

SEARCH FOR AXIONS VIA ASTROPHYSICAL OBSERVATIONS

The Theoretical and Mathematical Physics,

Astronomy and Astrophysics Division

Physics Department – University of Patras

Antonios Gardikiotis

July 2015

CERN-THESIS-2015-483
15/07/2015



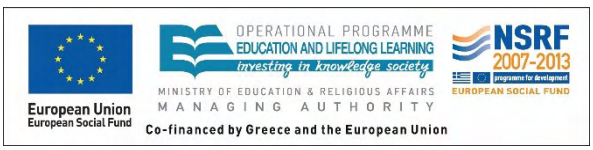

This research has been co-financed by the European Union (European Social Fund – ESF) and Greek national funds through the Operational Program "Education and Lifelong Learning" of the National Strategic Reference Framework (NSRF) - Research Funding Program: Heracleitus II. Investing in knowledge society through the European Social Fund.



ΑΝΑΖΗΤΗΣΗ ΑΞΙΟΝΙΩΝ ΜΕΣΑ ΑΠΟ ΑΣΤΡΟΦΥΣΙΚΕΣ ΠΑΡΑΤΗΡΗΣΕΙΣ

Τομέας Θεωρητικής και Μαθηματικής Φυσικής, Αστρονομίας και Αστροφυσικής

Τμήμα Φυσικής – Πανεπιστήμιο Πατρών

Αντώνιος Γαρδικιώτης

Ιούλιος 2015



Η παρούσα έρευνα έχει συγχρηματοδοτηθεί από την Ευρωπαϊκή Ένωση (Ευρωπαϊκό Κοινωνικό Ταμείο - ΕΚΤ) και από εθνικούς πόρους μέσω του Επιχειρησιακού Προγράμματος «Εκπαίδευση και Δια Βίου Μάθηση» του Εθνικού Στρατηγικού Πλαισίου Αναφοράς (ΕΣΠΑ) – Ερευνητικό Χρηματοδοτούμενο Έργο: Ηράκλειτος ΙΙ . Επένδυση στην κοινωνία της γνώσης μέσω του Ευρωπαϊκού Κοινωνικού Ταμείου.

To my father

Acknowledgments

I would like to thank Professor K. Zioutas who gave me the opportunity to be a member of the CAST collaboration and also being my supervisor. The support he gave me over the years was unconditional and I feel really grateful for his constant supervision.

I want also to thank co-supervisors Professors Smaragda Lola and Anastasios Liolios as members of my selection board for their continuous interest and understanding.

As a member of the Micromegas group at CAST I would like also to thank Ioannis Giomataris, Igor G. Irastorza and Thomas Papaevangelou for their support.

During the period 2009-2012 I have been working for the CAST experiment at CERN where I dedicated most of my time. In this scientific and international environment I met other CAST colleagues that encouraged me and helped me. I would like to thank CAST's technical coordinator Martyn Davenport as also Biljana Lakic, Annika Nordt, Jaime Ruz, Cenk Yildiz and Theopisti Dafni for their deep dedication to the experiment as also the rest collaborators of CAST who actually make possible to run the experiment thanks to their extended experience. I would like also to thank Jean Michel Laurent.

Η παρούσα εργασία έχει ως σκοπό την αναζήτηση αξιονίων (σωματιδίων Σκοτεινής Ύλης) μέσα από αστροφυσικές παρατηρήσεις. Από τις πρώτες παρατηρήσεις της ταχύτητας περιστροφής αστέρων σε σμήνη Γαλαξιών από τον Zwicky και μετά, έγινε σαφές στην επιστημονική κοινότητα πως η ύπαρξη σκοτεινής ύλης καθώς και η κατανόηση της είναι θεμελιώδους σημασίας για την Κοσμολογία. Το ποσοστό της σκοτεινής ύλης του σύμπαντος (~21%), σε σχέση με το αυτό της ύλης που παρατηρούμε (~4%), καθιστά σαφή την αναγκαιότητα για εντατική έρευνα στο πεδίο αυτό της Φυσικής. Ανάγκη δε, προκύπτει επίσης για την εξερεύνηση της σκοτεινής ενέργειας η οποία αποτελεί το υπόλοιπο ~75% του Σύμπαντος. Ένα μικρό μέρος της παρούσας έρευνας στο CERN έχει επικεντρωθεί και στην μελέτη Σκοτεινής ενέργειας καθώς, το πείραμα μέσα από το οποίο προσεγγίζεται η αναζήτηση αξιονίων (CAST – CERN Axion Solar Telescope), προσανατολίζεται συγχρόνως στην έρευνα σωματιδίων Σκοτεινής ενέργειας (χαμαιλέοντες) . Στο κεφάλαιο 10 αναπτύσσεται λεπτομερώς η έρευνα του πειράματος CAST για την ανίχνευση ηλιακών χαμαιλεόντων καθώς και η συμβολή της παρούσας εργασίας για την ανάπτυξη του ανιχνευτή KWISP.

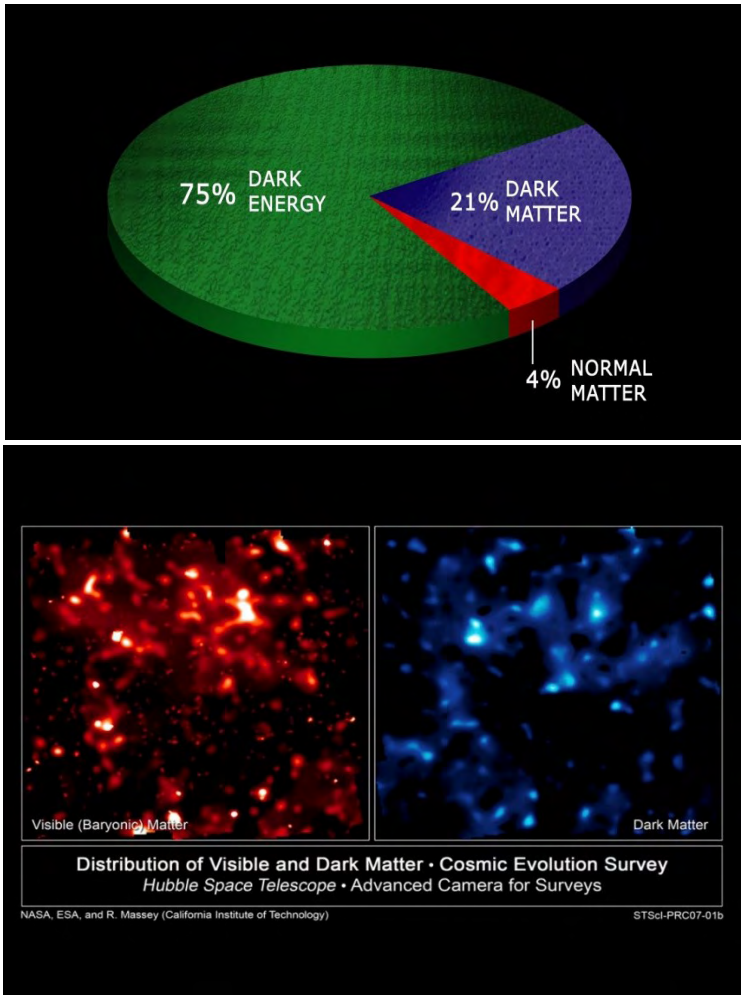

Εικονα 1. Πάνω, το ποσοστό κατανομής της ύλης στο Σύμπαν σύμφωνα με κοσμολογικές παρατηρήσεις. Κάτω, η κατανομή της ορατής (βαρυονικής) και της Σκοτεινής ύλης σε ένα σμήνος γαλαξιών όπως προκύπτει από Αστροφυσικές παρατηρήσεις από το Hubble Space Telescope (NASA-ESA).

Το καθιερωμένο πρότυπο της φυσικής έχει πλέον παγιωθεί μετά και από την ανακάλυψη του σωματιδίου Higgs. Παρά το γεγονός αυτό, άλλα αναπάντητα ερωτήματα εγείρονται, όπως αυτό της μη παραβίασης της CP (φορτίου - ομοτιμίας) συμμετρίας στις ισχυρές αλληλεπιδράσεις. Η QCD θεωρία της χρωμοδυναμικής προβλέπει μια παραβίαση της συμμετρίας CP η οποία όμως δεν επιβεβαιώνεται πειραματικά. Σαν λύση στο πρόβλημα της συμμετρίας, οι Peccei και Quinn (1977) πρότειναν τη διατήρηση της συμμετρίας CP υπό την παρουσία ενός ψευδοβαθμωτού σωματιδίου, του αξιονίου. Η νέα αυτή πρόταση των Peccei και Quinn αποτελεί μια ελάχιστη επέκταση του καθιερωμένου προτύπου.

Η αυθόρμητη ρήξη της συμμετρίας σε κάποια ενεργειακή κλίμακα f_{PQ} είναι η αιτία, κατά το θεώρημα Goldstone, για την εμφάνιση ενός σωματιδίου το οποίο ονομάστηκε «αξιόνιο».

Το σωμάτιο αυτό είναι ηλεκτρικά ουδέτερο, με σταθερά ζεύξης και μάζα που είναι αντιστρόφως ανάλογες της ενεργειακής κλίμακας f_{PQ}. Εάν η ενεργειακή αυτή κλίμακα είναι αρκετά μεγάλη, τότε πρόκειται για ένα πολύ ελαφρύ σωμάτιο και, σύμφωνα με κοσμολογικές παρατηρήσεις, τηρούνται οι προϋποθέσεις εκείνες ώστε το σωμάτιο αυτό να είναι ένας από τους βασικούς υποψηφίους σύστασης της σκοτεινής ύλης.

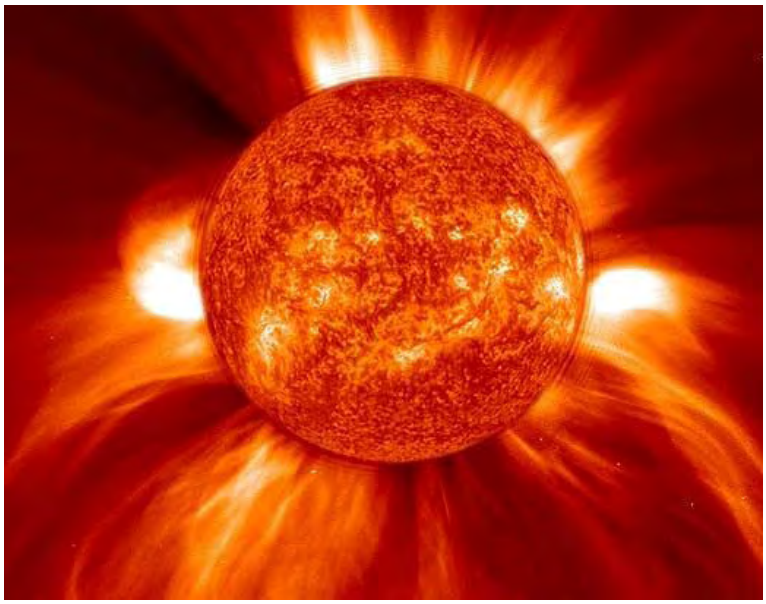

Εικόνα 2. Ο Ήλιος όπως αναφέρθηκε πρόσφατα [164] μπορεί να είναι μια αστείρευτη πηγή αξιονίων. Οι 12ετείς αναλύσεις δεδομένων από τηλεσκόπια φανερώνουν την ύπαρξη μεταβαλλόμενης ροής ακτίνων Χ από τον Ήλιο και αλληλεπίδραση της ροής αυτής με το μαγνητικό πεδίο της Γης, κάτι που ταιριάζει με την συμπεριφορά του αξιονίου. Σημαντικό είναι να τονιστεί πως, αν όντως αποδειχθεί πειραματικά η δημιουργία αξιονίων στον Ήλιο, ένα από τα πιο σημαντικά προβλήματα της φυσικής που είναι το Πρόβλημα της Ηλιακής Κορώνας, θα έχει λυθεί.

Αξιόνια μπορούν να παραχθούν στους πυρήνες των αστέρων, μέσω του φαινομένου Primakoff και λόγω της εγγύτητας του Ήλιου, πολλές αστροφυσικές παρατηρήσεις έχουν συγκεντρωθεί στο άστρο αυτό.

Αξιόνια μπορούν να παράγονται σύμφωνα με θεωρητικές μελέτες στο κέντρο του Γαλαξία ή με πειράματα Laser μέσα στο εργαστήριο. Επιπλέον, έχουν προταθεί πειράματα με σκοπό την αναζήτηση αρχέγονων αξιονίων από τον καιρό της Μεγάλης έκρηξης (ο χρόνος ζωής των αξιονίων είναι μεγαλύτερος από αυτόν του Σύμπαντος) αλλά σε αυτή την εργασία δίνεται βάση στην αναζήτηση αξιονίων με πηγή τον Ήλιο και σε μεθόδους ανίχνευσης μέσω Ηλιοσκοπίου.

Η ροή των αξιονίων προς την Γη λαμβάνοντας υπόψη το Ηλιακό μοντέλο δίνεται από τη σχέση

$$\frac{\mathrm{d}\Phi_{\alpha}}{\mathrm{d}E} = g_{10}^{2} 6.0 \times 10^{10} cm^{-2} s^{-1} keV^{-1} E^{2.481} e^{-E/1.205}$$

με σταθερά ζεύξης $g_{10}=g_{a\gamma}/10\ GeV^{-1}$. Η ροή των αξιονίων στην Γη δίνεται στο επόμενο διάγραμμα σε γραμμική-λογαριθμική και λογαριθμική-λογαριθμική κλίμακα.

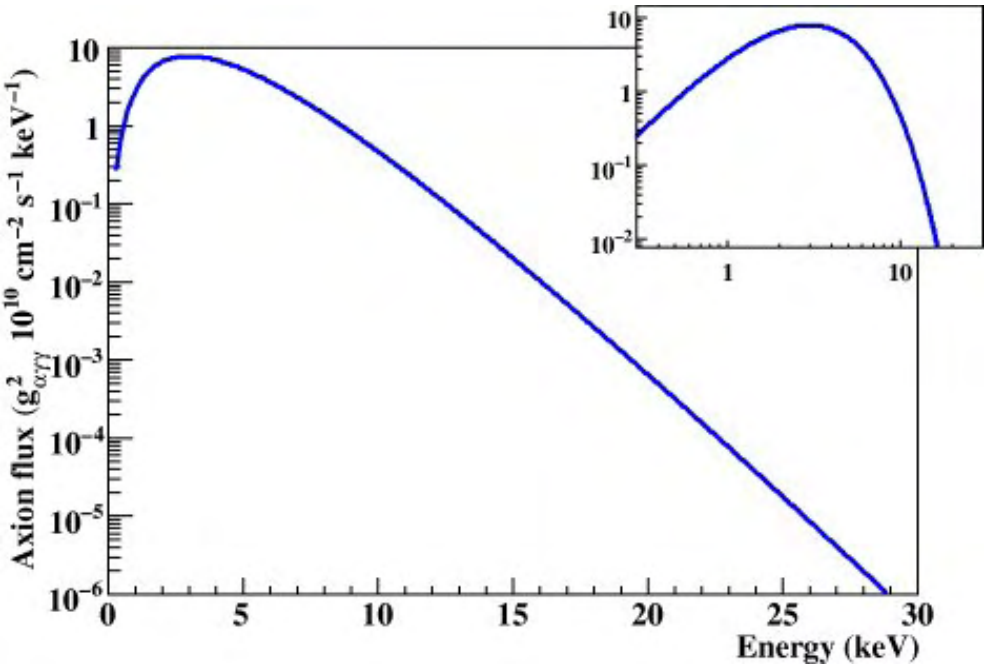

Σχήμα 1. Ροή των αξιονίων στην Γη. Η μέση τιμή της έντασης είναι στα ~4.2 keV. Η

Η μετατροπή του αξιονίου σε φωτόνιο λαμβάνει χώρα σε ισχυρά μαγνητικά πεδία και αυτή την αρχή χρησιμοποιεί το πείραμα CAST (Cern Axion Solar Telescope) στην Γενεύη προκειμένου να ανιχνεύσει ηλιακά αξιόνια ακολουθώντας την ιδέα του Sikivie. Το Ηλιοσκόπιο του CAST έχει έως τώρα την μεγαλύτερη ευαισθησία μεταξύ των πειραμάτων για την ανίχνευση αξιονίων.

Η αρχή λειτουργίας του όπως τονίστηκε είναι το φαινόμενο Primakoff: εισερχόμενα αξιόνια επιδρούν με το κάθετο μαγνητικό πεδίο του LHC μαγνήτη ο οποίος στοχεύει στο κέντρο του Ήλιου (κατά την ανατολή και την δύση του) και αναμένεται να μετατρέπονται σε φωτόνια ακτίνων Χ. Η πιθανότητα μετατροπής αξιονίου σε φωτόνιο είναι μέγιστη όταν το εισερχόμενο αξιόνιο και το μετατρεπόμενο φωτόνιο είναι σε συμφωνία (coherence).

Το βασικό στοιχείο του CAST είναι ο διπολικός του μαγνήτης μήκους 10 μέτρων και μπορεί να δημιουργεί μαγνητικό πεδίο έντασης 9 T. Ο μαγνήτης αυτός που κατασκευάστηκε ως πρότυπο για τον LHC στο CERN, λειτουργεί ως Ηλιοσκόπιο αφού μπορεί και ευθυγραμμίζεται με το κέντρο του Ήλιου για 3 ώρες περίπου την ημέρα κατά την ανατολή και την δύση του. Αυτό συμβαίνει επειδή ο μαγνήτης είναι εγκατεστημένος σε μια κινούμενη πλατφόρμα που του δίνει την ικανότητα να κινείται από -8° σε +8° στην κάθετη διεύθυνση και ±40° στην οριζόντια. Λόγω της μηχανικής εγκατάστασης, το Ηλιοσκόπιο δε μπορεί να ακολουθεί τον Ήλιο για περισσότερο από 1,5 ώρα κάθε φορά.

Τα αξιόνια που μετατρέπονται στον μαγνήτη μπορούν να ανιχνευτούν με την βοήθεια ανιχνευτών χαμηλού υποβάθρου ακτίνων X και στο CAST χρησιμοποιήθηκαν κατά την διάρκεια εκτέλεσης της παρούσας διατριβής 3 ανιχνευτές τεχνολογίας Micromegas και ένας ανιχνευτής CCD προσαρμοσμένος σε ένα τηλεσκόπιο ακτίνων X. Οι ανιχνευτές είναι τοποθετημένοι σε κάθε άκρο των 2 κοίλων σωλήνων του μαγνήτη καθένας από τους οποίους έχει διάμετρο 43mm.



Εικόνα 3. Η συνεργασία CAST με τα μέλη της μπροστά στον μαγνήτη του πειράματος. Χάρη στους 60 και πλέον συνεργάτες και τεχνικούς, υπό την καθοδήγηση του αρχηγού του πειράματος K. Ζιούτα, έγινε δυνατή η μελέτη και η μέθοδος αυτή ανίχνευσης Ηλιακών αξιονίων η οποία είναι ακόμα πρωτοπόρα μετά από 15 έτη.

Η παρούσα διατριβή έχει ως σκοπό την επεξεργασία των δεδομένων των ανιχνευτών της δυτικής πλευράς του μαγνήτη, τεχνολογίας Micromegas bulk και Micromegas microbulk. Οι ανιχνευτές τεχνολογίας microbulk αντικατέστησαν τους πρώτους αφού έχουν πολύ καλύτερη διακριτική ικανότητα, πολύ χαμηλή εγγενή ακτινοβολία και είναι ιδανικοί για πειράματα ανίχνευσης σωματιδίων χαμηλού ρυθμού.

Η ανάλυση των δεδομένων αφορά τις μετρήσεις που έγιναν τα έτη 2009 και 2010 στο πείραμα CAST καλύπτοντας το εύρος μάζας αξιονίου 0.66-1.01 eV/c^2. Το αέριο ^{3}He που βρισκόταν μέσα στις κοιλότητες του μαγνήτη αντιστοιχεί σε εύρος πίεσης 37.5–82.52 mbar σε θερμοκρασία 1.8 K.

Σημαντική είναι και η προσφορά στην μελέτη της θερμοδυναμικής κατάστασης του αερίου Ηλίου-3, μέσω προσομοίωσης με την μέθοδο των πεπερασμένων στοιχείων. Για την κατανόηση της στατικής και δυναμικής κατάστασης του αερίου μέσα στον μαγνήτη έγινε χρήση του προγράμματος Ansys 15.0 αφού πρώτα είχε σχεδιαστεί το μοντέλο που προσομοιάζει το αέριο και το μεταλλικό στέλεχος που το περιβάλλει, σε περιβάλλον CAD.

Η ποσοτική και ποιοτική ανάλυση της συμπεριφοράς του σπάνιου αυτού αερίου υπό καταστάσεις χαμηλής πίεσης και θερμοκρασίας εμπεριέχει μια από τις πιο σημαντικές παραμέτρους του πειράματος CAST που είναι το πραγματικό μήκος συνοχής. Το μήκος δηλαδή εκείνο του μαγνήτη κατά το οποίο το εισερχόμενο αξιόνιο και το μετατρεπόμενο φωτόνιο είναι σε συμφωνία (coherence). Η παράμετρος αυτή χρησιμοποιείται στην ανάλυση των δεδομένων των ανιχνευτών Micromegas.

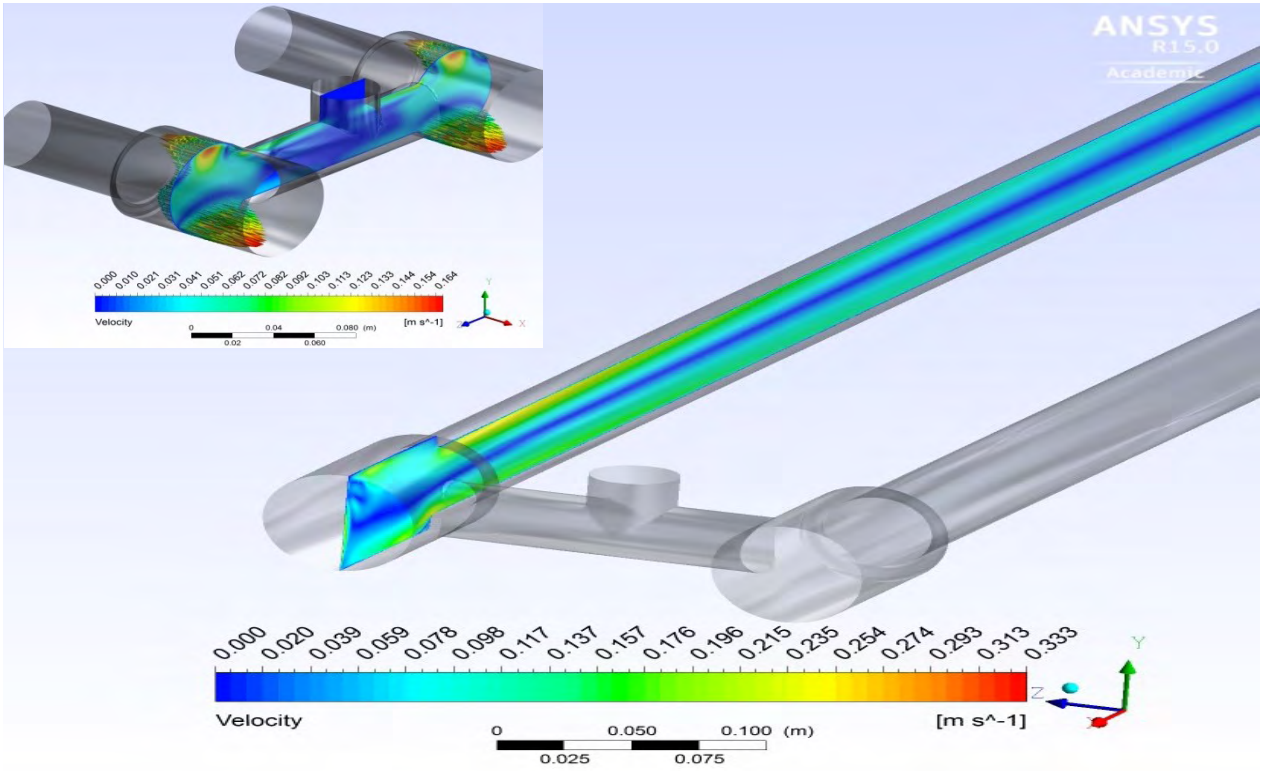

Εικόνα 4. Η κατανομή της ταχύτητας κατά μήκος της κοιλότητας του μαγνήτη και η κατανομή και η ένταση της ταχύτητας του ρευστού σε μια εγκάρσια τομή κάθετα στον μαγνήτη (μικρογραφία).

Κατά την εκτέλεση του πειράματος, μελετήθηκε επίσης η δυναμική του αερίου, καθώς ο μαγνήτης κινούταν σε διαφορετικές γωνίες κλίσης και προέκυψαν αποτελέσματα για το πεδίο ταχυτήτων, θερμοκρασίας και πυκνότητας σε κάθε σημείο του αερίου μέσα στον μαγνήτη.

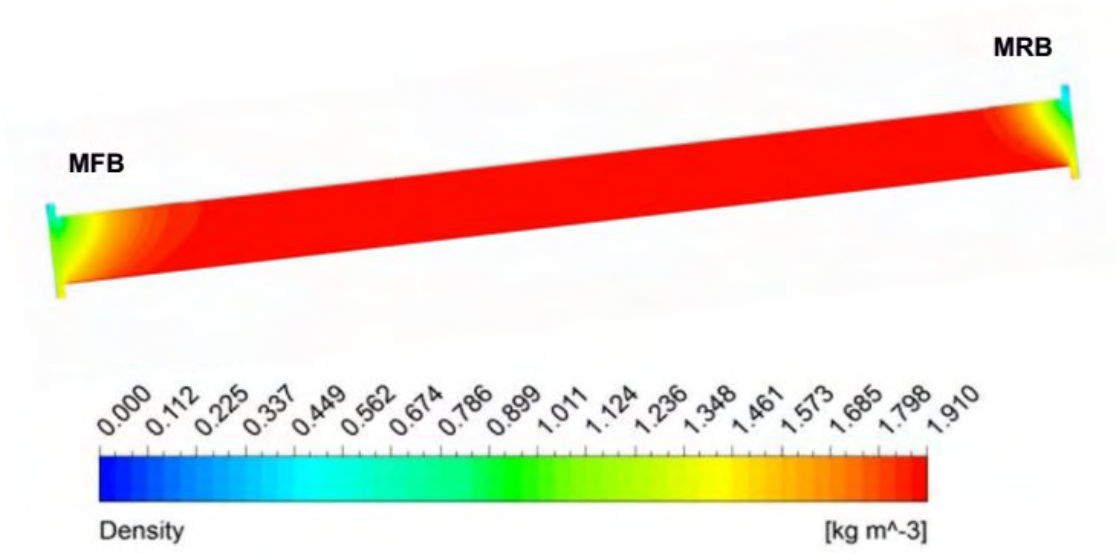

Εικόνα 5. Η κατανομή της πυκνότητας του αερίου ^{3}He όταν ο μαγνήτης βρίσκεται υπό θετική κλίση +4°. Όπως φαίνεται η πυκνότητα δεν είναι ομοιογενώς κατανεμημένη στα 9.26 m του μαγνήτη καθώς η υδροστατική πίεση και τα δυναμικά φαινόμενα μεταφοράς λόγω δινών επιδρούν με διαφορετική ένταση στα άκρα του μαγνήτη. Για καλύτερη απεικόνιση έχει γίνει μεγέθυνση με συντελεστή 15.

Το μήκος συμφωνίας (coherence length) συνεχώς μεταβάλλεται ανάλογα με την κλίση όπως φαίνεται στο παράδειγμα της Εικόνας 5. Η σχέση του μήκους συνοχής εισέρχεται στον υπολογισμό του σταθεράς ζεύξης του αξιονίου και από τα δεδομένα αυτά για την δυναμική του αερίου με ποσοστό ακρίβειας ~1% προκύπτει το διάγραμμα απόρριψης με τα δεδομένα των ανιχνευτών για τα έτη 2009-2010.

Τα δεδομένα των ανιχνευτών σε συνάφεια με την δυναμική του συστήματος Ηλίου-3 σε κάθε πίεση και κλίση του μαγνήτη, αποτυπώνονται στο παρακάτω διάγραμμα απόρριψης του πειράματος CAST στο οποίο απεικονίζονται οι φάσεις του πειράματος από το 2003.

Ο υπολογισμός του ορίου σταθεράς ζεύξης του αξιονίου έγινε με την μεγιστοποίηση της συνάρτησης Πιθανότητας. Στην παρούσα εργασία το όριο στην σταθερά $g_{\alpha\gamma}$ υπολογίστηκε ολοκληρώνοντας στο επίπεδο εμπιστοσύνης έως 95%, την Μπεϋζιανή πιθανότητα (Bayesian probability) και για το εύρος μάζας αξιονίου 0.65-1.01 eV/c^2 προκύπτει:

$$g_{\alpha\gamma} \leq 4.29 \times 10^{-10}\ GeV^{-1}\ at\ 95\%\ CL$$

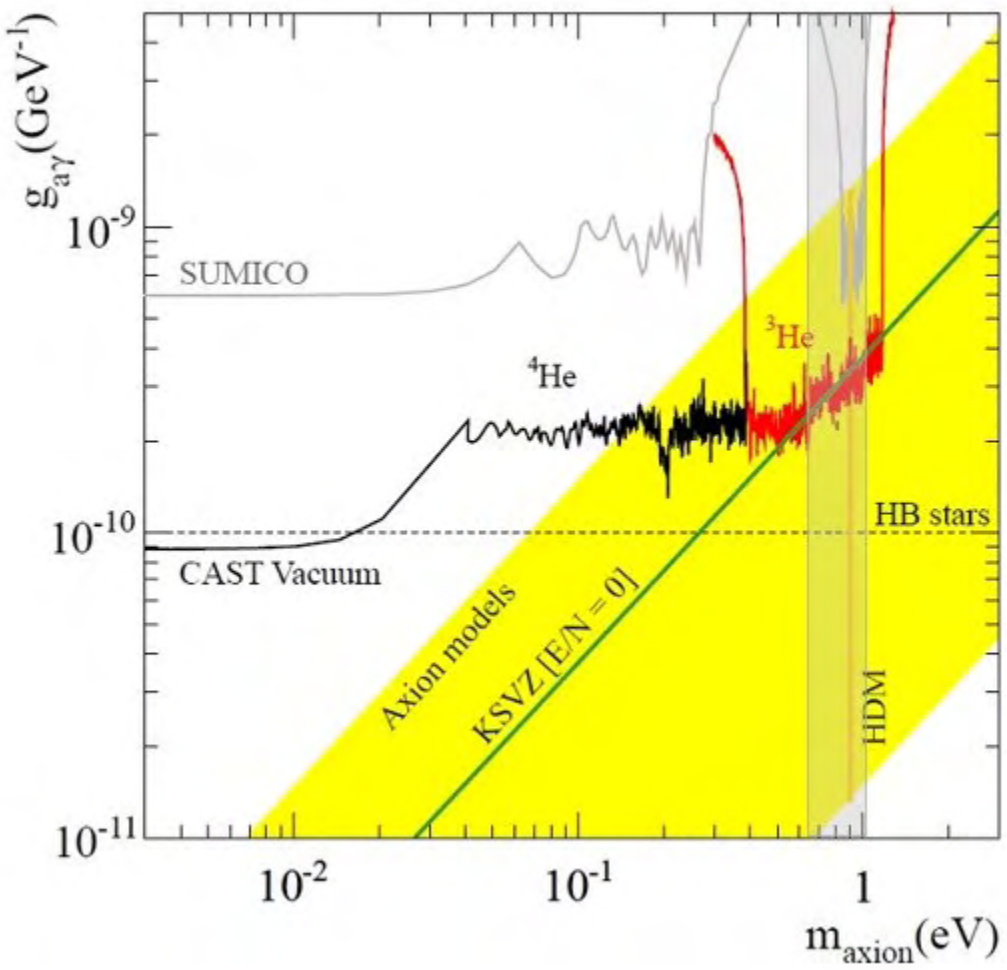

Εικόνα 6. Διάγραμμα απόρριψης γεγονότων του πειράματος CAST στο κενό, με την χρήση αερίου Ηλίου-4 και Ηλίου-3. Το διάστημα για το εύρος μάζας αξιονίου από 0.65-1.01 eV παρουσιάζεται στο γκρίζο διαφανές διάστημα. Η κίτρινη ζώνη παρουσιάζει τυπικά θεωρητικά μοντέλα ενώ διακρίνονται τα όρια από τους αστέρες του Οριζόντιου Τομέα (HD stars), τα όρια από την θερμή σκοτεινή ύλη (HDM) και η σύγκριση με το Ιαπωνικό Ηλιοσκόπιο SUMICO.

Σημαντική είναι επίσης η συμβολή της παρούσας εργασίας στην έρευνα για την αναζήτηση σωματιδίων Σκοτεινής Ενέργειας. Σωματίδια όπως οι χαμαιλέοντες, είναι σύμφωνα με πρόσφατα θεωρητικά μοντέλα, υποψήφια για την Σκοτεινή Ενέργεια η οποία επιταχύνει την διαστολή του σύμπαντος.

Οι χαμαιλέοντες μπορούν να δημιουργηθούν σε μια περιοχή του Ηλίου σε απόσταση 0.7 $R_\odot$ από το κέντρο του. Στο CAST έχουν ήδη γίνει μετρήσεις για την μέτρηση ηλιακών χαμαιλεόντων με την χρήση του Ηλιοσκοπίου σε κενό. Σε αντιστοιχία με το φαινόμενο Primakoff η ανίχνευσή τους μπορεί να γίνει με την εφαρμογή του εγκάρσιου μαγνητικού πεδίου του μαγνήτη και την χρήση του νέου ανιχνευτή χαμηλών ενεργειών ακτίνων X InGrid (<1 keV).

Τα πρώτα δημοσιευμένα αποτελέσματα του CAST βάζουν ένα άνω όριο στην σταθερά ζεύξης χαμαιλέοντα-φωτονίου

$$\beta_\gamma \leq 9.26 \cdot 10^{10}\ at\ 95\%\ C.L$$

Οι ηλιακοί χαμαιλέοντες μπορούν επίσης να ανιχνευτούν από την αλληλεπίδρασή τους με την ύλη μέσο της πίεσης της ακτινοβολίας τους (radiation pressure) σε μικρο-μεμβράνη η οποία μπορεί να μετακινείται μέσα σε μια οπτική κοιλότητα (Fabry-Perot). Ένας τέτοιος αισθητήρας (ονομαζόμενος KWISP) έχει κατασκευαστεί στο Ινστιτούτο INFN στην Ιταλία και πρόκειται να χρησιμοποιηθεί στο CAST αντικαθιστώντας τον InGrid ανιχνευτή.

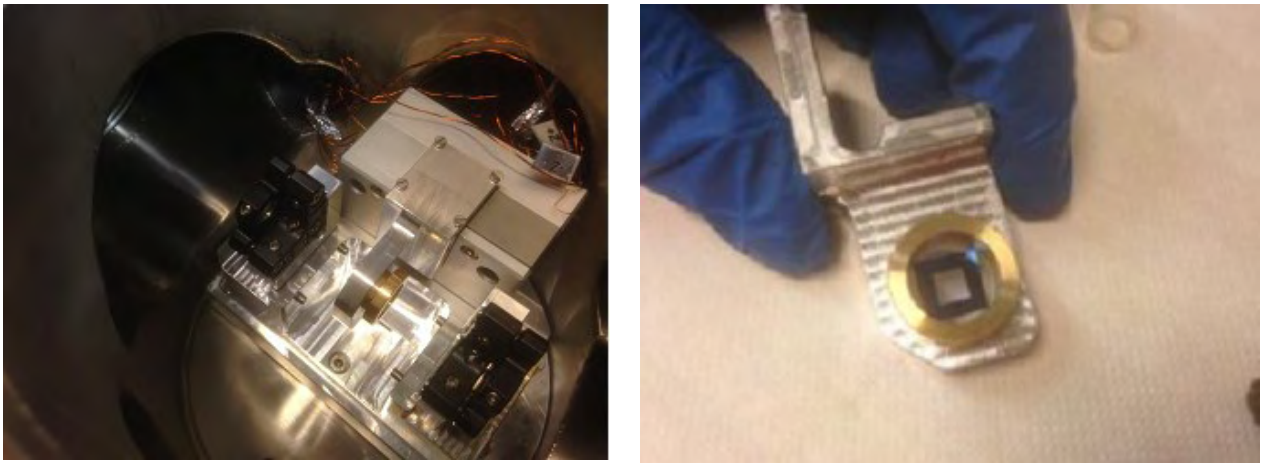

Εικόνα 7. Αριστερά η οπτική κοιλότητα Fabry-Perot μέσα στην οποία είναι τοποθετημένη η μικρομεμβράνη. Δεξιά φαίνεται η 5mm×5mm, πάχους 100 nm μικρομεμβράνη κατασκευασμένη από Si_3N_4.

Στην παρούσα εργασία έγιναν προσομοιώσεις όπως περιγράφονται στο κεφάλαιο 10.6, με την μέθοδο των πεπερασμένων στοιχείων για τον χαρακτηρισμό των ιδιοτήτων της μικρομεμβράνης. Με χρήση του προγράμματος Ansys 15.0 έγινε ο σχεδιασμός, η μοντελοποίηση και η ανάλυση των τρόπων ταλάντωσης της μεμβράνης η οποία έχει προένταση 800 MPa. Σκοπός της ανάλυσης αυτής ήταν να ελεγχθούν τα πειραματικά αποτελέσματα με το θεωρητικό μοντέλο της προσομοίωσης για:

1. Τον υπολογισμό της ευαισθησίας δύναμης (force sensitivity) του αισθητήρα με την χρήση της «σταθεράς ελατηρίου» της μεμβράνης. Η αρχική μοντελοποίηση είχε στόχο να προσομοιώσει την μικρομεμβράνη με ένα απλό ελατήριο.
2. Την εύρεση των κανονικών τρόπων ταλάντωσης της μεμβράνης καθώς και της ιδιοσυχνότητας αυτής.
3. Τον υπολογισμό του δείκτη ποιότητας (Quality factor) της μεμβράνης.

Τα αποτελέσματα ήταν πολύ ικανοποιητικά και σε πλήρη αντιστοιχία με τα πειραματικά αποτελέσματα τα οποία παρουσιάζονται αναλυτικά στο κεφάλαιο 10.6.

Contents

1. Dark Matter 16
1.1 Introduction 16
1.2 Dark Matter particles 21
2. Axions 23
2.2 Axions and the QCD vacuum 24
2.3 Approaches to the Strong CP Problem 26
Standard axion 28
2.3.1 Axion Properties 28
2.3.2 Axion Couplings 29
2.3.1.1 Axion -Gluon coupling 29
2.3.1.2 Axion-Photon coupling 30
2.3.1.3 Axion-fermion coupling 31
2.3.2 Axion models 34
Visible Axions 34
The invisible Axions 37
KSVZ Axion 38
DFSZ model 39
The Primakoff effect 40
2.4 Why are axions a DM candidate? 41
2.4.1 Topological axion production 42
2.4.2 Vacuum realignment mechanism 43
2.5 Astrophysical axion bounds 45
Globular clusters axion limits 47
White-dwarf cooling 48
Supernova 1987A 49
Axion detection experiments 51
Axion Haloscopes 52
2.6 CAST as an Antenna for relic axions 53
2.7 Optical and Radio Telescope searches 55
2.8 Laser Induced axion searches 56
2.8.1 Light shining through a wall 57
2.9 Detecting the magneto-optical vacuum properties 58

2.10 Bragg diffraction experiments 59
2.11 Axion Helioscope Experiments 61
2.12 Axion Like Particles (ALP) 62
3. Solar Axions 64
3.1 Axion flux from the Primakoff conversion in the Sun 64
3.2 Axions Detection Principle 67
3.3 Axion-electron coupling 70
4. The CAST Experiment 72
Introduction 72
4.1 CAST magnet set-up 72
4.2 Vacuum System 75
4.3 Solar tracking system 77
CAST platform movement 77
Solar tracking 78
4.4 GRID measurements 80
4.5 Sun filming 82
4.6 Slow control system 83
4.7 CAST scientific research program 84
4.8 The X-ray windows 87
4.9 The ^{3}He gas system 88
4.9.1 The ^{3}He metering system 89
4.9.2 Purging system 89
4.9.3 Expansion volume and recovery of ^{3}He 90
4.9.4 The PLC system 91
4.10 CAST detectors 92
The X-ray Telescope and the pn-CCD detector 93
The X-ray Telescope 93
The pn-CCD detector 95
5. ^{3}He CFD simulations for CAST 96
5.1 CFD introduction 96
5.2 CFD methodology 97
5.3 Thermodynamics of the simulated system 98
5.4 The CFD model 102
5.4.1 Model Geometry 102
5.4.2 Geometry domains 104

5.4.3 Boundary conditions 106
5.5 CFD model meshing 109
5.5.1 Cold bore meshing (Fluid) 110
5.5.2 MRB and MFB meshing (Fluid) 111
5.5.3 Solid meshing 112
5.5.4 Mesh Quality check 113
Orthogonal Quality 113
5.6 Physical properties of the model 114
5.6.1 ^{3}He (Helium-3) 114
5.6.2 Thermal properties 116
5.6.3 Solid Properties 119
Stainless Steel 119
Polypropylene (PP) 120
5.7 Physical modelling 121
5.7.1 Steady state model 121
5.7.2 Continuum flow assumption 122
5.7.3 Heat transfer model 122
5.8 Turbulence modelling 123
5.8.1 Turbulent models 125
5.8.2 Ansys- CFX transition model 126
5.8.3 Modelling Flow near the Wall 128
5.8.4 CFD model computation 130
5.8.5 Convergence 131
5.9 CFD model results 132
5.9.1 Validation of the results 139
5.10 Velocity, Temperature and Density profiles 142
5.11 CFD study of the tilted magnet 145
5.11.1 Problem description 145
5.11.2 CFD modelling 147
5.11.3 Turbulence model 148
5.11.4 CFD Simulations method 151
5.11.5 CFD Results 152
5.12 DST (Density Stability Threshold) 159
6. The Micromegas detector 162
6.1 Phenomenology of Gaseous chambers 162
6.1.1 Interaction of photons in a gas chamber 162

Photoelectric effect 163
6.1.2 Interaction of charged particles in a gas chamber 166
Electrons 167
6.2 Excitation and Ionization in Gases 170
Excitation Process 170
Ionization Process 171
6.3 The Fano factor 174
6.4 Ions and electrons transport in Gases 175
6.4.1 Drift of electrons and Ions in Gas chambers 175
Drift of Ions 179
6.4.2 Electron Diffusion 179
6.4.3 Electron attachment and recombination 181
6.4.4 Avalanche Multiplication of electrons 182
6.4.5 Signal generation 184
6.4.6 Gas choice for Micromegas detectors 185
6.5 Gaseous detectors 185
6.6 Micromegas detector: A Micro-Pattern Gas Chamber 188
6.6.1 Micromegas properties 190
Gain 190
Energy Resolution 191
Spatial Resolution 193
Aadvantages of Micromegas detectors 194
6.7 CAST Micromegas detectors 194
Fabrication 195
6.7.1 Bulk Micromegas technology 195
6.7.2 Microbulk Micromegas 196
6.8 The CAST Micromegas detector 197
6.9 Sunset Micromegas System 199
6.9.1 Vacuum system 200
6.9.2 CAST Micromegas Efficiency 202
6.9.3 Calibration System 203
6.9.4 The Sunset Micromegas Background and Shielding 204
6.10 The Sunset Micromegas upgrades 207
6.10.1 Cable Trays 207
6.10.2 2012 upgrade of the Sunset setup 208

6.10.3 Muon Veto setup 209
6.10.4 Calibration system 210
6.11 Data Acquisition System of Micromegas 210
Read out electronics 210
6.11.1 Strips Signal 210
6.11.2 Mesh Signal 212
6.12 Data Acquisition system 213
7. Raw Data Analysis of the Sunset Micromegas Detectors 215
7.1 Raw-Data Format 216
7.2 Raw Data Reduction 217
7.2.1 Strips signal analysis 217
7.2.1.1 Pedestal subtraction 217
7.2.1.2 Clustering 218
7.2.2 Mesh signal and Pulse shape analysis 220
7.2.3 Sunset detector's Calibration and files implementation 221
7.3 Background discrimination 223
7.3.1 Manual selection cuts 224
7.3.2 Automatic selection cuts 224
7.3.2.1 2D Multiplicity Cut 225
7.3.2.2 2D sigma cut 225
7.3.2.3 2D mesh defined selection cuts 226
7.3.2.4 Baseline Fluctuation 229
7.3.3 Conclusions 229
8. Sunset Micromegas data taking and background levels of 2009 and 2010 230
8.1 Introduction 230
8.2 Data taking overview in the 2009 run 230
8.3 Sunset Detectors Data Taking in 2009 232
8.3.1 Sunset detectors stability and gain performance 234
8.3.2 Efficiency of the selected criteria 236
8.3.3 Background and Tracking Data of 2009 241
8.4 Data taking overview in 2010 247
8.4.1 Sunset detectors Data taking in 2010 249
8.4.2 Sunset detectors stability for 2010 250
8.4.3 Efficiency of the Sunset detectors in 2010 252
8.4.4 Statistical evaluation of the 2010 data 257
9. A limit for the axion-photon coupling constant 259

9.1 The CAST expected X-ray signal 259
9.2 Unbinned Likelihood method 263
9.3 The Sunset Micromegas limit obtained for 2009-2010 mass range scanning 266
10 Dark energy 270
10.1 Introduction 270
10.2 Quintessence 272
10.3 Solar Chameleons 274
10.4 Detection of Solar Chameleons with the Inverse Primakoff effect 276
10.5 Detection of Solar Chameleons through Radiation Pressure 279
10.6 Finite elements simulations of the KWISP membrane 282
10.7 Conclusions 293
References 300

1. Dark Matter

1.1 Introduction

Dark matter is a non-baryonic type of matter that accounts for the total amount of mass in the Universe. After many observations, starting with the pioneering ones, of Jan Oort in 1932 and Fritz Zwicky in 1933, physicists have discovered that a large mass constitute of the Universe exists in a non-luminous and non-absorbing form. The evidence of the missing mass came up by observing the rotation curves and orbital velocities of stars in the Milky Way, as also the orbital velocities of galaxies in clusters of galaxies. The velocities of various luminous objects (stars, gas clouds or entire galaxies) reveal that these objects move faster than expected if they only felt the gravitational attraction of other visible objects. The existence of Dark Matter (DM) became plausible after the observed gravitational lensing of background objects by galaxy clusters, the temperature distribution of hot gas in galaxies and clusters of galaxies and recently the pattern of anisotropies in the cosmic microwave background.

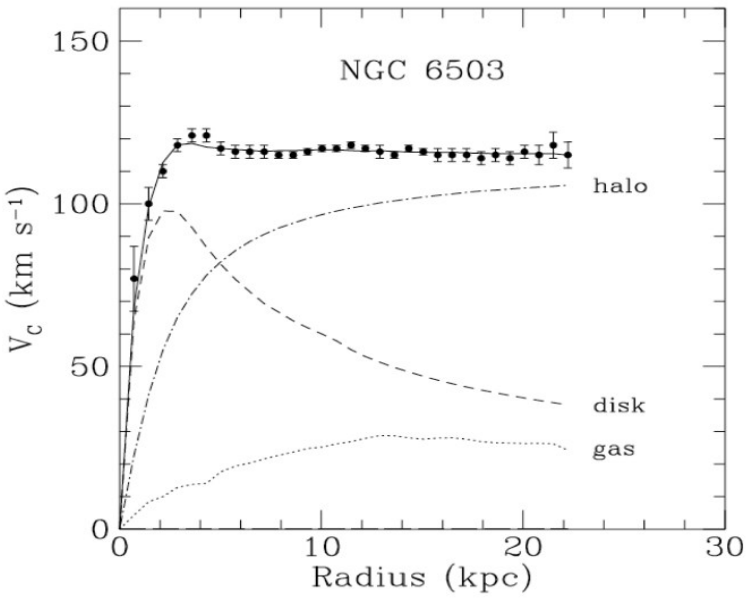

Figure 1.1 Radial velocity of NGC 6503 cluster. The halo, disk and gas velocities contributions are also shown.

F. Zwicky, observing the radial velocities of eight galaxies in Coma cluster [2], found an unexpectedly large velocity dispersion σ_v = 1019±360 km s^{-1}. From these observations, he concluded that for a velocity dispersion of ~1000km $s^{-1,}$ the mean density of the Coma cluster would have to be ~400 times greater than that derived from luminous matter. According to the observations there should be some kind of matter to hold galaxies together in the cluster.

In our typical spiral galaxy Milky Way, we live at a distance ~8.5 kpc from its center, while stars and gas extended out to a distance ~10kpc. If the visible stars and gas provided all the mass in the Galaxy, according to the Keplerian relation $v^2=GM_{obs}/r$, the rotation velocity should decline at a distance larger than 10kpc. Instead, one observes that rotation curve remains constant at much larger radii.

The DM envelops the galactic disc and extends well beyond the edge of the visible galaxy. This is the called Galaxy Dark Matter Halo and it consists of DM that cannot be observed directly. Radio observations from light emission from neutral atomic Hydrogen reveal the absence of any visible matter to account for the increase of the rotation velocity and implies the presence of unobserved (i.e. dark) matter.

The DM halo, with mass density $\rho(r) \sim 1/r^2$, leads to a lower bound of the DM density, $\Omega_{DM}>0.1$, where $\Omega_X=\rho_X/\rho_{crit}$, and ρ_{crit} being the critical mass density that corresponds to a flat Universe.

Another evidence for the existence of DM in the Universe is by making accurate measurements of the cosmic microwave background fluctuations. WMAP is able to measure the basic parameters of the Big Bang model including the density and composition of the universe. WMAP measures the relative density of baryonic and non-baryonic matter with an accuracy of order 1 to 10**5**. The *cosmic microwave background (*CMB*)* is an almost-uniform background of radio waves that fill the universe. The CMB is, in effect, the leftover heat of the Big Bang itself - it was released when the universe became cool enough to become transparent to light and other electromagnetic radiation~100,000 years after its birth.

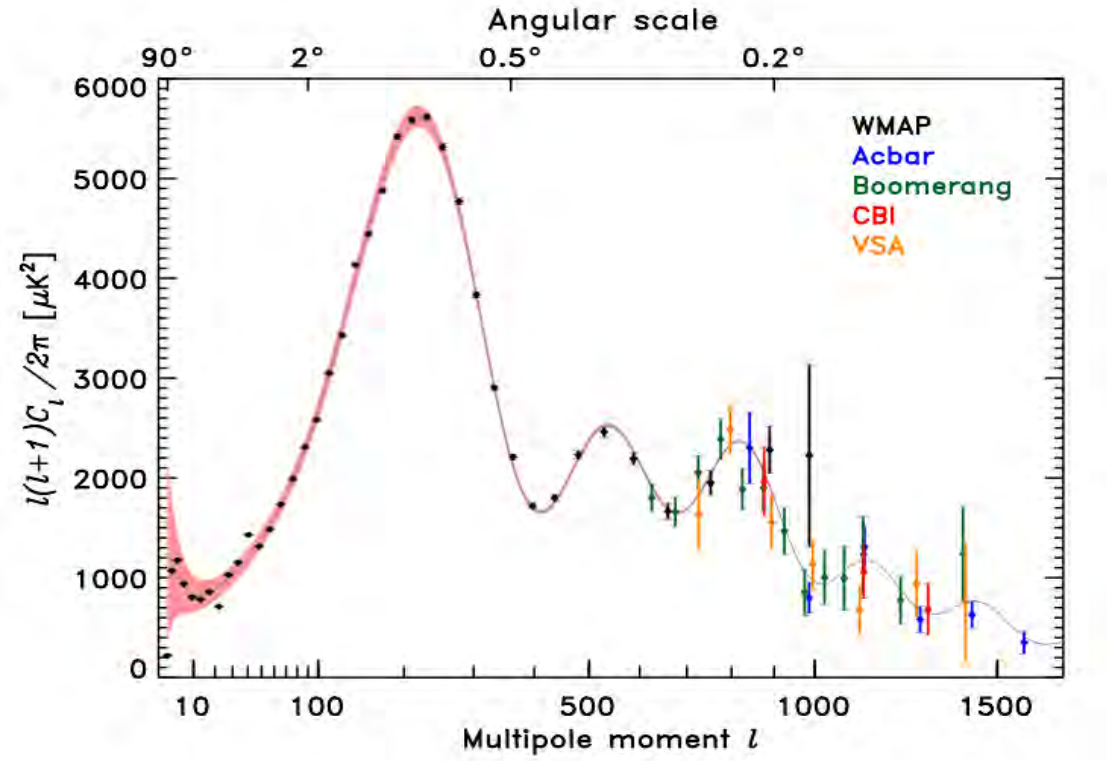

Figure 1.2 The angular fluctuations in the cosmic microwave background (CMB) spectrum provide evidence for dark matter.

The small scales anisotropies in the Cosmic Microwave Background (CMB), which are found by studying its power spectrum, can give us information about the dark matter density. The angular scale of the first peak determines the curvature of the universe. The next peak—ratio of the odd peaks to the even peaks—determines the reduced baryon density. The third peak can be used to acquire information about the dark matter density.

According to the WMAP team, the universe is 13.798 ± 0.037 billion years old, and contains 4.9% ordinary matter, 26.8% dark matter and 68.3% dark energy.

Dark matter plays a key role in structure formation because it feels only the force of gravity. As a result, dark matter begins to collapse into a complex network of DM halos, well before ordinary matter. Without DM, the epoch of galaxy formation would occur substantially later in the universe than observed. The dark matter is therefore crucial for understanding the evolution and present structure of galaxies, clusters, superclusters and voids. The rate at which structures formed in the universe, implies a matter density of $1/4 < \Omega_m < 1/3$, which is far more than observed in our local universe.

There is another constraint that can be extracted from the Big Bang nucleosynthesis (BBN) era. BBN takes place between eras with (CMB) temperatures T~ 3 MeV and T ~ 10 keV, in the cosmic time window $t \approx 0.1 - 10^4$ sec, and may be characterized as a freeze-out from nuclear statistical equilibrium of a cosmic plasma at very low (~ 10^{-9}) baryon-to-photon number ratio. It produces the bulk of ^{4}He and ^{2}H (D), as well as good fractions of the ^{3}He and ^{7}Li observed in the current Universe, whereas all other elements are believed to be produced either by stars or cosmic rays. A part of the dark matter can be in the form of dense baryonic matter, such as planets and black holes. BBN however places a firm upper limit on the maximum baryonic density. To develop a consistent ratio with absorbed abundance ratios, it requires the baryon density to be far below the total matter density Ω_m, with value: $\Omega_b < 0.05$.

Another way to study DM is by its gravitational effects on more easily visible particles. The most direct method for this is “gravitational lensing”, the deflection of photons as they pass through the warped space-time of a gravitational field. Light rays from distant sources are not “straight” (in a Euclidean frame) if they pass near massive objects, such as stars, clusters of galaxies or dark matter, along our line of sight. In practice, the effect is similar to optical refraction, although it arises from very different physics. The effect was first observed in 1919, during a solar eclipse in front of the Hyades star cluster, whose stars appeared to move as they passed behind the mass of the sun. This was also the first verification experiment of general relativity. Although neither Einstein nor the observers saw any further uses for the effect [3], Zwicky suggested that the ultimate measurement of cluster masses would come from lensing [4], and it has indeed become the most successful probe of the dark sector.

Gravitational lensing is most easily observable around a dense concentration of mass like the core of a galaxy or cluster of galaxies. In the “**strong lensing**” regime, nearby space-time is so warped that light can travel along multiple paths around the lens, and still be deflected back towards the observer. The effect is strong enough to produce multiple images, arcs or even Einstein rings.

Most lines of sight through the Universe do not pass near a strong gravitational lens. Far from the core of a galaxy or cluster of galaxies, the light deflection is very slight. **Weak gravitational lensing** is thus an intrinsically statistical measurement, but it provides a way to measure the masses of astronomical objects without requiring assumptions about their composition or dynamical state.



Figure 1.2 On the left strong gravitational lensing as observed by the Hubble Space Telescope in Abell 1689 cluster. The strong gravitational lensing creates multiple images near the cluster core. On the right The Bullet Cluster of galaxies is depicted. The total projected mass distribution reconstructed from the weak and strong gravitational lensing is shown in blue, while the x-rays emitted hot gas is shown in red (Chandra X-ray Observatory)

Historically, three categories of dark matter candidates had been postulated.

-**Cold dark matter** (CDM), the form of DM that the constituent particles move slowly compared with the speed of light when structures formed in the universe. Cold matter is necessary to explain the large-scale structure of the universe.

-**Hot dark matter**, which consists of particles that travel with ultra-relativistic velocities. The best candidate for the identity of hot dark matter is the neutrino. They only interact by weak interaction and gravity. Hot dark matter cannot explain how individual galaxies formed from the big bang. The microwave background radiation as measured by the COBE satellite is very smooth and fast-moving particles cannot clump together on this small scale from such a smooth initial clumping.

Warm dark matter (WDM), has properties between those of hot DM and cold DM. The most common WDM candidates are sterile neutrinos and gravitinos.

CDM matter is currently the area of greatest interest for DM research, as hot dark matter does not seem to offer viable ways for galaxy and galaxy cluster formation, while most particle candidates become non-relativistic at very early times, hence are classified as cold.

1.2 Dark Matter particles

All current models of DM use the standard concept of quantum field theory to describe the properties of elementary DM particle candidates [3]. They can be characterized by the mass and spin of the DM particle. The mass of the proposed candidates spans a very large range as can be seen in the Table 1.

Type	Particle Spin	Approximate Mass Scale
Axion	**0**	**μeV- meV**
Inert Higgs Doublet	**0**	**50 GeV**
Sterile Neutrino	**1/2**	**keV**
Neutralino	**1/2**	**10 GeV - 10 TeV**
Kaluza-Klein UED	**1**	**TeV**
Weakly-interacting massive particles (WIMPs)	**-**	**10 GeV − TeV**

Table 1. Properties of various Dark Matter Candidates

WIMPs are considered one of the main candidates for cold dark matter, the others being massive compact halo objects (MACHOs) and axions.

WIMP-like particles are predicted by R-parity-conserving supersymmetry, a popular type of extension to the standard model of particle physics, although none of the large number of new particles in supersymmetry has ever been observed. The main characteristics of a WIMP are:

- Interaction only through the weak force and gravity and possible interactions with cross-sections no higher than the weak scale.
- Large mass compared to standard particles.

The axion remains one of the earliest suggestions of a viable particle candidate for dark matter, and in fact one of the most attractive. This is not least due to the fact that its existence was motivated by solving the strong CP problem in particle physics.

The **axion** is a hypothetical elementary particle postulated by the Peccei–Quinn theory in 1977 to resolve the strong CP problem in quantum Chromodynamics (QCD) [5].

The basic properties of a candidate DM must satisfy the following

1. It must be stable or long lived, which can be achieved by an appropriate symmetry
2. it should be electrically and color neutral, as implied by astrophysical constraints on exotic relics
3. it has to be non-relativistic, which is usually guaranteed by assuming that it is adequately massive, although even very light particles such as axions can be non-relativistic for different reasons

2. Axions

The Strong CP problem

Elementary particle physics is described by the gauge theory of the standard model including the strong, weak and electromagnetic interactions. But there is still an unresolved problem in the theory that cannot explain why the predicted violation in weak interactions, that is the charge conjugation times parity (CP) symmetry, is not observed in strong interactions.

This is the unsolved question that is widely known as **the strong CP problem**.

Quantum Chromodynamics (QCD) is a non-Abelian field theory that describes the mechanism of strong interactions between colored quarks and vector gluons. The calculations in the theory are generally perturbative, meaning that particles and interactions are defined by expanding the field around the ground state or vacuum.

The QCD Lagrangian that describe the interactions between quarks and gluons is

$$L_{pert} = \sum_f \overline{q_f}\left(i\gamma^\mu D_\mu - m_f\right)q_f - \frac{1}{4}G^\alpha_{\mu\nu}G^{\mu\nu}_\alpha \qquad (2.\ 1)$$

where *f* is referred to all flavors of quarks, q are the quark fields with constituent quark masses m_f, G_a are the eight vector gluon fields with α=1,...,8. D_μ represents the covariant derivative and is defined as

$$D_\mu \equiv \partial_\mu + igT_\alpha G^\alpha_\mu \qquad (2.\ 2)$$

The terms γ^μ, are Dirac matrices connecting the spinor representation to the vector representation of the Lorentz group.

In the limit of vanishing quark masses $m_f \to 0$, the QCD Lagrangian for f flavors is invariant under global axial and vector transformation and has a global symmetry: $U(f)_V \times U(f)_A$. As m_u and m_d $<<\Lambda_{QCD}$ are relatively small compared to the dynamical scale of the theory, one would expect the strong interactions to be approximately $U(2)_V \times U(2)_A$ invariant.

Experimentally, it is found that the vector symmetry corresponding to isospin times baryon number, $U(2)_V = SU(2)_I \times U(1)_B$, is a good approximate symmetry of nature and leads to baryon number conservation. But quark condensates $<\bar{u}u>$, $<\bar{d}d>$ are breaking down the axial symmetry spontaneously. The axial symmetry $U(1)_A = U(2)_{L-R}$ should lead to a symmetry between left and right handed quarks, which has not been observed in nature. As a general

theorem, whenever a continuous global symmetry is spontaneously broken, the spectrum will have a massless spin-zero boson (Nambu-Goldstone boson)

Following the above mentioned theorem– four Goldstone bosons are expected according to the Lagrangian (Equation 2.1). Three of them (corresponding to the $SU(2)_A$ breaking) have been noticed. The pion triplet π^-, π^0, π^+.However the expected fourth boson that in case of SU(2)×SU(2) symmetry is the η, has a mass of 548 MeV and it is far too high compared to that of pions. The absence of a satisfactory candidate for the fourth Goldstone boson is known as the $U(1)_A$ problem [6].

2.2 Axions and the QCD vacuum

The resolution of the $U(1)_A$ problem came through the realization by 't Hooft [7] that the QCD vacuum has a more complicated structure.

't Hooft [[3], [6]] bypassed the problem by introducing an anomalous breaking of $U(1)_A$, which resulted in an additional term L_θ to the Lagrangian. Anomalous here has the meaning that it is not a really anomalous one, but it is broken by quantum effects.

QCD vacuum has infinitely degenerate vacua, topologically different and the transition from one vacuum class to another is classically forbidden. But because of the quantum tunneling, the transition has a non-zero amplitude. Instantons can give a solution, in which a vacuum of class n−1 evolves into another vacuum of class n. The integer n is the topological winding number that labels each of the vacua. The superposition of an infinite number of vacuum states, that is the ground state denominated as θ-vacuum, can be expressed as:

$$|\theta>=\sum_{n=-\infty}^{\infty} e^{-in\theta}|n> \qquad (2.\ 3)$$

By taking into account the electroweak interactions, the parameter θ is transformed as:

$$\bar{\theta} = \theta + \arg(\det M) \qquad (2.\ 4)$$

where M is the quark mass matrix and θ effectively takes into account both QCD and electroweak information.

The effect of the θ -vacuum is introduced in the Lagrangian of the QCD as an additional term:

$$\mathcal{L}_{QCD} = \mathcal{L} + \mathcal{L}_\theta \qquad (2.\ 5)$$

The following term in the Lagrangian allowed by the gauge symmetry is

$$\mathcal{L}_{\bar{\theta}} = \bar{\theta}\frac{g^2}{32\pi^2}G^{\alpha}_{\mu\nu}\tilde{G}^{\mu\nu}_{\alpha} \quad (2.\ 6)$$

where g is the coupling constant and G_α is the gluons field strength tensor. Its dual $\tilde{G}_\alpha$ is given by

$$\tilde{G}^{\mu\nu}_{\alpha} = \frac{1}{2}\varepsilon^{\mu\nu\,\rho\sigma}G^{\alpha}_{\rho\sigma} \quad (2.\ 7)$$

The arbitrary parameter θ is an angle between 0 and 2π.

The CP-violating term is not invariant under CP transformations, so it could be large unless the parameter could be really small. Experimentally, CP violation is not observed in strong interactions.

The CP-violating term contributes to the neutron electric dipole moment (nEDM) of order [8]

$$\mathrm{d}_n \cong \frac{e\bar{\theta}m_q}{m_N^2} \quad (2.\ 8)$$

where

$$m_q = \frac{m_u m_d}{m_u + m_d} \quad (2.\ 9)$$

and m_N is the neutron mass.

Recent experimental bound on the NEDM reads $|d_n| < 2.9\times 10^{-26}$e cm (90% CL) [9]. This leads to the constraint on the θ parameter as $\theta < 0.7 \times 10^{-11}$. This low θ value is allowed, but it would imply that either both contributions in Equation 2.5 are really small, or that they cancel themselves, leading to a fine tuning of both parameters.

There seems to be no reason in the SM why θ must be so small. The question of why, the term that violates the CP symmetry cannot be omitted by the theory because of the vacuum topology and the $\bar{\theta}$ parameter that emerges from two independent contributions is so small, is known as "**the Strong-CP problem**". The strong CP problem cannot be solved in the Standard model theory approach [11], [12].

2.3 Approaches to the Strong CP Problem

One easy and attractive way to solve the strong CP problem of QCD is to introduce a massless quark. If the lighter u quark had only a bare mass, meaning that has no interaction with the Higgs field, but it became massive only by the other quark interactions through quantum effects and by instantons interactions, the CP problem would not exist.

An axial global transformation of u quark can modify the $\mathcal{L}_\theta$ Lagrangian by $\theta'=\theta+\alpha$ but can also introduce a complex mass component in m_u that is physically forbidden. But in the case that $m_u = 0$, we can freely rotate the fermionic field and cancel the anomaly term, leaving unaltered the Lagrangian. The massless quark solution, from a theoretical point of view, solves the problem by ejecting the θ term that violates the CP symmetry. But experimentally, one cannot insist that the lighter u, d, s quarks are massless, though, the experimental errors that incorporate into the mass ratio of $m_u/m_d$and $m_d/m_s$are enormous. [13]. One can estimate that m_u~4MeV and that $m_u/m_d \approx 0.56$. So it seems that the massless quark scenario is not viable although the small quark mass could emerge from instanton effects with heavier quarks.

Another possible solution to the strong CP problem is given by considering the CP symmetry spontaneously broken. This is interesting and one can set $\theta = 0$ at the Lagrangian level. Theories of spontaneously broken CP symmetry, although seemingly attractive, need complex vacuum expectation values (VEVs), leading to more difficulties in the theory. The biggest drawback of this "solution" to the strong CP problem, is that experimental data are in excellent agreement with the Cabibbo-Kobayashi-Maskawa model where CP is explicitly, not spontaneously broken.

Peccei and Quinn approach to the Strong CP problem, was, that they introduced a spontaneously broken global chiral symmetry, $U(1)_{PQ}$ for the QCD Lagrangian, that effectively, rotates the θ-vacua away. This solution is perhaps the most cogent to the strong CP problem.

They proposed to solve the strong CP problem treating θ not as a parameter, but as a dynamical variable which allows different states with a vacuum state at $\bar{\theta} = 0$, leaving no strong-CP violation. From the breaking of the symmetry a pseudo Nambu-Goldstone boson emerges, the **axion**. The chiral symmetry $U(1)_{PQ}$, which is spontaneously broken at the energy scale, f_α, resulting in the Lagrangian which introduces the axion field α and its coupling to gluons.

$$\mathcal{L}_\alpha = \frac{a}{f_\alpha}\xi\frac{g^2}{32\pi^2}G_\alpha^{\mu\nu}\tilde{G}_{\mu\nu}^{\alpha} \qquad (2.\ 10)$$

where ξ is a model depended parameter, and f_α a free parameter that is well known as the Peccei-Quinn scale.

The axion field under a $U(1)_{PQ}$ transformation, translates to

$$a(x) \to a(x) + a f_\alpha \tag{2. 11}$$

In order to make the Lagrangian of the Standard model $U(1)_{PQ}$ invariant, the axion interactions must be augmented.

$$\mathcal{L}_{QCD} = \mathcal{L}_{pert} + \bar{\theta}\frac{g^2}{32\pi^2} G_\alpha^{\mu\nu}\tilde{G}_{\mu\nu}^{\alpha} + \mathcal{L}_a \tag{2. 12}$$

$$\mathcal{L}_a = -\frac{1}{2}\left(\partial_\mu a\right)^2 + \xi\frac{\alpha}{f_\alpha}\frac{g^2}{32\pi^2} G_\alpha^{\mu\nu}\tilde{G}_{\mu\nu}^{\alpha} \tag{2. 13}$$

The first term in 2.13 is the kinetic energy of the axion field and the second term represents the interaction of axions with gluons.

$\mathcal{L}_a$ is the additional contribution of the axion field to the effective potential V_{eff} of the QCD Lagrangian and the minimum of this potential determines the vacuum expectation value (VEV) of the axion field $< a >$

$$\langle\frac{\partial V_{eff}}{\partial\alpha}\rangle = -\frac{\xi}{f_\alpha}\frac{\alpha}{f_\alpha}\frac{g^2}{32\pi^2}\langle G_\alpha^{\mu\nu}\tilde{G}_{\mu\nu}^{\alpha}\rangle|_{<\alpha>} \tag{2. 14}$$

It forces the VEV of the axion field to have a value

$$\langle\alpha\rangle = -\frac{f_\alpha}{\xi}\bar{\theta} \tag{2. 15}$$

For this value the term $G_\alpha^{\mu\nu}\tilde{G}_{\mu\nu}^{\alpha}$ vanishes, so it cancels out the $\bar{\theta}$ term and provides a dynamic solution to the strong CP problem.

Obviously, the Lagrangian (1.23) no longer has a CP-violating $\bar{\theta}$ term. Expanding V_{eff} at the minimum gives the axion a mass because of the potential curvature.

$$m_\alpha^2 = \langle\frac{\partial^2 V_{eff}}{\partial a^2}\rangle = -\frac{\xi}{f_\alpha}\frac{g_S^2}{32\pi^2}\frac{\partial}{\partial\alpha}\langle G_\alpha^{\mu\nu}\tilde{G}_{\mu\nu}^{\alpha}\rangle|_{<\alpha>=-\frac{f_\alpha}{\xi}\bar{\theta}} \tag{2. 16}$$

In that way the axion, is the most attractive and elegant solution to the strong CP problem and what is left is for it to be discovered.

Standard axion

The SM of particle physics does not contain any particle qualified as a dark matter particle. But extensions of the SM do, providing viable particle candidates as axions. The axion being the pseudo-Nambu-Goldstone boson of the Peccei-Quinn solution to the strong CP problem is a strongly motivated particle candidate. As shown by Gerardus't Hooft, QCD possess a non-trivial vacuum structure that permits the CP violation. The strong CP violating term $\bar{\theta}$, which includes the weak interactions effect, appears as a SM input parameter. Although, large CP violating terms would induce a large electric dipole moment of the neutron (nEDM), that is not experimentally observed, leading us to the conclusion that the $\bar{\theta}$ parameter must be extremely small.

By introducing the axion with appropriate properties the strong CP problem can be solved. In the original PQ model [13], they proposed to implement the $\bar{\theta}$ parameter as a dynamical field (particle). This is accomplished by adding a new global symmetry ($U(1)_{PQ}$ symmetry) that is spontaneously broken and as a result the axion appears relaxing the CP violation term $\bar{\theta}$ to zero. This is the reason Wilczek gave this new particle the name of a laundry detergent. It has the notion that axion can "clean up" the strong CP problem in physics.

2.3.1 Axion Properties

The axion, being a very light neutron pseudoscalar particle, interacts very weakly with matter and its properties depend on the Peccei-Quinn breaking scale f_α. Axion properties can be defined via the axion mass m_α and its coupling to other particles, which are inversely proportional to f_α.

$$m_\alpha \sim 1/f_a \;\&\; g_{\alpha i} \sim 1/f_{\alpha i}$$

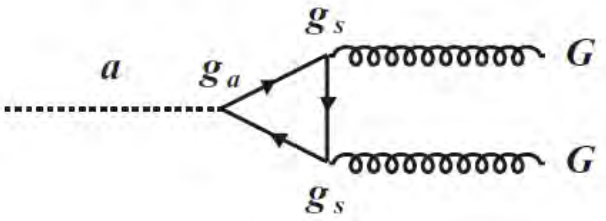

Figure 2.1 The triangle loop of the interactions of axions to gluons, where g_s is the strong coupling constant and g_α the axion-fermion Yukawa coupling.

2.3.2 Axion Couplings

Axion models are related to axions interactions with various fundamental particles. Axions interact mainly with gluons and photons. In some models however axions can interact with fermions, like electrons or nucleons [16]. The models that have been proposed can be divided in two categories, depending on the size of f_α, and the coupling to other particles $g_{\alpha i}$.

2.3.1.1 Axion -Gluon coupling

The global $U(1)_{PC}$ symmetry is spontaneously broken due to the axion's anomalous triangle coupling to gluons as can be seen in Figure 2.1.

The coupling to gluons, as a result of the chiral anomaly of the $U(1)_{PC}$ leads to the

$$\mathcal{L}_{aG} = \frac{\alpha_S}{8\pi f_\alpha} \alpha G_\alpha^{\mu\nu} \tilde{G}_{\mu\nu}^{\alpha} \quad (2.\ 17)$$

where α_S is the fine structure constant of the strong interactions. Although axions are massless, they obtain their mass via the interaction with gluons following the equation above.

This interaction can induce transitions to $q\bar{q}$ states leading to the neutral pion. That means that axion and π^0 are mixing with each other so the axion acquires a small mass given by the relation $m_\alpha f_\alpha \sim m_{\pi^0} f_\pi$ where m_{π^0}=135 MeV and f_π ~92 MeV [16]. In more detail one finds

$$m_A = \frac{z^{1/2}}{1+z} \frac{f_\pi m_\pi}{f_A} = \frac{0.60\ meV}{f_A/10^{10} GeV} \quad (2.\ 18)$$

where $z = m_u/m_d$. The value z =0.56 is used, but the range z =0.35-0.60 is also acceptable.

2.3.1.2 Axion-Photon coupling

The axion two-photon interaction is the most important and arises because of the axion-pion mixing. This interaction plays a key role for many searches and is described by the Lagrangian

$$\mathcal{L}_{int} = -\frac{1}{4} g_{\alpha\gamma} F_{\mu\nu} \tilde{F}^{\mu\nu} a = g_{\alpha\gamma} \vec{E} \cdot \vec{B} \alpha \quad (2.\ 19)$$

where F is the electromagnetic field-strength tensor, $\tilde{F}$ its dual and α the axion field. The axion-photon coupling strength $g_{\alpha\gamma}$ with the dimension (energy)$^{-1}$ is given by

$$g_{\alpha\gamma} = -\frac{\alpha}{2\pi f_\alpha}\left(\frac{E}{N} - \frac{2}{3}\frac{(4+z+w)}{(1+z+w)}\right) \quad (2.\ 20)$$

where α =1/137 is the fine structure constant and z, w are the mass ratio of the *u* to the *d* quark and the *u* to the *s* quark respectively.

$$z \equiv m_u/m_d \cong 0.553 \pm 0.043 \quad (2.\ 21)$$

$$w \equiv m_u/m_s \cong 0.029 \pm 0.004 \quad (2.\ 22)$$

Using the quark mass ratios for z and w, the coupling strength can be re-written as:

$$g_{\alpha\gamma} = \frac{\alpha}{2\pi f_\alpha}\left(\frac{E}{N} - 1.95 \pm 0.08\right) = \frac{\alpha}{2\pi f_\alpha} C_{\alpha\gamma} \quad (2.\ 23)$$

The coupling constant depends on the model-dependent factor $\frac{E}{N}$, the ratio of two anomaly coefficients, $E = 2\sum_f X_f Q_f^2 D_f$ the electromagnetic anomaly and $N = \sum_f X_f$ the color anomaly of the axion current, where X_f and Q_f denote the PQ and the electric charges respectively. In the existence of external electric or magnetic fields, this type of coupling allows both the axion decay $\alpha \to \gamma$ and conversion through the Primakoff effect $\alpha \leftrightarrow \gamma$.

Large values of $\frac{E}{N}$ can enhance the axion-photon coupling, while values of $\frac{E}{N}$~2 suppress it.

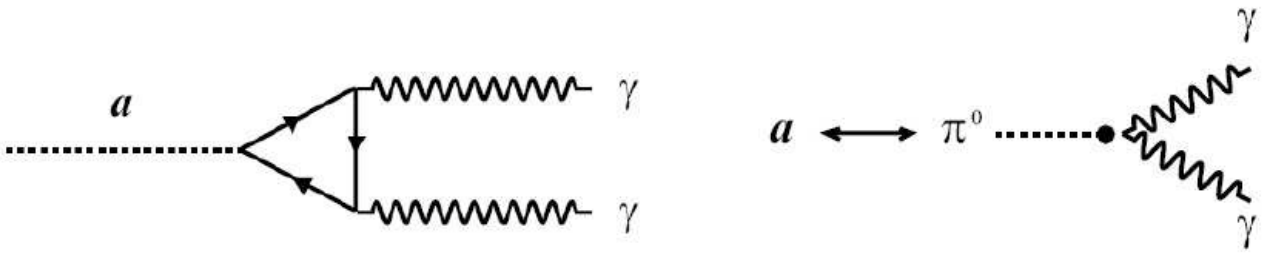

Figure 2.2: Diagram for the interaction of an axion with two photons via a fermion triangle loop. Two Feynman diagrams contribute to the axion-photon coupling: coupling of the axion to two photons via a triangle loop through fermions carrying PQ and electric charges (left image), and axion-pion mixing (right image)

2.3.1.3 Axion-fermion coupling

In some models axions can also couple with fermions, like electrons and nucleons. Electrons and quarks would show Yukawa coupling to axions if they carry PQ charge. Free quarks do not exist due to confinement below the QCD scale ~200MeV, so one can study the effective coupling of axions to nucleons.

The interaction with a fermion can be described in a general form:

$$\mathcal{L}_{af} = \frac{C_f m_f}{2f_\alpha}\bar{\Psi}_f \gamma_\mu \gamma_5 \Psi_f \partial_\mu \alpha \qquad (2.\ 24)$$

where C_f is the effective PQ charge, m_f is the fermion mass and Ψ_f is the fermion field.

The dimensional parameter

$$g_{\alpha f} = \frac{C_f m_f}{2f_\alpha}$$

plays the role of a Yukawa coupling with the fermion. The axion coupling for electrons in terms of the axion mass is given by

$$g_{\alpha e} = \frac{C_{\alpha e} m_e}{f_\alpha} = C_{\alpha e} 0.85 \times 10^{-10} \frac{m_\alpha}{eV} \qquad (2.\ 25)$$

where m_α is expressed in eV and $C_{\alpha e}$ is a model depended parameter.

In the KSVZ axion model $C_{ae} = 0$ at the tree level[1] although some couplings induced by radiation can exist [17].

In the DFSZ model

$$C_{ae} = cos^2\beta/N_f \quad (2.\ 26)$$

where $cos^2\beta$ is the vacuum expectation values x and N_f the number of families, which is 3.

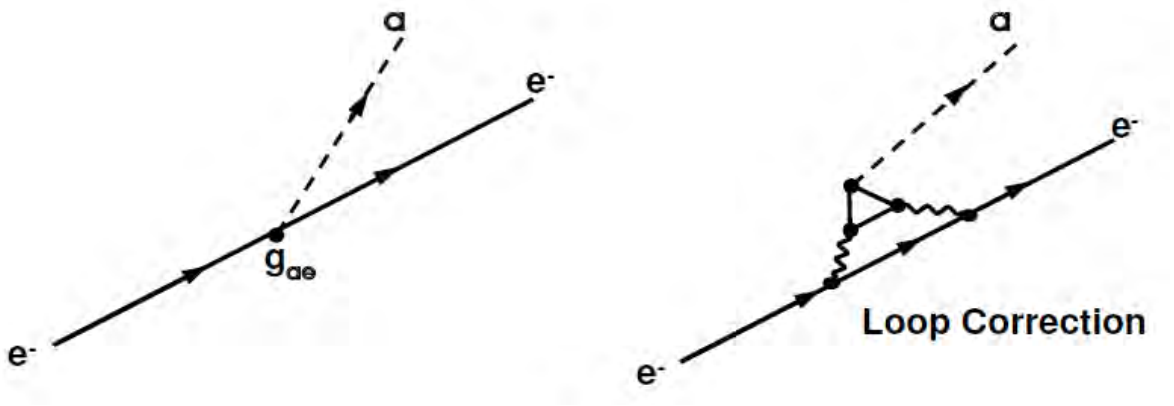

Figure 2.3 Direct coupling of an axion with an electron on the left, which is valid only for DFSZ axions. Right image: higher order coupling of an axion and an electron [16]

When two nucleons collide in a dense hot star as in a supernova, one of the axion emission processes appears and it is the nucleon bremsstrahlung as shown in the Figure 2.4. In the axion-nucleon coupling the PQ charge is given by ~30% of protons and 70% of neutrons in the supernova core region[2].

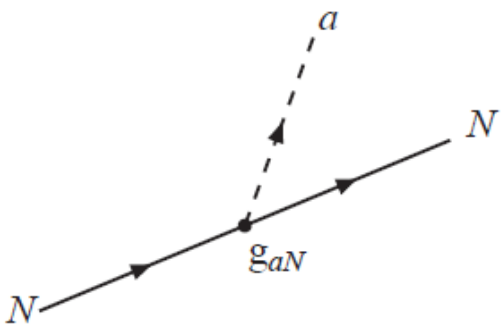

Figure 2.4 Coupling of an axion with a nucleon

[1] In general tree diagrams are those without closed loops. Loop diagrams (those with internal closed loops) tend to have larger powers of the coupling constant ; i.e. the right image of the Feynman diagram in Figure 2.3

[2] When the iron core of the supernova begins to collapse the ratio of protons and neutrons is $N_p/N_n \sim 0.4$. Later on N_p decreases because during the infall phase the ν_e escape before all neutrinos are trapped.

$$C_{\alpha N} \equiv \sqrt{0.3C_{\alpha p}^2 + 0.7C_{\alpha n}^2} \quad (2.\ 27)$$

The axion couples to the axial vector current of the fermions, i.e. to the particle's spin, so that the axion-proton interaction strength depends on the proton spin.

The mixing of axions with π^0 and η can lead to an effective coupling with nucleons with equivalent PQ charge $X_p{}'$ for protons and $X_n{}'$ for neutrons according to $C_f = X_f{}'/N$ where $N = \sum_{quarqs} X_f$ represents the absorption of the color anomaly. The coupling strength to nucleons is related to the axion mass m_α according to the relation

$$g_{\alpha N} = \frac{C_N m_N}{f_\alpha} = C_N \cdot 1.56 \cdot 10^{-7} m_\alpha \quad (2.\ 28)$$

The charges for proton and neutron are [17]

$$C_{\alpha p} = (C_u - \eta)\Delta u + (C_u - \eta z)\Delta d + (C_s - \eta w)\Delta s \quad (2.\ 29)$$

$$C_{\alpha n} = (C_u - \eta)\Delta d + (C_d - \eta z)\Delta u + (C_s - \eta w)\Delta s \quad (2.\ 30)$$

where $\eta = (1 + z + w)^{-1}$ and Δu is the fraction of the nucleon's spin carried by the u quark and the rest respectively

$$\Delta u = +0.85$$

$$\Delta d = -0.41$$

$$\Delta s = -0.08$$

with uncertainties of ±0.03 each [16].

In the DFSZ axion model,

$$C_u = \frac{sin^2\beta}{N_f} \quad (2.\ 31)$$

$$C_d = C_s \frac{cos^2\beta}{N_f} \quad (2.\ 32)$$

Using the relations

$$C_u + C_d = 1/N_f \quad (2.\ 33)$$

$$C_u - C_d = -cos2\beta/N_f \quad (2.\ 34)$$

$$C_d = C_s = C_{\alpha e} \quad (2.\ 35)$$

with number of families $N_f = 3$ we obtain the proton and neutron PQ charge

$$C_{\alpha p} = -0.10 - 0.45cos^2\beta \quad (2.\ 36)$$

$$C_{\alpha n} = -0.18 + 0.39cos^2\beta \quad (2.\ 37)$$

where β is a parameterization of $C_e = cos^2\beta/N_f$. In the KSVZ axion model which only assumes axion interactions with hadrons and $C_u = C_d = C_s = 0$ the relation gives

$$C_{\alpha p} = -0.39$$

$$C_{\alpha n} = -0.04$$

2.3.2 Axion models

Axion properties and the coupling to matter depend on the axion model used. The axion can be seen in the context of different models. The parameters that distinguish the two major axion model classes are the size of the PQ scale f_α, which is inversely proportional to the axion mass m_a as mentioned. Axions in generally can mix with pions in a way that the axion mass and its coupling to photons must be f_π/f_α times those of π^0. *The* two main axion model branches are:

- f_α small → m_a large: Visible axion
- f_α large →m_a small: Invisible axion

Visible Axions

The standard axion model as it was originally proposed by Peccei Quinn and extended by Weinberg and Wilczek (PQWW) [11]. In this model the axion has, a decay constant that is related to the electroweak constant $f_\alpha - f_{weak} \sim 250GeV$, implying an axion mass of the order of m_α ~200 keV. In this model, one needs to introduce two independent Higgs fields, Φ_1 and

Φ2, in order to describe the PQ mechanism. Quarks, leptons and intermediate bosons of PQWW theory acquire a mass, because the vacuum expectation values of the Higgs doublets are supposed to be non-zero. The symmetry must be spontaneously broken at an energy scale f_α that is equal to the electroweak scale [21].

The vacuum expectation values of the fields are $f_1/\sqrt{2}$ and $f_2/\sqrt{2}$ and the they follow the relation

$$\sqrt{f_1^2 + f_2^2} = f_{weak} \tag{2. 38}$$

$$\mathcal{L}_Y = f_d^* \bar{Q}_L \Phi_d d_R + f_d \bar{d}_R \Phi_d^\dagger Q_L + f_u^* \bar{Q}_L u_R + f_u \bar{u}_R \bar{\Phi}_d^\dagger Q_L \tag{2. 39}$$

The ratio of the vacuum expectation values of the Higgs field is denoted by $x = f_1/f_2$. Bardeen and Tye [126] used current algebra methods to estimate the axion mass in the PQWW model. PQ current has a color anomaly and the axion gets its mass.

The axial vector current is constructed form the axion and quark - lepton transformations under the CP symmetry are:

$$J_{PQ}^\mu = f_\alpha \partial^\mu \alpha + \frac{x}{2} \sum \bar{u}\, \gamma^\mu \gamma_5 u + \frac{1}{2x} \sum \bar{d}\, \gamma^\mu \gamma_5 d + (lepton\ currents) \tag{2. 40}$$

where α is the axion field, u is the +2/3 quark charge and d is the -1/3 quark charge. The lepton current is neglected for the axion mass estimation. Using standard current algebra methods the axion mass is estimated by the divergence of the anomaly free chiral current.

$$\partial_\mu \tilde{J}_{PQ}^\mu = N(x + \frac{1}{x}) \frac{m_u}{m_u + m_d} \left(\bar{u} \gamma^\mu \gamma_5 u + \bar{d} \gamma^\mu \gamma_5 d \right) \tag{2. 41}$$

The above equation gives:

$$\begin{aligned} m_\alpha^2 f_\alpha^2 &= N^2 \left(x + \frac{1}{x} \right)^2 \frac{Z}{(1+Z)^2} \left(-m_d \langle \bar{u} u \rangle - m_u \langle \bar{d} d \rangle \right) \\ &= N^2 \left(x + \frac{1}{x} \right)^2 \frac{Z}{(1+Z)^2} m_{\pi^0}^2 f_\pi^2 \end{aligned} \tag{2. 42}$$

where $m_{\pi^0} = 135 MeV$ and $f_\pi = 93\, MeV$ for the pion mass and decay constant respectively, and $Z = m_u/m_d \sim 0.56$ and N the number of quark doublets.

Then the axion mass is obtained as:

$$m_\alpha = N\left(x+\frac{1}{x}\right)\frac{\sqrt{Z}}{1+Z}\frac{f_\pi m_{\pi^0}}{f_\alpha} \cong 25N\left(x+\frac{1}{x}\right)\ keV \quad (2.\ 43)$$

and it is at least ~100 keV. However, several experiments have excluded the existence of the '*visible*' axion. Such a quite light axion (O(100 kev)) has decay time (O(10^{-1} sec)) but in the Crystal Ball experiment such a signal was excluded. They estimated the axion coupling with gluons by determining the branching ratios for both J/ψ and Y decays to $\gamma+\alpha$ [127].

- **J/ψ and Y decay**

From the heavier meson decays J/ψ ($c\bar{c}$) and Y ($b\bar{b}$) we can extract useful information. The decay rate of the heavier meson J/ψ to a photon plus an axion is given by:

$$B(J/\psi \to \gamma\alpha) \propto x^2 \quad (2.\ 44)$$

and for Y decay :

$$B(Y \to \gamma\alpha) \propto 1/x^2 \quad (2.\ 45)$$

where the free parameter x is the ratio of the vacuum expectation values of the two Higgs fields. To eliminate the free parameter we combine the equations (2. 44) and (2. 45)

$$B(J/\psi \to \gamma\alpha)\cdot B(Y \to \gamma\alpha) = B(J/\psi \to \mu^+\mu^-)B(Y \to \mu^+\mu^-)\frac{(G_F m_c m_b)^2}{2\pi^2\alpha^2} \quad (2.\ 46)$$
$$= (1.4 \pm 0.3)\times 10^{-8}$$

G_F is the Fermi coupling constant, $m_c = 1.44GeV$ is the mass of the charmed quark and $m_b = 4.9\ GeV$ is the mass of the bottom quark and α is the fine structure constant.

The Crystal Ball experiment obtained an upper limit for [22]

$$B(J/\psi \to \gamma\alpha)\cdot B(Y \to \gamma\alpha) < 5.6\times 10^{-10} \quad (2.\ 47)$$

from which we conclude that

$$f_a > 10^3 GeV \ \ or \ \ m_\alpha < 6\ keV \quad (2.\ 48)$$

Hence the experimental search ruled out the originally proposed axion of the PQWW model.

The invisible Axions

After the experimental exclusion of the PQWW axion, new ideas came up for the solution of the strong CP problem keeping alive the attractive and elegant way of the PQ symmetry. The main problem of the PQWW axion and the $U(1)_{PQ}$ symmetry breaking scale f_a was that it was related to the electroweak symmetry breaking scale f_{weak}. Physically, there is no favorite way of nature to do that. Instead, new extensions of the PQWW theory appeared in a way that the symmetry breaking scale could be much higher than the electroweak one $f_a \gg f_{weak}$. In that case the coupling of axion becomes weaker so much that it can have eluded all experimental searches. It would be 'invisible'. In the invisible axion model the symmetry scale is an arbitrary parameter, implying that the coupling of axions is not fixed. It is therefore preferable that the adjustment of the strong CP parameter $\bar{\theta} = 0$ works for any scale of f_a. The invisible axion models introduce a new electroweak Higgs complex scalar field σ with vacuum expectation value $\langle\sigma\rangle = \frac{f_a}{\sqrt{2}} \gg f_{weak}$. The σ field is not participating in electroweak interactions. $U(1)_{PQ}$ symmetry should be broken by the vacuum expectation value of the scalar field σ and the axion field, it is just the phase of the singlet complex scalar field that can be described by the Lagrangian [23]

$$\mathcal{L} = \left(\partial_\mu\sigma\right)^*(\partial^\mu\sigma) - V(\sigma) = \left(\partial_\mu\sigma\right)^*(\partial^\mu\sigma) + \mu^2\sigma^*\sigma - \lambda(\sigma^*\sigma)^2 \qquad (2.\ 49)$$

where μ is the mass and λ the coupling. This Lagrangian is invariant under the chiral phase transformation of the form:

$$\sigma \rightarrow e^{ia}\sigma \qquad (2.\ 50)$$

where a is a constant. This chiral symmetry is often referred to as the Peccei-Quinn (PQ) symmetry $U(1)_{PQ}$ .The potential $V(\sigma)$ is chosen to be a “Mexican” hat, with absolute minimum at $|\sigma| = f_{PQ}/\sqrt{2}$ where f_{PQ} is some large energy scale. Ground state is characterized by a non-vanishing vacuum expectation value

$$\langle\sigma\rangle = \left(f_a/\sqrt{2}\right)\varepsilon^{i\varphi} \qquad (2.\ 51)$$

where φ is an arbitrary phase. It spontaneously breaks the PQ symmetry because it is not invariant under the transformation of equation 2.49.

Then we may write

$$\sigma = \frac{1}{\sqrt{2}}(f_\alpha + \rho)\varepsilon^{i\alpha/f_\alpha} \tag{2. 52}$$

in terms of two real fields a and ρ which represent the “axial” and “angular” excitation. The $V(\sigma)$ potential provides a large mass for ρ, which will be of no interest for our low-energy case. [24]

The main groups of models that have been considered in the invisible axion theory are the:

One is the Dine-Fischler-Srednicki-Zhitnitskii (DFSZ) axion, the so called GUT axion, where one introduces additional Higgs doublets and they carry non-vanishing PQ charge as the light quarks does [23].

The other is the Kim-Shifman-Vainshtein-Zakharov (KSVZ) axion, the so called hadronic axion or heavy quark axion that has to introduce heavy quarks [24].

KSVZ Axion

In the frame of this scenario, axions decouple from ordinary particles, implying that axion interactions with matter take place through the axion-gluon coupling introduced by PQ. Leptons and quarks do not carry PQ charge while some exotic heavy quarks do. The statement that $C_e \equiv C_u = C_d = C_s = 0$, implying that the KSVZ axions do not interact with electrons and quarks at the tree level and this is why they are called hadronic axions.

Simplifying equation (2. 28) and taking into account that $w \ll z$ it follows that,

$$g_{\alpha\gamma} = \frac{\alpha}{2\pi}\left(\frac{E}{N} - \frac{2}{3}\frac{4+z}{1+z}\right)\frac{1+z}{\sqrt{z}}\frac{m_\alpha}{m_\pi f_\pi} \tag{2. 53}$$

In the standard KSVZ model the ratio E/N is equal to zero, but different assumptions depending on an anomaly for the E/N ratio, related with the electric charge of the new heavy quark introduced, can give values between 0 and 6.

That is

$$\frac{E}{N} = 6Q_{em}^2 \tag{2. 54}$$

and the charge Q_{em} can take values $Q_{em} = 2/3, -1/3, 1, 0$ [25]. In general there is no physical motivation to introduce a new heavy quark.

DFSZ model

This model was introduced by Dine, Fischler, Srednicki, Zhitnitskii [27] and allows axion coupling to ordinary quarks and leptons. Because fermions carry PQ charge, there is no need for exotic quarks and the axion couples directly to the Standard Model matter fields. The DFSZ model can be introduced in GUT theories. In that case one should consider that in models where the inflationary scale is super-heavy (SUSY GUT scale), large axion contribution to the CDM is disfavored because WMAP set stringent bounds to the isocurvature perturbations that emerge at the QCD phase transition.

The PQ field emerges with non-zero value at the end of inflation era, because the θ -angle acquires a superhorizon spectrum of perturbations and these perturbations turn into an isocurvature perturbation in axion energy density. Kasuya and Kawasaki proposed an axion model with isocurvature fluctuations and large scale structure observations or even the PLANCK mission, which could see such existence with a huge blue tilt. However in the DFSZ model, GUT theories predict $E/N = 8/3$ and the value of $g_{\alpha\gamma}$:

$$g_{\alpha\gamma}^{DFSZ} \approx -0.75 \frac{\alpha}{2\pi f_\alpha} \tag{2. 55}$$

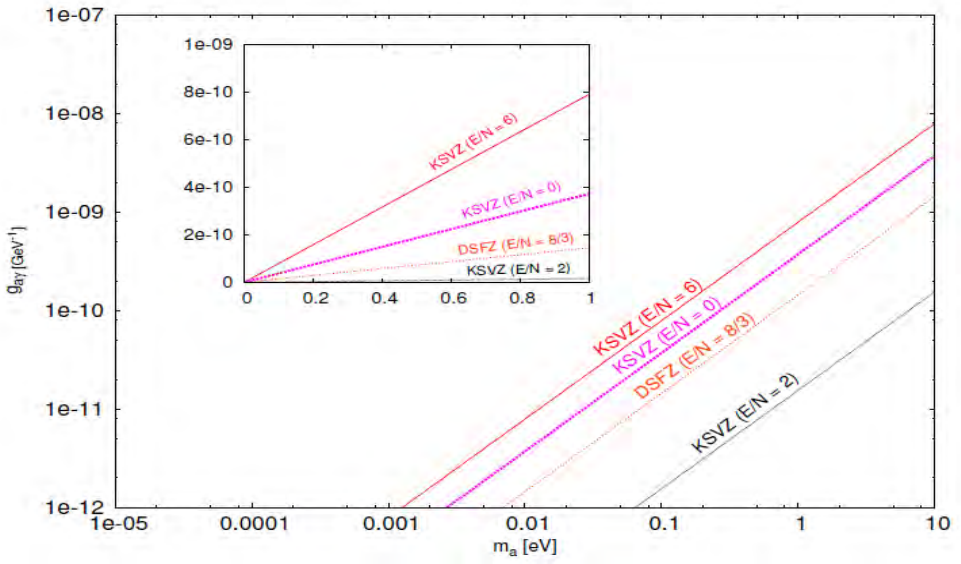

Figure 2.6 The various axion models coupling strength as a function of axion mass. [169]

The Primakoff effect

The most interesting mechanism for axion production is the Primakoff effect [26] according to which a real photon interacts with the static Coulomb field of a charged particle (usually a nucleus) and an axion is produced. For hadronic axions that are not coupled to leptons, this is the main production and detection mechanism. The differential cross section for this process is:

$$\frac{d\sigma_{\alpha\to\gamma}}{d\Omega} = \frac{g_{\alpha\gamma\gamma}^2 Z^2 \alpha_{em}}{8\pi} \cdot \frac{\left\|\vec{p}_\alpha \times \vec{p}_\gamma\right\|^2}{\left\|\vec{p}_\alpha - \vec{p}_\gamma\right\|^4} \qquad (2.\ 56)$$

where Z is the nucleus charge that produces the Coulomb field and the axion interaction takes place.

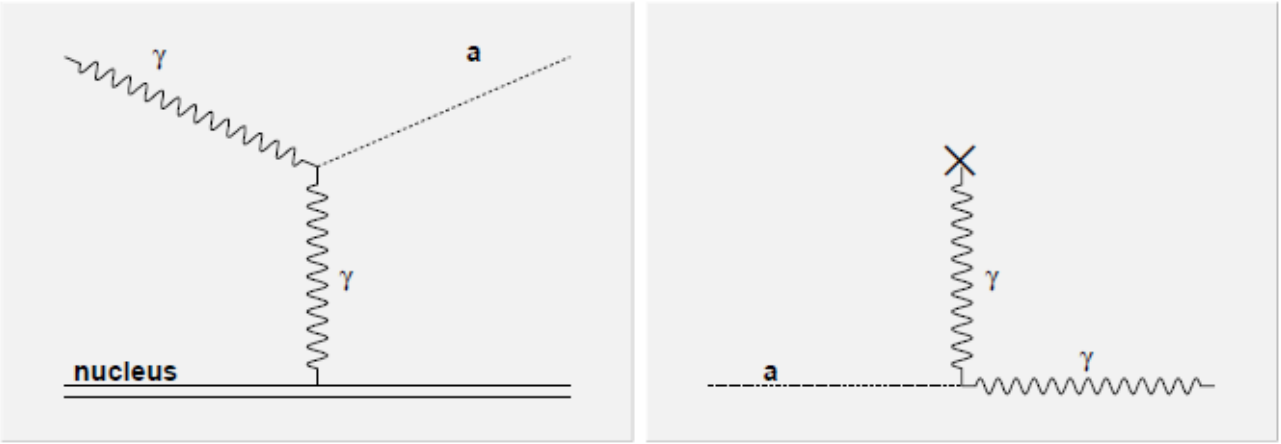

Figure 2.5 Left: A photon interacts with the electromagnetic field of a nucleus and an axion is produced. Right: an axion is transformed to a photon in an external electromagnetic field.

2.4 Why are axions a DM candidate?

As mentioned, WMAP measurements predict that 22% of the energy density of the present Universe consists of CDM. The nature, origin and composition of this important component, is still being explored and Particle physics along with Astrophysics can provide the candidate particles out of which CDM can be made. The main properties of such a candidate must satisfy the following:

1) It should be stable and long lived, which can be provided by an appropriate symmetry
2) It should be color and electrically neutral as implied by astrophysics constraints on exotic relics
3) It has to be non-relativistic assuming that it is adequately massive, although it can be very light.

The Standard Model of particle physics does not contain a particle that qualifies as a DM particle. Extensions to the standard model do, however providing viable particle candidates. The axion, that is the pseudo-Nambu-Goldstone boson of the Peccei-Quinn solution to the strong CP problem, is a strongly motivated candidate particle. The axion has a lifetime comparable to the age of the Universe today, $t_0 \cong 14\ Gyr$. Because of their weak coupling to matter, axions have a very low decay rate, i.e. the lifetime of the axion is governed by the decay $\alpha \to \gamma$ and it is:

$$\tau_\alpha \cong 4.6 \cdot 10^{40} s \left(\frac{E}{N} - 1.92\right)^{-2} \left(\frac{f_\alpha/N}{10^{10} GeV}\right)^{5} \quad (2.\ 57)$$

for $E/N = 0$, this relation leads to an axion lifetime $\tau_\alpha > t_0$ for $f_\alpha/N > 3 * 10^5 GeV$ and thus $m_\alpha < 20\ eV$ that is a favored region as can be seen in the following section, from astrophysical and cosmological constraints.

Axions satisfy the criteria necessary for cold dark matter:

(1) A non-relativistic population of axions could be present in our universe in sufficient quantities to provide the required dark matter energy density and

(2) They are effectively collisionless, i.e., the only significant long-range interactions are gravitational [28]. Axions have a very small mass

$$m_\alpha \cong 6 \times 10^{-6} eV \left(\frac{10^{12} GeV}{f_\alpha}\right) \quad (2.\ 58)$$

but axion DM is non-relativistic, because cold populations are produced out of equilibrium. Since axion mass is an arbitrary parameter, axions could favor the HDM contribution component, in case that its coupling strength is strong enough, or the CDM component for larger PQ scale factor, f_α.

The HDM axions contribution could have been produced in the early Universe and thermalized before the QCD phase transition (T~200MeV), in case $f_\alpha \leq 10^8\ GeV$.

There are three mechanisms via which CDM axions are produced: vacuum realignment, string decay and domain wall decay.

2.4.1 Topological axion production

One important parameter is the temperature at which the PC symmetry breaks, T_{PQ}. Which of the three mechanisms contribute to the cold dark matter population depends on whether this temperature is less or greater than the inflationary reheating temperature, T_R. It is the temperature at which the axion mass, arising from non perturbative QCD effects, becomes significant [30]. The axion mass becomes important at time t_1, when $m_\alpha t_1 \sim 1$ and the temperature of the universe at that time is $T_1 \sim 1\ GeV$. At an early age, the universe temperatures are greater than T_{PQ} and the PQ symmetry is unbroken. At T_{PQ}, the symmetry breaks spontaneously and the axion field can have any value. Axion strings appear as topological defects. If $T_R < T_{PQ}$ the axion field is homogenized over vast distances and the string density is diluted by inflation. When $T_R > T_{PQ}$ the strings radiate cold massless axions until QCD effects appear at temperature T_1. Axion decay from string radiation has two possibilities to occur in order to fulfill the expected axion spectrum. Either strings are oscillating many times before complete decay, or a more rapid decay occurs. Rapid decay produces ~ 70 times less axions than slow string decay[3]. At the time t_1, when the universe temperature cools down to T_1, the axion strings become the boundaries of N domain walls. In the case where $N > 1$, the domain wall problem arises because the vacuum is multiply degenerate and there is at least one domain wall per horizon. For the case where $N = 1$ or $T_R < T_{PQ}$, axion string density is diluted by inflation. In the case where $T_R > T_{PQ}$, string and wall decay contribute to the axion energy density, but in both cases there is no significant contribution to the density of cold axions.

[3] Either strings oscillate many times before they completely decay and axion production is strongly peaked around a dominant mode or much more rapid decay occurs, producing a spectrum inversely proportional to momentum [28]

Axion models have spontaneously broken $U(1)_{PQ}$ symmetries and inflation, if occurred, it occurred after the spontaneous breaking of this symmetry. Thus the axion production by this mechanism depends on the average energy of the axion produced by string dissipation at time t. The contribution of the axionic strings that turn into axions would be

$$\Omega_{string}h^2 \cong \frac{m_\alpha eV^{-1.175}}{10^{-3}} \tag{2. 59}$$

restricting the axion mass to $m_\alpha \geq 10^{-4}eV$. Sikivie et al's reasoning [29] assumed that string radiation goes more into kinetic axion energy and these axions would not increase significantly the relic axion density, at least no more than the "misalignment mechanism" defying an axion mass bound:

$$m_\alpha \geq 10^{-6}eV \tag{2. 60}$$

2.4.2 Vacuum realignment mechanism

Cold axions could have been produced by vacuum realignment for any T_R. For $T_R < T_{PQ}$, inflation could lead to homogenization and the axion field should be single valued. The axion field acquires a potential because of QCD effects and the axion field will oscillate in its potential. These oscillations do not decay and contribute to the energy density of axions. The axion expectation value in the early Universe is zero ($\theta = 0$) but as it cools down to a temperature range comparable to the PQ scale the axion field acquires a value θ_1 (initial "misalignment"). At $T \sim \Lambda$, where Λ is the confinement scale, non-perturbative QCD effects give the axion a mass, which is temperature and time dependent. An effective potential is created

$$\widetilde{V}(\theta) = m_\alpha^2(T)f_\alpha^2(1 - \cos\theta) \tag{2. 61}$$

in this case the initial axion field takes the value

$$\alpha_i = f_\alpha\theta_\iota \tag{2. 62}$$

where θ the initial misalignment of the θ parameter and $0 \leq \theta \leq \pi$. At early times, the axion mass is insignificant and θ can have a constant value but when the universe cools down to the critical temperature, the axion field will begin to oscillate in its potential. [31]

In the realignment mechanism, a field can take any value in the early universe, but later on it rolls down towards the minimum of the potential. When it reaches the bottom, it overshoots the minimum and starts to oscillate. In the case that the quanta of the field are cosmologically

stable, these oscillations behave as a cold dark matter fluid. A scalar field φ of mass m_φ has a Lagrangian of the form:

$$\mathcal{L} = \frac{1}{2}\partial_\mu\varphi\partial^\mu\varphi - \frac{1}{2}m_\varphi^2\varphi^2 + \mathcal{L}_\mathrm{I} \tag{2. 63}$$

where $\mathcal{L}_\mathrm{I}$, includes the interactions of the field with itself and the rest of the particles in the primordial soup. In each causally connected patch of the universe the scalar field has an initial value φ_i .

If inflation already happened, φ is equal to φ_i for all the times of the universe. The equation of motion in the expanding universe for the scalar field is given by the relation:

$$\ddot{\varphi} + 3H\dot{\varphi} + m_\varphi^2 = 0 \tag{2. 64}$$

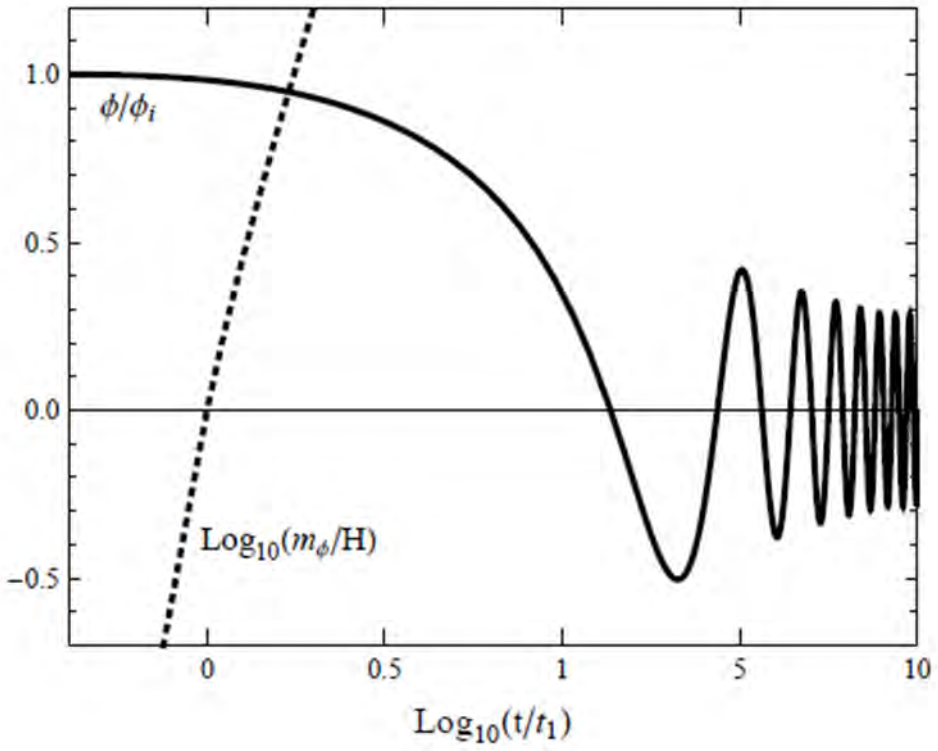

Figure 2.7 At the time $t_1 = 2\times10^{-7}s\ \left(\frac{f_\alpha}{10^{12}GeV}\right)^{\frac{1}{3}}$, characterized by $3H(t_1) = m_\varphi(t_1)$, the potential starts to oscillate [28]

The energy density in these oscillations of the axion field should not exceed the energy density which closes the universe and can be defined as

$$\Omega_\alpha h^2 \approx 1.9\times3^{\pm1}\left(\frac{1\mu eV}{m_\alpha}\right)^{1.175}\Theta_i^2 f(\Theta_i) \tag{2. 65}$$

where $f(\Theta_i)$ is a function that incorporates all the inharmonic corrections on the axion potential and h the Hubble constant .

Coherent oscillations produce the initial energy density that can be expressed as

$$\rho_1 = \frac{1}{2} f_\alpha^2 m_\alpha^2(t_1)\theta_1^2 \tag{2. 66}$$

where θ_1 is the initial, "misalignment" angle. The production of axions by this mechanism accounts for the contribution to the dark matter density for some values of f_α, which are given by [150]

$$\Omega_\alpha h^2 \approx 0.3\left(\frac{f_\alpha}{10^{12}}\right)^{7/6} \tag{2. 67}$$

which can be compared to the total cold dark matter density $\Omega_{CDM} * h{\sim}0.13$. That implies that axions with mass $\sim 10\ \mu eV$ would be the only dark matter candidate, assuming abundance for the axions of the same order. This value varies according to different producing mechanisms (string and domain walls as also non-zero modes of the axion field) and a conservative limit for the axion mass could be

$$m_\alpha \geq 10^{-5}\ eV \tag{2. 68}$$

The results are defined in the case where axions were never in thermal equilibrium, the scale f_α is quite large $(f_\alpha \geq 10^8\ GeV)$ and axions are weakly interacting. In the case where axions would have been in thermal contact with the hot plasma, there should exist an invisible sea of background axions but astrophysical arguments do not support this idea.

2.5 Astrophysical axion bounds

Axion emission by hot and dense plasma is an energy loss channel for stars. The rate of this loss modifies the solar sound-speed profile, solar neutrino flux, helium burning lifetime of globular cluster stars and also accelerates the white-dwarf cooling and alters the neutrino burst duration of the supernova SN 1987A. Astrophysical phenomena provide us a natural laboratory for high and low energy exploration of elementary particle physics. Especially for axions, stars are well suited for sensitive axion tests because of the high energy available. Stars are potential powerful sources of weakly interacting particles such as neutrinos, gravitons, axions and others. The properties of stars should be altered in the case when those particles provide an additional energy loss mechanism. Extensive research can show up these properties.

The Sun would be ubiquitous the brightest axion source in the sky, since a photon can convert into an axion in the presence of an external magnetic or electric field by means of the two photon coupling:

$$L_{\alpha\gamma\gamma} = \frac{g_{\alpha\gamma\gamma}}{4} F_{\mu\nu}\tilde{F}^{\mu\nu}\alpha = -g_{\alpha\gamma\gamma} E \cdot B\alpha \quad (2.\ 69)$$

$g_{\alpha\gamma\gamma}$ is the axion to γ-γ coupling constant, F the electromagnetic field-strength tensor and E, B the electric and magnetic field respectively.

This is the so called Primakoff effect, which was first proposed for the creation of mesons in the nuclei electric field. The high concentration of thermal photons in the presence of a strong electromagnetic field of the stellar plasma, makes the Sun and stars in general, a rich source for axion production and other similar particles like ALP's (axion like particles) paraphotons and chameleons (Dark energy particles).

Using the standard solar model, the calculated solar axion luminosity is

$$L_\alpha = g_{10}^2 1.85 \times 10^{-3} L_\odot \quad (2.\ 70)$$

where $L_\odot = 3.90 \times 10^{25}$ W is the solar luminosity and

$$g_{10} = g_{\alpha\gamma\gamma}/(10^{-10} GeV^{-1}) \quad (2.\ 71)$$

Solar axion luminosity cannot exceed the photon luminosity and that constrains

$$g_{\alpha\gamma} < 3 * 10^9 GeV^{-1} \quad (2.\ 72)$$

In case $g_{\alpha\gamma} \sim 2 - 5 * 10^{-6} GeV^{-1}$ the Sun could live only for 1000 years. A more stringent constraint could be given by a deeper study of the solar physics model. Existence of axions with a stronger coupling constant would imply modifications in the actual Helium abundance in the core of the Sun and this would change substantially the sound speed profile of the star that can be diagnosed by Helioseismology. This provides a conservative limit

$$g_{\alpha\gamma} < 1 * 10^{-9} GeV^{-1} \quad (2.\ 73)$$

that corresponds to $L_\alpha \leq 0.20 L_\odot$.

Enhanced solar axion emission increases the energy loss by nuclear burning and that would increase the Sun temperature. Solar models with axion losses make it clear that a $g_{\alpha\gamma} \sim 4.5 * 10^{-6} GeV^{-1}$ implies a 20% increase of the solar ^{8}B neutrino flux. [31].

The all-flavor measured value for ^{8}B neutrino flux is $4.94 * 10^{6} cm^{-2} s^{-1}$. Therefore, the measured neutrino fluxes put a limit on the coupling constant

$$g_{\alpha\alpha\gamma} \leq 5 \times 10^{-10} GeV^{-1} \quad (2.\ 74)$$

and that value corresponds to $L_{\alpha} \leq 0.04 L_{\odot}$ [164].

Globular clusters axion limits

A more restrictive limit on axion photon coupling $g_{\alpha\gamma}$, can be obtained by globular cluster stars, i.e. stars that belong to a gravitationally linked system that formed at the same time and differ in their mass. Stars on the horizontal branch (HB) have reached helium burning and they have masses below $M_{\odot}$. They can be classified using a color-magnitude diagram (see Figure 2.8) that represents the surface brightness vs. surface temperature. From this diagram one can identify their state of evolution and estimate the accelerated consumption of helium due to axion production that is related with the axion coupling.

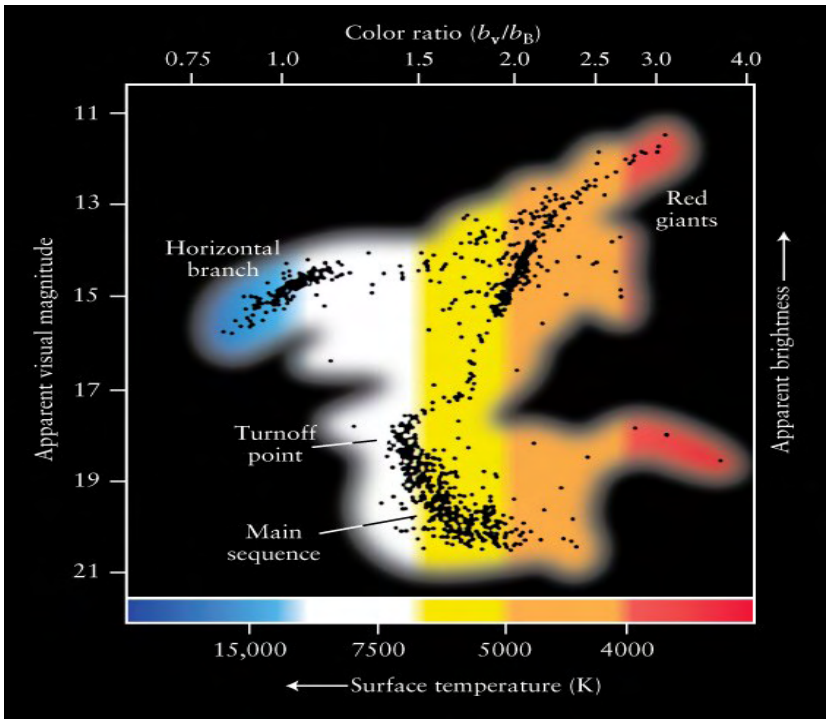

Figure 2.8 A globular cluster color-magnitude diagram where the different evolutionary stages of stars have a representative pattern distribution. The y-axis represents the brightness of the star, while the x-axis is related with the surface temperature of the star, hot stars laying at the left of this plot. In this map different types of stars can be distinguished, main sequence (MS): core hydrogen is burning, main-sequence turnoff (TO): central hydrogen is exhausted, red-giant branch (RGB): growing radius till helium ignites, and horizontal branch (HB) stars: helium burning in the core, between others. Extracted from Ref. [31]

The Primakoff energy loss rate should accelerate the helium consumption and reduce the HB lifetime. The HB lifetime is calculated by the axion production and it could be reduced by a factor of $1/\left(1+3\left(g_{10}\right)^{2}/8\right)$ and can be measured relative to the red giant branch (RGB) time evolution which is the ratio between the HB and RGB stars. This number ratio agrees with expectations within 20-40% in any globular cluster and this error is of statistical origin because the number of HB stars measured is typically around 100. The helium burning lifetime estimated by 15 globular clusters, agrees with expectations within 10-15% and a reasonable conservative limit for the coupling constant is [20]

$$g_{\alpha\gamma\gamma} < 10^{-10} GeV^{-1} \tag{2. 75}$$

This globular cluster limit varies due to uncertainties and precludes Primakoff production of axions, that is $\gamma + Z\varepsilon \rightarrow \alpha + Ze$.

White-dwarf cooling

After the HB phase, stars ascend through the red giant branch evolving to the asymptotic red giant branch (AGB). AGB stars have a degenerate carbon-oxygen core and helium burning in a shell. The fast mass loss creates a “planetary nebula” which surrounds a compact remnant, which is a white-dwarf, cooling down firstly by neutrino emission and later by surface photon emission. The observed luminosity reveals that the cooling speed can constrain axion emission.

The derived limit results of the axion-electron coupling is

$$\alpha_{\alpha ee} \leq 1 \times 10^{-26} GeV^{-1} \tag{2. 76}$$

and it is similar to the globular cluster limit (2. 75). This limit evaluated according to recent analyses allowing one to set a limit that corresponds to axion losses according to

$$g_{\alpha e} < 4.3 \times 10^{-13} GeV^{-1} \tag{2. 77}$$

at a statistical 95% CL.

This axion limit is from the GC M5 (NGC 5904) and it is based on a large set of observations from high precision photometry, while the predictions are based on contemporary stellar evolution theory.

Axions can interact with electrons in the vertex form

$$C_e \bar{\psi}_e \gamma^{\mu} \gamma_5 \psi_e \partial_{\mu} \alpha / 2 f_{\alpha} \tag{2. 78}$$

where C_e is a model-dependent coefficient and the Yukawa coupling is usually defined as

$$g_{\alpha e} = C_e m_e / f_\alpha \quad (2.\ 79)$$

In the case of the DFSZ model the coupling with electrons is defined explicitly as

$$g_{\alpha e} = \frac{1}{3} tan^2(\beta) m_e / f_\alpha \quad (2.\ 80)$$

where $tan\beta$ is the ratio between the two-Higgs field expectation value. In WD's a bremsstrahlung process that an axion-nucleus can increase the cooling rate of a white-dwarf as follows

$$e + Ze \rightarrow Ze + e + \alpha \quad (2.\ 81)$$

The cooling speed of a WD can also be tested by the period decrease of pulsating WD's (ZZ Ceti stars). The additional cooling required, corresponds to $\widetilde{m}_a \sim 15 - 20\ meV$

where

$$\widetilde{m}_a = m_\alpha cos^2 \beta \quad (2.\ 82)$$

Supernova 1987A

The lowest-lying upper bound for the axion mass can be extracted from the SN1987A. The core-collapse of a massive star evolves to a proton-neutron star of enormous density such as that even neutrinos cannot escape. Remarkable, this collapse can produce in a few seconds as much radiation as the Sun in its total lifetime. The axions produced in a proton-neutron star are emitted by nucleon bremsstrahlung $N + N \rightarrow N + N + \alpha$ and depends on the axion-nucleon Yukawa coupling $g_{\alpha NN}$. In such a case, energy loss of the SN1987A would have the following effects:

Firstly decrease the observed neutrino pulse in the IMB and Kamioka water Cherenkov detectors (19 neutrinos in 10 seconds). The axion-nucleon coupling $g_{\alpha NN}$ can affect the cooling time process by this additional energy loss channel. For small axion-nucleon coupling, axion emission is too weak to alter the burst duration time. For larger coupling the burst duration becomes shorter as the axion emission increases. Then it reaches the minimum in the case where the axion mean free path is about the size of the SN. When axion-nucleon coupling becomes larger, axions are trapped and they are emitted from an “axion sphere”.

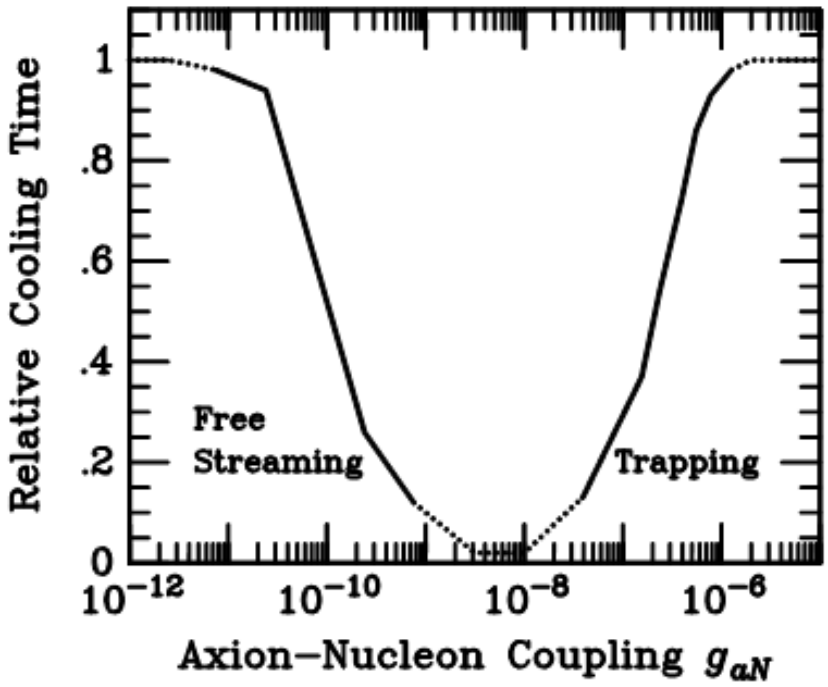

Figure 2.9 Burst duration in seconds vs. axion-nucleon coupling. On the left side, axions are emitted freely from the entire core but on the right side axions cannot escape [166].

Secondly, in the case of "strongly" interacting axions, axions would have interacted with oxygen nuclei, leading to γ rays and increase the number of events to the detectors that registered the SN1987A. So according to the observations axion-nucleon coupling range between

$$3 \times 10^{-10} GeV^{-1} \leq g_{\alpha N} \leq 3 \times 10^{-7} GeV^{-1} \quad (2.\ 83)$$

is excluded resulting in an exclusion range for the axion mass:

$$0.01\ eV \leq m_{\alpha}^{KSVZ} \leq 10\ eV \quad (2.\ 84)$$

The detection of the neutrinos measured by the SN 1987A might lead to some uncertainties in the axion mass range excluded. The statistics from the detectors mentioned is low and this can lead to some incompatibilities. These results however plus the calculated astrophysical and cosmological bounds on axion properties leaves only a relatively narrow window open to the axion mass range.

CAST continues the exploration and the searching of axions in that allowed range. In the figure below the astrophysical and cosmological bounds are summarized in parallel with the sensitivity of some axion experiments that will be referred in the next section.

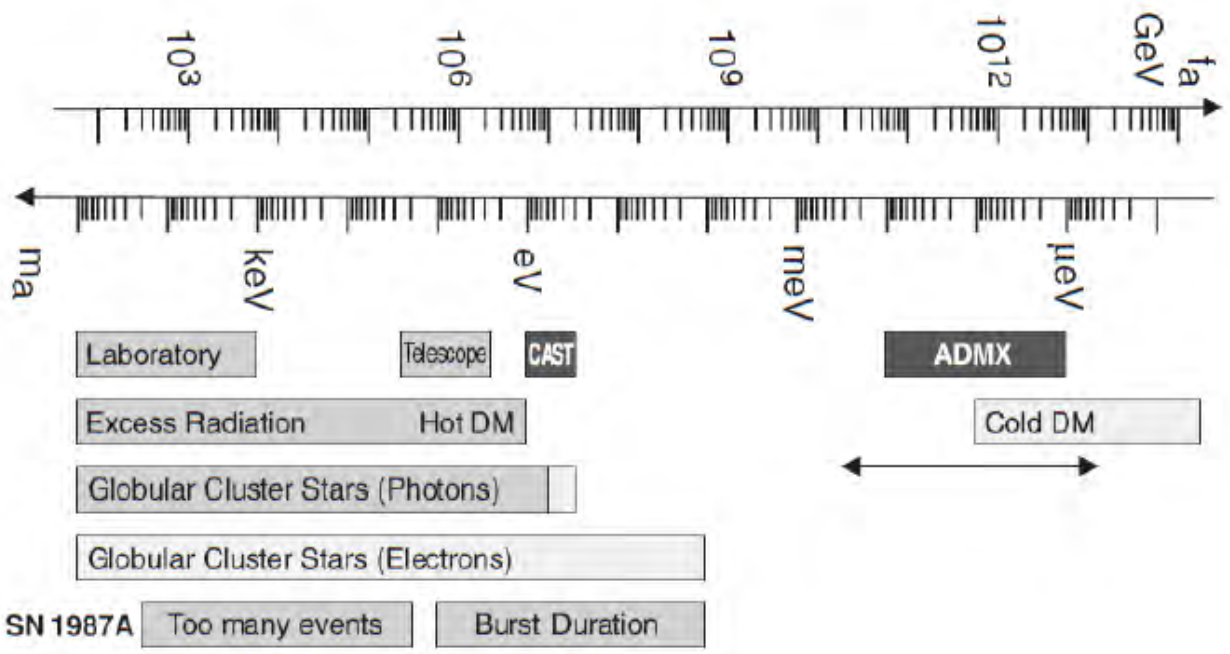

Figure 2.10 Excluded axion mass regions according to astrophysical and cosmological bounds [31]

Axion detection experiments

In 1983, Sikivie [32], proposed that invisible axions could be traced by several experiments, all based in the axion-photon conversion i.e. the Primakoff effect. The Primakoff effect describes the conversion of photons into axions in the presence of virtual photons produced by external electric or magnetic fields. These fields can be provided by the Coulomb field of the nucleus, the electric field of charged particles in the dense hot plasma of astrophysical origin (Stars, WD's etc.) or even a strong magnetic field in the laboratory. We can use the inverse process, which is the axion to photon conversion to detect axions in most of experiments. Experiments in which axions or axion like particles couple to photons can be distinguished in three types

- Axions of galactic origin → Axion Haloscopes
- Axions produced in the Sun → Axion Helioscopes
- Laboratory Axions → Laser experiments

Axion Haloscopes

Microwave cavity experiments are searching for galactic halo axions that are resonantly converted into RF photons, in a microwave cavity permeated by a strong magnetic field. Tuning the cavity to adjust the resonant condition i.e. the cavity resonant frequency (ω) matches the axion mass m_α, that is

$$h\nu = m_\alpha c^2\left(1 + \mathcal{O}(\beta^2 \sim 10^{-6})\right) \quad (2.\ 85)$$

and axions will convert resonantly to photons according to conversion power

$$P = g_{\alpha\gamma\gamma}^2 \frac{VB^2\rho_\alpha Q}{m_\alpha} \quad (2.\ 86)$$

where B is the magnetic field strength, V is the volume of the cavity and Q is the quality factor of the cavity. The converted photons are measured by sensitive microwave receivers which respond to the increased power related to the increased number of photons that have been converted. For example a $5\ \mu eV$ axion quasi at rest would convert to a $1{,}2\ GHz$ photon. The predicted halo axion velocities $\beta \sim 10^{-3}$ can cause a spread in the axion energy and the relation

$$E \cong m_\alpha c^2 + \frac{1}{2} m_\alpha c^2 \beta^2 \quad (2.\ 87)$$

would cause a variation of the order $10^{-6}$and this translates into a $1.2\ kHz$ upward spread in frequency of the converted photons.

Early attempts were made by the Rochester-Brookhaven-Fermilab (RBF) [34] and the University of Florida Experiment (UF) [167]. These were proof-of-concept experiments because of their small cavity size and high noise temperatures but they were able to scan and preclude a range in the mass of axions

$$4.5\ \mu eV \leq m_\alpha \leq 16.3\ \ \mu eV$$

although they were not sensitive enough to reach the prediction of the theoretical axion models (Figure 2.11)

A second generation experiment, the ADMX (Axion Dark Matter eXperiment) was built at the Lawrence Livermore National Laboratory (LLNL) and has provided some constrains in the region $m_\alpha = 1.9 - 3.5\ \mu eV$, which translates into $f_\alpha = 1.8 \times 10^{12} - 2.2 \times 10^{12}\ GeV$.

A new experiment, called ADMX-HF is planned to operate at Yale University with better sensitivity so to scan the parameter space of ALPs in the range $10 - 100\ \mu eV$ and reach the axion band.

A smaller experiment in Japan, CARRACK I (Cosmic Axion Research using Rydberg Atoms in a resonant cavity in Kyoto) has been built, using Rydberg atoms and has searched for axions at the 10μeV region. The experiment has been upgraded to CARRACK II, which intend to probe in higher mass ranges and cover masses between $2 - 50\ \mu eV$.

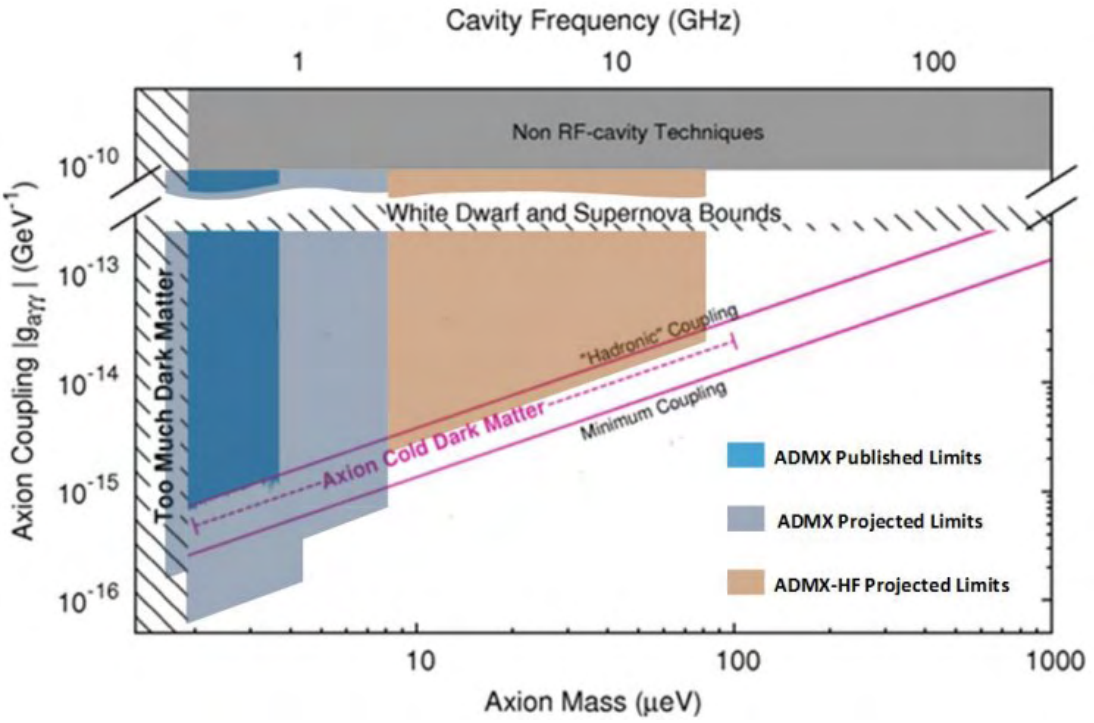

Figure 2.11 Axion exclusion plot showing published and "long term" projected sensitivity of ADMX and ADMX-HF programs. The KSVZ limit is called "hadronic" and the DFSZ limit is labels as Minimum coupling.

2.6 CAST as an Antenna for relic axions

The last years in CAST the idea of implementing at one of the magnet pipes end, a "dish antenna" that can transform CAST to an antenna for direct dark matter axions, is under development [35]. The Dish Antenna can be also used for Axion Like Particles (ALP's) and paraphotons. By using the antenna at the end of the CAST's magnet bore, the experiment is transformed to a suitable Haloscope for streaming axions and other exotica. The antenna reflective surface can effectively convert the dark matter particles into electromagnetic radiation emitted perpendicular to the surface as shown in the Figure 2.12. By using a spherical surface the emitted radiation is concentrated in the center of the sphere detector where it can be detected. The advantages of this setup over conventional resonant cavities searches are the following

- the emitted power is proportional to the surface area and therefore possible to scale up
- The setup is sensitive to the whole mass range in one measurement without the need to scan
- It provides sensitivity to higher masses that are difficult to access in cavity experiments

The limit for the axion mass provided for such a setup in the CAST experiment is

$$m_\alpha \geq 10^{-4} \frac{eV}{c^2} for\ \lambda \leq 1\ cm$$

In principle, the concentration mechanism is effective for the sensitivity of such an experiment as long as the diffraction is small. The wavelength of the incoming particle should be much smaller than the size of the dish antenna.

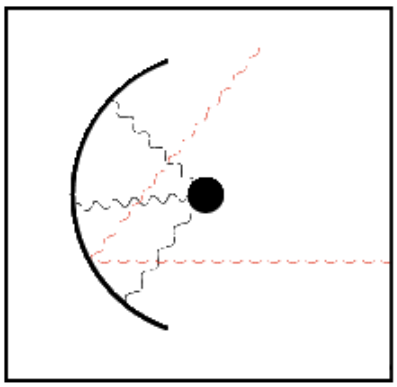

Figure 2.12 Non-relativistic dark matter particles are converted to monochromatic photons (black line) emitted from the surface of a spherical dish antenna. The electromagnetic radiation is focused in the center of the dish where a broadband detector is placed. The red line represents photons emitted from other boundaries or from distant sources that are typically not focused.

2.7 Optical and Radio Telescope searches

A search for optical line emission from the two-photon decay of thermally produced axions can be searched with optical telescopes. The two-photon coupling of the axion will lead to monochromatic line emission from axion decays to photon pairs. The axion life-time is much longer than the Hubble time, but the density of axions in a galaxy cluster is high enough so that the optical line emission of such decay could be detectable. This line should be detected through the density profile of the galaxy cluster. Telescope searches for this emission line were first attempted by observations of well-studied clusters (Abell 1413, 2218 and 2256) at Kit Peak National Observatory, in which a null search imposed an upper limit to the two-photon coupling of the axion in the mass window

$$3\ eV < m_{\alpha} < 8\ eV$$

Recent observations [128] using spectra of the galaxy cluster Abell 2667 (A2667) and Abell 2930 (A2930), obtained with the Visible Multi-Object Spectrograph (VIMOS) Integrated Field Unit (IFU) set up new upper limits to the two-photon coupling of the axion in the mass window

$$4.5\ eV \leq m_{\alpha} \leq 7.7\ eV$$

that is a limit where many improvement factors have been used. The collecting area of the telescope, the integration time and the observed collected area give a factor of ~13 more stringer bound than in Ref [37].

Radio telescope searches include axions that would have decayed into photons in the radio power spectra band. The assumption is that axions that decay in this radio emission line dominate potential walls. The radio telescope at the Haystack Observatory was able to rule out coupling constants of

$$g_{\alpha\gamma} < 1.2 \times 10^{-9} GeV$$

and axion masses in the range

$$298\ \mu eV\ \leq m_{\alpha} \leq 363\ \mu eV$$

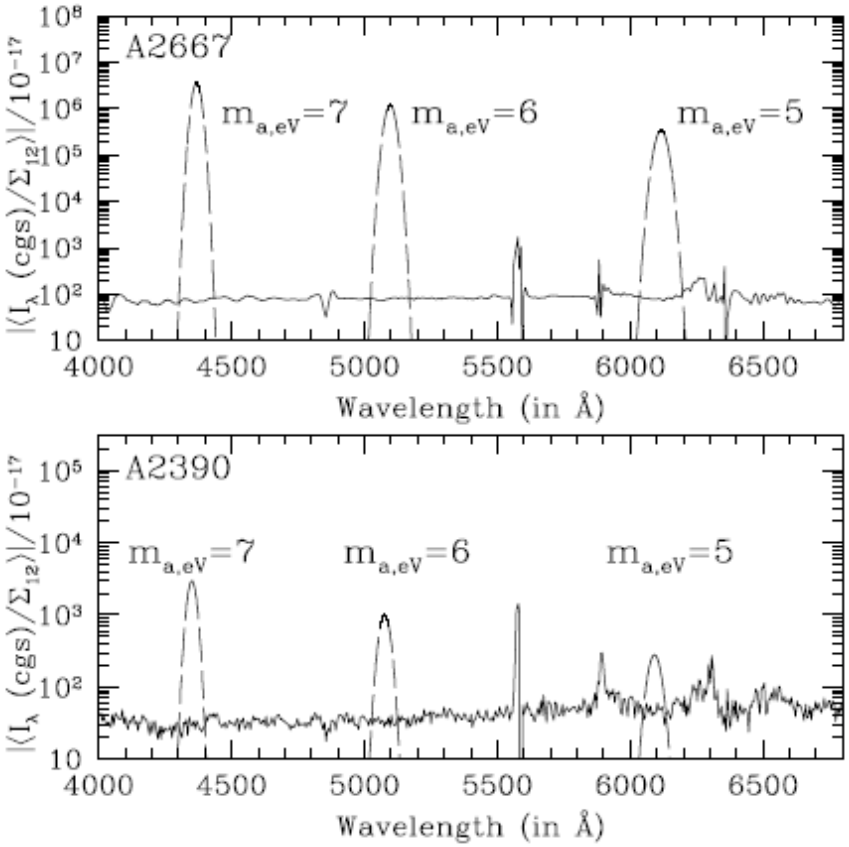

Figure 2.13 Constraints on intensity as a function of wavelength for A2667 and A2390. CGS units for specific intensity are $erg\ cm^{-2}s^{-1}\text{Å}^{-1}arcsec^{-2}$, and $\Sigma_{12} = \Sigma/\left(10^{12}M_{\odot}\text{pix}^{-2}\right)$, where Σ is the projected mass density of the cluster, measured using strong lensing. The over-plotted dashed lines are theoretical Gaussian spectra for axion decays, with central wavelength λ_0, corresponding to an axion mass of $m_{\alpha,eV} = 24{,}800\text{Å}(1+z)/\lambda_0$.

2.8 Laser Induced axion searches

While solar axion experiments probe axions that would escape from the Sun, laboratory laser experiments should produce axions from a polarized magnetic field in a transverse magnetic field. The production and detection mechanism is still the same: the Primakoff effect. In this way, purely laboratory bounds on axions or generalized pseudoscalars have also been established. In addition to astrophysical axion searches, laser-based experiments can also perform precise QED tests and search in parallel for other scalar or pseudoscalar (paraphotons, milicharged etc.) particles that couple to photons . The principle mechanism is that axions are produced through the interaction of polarized photons with the virtual photons of the applied magnetic field.

$$\gamma + \gamma_{virtual} \rightarrow \alpha$$

In general, laser based experiments can be divided to the following categories:

- the so called “Shining through the wall” or “photon regeneration” experiments
- Experiments that can probe the magneto-optical vacuum properties

2.8.1 Light shining through a wall

Axions can be coherently created by shining a light beam (usually laser) through a transverse dipole magnet, and reconverted to real photons in a collinear dipole magnet on the other side of an optical barrier (wall).

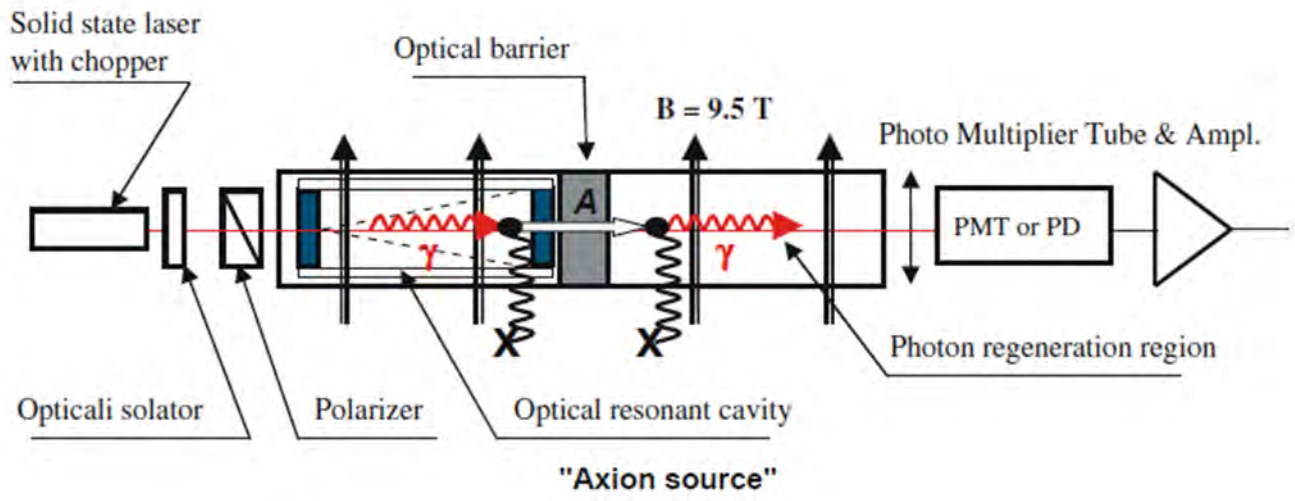

Figure 1.7: Schematic view of the principal of operation of “Photon regeneration” or “light shining through the wall experiments” [41]. A fraction of the laser photons can be transmuted to axions or similar. The laser light is absorbed by the wall while axions would pass it. A second magnetic field is used to reconvert the axions to photons.

This method performed by the Brookhaven-Fermilab-Rutherford-Trieste (BFRT) collaboration and since no signal was found they could set an upper limit of the coupling constant and the axion mass [41]

$$g_{\alpha\gamma} < 6.7 \cdot 10^{-7}\ GeV\ for\ m_{\alpha} < 10^{-3} eV$$

Current limits from photon regeneration can be set from a new experiment at CERN. The Optical Search for QED vacuum birefringence, Axions and photon Regeneration (OSQAR) experiment using two 15m long LHC superconducting dipole magnets could set an upper limit, constraining the coupling of scalar or pseudoscalar particles that can couple to two photons to be less than

$$g_{\alpha\gamma} < 8.0 \times 10^{-8}\ GeV^{-1}$$

2.9 Detecting the magneto-optical vacuum properties

The second kind of laboratory experiments searching for axions and axion-like particles is based on the theoretical prediction that these particles can affect the polarization of light that propagates in vacuum through a transverse magnetic field $\boldsymbol{B}$, because of their two photons coupling. If a light beam is linearly polarized at an angle θ with respect to magnetic field direction, it is expected to acquire an ellipticity Ψ (Linear birefringence) and a rotation Θ (Linear dichroism), according to the formula and as explained in the figure.

$$\Psi \approx N \frac{B^2 L^3 m_\alpha^2}{96\omega M^2} \sin(2\theta) \tag{2. 88}$$

$$\Theta \approx N \frac{B^2 L^2}{16 M^2} \sin(2\theta) \tag{2. 89}$$

where m_α is the axion mass, $M = 1/g_{\alpha\gamma\gamma}$ is the inverse of the coupling constant to two photons, ω is the photon energy, L is the effective path length and N is the number of paths that the light travels. Any result that could predict a measurable effect and an even small value for ellipticity and rotation, would manifest a deviation from the QED where no such effects are expected.

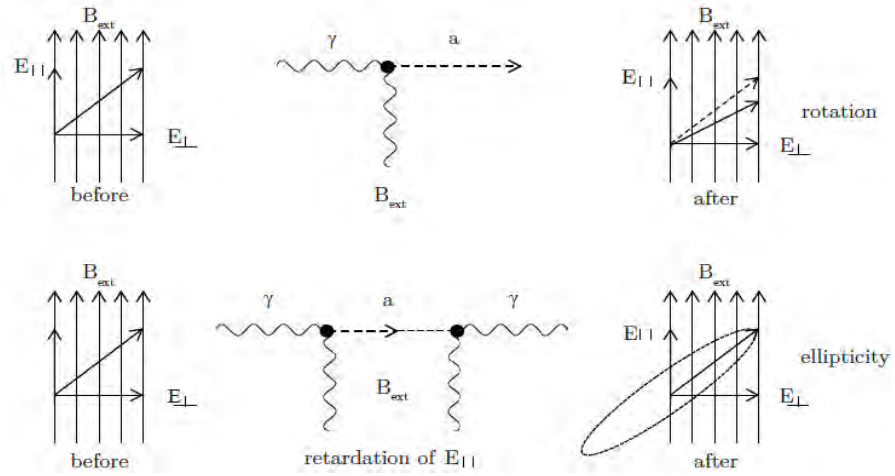

Figure 2.14 The axion induced linear dichroism (upper figure) together with linear birefringence (bottom figure) is portrayed.

The first attempt to search for axions using this method was carried out in the BFRT experiment, setting a bound on the axion-to-photon coupling constant

$$g_{\alpha\gamma\gamma} < 3.6 \times 10^{-7} GeV^{-1}$$

for axion masses

$$m_\alpha < 5 \times 10^{-4}\ eV$$

at the 95% CL.

The Polarizzazione del Vuoto LASer (PVLAS) collaboration [38] has been taking data to test the vacuum birefringence in a presence of a magnetic field having magnitude 5.5 T, created from a 1m long dipole magnet. In 2006 they claimed that they have found a signal for the amplitude of the rotation ε of the polarization plane, but later it was excluded by several experiments including PVLAS itself. [39]

2.10 Bragg diffraction experiments

A pioneering idea and a different approach to search and detect solar axions, was proposed by E. A. Paschos and K. Zioutas [42]. The detection principle uses the intense Coulomb field of the nuclei in a crystal lattice instead of an external magnetic field to convert axions to photons according to the Primakoff effect. The crystal can be used solely as an axion converter or as a thin film that covers a reflective parabolic antenna that focuses the converted photons on a detector in their focal plane. The electric field at $0.1\ \text{Å}$ from a nucleus with Z=10 is equivalent to a magnetic field of 5*10^5 T. The axion mass can be considered extremely small compared with the nucleus mass in the crystal so recoils from the crystal nuclei can be neglected. The differential cross section for the conversion is given by

$$\frac{\mathrm{d}\sigma}{\mathrm{d}\Omega} = \frac{g_{\alpha\gamma\gamma}}{16\pi^2} F_\alpha^2(\mathrm{q}) sin^2(2\Theta) \qquad (2.\ 90)$$

where 2Θ is the scattering angle and F_α is a form factor that describes the crystal atomic structure. Using the Sun as an axion source where the mean axion energy is $E_\alpha \sim 4\ keV$, the axion wavelength λ can be comparable to the lattice spacing d of the crystal (a few Å), so a Bragg-reflection pattern could be expected. Constructive interference can occur in the case where reflected waves from different lattices are in phase. The Sun is a moving source so care should be taken for the detector movement to be synchronized with the Sun's rotation so as to keep the entrance angle constant. There are several underground experiments using different detector materials such as Germanium (CDMS [43] SOLAX, COSME) or NaI(Tl) (DAMA) with their main purpose the search of WIMPs, but by analyzing their data they were able to provide mass-independent bounds to the axion to photon coupling.

$$g_{\alpha\gamma} < 2.7 \times 10^{-9} GeV^{-1} \text{ (SOLAX)}$$

$$g_{\alpha\gamma} < 2.8 \times 10^{-9} GeV^{-1} \text{ (COSME)}$$

$$g_{\alpha\gamma} < 1.7 \times 10^{-9} GeV^{-1} \text{ (DAMA)}$$

$$g_{\alpha\gamma} < 2.4 \times 10^{-9} GeV^{-1} \text{ (CDMS)}$$

The CDMS experiment is using Germanium and Silicon detectors and it can also search for galactic axions.

The bounds provided from the Bragg-diffraction experiments are in the same range and have a major advantage; its sensitivity does not depend on the axion mass. Nevertheless their sensitivity cannot compete with the sensitivity provided from the Helioscopes.

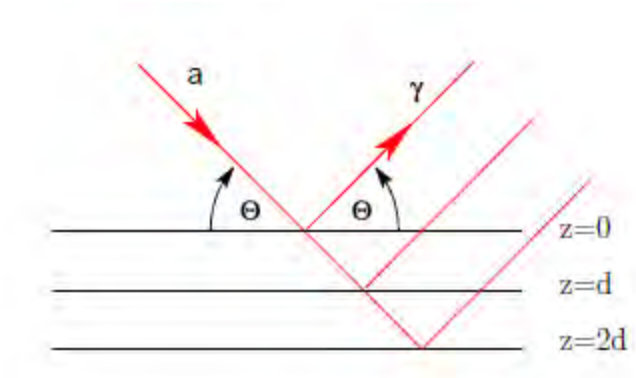

Figure 2.15 Schematic view of the axion Bragg-reflection from different layers in a crystal. The axion enters at an angle Θ. In the case that the Bragg condition holds, the reflected x-ray waves from different layers can interfere constructively and enhance the signal.

2.11 Axion Helioscope Experiments

The most sensitive experiments up to date are based on the idea presented by Sikivie in 1983 [46] and they are composed by a powerful magnet with their magnetic field transverse to the axion source; the Sun. Axions that are produced in the hot solar core, will reach the Earth after 500sec as a parallel axion beam. For the axion detection, they make use of the inverse Primakoff effect, i.e. $\alpha + \gamma_{virtual} \rightarrow \gamma$ where the axion interacts with the virtual photon provided by the transverse magnetic field and reconverted to a real photon that can be detected. The photons created in the magnet from the axion-to-photon conversion have the same energy and momentum as the incoming solar axions, so their energy distribution is the same to the solar axion energy spectrum scaled down by the conversion probability. A low energy X-ray detector can be used to detect the reconverted photons, placed at the end of the magnetic field and search for the axion signal above the detector background as shown in Figure 2.16. These kinds of experiments can search for axions in a wide mass range of

$$10^{-5} eV \leq m_{\alpha} \leq 1.16\, eV$$

The first axion helioscope was performed by Lasarus et al. [45] at the beginning of the 90's and they explored two regions in the mass range

$$g_{\alpha\gamma} < 3.6 \times 10^{-9} GeV^{-1}\ for\ m_{\alpha} < 0.03\, eV$$

and

$$g_{\alpha\gamma} < 7.7 \times 10^{-9} GeV^{-1}\ for\ 0.03 < m_{\alpha} < 0.11\, eV$$

Later on, an improved in sensitivity experiment of this kind (Tokyo Axion Helioscope) continued the search for solar axions setting a more restrictive limit at that time [46]

$$g_{\alpha\gamma} < 6 \times 10^{-10} GeV^{-1}\ for\ m_{\alpha} < 0.03\, eV$$

and

$$g_{\alpha\gamma} < 6.8 - 10.9 \times 10^{-10} GeV^{-1}\ for\ m_{\alpha} < 0.3\, eV$$

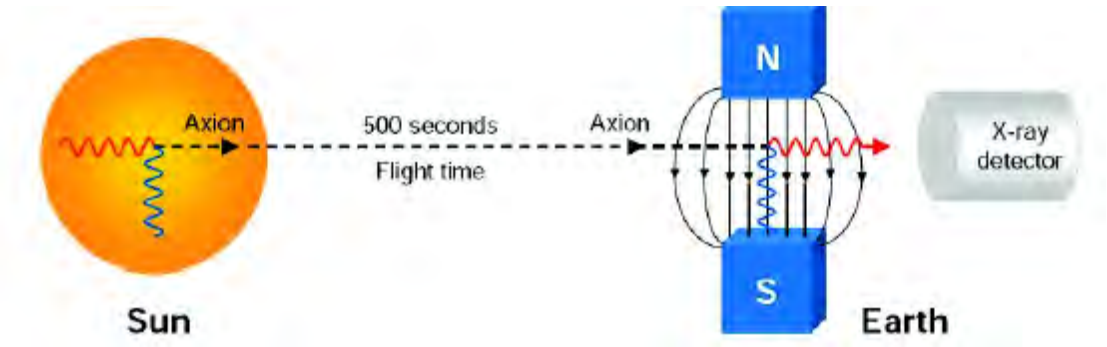

Figure 2.16 Detection principle of Sikivie's idea. The Sun is used as an axion source and the magnetic field converts the axions to detectable x-ray photons.

The CERN Axion Solar Telescope (CAST) is by far the most sensitive helioscope up to date and has provided the most restrictive experimental limits. It is the main topic of this thesis and will be fully described on chapter 4 where the research program of the past and the future is analyzed in detail and in parallel with the coupling limit values reached.

2.12 Axion Like Particles (ALP)

There are many theories that extend beyond the Standard model of particle physics and they have new symmetries. Anytime, one of them is spontaneously broken, if it is a global symmetry, a Goldstone or a pseudo Goldstone boson appears. An example is the lepton number symmetry that would produce majorons or symmetries related to particle flavor or the R-symmetry in supersymmetry. In general, in theories beyond the standard model there are many light scalar and pseudoscalar particles and since phases are dimensionless, the canonical normalized theories at low energies, always include the combination φ/f_φ where f_φ is the scale of the spontaneous symmetry breaking. We denote these new light particles as axion-like-particles (ALPs) for the scalar and pseudoscalar cases. [48]

The ALPs potential can be defined as

$$V(\varphi) = m_\varphi^2 f_\varphi^2 \left[1 - cos\left(\frac{\varphi}{f_\varphi}\right)\right] \tag{2. 91}$$

The new particle that we call φ, will couple to two photons. In case φ is a scalar

$$L'_{\varphi\gamma\gamma} = \frac{1}{4} g_{\varphi\gamma\gamma} F_{\mu\nu} F^{\mu\nu} \varphi \tag{2. 92}$$

and when φ is pseudoscalar

$$L_{\varphi\gamma\gamma} = \frac{1}{8M}\varepsilon_{\mu\nu\,\rho\sigma}F^{\mu\nu}F^{\rho\sigma}\varphi \quad (2.\ 93)$$

In general, there is no relation between the mass of the ALP particle and its couplings, as it is for the axion. Through analyzing ALP models we can focus in two independent parameters which are the mass of the light particle and the energy scale M of the new physics. It is convenient to focus on the coupling of the light particle to two photons as this is the case used by most experiments searching for axions. The bounds of the ALPs are looser than those of axions as in the case of the SN1987A because one assumes only the $\varphi\gamma\gamma$ coupling, and measurements from the Solar Maximum Mission satellite, imply a bound on the coupling

$$M > 3 \times 10^{11}\ \mathrm{GeV} \quad (2.\ 94)$$

In the same way based on coherent axion-photon conversion in a strong magnetic field that Sikivie realized, ALP can couple to two photons. In the case that the particle is a pseudoscalar one can define

$$L_{\varphi\gamma\gamma} = g_{\varphi\gamma\gamma}E \cdot B\varphi \quad (2.\ 95)$$

while in the scalar case

$$L'_{\varphi\gamma\gamma} = \frac{1}{2}g_{\varphi\gamma\gamma}(E^2 - B^2)\,\varphi \quad (2.\ 96)$$

Both, axions and ALPs, induce photon-ALP transition in a strong external magnetic field. The probability of the $\varphi - \gamma$ transition is always multiplied by the factor $1/M^2$. If $\varphi - \gamma$ conversion in the magnetic field is coherent, the probability P is enhanced. This conversion is coherent provided that there is an overlap in the wave functions of the axions and photons while they are propagating in a linear path of distance L, i.e.

$$\left|k_{\gamma\prime} - k_{\varphi\prime}\right|L < 2\pi \quad (2.\ 97)$$

Then the probability of conversion becomes

$$P(\gamma \to \varphi) = \frac{1}{4}g^2_{\varphi\gamma\gamma}B_T^2L^2 \quad (2.\ 98)$$

3. Solar Axions

3.1 Axion flux from the Primakoff conversion in the Sun

Standard Solar Model explains the stellar nucleosynthesis and provides the physics of the energy source and energy losses in stars. Hans Bethe, winning the Nobel Prize for his paper "Energy Production in Stars" in 1939, revealed the two main processes of stars energy loss: the proton-proton chain and the Carbon-Nitrogen-Oxygen cycle. Proton-proton chain can provide more than 98% of the energy required to produce the observed solar luminosity. Fusion reactions from the proton-proton chain in the solar core produce a vast amount of heat with T_C ~ $1{,}55\times10^7$ K. Solar core is about 20% of the solar radius and has a density 156 g/cm^3. The plasma frequency in the solar core is ~ 0.3 keV and near the solar center, the Debye-Huckel radius is κ~ 9keV [49].

The Sun is a powerful axion (or axion like particles) source because the solar core can offer the electric fields of nuclei and electron targets in its hot plasma, that will consequently convert photons to axions due to the *E*B* fluctuation caused by the presence of electromagnetic radiation as also by the collective and random motion of charged particles [52]. The magnetic field term can be provided by the propagating thermal photons. Small momentum transfer cases produces axions via coherent plasma field fluctuations [56] while the large momentum transfer can be viewed as the manifestation of the Primakoff effect in Figure 3.1

$$\gamma + (e^-, Ze) \rightarrow (e^-, Ze) + \alpha \qquad (3.\ 1)$$

Recoil effects can be neglected because of the small photon energies (few keV) compared to the electron mass.

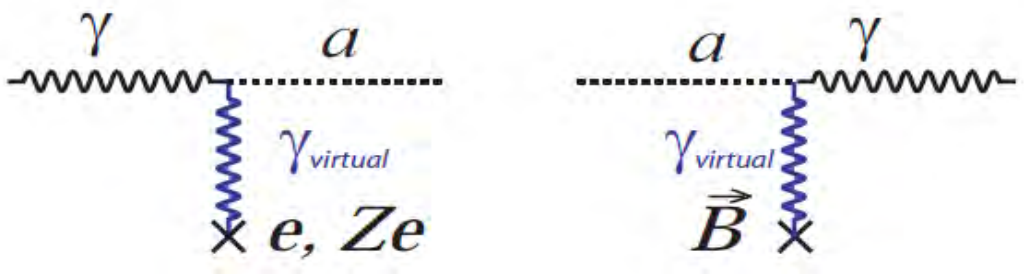

Figure 3.1 On the left is presented the Feynman diagram of the incoherent Primakoff effect by the interaction with a virtual photon by an electric field produced by a nuclei or a certain electron density in the solar core, while on the right the diagram represents the inverse laboratory process for the axion detection that is the coherent process in a magnetic field. The external magnetic field compensates the spin and momentum mismatch in case of axion-photon oscillation [56]

Standard Solar Model provides us information for the energy loss channels of the axion interactions and the solar fluxes derived can consider the Primakoff effect as the manifestation of the axion production mechanism in the Sun.

In the solar core, a charge distribution $\vec{\rho}$ is able to provide an external electric field $\vec{E}$ in which a photon of energy $\omega = kc$ could convert into an axion. The differential cross section ignoring recoil effects for a target charge Z·e is:

$$\frac{d_{\sigma_{\gamma\to\alpha}}}{d\Omega} = \frac{g_{\alpha\gamma}^2 Z^2 \alpha}{8\pi} \frac{\left|k_\gamma \times k_\alpha\right|^2}{q^4} \tag{3. 2}$$

where q = $k_\gamma - k_\alpha$ is the momentum transfer while the axion and photon energies are the same. It is clear that the maximum differential cross section is reached when the axion-photon interaction is transversal. The calculation of the solar axion flux is straightforward but the screening effects of the long range Coulomb cut off should be included. The differential cross section is modified by a factor

$$q^2/(k_S^2 + q^2) \tag{3. 3}$$

In the non-degenerate solar plasma core the screening scale is expressed by the Debye-Hückel formula

$$\kappa_S^2 = \frac{4\pi\alpha}{T}\left(n_e + \sum_{nuclei} Z_j^2 n_j\right) \tag{3. 4}$$

where n_e is the electron density and n_j is the density of the jth ion of charge Z_j and κ_S modifies the Coulomb potential as

$$V(r) = \frac{Ze}{4\pi} \cdot \frac{e^{-\kappa_S r}}{r} \tag{3. 5}$$

The transition rate of a photon of frequency ω into an axion of the same energy can be derived by summing over all targets assuming non-relativistic plasma

$$R_{\gamma\to\alpha} = \frac{g_{\alpha\gamma}^2 T \kappa_S^2}{32\pi}\left[\left(1 + \frac{\kappa_S^2}{4\omega^2}\right)\ln\left(1 + \frac{4\omega^2}{\kappa_S^2}\right) - 1\right] \tag{3. 6}$$

The effective photon mass and the axion mass are considered very small compared to the energy *E.* The energy loss per unit volume is calculated by integrating the decay rate

$$Q = \int \frac{2d^3\overrightarrow{k_\gamma}}{(2\pi)^3} \frac{\Gamma_{\gamma\to\alpha} E}{e^{E/T} - 1} = \frac{g_{\alpha\gamma}^2 T^7}{4\pi} F(k^2) \tag{3. 7}$$

where *F* is a function of order unity. From the transition rate, van Bibber et al [52] integrated the energy loss equation over the solar model to calculate the axion luminosity.

$$L_\alpha = g_{10}^2 1.7 \times 10^{-3} L_\odot \tag{3. 8}$$

Where $L_\odot$ is the solar luminosity and $g_{10} = g_{\alpha\gamma} \times 10^{10}$GeV. In order to obtain the differential flux of axions on Earth, the transition rate must be folded over the blackbody photon distribution of the Sun and by integrating over a standard solar model Raffelt [49] calculated the total differential axion flux

$$\frac{\mathrm{d}\Phi_\alpha}{\mathrm{d}E} = g_{10}^2 6.0 \times 10^{10} cm^{-2} s^{-1} keV^{-1} E^{2.481} e^{-E/1.205} \tag{3. 9}$$

where E_α is measured in keV. It is essentially a blackbody distribution of the thermal conditions in the solar interior. The differential axion flux presents a maximum at 3 keV and has a mean energy value of <E_α> = 4.2 keV. The reason for the higher energy values reached than that in the solar core (kT ~ 1 keV) is that the low energies are suppressed in total by a factor of ~ 25 due to the screening effects.

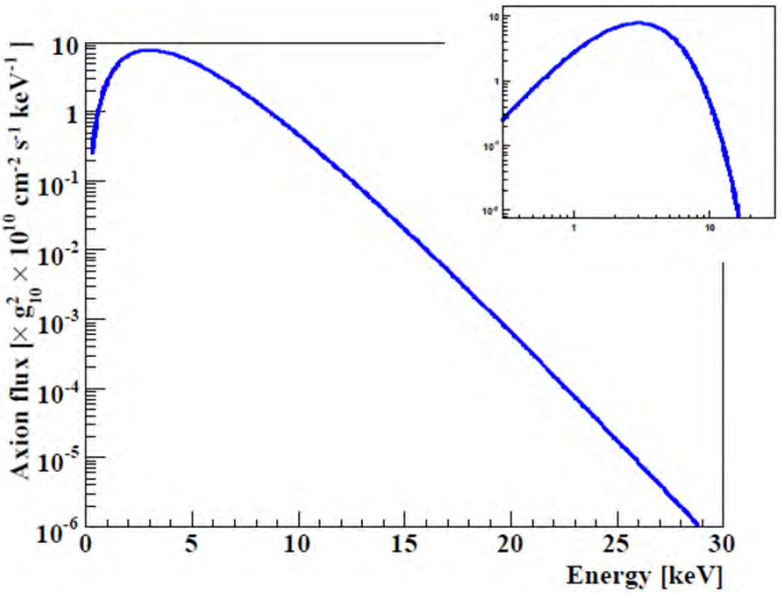

Figure 3.2 The differential solar axion flux on Earth from the Primakoff conversion of photons in the Sun plotted in log-linear and inverted log-log scales. The maximum axion intensity is reached at 3 keV while the average axion energy is <E_α >= 4.2 keV. The sub-keV energy range was experimentally not accessible before. Axion Helioscopes are best suited for low energy searches because the screening effects that appear in dense materials are quasi-suppressed.

Axion emission from the Sun is directly related with its plasma core temperature and since there is a gradient of the interior temperature, the flux of axions relative to the Sun radius is considered. The flux is also calculated according to the blackbody radiation spectrum applied to the temperature of the solar core (Figure 3.2).

3.2 Axions Detection Principle

Solar axions detection with Helioscopes is based on the inverse coherent Primakoff effect (Figure 3.1). The solar axions that escape from the Sun will be re-converted to x-ray photons in the presence of a strong transverse magnetic field. The conversion is only effective when the polarization of the outcoming photon is parallel to the magnetic field that has to be transversal to the propagating axion [53]. The axion field *α* is characterized by its amplitude and in case where it is propagated in a media along the *z* axis the relation of the field state is given by the relation

$$i\partial_z \begin{pmatrix} A \\ \alpha \end{pmatrix} = \begin{pmatrix} \frac{E_\alpha - m_\gamma^2}{2E_\alpha - i\Gamma/2} & \frac{g_{\alpha\gamma}B}{2} \\ \frac{g_{\alpha\gamma}B}{2} & \frac{E_\alpha - m_\gamma^2}{E_\alpha} \end{pmatrix} \begin{pmatrix} A \\ \alpha \end{pmatrix} \tag{3. 10}$$

Where A is the parallel photon component, B is the transversal magnetic field, Γ is the inversion absorption length for x-rays in the medium and m_γ is the effective photon mass corresponding to the plasma frequency, that is given by the buffer gas as a function of the number of electrons, which is expressed as $(\hbar = c = 1)$

$$m_\gamma = \omega_p = \sqrt{\frac{4\pi\alpha n_e}{m_e}} \tag{3. 11}$$

Where n_e is the number of electrons of the buffer gas and it is related with the gas density according to the relation

$$n_e = Z\frac{N_A}{W_A}\rho \tag{3. 12}$$

In this relation Z is the gas atomic number and W_A is the atomic weight. The relation 3.11 can be re-written as a function of the gas density

$$m_\gamma \left[\frac{eV}{c^2}\right] \cong 28.77 \sqrt{\frac{Z}{A}\rho \left[\frac{g}{cm^3}\right]} \quad (3.\ 13)$$

The axions that have been transformed to photons in the buffer medium inside the magnetic field can be seen in X-ray detectors located outside the magnetic field region. The number of photons that is expected to reach these detectors is given by the relation

$$N_\gamma = \int \frac{\mathrm{d}\Phi_a}{\mathrm{d}E} P_{\alpha\to\gamma} A t \mathrm{d}E \quad (3.\ 14)$$

Where $\mathrm{d}\Phi_a/\mathrm{dE}$ is the solar axion spectrum expected at the Earth, $P_{\alpha\to\gamma}$ is the probability of axion-to-photon conversion, t is the time of observation and A is magnet aperture area.

The conversion probability for a uniform optical medium inside a transverse homogeneous magnetic field extend of coherence length L can be expressed as [52]

$$P_{\alpha\to\gamma} = \left(\frac{g_{\alpha\gamma}B}{2}\right)^2 \frac{1}{q^2 + \Gamma^2/4}\left[1 + e^{-\Gamma L} - 2e^{-\Gamma L/2}\cos qL\right] \quad (3.\ 15)$$

The photon mass m_γ has been encoded in the momentum transfer of the axion–photon interaction and is given by the relation

$$q = \left|\frac{m_\gamma^2 - m_\alpha^2}{2E_\alpha}\right| \quad (3.\ 16)$$

In case where the medium inside the magnetic field region is vacuum it follows that $\Gamma = 0$, $m_\gamma = 0$ and the momentum transfer becomes

$$q = \frac{m_\alpha^2}{2E_\alpha} \quad (3.\ 17)$$

In the next figure, the axion conversion probability is plotted against the axion rest mass by assuming an axion coupling constant of $g_{\alpha\gamma\gamma}$=1×10^{-10} GeV^{-1}.

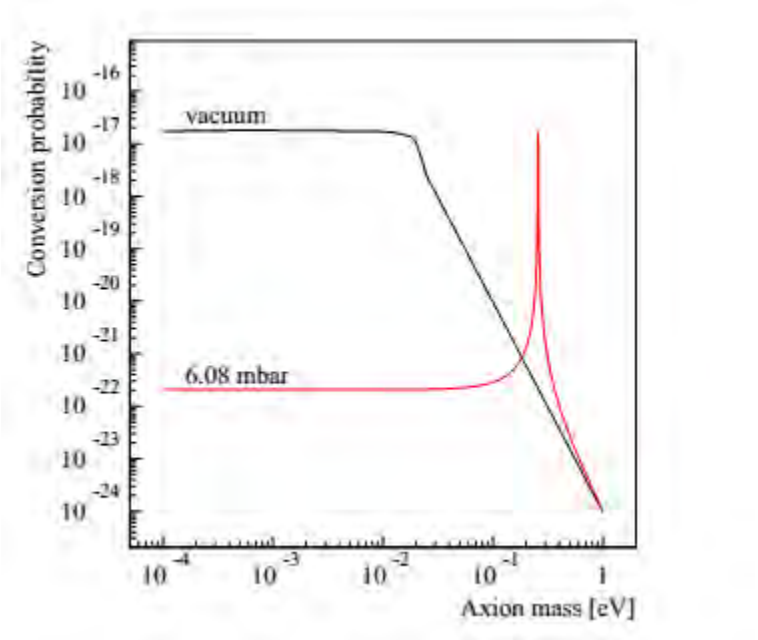

Figure 3.3 In black, the line shows the conversion probability inside a 10 m long pipe of magnetic field at 9T. Above the limit of the axion mass in the vacuum (m_α<0.02 eV) the conversion efficiency breaks down because of deconstructive interference. In red line, the conversion probability is shown for a specific Helium density. The resonance curve has a very narrow width for which coherence is restored over the whole magnetic length.

The maximum conversion probability can be achieved in case of zero momentum transfer $(q \to 0)$, where both axion and photon field remain at phase over the magnetic field length. This coherence condition is met when $qL \leq \pi$ which yields an axion limit in vacuum of $m_\alpha < \sqrt{2\pi E_\alpha / L}$. This limits CAST to the axion mass sensitivity in vacuum at $m_\alpha < 0.02$ eV. In case where the magnetic field region of CAST is filled with a buffer gas the coherence condition is fulfilled in a narrow mass range

$$\sqrt{m_\gamma^2 - \frac{2\pi E_\alpha}{L}} \leq m_\alpha \leq \sqrt{m_\gamma^2 + \frac{2\pi E_\alpha}{L}} \qquad (3.\ 18)$$

3.3 Axion-electron coupling

In non-hadronic axion models however, where there is a tree-level axion-electron interaction, the Sun can produce a strong flux by bremsstrahlung, Compton scattering and axio-recombination, a process that is known as the "BCA process". In the DFSZ non-hadronic axion model, axions can couple to electrons and thus new axion-production channels are opened in stars, which could be more effective than the Primakoff effect. The most important processes summarized are:

- The Primakoff effect: $\gamma + Q \rightarrow Q + \alpha$
- Compton scattering: $\gamma + e \rightarrow e + \alpha$
- Electron-Ion bremsstrahlung (free- free transition): $e + I \rightarrow e + I + \alpha$
- electron-electron bremsstrahlung: $e + e \rightarrow e + e + \alpha$
- Axio-recombination (free- bound transition): $e + I \rightarrow I^- + \alpha$
- Axio-deexcitation (bound – bound transition): $I^* \rightarrow I + \alpha$

where Q refers to any charged particle, e for electrons, I for ions and I^* is the excited ion state.

The Primakoff effect dominates when coupling to electrons is absent at the tree-level. When this is not the case the BCA process dominates.

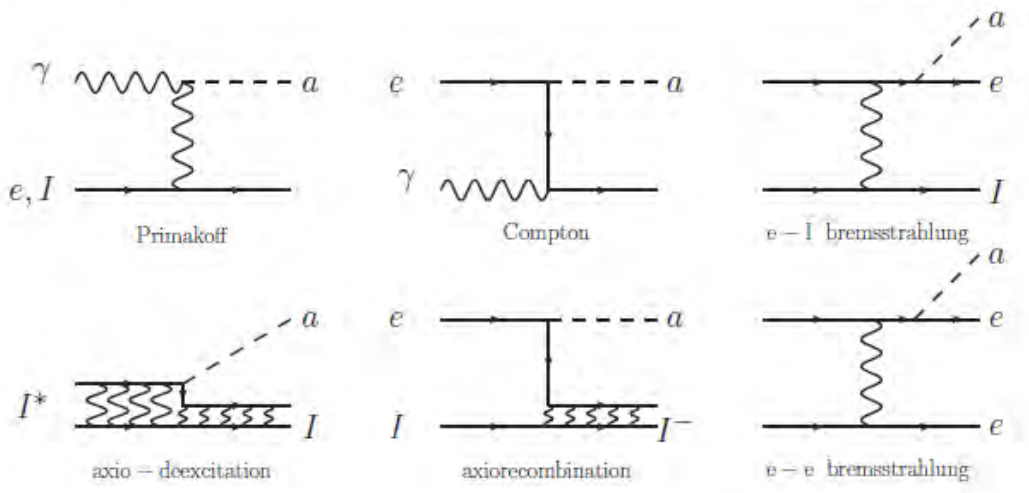

Figure 3.3 The Feynman diagrams for the processes of solar axion emission. The Primakoff effect depends on the two-photon coupling. BCA process comes from bremsstrahlung on hydrogen and helium nuclei for low energy axions when the Primakoff effect is absent, axio-recombination of metals (O, Ne, Si, S and Fe) contribute at intermediate energies and Compton take over for higher energies. Axio-deecxitation is mainly dominated by Lyman transitions and the axion flux energy peak ~ 6.5 keV.

The total solar axion flux on Earth including all the processes mentioned above can be represented in the following figure [61]

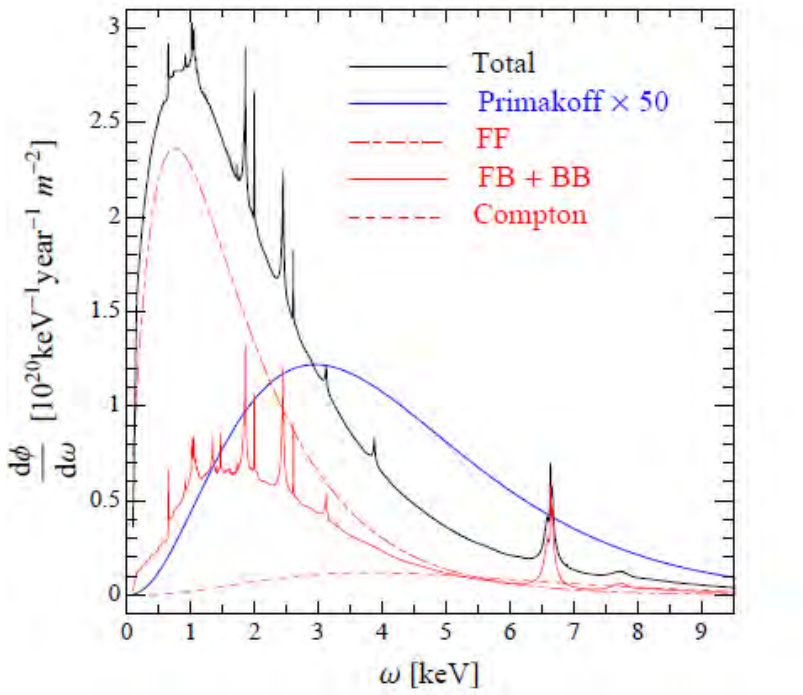

Figure 3.4 A DFSZ model solar axion flux on Earth with interaction strength to electrons g_{ae} =10^{-13} GeV. The blue line corresponds to the Primakoff flux scaled by a factor of 50, and the red lines show the different components of the BCA flux. FF is free-free (bremsstrahlung), FB is the free-bound (axio-recombination) and BB is the bound-bound(axio-deexcitation). The black line represents the total flux.

In the analysis of CAST data in search for non-hadronic axions, there was set a new upper bound on g_{ae}×$g_{a\gamma}$, that is the product of the electron-axion coupling and the two-photon coupling. For axion masses $m_a \leq 10$ meV CAST data analysis constrains

$$g_{a\gamma} \times g_{ae} < 8.1 \times 10^{-23}\text{GeV}^{-1}(95\%\ \text{CL})$$

4. The CAST Experiment

Introduction

The CERN Axion Solar Telescope situated at the LHC Point 8 of CERN (**C**onseil **E**uropéenne pour la **R**echerche **N**ucléaire) is an axion helioscope that aligns a traverse magnetic field created from a decommissioned LHC (Large Hadron Collider) superconductive dipole magnet to the solar core; i.e. allows the axion to photon conversion according to the Primakoff effect. The magnet is installed on top of a moving platform and can move vertically and horizontally in order to align with the Sun twice a day (during sunrise and sunset) for about 1.5 hours each time. The twin aperture LHC magnet is about 10m long and can reach a field of 9T [57]. This prototype magnet is fabricated to have its bores straight in comparison with standard LHC magnets, so that their bores are bended in order to have all together (~2700 magnets) the LHC machine radius of curvature. In each end of the bore tubes four low-background X-ray detectors are mounted in order to identify converted X-ray photons generated in the strong magnetic field. These state of the art detectors are implemented by the CAST collaborators in places like Paris (Saclay), Saragossa (University of Saragossa), Athens (NTUA), Thessaloniki (Aristotle University) and Geneva (CERN), improving their sensitivity, reducing their background as also updating the analysis code and upgrading their data acquisition systems and electronics.

4.1 CAST magnet set-up

A decommissioned LHC superconductive magnet forms the basis of the CAST experiment. Each bore of the twin aperture prototype magnet has a cross section area A = 14.5 cm^2 and the applied nominal field is 9T over a length of 9.26 m. A schematic view of the cross-section of the CAST magnet is shown in Figure 4.1

The high magnetic field of this magnet is provided by a current of over 13kA and the magnet has to be operated at a temperature of 1.8K (niobium-titanium coils become superconductive below 4.5K). This temperature can be achieved by a whole cryogenic plant in order to cool down the dipole magnet and keep it superconductive. The cooling systems needed to support and maintain the operation of the magnet were adapted from the dismounted e^+e^- LEP collider and DELPHI, while a new purchased Roots pumping group provides the final stage of cool down and operation.

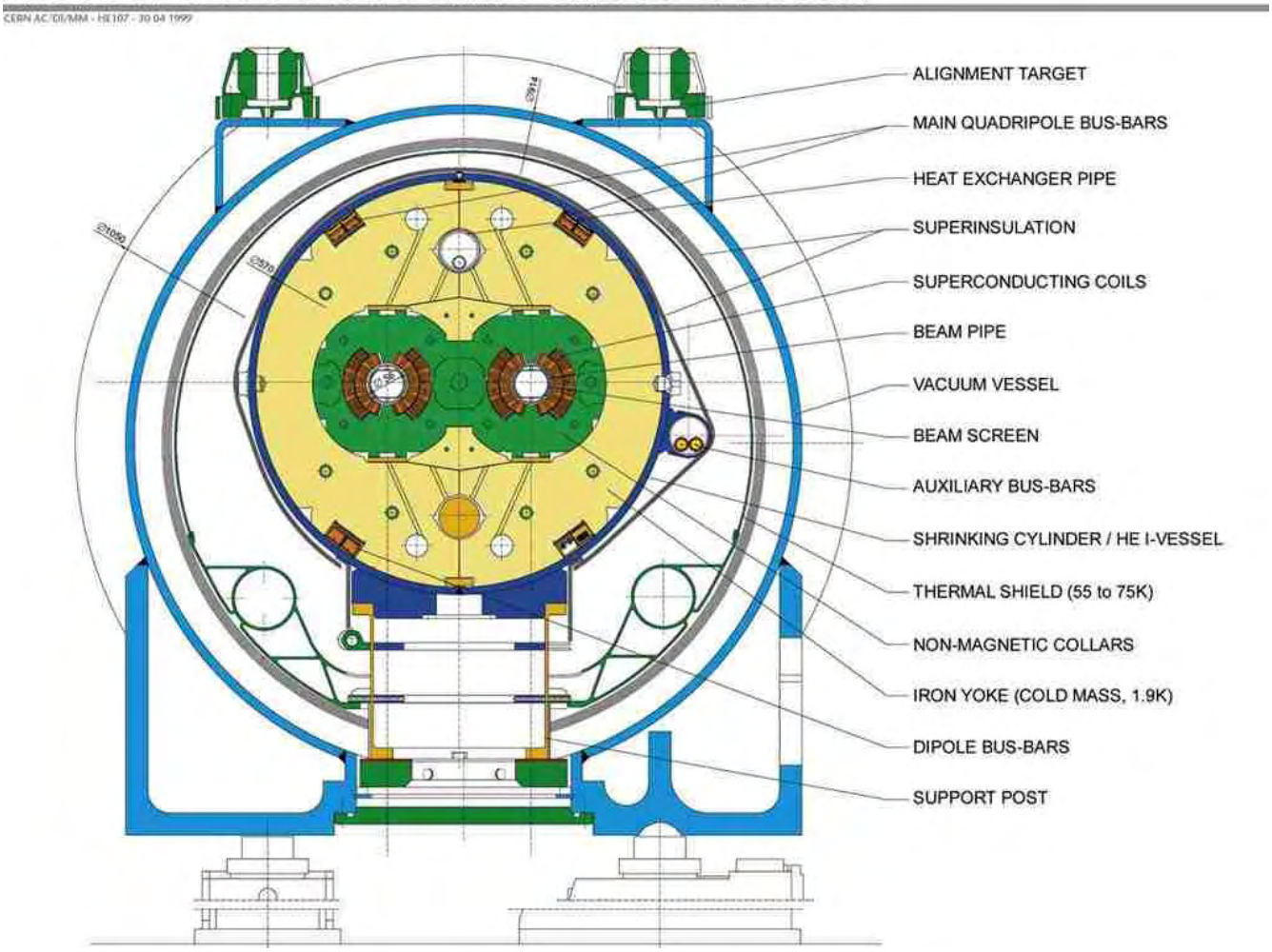

Figure 4.1 Cross-section of the CAST magnet

In Figure 4.2 the orientation of the magnetic field and its strength that is position dependent is shown inside the magnetic cross section.

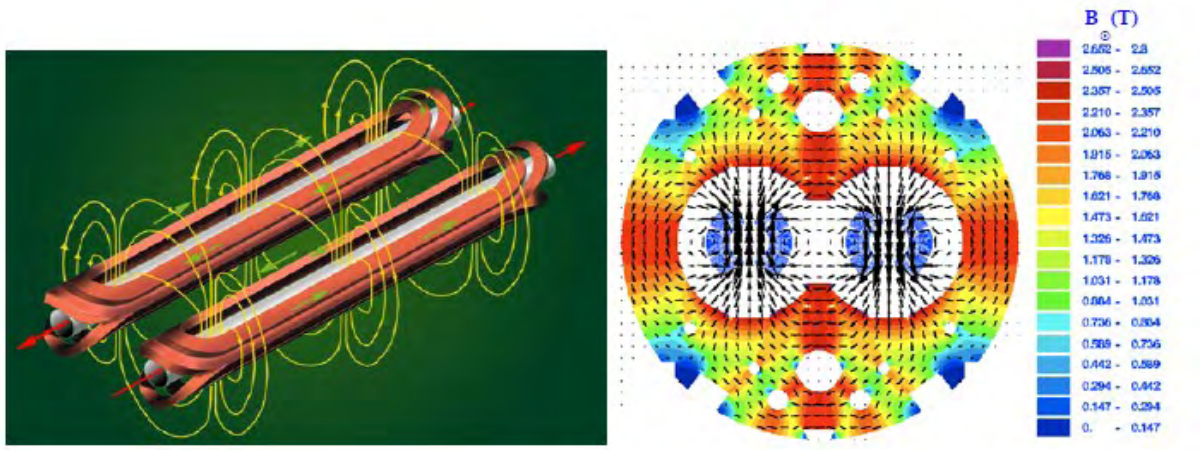

Figure 4.2: The magnetic field configuration of the CAST dipole magnet.

The Magnet Feed Box (MFB) is fixed on top of the magnet towards its western end (see Fig 4.3) supplying the magnet with all needed cryogenic and electrical feeds while the other side of the dipole is closed by the Magnet Return Box (MRB, see Fig. 4.3). The MFB is connected to the liquid helium supply, the gaseous helium pumping group and the quench recovery system via seven flexible transfer lines as shown in the left picture of fig 4.3. The transfer lines were designed to allow the magnet movement without any interruption of the helium flow. The “Potence”, a movable gibbet is required for the power supply lines movement.

The magnet bores, denominated also as *cold bores*, are isolated from the environmental temperature via the isolation vacuum inside the cryostat where liquid nitrogen flows and cools down the system to about 77K in a first cooling stage. Further details of the cryogenics can be found in Ref. [58]

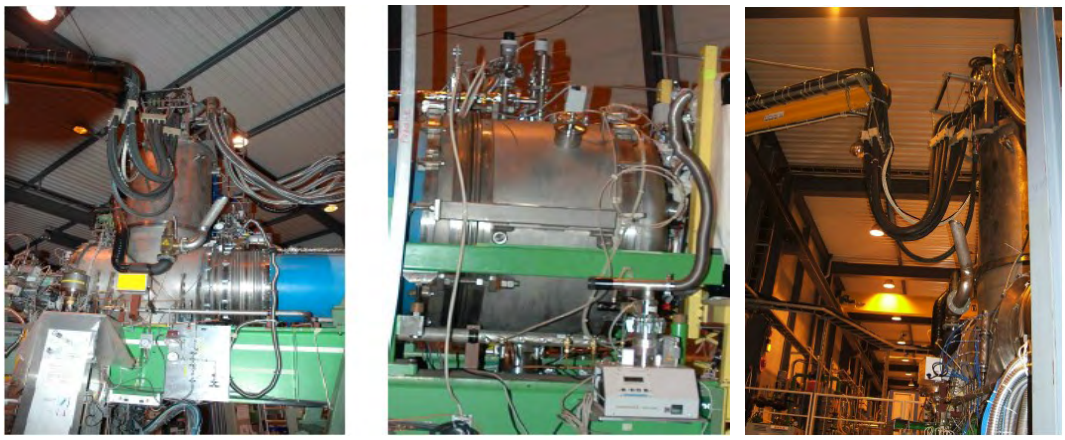

Figure 4.3: Image of the CAST’s Magnet Feed Box (MFB) on the left, the Magnet Return Box (MRB) in the middle and the Potence gibbet for the power supply lines on the right.

A very important part of the cryogenic system is the quench recovery system that is activated when there is a sudden change in the superconductive coil and a part of it enters in its resistive state. Certain cases, like a power cut or a fluctuation of the current, can lead the superconductor to its normal-conductive state in which an electric resistance occurs. In this situation the magnet temperature increases rapidly and so does the pressure inside the dipole. In order to prevent both the cryogenic plant and the magnet from damage, a fast discharge of the current is triggered along with the closing of the liquid helium supply valve. The heat that is generated by the Joule effect is dissipated during the quench by the presence of cold helium in the magnet cryostat. When a quench is triggered Helium gasifies and generates an overpressure of Helium gas in the cryostat that must be released as it is shown in figure 4.4



Figure 4.4 Quench in the CAST experiment. In the case of a sudden change of the magnet from its superconducting state to its normal-conducting state the cooling helium is released in order to protect the system from damage.

After a quench, the re-start of the automatic cool-down system is necessary in order to achieve the 1.8K in the cold mass plant (that was warmed up to 40K as a result of the dumped energy). This procedure requires a manual acknowledge by the operator and it usually takes 6-8 hours to accomplish.

4.2 Vacuum System

A system of vacuum pumps is connected to the CAST magnet setup in order to evacuate the cold bore while the detector vacuum is pumped independently. There are in total four gate valves (VT1-VT4), each one installed at every detector bore end, in order to separate the cold bore from the detector side. The detector vacuum is the vacuum between each detector and the corresponding gate valve. The gate valves separate the detector vacuum from the CAST general vacuum. The CAST general vacuum is separated by the cold bore area where the buffer gas is included by the Cold windows as shown in figure 4.6. Blue color dedicates the cryostat vacuum that provides thermal insulation of the cold magnet and the cooling helium system against ambient temperature. A system of interlocks provides the function algorithm in parallel with a PLC (Programmable Logic Controller) for the pn-CCD detector. The interlocks system automatically protects the vacuum setup, the buffer gas, the detectors vacuum side and the cryostat whenever a problem occurs. Various pressure probes and the corresponding

gauges are installed to the vacuum as also in the buffer gas system and they are able to send warnings or alarms in cases of irregularities in the experiment or even in a possible vacuum breakdown. The interlock system will close the gate valves (VT1-VT4) and thus can protect the whole system. Other alarms can be triggered in case of a quench, where a proper sequence of logic interlock functions protects the magnet and the vacuum system from damage. This safety protection system is also triggered in case of a gaseous leak, a vacuum malfunction or even CAST user erroneous manipulations.

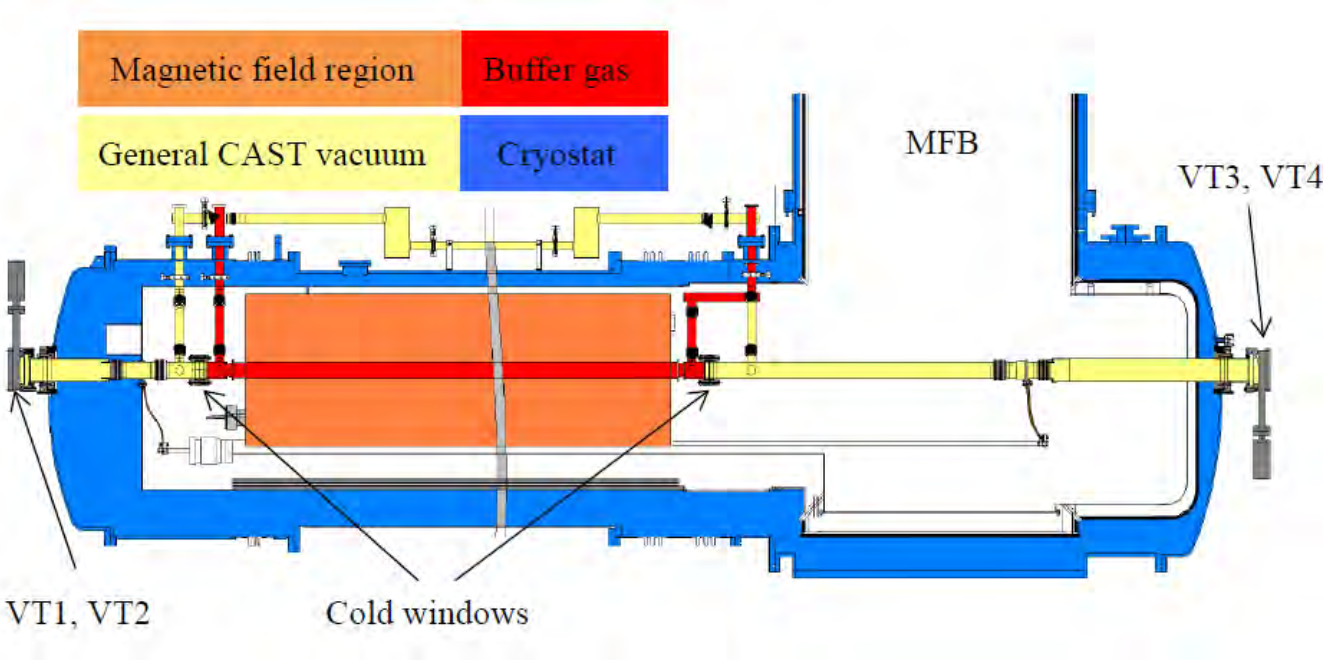

Figure 4.6 Different vacuum systems of the CAST magnet.

The vacuum system is also equipped with two residual gas analyzers (RGA) in order to detect any possible gaseous leak in the CAST vacuum system. They are working as mass spectrometers and allow the real time identification of various gases that can be found in the CAST magnet.

4.3 Solar tracking system

CAST platform movement

CAST as an axion helioscope has to track the solar core with an accuracy of better than 0.01º. In order to achieve this accuracy an extremely precise system is essential to move the CAST setup with its weight that is over 40 tones. A movable platform (girder) was built in order to allow the magnet to track the Sun for the longest possible period (and so increase the data taking time). The magnet is supported by the moving platform which consists of two metallic supports and thus allows the movement of the whole structure horizontally and vertically as it is shown in Figure 4.7.

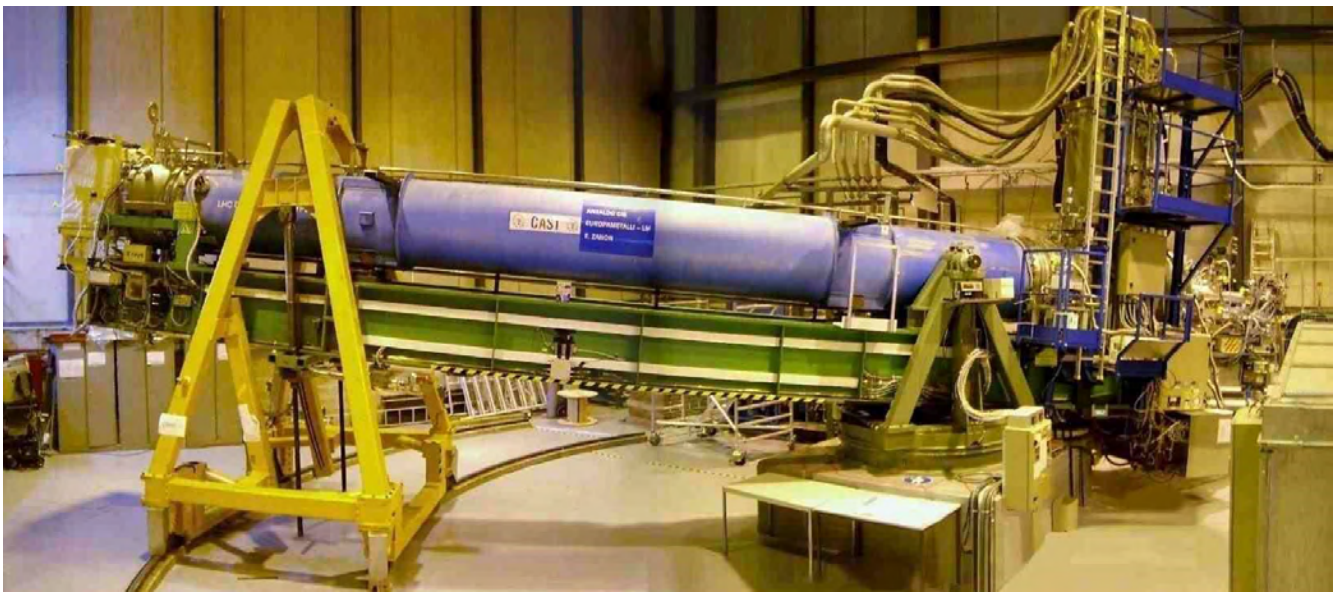

Figure 4.7 The CAST 10m magnet is moving sitting on a platform that is adjusted on a turntable on the right (that allows the magnet to move ±40º horizontally) and a girder on the left that using two screws can move the magnet vertically ±8º. The turntable can hold the weight of the MFB where the flexible helium transfer lines do not disturb the cryogenic operation, while the less weighted MRB side is held by the screws of the girder.

Mechanical constraints were imposed by the magnet manufacturer taking into account the magnet cryogenics. The mechanical strains in the cryostat that sits inside the metallic vessel (blue color in figure 4.7), which is connected via thermally isolated feet, put a maximum allowed limit for the vertical movement of the platform and it is constrained to ±8º. Mechanical constraints allow the magnet to be aligned with the Sun for approximately 3 hours per day (1.5 hour during sunrise and the same time during sunset).

Solar tracking

The movable platform is roll along by two motors (accompanied by two encoders each), one of them is responsible for the vertical movement and it is used to rotate two lifting jacks in the MRB side, while the horizontal movement is achieved by using the other motor (also placed in the yellow girder). In order to track the Sun, the motorized system is taking orders from a software program that directs the magnet. This software is also responsible to move the magnet or to point it to any other direction like the center of the galaxy. To perform a tracking for data taking, CAST makes use of the ephemeris of the Sun.

An ephemeris is a look up table that provides the position of celestial bodies like the Sun or planets at a given time. In order to calculate the Sun's ecliptic[4] CAST uses NOVAS (Noval Observatory Vector Astrometry Subroutines) software that is provided by the U.S. Naval Observatory [54]. CAST uses NOVAS that is implemented in the LabView (Laboratory Virtual Instrumentation Engineering Workbench) control software for tracking. The tracking software system guides the magnet movement and it also records all the necessary information (ambient temperature, pressure and the magnet field intensity, tracking or no tracking) about data taking conditions to log files that later can be used as input for the data analysis. The software reads out the time and date of the computer and can calculate exactly the azimuth (AZ) and zenith distance (ZD) of the Sun for the specific CAST coordinates[5] at every minute. The AZ and ZD values can be transformed into motor encoder values V_x(AZ,ZD) and V_y(AZ,ZD) with an accuracy of 0.001º. This accuracy is achieved with the help of the surveyors of the EST[6] division at CERN by recording a large number of magnet positions and converting them to encoder values (1 vertical encoder unit = 30μm of magnet movement, 1 horizontal encoder unit = 35μm of magnet movement).

Gaps between discrete data points provided by the surveyor's measurements can be filled by using the spline interpolation.

The magnet movement has also many emergency stops in the magnet setup to prevent any damage. These stops are hardware switches as also software limits to magnet positions beyond the proper safety angles that the magnet can move.

[4] Ecliptic is the geometric plane that contains the orbit of the Earth. Most of the Solar System planets are close to this plane
[5] 46º 15′ N, 6º 5′ E ,330m above sea level
[6] Engineering Support and Technology



Figure 4.8 Image of the vertical encoder (left) that converts the magnet position in encoder values. On the right the vertical movement system is shown.

Of similar importance for the tracking software is also the time synchronization. The system checks –and corrects if necessary- the clock of the hosting PC. The checking is performed by the two CERN time servers and it is running a NTP[7] demon that produces time synchronization with an accuracy of 1ms. According to the previous paragraphs a sketch that depictures the tracking software algorithm is the following

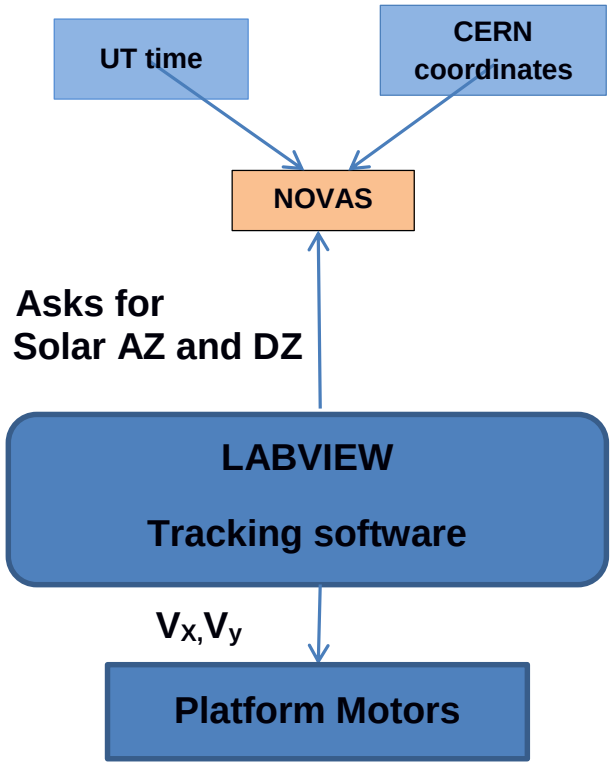

Figure 4.9 The operation principle of the tracking software.

[7] Network Time Protocol (NTP) is a networking protocol for clock synchronization between computer systems over packet-switched, variable-latency data networks. In operation since before 1985, NTP is one of the oldest Internet protocols in current use

The precision of the tracking system is maintained by some specific tests that can provide the magnet alignment accuracy. Before CAST first data taking in 2002, some specific tests that measured the alignment accuracy were accomplished. The required tracking accuracy that should be less than 1 arcmin was fulfilled. The method used was a GRID measurement. Another method to provide the necessary tracking accuracy is the Sun filming. A snapshot of the tracking software implemented in LabView is shown in figure 4.10

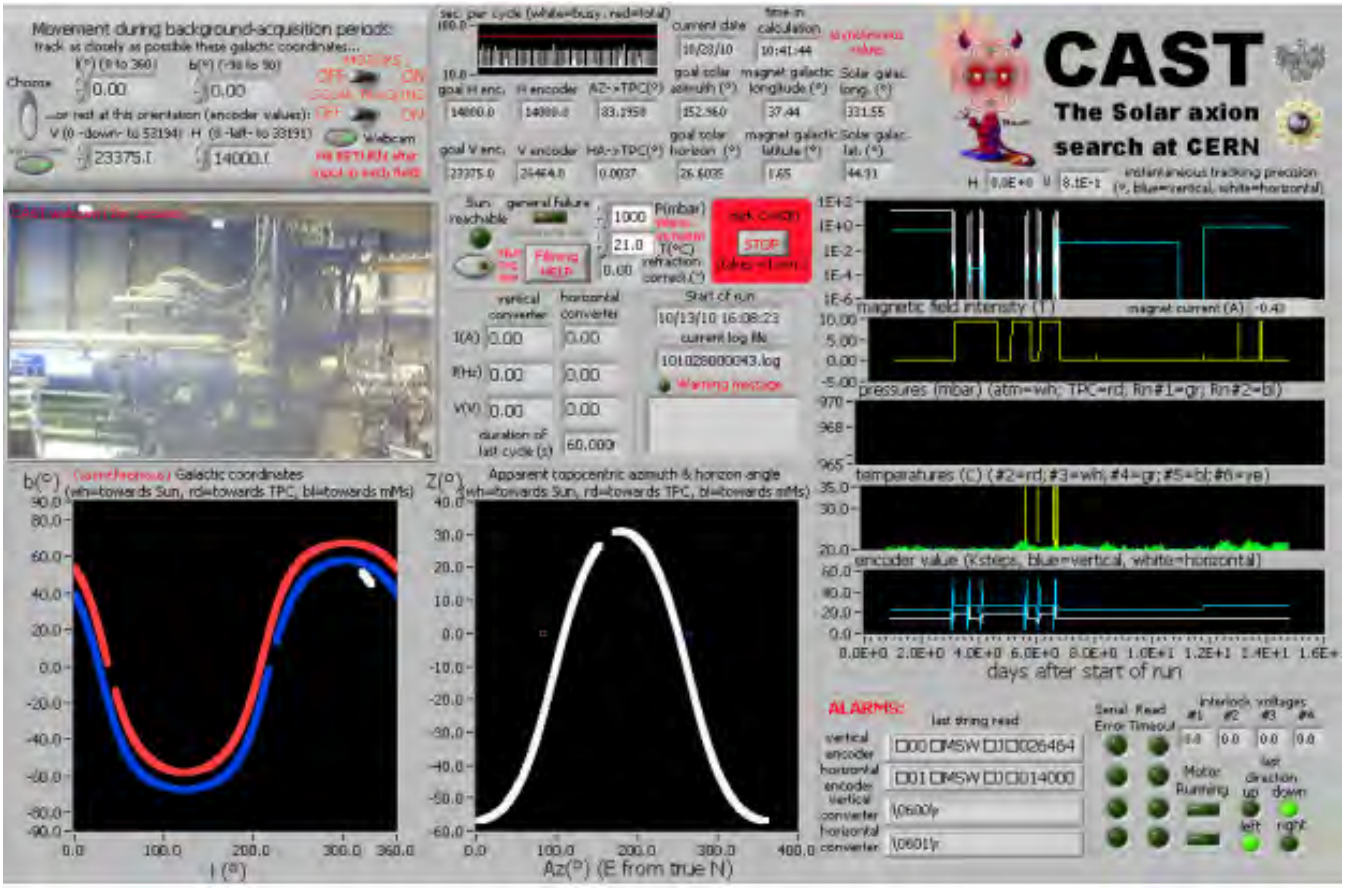

Figure 4.10 Picture of the user interface of the tracking software that controls the magnet movement and saves log data for time, position tracking and other useful information for data analysis.

4.4 GRID measurements

In order to confirm the stable and accurate operation of the tracking system a GRID measurement is performed regularly in CAST with the help of the Survey group of CERN. The first calibration of the encoding of the motors has been done in 2002. The GRID measurements consist of a set of independent magnet positions in a set of reference coordinates (GRID) that cover a wide range of the magnet's allowed movement range. According to the first calibration in 2002, every year this measurement is reproduced in order to detect any drift in the point accuracy of the system. A second reference GRID performed in 2007 showed no significant

deviation from the original measurement in 2002 (all the prefixed positions had a deviation less than 1 arcmin). The latest measurement in 2011 found the system substantially unchanged with respect to the reference values of the previous GRID measurements as can be seen in figure 4.11. In this figure a comparison between 2007 and 2011 GRID measurements is shown and the results are represented in a projected plane at 10m in order to compare any deviation from the required precision. The 10% of the Sun's core projected at 10m is also shown for comparison purpose.

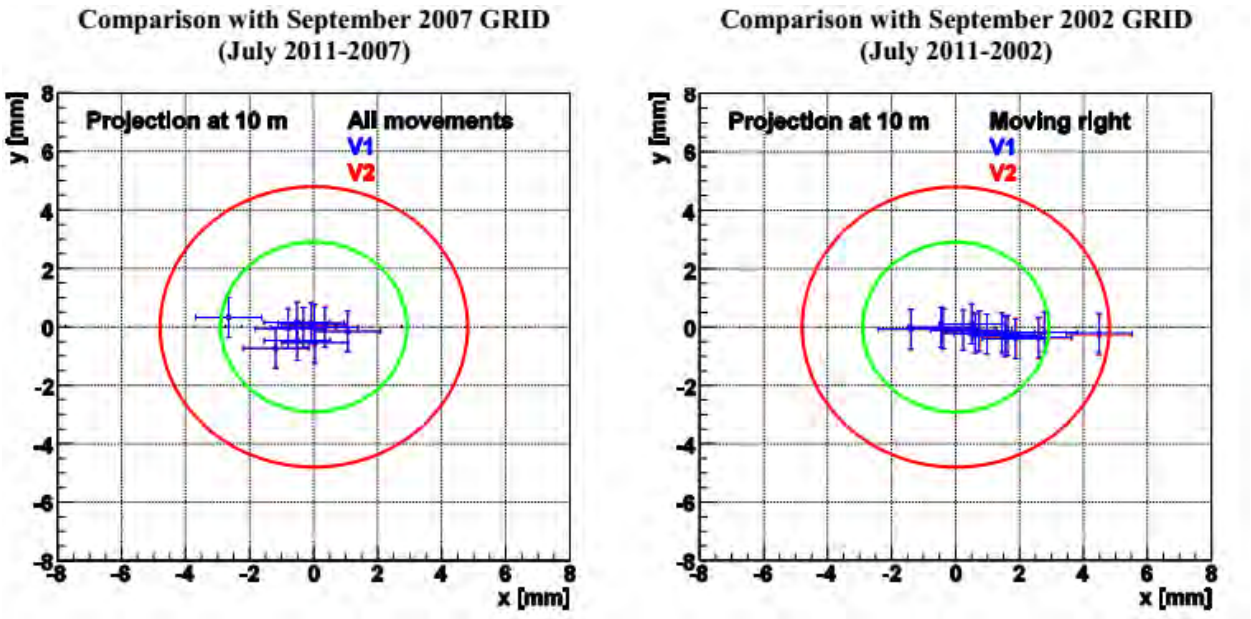

Figure 4.11 GRID measurements performed in 2007 and in 2011 compared with the initial calibration in 2002 for both magnetic bores V1 and V2. The green circle indicates the required precision of 1 arcmin while the red circle represents the 10% of the Sun projected at 10m. The point located out of the green circle on the right, referred to a position that lies in the limit of the magnet movement range and so is of no importance.

4.5 Sun filming

In order to cross-check the tracking system precision, the Sun-filming measurement is required. This measurement is performed by directly observing the Sun and testing whether the CAST magnet setup is able to point to the Sun twice per year. In the CAST host building a window is specifically positioned for this purpose. This measurement can provide enough information in parallel with the GRID measurement for the system accuracy. Sun-filming can be done twice per year during March and September when the Sun passes through a special window of the building if weather permits. The tracking software[8] points the magnet to the Sun and a SLR camera that is aligned to the axis of the magnet with laser targets can film for less than 5 minutes. Analysis of the Sun's images using the LabView software is shown in figure 4.12 where the center of the Sun is calculated.

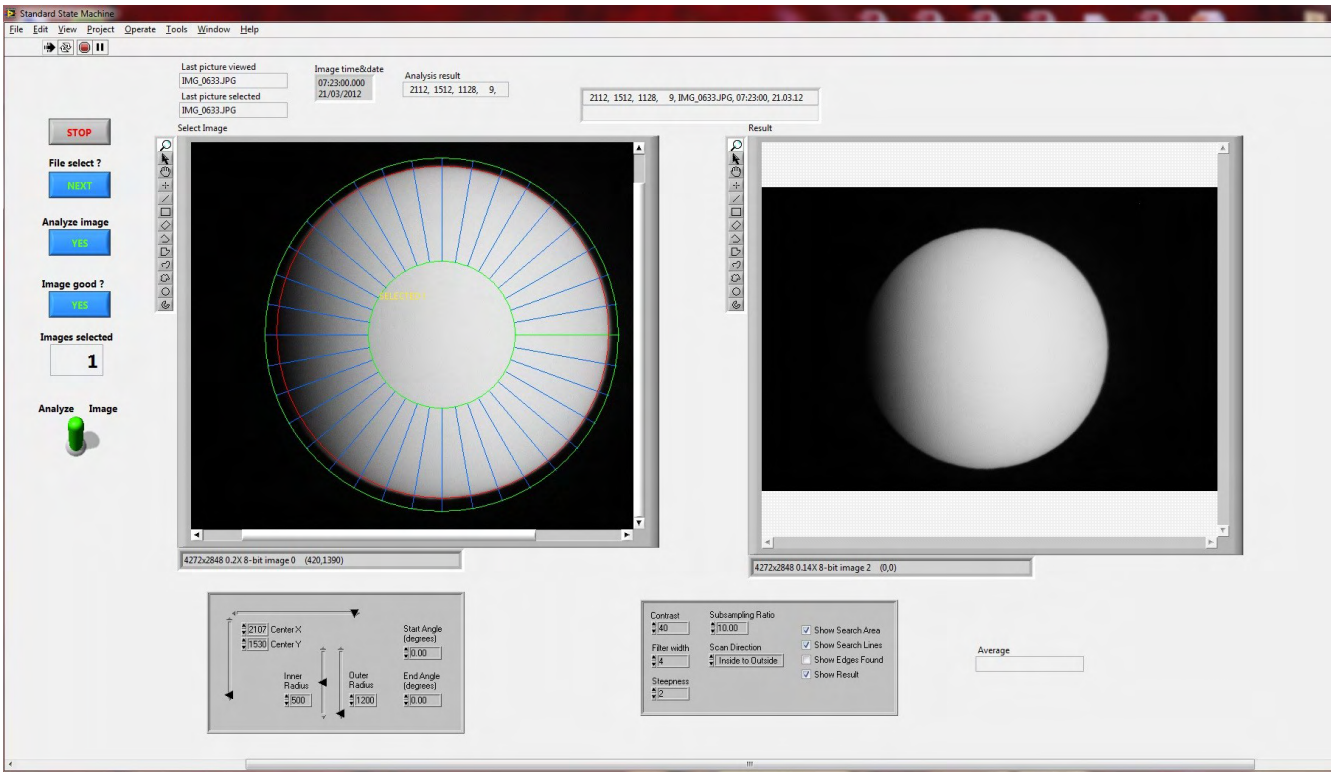

Figure 4.12 A snapshot of the LabView program analyzing Sun's images. Many pictures are used to calculate the center of the Sun in average and so the standard deviation is used as the error.

In table 4.1 the total estimated CAST tracking precision is given and it is better than 0.01º taking into account all the error sources.

[8] This is another version of the tracking software where the refraction of light in the atmosphere is taken into account.

Source of Error	Typical value	Maximum value
Astronomical calculations	0.002º	0.006º
Uncertainty of coordinates	~0.001º	
Clock time	~0º	
Grid measurements (0.2mm precision)	0.001º	
Interpolation of Grid measurements	~0.002º	<0.01º
Horizontal encoder precision	~0.0014º	
Vertical encoder precision	~0.0003º	
Linearity of motor speed	<0.002º	
TOTAL	<0.01º	

Table 4.1 Summary table of the main error sources in the tracking accuracy

4.6 Slow control system

To monitor and log the main parameters of the CAST experiment is of great importance. For this purpose a dedicated software program has been built since 2003 based on LabView language. The system uses the information of several NI (National Instrument) cards that acquire analog and digital signals from many sensors and gauges and produce output signals. The software is continuously upgraded and more signals have been added. Among others the Slow Control application can check and log information as

- Vacuum and cryostat pressure as also pressures in the cold bores – detectors
- Various temperatures in different parts of the magnet
- Magnet movement parameters (loads on lifting screws), motor encoder values, angles
- Magnet valves status (open or closed)
- Safety of the system and alarms

All the values of CAST measured by the Slow Control are recorded every minute. Abnormal variations in system values out of their safety range can trigger alarms, or trigger the fast acquisition and logging mode and can finally send warning messages and emails to the responsible people.

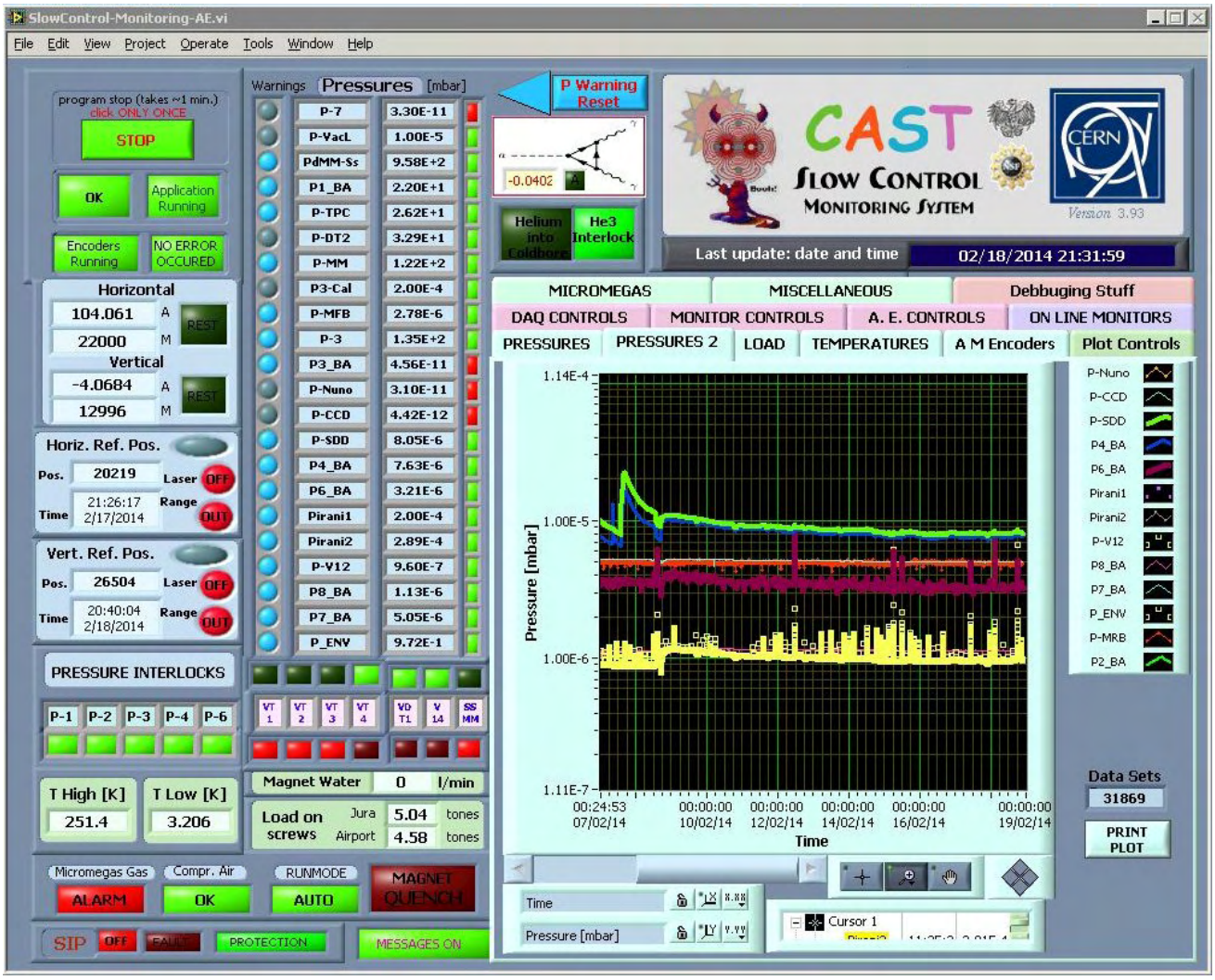

Figure 4.13 Snapshot of the Slow Control system user interface.

4.7 CAST scientific research program

The CAST experiment started taking data since 2003 and has since then provided the most restrictive experimental limits on the axion-photon coupling for a wide range of axion masses. In 2003 and 2004, CAST operated with vacuum inside the magnet bores (CAST phase I) and set the best experimental limit for the axion-photon coupling constant for axion masses up to $m_\alpha \leq 0.02\text{eV}/c^2$ [63].

Phase I completed in 2004 using a conventional time projection chamber (TPC), a gaseous chamber Micromegas and an X-ray telescope with a charge coupled device (CCD) as data taking detectors. The axion signal should appear as an excess of photons above background in the three different X-ray detectors.

The best fit values of $g_{\alpha\gamma}^4$ obtained for each of the detector's 2004 data and the combined result in addition with the Bayesian probability function of 2003 data analysis give the final limit for the CAST vacuum setup of

$$g_{\alpha\gamma} < 8.8 \cdot 10^{-11}\ \mathrm{GeV}^{-1} \text{ at } 95\%\ \mathrm{CL}$$

In the second phase (CAST phase II) a buffer gas was used in order to restore coherence. Beyond 0.02 eV for the axion mass the coherence is lost and ^{4}He gas filling the magnet bores provides a higher effective mass to the transformed photon. The refractive buffer gas maximizes the probability that axions can be converted into photons for a mass-range higher than in CAST Phase I and up to about 0.39 eV [64]. ^{4}He has a saturation vapor pressure of 16.405 mbar at 1.8K, so in order to avoid problems like He^4 liquefying, CAST made use of ^{3}He and extended the sensitivity to axion masses up to ~1.16 eV.

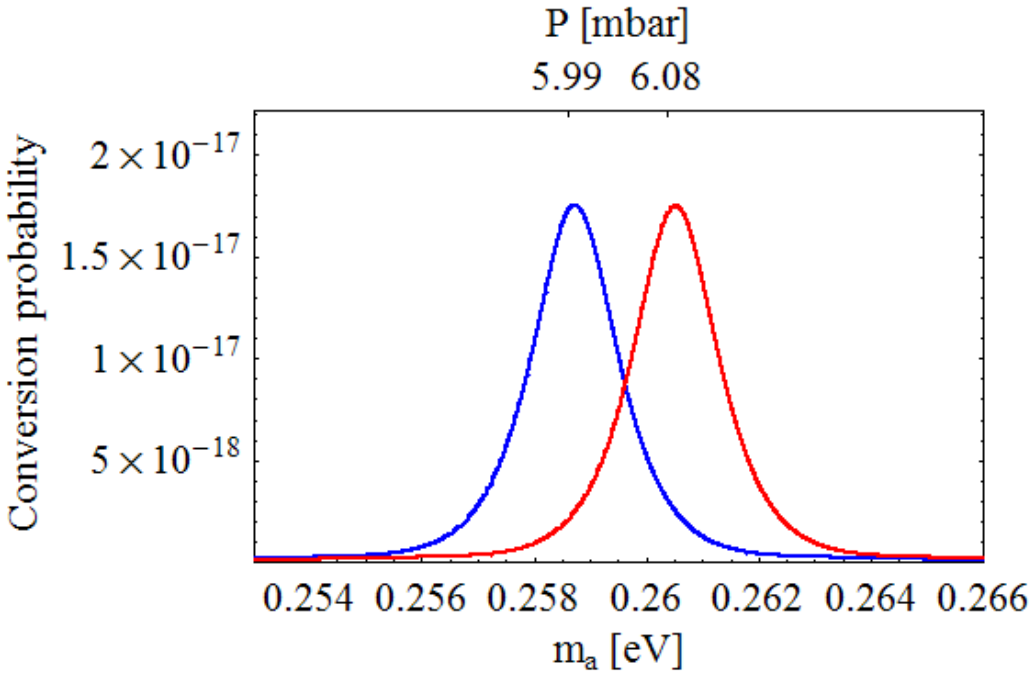

Figure 4.14 The axion mass coverage in terms of conversion probability. The probability is directly related to the number of axions that CAST is able to detect at a given axion mass.

In order to cover the axion mass range by using a buffer gas, the density was increased in small equal steps such as to assure a smooth coverage for different axion masses (Figure 4.14). These steps corresponded to 0.08 mbar (or 1 dP that is the nominal pressure setting) at 1.8K in the cold bore.

In 2007 CAST finished its extensive research using ^{4}He as a buffer gas and after upgrades in the helium CAST system, the magnet bores have been filled with ^{3}He. By using ^{4}He an

improved limit for the axion to photon coupling constant that was inside the theoretically favored region has been derived [70]

$$g_{\alpha\gamma} \leq 2.17 \cdot 10^{-10}\ \text{GeV}^{-1} \text{ at 95\% of CL}$$

$$\text{for } 0.02\ \text{eV} < m_{\alpha} < 0.39\ \text{eV}$$

With this result CAST is the first helioscope to have crossed the KSVZ model line. The replacement of ^{4}He by ^{3}He extended the research to higher axion masses and finished at the end of July 2011. The CAST experiment has covered axion masses up to 1.18 eV closing the hot dark matter limit and actually overlapping with it. The limit in the range 0.39 eV/c^2 ≤ m_{α} ≤ 0.64 eV/c^2 has been published in PRL and the limit provided in [64] was

$$g_{\alpha\gamma} \leq 2.3 \cdot 10^{-10}\ GeV^{-1} \text{at } 95\% \text{ of CL}$$

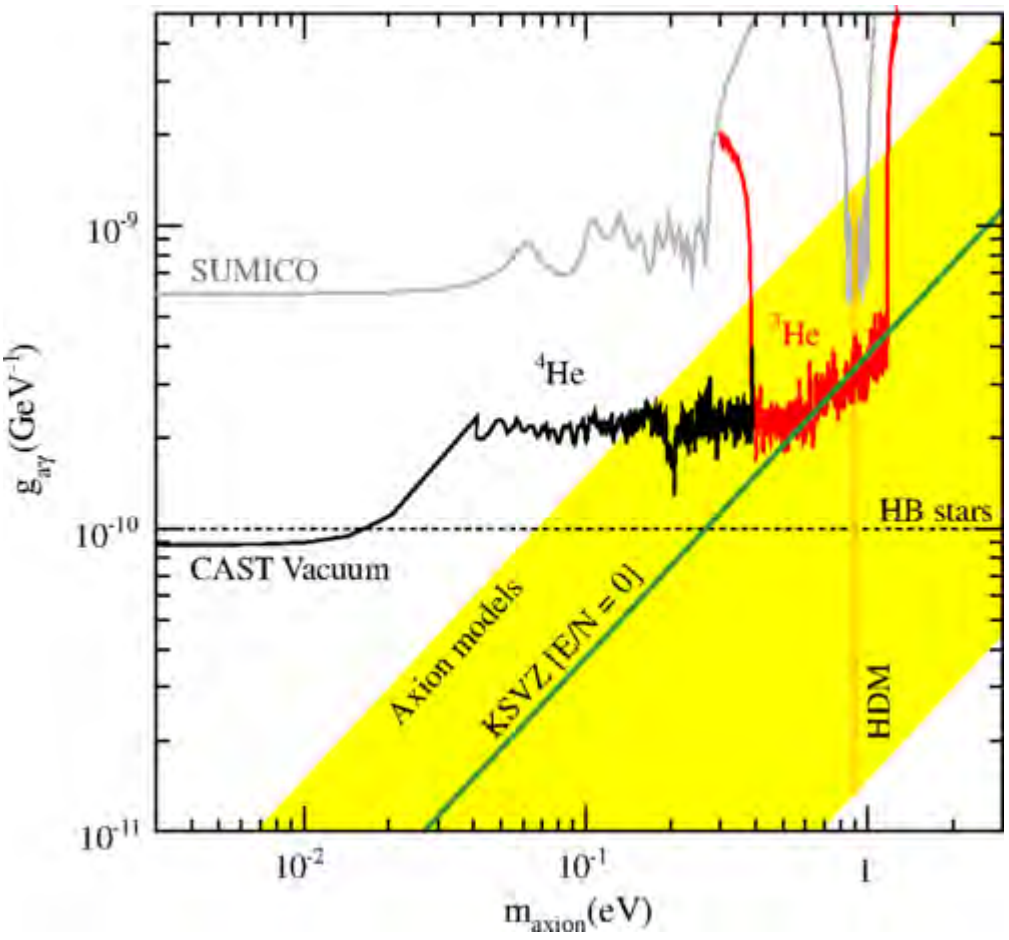

Figure 4.15 Exclusion region for the axion-photon coupling constant versus axion mass achieved by CAST in the vacuum pipes, ^{4}He and ^{3}He results appears in red [71]. Constraints set by the Tokyo helioscope are shown in grey [129], the horizontal branch (HB) stars and the hot dark matter (HDM) bounds are also shown. The yellow band represents theoretical models with |E/N -1.95| = 0.07-7. The green solid line corresponds to E/N = 0.

4.8 The X-ray windows

In order to confine the gas in the magnet bores, four cold windows were developed at the CERN cryolab. The original design given by CEA-Saclay for the cold windows consists of a 15μm thick polypropylene foil that is protected from pressure differences by being glued onto the stainless steel strongback. The strongback is attached to the polypropylene layer sitting at the vacuum side and forming a grid of square mesh as can be seen in figure 4.16

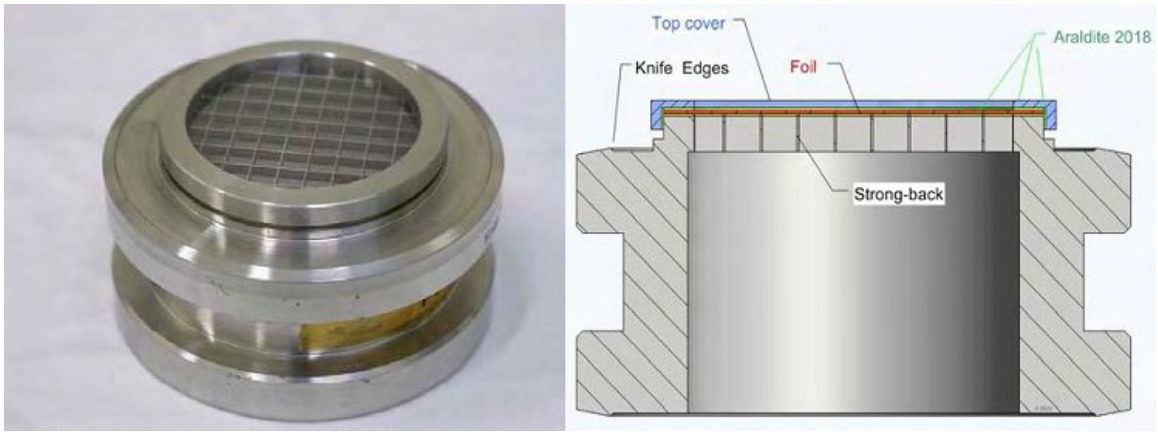

Figure 4.16 A picture of a cold window (left) and a cross section view of the design (right).

The cold windows position in the CAST gas system can be seen in figure 4.6. These windows have to operate at low temperatures (1-120K), must have a high X-ray transmission of 1-7 keV, robustness and tightness. The differential pressure between the buffer gas in the cold bores and the vacuum in front of the detectors can reach the value of 1.2 bars in case of a quench. To achieve the aforementioned requirements the cold windows were leak and pressure tested at CERN cryolab by applying sudden pressure changes and measuring the leak rate that was found less than $1 \cdot 10^{-7}$ mbar·l/s.

The X-ray windows are in contact with the helium gas at 1.8K, so in order to keep the windows at a constant temperature, it is required that a heater system is applied on them. The windows were heated up to 120K in ^{4}He phase while in ^{3}He phase the temperature was about 80K. Once every two months a procedure called *bake out* was taking place by emptying the magnet bores and by applying the maximum heater power to the windows. The purpose of this procedure was mainly to evaporate frozen air or water molecules that could probably have stacked in the polypropylene foil. Another advance of the bake-out was to provoke the outgassing of the molecules absorbed by the foil.

4.9 The ^{3}He gas system

Once the saturation pressure of the ^{4}He was reached, a significant upgrade of the CAST gas system took place in order to use ^{3}He as a buffer gas of the CAST magnet and thus, to access higher axion masses. The gas system needed to accomplish the second phase of CAST by using ^{3}He had to be accurate, stable and capable to precisely measuring small quantities of gas inserted into the cold bore volume in a reproducible way. The design of the whole system was based on a small error in any pressure setting needed to be reproduced, of about 0.01mbar. The metering system was upgraded for accurate and metered transfer of gas into the cold bores of the magnet. (Section 4.3.1)

The ^{3}He gas is extremely valuable so one of the main specifications was to avoid any gas loss. A safe storage volume and a carefully designed transfer system of gas pipes were installed. (Section 4.9.1)

A purging system to purify the ^{3}He gas was installed to avoid any contamination from the pumping system. (Section 4.9.2)

A system to recover the ^{3}He gas was also installed in order to save the gas in case of a quench and also to prevent any damage from the sudden increase of pressure in the cold windows. (Section 4.9.3)

A PLC system to control and monitor the valves, pumps flow meters and all the gas system sensors was also installed. (Section 4.9.4)

A detailed behavior of the ^{3}He gas in the cold bore is also needed in order to calculate the density profile and the actual length of the pipes where coherence is restored for the axion conversion. A detailed model based on CFD (Computational Fluid Dynamics) simulates the gas inside the cold bores. (Chapter 5)

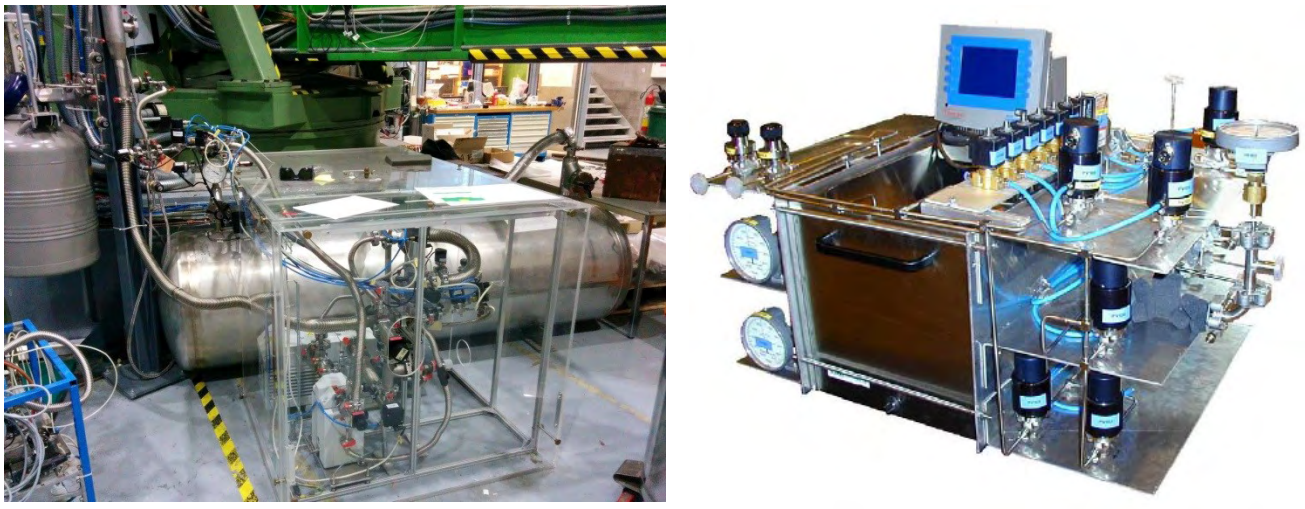

Figure 4.17 A picture of the CAST ^{3}He system (left) and the metering system (right).

4.9.1 The ^{3}He metering system

The metering system (Figure 4.17) consists of two cylindrical metering volumes of different capacities. The small one (MV2) has a volume of 1.63 liters and its purpose is to increase the gas density in the magnet bores in the middle of the Sun's tracking. The larger volume (MV10) contains 8.58 liters and is suitable for injecting large amounts of gas into the magnet bores in a short period of time (in case of a quench or a bake-out). The accuracy of using the metering system was reproduced via the pressure difference measurement and by keeping the volumes into a thermal bath at a constant temperature of 309K. The pressure is measured with high accuracy before and after the gas injection in the magnet bores. The temperature is also kept constant with stability of about ±0.01K. A LabView based software was developed that can record the bath temperature at any moment and send alarms in case of any system change.

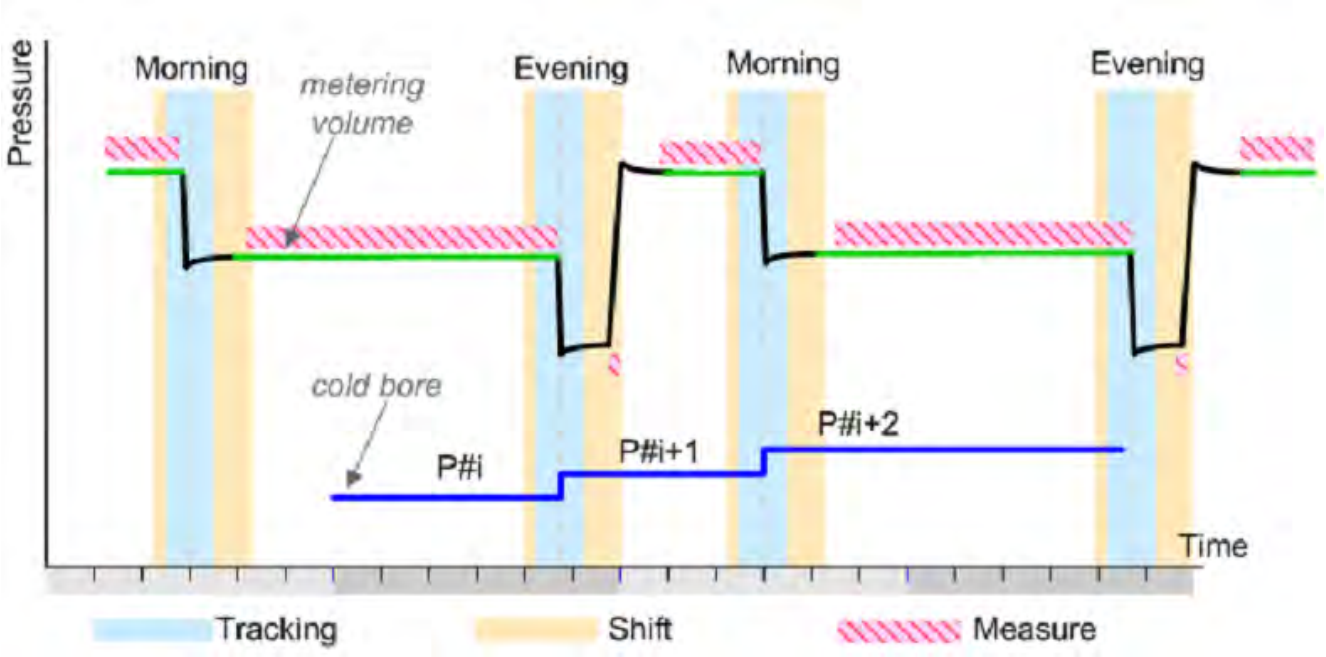

Figure 4.18. The filling scheme of the metering volume for the ^{3}He gas injection. An accurate system filling for gas density increase at each pressure setting is shown. In this filling scenario that has been chosen as the most attractive in CAST collaboration, the density inside the cold bores is increased in the middle of each tracking by one pressure setting.

4.9.2 Purging system

The impurities of the gas must be removed and thus a system of two charcoal traps is used. The first one (RT) is at room temperature and its purpose is to trap water vapor and oil from the gas system pumps while the second one (LN) is immersed in a liquid nitrogen bath of about 77K and removes the rest of impurities. The traps need to be periodically purged and regenerated to maintain their efficiency.

4.9.3 Expansion volume and recovery of ^{3}He

In the case of a natural quench event or a quench event provoked by interlocks, the magnet temperature raises rapidly. The temperature rises in case of a quench by a factor of 21 in 200sec (40K). In order to protect the cold windows from damage because of the gas volume increase, a 10 meter long, 450 liter volume has been installed above the magnet (Expansion volume) as can be seen in Figure 4.19.

The cold bore is connected to the expansion volume via safety valves that can be triggered when the pressure is raised above the safety range. The valves are opened by the quench alarm interlocks and the ^{3}He gas is transferred to the expansion volume. The expansion volume has been designed to sustain with a safety factor of 1.2, the amount of gas in the cold bore that has pressure 140 mbar at 1.8 K.

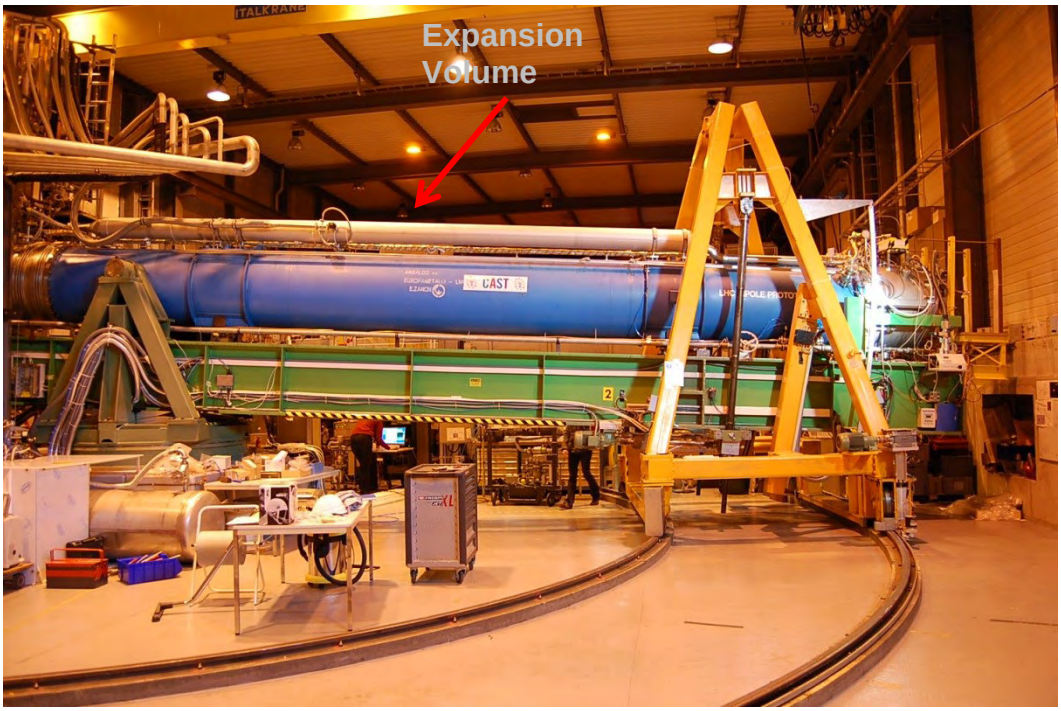

Figure 4.19 The expansion volume above the CAST dipole magnet.

A hermetic ^{3}He pump recovers the gas into the Storage Volume, that is a container of 963 liters and it is designed to contain the whole gas supply at room temperature and pressure below the atmospheric. The following diagram represents the ^{3}He system and the procedure followed.

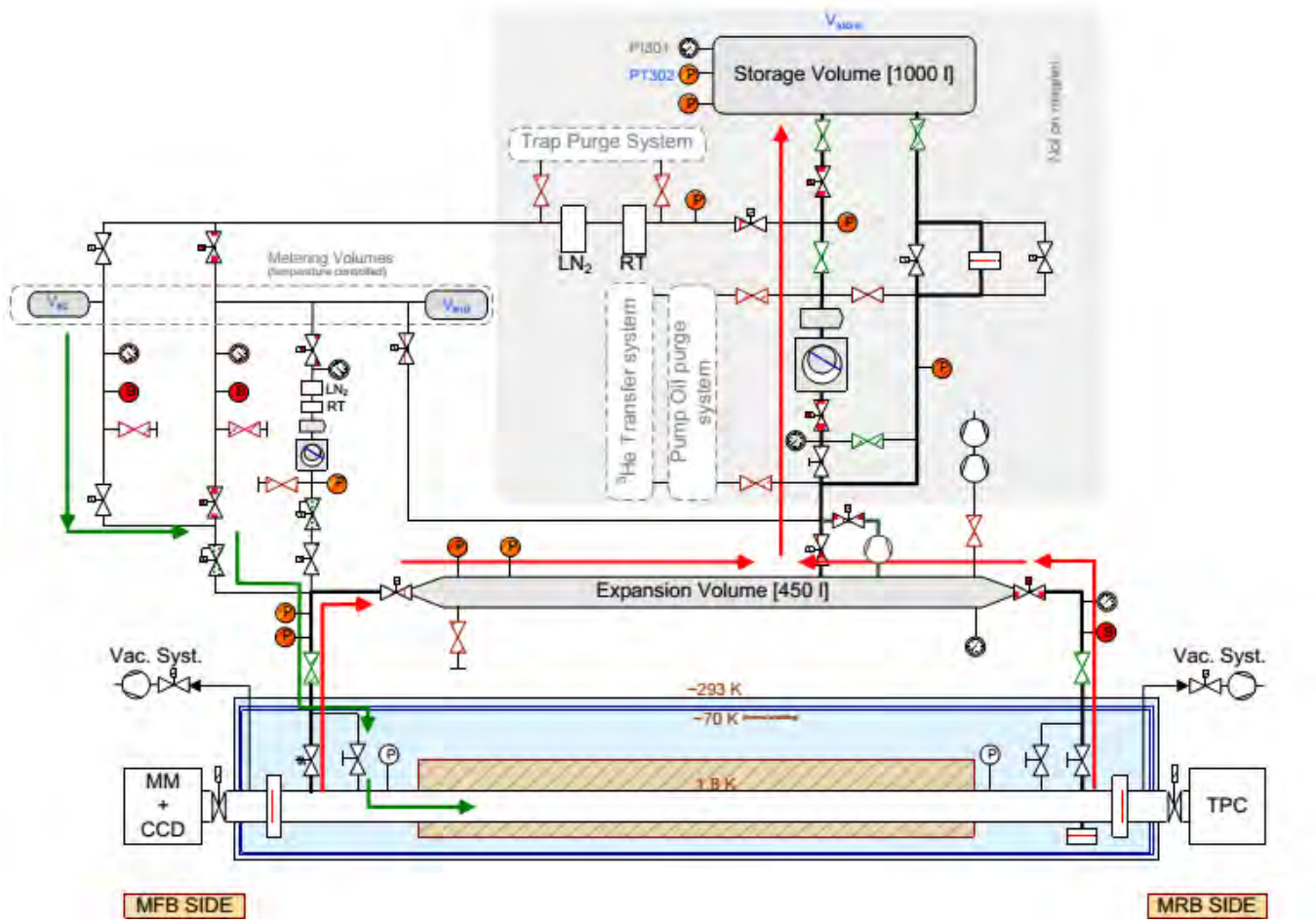

Figure 4.20 The ^{3}He gas system of CAST. The green arrows indicate the filling procedure of a small amount of gas from the metering volume to the cold bores, while the red ones show the transfer line of the gas in case of a quench event.

4.9.4 The PLC system

A Programmable Logic Controller (PLC) is used to control and supervise the gas system. The high complexity of the ^{3}He gas, the large amount of signals involved from the large number of instruments that have to be monitored, remote controlled and provide safety led CAST to choose a PLC. A Supervisory Control and Data Acquisition system (SCADA) based on PVSS II was set up using the standard control architecture developed at CERN. SCADA provides a graphical user interface for the PLC as can be seen in Figure 4.20. The relative simple user interface can help the user to perform tasks like the gas recovery, refilling of the metering volumes and of most importance for every CAST shifter to fill the magnet bores in the middle of the tracking.

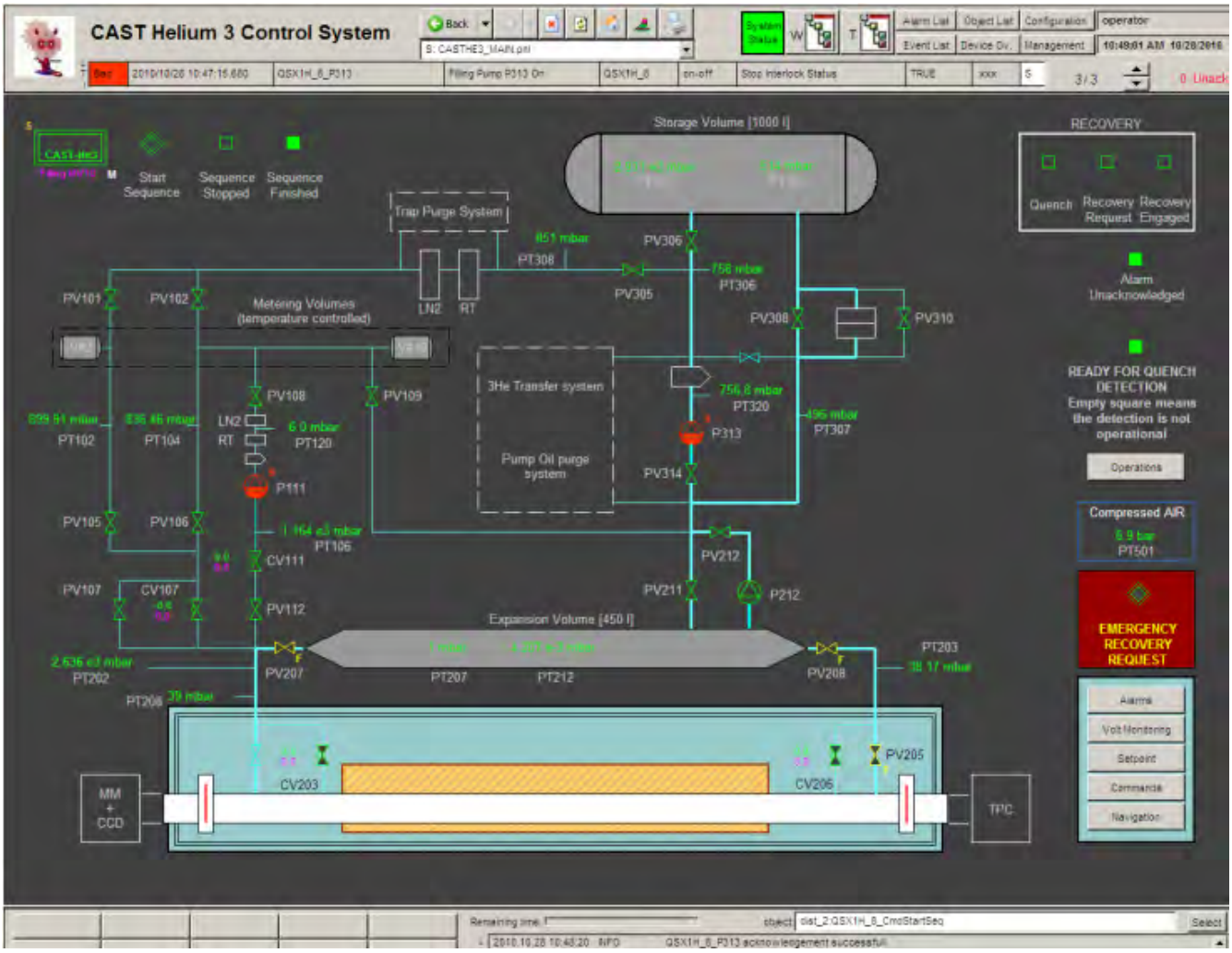

Figure 4.21 The SCADA interface of the PLC. Manual and automated processes can be performed involving valves and pumps control and monitoring of sensors levels. UNICOS (UNified Industrial COntrol System) is an industrial framework that targets to Siemens PLC hardware and uses PVSS II at the supervision level.

4.10 CAST detectors

In order to detect the X-ray photons originated from the axion-to-photon conversion in the strong magnetic field, CAST setup has four X-ray detectors sensitive to 1-10 keV range. There are three Micromegas (MICRO pattern GAseous Structure) and one pn-CCD (Charged-Coupled Devise).

The two MRB (sunset side) bores are covered by two Micromegas detectors while on the MFB side (sunrise), one Micromegas and one pn-CCD detector placed at the end of an X-ray telescope are installed. The detectors are characterized by their low background and high efficiency and they are suitable for the x-ray photons that can be converted in CAST's magnet bores. The Micromegas detector and the detector data analysis of 2009-2010 will be reviewed in next chapters.

In sunrise, Micromegas and the CCD are taking data for about an hour and a half while in sunset the other two Micromegas are taking data for the same time. The remaining time, background measurements are performed for each detector.

The X-ray Telescope and the pn-CCD detector

A very sensitive detector of CAST was a combined X-ray mirror telescope and a CCD detector placed at the focal plane. In the sunrise side the telescope is assembled in front of one of the magnet bores and it is able to focus the photons emerging from the 1452 mm^2 aperture to a spot size of 9 cm^2 of the CCD chip. The focusing of photons improves the signal to noise ratio by two orders of magnitude (without taking into account that the mirror system efficiency is 35%). Another advantage of the system is the simultaneous measurements of signal and background, diminishing the systematic effects.

The X-ray Telescope

The X-ray telescope of the CAST experiment [65],[66] is a prototype Wolter I[9] telescope that was developed for the German X-ray satellite mission ABRIXAS[10] [67] that finished in 1999. Its focal length is of 1600 mm and consists of 27 gold coated Ni parabolic and hyperbolic mirror shells. The maximum aperture of the outermost shell is 163 mm while the smallest one has a diameter of 76 mm. There is a spider-like structure that supports the individual mirror shells and divides the aperture of the telescope in six sectors. The CAST's magnet bore is 43 mm in diameter so only a fraction of the telescope is used; thus only one of the six sectors is used to focus axions converted into photons. The telescope efficiency for each of the six sectors was measured at PANTER [68] facilities and the best in performance sector was chosen for CAST usage. The transmission efficiency is decreased by any contamination on the mirror reflective area; therefore the telescope is operated under vacuum conditions (below 10^{-5} mbar).

[9] Wolter I is parabolic-hyperboloid type of telescope with internal reflections
[10] A BRoad-band Imaging X-ray All-sky Survey

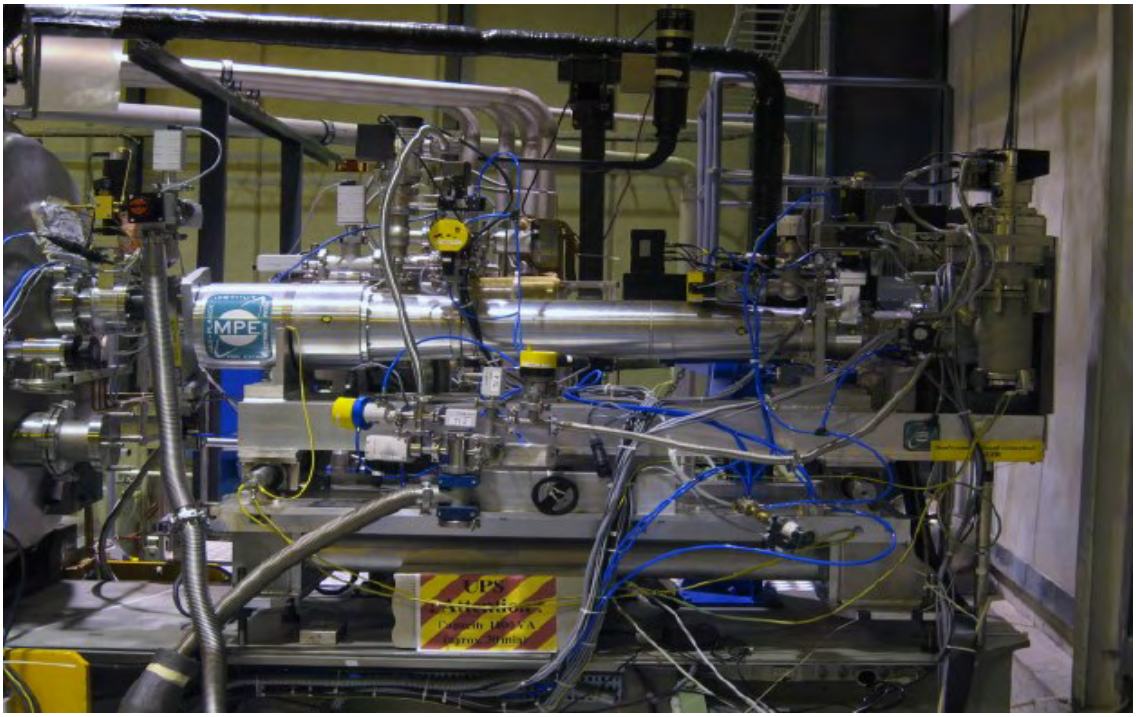

Figure 4.22 CAST's X-ray telescope mounted at the MFB (sunrise) side of the magnet

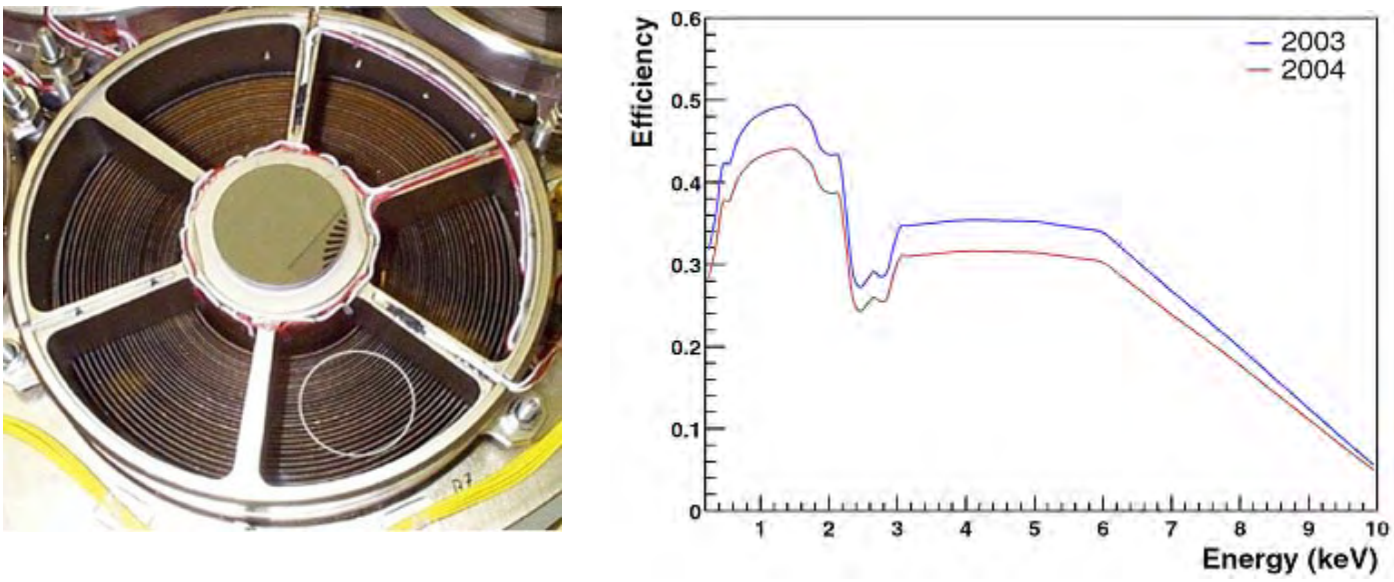

Figure 4.23 The front view of the X-ray 27 nested mirror shells on the left. CAST's magnet bore side is indicated by the the white circle. On the right a plot represents the telescope efficiency as a function of the photon energy. The on-axis angular resolution of the telescope is 34 arcsec and 43 arcsec (~0.01°) Half Energy Width at 1.5 KeV and 8.0 KeV respectively. That is a factor 10 better than the expected axion spot size of the Sun (~0.1°).

The pn-CCD detector

The detector that is mounted on the focal plane of the X-ray telescope is a fully depleted pn-Charged Coupled Device (CCD); it is a prototype developed for the XMM Newton[11] mission of ESA[12] [69]. The detector is 280 μm thick and its sensitive area is 2.88 cm^2 that is divided into 200×64 pixels. Each pixel covers a region of 150 × 150 μm^2. The detector's design is based on the silicon drift detector proposed in 1983 by E.Gatti and P. Rehak. It has the advantage of low background applications because of the passive shielding of Cu and Pb, as also the advantage of high quantum efficiency (95%). A Stirling cooling system is used to keep the detector operation stable over time at a temperature of about -130º C and a very thin entrance window (20 nm) at the backside of the chip, allows the chip to operate in vacuum directly connected to the magnet vessel.

The axion signal coming from the Sun's core covers an effective area on the CCD chip that is of diameter of about 2.83mm (19 pixels).That feature enables the simultaneous measurement of the signal inside the spot mentioned and the background in the rest of the detector's area. The background reduction was improved by a shielding of Cu and lead inside the detector's vessel as can be seen in Figure 4.23

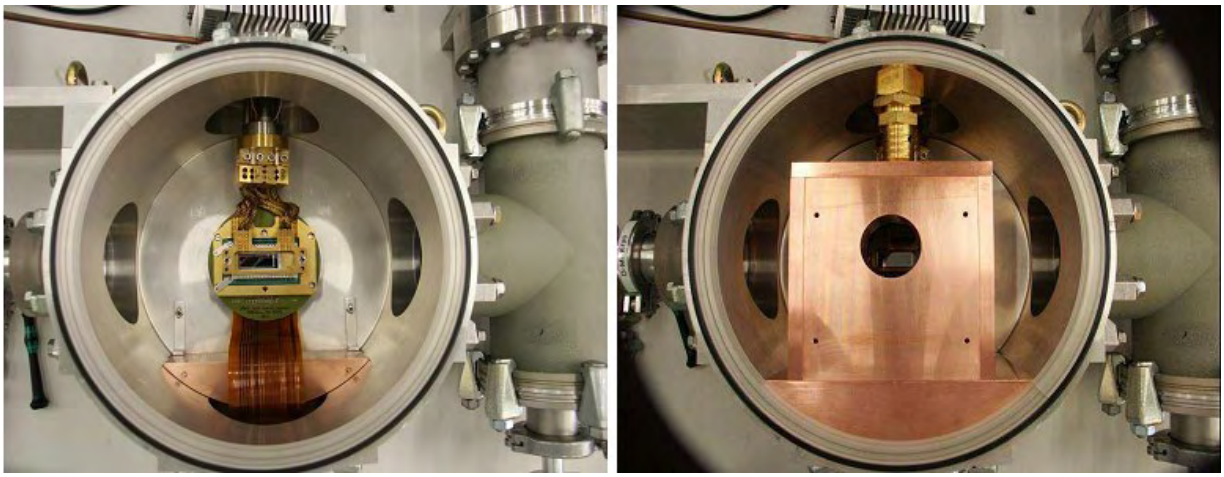

Figure 4.24 Front view of the pn-CCD detector on the left. The black area in the center is the active area of the CCD chip. On the right an inside view of the detector with the Cu shielding. The shielding reduces the background produced from external sources like cosmic rays.

[11] X-ray Multi Mirror design that honors Sir Isaac Newton
[12] European Space Agency

5. ^{3}He CFD simulations for CAST

5.1 CFD introduction

CFD is not a science by itself but a method to apply the techniques of one discipline (numerical analysis) to another (heat and mass transfer). CFD is a branch of Fluid Mechanics that uses numerical methods to solve and analyze fluid flows. The main purpose of using this method, is the determination of entire fields like temperature T(x,t), velocity v(x,t) or density $\rho(x,t)$. Computational power is needed to perform the required calculations to simulate the interactions of liquids or gases with solid surfaces that can be defined as boundary conditions.

The set of equations that describe the process of momentum, heat and mass transfer are known as the Navier-Stokes equations. These are partially differential equations with no analytical solution but can be discretized and solved numerically. There are different numerous solutions that can solve the CFD codes but the general one is known as the finite volume method. In this method the fluid region of interest is divided into small sub-regions, the control volumes. The equations are discretized and are solved iteratively for all the control volumes. The variable of interest is solved approximately for any specific point in the control volume. In this way a full picture of the flow behavior can be obtained.

Navier-Stokes equations are derived by application of Newton's second law for an arbitrary portion (control volume) of the fluid, assuming that the stress in that fluid portion is the sum of a diffusing viscous term and a pressure term. The solution of these equations dictates a velocity field or a flow field rather than some discrete point's trajectories. Convective acceleration produces nonlinearity in Navier-Stokes partial differential equations because of change in velocity over position. The nonlinearity is due to convective associated which is an acceleration associated with the change in fluid velocity over position.

Turbulence is a chaotic behavior that can be experimentally seen in many fluid flows. It is a rather complicated phenomenon due to the fluid's inertia as a whole. To properly describe the turbulence length scales in most simulation models, the control volumes (especially those that surround the region of interest) should be very small. A very fine mesh (topology of the control volumes) should be produced but in some cases the computational time and cost became infeasible.

In the general case the Navier-Stokes equations together with supplemental equations, like conservation of mass and well defined boundary conditions, seem to model fluid flows accurately. They can be used to model the weather, ocean currents, fluid flows in a pipe or the flow of air around a wing. Coupled with Maxwell's equations they can be used to model and study magnetohydrodynamics.

In an inertial frame of reference, conservation of momentum alongside with mass and energy conservation, the general form of the Navier-Stokes equations of fluid motion is

$$\rho\left(\frac{\partial v}{\partial t} + v \cdot \nabla v\right) = -\nabla p + \nabla \cdot T + f \tag{5.3}$$

where v is the flow velocity, p is the pressure, T is the stress tensor component of order two and f are the body forces that are acting on the fluid volume.

5.2 CFD methodology

A graphical user interface is used to define preprocessor procedures where

- Physical bounds of the real geometry are defined
- The geometry volume is discretized by the cells (volume controls). That is called a mesh
- Physical properties are also defined, that is the fluid properties, thermodynamics of the system simulated and equations of motion
- Boundary conditions are set. The fluid or solid properties (behavior) at the fluid boundaries are specified.
- The simulation can be solved iteratively as a steady-state (at a specified moment) or transient (where the simulation evolves with time)

The discretization method is applied by integration of an equation (momentum equation) over the control volume of a computational cell. Ansys CFX, that is the software used[14] to simulate CAST ^{3}He gas dynamics, uses an element base finite volume method to discretize the spatial domain using a mesh. The mesh is three dimensional but for simplicity the figure below shows a two dimensional mesh.

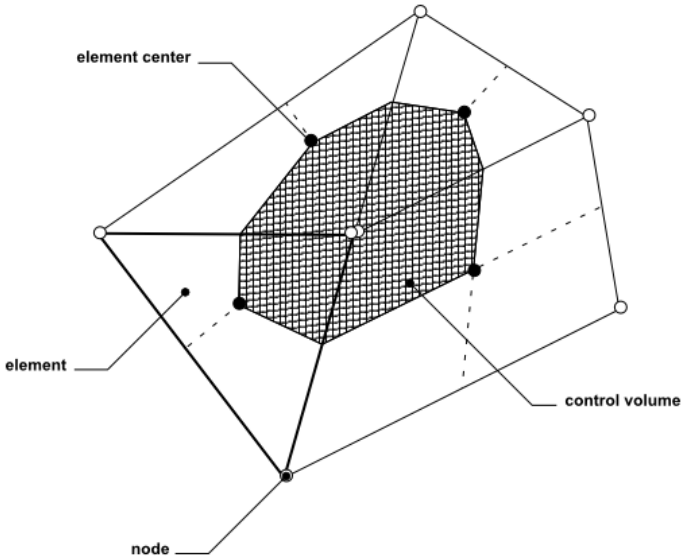

Figure 5.3 Control volume definition sketch. All solution variables and fluid properties are stored at the nodes i.e. at the mesh vertices

[14] Star-CCM+ was also used for this study but will not be presented

5.3 Thermodynamics of the simulated system

The cold bore temperature should be constant[15] at 1.8K, but as can be seen in Figure 5.4 the cold bores ends are connected with other pipework beyond the limits where magnet cryogenics keep the temperature down to 1.8K. Those volumes (pipework's connections) in MRB and MFB side will transfer heat loads by the ***conduction*** mechanism. The heat is transferred through the cold windows and this can be measured by the temperature sensors placed in a hole made over each cold window flange. The measured temperature of the sensors is around 20K. The law of heat conduction, known as Fourier's law, states that the time rate of heat transfer through a material is proportional to the negative gradient in the temperature and the area, at right angles to that gradient, through which the heat flows. The heat flux density $\vec{q}$, that is the amount of energy flowing through a unit area per unit time is

$$\vec{q} = -k\,\nabla T \tag{5.4}$$

where k is the material's conductivity and ∇T is the temperature gradient.

Heat is transferred by *conduction* from the gas inlet tube where a temperature sensor is also installed and indicates the phenomenon. The displayed temperature at the inlet and outlet is also higher than 1.8 K. In the outlet there is a needle valve that insulates the gas system from the rest of pipework. Gas is transferred through a small diameter tube (2 mm capillary tubes that their orifices have a diameter of 0.7 mm) and thus heat transfer is minimized. This assembly configuration assumes an adiabatic boundary condition at the outlet or the same temperature as the inlet. The outlet configuration is shown in Figure 5.4

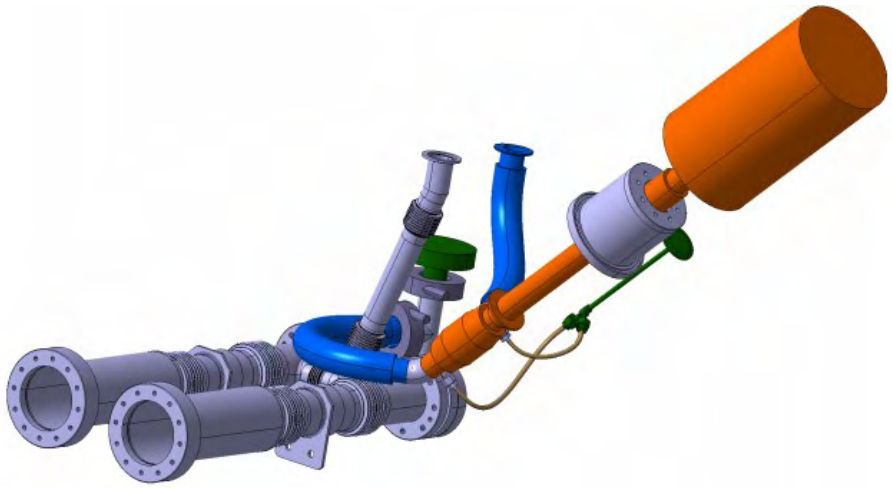

Figure 5.4 Catia design shows the vacuum pipework attached to the ^{3}He gas system. The outlet is shown in blue. Cryogenic valves are shown in green and the by-pass pipe in yellow.

[15] There is a variation of ±(10-15) mK in the cold bore temperature when magnet tilting occurs due to cryogenic circuit

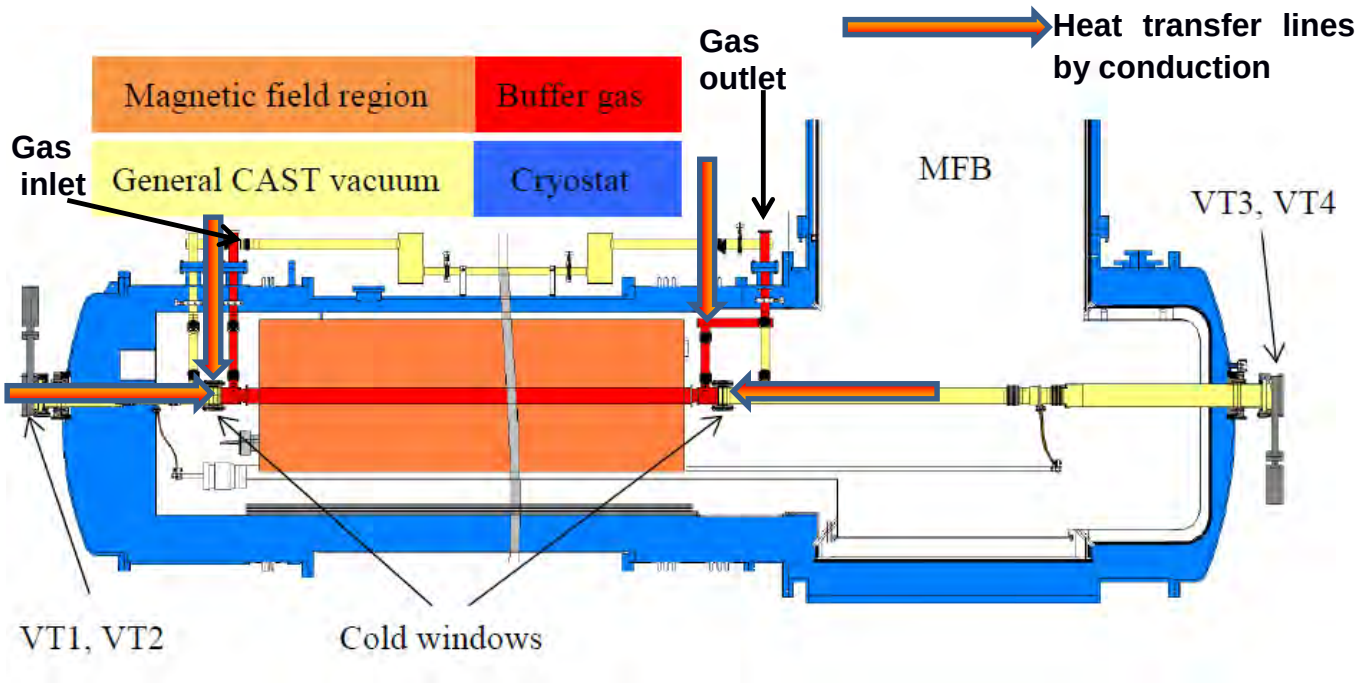

Figure 5.5 Arrows show the transfer of heat by conduction. The cold bore is connected via pipework to the system and since there is a temperature difference with the general CAST vacuum system, the conduction mechanism is applied [76]. Gas inlet and outlet are also shown.

According to the pipework configuration and the cold windows construction parts[16], the heat will flow:

- Through the metallic parts that surround the fluid, to the fluid according to the heat transfer coefficient between stainless steel walls and gas
- Through the Polypropylene (PP) attached to the cold window metal grid
- Between the metallic parts according to their thermal conductivity

The metallic walls close to the cold windows are hotter than the walls in the cold bore and the fluid will become less dense in these regions because the temperature gradients will cause ***convective*** heat transfer. The convective heat transfer implies the mass transfer of gas by advection and diffusion. The temperature gradient close to the hotter regions of metallic boundaries will cause the fluid to increase its temperature, becoming less dense and it follows that it will rise, while the cooler gas that is denser will occupy its place. The density differences due to temperature gradients will cause a mechanism known as natural convection. The driving force of this mechanism is buoyancy.

The expression that describes the convective heat transfer from the solid walls to the fluid is

$$\frac{dQ}{dt} = -hA_s(T_s - T_\infty) \tag{5. 5}$$

[16] A 15μm Polypropylene (PP) foil is glued onto the stainless steel strongback , forming a grid of a square mesh

- h is the heat transfer coefficient
- A_s is the solid wall area in contact with the fluid
- $T_s - T_\infty$ is the temperature difference between solid wall and the fluid temperature away from the wall

Convection currents will increase heat and mass flow at the ends of the cold bore giving rise to turbulence effects. The gas inside the cold bore should remain still at a great extent. The cooling system forces the gas to have a temperature of 1.8 K. But close to the end of the cold bores natural convection phenomena arise and buoyancy is the main force that drives the gas in a circulation at MRB and MFB side respectively.

The fluid at these ends is less dense and turbulence effects that should be studied arise. Natural convection stops being the dominant heat transfer mechanism at the region where fluid is cooled down to 1.8 K inside the cold bore. Conduction phenomena are taking place and the gas becomes denser.

Radiation effects are neglected as not important for the ^{3}He system study due to very low temperatures involved.

The situation becomes more complicated when the magnet moves and ***hydrostatic*** pressure is taking place by the tilting of the magnet. The contribution of the hydrostatic pressure induced is considered small but not negligible due to the small ^{3}He gas density.

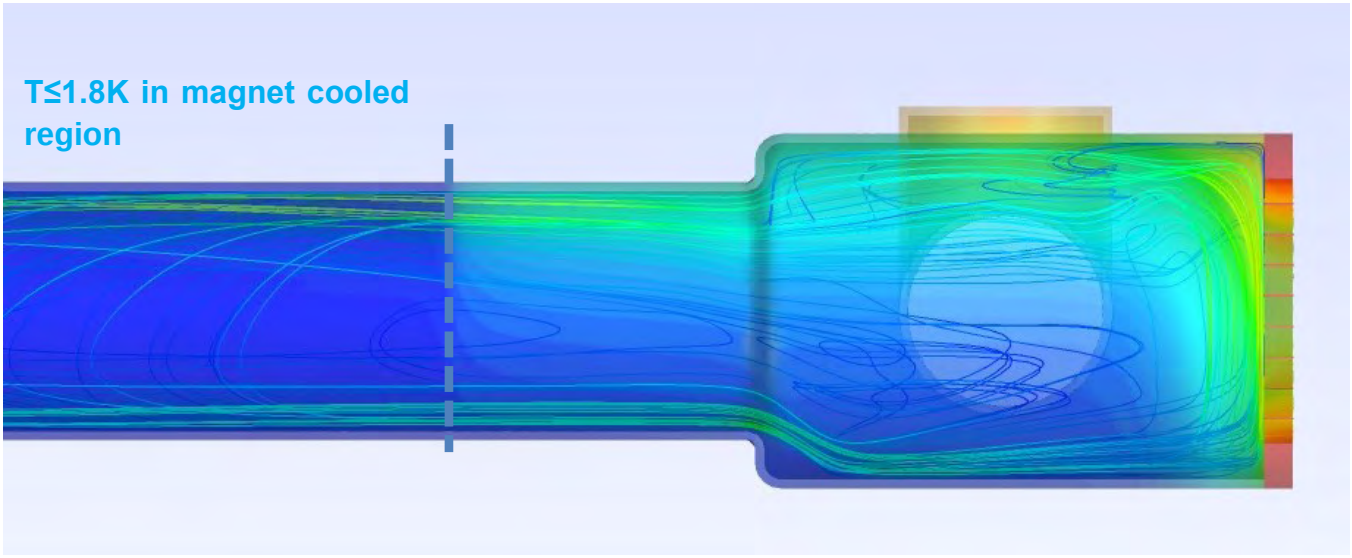

Figure 5.6 Heat transfer in the CFD model. The blue metallic region indicates the cooling of the cold bore at 1.8K. The red region is the cold windows at a temperature around 20K. Heat is transferred by conduction between solid parts (steel – polypropylene). The streamlines inside the solid region indicate that the convection mechanism is stronger close to the warmer windows. The heat and mass transfer from warmer regions to the cooled denser gas inside the cold bore indicate the natural convection mechanism through which buoyancy is driven.

In Figure 5.7 the expected behavior of ^{3}He gas is shown and the regions of the dominant heat transfer mechanism are specified.

It is important to mention that the full model solution requires a Steady State Thermal solution from Ansys Workbench[17]. The output of this solution should be a contraction of the whole steel structure i.e. shrinkage of the cold bore because of its very low temperature. This could change the volume of the gas system and potentially it could affect the result of the simulations. In this study it is considered that the effect of contraction is infinitesimal.

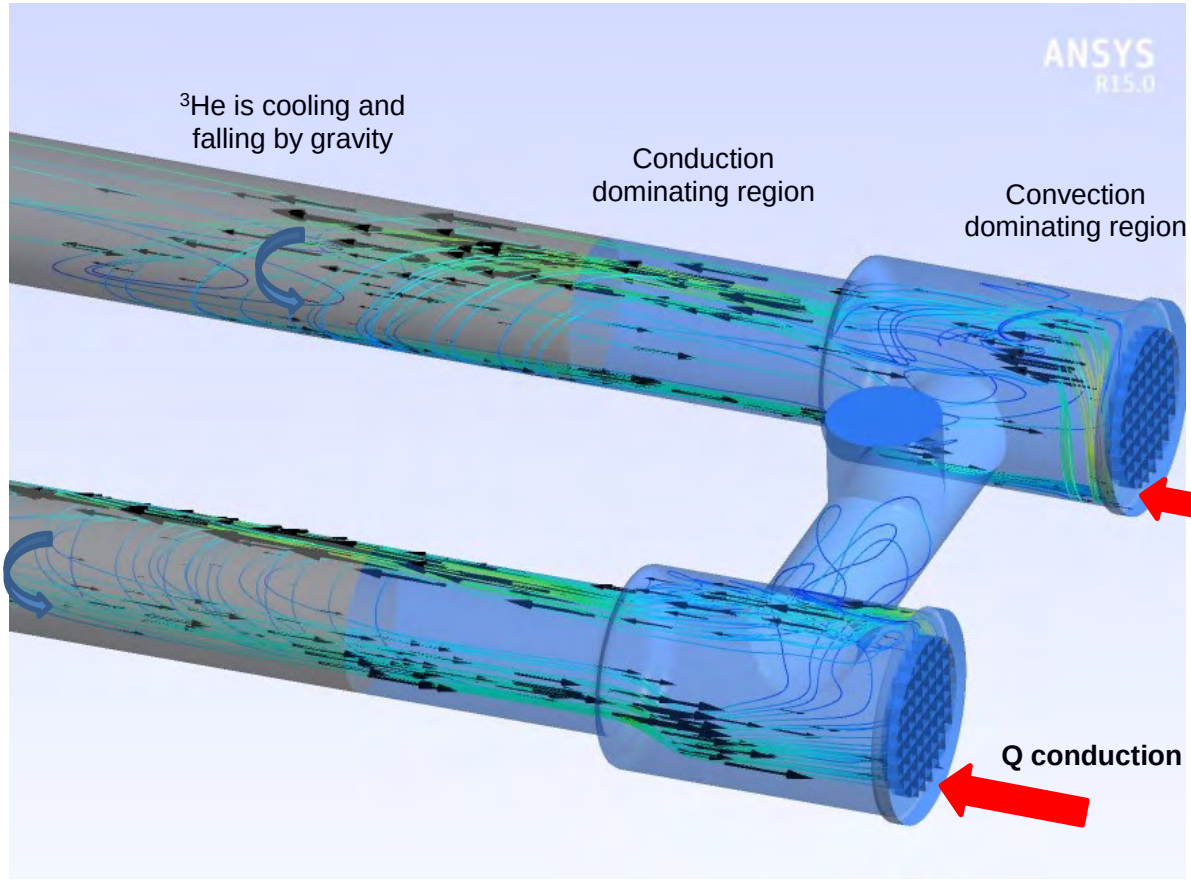

Figure 5.7 The 3D arrows indicate the flow of ^{3}He at some depth inside the cold bore. In convective regions the fluid gets warmer and less dense by absorbing the heat of the hotter windows. Natural (free) convection phenomena arise because of density gradients in the vicinity of the hotter windows and mass (fluid) transfer occurs. The lighter and warmer gas will flow upwind and a stream will start because colder and denser gas should occupy the upward gradient flow of mass. The natural convection current appears at both magnet ends (MRB and MFB) [76] with intensity that is analogous to the corresponding cold window temperature and the tilting angle[18]. In conductive regions the transferred hotter fluid that follows the upper bound of the tube trajectory gets colder by means of conduction. Therefore at this region the gas will increase its density and as the blue arc arrows show, it will fall down by gravity.

[17] This model has been worked out in Ansys 14.5
[18] Hydrostatic pressure induced by tilting the magnet

5.4 The CFD model

The CFD simulation's purpose is to understand the real behavior of the ^{3}He gas in the CAST cold bore and quantify the effects mentioned as the transfer of heat into the regions of interest. To accomplish that, a model resembling the real CAST geometry should be made. However, the real sketch up of CAST ^{3}He system cold bore and surrounding pipework in addition with the cold windows is too complicated as seen in Figure 5.8; therefore a simpler geometrical model should be made. This can be achieved thanks to the sensors that measure the necessary information like pressure and temperature at different points. Sensor's experimental values can be used as boundary conditions to a simpler model and these values are the CFD input parameters. In the following, tables with the specified values that had been used as boundary conditions to the model simulated will be presented.

The CAST model for CFD simulations is an assembly of parts like stainless steel, Polypropylene and the gas itself. Geometric simplifications have been made taking into account the computational cost and time cost for the opposite choice.

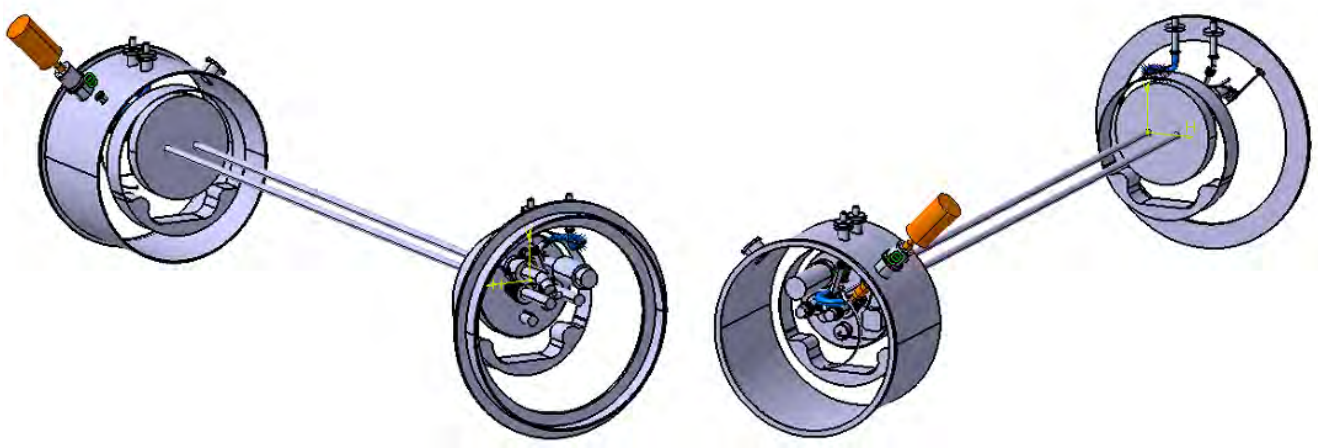

Figure 5.8 CATIA designs of the 10 m cold bore and pipework connections. To fully define the model, dead volumes should be added to the model geometry. Instead, having all the required information needed, a simpler geometrical model can be made.

5.4.1 Model Geometry

The model's volume is totally closed at both ends (MRB and MFB) by the cold windows and Polypropylene foil as also the inlet and outlet of the system is closed by a closing surface. The metallic bellows that absorb the contraction or extraction of the gas volumes were not modeled (Figure 5.9). Smooth edges have been designed as in the real construction model for a change in the pipe diameter from 63.5 mm to 46.2 mm at the end of the bores. This has an impact on

the turbulence model and the fluid flow. In the case where smooth edge change is not used, turbulence effects should be different than in reality.

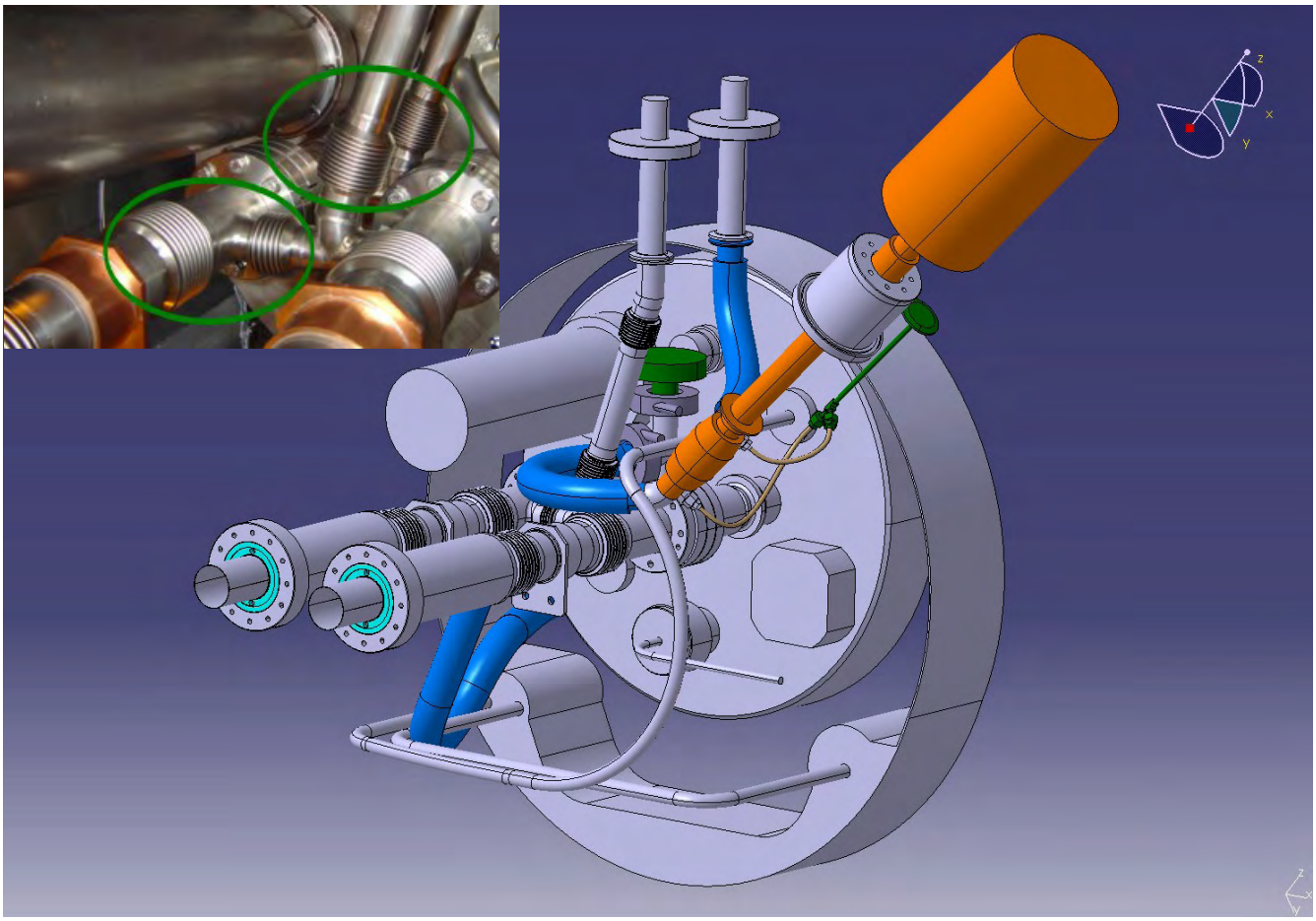

Figure 5.9 CATIA design view of the MRB end of the model. The picture included shows the real configuration and the bellows exposed.

The model for the CFD simulations has been built using Ansys CFX geometry. It consists of

- Stainless steel (SS) cold bores of 1.6 mm thickness
- MFB and MRB ends of SS of the same thickness as the cold bores
- Polypropylene (PP) foil of 15μm thickness attached at the end of MRB and MFB ends respectively, closing the MRB and MFB ends
- Windows SS net as shown in Figure 5.10 that is attached to the PP foil
- Inlet and outlet closing surfaces (SS) at MFB and MRB ends of 1.6 mm thickness
- ^{3}He gas that is a continuum inside the closed metallic structure.

5.4.2 Geometry domains

The cold bore domain consists of two parallel tubes and is inside the magnet's cryogenic cooling system. The cooling power is sufficient to cool down the cold bores to 1.8K so it is reasonable to assign this temperature to the external cold bore surface.

The tubes of the cold bore are closing by the MRB and MFB domains made of stainless steel as the cold bore, having also the same thickness. The inlet and the outlet are closed surfaces and thanks to a sensor attached to the inlet MFB end, the temperature is known and can be used as a boundary condition. The inlet temperature value can be assigned to the closing surface of the outlet, although there is no sensor in the outlet domain. In case where the magnet is horizontal this is reasonable, but when the magnet is tilted this assumption can lead to deviations from reality since the gas flow and heat modifies the outlet temperature value.

In Figure 5.10 a thermal study shows the temperature gradients in the pipework attached to the CAST's inlet and outlet. However, the results of this study cannot be used in this model since the fluid-solid interaction has not been taken into account.

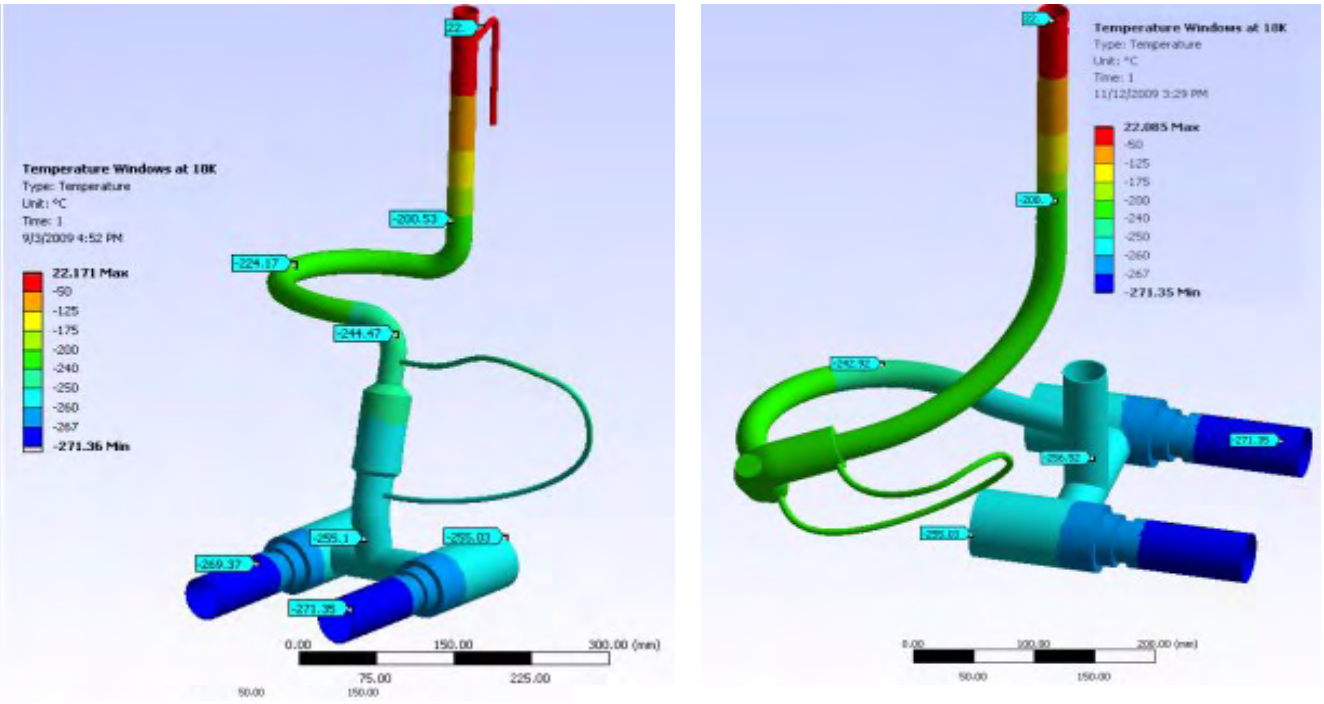

Figure 5.10 MFB (left) and MRB (right) temperature distribution of the inlet and outlet pipework attached respectively. This study contains no fluid-solid interaction. It is shown as a visualization of the temperature distribution from the cold bore domain to the hot (ambient temperature) outside world.

The cold windows attached to the MRB and MFB ends have a strongback net where the Polypropylene (PP) foils of 15 μm thickness each are glued. Since there are 4 sensors at each cold window there is no need for it to be designed as a whole structure (Figure 5.11). Instead the stainless steel net strongback is suitable, closing the MRB and MFB ends attached the PP foil.

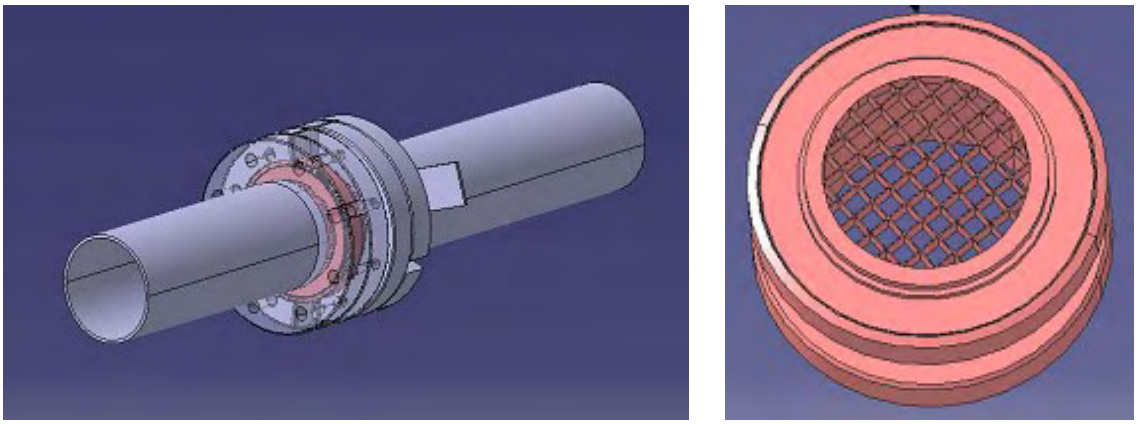

Figure 5.11 Cold window and the pipework attached (left). On the right a CATIA design view of the window. The foil is attached to the metal grid.

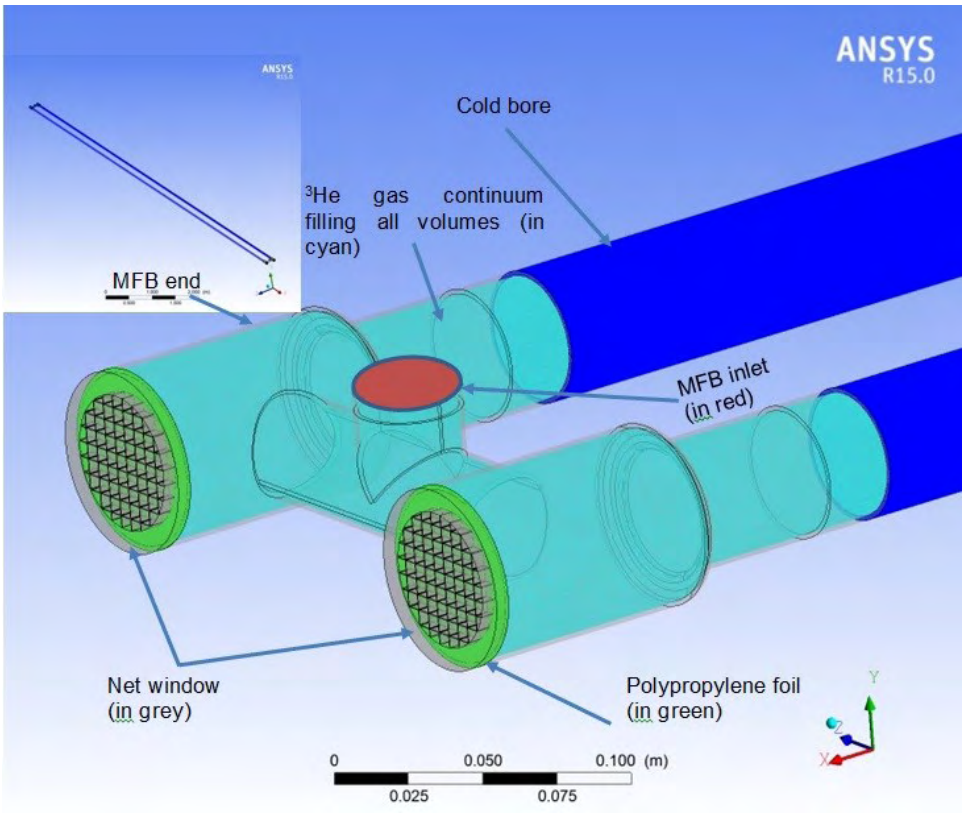

Figure 5.12 The geometry model in the MFB side. Each domain is pointed by arrows. The same configuration exists in the MRB side. The full model is attached. Bellows have been neglected

The geometry model was designed in Ansys CFX Geometry application using the CATIA software 3D model. Using the geometry software provided by Ansys the regions and domains mentioned have been defined. Parts that are composing bodies have been defined as regions where boundaries or interfaces have been created. The continua that are either solids or fluids are assigned to the regions created.

The continua created are

- ^{3}He *gas* that is assigned to the MFBIN, MRBIN and CBIN regions
- Stainless steel *solid* assigned to the CBOUT, MFBOUT, MRBOUT and the WINMFB and WINMRB regions
- *Solid* Polypropylene that composes the PPMFB and PPMRB regions

Geometry has been designed using the following sketch that CAST provided.

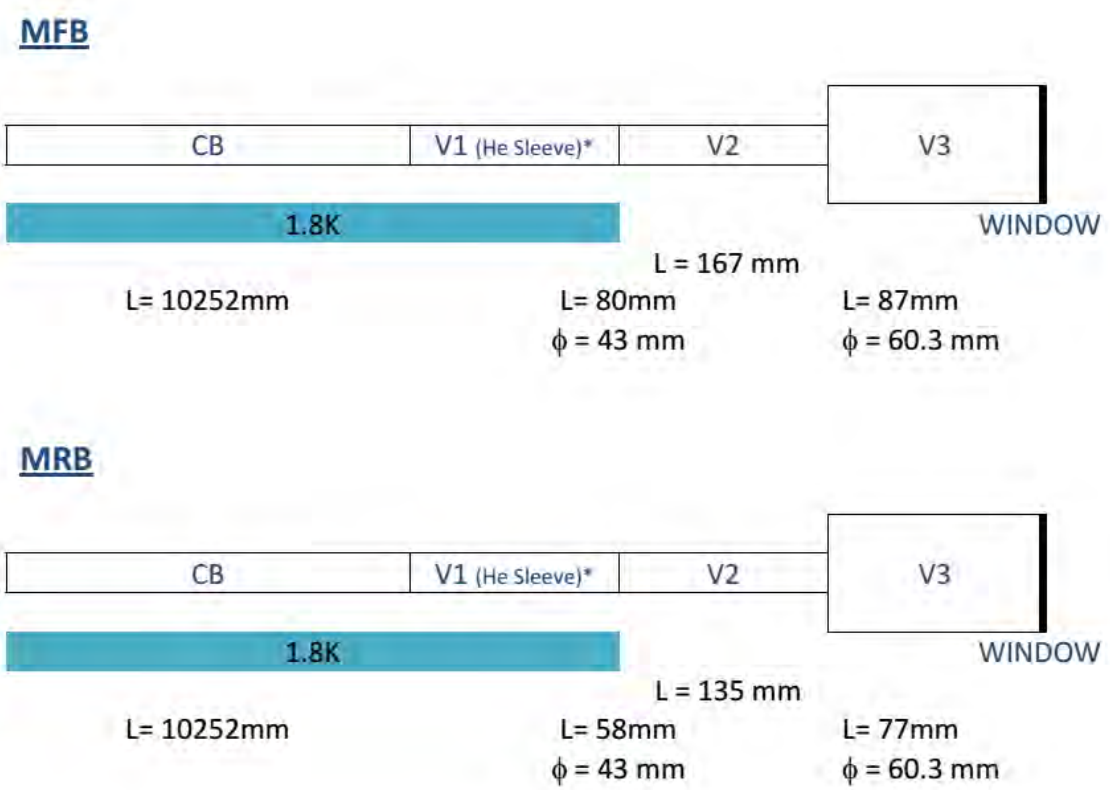

Sketch 5.1 Geometry dimensions that CAST provides. L_{Sleeve} = 25mm, Distance between center of each cold bore = 180 mm and CB connection pipes in between have a φ= 34 mm and V = 0.12984 liters

5.4.3 Boundary conditions

By specification of conditions applied on a domain boundary, the equations related to the fluid flow can be numerically closed. The boundary conditions produce the solution for a given geometry and the sets of physical models. It is the boundary conditions that determine to a large extent the characteristic of the solution, so it is important to set boundary conditions (BC) accurately in order to obtain accurate results. Boundary conditions are a set of properties on surfaces of domains that are required to fully define the flow simulation.

The sensors installed in the gas system are suitable monitors of the values that can be used as boundary conditions. The information provided is temperature and pressure.

The windows temperature is measured by four sensors installed in a hole made over each window flange. There are also heaters attached to the windows flanges in order to heat up the windows in a bake out case or in case CAST wants a higher windows temperature measurement. The sensors (CERNOX) uncertainty is 0.01 K.

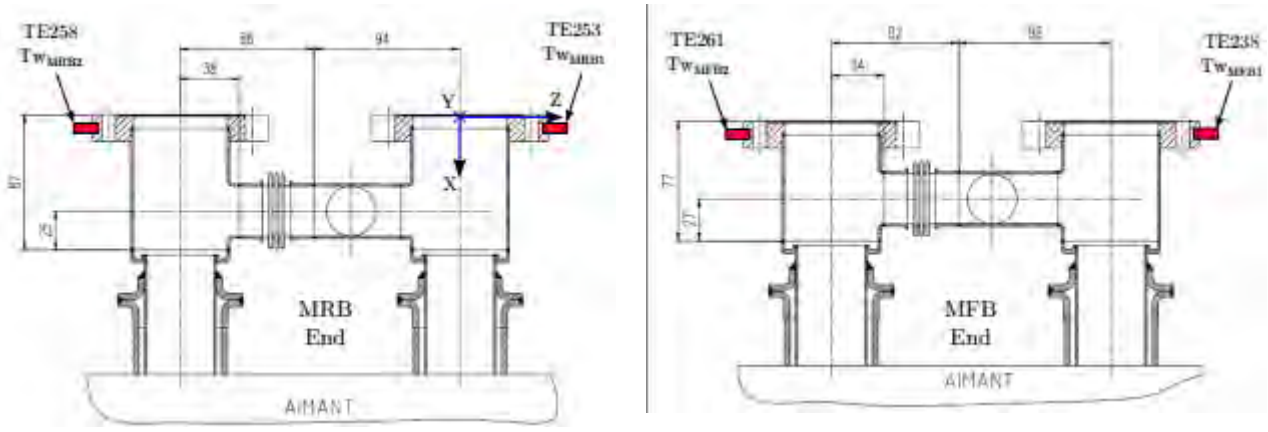

Figure 5.13 Position of the temperature sensors attached in the windows flanges

There are sensors also installed in the inlet and outlet region. The value provided by these sensors can be used as BC's in the CFD model. A pressure sensor is also installed in the MRB end (Baratron 690A) [77]. The sensor is inside the gas volume and its accuracy provides the necessary information of pressure at any moment. The sensor uncertainty of the pressure inside the gas volume is 62 ppm.

The ^{3}He gas mass can be measured accurately before injection in the cold bore. The gas system setup with the thermal bath and its constant temperature (309.15 ±0.01 K) in addition with the pressure valve used, can provide accurate measurement of the amount of gas released from MV2 (metering volume). However, it should be considered that a small amount of gas could be trapped inside the pipework. In this study, the amount of gas that can be trapped is considered negligible because the pipework is at high temperature (room temperature) and it is assumed that all gas flows towards the cold bores where temperature is at 1.8 K. The uncertainty of the number of moles of gas measured is about 37 ppm.

The number of moles N can be used as a boundary condition that tests the validity of the simulations. In the CFD simulation program one should set the pressure inside the gas volume (close to the experimental measurement place – if there is no recirculation of gas at this point) and after solving the problem can integrate over the volume and extract the mass of the gas. The reverse process is not allowed, meaning there is no way to set as input (BC) the number of moles inserted and measure the pressure as an output in the CFX program.

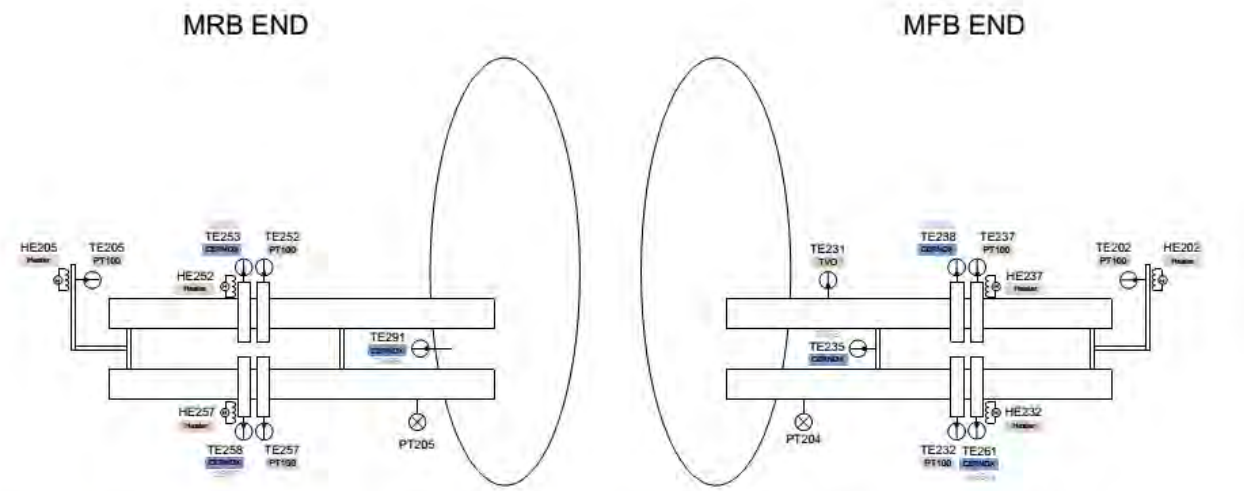

SENSOR	TYPE	LOCATION	READOUT INSTRUMENT	LABVIEW VI
TE205	PT100	Thermalisation à 60K	Lakeshore	LSCI TEMP MON
TE252	PT100	Bride ext. fenêtre droite	Lakeshore	LSCI TEMP MON
TE253	CERNOX	Bride int. fenêtre droite		
TE257	PT100	Bride int. fenêtre gauche	Lakeshore	LSCI TEMP MON
TE258	CERNOX	Bride ext. fenêtre gauche		
TE291	CERNOX	A gauche	Logtherm	Quench-He
HE205		Thermalisation à 60K		
HE252		Bride fenêtre droite	Hameg	
HE257		Bride fenêtre gauche	Hameg	
PT205	Themal Acoustic Oscilations			

SENSOR	TYPE	LOCATION	READOUT INSTRUMENT	LABVIEW VI
TE202	PT100	Thermalisation à 60K	Lakeshore	LSCI TEMP MON
TE231	TVO	Tube faisceau droit	Picowatt	AVS47
TE232	PT100	Bride int. fenêtre gauche	Lakeshore	LSCI TEMP MON
TE235	CERNOX	Pont tube faisceau	Logtherm	Quench-He
TE237	CERNOX	Bride int. fenêtre droite		
TE238	PT100	Bride ext. fenêtre droite	Lakeshore	LSCI TEMP MON
HE202		Thermalisation à 60K		
HE232		Bride fenêtre gauche	Hameg	
HE237		Bride fenêtre droit	Hameg	
PT204	Themal Acoustic Oscilations			

Figure 5.14 Schematic view of the sensor's location in the CAST gas system.

The configuration of the BC's can be seen in Figure 5.14. Apart of the solid-gas interfaces along the whole structure, the uniform temperature in the cold bore and the adiabatic conditions that the MRB-MFB ends and the PP foil have been set, it is important to mention that the temperature of the windows-net is applied in the stongback net perimeter as shown in red. The inlet and outlet temperature BC's have been applied in the red region (Figure 5.14) that closes the MFB and MRB ends respectively.

The cold windows temperature value is measured continuously and each sensor value can be used independently, applied in the perimeter of the window as seen in Figure 5.15. To apply the sensor's value in the window perimeter is the best choice, rather than applying it to the whole strongback net. This is firstly because the sensor is located at this point (although in the outer side of the perimeter) and secondly because by applying adiabatic BC at the rest of the net domain inner fluid-solid interactions are taken into account.

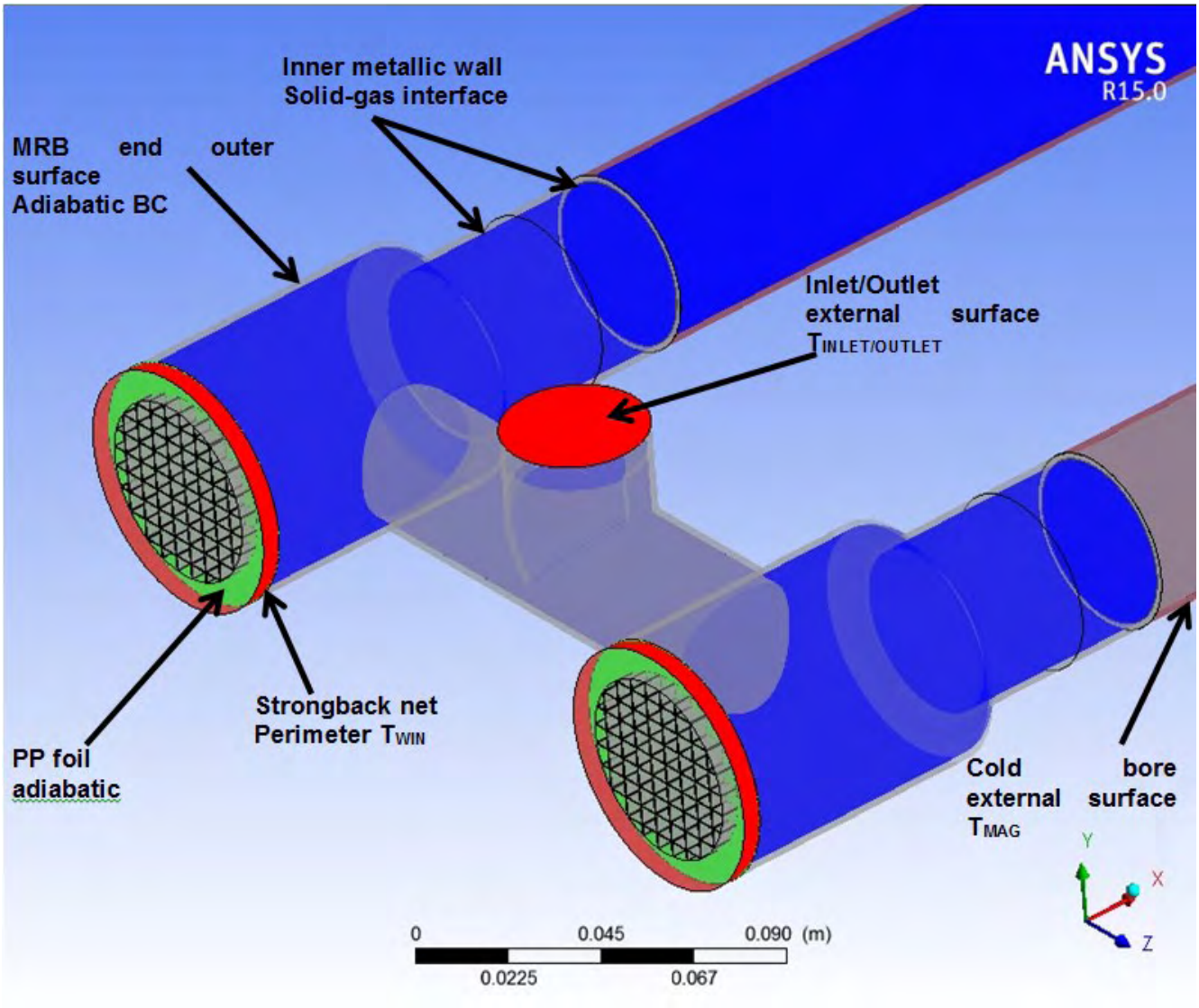

Figure 5.15 Boundaries condition configuration. Sensor's values have been applied at the specified regions and fluid-solid interfaces have been created.

5.5 CFD model meshing

In this study a CFX-Mesh has been used, that is a mesh generator aimed at producing high quality meshes for CFD simulations. The CFD mesh requires meshes that can resolve boundary layer phenomena. CFX-Mesh produces meshes containing tetrahedral, prism, pyramids and hexahedra [78].

The meshing purpose is to discretize each domain, create small elements called cells where integral Navier-Stokes equations can be solved numerically. Meshing the fluid domain is a very crucial operation for the accuracy of the solution and convergence. Important physical phenomena could be overlooked if cells are too big or if meshing is too coarse. It is then mandatory to find the optimal solution between a refined mesh (computational time cost) and a coarser one that is less costly.

The CAST model includes a scoped method control mesh (Sweep or Multizone) for the cold bore fluid area (Multizone method) and a sweep method for the outer metallic cold bore area. Automatic method has been used for the MRB and MFB outer metallic ends.

Ansys CFX- mesh uses as its automatic method a tetra mesh method that is based in Delaunay triangulation with an advancing-front point insertion technique used for mesh refinement. The Patch conforming Tetra mesh method applied to the MRB and MRB fluid ends, as it is, supports the 3D inflation. The method creates tetrahedrons that can be adjusted in size by Face sizing tools.

5.5.1 Cold bore meshing (Fluid)

Multizone meshing has been applied to the cold bores of the CFD model. The mapped mesh type is hexahedra and the surface mesh method is uniform. Face sizing and inflation have been applied to the domain. The inflation method used is the First Layer thickness option with first layer height of 1e-02mm, growth rate 1.1 and maximum height of the inflation layer 3mm.

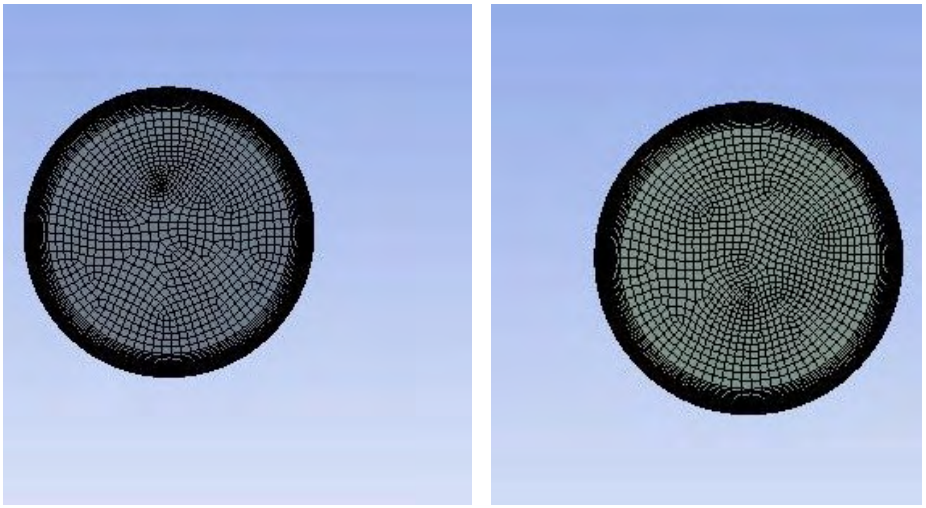

Figure 5.16 Cross view of the interface of the cold bore at the MRB end. Multizone meshing and inflation is shown.

5.5.2 MRB and MFB meshing (Fluid)

The MRB and MFB ends, are meshed using tetrahedrons with the Patch conforming method. Inflation has also applied using the Last Aspect ratio option. This option controls the heights of the inflation layers by defining the aspect ratio of the inflations that are extruded from the inflation base. The *aspect ratio* is defined as the ratio of the local inflation base size to the inflation layer height.

Inflation is useful for CFD boundary layer resolution, especially for eddies currents that can be resolved close to the wall. The layers have been created in every fluid domain are 21. A detail of the layers used can be seen in Figure 5.16

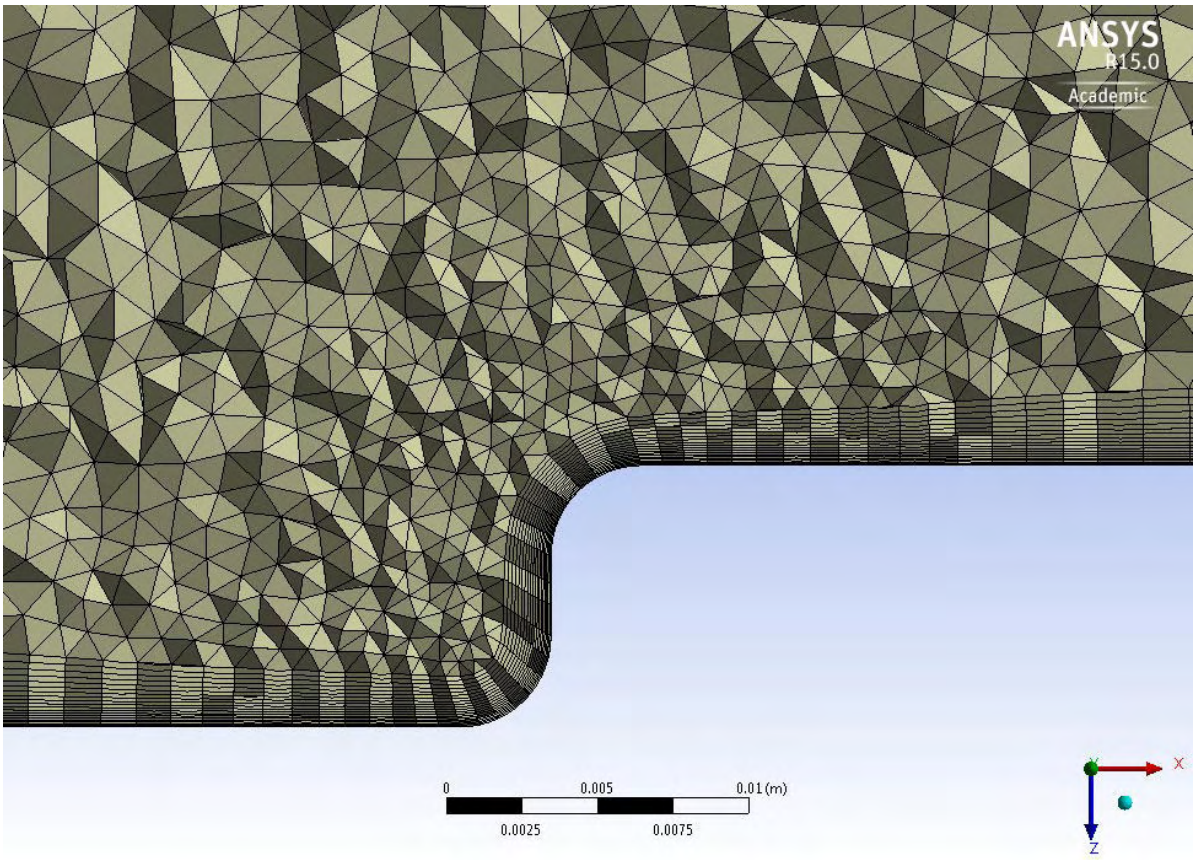

Figure 5.17 The “Last Aspect Ratio” method which has been used is the Base/Height ratio. In MRB and MFB fluid domains, the ratio is 5.5 and the inflation result can be seen in the figure. The Patch conforming method builds tetrahedrons and by use of a “Face control” option, elements are created with a smallest size of about 8e-004m. Growth rate is 1.05, so from a small element, a smooth growth is preserved to neighbored elements. Same condition is applied to the inflation elements. The first layer height is 5e-002 mm.

5.5.3 Solid meshing

Solid domains of stainless steel and polypropylene are meshed in a default way using fewer elements except than the strongback net where the inflation algorithm has been applied. The automatic method was used for the PP foils and the mesh system choice was the Multizone method.

The mesh should be as fine as possible but there is a limit in this study depending on the memory of the computer used and the number of the available solver CPU's. A detailed table of the mesh elements for each domain is given in table 5.1. A symmetry plane could possibly resolve this issue but since the results, using about 12 million elements, show nice behavior and converge, it is physical and reasonable to keep this configuration.

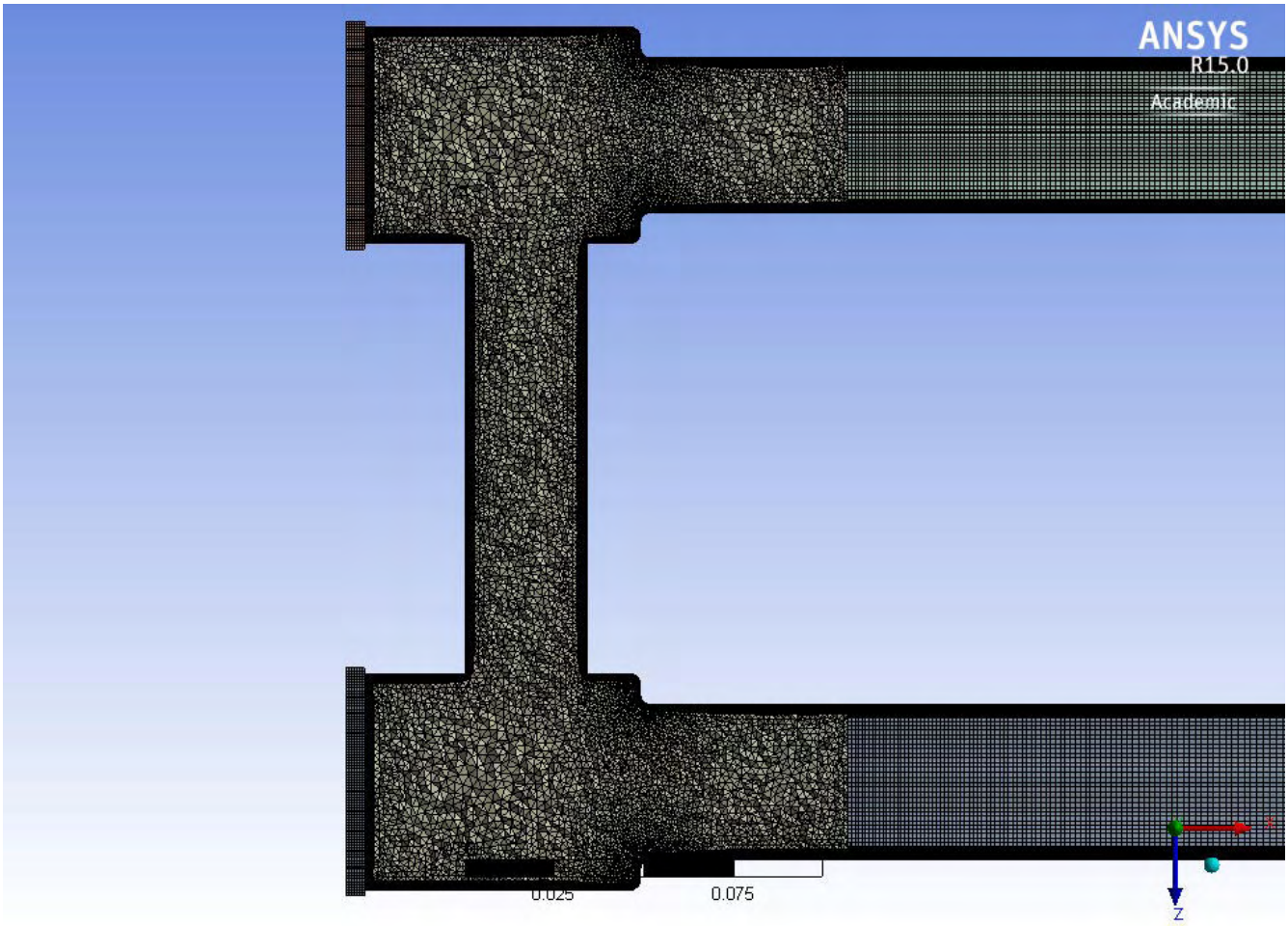

Figure 5.18 : The final mesh setup. MRB end and a part of the cold bore domain are shown (Fluid). At the MRB fluid domain end, the solid inflated strongback net is also depictured.

5.5.4 Mesh Quality check

A check for measuring the mesh quality is the Skewness. Skewness is one of the primary quality measures for a mesh. Skewness determines how close to ideal (i.e., equilateral or equiangular) a face or a cell is.

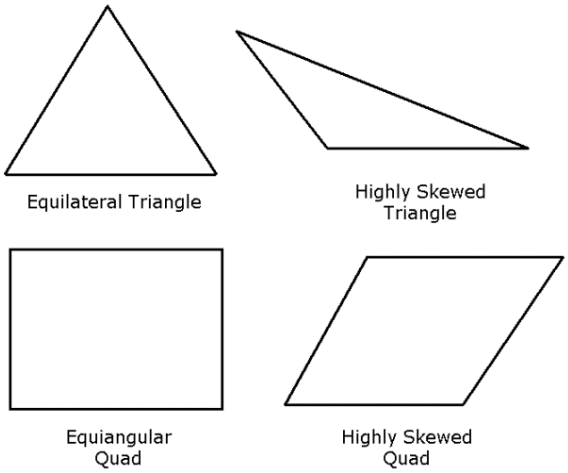

Figure 5.19 Ideal and Skewed Triangles and Quadrilaterals

Mesh Skewness check in the CFD model revealed that the minimum value is 1.305E-10, maximum value is 0.88 and the average value is 0.12. There are only few elements with Skewness value above 0.75 that is characterized as poor and convergence is achieved not easily.

Orthogonal Quality

The orthogonal quality for cells is computed using the face normal vector, the vector from the cell centroid to the centroid of each of the adjacent cells, and the vector from the cell centroid to each of the faces. Figure 5.18 illustrates the vectors used to determine the orthogonal quality for a cell. The range for orthogonal quality is 0-1, where a value of 0 is worst and a value of 1 is best.

The Mesh metric “Orthogonal quality” has been checked in the CFD model and the minimum value is 0.167, the maximum value is 1 and the average value is 0.951.

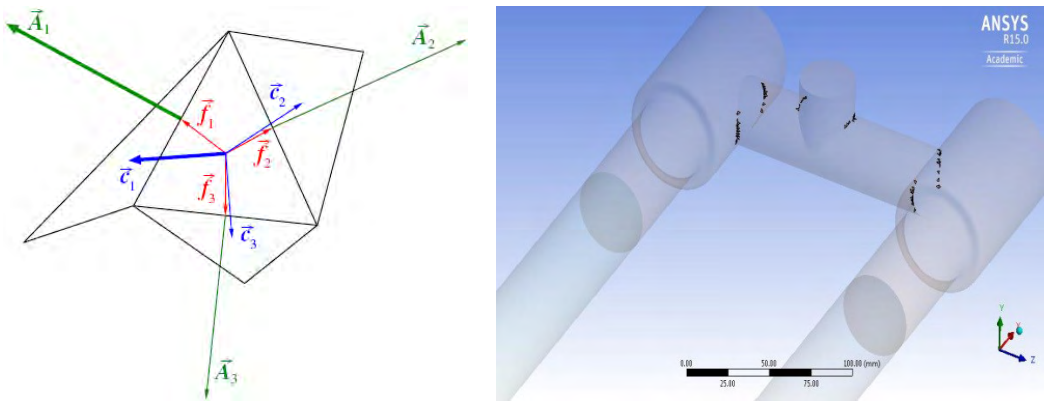

Figure 5.20 On the left Vectors used to compute orthogonal Quality for a cell. On the right some elements created with orthogonal quality of about 0.2 are shown.

5.6 Physical properties of the model

Physical and thermal properties of the continua used to the CFD model are of excessive importance for the accurate problem description. The properties of ^{3}He will be described as also the solids used in the model, which are stainless steel and polypropylene.

5.6.1 ^{3}He (Helium-3)

Helium-3 is a very rare light isotope of helium with two protons and one neutron. It is used for neutron detection, ultra-low temperature research and fusion reactions. CAST uses helium-3 because its high saturation pressure makes it suitable for research of axions having higher masses.

National Institute of Standards and Technology (NIST[19]) [74] database provides the properties of ^{3}He in comparison with ^{4}He.

Property	Helium-3	Helium-4
Formula	^{3}He	^{4}He
Molar mass (M) [g mol^{-1}]	3.01603	4.002602
Critical temperature (T_c) [K]	3.3243	5.1953
Critical pressure (p_c) [Pa]	116000	116000
Saturation pressure (p_{Sat} [mbar]) at 1.8 [K]	135.58	16.405

[19] NIST: it is the National Institute of Standards and Technology: http://www.nist.gov/srd/nist23.cfm

Table 5.2 NIST database properties of ^{3}He and ^{4}He.

In order to fully describe the thermodynamic properties of the fluid, an equation of state is needed, that is a relation between state variables such as temperature, pressure and volume. The fluid in the CFX-Pre program of Ansys [79] can be considered as an ideal gas or a real gas. In the case where the fluid is considered as ideal, intermolecular forces would be neglected.

Van der Waals in 1873 proposed an equation of state that takes into account intermolecular forces and in his remarkable equation he introduced an attractive and a repulsive parameter. Nowadays more complex equations describe the real gases more accurate.

Since the beginning of this CFD study the equation of state proposed and used throughout all models developed is the Peng-Robinson equation. The equation proposed in 1976 satisfies the following requirements

- ✓ The parameters are expressible in terms of critical properties and the acentric factor[20]
- ✓ The model provides accuracy close to the critical point
- ✓ The equation should be applicable to all calculations of all real fluids

This equation of state is the most complete among the real gases although new extensions concerning the centricity have been developed.

The formula of the Peng-Robinson equation is

$$P = \frac{RT}{V_m - b} - \frac{a(T)}{V_m^2 + 2V_m b - b^2} \tag{5. 6}$$

Where P is the pressure, V_m is the relative volume, T is the fluid temperature and R the molar gas constant. The constants a and b are defined as

$$b = 0.778\frac{RT_c}{p_c} \tag{5.7}$$

and

$$a(T) = a_0\left(1 + n\left(1 - \sqrt{\frac{T}{T_c}}\right)\right)^2 \tag{5.8}$$

[20] The acentric factor is a measure of the non-sphericity (centricity) of molecules

$$a_0 = 0.45724 \frac{R^2 T_c^2}{P_c} \quad (5.9)$$

and the parameter n is computed as a function of the acentric factor, ω:

$$n = 0.37464 + 1.54226\omega - 0.26993\omega^2 \quad (5.10)$$

NIST developed a preliminary Helmholtz equation of state based on experimental measurements for ^{3}He. The equations of state mentioned are compared in a single plot (Figure 5.21) of density versus temperature for constant pressure.

The density at low temperatures is high and density gradients at this temperature range (1.7-1.9 K) should be taken into account in the CFD model. The equation of state and fluid transport properties that are temperature dependent can include all the fluid transport phenomena. The scales at which such variations in density exist are very small and hence the mesh refinement should consider such effects. The Peng-Robinson equation of state is implemented in the Ansys-CFX program that is the setup environment of this CFD model.

In the Ansys-CFX program thermal conductivity and heat capacity at constant pressure are expressed as functions of temperature.

5.6.2 Thermal properties

Thermal conductivity and dynamic viscosity have been considered as temperature dependent neglecting the influence of pressure. Data has been obtained from Hurly and Moldover (2000) for T ≤ 50K and Lemmon (2011) for T > 50K [75]. The plots in Figure 5.22 show the thermal conductivity[21] and dynamic viscosity[22] versus temperature.

[21] It is the property of a material to conduct heat
[22] It is the amount of heat needed to provide to 1 kg of substance to increase its temperature by 1 K.

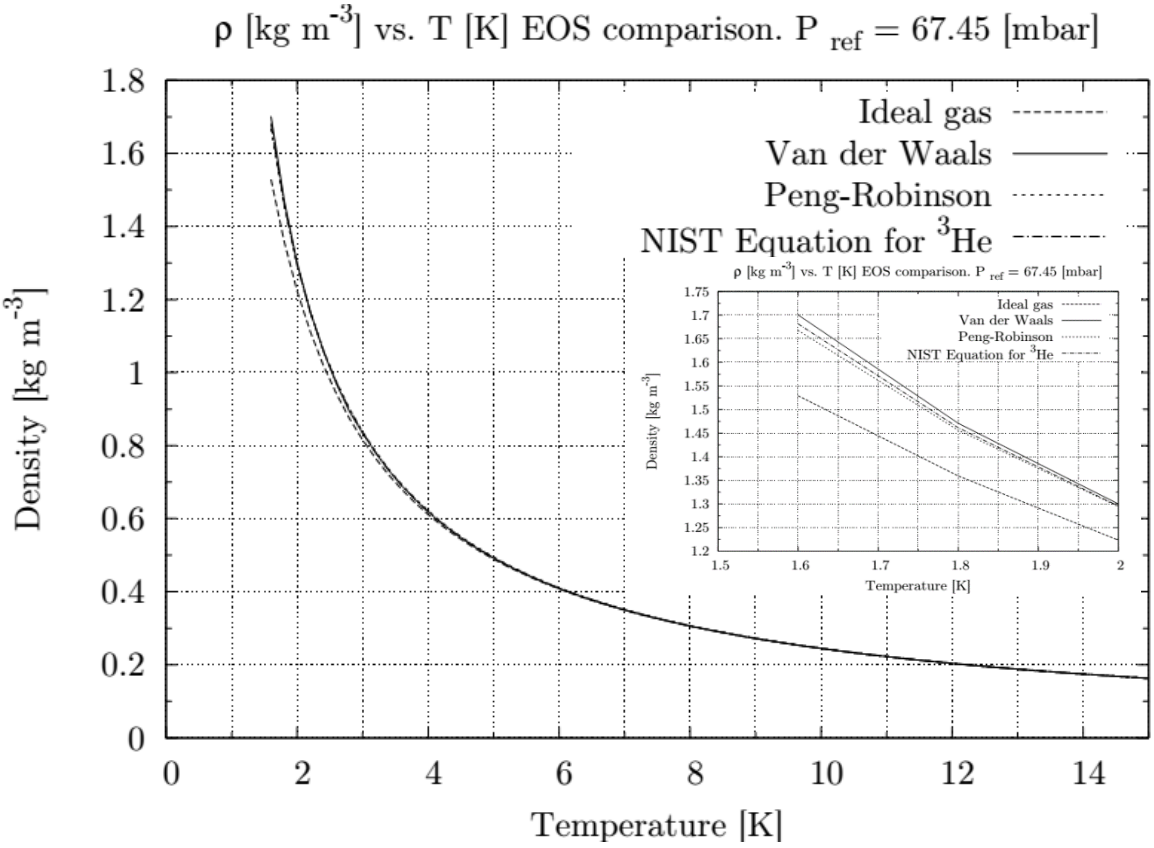

Figure 5.21 Equation of State (Eos) plot. Density is plotted as a function of temperature for a given pressure (setting) P=67.45 mbar. The detailed plot includes the differences in low temperatures and the deviation from the real gas behavior is obvious.

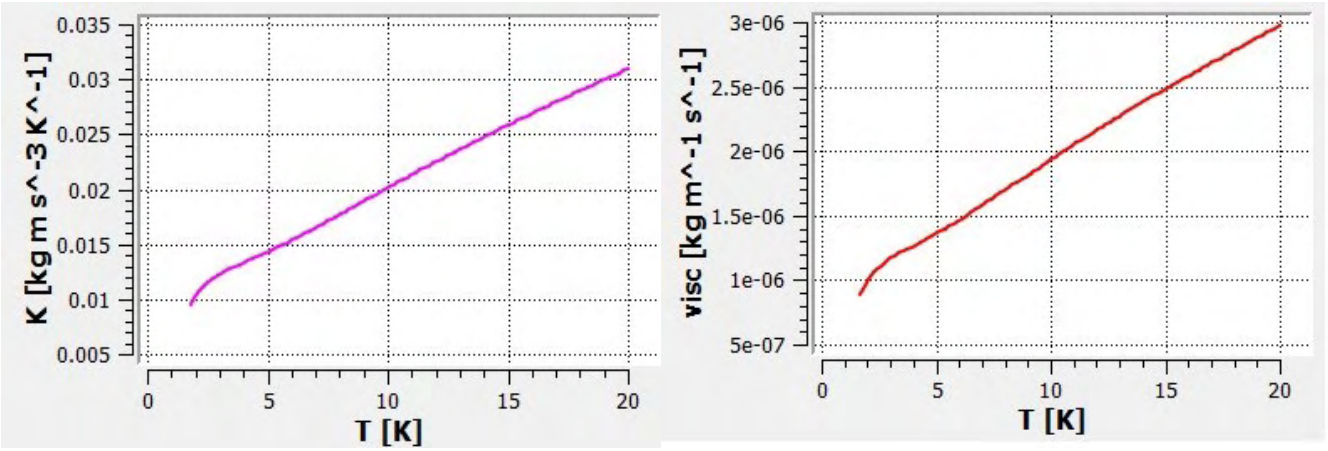

Figure 5.22 Thermal conductivity on the left and viscosity plot on the right as a function of temperature.

The influence of pressure and temperature should be taken into account for heat capacity at constant pressure Cp[23] evaluation. For each pressure value used in the CFD model, a different temperature dependent polynomial equation is plotted and by applying fitting methods, the fifth

[23] It is the amount of heat needed to provide to 1 kg of substance to increase its temperature by 1 K.

order polynomial coefficients are extracted. Ansys-CFX program uses NASA format to specify the heat capacity of ^{3}He. The formula used is the following

$$\frac{C_p^0}{R} = \ a_1 \ + \ a_2 T + a_3 T^2 + a_4 T^3 + a_5 T^4 \qquad (5.\ 11)$$

Ansys-CFX uses a temperature limit that defines two temperature ranges for the upper and the lower interval. The same method is applied for extracting the polynomial coefficients for specific enthalpy

$$\frac{H^0}{R} = \ a_1 T + \frac{a_2}{2} T^2 + \frac{a_3}{3} T^3 + \frac{a_4}{4} T^4 + \frac{a_5}{5} T^5 + a_6 \qquad (5.\ 12)$$

and specific entropy

$$\frac{S^0}{R} = \ a_1 \ln T + a_2 \ T + \frac{a_3}{2} T^2 + \frac{a_4}{3} T^3 + \frac{a_5}{4} T^4 + a_7 \qquad (5.\ 13)$$

There are seven coefficients in each interval for a total of 14 coefficients. Figure 5.23 shows a plot of Cp for different pressures versus temperature. The fitting method to extract the coefficients is a polynomial of fourth order. The fit is accomplished using ROOT software chi-square method.

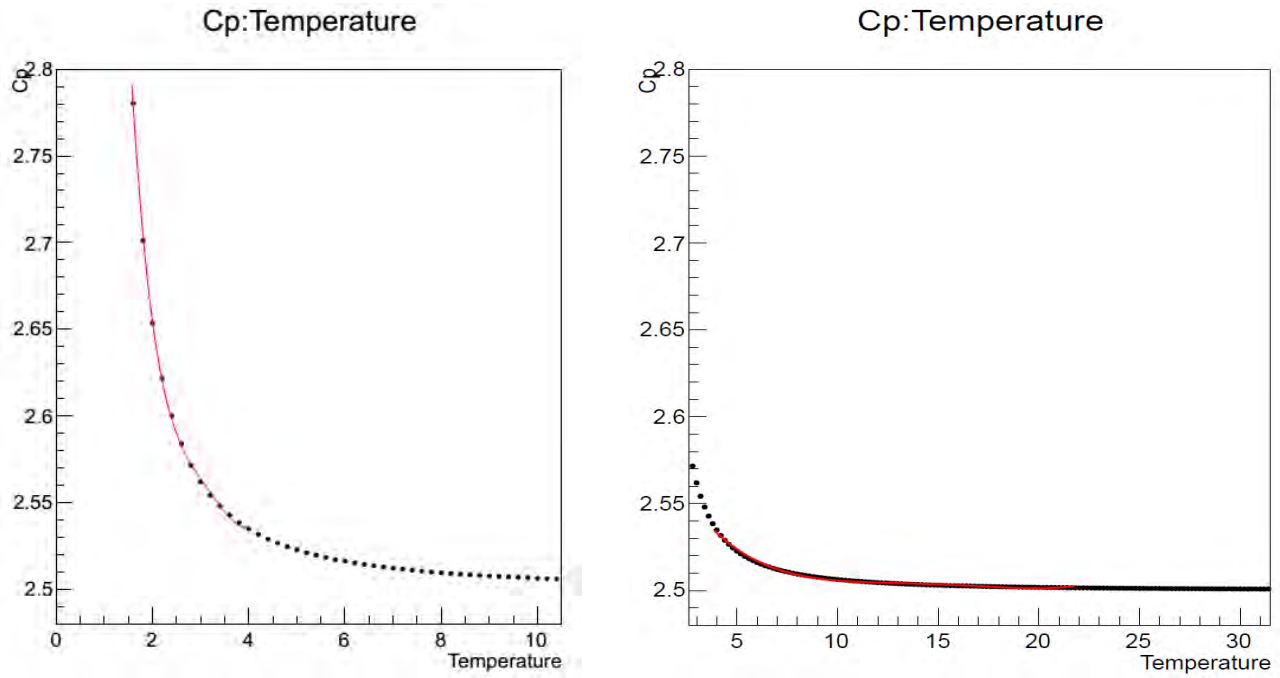

Figure 5.23 Cp/R fit method. The polynomial fit is a fourth order one. There are two NASA coefficients intervals and in this example of 83 mbar, the Cp/R is fitted at the temperature range 1.5- 4K on the left while on the right plot the fit is between 4 and 23K.

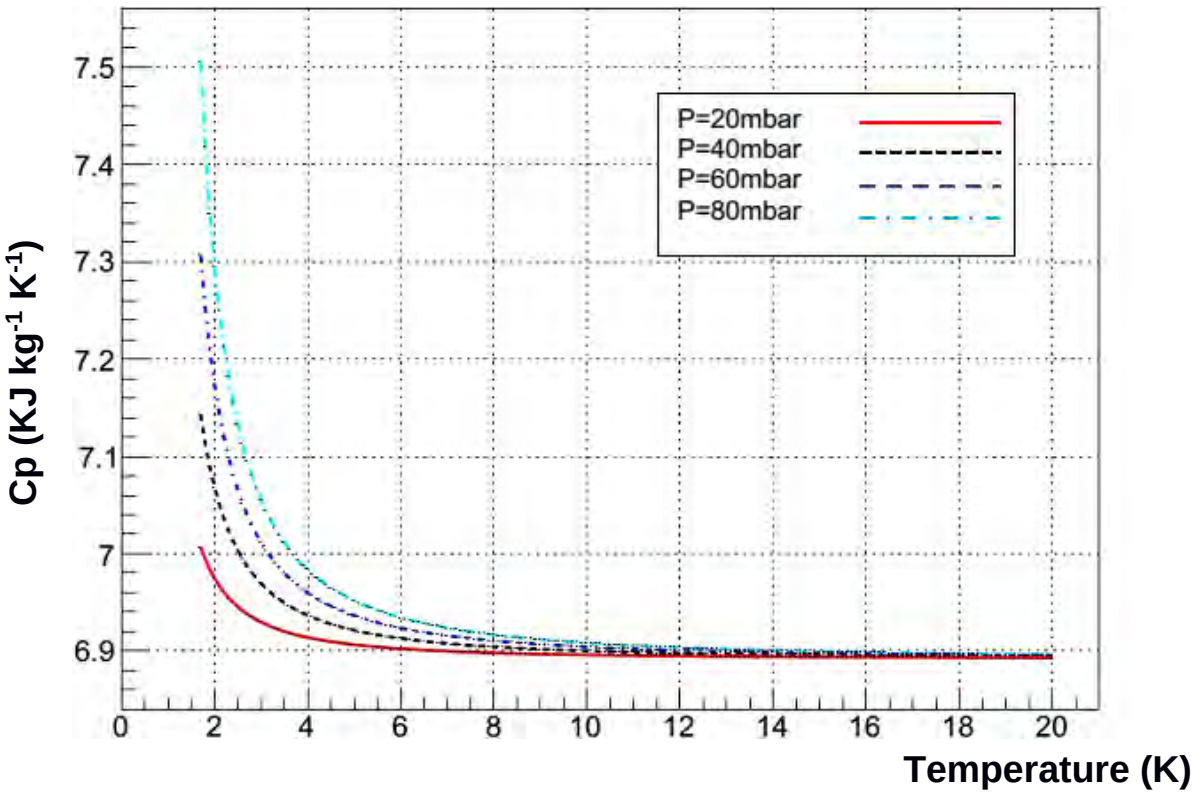

Figure 5.24 Heat capacity is plotted against various pressures. As temperature decreases the capability of the gas to store energy is greater.

5.6.3 Solid Properties

Stainless Steel

Pipework thickness as also the strongback nets are made of steel. A stainless steel coded as AISI 316NL has been used by CAST. The type used is the Cr-Ni, austenitic stainless steel AISI 316LN type (designated UNS S31653 under the UNS). Due to the difficulty to find the thermal properties of this particular stainless steel at the low temperatures occurring in the problem, they have been assumed similar as the kind of stainless steel from the same series, UNS S31600. Thermal Conductivity values have been obtained from Marquardt et al. (2000), while constant heat values have been obtained from Du Chatenier (1965) for 1 K < T < 3 K and Marquardt et al. (2000) for T > 3 K. [80].

The data obtained have been implemented in Ansys-CFX as functions. Then, expressions are created based on the functions generated for each variable. The following plot in figure 5.25 reveals the trend of thermal conductivity and heat capacity of the SS used as implemented in Ansys-CFX.

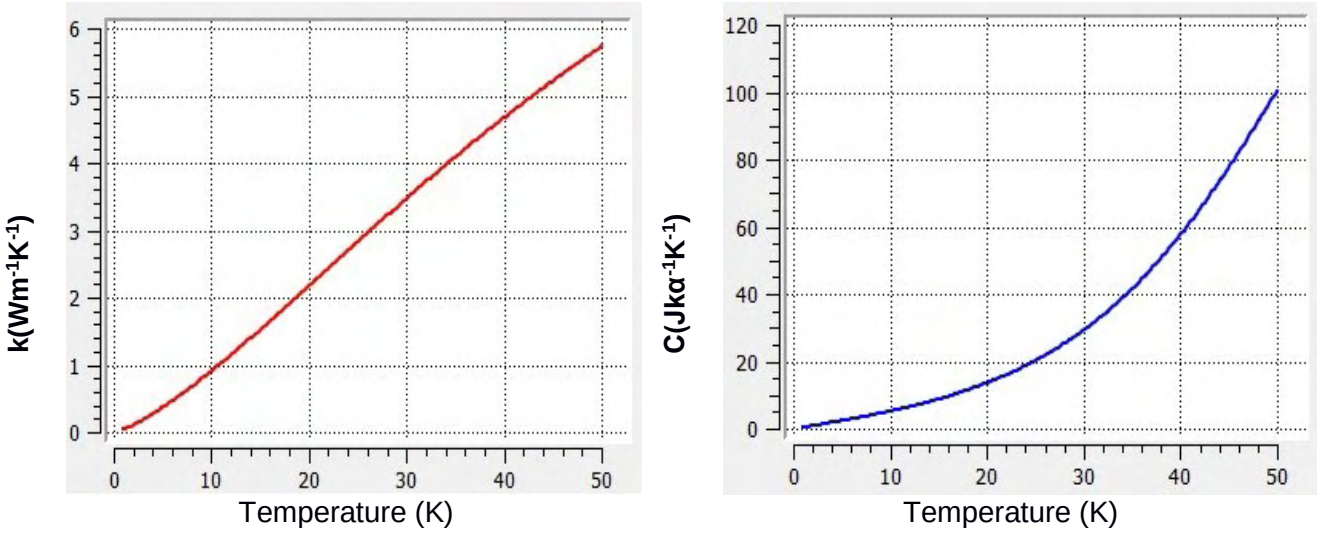

Figure 5.25 On the left, thermal conductivity is plotted versus temperature for SS 316 in Ansys-CFX. The low values of thermal conductivity-k close to absolute zero temperatures means that heat will flow towards the fluid instead of being transferred by conduction to the pipework. On the right, Heat capacity is plotted against temperature for SS 316 in Ansys-CFX. Close to absolute zero temperatures, the capacity of steel to store heat is decreasing and subsequently the heat will flow into the fluid.

Polypropylene (PP)

The cold windows at each end of the CAST telescope consist on a 15 μm thick polypropylene (PP) foil attached to a metallic strongback net. There are several types of PP depending on its tacticity[24] and on its crystallinity. The PP is a thermoplastic polymer, formulated -$(C3H6)_n$ -. The PP foils in CAST can be assumed as isotactic, with 65% of crystallinity[25] [77]. Thermal conductivity values have been obtained from Choy and Greig (1977), while constant heat values have been obtained from Gaur and Wunderlich (1981). Ansys-CFX stores the data mentioned and a linear interpolation is used to create the following graphs (Figure 5.26).

Since the heat capacity and thermal conductivity of both solid materials (Stainless steel and PP) are quite low at low temperatures, heat would flow towards the fluid. The heat will flow from the PP foil to the steel or to the gas because of its low thermal properties values. It is then natural to assume that in the data taking period considered, incoming heat will be transferred to the fluid because of the low capacity values of SS and PP.

[24] Tacticity (from Greek τακτικός *taktikos* "of or relating to arrangement or order") is the relative stereochemistry of adjacent chiral centers within a macromolecule

[25] Crystallinity refers to the degree of structural order in a solid. In a crystal, the atoms or molecules are arranged in a regular, periodic manner

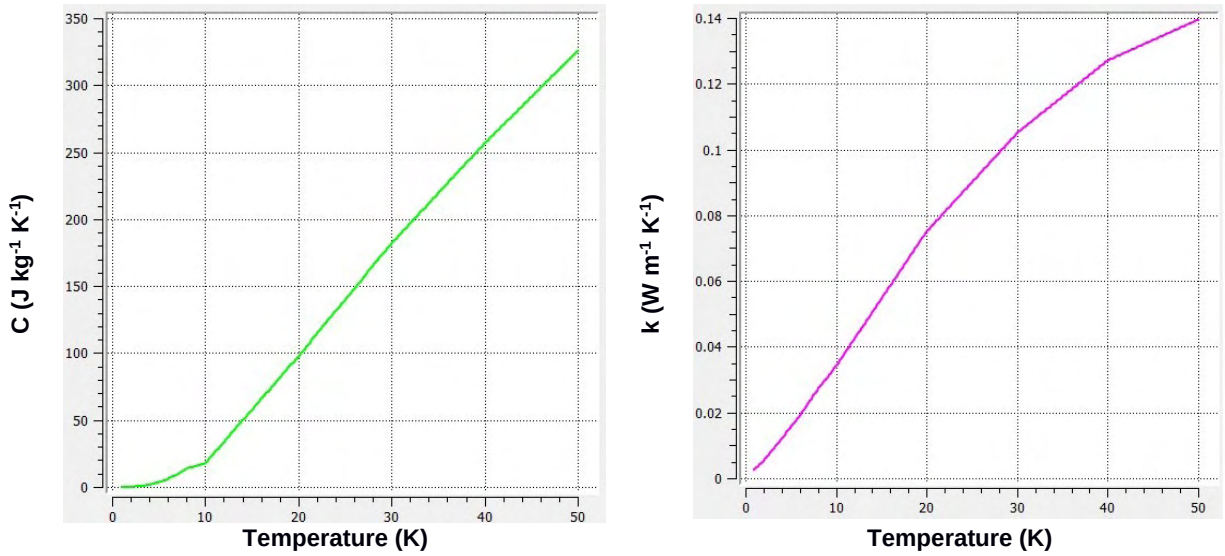

Figure 5.26 On the left Heat Capacity of PP foil is plotted against temperature. On the right, a plot of thermal conductivity versus temperature is shown

5.7 Physical modelling

Since fluid domains that define the region of the fluid flow have been defined, it is natural to define the physical nature of the flow. The accuracy of the physical modeling specifies the CFD model accuracy.

5.7.1 Steady state model

First it is of great importance to specify if the time dependence of the flow characteristics is a steady state or a transient one. Steady state simulations, by definition, are those whose characteristics do not change with time and whose steady conditions are assumed to have been reached after a relatively long time interval [81].

Transient simulations require real time information to determine the time intervals at which the CFX-Solver calculates the flow field. Transient flows can be caused by the initially changing boundary conditions of the flow or in cases that the flow is driven by buoyancy.

In the CFD model created, steady state simulations have been performed and although buoyancy is activated as the natural convection source, by changing the pseudo-timestep size of the steady state simulation, any oscillations of the residual plots disappears. It is also physical to assume a steady state simulation since the rotational velocity is very low.

5.7.2 Continuum flow assumption

The validity of Navier-Stokes equations that describe the fluid motion is set by a threshold value that is known as the Knudsen number. In case where the pressure in the medium is very low as in CAST, the Knudsen number that express the ratio between the mean free path of ^{3}He molecules and a representative physical length scale should be examined.

The Knudsen number determines whether statistical mechanics or the continuum mechanics formulation of fluid dynamics should be used. If the Knudsen number is ≥1, the mean free path of a molecule is comparable to a length scale of the problem, and the continuum assumption of fluid mechanics is no longer a good approximation. In this case statistical methods must be used. The formula that expresses the dimensionless Knudsen number is

$$Kn = \frac{\lambda}{L} \tag{5. 14}$$

The mean free path can be calculated from the following expression

$$\lambda = \frac{k_B T}{\sqrt{2\pi\sigma^2 p}} \tag{5.15}$$

Where k_B is the Boltzmann constant, T is the mean temperature of the fluid system, σ is the particle hard shell diameter and p is the total pressure. Calculating the above expressions it follows that Knudsen number is ≤ 1 so it is natural to use the continuum assumption of fluid mechanics instead of a statistical method.

5.7.3 Heat transfer model

Heat transfer that is modeled is used to predict the temperature throughout the flow. The mechanisms involved, consist of conduction, convection, and (where appropriate) turbulent mixing and viscous work. The model includes the transport of enthalpy and kinetic energy effects. This option is necessary for buoyancy modeling in Ansys-CFX. The heat transfer model used is the “Total Energy” in Ansys-CFX. Turbulent Flux closure for Heat transfer option is not selected, as the turbulent Prandtl number is not a constant in the model used. Details of the turbulence physical analysis used are given in the next paragraph.

Reference pressure

The pressure set in the CFD model is a relative value that describes the system pressure. This is because there is not any closed pressure boundary in the model and as a consequence a reference pressure should be set at some point. All relative pressure specifications set in CFX are measured relative to this **Reference Pressure** value. The **Reference Pressure** will affect the value of every other pressure set in the simulation. The reference pressure has been set

equal to zero at the MRB end connection domain in coordinates (-10.34, 0.005, 0.005) as shown in figure 5.23

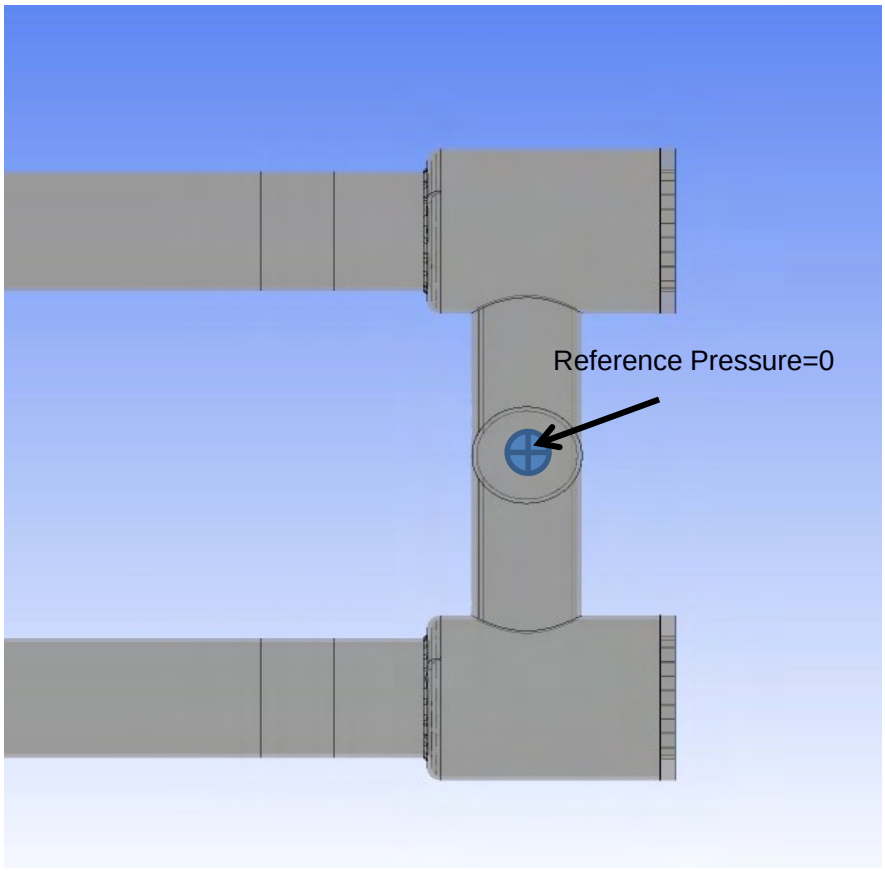

Figure 5.27 Reference pressure set equal to zero at the point specified. In case where there is no tilting simulated it follows that $P_{Abs}=P_{CB} + P_{Ref}$

5.8 Turbulence modelling

Turbulence models are used to predict the effects of turbulence in fluid flow without resolving all scales of the smallest turbulent fluctuations. In the case of the CAST model, turbulence is expected at the regions close to both model ends. The temperature in the cold bore is very low (~1.8 K) and because of its long length, the fluid flow is expected to be laminar. Laminar flow is governed by the unsteady Navier-Stokes equations. The laminar case applies when the energy transfer in the fluid is accomplished by molecular interaction (diffusion). When the speed of flow increases, the work of the viscous stresses can also contribute to the energy transfer.

In fluid mechanics, a dimensionless quantity that can predict similar flow patterns in different fluid flow situations is the Reynolds number and it is defined as the ratio of inertial forces to viscous forces. It is therefore a consequence of this number to describe the importance of the two types of forces acting on a fluid for given flow conditions. Reynolds number is used to characterize different flow regimes within a similar fluid, such as laminar or turbulent flow. Laminar flow occurs at low Reynolds numbers ($Re \leq 1000$) where viscous forces are dominant

and the flow is smooth and constant; turbulent flow occurs at high Reynolds numbers and inertial forces dominate. In turbulent flow chaotic eddies, vortices and flow instabilities occur.

Turbulence intensity is another parameter that can define the turbulent kinetic energy and in the CAST-CFD model is more useful to characterize the flow. Turbulence intensity is defined as the ratio of the root-mean-square of the velocity fluctuations, u', to the mean flow velocity, u_{avg}.

$$I = \frac{u'}{u_{avg}} = 0.16\left(Re_{D_H}\right)^{-\frac{1}{8}} \tag{5. 16}$$

where Re_{D_H} is the Reynolds number in a flow field of Hydraulic Diameter DH. $u'$is defined as

$$u' = \sqrt{\frac{2}{3}K} \tag{5. 17}$$

where K is the turbulent kinetic energy in J/K. The distribution of turbulent kinetic energy can be seen in Figure 5.23. Calculation of the turbulent intensity results in a value close to 20% at regions close to MRB and MFB ends. The turbulence in these regions would be intense, as seen in Figure 5.28, while the fluid remains constant in a laminar behavior inside the cold bore. A turbulence intensity of 1% or less is generally considered low and turbulence intensities greater than 10% are considered high. Transitional effects should rise in between of those two regions.

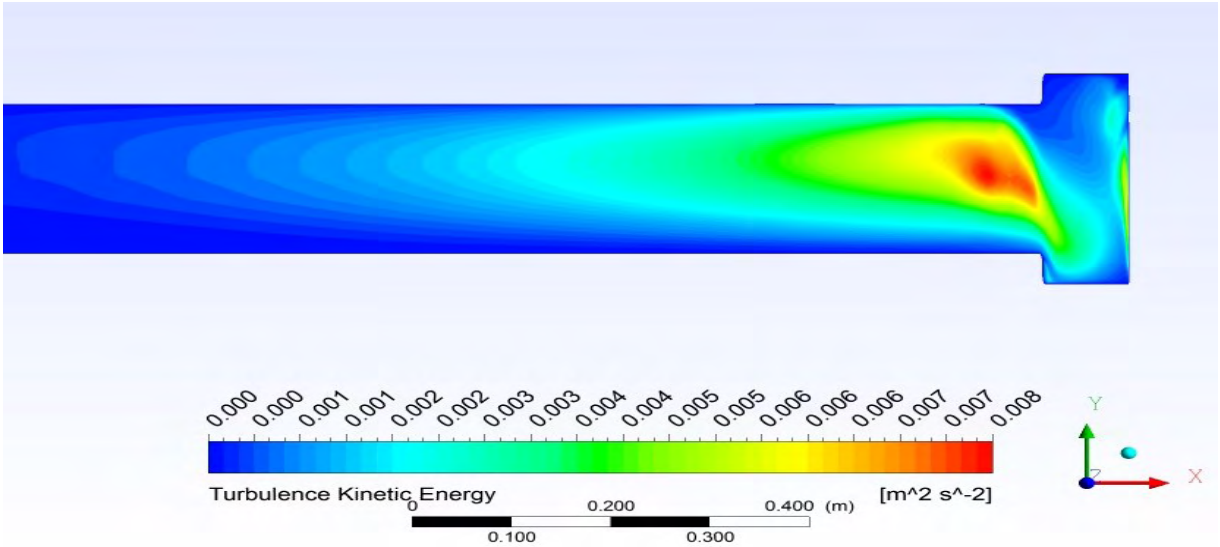

Figure 5.28 Turbulent kinetic energy contour of a plane in the middle of one cold bore is shown. The contour shows the MFB region with high turbulence intensity (I ≥ 20%). Inside the cold bore region, blue region indicates that the turbulent intensity drops to zero and laminar flow develops. The case plotted is for P_{CB}=83mbar and the contour is scaled in the Y axis by a factor of 5.

5.8.1 Turbulent models

A number of models have been developed that can be used to approximate turbulence based on the Reynolds Averaged Navier-Stokes (RANS) equations. In this CFD study, firstly the k-epsilon model was tested and results have been analyzed. K-epsilon is a model implemented for general purpose CFD codes and is considered the industry standard model. K-epsilon model has proven to be stable and numerically robust and has a well-established regime of predictive capability. For general purpose simulations, the k-epsilon model offers a good compromise in terms of accuracy and robustness. Within Ansys-CFX, k-epsilon model uses the scalable wall-function approach enabling solutions on arbitrarily fine near-wall grids, which is a significant improvement over standard wall functions.

K is the turbulent kinetic energy and is defined as the variance of the fluctuations in velocity and epsilon (e) is the turbulence eddy dissipation (the rate at which the velocity fluctuations dissipate).

Although the k-e model provides good predictions for many engineering flows, there are some limitations for applications as

- Flows with boundary layer separation.
- Flows with sudden changes in the mean strain rate.
- Flows in rotating fluids.
- Flows over curved surfaces.

A challenge in turbulence modeling is the accurate prediction of flow separation from a surface. Standard two equations turbulent models usually fail to predict the onset and the amount of flow separation under pressure gradients. The most accurate model was the k-ω turbulent model of Menter [82]. Later on, a k-ω based turbulence model, the Shear-Stress-Transport (SST) was designed to give more accurate results and predict the onset and the amount of fluid separation by inclusion of transport effects into the formulation of the eddy-viscosity. The SST model is recommended for high accuracy boundary layer simulation, as CAST needs, and for free shear flows, the SST model is identical to the k-ε model. This model was developed to overcome deficiencies in the k-ω turbulence model like the transport of the turbulent shear stress.

To include transitional effects two more equations are added to the SST model; the intermittency and the transition onset criteria, in terms of momentum-thickness Reynolds number. An ANSYS empirical correlation (Langtry and Menter [83]) has been developed to cover standard bypass transition as well as flows in low free-stream turbulence environments. An option was added to the code so the user can add a user-defined correlation that is used to control the transition onset momentum thickness Reynolds number equation.

5.8.2 Ansys- CFX transition model

When a laminar flow is becoming turbulent, the phenomenon is known as laminar-turbulence transition. The process is so complicated that at present it is not yet fully understood. Despite the difficulties occurring with transitional flows, even after decades of intensive research, certain features have become gradually clear. In figure 5.29 a schematic view of the transition region is depicted. Flow starts as laminar but after some distance, small chaotic oscillations start to develop in the transition region and eventually the flow becomes fully turbulent.

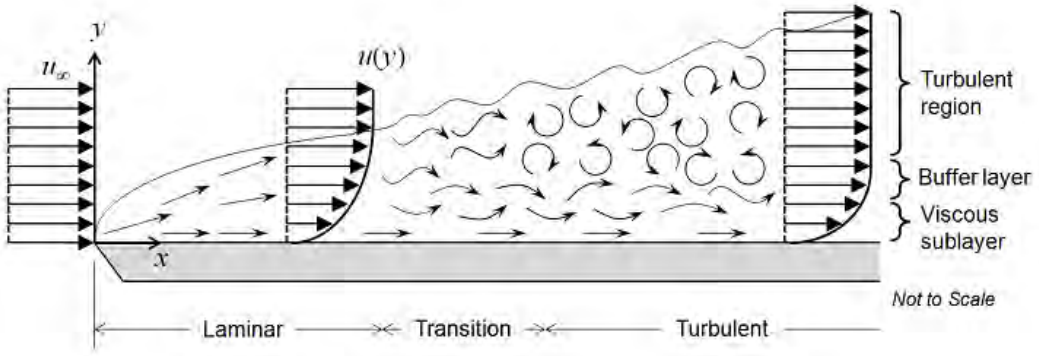

Figure 5.29 The transition region is shown. The near-wall region can be subdivided into two layers. The innermost one is called viscous sub-layer and the flow is almost laminar-like. In this layer molecular viscosity plays a dominant role in momentum and heat transfer. Further away from the wall, in the buffer layer, turbulence effects and molecular viscosity are of equal importance.

The transition between these three regions can be defined in terms of the Reynolds number,

$$Re = \rho u L/\mu \tag{5. 18}$$

where ρ is the fluid density, u is the velocity, L is the characteristic length (in this case, the distance from the leading edge) and μ is the fluid dynamic viscosity.

Using low-Reynolds number turbulent models where the wall damping functions trigger the transition onset is an attractive solution as in the most k-ω models. However, experiments and experience have shown that this approach cannot reliably capture the influence of parameters as such as free-stream turbulence, pressure gradients and separation.

The transition model makes use of experimental correlations that relate the turbulent intensity, *Tu*, in the free-stream, to the momentum-thickness Reynolds number, $Re_{\theta t}$, at transition onset. The momentum thickness Reynolds number is given by

$$Re_{\delta_2} = \frac{\rho u_\infty \delta_2}{\mu} \tag{5. 19}$$

Where ρ is the fluid density, μ is the dynamic viscosity u_∞ is the fluid velocity far away from the boundary layer and δ_2 is the momentum displacement that can be defined as a layer into the boundary that the fluid loses momentum.

In Ansys-CFX, a locally formulated transport equation has been developed for intermittency that is used to trigger transition. The other equation is applied to check criteria related to the momentum thickness Reynolds number. This model is called the "Gamma-Theta model" and it uses a new empirical correlation (Langtry and Menter) [84] that has been developed to cover standard bypass transition as well as flows in low free-stream turbulence environments. The built-in correlations have been extensively validated within the SST turbulence model for a wide range of transitional flows.

The relative percentage of laminar flow can be estimated by using the following formula

$$\frac{Re_{xt}}{Re_x} = \frac{380000(100\,Tu)^{-5/4}}{(\rho/\mu)VL_{Device}} \qquad (5.\ 20)$$

Where Re_{xt} is the transition Reynolds number (that is a user input for the Ansys-CFX program), Re_x is the device Reynolds number, L_{Device} is the device length, V is a representative velocity and Tu is the free-stream turbulence intensity that is defined as follows.

$$Tu = \frac{(2k/3)^{0.5}}{V} \qquad (5.21)$$

where k is the turbulence kinetic energy.

The CAST CFD model has to predict the transitional flow close to the MRB and MFB ends and at the region of the cold bore where laminar flow starts to develop. This is crucial because the transition region finally determines the region of the cold bore that laminar flow dominates (with a density variation ~ 10^{-3}) and this region length will predict the magnet's coherence length. Transition Gamma-Theta model is a suitable tool to predict in high accuracy the CAST simulations.

Figure 5.28 proves that ^{3}He flow will be mainly turbulent at the volume ends (MRB and MFB fluid regions) while it will remain static at the central part of the cold bore. The region between the laminar and turbulent flow would be a transitional region, that the more accurately simulated the higher the correct calculation of the coherence length. It is also pointed out that the correct transition onset prediction should give the amount of gas expected inside the volume according to the pressure set.

5.8.3 Modelling Flow near the Wall

Near the CFD model walls there are strong gradients of the dependent variables. It has been also observed that viscous effects of transport processes are quite large. It is a crucial issue that the simulation accounts for the wall viscous effects and accurately resolves the rapid variation of flow variables within the boundary layer.

In the Gamma-Theta transition model used, the requirement is a finer grid that is typically used for routine design purposes. The max grid y^+ should be approximately equal to one. The Yplus (y^+) variable is given by the standard definition used in CFD

$$y^+ = \frac{\sqrt{\tau_\omega/\rho}\Delta n}{\nu} \quad (5.\ 22)$$

Where Δn is the distance between the first and the second point of the wall, τ_ω is the wall-shear –stress in the log-raw region, ρ is the fluid density and ν is the dynamic viscosity.

Two more boundary layers have to be resolved in order to identify the fluid behavior near the wall: the momentum boundary layer and the thermal boundary layer. The Prandtl number is a dimensionless number that is defined as the ratio of momentum diffusivity to thermal diffusivity.

Prandtl number is expressed as

$$Pr = \frac{v}{a} = \frac{viscous\ diffusion\ rate}{thermal\ diffusion\ rate} = \frac{C_p\mu}{k} \quad (5.\ 23)$$

- Where v is the kinematic viscosity
- a is the thermal diffusivity
- C_p is specific heat
- μ is dynamic viscosity

The Prandtl number (Pr) controls the relative thickness of the momentum and thermal boundary layers. When Pr is small, the heat diffuses very quickly compared to the momentum. This is the case for the CAST model ($Pr \leq 1$) as can be seen in Figure 5.30.

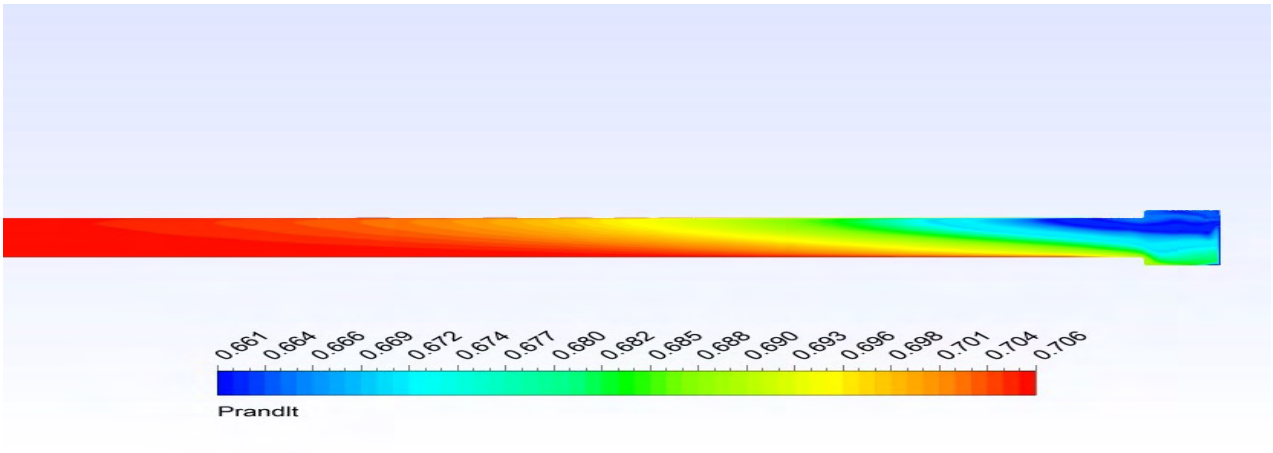

Figure 5.30 *Pr number* is less than one, so the thermal boundary layer is thicker than the momentum layer. *Pr* is plotted in the central longitudinal section of cold bore and MFB at a pressure of 43mbar. The windows temperature is ~20K. The scale of the contour is 2.

For vertical flat plates a dimensional number known as Grashof number (Gr), can predict transitional flow when it is lying in the range $10^8 \leq Gr \leq 10^9$. In flows like the one being modeled for CAST, the Gr number cannot predict the transition regime. The Gr number in the central longitudinal section in CB and MFB is plotted in Figure 5.31.

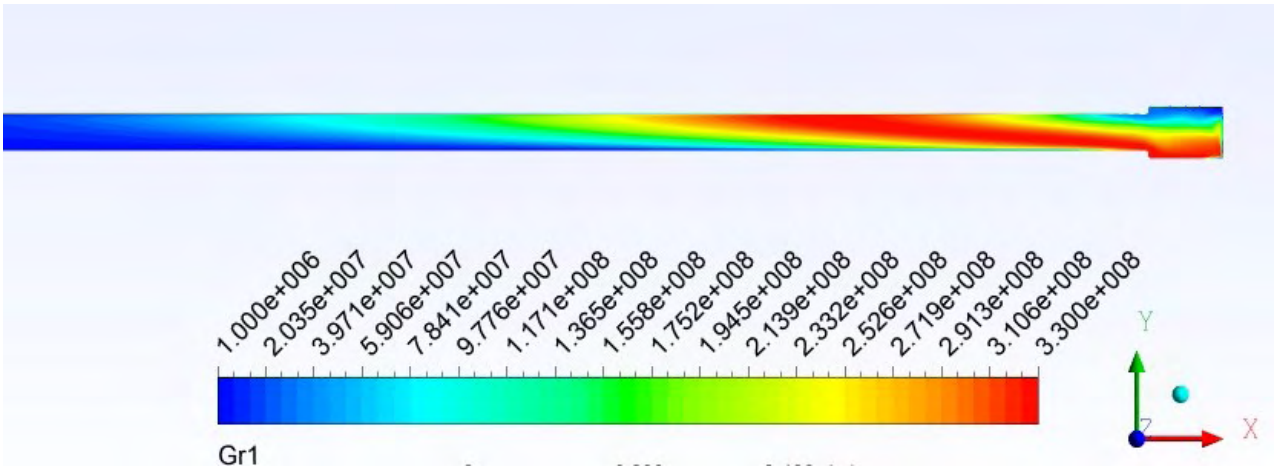

Figure 5.31 Grashof number contour for P_{CB}=67mbar and T window ~ 20K

The Grashof number is defined as the ratio of the buoyancy to viscous forces acting on the fluid. The formula that defines the Grashof number is

$$Gr = \frac{g\beta(T_S - T_\infty)D^3}{\nu^2} \quad (5.\ 24)$$

- Where g is the gravity acceleration
- β is the volume expansion coefficient . For Ideal gases it is assumed that $\beta \sim T^{-1}$
- T_S is the wall temperature
- T_∞ is the bulk temperature

- D is a characteristic length of the device
- ν is the dynamic viscosity

CAST's CFD simulation is a complicated problem and the model that has been built takes into account all the phenomena of a transitional flow that are emerging from natural convection forces. The fluid into consideration (^{3}He) has also specific properties that diverge from usual fluids.

The onset of the transitional region is a compromise between the turbulent flow observed at the MRB and MFB ends and the laminar flow expected in the cold bore central region. It is of great importance for the simulation to properly adjust the physics of the model and a turbulence model that can resolve the boundary layers close to the wall. The Gamma Theta turbulence model is the most appropriate tool for boundary layer resolution because of the use of experimental correlations that can be defined by the user. One correlation is introduced via the intermittency term that ranges between 0 and 1 (0 for laminar flow and 1 for fully turbulent) and the Re_{th} term, that drives the onset of transition according to the "transition onset Reynolds number", that is user defined.

The transition model adopted in this study requires the solution of extra transport equations, which require additional computation costs. It is also necessary to create a finer grid for the model in order to achieve y^+ values bellow one. In the next section the computational solver management and the numerical strategy is explained.

5.8.4 CFD model computation

Ansys CFD provides a software called CFX-Solver manager [85] that sets up the simulation model solution requirements. The points that can establish an accurate solution of the simulation are the problem initialization and the results validation, in parallel with the numerical strategy followed.

First the initial conditions of the problem should be set. Typical fluid properties should be defined and concerning parameters such as pressure, temperature, velocity and turbulence parameters should be set at their initial value. The metal cold bore temperature for example, could be used as an initial condition for the fluid temperature inside the cold bore. Velocities should be rather low in the cold bore region while at the MRB and MFB ends should be set at a higher value.

In CFX-Pre software initialization can be used for any region or domain. For turbulence, there is an option to use between low intensity (1%), medium intensity (5%) or high intensity (10%), or to use real values for the k-ω model like the turbulence kinetic energy and turbulence eddy frequency. Many models have been created and turbulence initialization takes the form of the previous solutions values provided, in order to decrease the solution's computational time.

The numerical approach used in CFX to solve the simulation is a pressure-velocity coupling. This option is known as a coupled solution. The advantage of using a coupled solver is that this scheme obtains a robust and efficient single phase implementation for steady state flows. The performance is superior compared to the simple or segregated[26] methods. The coupled algorithm solves the momentum and pressure-based continuity equations together. The full implicit coupling is achieved through an implicit discretization of pressure gradient terms in the momentum equations, and an implicit discretization of the face mass flux, including the pressure dissipation terms.

5.8.5 Convergence

The convergence[27] of the solution is an association of parameters that have to be satisfied in the CFD model simulated. At convergence of a simulation the following conditions should be fulfilled

- All discrete conservation equations (momentum, energy etc.) are obeyed in all cells
- Overall mass, energy and scalar balances are achieved
- By monitoring convergence via residual monitors, a decrease in residuals by three orders of magnitude indicates at least a qualitative convergence

On monitor tabs of Ansys-CFX Solver, history plots and user defined plots are shown. The convergence history section details the state of the solution as it progresses. Equation residual information at specified locations enables us to monitor the convergence. Convergence difficulties can often be pinpointed to a particular part of the solution.

Solver residuals represent the absolute error in the solution of each variable from the Navier-Stokes equations numeric calculation. At each iteration, the residuals should become lower or remain stable and this is an indication of solution convergence. As pointed out, residuals are not reliable enough to show a fully converged problem.

The solution to the linearized set of Navier-Stokes equations takes the form

$$Ax = b \tag{5. 25}$$

The iterative method, generates a sequence of approximate solutions to the system that converges to the exact solution

After *k* iterations, an approximation is obtained for the exact solution

$$Ax^{(k)} = b - r^{(k)} \tag{5. 26}$$

[26] In the segregated method, the solver solves the flow equations independently. One equation is solved for each velocity component and one for the pressure.
[27] In mathematics, a convergence limit is the value that a function or sequence "approaches" as the input or index approaches some value

where $r^{(k)}$ is the residual after *k* iterations. Defining

$$\varepsilon^{(\kappa)} = x - x^{(k)} \tag{5. 27}$$

as the difference between the exact and approximate solution, we obtain

$$A\varepsilon^{(k)} = r^{(k)} \tag{5. 28}$$

The purpose of the iterative method is convergence and this is achieved if the corresponding sequence converges for the given initial approximations.

It is also important to plot certain variables like temperature or density and pressure at specified points set by the user. The variables behavior and tendency could indicate that the problem converges. Plots of the energy imbalance are also available; for a given control volume the balance of energy crossing its boundaries is considered. The closed volume should obey to the First law of Thermodynamics and since the ^{3}He mass remains constant the energy exchange should be balanced. The heat transfer rate $(\dot{Q})$ at every domain boundary should remain null. Plots of energy balance should show values close to zero.

Mass flow rates at cross sections of the model boundaries should also remain zero. Transverse sections mass flow rate plots can show the mass balance of the system.

5.9 CFD model results

The results that have been obtained by the simulations will be reported and analysed in this section, in order to extract the conclusions needed to understand the simulated physics of the ^{3}He flow and behaviour. The simulations obtained, cover the 2009-2011 period where the windows were not heated. The same model can be used to simulate the 2008 period where the windows have a temperature of about ~70K.

The CFD model was used to check the influence of the magnet tilting at some specific pressure (83mbar) in order to investigate the hydrostatic effects as also the natural convection mechanism at specified angles of the system. The tilted positions simulated in steady state conditions imply that the rotation is very slow and the model is capable to analyse the phenomena produced at small degrees.

The study of specific pressure settings is capable to describe the thermodynamic behaviour of the gas inside the magnet cold bores according to the experimental conditions set. The specified settings that are provided via the boundary conditions and the physics described are adequate to validate the results obtained.

These results will be used for the Micromegas analysis and explained in next chapters. The simulation results can analyse and explain the real experiment of CAST. A set of the pressure settings used for the first part of this study is shown in the following table.

P_{CB}(mbar)	Date of the experiment	T_{mag}(K)	T_{WIN} (K) MFB_1	T_{WIN} (K) MFB_2	T_{WIN} (K) MRB	T_{INLET} (K)	T_{OUTLET} (K)	Number of moles (n)
43.650	29.04.09	1.725	20.0	18.25	13.17	16.9	16.9	9.49158
67.500	10.10.10	1.725	19.5	17.75	11.50	16.	16.	15.18449
83.390	09.12.09	1.758	19.0	16.50	11.20	15.6	15.6	18.88742
97.600	05.07.11	1.725	18.5	17.30	10.40	16.3	16.3	23.10908

Table 5.3 The BC's used for each pressure setting (P_{CB}). The temperature for the MFB windows boundary condition is the mean value of MFB_1 and MFB_2. The MRB boundary condition is set by a sole sensor since the second one cannot be characterized as reliable for this study. T_{INLET} and T_{OUTLET} are boundaries located in MRB and MFB domains as explained in a previous section. The amounts of moles are the experimental value expected to result as the output of each setting. Detailed study of the influence of each boundary condition will be presented in a next section.

The effective length (L_{eff}) of the magnetic field inside the cold bore, where density is uniform, can be considered as a reference density that does not alter the physics of CAST. Convection currents can change as pointed in previous sections the effective magnet length where axions can be coherently transformed into photons. The shortening of the actual magnet length depends on the x-ray windows temperature, which can drive forces that alter the homogeneity in the magnet cold bore gas. The reference density can be calculated as pointed out in figure 5.32.

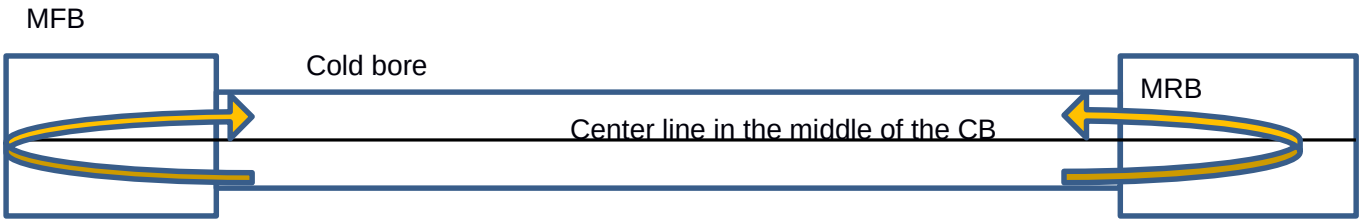

Figure 5.32 Schematic view of the centerline chosen in the middle of the CB. The density will be measured in the center line shown. The arrows show the convection currents that can alter the homogeneity of the density inside the magnetic length.

The criteria that a uniformity in density has been established in the cold bore region is

$$\Delta\rho \leq \rho_0 \, [kg\, m^{-3}] \tag{5. 29}$$

Where ρ_0 is the difference in density $\rho_{ref} - \rho$ bellow which any density variation is assumed to be negligible and does not alter CAST's physics results. The $\Delta\rho$ threshold has been set as

$$\Delta\rho \leq 0.003 [kg\, m^{-3}] \tag{5. 30}$$

Bellow this threshold the ^{3}He density can be considered as uniform although this condition will be re-examined in a next section. The L_{eff} is calculated by taking into account the condition of $\Delta\rho$ as a threshold by the density value in the center line in the middle of the CB. The density distribution in the center line mentioned can be plotted as shown in figure 5.33.

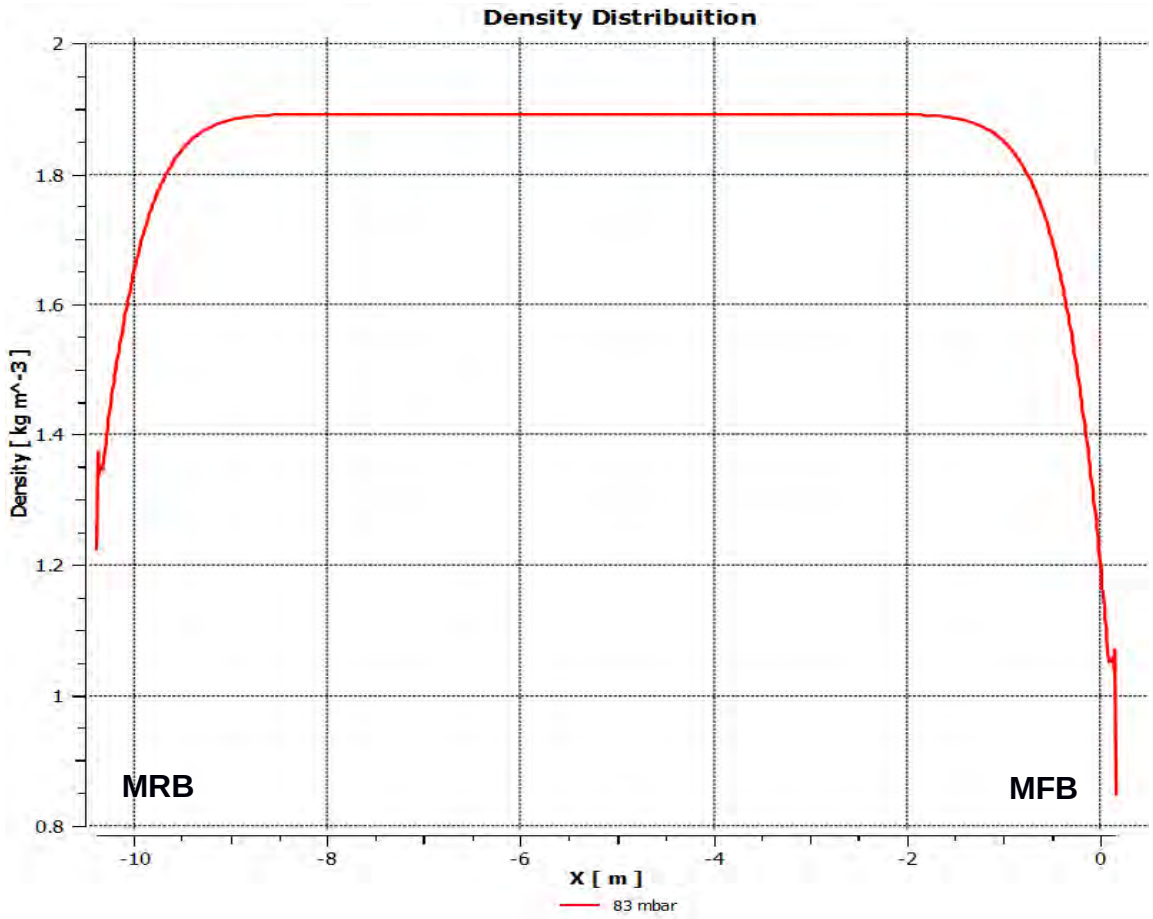

Figure 5.33 The density distribution along the axis of the central line as shown in figure 5.32 is plotted. The plot shows the distribution at a pressure setting P_{CB}=83mbar. The density is homogeneous for an effective length L_{eff}. At the MRB and MFB ends, as also at some length inside the CB, the density decreases as convection currents heat up the helium gas. The MFB is located at zero X coordinate while the MRB end at a negative X value.

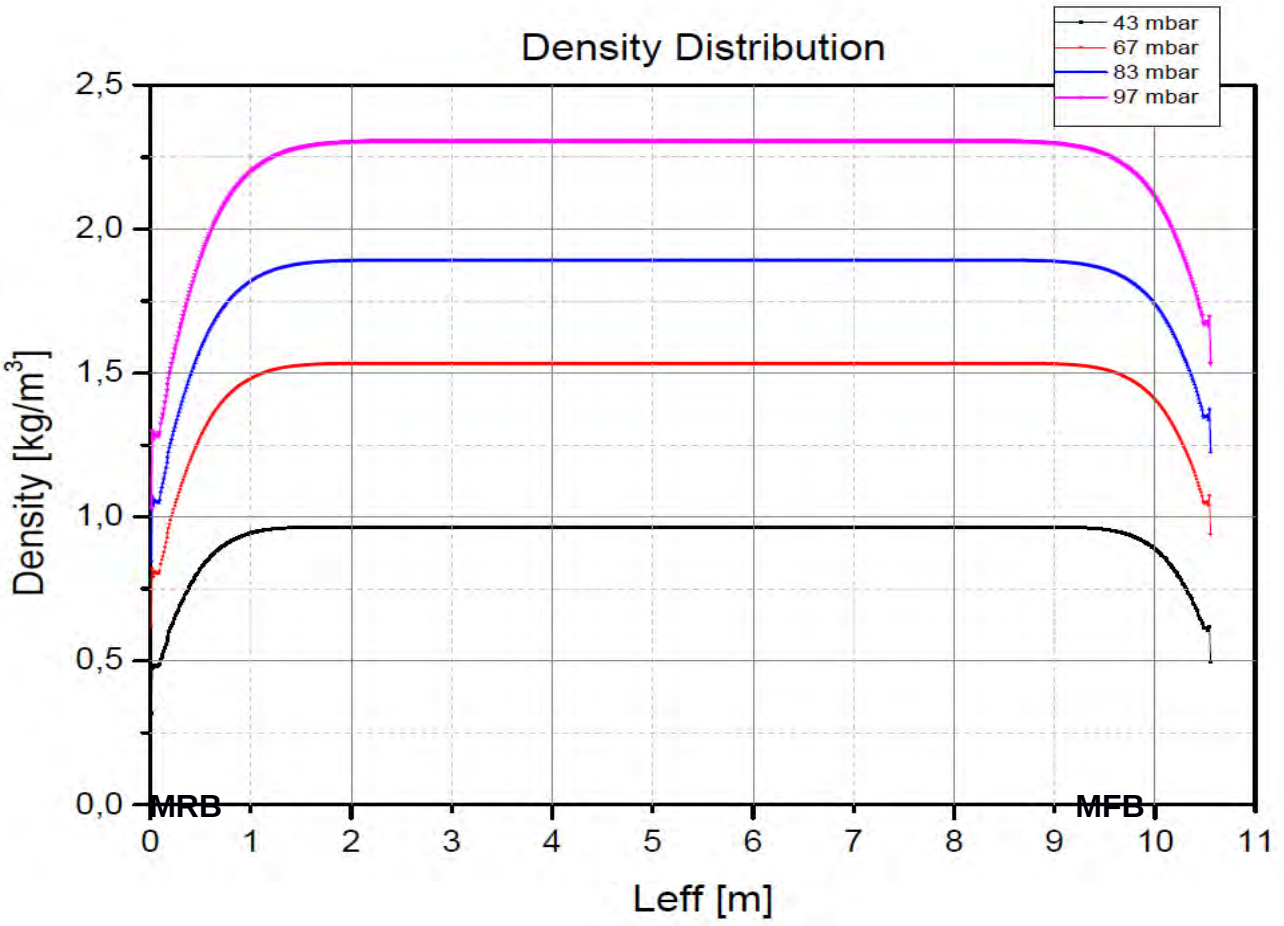

Figure 5.34 Density distribution for the pressure settings referred on table 5.3. The boundary conditions used are the same as in the table 5.3. MRB and MFB ends are shown in the plot. The density decreases at the ends because of the higher temperature of the x-ray windows.

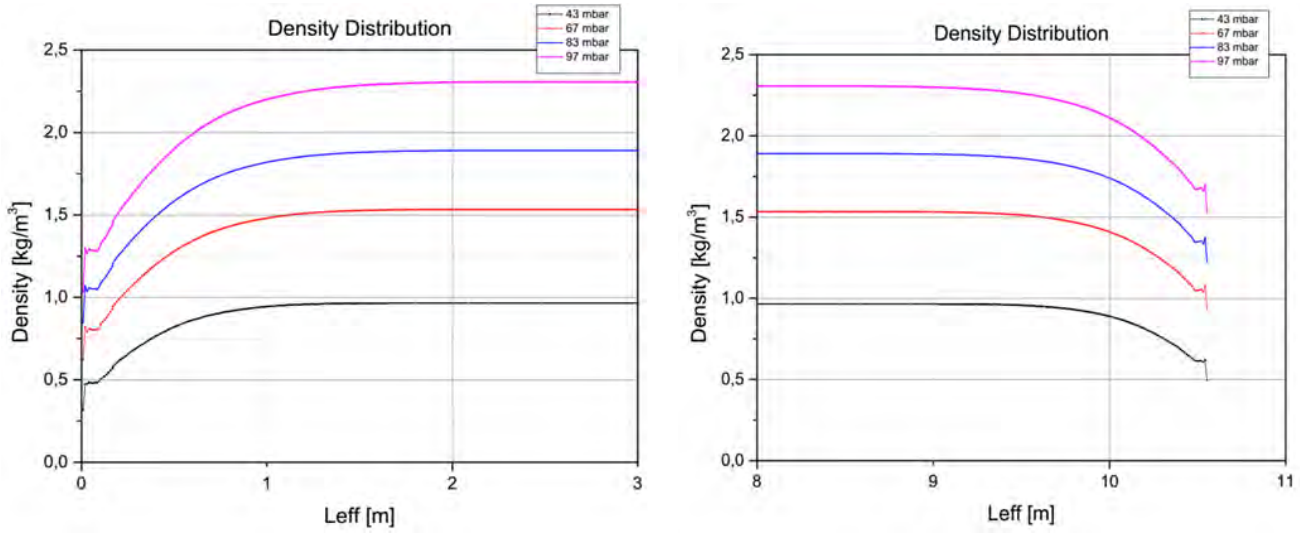

Figure 5.35 On the left is the MRB end plot of the density distribution for various pressures as in figure 5.34. On the right a detailed plot for the MFB end is shown.

For every simulation performed, the density distribution is extracted as also temperature profiles at the center line of the cold bore or at specified points that can be defined as probes. The distributions from the four simulated pressure settings, referred to in table 5.3, using the according boundary conditions can be seen in Figure 5.34. The center line has been divided in a thousand points and at each point the reference density is extracted. At the MRB and MFB ends the density is decreased as expected. The total number of moles is computed by summing the volume integral of the mass contained in each domain; cold bore, MRB and MFB.

$$n_{CFD} = n_{CB} + n_{MRB} + n_{MFB} \tag{5. 31}$$

The central part of the cold bore remains at a constant density and the part of it that fulfills the condition

$$\Delta\rho \leq 0.003 \mathrm{kg} m^{-3} \tag{5. 32}$$

can be assigned as the effective length of the magnet where axions can be transformed into photons.

P_{CB} [mbar]	T_{MAG} [K]	ρ_{ref} [kg m^{-3}]	L_{eff} [m]
43.650	**1.725**	**0.9640**	**7,45**
67.500	**1.725**	**1.5330**	**7.101**
83.390	**1.758**	**1.8900**	**6,845**
97.600	**1.725**	**2.3070**	**6,612**

Table 5.4 Effective length (L_{eff}) is shown for the simulated pressure settings.

The effective length obtained from the steady state simulations can be plotted against the pressure of the cold bore, as can be seen in Figure 5.36. The trend of the linear fit shows a decrease in the L_{eff} as the pressure increases. Any deviation occurring from the trend line is because of the differences in the T_{magnet}, which is not constant in all simulations performed. Nevertheless, from this plot the behavior of the density distribution inside the magnet can be extracted and the value of any pressure setting can be assigned to a corresponding length for the CAST's data analysis. The equation that describes the trend of the effective length is

$$L_{eff} = -0.015684 \cdot P_{CB@1.8K} + 8.13519 \tag{5. 33}$$

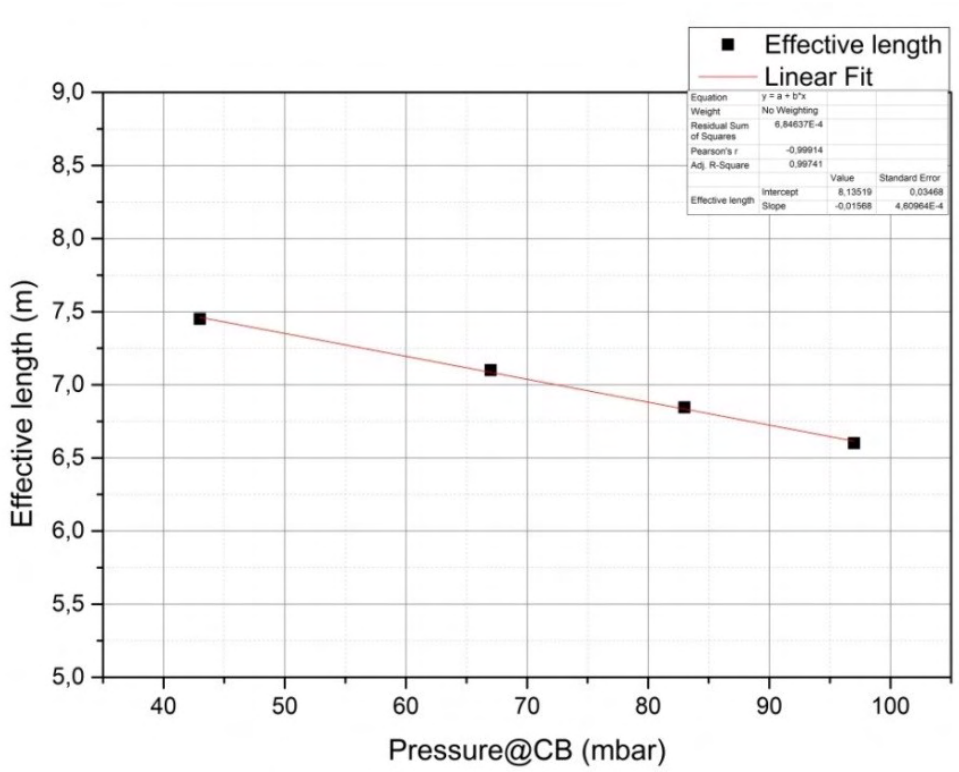

Figure 5.36 Effective length (L_{eff}) is plotted versus the P_{CB}. The linear fit provides the trend of the length as the pressure increases.

Although one can assume similar boundary conditions to the four simulations performed, the difference because of the "small" pressure change is huge. There are several parameters for this enormous change that take effect when pressure changes. It is important to notice the change of the specific heat capacity Cp of ^{3}He as shown in Figure 5.24. As pressure increases, the heat capacity of the fluid is increasing too, so the amount of energy that can be transferred into the fluid is higher. By assuming the same temperature differences on the system boundaries, a higher specific heat capacity (for higher pressure) can transfer more energy through the fluid. Thus, the heat produced on the x-ray windows can be transferred in a longer distance inside the cold bore, "disturbing" the density homogeneity and resulting in a smaller effective length. When pressure is increasing, density is increasing too as can be seen in Figure 5.37 from the NIST database of ^{3}He. The increase of density results in a series of physical results

- Increase of the heat transfer coefficient that is a fluid-solid property, can result in a higher conductive heat transfer mechanism in the wall layer
- Reynolds number is increasing and turbulence should be more intense for the same boundary conditions. This can also alter the heat transfer coefficient (increase) because the coefficient is enhanced in turbulence wall regions.
- As the fluid-solid heat transfer mechanism is stronger in higher pressures the ^{3}He will receive more heat from the hotter boundaries, resulting in an amplification of natural convection and an increase of observed density gradients.

- The increased heat capacity should transfer more heat into the cold bore and homogeneity is disordered

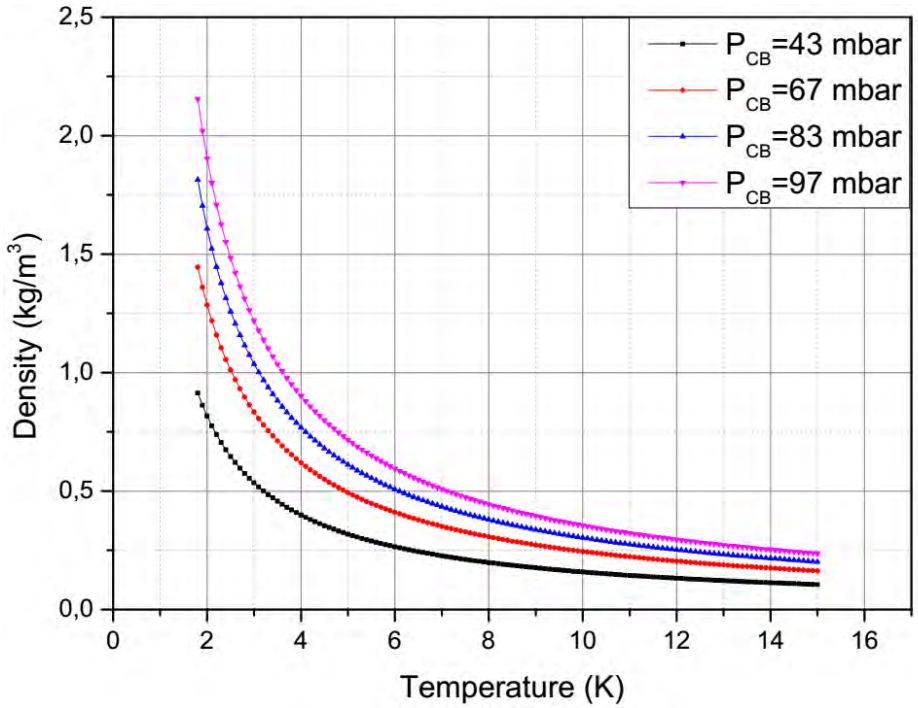

Figure 5.37 Evolution of the density for various pressures according to the equation of state that NIST provides for ^{3}He

The results validity can be confirmed by a set of parameters that will be described below. One parameter of great importance is the CFD mass output result; i.e. the number of moles that the CFD model computes with a given pressure (P_{CB}) and the corresponding boundary conditions. If the CFD model is capable to reproduce the experimental amount of mass that occupies the fluid domains, it is assumed that the model can be characterized as correct. A set of various systematic errors can be reproduced inside the model as

- A measured experimental boundary condition. For example, T_{mag} in the metallic surface of the cold bore is known to have a variation of ~10-15 mK
- Dead volumes of the pipework were not modeled and it is assumed that a meaningful amount of mass is occupied in this volume, although with some uncertainty
- The shrinkage of metallic pipes because of contraction that is not taken into consideration
- The equation of state used. It is known that the Peng-Robinson EoS can describe the ^{3}He in an accurate way, although a small deviation occurs as seen in Figure 5.21 from NIST experimental data for very low temperatures
- The turbulence model used. The model is known for its accuracy but the transition region case modeling is still a field of intensive research
- Computational errors like a non-fully convergent simulation

The parameters described as a source of uncertainty can lead to the assumption that an error in the CFD mass of 1% deviation is acceptable. The total mass of the fluid is obtained by

volume integration for each domain that is the MFB, MRB and the CB. The opposite procedure is not available; i.e. to set the amount of moles as a boundary condition and this is because the mass is computed as a volume integral. In the table 5.5 the moles that occupy the fluid domain for each pressure setting are shown and the deviation of the experimental value is also shown.

P_{CB} [mbar]	Experimental number of moles -n_{exp}	CFD-computed number of moles- n_{CFD}	Deviation [%]
43.650	9.49158	9.588200	1.01
67.500	15.18449	15.26682	0.54
83.430	18.88742	18.85700	0.16
97.600	23.10908	22.97700	-0.53

Table 5.5 Comparison of the experimental number of moles and the computed number of moles provided from the simulations at the specified pressures. The deviation in percentage is shown.

The deviation of the calculated number of moles is calculated from the following expression

$$Deviation = \frac{n_{CFD} - n_{exp}}{n_{exp}} \cdot 100 \ (in\ \%) \qquad (5.\ 34)$$

The simulations according to the results can be considered as valid, since the mass obtained is less or equal of ±1%. In this study of the CAST model one could consider as a source of error the 4th order polynomial fit to the specific heat data obtained from NIST database. The fit cannot reproduce in a great accuracy the data trend by using only a fourth order polynomial. This limitation that the software provides can't be overcome. A polynomial fit of higher order is much more accurate as noticed, but for the coefficients extraction a 4th order polynomial fit is necessary.

The volume contraction, if taken into account, should have a positive effect towards the deviation limitation.

5.9.1 Validation of the results

Results obtained can be considered as valid by convergence examination, as also by checking other simulation parameters as the velocity and temperature profiles.

Residuals as noticed should be examined for every simulation convergence. In this study residuals are below 10^{-6} for most of the parameters as can be seen in Figure 5.38

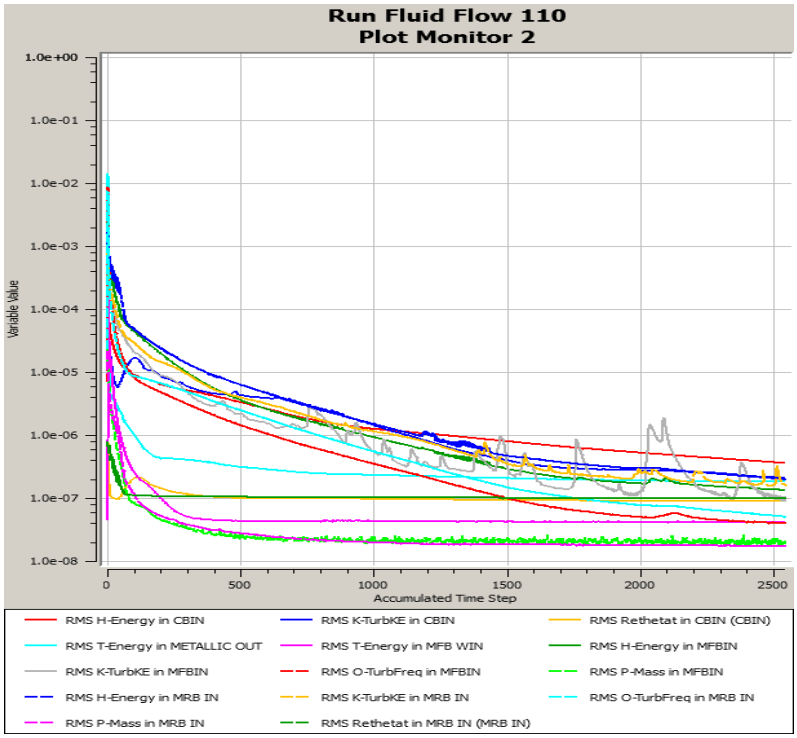

Figure 5.38 Residual plot for the 67 mbar simulation run

In order to check the mass accumulated in the fluid domains another user plot is checked that is the total amount of moles divided by a thousand. A monitor point set by the user can show the evolution of the total mass accumulated.

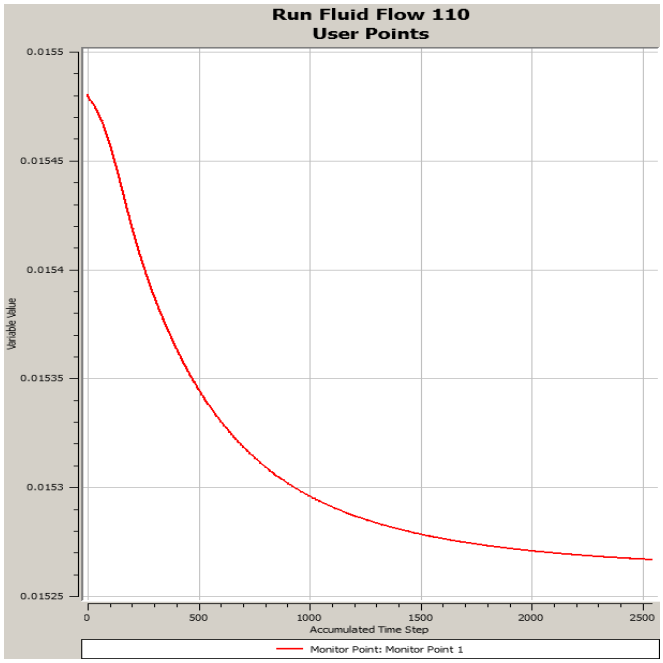

Figure 5.39 The plot shows a monitor point that estimates the (total amount of moles)/1000. In this plot the 67 mbar case is shown.

It is also important to crosscheck the thermal energy flow in solid domains as also the imbalance of energy in fluid; that is whether the equation of energy has fully balanced. This statement can be expressed from the following equation by integration across the entire simulation domain.

$$Energy_{\ input} - \ Energy_{stored} = Energy_{output} \qquad (5.\ 35)$$

The following plot presents the energy imbalance of the fluid domains involved in the 67 mbar simulation.

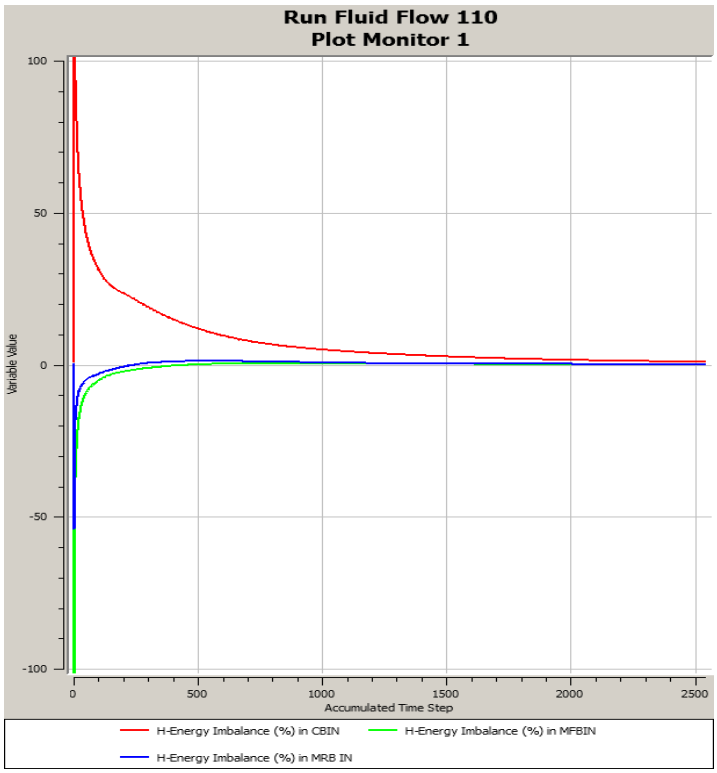

Figure 5.40 Energy imbalances in the fluid domains of the 67 mbar simulation are shown.

The mass flow rate has also have been checked and the values produced from all sections are very close to zero indicating that convergence has been performed.

It should be noted that the complexity of the CFD system under investigation is high and the purpose of this study is not to achieve 100% accuracy but to explore and analyze the system behavior in an accurate way. CFD is not an exact science but a way to model physical phenomena in a great accuracy.

Another parameter that limits the simulations accuracy is the computational time. The simulations for this study were performed by using the CERN Remote Solver Manager (RSM) cluster that has some time limitations because of CERN users needs and the few queues available.

5.10 Velocity, Temperature and Density profiles

The velocity profile across the middle section of the cold bore can provide some information about the fluid behavior, direction and intensity of the velocity field.

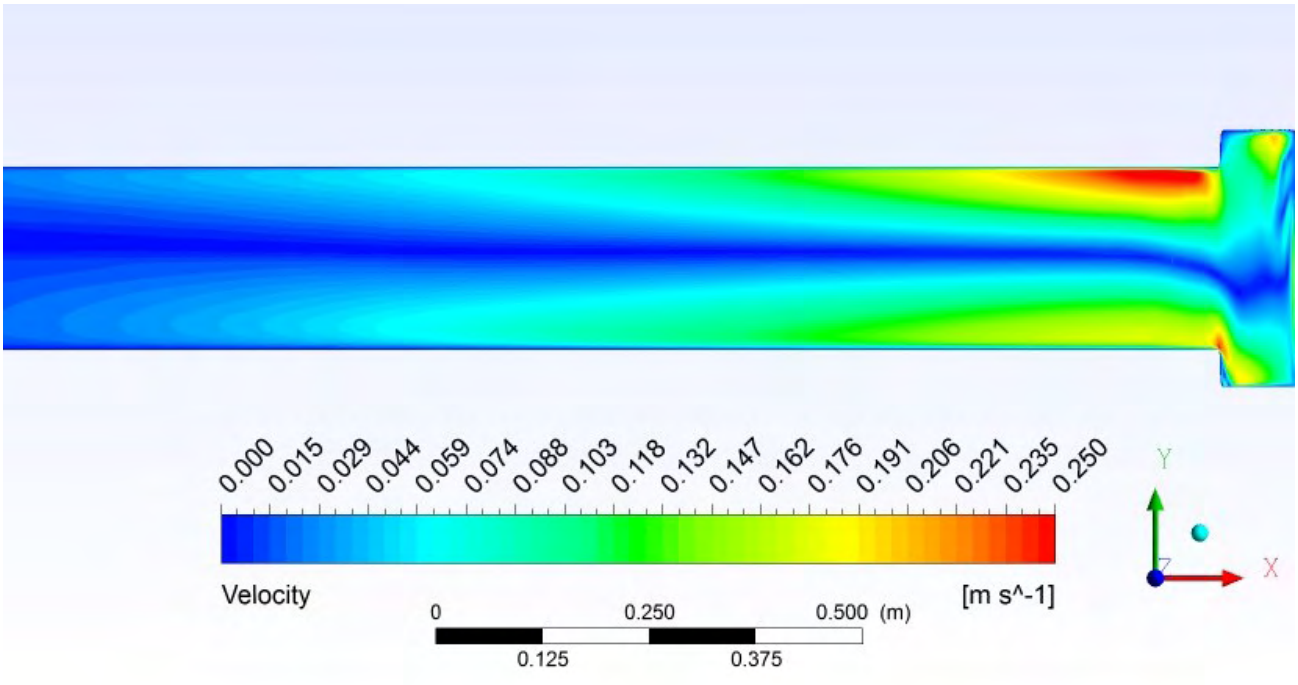

Figure 5.41 Velocity field of the MFB side of the magnet. The plane is a section in the middle of one of the cold bores as can be seen in the Figure 5.42. The pressure is 67 mbar.

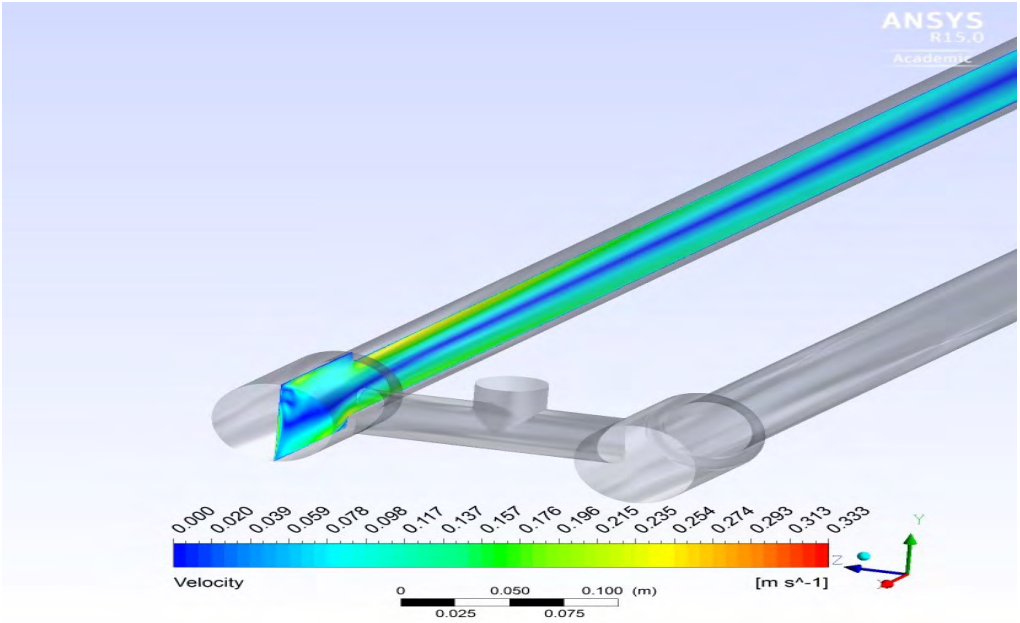

Figure 5.42 The sectional plane of the velocity field that crosses MRB, MFB and the CB

To investigate the velocity field not only the magnitude and the intense regions are important, but the flow direction too. In the next figure 3D arrows show the fluid direction as pointed out in the previous section.

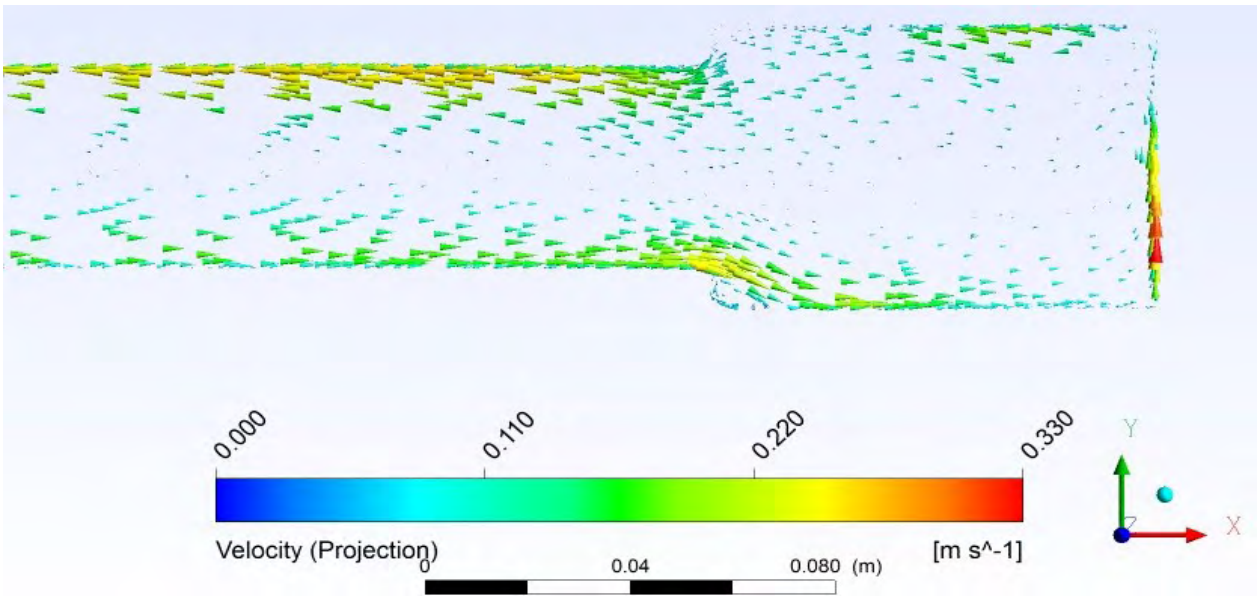

Figure 5.43 The arrows are projected tangential to the sectional plane indicating the flow direction. The windows heat the fluid and accelerate it inside the medium. Hot gas direction is upwind and then it is transformed inside the CB. The hotter fluid becomes less dense and by moving inside the tube, a downstream flow of colder fluid comes from the CB, replacing the hotter gas released.

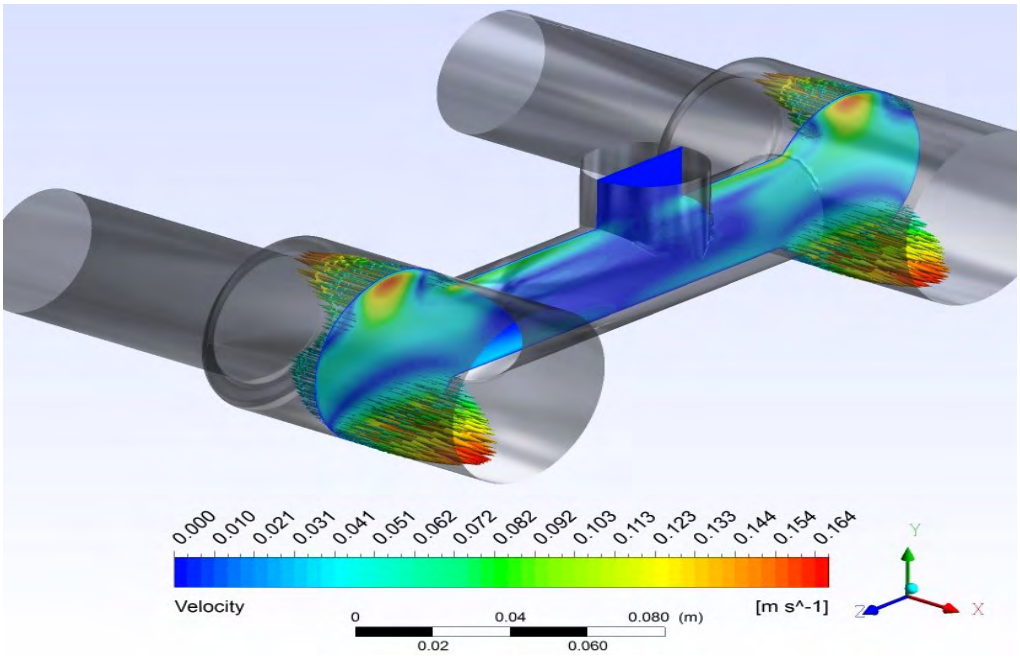

Figure 5.44 Another interesting feature of the velocity behavior can be extracted from the MRB end, were turbulence effects take place in a region of a not so hot environment. A section of the velocity plane is shown and the projection of 3D velocity arrows is normal to this plane.

The density profile in the central cold bore longitudinal section can be seen in the Figure 5.45

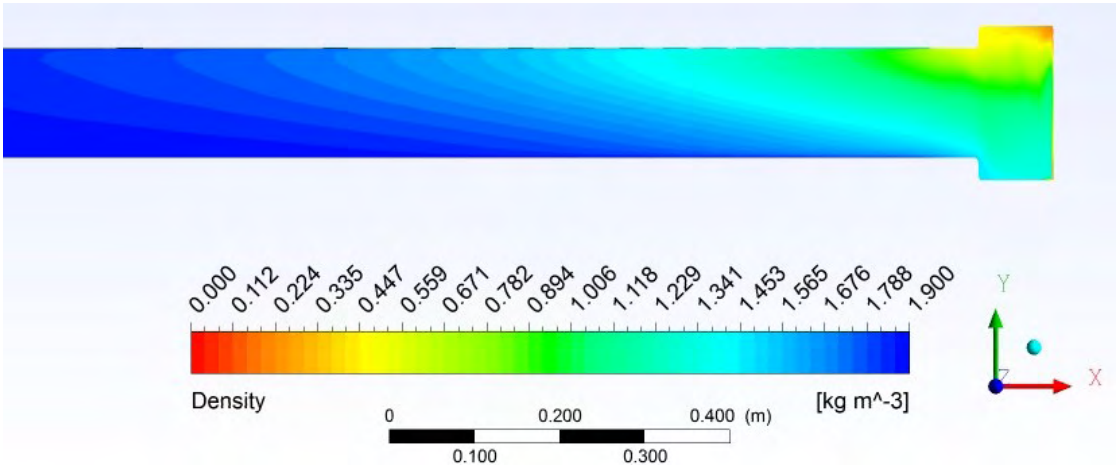

Figure 5.45 Density profile of the 67 mbar pressure setting. Close to the x-ray windows of the MFB side the fluid is less dense because of higher temperatures. The density gradients are more intense close to the windows and this produces a stronger natural convection.

The stratification occurring in the cold bore is characteristic; the cold heavier gas remains in the bottom of the tube while the lighter and warmer ^{3}He occupies the upper level. The heat is transferred from the outer perimeter of the strongback net to the PP foil and through the foil to the ^{3}He fluid. Conduction mechanism transfers the heat from the metallic part, mainly in MRB and MFB sides, to the fluid. This can be depicted in the Figure 5.46 that shows the temperature distribution in the solid and fluid domains of the MFB side.

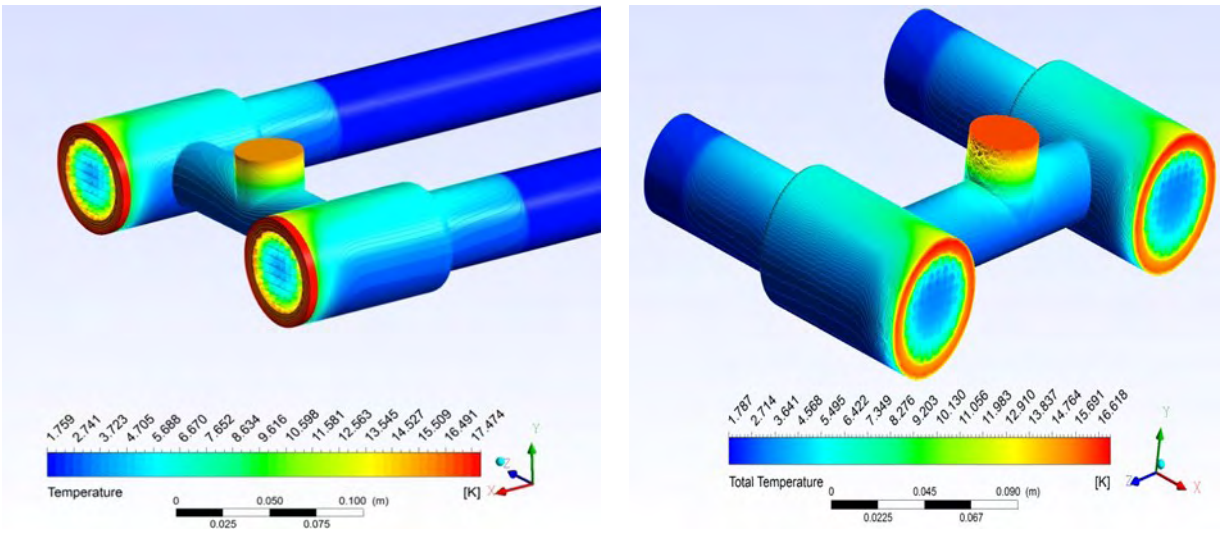

Figure 5.46 On the left, the metallic part of the model is shown. The highest temperature is observed as expected at the strongback net perimeter. On the right, the fluid walls are shown for the case of 97 mbar. The effect of the net is obvious, although not very well resolved.

5.11 CFD study of the tilted magnet

5.11.1 Problem description

When the magnet is horizontal, the central gas density inside the cold bore can be calculated from the equation of state (EoS), the magnet temperature T_{mag} and the pressure inside the cold bore P_{cb}. During the solar tracking the P_{cb} is changing due to hydrostatic effects and because of a variation of T_{mag} (10-15 mK) that the cryogenic circuit causes. The variation of the T_{mag} against time is plotted in figure 5.47.

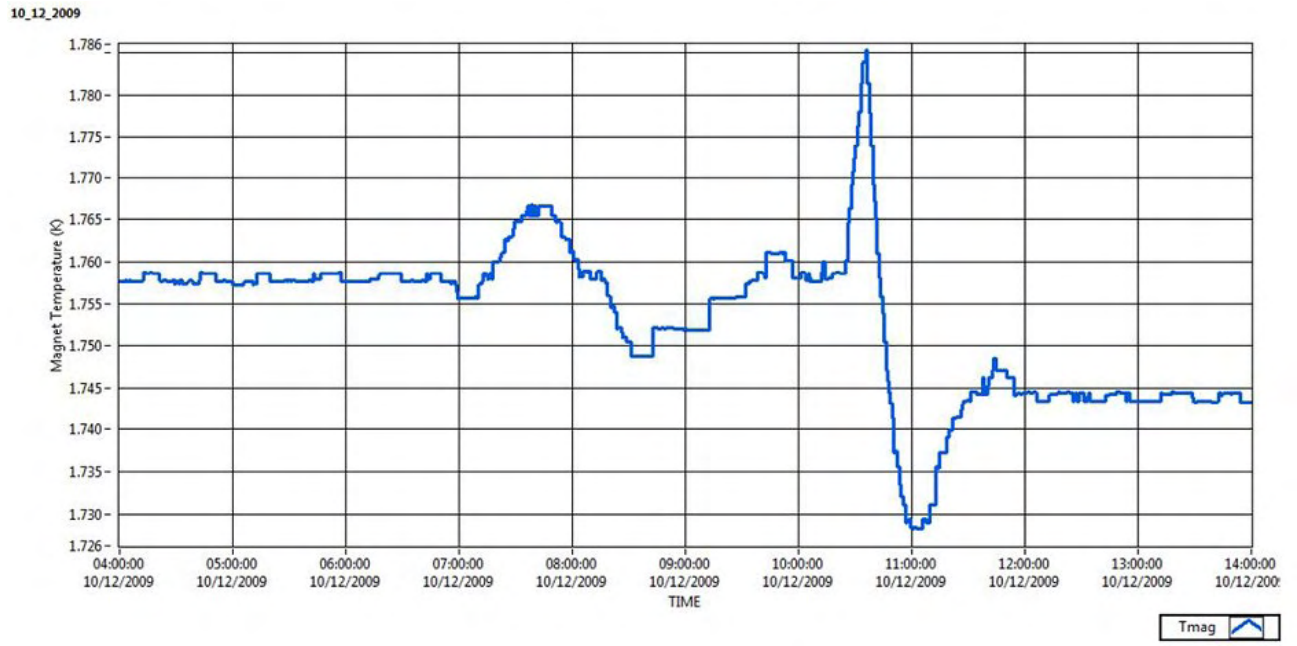

Figure 5.47 The plot shows the variation of magnet temperature versus time. The T_{mag} decline starts at 07:00 in time axis and ends at ~09:00, which is the time interval under consideration due to solar tracking.

The variation of pressure is enormous but follows the trend of T_{mag} as expected. As noticed for example at 84 mbar, a vertical movement of the magnet at +6 degrees increases the measured pressure in the cold bore 1.05 mbar as can be seen in figure 5.48. The hydrostatic and the T_{mag} effects account for the 0.65 mbar. Tilting can cause a modification in fluid dynamics effects that alter the x-ray windows temperature as expected and the effective length of the magnet. The fluid dynamics can affect dramatically the density distribution inside the cold bore. The question rises; are the physical effects taking place inside the cold bore as strong and intense as to observe a change of pressure P_{cb} by ~1 mbar?

In this study of the tilted magnet, simulations have been performed at 83 mbar pressure at various angles in a steady state condition in order to investigate the fluid behavior, observe and model the density distribution and finally quantify the effective length.

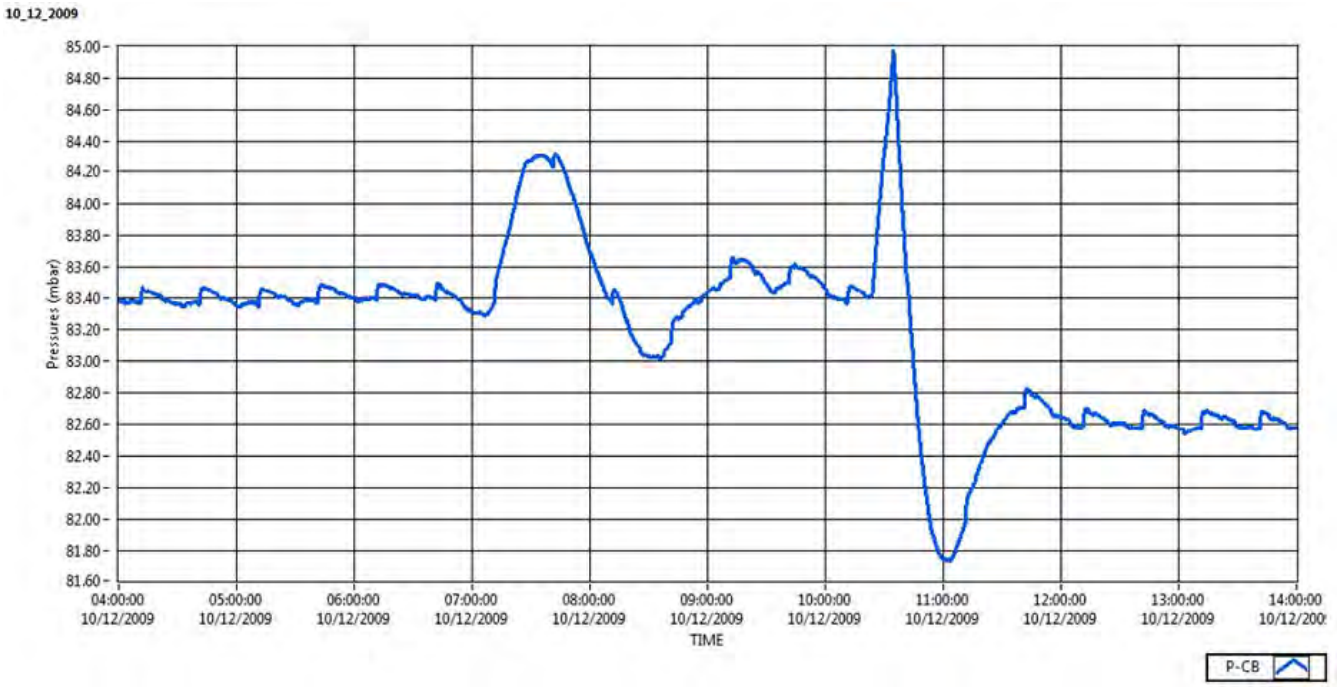

Figure 5.48 The cold bore pressure is plotted against the time of the experiment. The trend is similar to the T_{mag} variation (Figure 5.39). The shift in pressure of ~1 mbar can be caused by the temperature shift (cryogenic circuit) and fluid dynamics phenomena.

Case	N_T	T_{MAG}	$T_{W\text{-}MFB1}$	$T_{W\text{-}MFB2}$	$T_{W\text{-}MRB}$	T_{LINK}	θ [degrees]	P_{CB}
#	[moles]	[K]	[K]	[K]	[K]	[K]		[mbar]
A	18.887	1.765	20.2	17.8	10.5	17.6	-6	84.30
B	18.887	1.766	20.2	18.0	10.5	17.1	-4	84.20
C	18.887	1.761	19.9	17.3	10.7	16.4	-2	83.72
D	18.887	1.759	19.1	16.5	11.0	15.7	0	83.43
E	18.887	1.750	18.9	16.2	11.8	15.5	+2	83.04
F	18.887	1.749	18.9	16.0	12.8	15.5	+4	83.11
G	18.887	1.752	18.8	16.0	14.1	15.5	+6	83.42

Table 5.6 N_T is the number of moles in the system. The magnet temperature T_{MAG} and the T_W (windows) temperature is given for each window sensor. T_{LINK} is the temperature in the link tube (MFB) but the same temperature can be set to the MRB link. The parameter θ is the angle of the magnet and P_{CB} is the pressure measured at each angle. Positive tilting means MRB above MFB

The density profile of the cold bore is needed at various angles in order to qualify and quantify the effective length of the magnet. CFD modeling can help in this direction, assuming that the boundary conditions given (windows temperature, cold bore pressure and magnet temperature), are correct and not influenced by any disturbance during the experimental time.

The simulations performed in this study are based on measurements at 83 mbar pressure in the cold bore and for the angles presented in the table 5.6. For each vertical rotation angle of the magnet the boundary conditions for the windows and magnet temperature are also given.

5.11.2 CFD modelling

The CFD model used in the horizontal case will be used for the tilted case at various angles and specified boundary conditions as shown in Table 5.6. For the tilted case needs, a new coordinate system is specified close to the MFB side at the reference point of magnet rotation. A model sketch is presented in Figure 5.49 in a positive angle so that the MRB side is brought above the MFB side. The geometry of the model, as also mesh and turbulence model used, remain the same as in the horizontal case.

The regions of interest, that is the MFB and MRB sides, are affected by hydrostatic pressure that is induced because of the magnet tilting. In the software the gravity vector is changed according to the tilted angle simulated. With this modification the fluid is under the influence of gravity (at any specified angle provided) that is projected in X and Z axis as shown in the Figure 5.49.

The solution of the 83 mbar simulation setting is taken as a reference model (initial condition) at 0 degrees and according to the boundary conditions specified in table 5.6 the tilted case will be examined. When the model is tilted, natural convection phenomena should be enhanced at the bottom (MFB side in Figure 5.49), while the same mechanism appears suppressed at the top (MRB side in Figure 5.49). The red arrows in Figure 5.49 indicate the intensity of the natural convection mechanism for a positive angle.

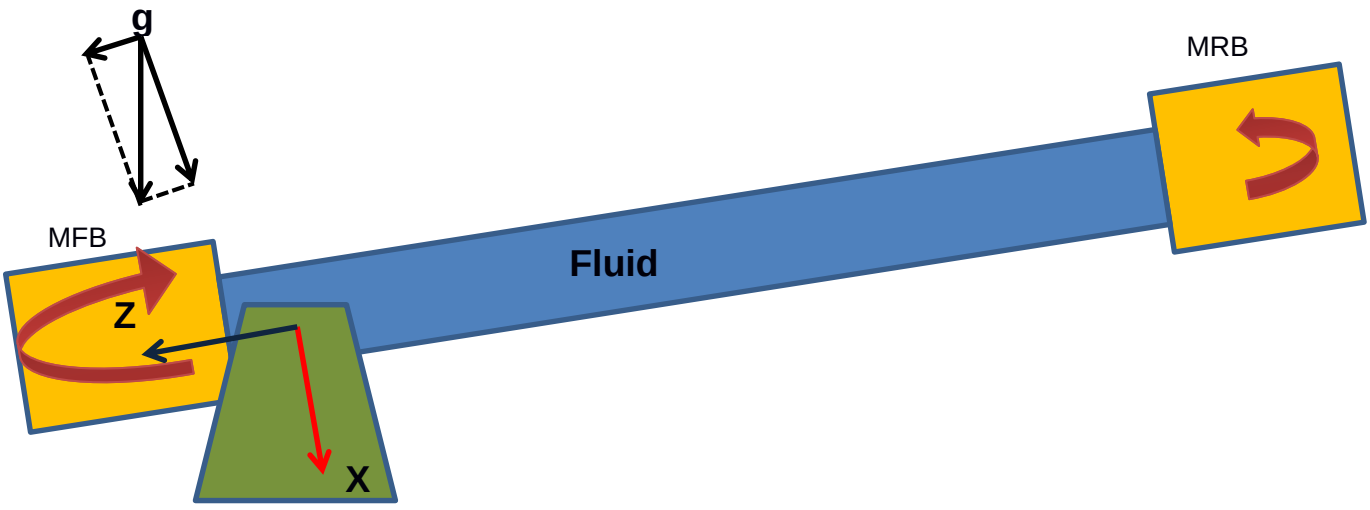

Figure 5.49 The tilted CFD model is sketched. A new coordinate system is introduced at the reference point of rotation. The natural convection mechanism is enhanced at the bottom (MFB) while it is suppressed at the top (MRB). The sketch shows a positive tilting angle.

5.11.3 Turbulence model

The CFD model for the tilted case makes use of the SST k-ω based turbulence model as described in the first sections of the horizontal case modeling. The tilted case is much more demanding than the horizontal case since there is redistribution of mass according to the tilted model position and that mass change is accompanied by an analogous pressure change. The turbulence model used is a transitional model and is supposed to be capable of reproducing any laminar to turbulent transition. The Gamma Theta model used is theoretically able to solve the opposite mechanism that is taking place for this study; that is the turbulence to laminar transition. The intermittency parameter involved sets the onset of the critical Reynolds momentum thickness as it has been defined by the user explicitly for this model. Although the model needs for high transition accuracy is set by the requirement y^+ ~ 1 (approximately), in this model some small regions in the cold bore has revealed values of y^+ at the level of ~1.5. This of course will set the transition onset location upwards but the computational sources used cannot overcome this limit. The theory of Ansys Solver sets the large onset of transition when $y^+>5$.

Another interesting feature is that the turbulence model used has been verified and analyzed in flows of airfoils, but not for the also complex flow system of CAST where temperature and density gradients (because of the fluid involved) are enormous. It is known in the literature that this model of turbulence may over-predict the transition and this feature can alter the accuracy of the density distribution. It should be emphasized however that the same model can give higher accuracy if the necessary computational sources are available. The Gamma Theta model can overcome the usual difficulties of relaminarization occurring in the standard SST model by the introduction of two more equations where the real conditions of transition can be specified by the user.

When the magnet starts tilting towards positive angles, the top end (MRB) starts a flow that resembles to be laminar because natural convection is suppressed at the top end. The density increases and pressure starts to decrease at the MRB region where the transition from turbulent to laminar occurs. The opposite effect can be observed at the bottom side (MFB), where natural convection is enhanced because of gravity and pressure increase (hydrostatic effect). Velocity gradients can change the so called Modified Pressure in the system when an extra term is added

$$p = p' + \frac{2}{3}\rho k + \frac{2}{3}\mu_{eff}\frac{\partial U}{\partial x} \qquad (5.\ 36)$$

where ρ is the density, k is the turbulence kinetic energy, μ_{eff} is the effective viscosity and $\frac{\partial U}{\partial x}$ is the divergence of velocity. The last term is usually omitted by CFX. Hydrostatic effects are also of great importance for the system when it is tilted and this effect by itself is capable to change the density distribution along the cold bore.

When the system is tilted at positive angles, the MFB window at the bottom is getting colder because of the increased convective cooling power, driven by the ^{3}He flow. The opposite effect is observed in the MRB window at the top, where less intense natural convection flow warms up the window temperature as can be seen also from the table 5.6. It is then clear that laminar to turbulent and turbulent to laminar effects are taking place in parallel with temperature variation at the x-ray windows as also with the imposition of the hydrostatic pressure. All these effects make the simulation model more complex compared with the horizontal case. Although complex enough, and natural convection driven, the problem can be solved by using the steady state simulation. The rotation of the system is very slow and the vertical movement downwards from 0 degrees to -6 degrees has a speed of

$$\boldsymbol{\omega_{tilt} = 0.15\ [\frac{deg}{min}]} \qquad (5.\ 37)$$

Potential inertial forces are not expected to occur during the tracking time because of the low velocity of the system which cannot have some measurable impact to the gas stability.

The effect of the turbulence model used and the phenomena induced to the system by applying a positive angle rotation of +4 degrees can be seen in Figure 5.50

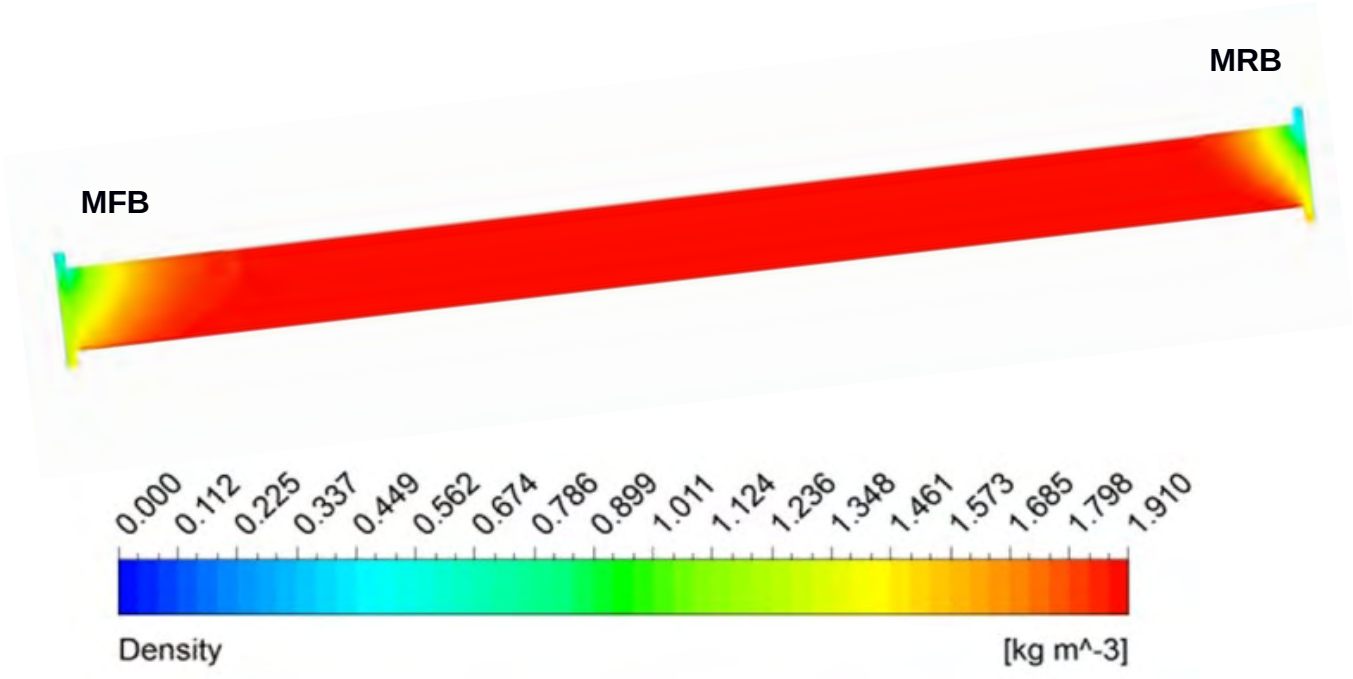

Figure 5.50 The density distribution of the tilted CFD model is shown in a positive angle +4 degrees. The density is suppressed at the top (MRB) while it is enhanced at the bottom. The model is shown in a scale of 15. As can be seen, the relaminarization has been “introduced” at the top side where previous turbulence has been suppressed. The MFB side is a turbulence enhanced region. The red region is not a truly constant density region because hydrostatic pressure disturbs homogeneity, but as can be seen, the red region is a laminar region that the CFD model reproduces as expected. However the turbulence model might have some limitations and not accurately predict the flow dynamics and the laminar region extent.

An important feature that can also give information about the turbulence occurring at the ends of the CFD model is the Turbulence Kinetic Energy plot that is shown in the next figure.

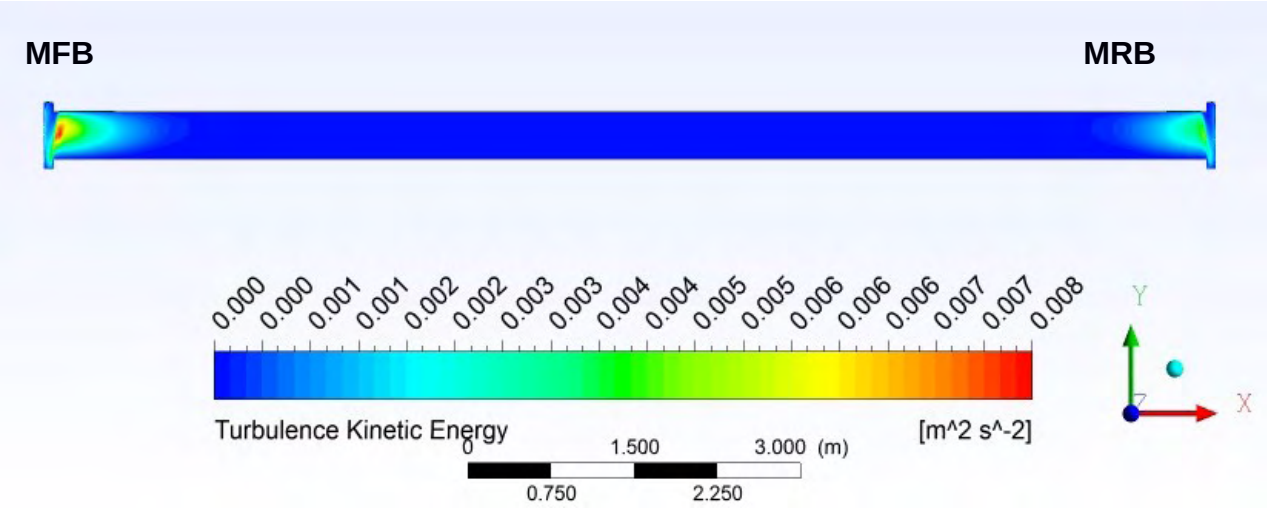

Figure 5.51 Turbulence kinetic energy of the CFD model at 83 mbar when the magnet is horizontal. The turbulence is more intense in the MFB side because of the higher temperature applied.

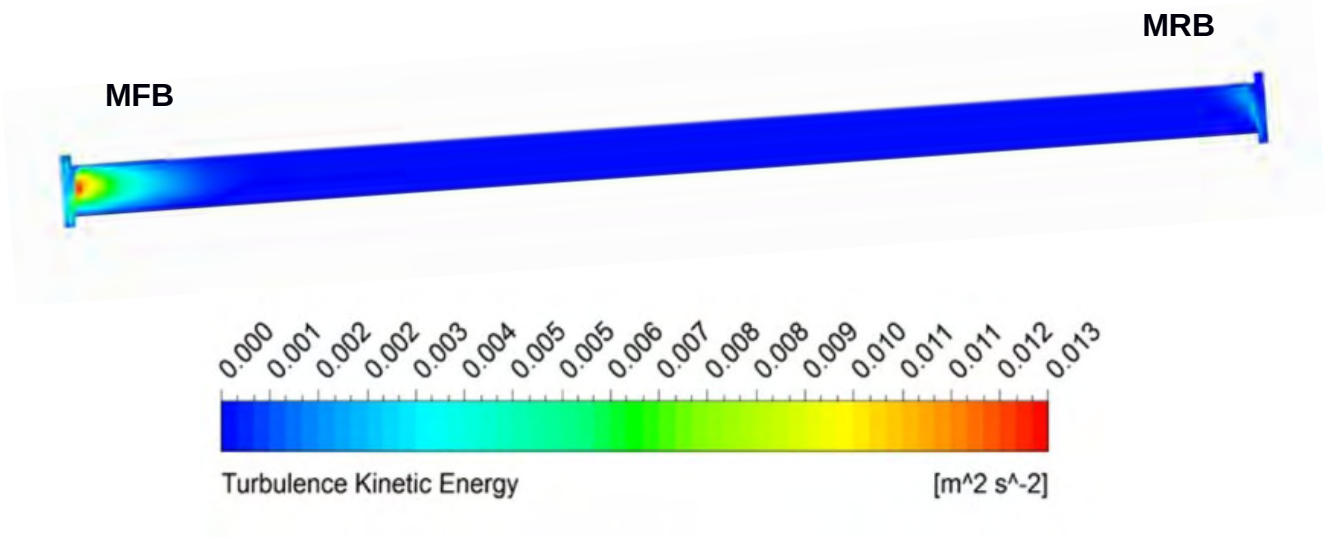

Figure 5.52 The Turbulence kinetic energy is shown when the model is tilted at +6 degrees. The turbulence has almost vanished in the MRB side on the top. MFB bottom side has enhanced turbulence as expected. The blue area indicates laminar flow.

It is then clear that the turbulence to laminar, while laminar to turbulence effects occurring in the CFD model can be resolved by using the Gamma Theta SST turbulence model. The extent of the boundary resolution is unfortunately not clear by testing only turbulence. In the next section the methodology to acquire more information about the model and finally for the very important effective length is analyzed.

5.11.4 CFD Simulations method

This CFD study purpose is to qualitatively predict the ^{3}He behavior inside the cold bore when the magnet is rotated during data taking. The information that can be extracted from this study is of utmost importance for CAST in order to specify the effective coherence length involved in the data analysis from the detectors used. In order to specify the fluid processes and the system dynamics the following strategy has been followed in this study

- Tilted steady state simulations for the cases (A, ..G) are referred in the table 5.6 according to the boundary conditions given
- Analysis of the number of moles extracted from the above simulations and the deviation observed between experimental values and the CFD model results.

As mentioned, there is a “discrepancy” between the cold bore pressure observed in figure 5.48 of the 83 mbar setting, and the pressure that is expected to be observed. The shift observed at P_{cb} = 83 mbar, but as a consequence of the vertical movement of the magnet of 6 degrees it is actually +1.06 mbar.

In the corresponding T_{mag} versus time plot of the 83 mbar setting (Figure 5.47), there is a variation of temperature during data taking time as mentioned. This variation of T_{mag}, as also the hydrostatic pressure induced, accounts for the +0.65 mbar shift. The remaining contribution of ~0.4 mbar is ascribed as fluid dynamics changes that can alter the pressure inside the cold bore. The phenomena arising can influence, as noted in the previous section, the distribution of the fluid in the extremities and the change of mass distribution can change to analogous amount of the system’s pressure. It is of importance to testify the “discrepancy” observed and clarify the final density distribution in the cold bore so as to be confident for the coherence length used by CAST’s analysis.

The pressure difference can be ascribed to the convection effect that is enhanced at the bottom end and suppressed at the top of the model. In case where the convection effect can be resolved in a great detail in the CFD model used, reliability can be assigned to the simulations and thus the actual coherence length can be predicted accurately.

The simulations method relies on the fact that the boundary conditions (sensors values) at the moment of the measurement are “real”. That means that the effect of external cooling or warming of the windows is depicted at that moment to the sensor values. It is clear that as the boundary condition of pressure P_{cb} or the magnet temperature can be used as a “standard” inputs to the model (although they are influenced by the fluid dynamics phenomena), in the same way, windows temperature BC’s can be used as “standard” input parameters (BC’s) for the model solution. At the specific moment for each one of the cases A…G (Table 5.6) that the measurement is taking place, the total physical phenomena are depicted in that measurement and the CFD model should reproduce it.

5.11.5 CFD Results

In order to obtain the effective length for the tilted case and a relation of the density distribution according to the magnet's angle, simulations have been performed for the tilted cases referred in the table 5.6. The number of moles that are distributed inside the cold bore as also to the MRB and MFB ends, amount for the total mass injected inside the system. In case where the simulation can provide a realistic approach at a high accuracy of the model used and the appropriate boundary conditions given, we can rely on the model built and the density distribution that each simulation provides.

As can be seen in the plot of Figure 5.45 the phenomena described are obvious; Tilting the magnet by +6º (the MRB is above MFB), the top end (MRB) gets denser because of convection suppress. The MFB becomes less dense and the gas is pushed to the MRB side.

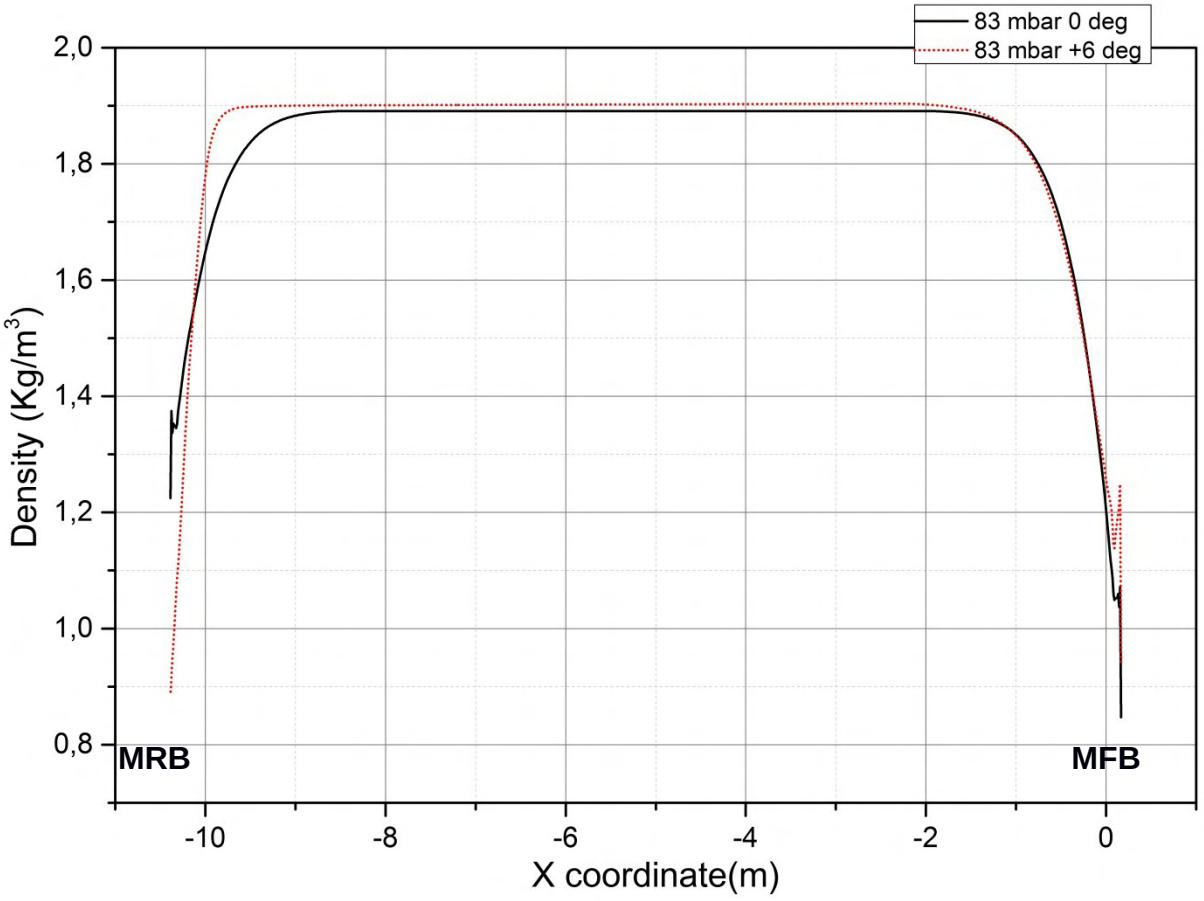

Figure 5.53 Density distributions along the center longitudinal line of the model. The red dashed line indicates the density of the tilted CFD model at +6º. The MFB side end is located at 0 m of the X coordinate axis, while the MFB end is at ~ -10.5 m. The pressure in the cold bore is P_{cb}=83.42 mbar and the magnet temperature is 1.752K. The BC's for the 0º is T_{mag}=1.759K and P_{CB}=83.43 mbar. The MFB windows temperatures have been decreased and the MRB windows temperatures have been increased in positive tilting.

A hydrostatic effect destroys the density homogeneity as can be seen in figure 5.54 and the density variation threshold of $\Delta\rho \leq 0.001$ [kg/m^3] applies only for a much shorter density length. This effect is irrelevant of the pressure BC and applies for all settings that have been used with CAST. This density threshold defined also as Density Stability Region (DST) will be analyzed in next section where the coherence length condition should be defined.

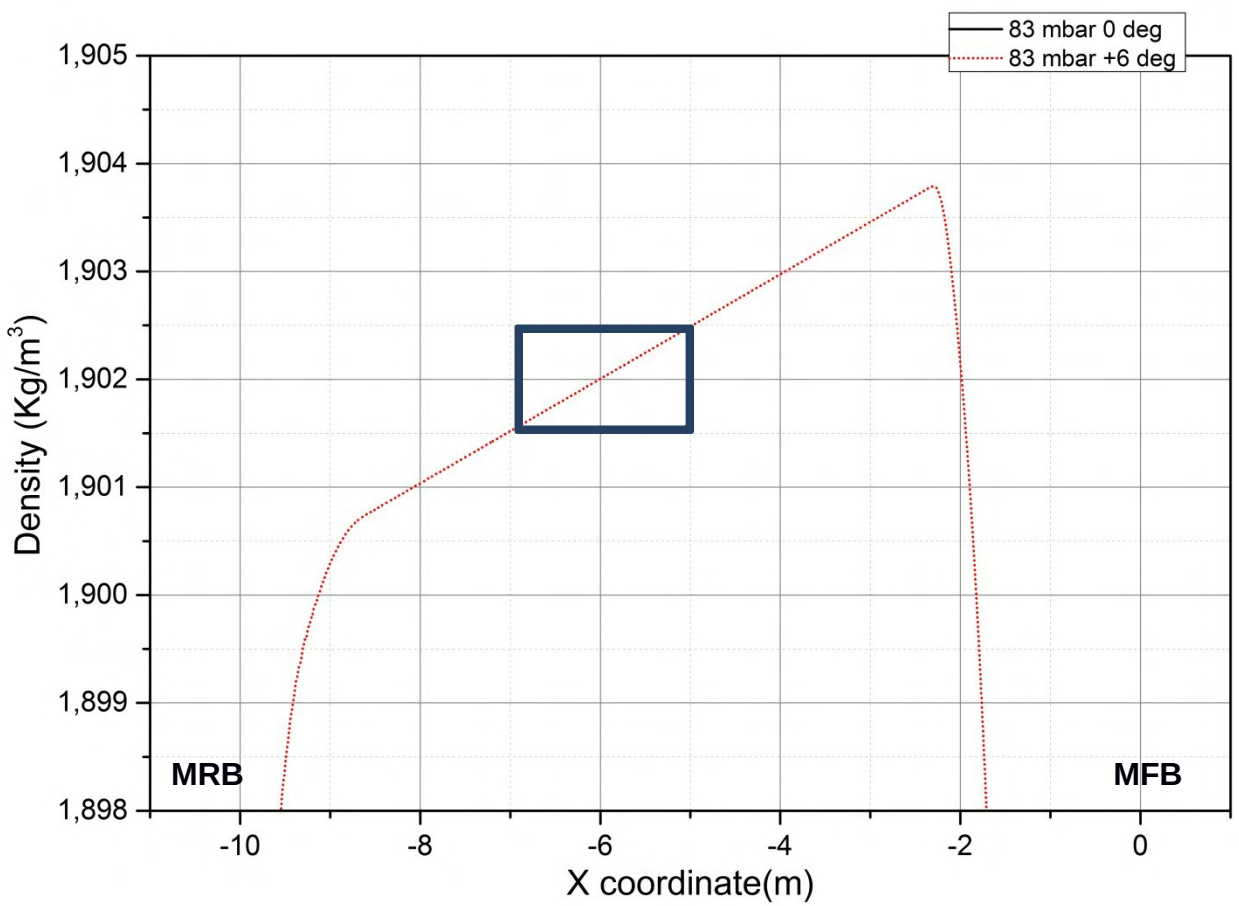

Figure 5.54 The Hydrostatic effect is shown on the +6º tilting at 83 mbar setting. Homogeneity of density is distorted and the blue window indicates the region of constant density below the 0.001 kg/m^3 density threshold. In the case where the DST (density stability region) is defined as 0.0025 kg/m^3, the effective length can be about 5.5 m.

The simulations performed for the tilted cases A to G, as specified in the table 5.6 (0º excluded), show that the effect of hydrostatic pressure is very important and influences drastically the CAST's coherence length. The CFD model can provide information for the horizontal case deviation while the magnet is tilted and provide the accurate coherence length to the analysis group for all magnet positions. The accuracy of the "real" coherence length provided is in accordance with the accurate results of the simulations performed. Deviations from the experimental number of moles calculated from the CFD model could impose some non-reliability of the solution proposed. As mentioned in the horizontal case results, there are some sources of error that could lead the CFD model to deviate from experimental measurements.

The pressure sensor (MKS Baratron 690A) placed at the MRB side is supposed to be accurate enough in the range of 100 torr (named B-100), even when the magnet is rotated. The MKS Company provides accuracy [personal communication] of 10 millitorr when the capacitance manometer is rotated at 90º. There have been also many studies about the T_{mag} accuracy and it has been found that the magnet temperature measurements suffer from an error of about ~1mK. The dead volumes (pipework) that are not modeled can also be a source of error but the amount of gas inside them is negligible. The shrinkage of the system is not taken under consideration. Another source of error is also the EoS used because the density difference between the Peng Robinson equation used and the NIST experimental data is of the order ~3.3 10^{-2} kg/m^3.

The table that summarizes the results obtained is the following.

Case #	T_{MAG} [K]	θ [degrees]	P_{CB} [mbar]	N_T experimental [moles]	N_T CFD [moles]	Deviation [%]
A	1.765	-6	84.30	18.887	19.00585	0.60
B	1.766	-4	84.20	18.887	18.94777	0.30
C	1.761	-2	83.72	18.887	18.88416	-0.01
D	1.759	0	83.43	18.887	18.856	-0.16
E	1.750	+2	83.04	18.887	18.8630	-0.13
F	1.749	+4	83.11	18.887	18.90381	0.09
G	1.752	+6	83.42	18.887	18.93752	0.26

Table 5.7 The calculated number of moles obtained from the simulations according to the BC's specified for each case. Higher deviation is observed for higher angles of tilting.

It is obvious that according to the results obtained and the error sources, it cannot be a perfect solution to the problem. CFD simulations are methods to investigate the fluid phenomena and cannot reproduce the real experiment at 100% accuracy.

What is interesting and important for CAST is the qualitative behavior of the ^{3}He gas inside the tubes of the CAST magnet. The number of moles obtained in addition with NIST database for ^{3}He can provide the information needed to represent the physics involved.

By applying the BC for each case one should expect that the pressure set in addition with the magnet temperature should produce the experimental number of moles. In low angles the accuracy is high while by tilting the magnet in extreme positions (negative or positive angles) the accuracy gets worst. It is reasonable to assume that a source or sources of errors are getting involved to the solution. Because of the tests that have been performed for the T_{mag} and the P_{cb} sensor's accuracy and showed no problematic behavior, it is reasonable to assume as a main source of deviation the solution implementation. The ^{3}He gas dynamics cannot be accurately reproduced by the Peng-Robinson EoS. The difference between experimental measurements of NIST for ^{3}He and the EoS used, that is the Peng Robinson, can be seen in the next plot, using the same actual simulated temperature and pressure P_{cb}= 83.43 mbar at 0º inclination.

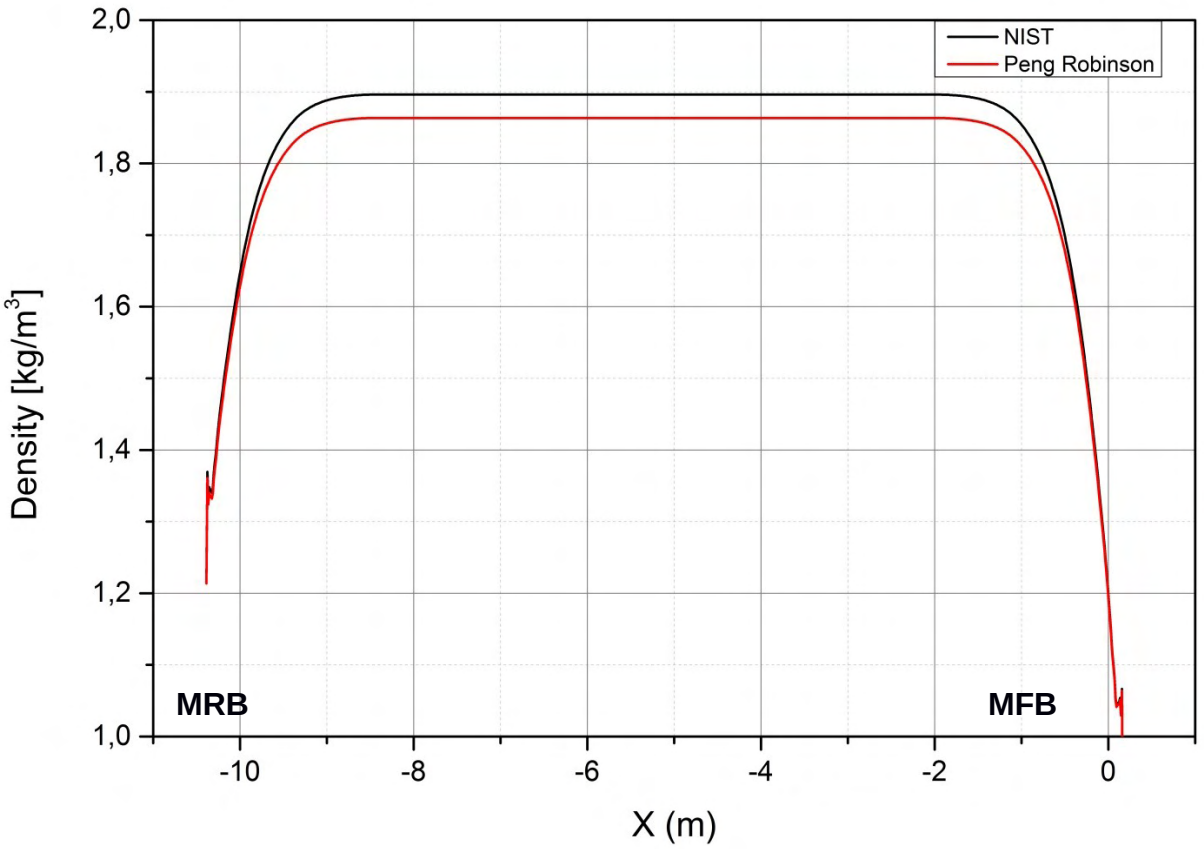

Figure 5.55 The difference of the real ^{3}He behavior expressed as NIST(black line) and the Peng-Robinson EoS (red line) result for the temperature of the fluid along the tubes in pressure P_{cb}= 83.43 mbar. The result is for zero tilting. The deviation for small temperatures is obvious.

The parameters of ^{3}He (like specific heat, viscosity etc.) have been extracted from the NIST database of experimental measurements, although the software will use the Peng-Robinson

equation as set. The Peng-Robinson EoS will always result in a smaller density as figure 5.55 indicates.

The hydrostatic effect (because of tilting) is changing the density distribution profile and the coherence length computed is always less than in the horizontal case. As the tilting increases to higher angles the coherence length becomes smaller. The hydrostatic pressure effect can be seen in the next plot.

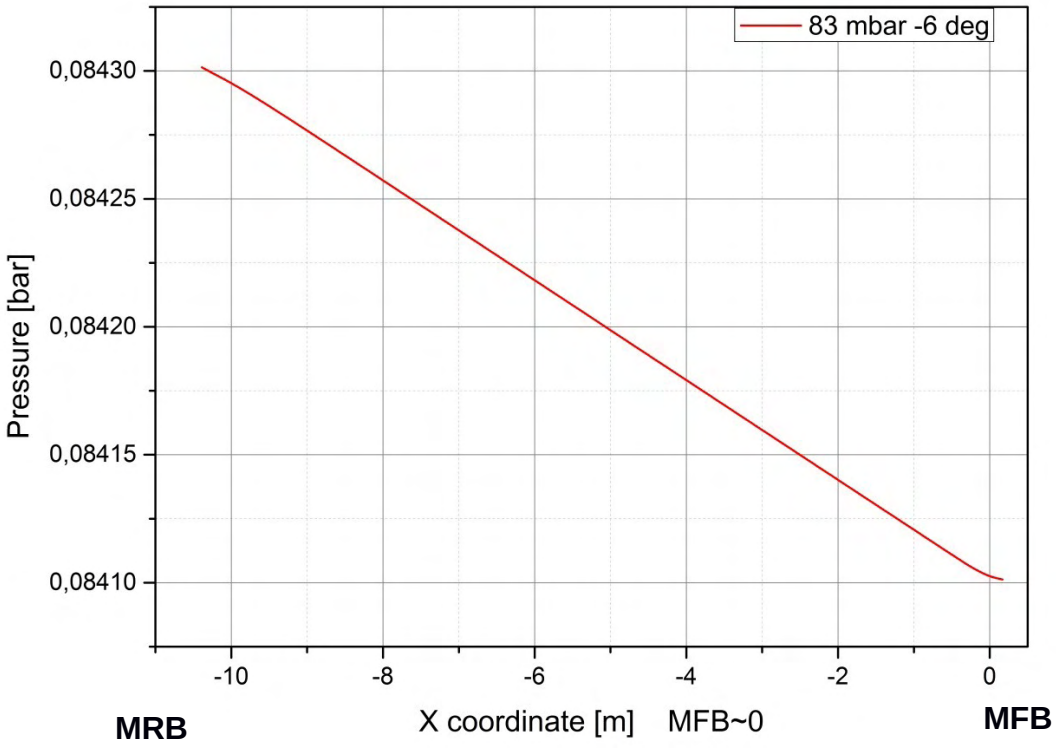

Figure 5.56 The hydrostatic effect when the magnet is tilted at -6º. The MFB region is located close to 0 coordinate and is at the bottom while the MRB pressure includes the hydrostatic pressure that is the reference pressure set as a BC (P_{CB}=84.3 mbar at -6 degrees). Therefore the "experimental" pressure measured and set as BC, includes the Hydrostatic pressure appearing for the specified magnet position.

The modified pressure known also as motion pressure is responsible for driving another part of the flow. An interesting effect that appears in the ^{3}He flow is that the pressure gradients sustain a flow inside the cold bore. This flow is forced by the hydrostatic pressure that appeared in high and low level regions. For example the pressure is higher at the MFB end when the magnet is tilted in positive angle and lower at the MRB end. This effect can alter the density inside the cold bore by a microscopic amount and does not significantly alter the coherence length.

Coherence length is affected by the convection effects intensity. In either side of the magnet when tilted, convection alters the coherence length by the amount of fluid being in turbulence or in transition flow. The uncertainties involved and the error sources can dramatically show a different flow behavior.

The influence of T_{mag} in the system's pressure and density is noticeable. Temperature variations because of cryogenic circuit phenomena can alter the pressure in the cold bore and as a consequence the density inside the magnetic field where the coherence length condition should apply. The density distributions of all cases specified in the table 5.6 are shown in the next plot.

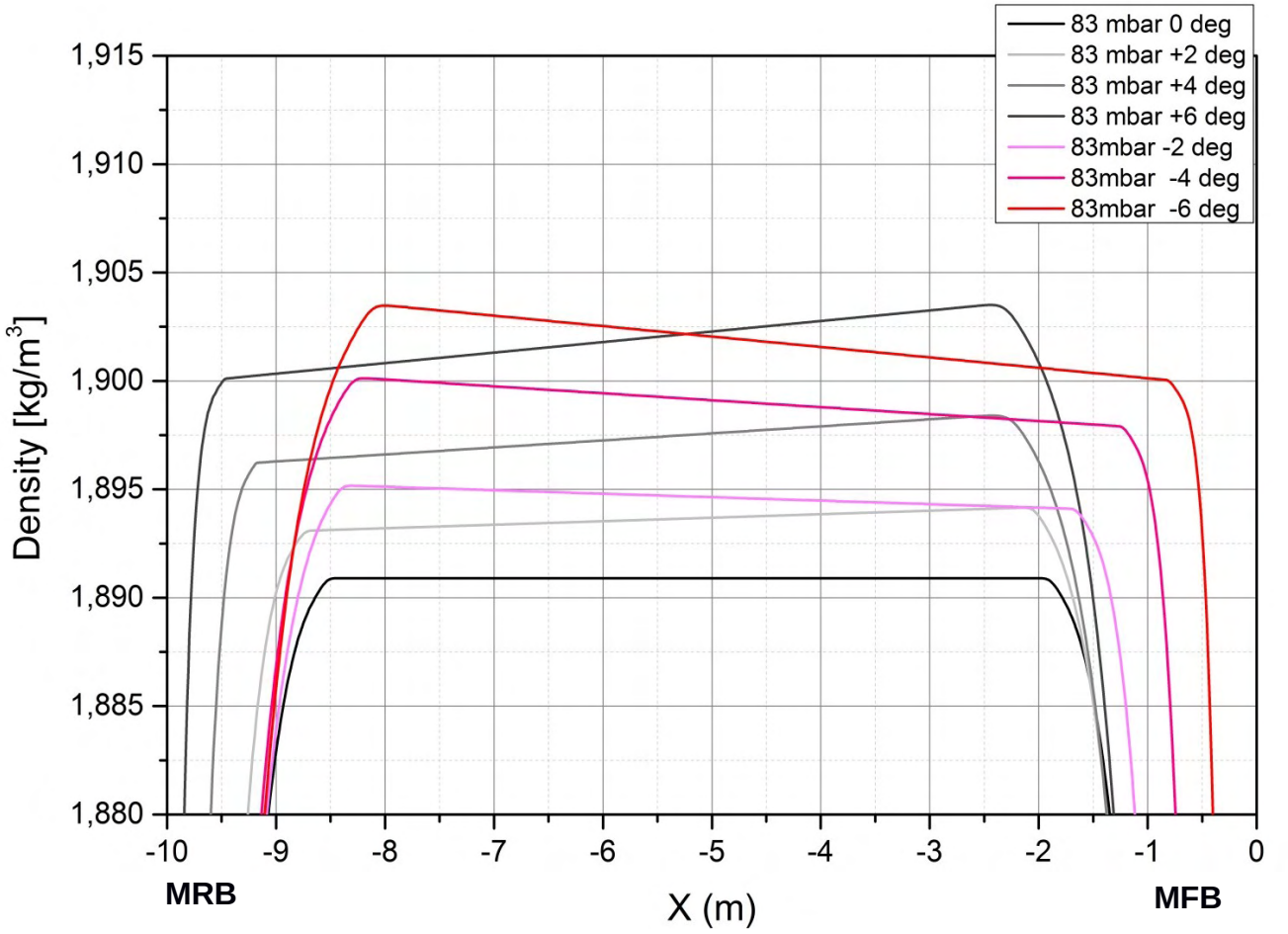

Figure 5.57 Density profiles of all angles are shown in reference with the horizontal case (black line). Light grey, grey and dark grey lines show the density while the magnet is tilted in positive angle. The trend of positive angles shows the density increase, the hydrostatic effect and that the MRB side at the top become denser. The opposite effect is shown when the magnet is tilted in negative angles by the magenta, pink and red lines.

The next plot (Figure 5.58) shows the distribution of moles for each angle according to the pressure set in the cold bore. The number of moles for each angle should be constant but since the magnet temperature is changing and due to tilting, there is a corresponding change of the pressure and density. The overall deviation of the experimental number of moles computed from the simulation is bellow ±0.6 %. The EoS deviation from NIST experimental values could be an issue as also the sources of uncertainty mentioned. The fluid behavior is well described and the Gamma-Theta turbulence model used can provide accurately enough the dynamic phenomena observed. CFD can be used as a tool to investigate and analyze thermodynamic phenomena in a great detail and provide the adequate information needed for CAST's scientific

research program. CFD is not a science by itself but can be used as a tool to investigate thermodynamic phenomena participating in astrophysical experiments like CAST.

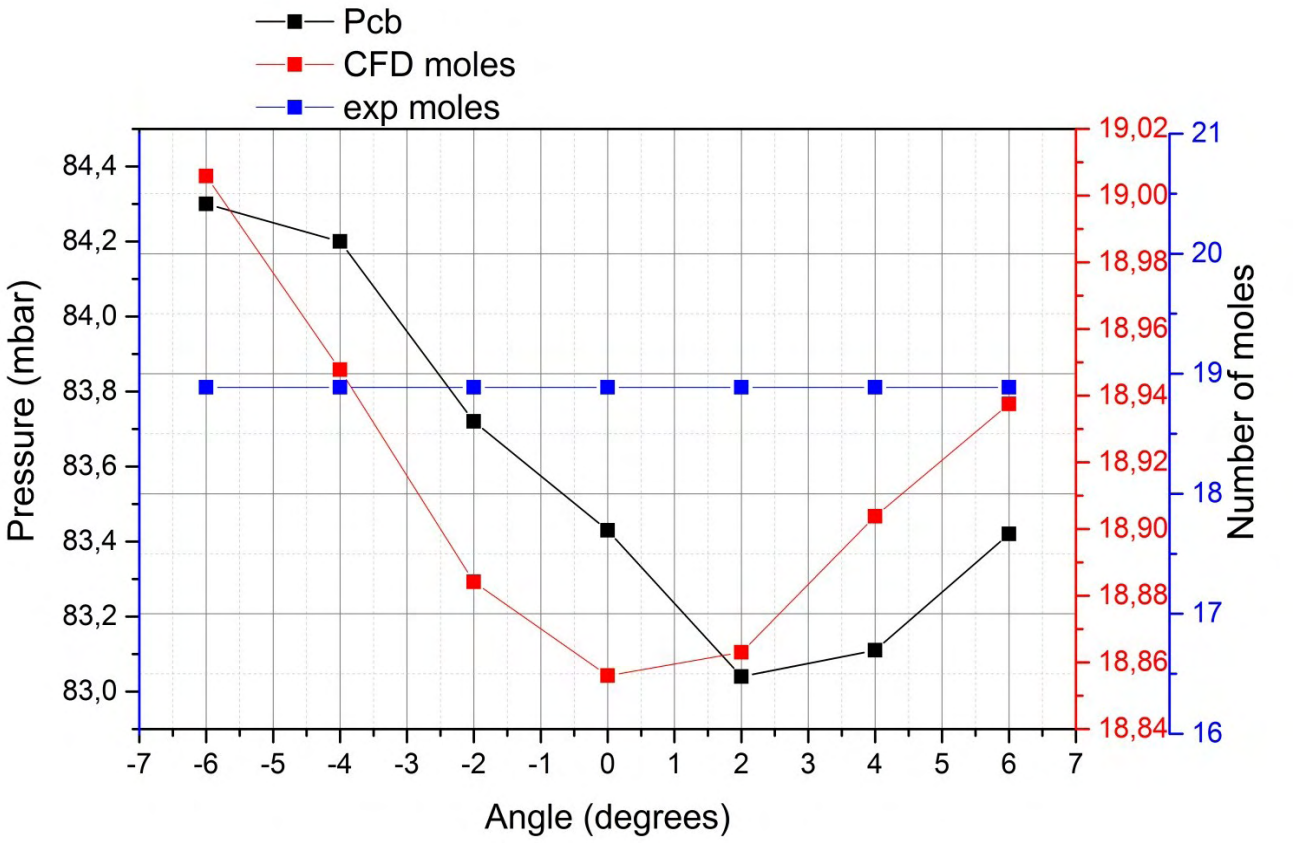

Figure 5.58 A 3Y plot of the computed number of moles provided by CFD simulations is shown in addition with the experimental number of moles and the trend of the cold bore pressure experimental value.

Studies have also been made in STARCCM+ software for each temperature influence on the fluid behavior and the total deviation from the experimental measurements. The studies accomplished were

- the influence of the MRB window change by ±5 K
- The influence of the MFB window change by +10 K
- The effect of T_{mag} if changed by 0.03 K
- The total effect of all the above parameters

These studies had as a purpose to investigate the fluid behavior for each boundary condition change, but they were accomplished in different software for the “hot windows” case (the windows at 2008-2010 were at temperature around ~70K). So these results will not be presented for this study.

5.12 DST (Density Stability Threshold)

This threshold as noticed is the value that is allowed for density variations in order to endure the coherence length over the maximum magnet length. The magnet's tube length is 9.26 m in total but this value does not account for the total coherence length because of the density distribution variations inside the cold bore. In the case where the DST is very strict, the overall CAST sensitivity decreases accordingly.

The fractional density that should be fulfilled in order to satisfy the coherence condition as referred by Zioutas et al [86] for axion (-like) particles can be written as

$$\frac{d\rho}{\rho} = 2\frac{dm}{m} \equiv \frac{4\pi \cdot E_\alpha}{L \cdot m_\alpha^2} \tag{5. 38}$$

where ρ is the density of the buffer gas, E_α is the axion energy, m_α is the axion mass and L the magnetic length.

The formula that expresses the axion mass via the buffer gas density is the following

$$\rho = 24.77\sqrt{\rho\frac{Z}{A}} \tag{5. 39}$$

Z is the atomic number of gas with mass A. when coherence condition applies $m_\alpha \equiv m_\gamma$ so ρ becomes

$$\rho \equiv \frac{3}{2}\left(\frac{m_\alpha}{28.77}\right)^2 \cdot 1000\ [\frac{kg}{m^3}] \tag{5. 40}$$

Where m_α is expressed in eV. By substituting equation (5. 40) in (5. 38) and rearranging the terms it follows that

$$d\rho = 6.05223 \cdot 10^{-3} \cdot \frac{E_\alpha}{L} \tag{5. 41}$$

E_α is measured in keV and L in meters.

The allowed density variation $d\rho$ is not dependent on axion mass or on gas density, but it only depends on the axion energy and the magnetic length. The allowed density variation for L =9.26 m, is plotted in figure 5.59

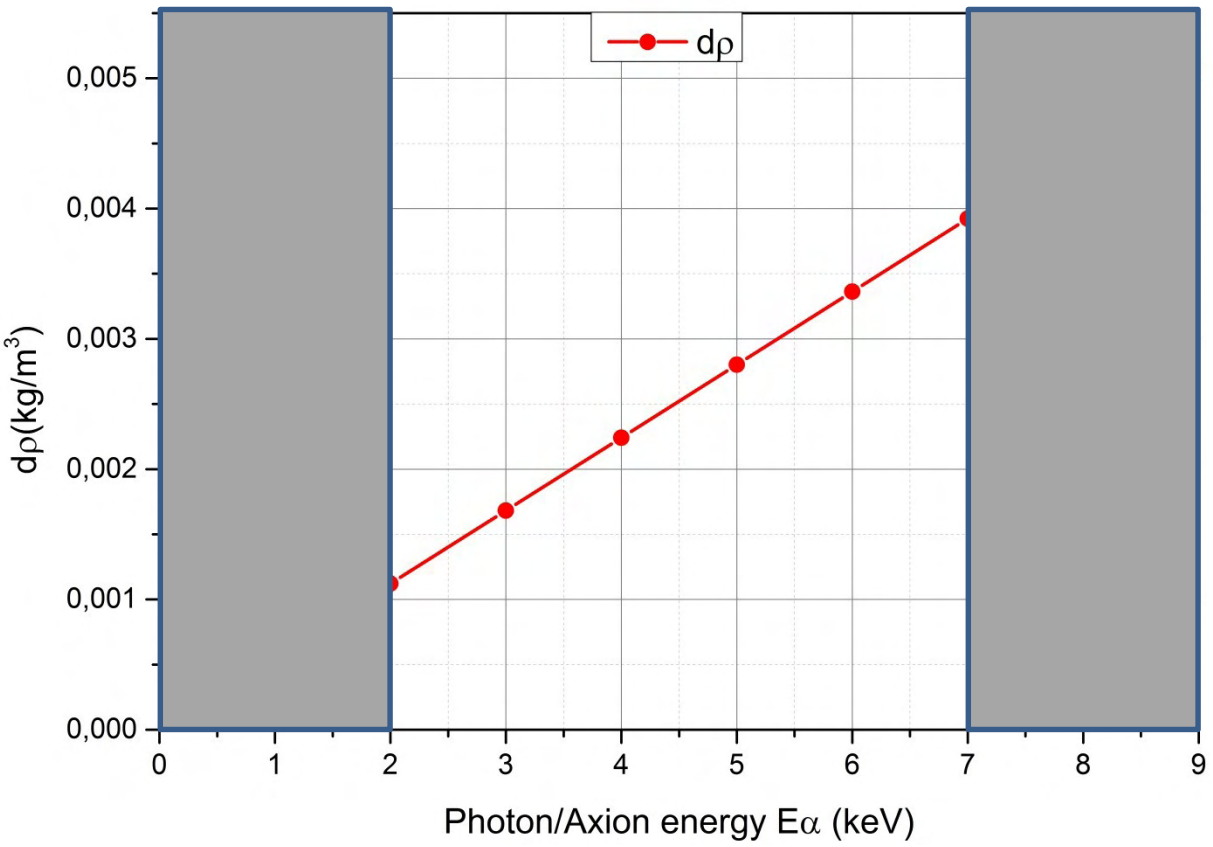

Figure 5.59 Allowed density variation dρ for L=9.26m. The dark regions are outside the region of interest.

For the CAST system with magnetic length 9.26 m, the density stability region specifies the threshold that is proportional to axion energy. For axion energy at 2 keV the threshold is 1.3×10^{-3} kg/m^3, while for 7 keV the threshold becomes 4.6×10^{-3} kg/m^3. It is clear that the threshold of 0.001 kg/m^3 is rather conservative and higher values of DST are allowed for energies above 2keV.

The effective length can be parameterized with respect to the density fluctuation and the cold bore pressure according to the formula

$$L_{eff} = \alpha \cdot d\rho^{\beta} \tag{5. 42}$$

Where α and β are given by the following relations [87]

$$a = -1.0442 \cdot 10^{-2} P_{1.8K} + 10.079 \tag{5. 43}$$

And β is given by

$$\beta = 2.57198 \cdot 10^{-4} P_{1.8K} + 2.07989 \cdot 10^{-2} \tag{5. 44}$$

Where $P_{1.8K}$ is the pressure inside the cold bore corrected by the magnet temperature.

So finally the effective length is given by the relation

$$L_{eff} = \alpha \left(6.0518 \cdot 10^{-3} \frac{E_a}{a}\right)^{\frac{\beta}{\beta+1}} \quad (5.\ 45)$$

This equation provides the effective length in the “cold windows” case as has been studied in this section.

6. The Micromegas detector

Three of the four X-ray detectors used in CAST during the data taking period of this work (2009-2011) were Micromegas. The principle of operation and the detailed description of the gaseous detector is given in this chapter. An introduction of the phenomenology of gaseous chambers is also reported in the next sections.

6.1 Phenomenology of Gaseous chambers

In order to detect a particle and measure its properties (like energy, mass, momentum etc.) an interaction with the gaseous part of the Micromegas should take place. There are many types of detectors, according to the application of measurement, that aim to detect specific types of particles. Gaseous chambers are instruments that are used for particle detection. These types of detectors are based on the idea that any particle can interact with a gas mixture inside the chamber and by applying an electric field, free charges that have been produced from the interaction of a particle of interest with the gas can be accumulated and measured. Gaseous detectors can detect photons, electrons and heavy charged particles like muons or alphas etc.

6.1.1 Interaction of photons in a gas chamber

A beam of photons with intensity I_0 after passing by a medium of thickness χ will have an intensity of[28]

$$I = I_0 e^{-\mu\chi} \tag{6. 1}$$

where μ is the total photoabsorption coefficient and is given by the formula

$$\mu = N\sigma \tag{6. 2}$$

N is the density of atoms and σ is the total cross[29] section per atom.

There are four types of interactions that can occur when the photon travels through the matter depending on its energy.

- Photoelectric effect: where the photon is absorbed by an atomic electron
- Compton scattering: where part of the photon energy is transferred to an atomic electron. For low energies it is called Thomson scattering
- Pair production: where the photon traversing the electromagnetic field of a nucleus materializes into an electron-positron pair.

[28] Beer-Lambert law
[29] The effective area that is used to express the likelihood of some scattering or absorption event

- Rayleigh scattering: where the photon is scattered by the atom or molecule (coherent scattering)

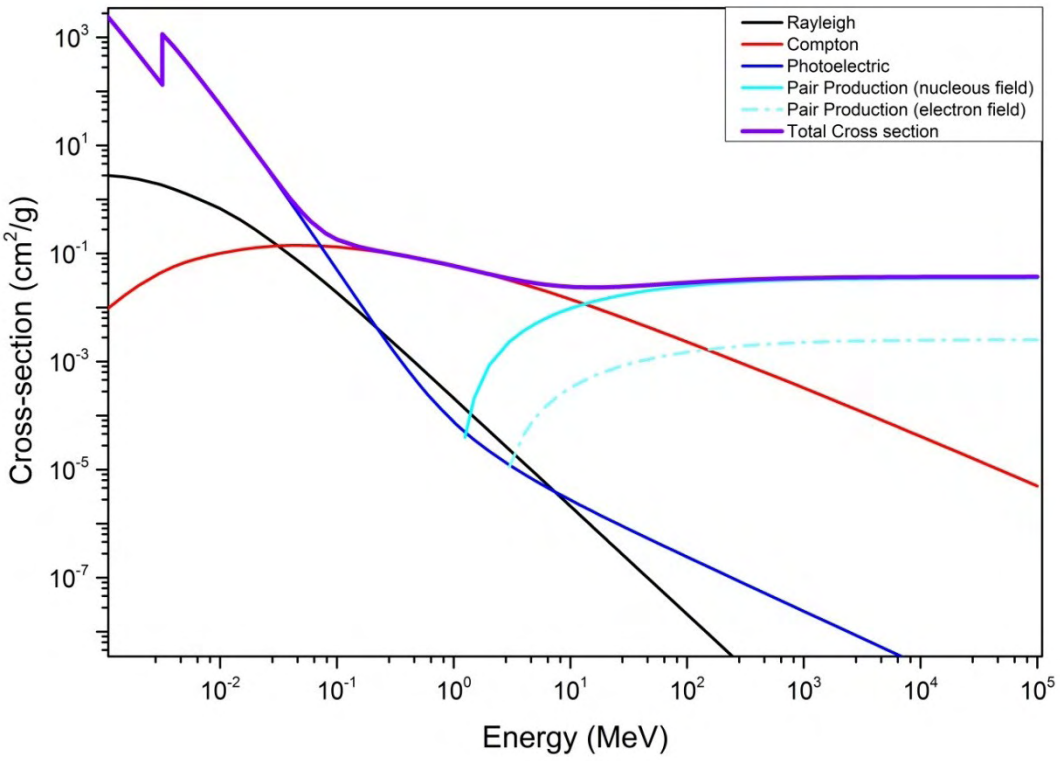

Figure 6.1 Cross-section of each process that photons experience when passing through a mixture of 90% Ar- 10% Isobutene. Units of Cross-section are given in cm^2/g for the specific mixture at standard pressure. The sharp increase of the total cross-section comes from the atomic K-edge that is observed above 3.19 keV for Ar [89]

Photoelectric effect

Each one of the three mechanisms contribute a cross section factor to the equation of the total cross section that can be defined as

$$\sigma = \Phi_{photo} + Z\sigma_c + \tau_{pair} + \sigma_{Rayleigh} \quad (6.\ 3)$$

The total cross section per atom consists of the photoelectric effect term, the Compton scattering term and the pair production one. The lower part of the spectrum up to several keV, is ruled by the photoelectric effect, next comes the Compton scattering up to hundreds of keV and above 1.22MeV the pair production mechanism dominates. The cross section of each interaction depends on the photon energy, the atomic number and the density of the material.

As an example, the Cross-section for the mixture of 90% Ar -10% Isobutene is shown in figure 6.1

The phenomenon where a photon of energy $E_o = h\nu$ is absorbed by an atomic electron and is followed by an electron ejection (photoelectron) is called photoelectric effect. The binding energy of the electron is E_B and the photon that is ejected has energy

$$E = h\nu - E_B \tag{6. 4}$$

When the photon energy is higher than the binding energy of a shell, the electrons of this shell can become photoelectrons. In order to estimate the total cross-section for the photoelectric effect, one must sum the cross-sections for the photoelectric effect of various shells where the effect is energetically allowed.

In the non-relativistic limit where $h\nu << m_e c^2$ and for photons energy higher than the binding energy of the K-shell, the cross-section for the photoelectric effect is given by

$$\Phi_{photo} = 4\alpha^4\sqrt{2}Z^5\frac{8\pi r_e^3}{3}\left(\frac{m_e c^2}{E_o}\right)^{7/2} \tag{6. 5}$$

where $\alpha = \frac{1}{137}$ is the fine structure constant, r_e is the electron radius, m_e is the electron mass, Z is the material atomic number and E_o is the photon energy. The formula is valid up to energies of 500 keV and it shows the strong dependence of the cross-section on the number of electrons in the medium.

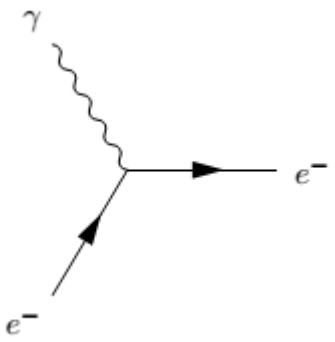

Figure 6.2 Feynman diagram of the photoelectric effect.

After the photoelectron has been ejected from the atomic shell, a vacancy is created in the shell. The electron ejection causes a re-arrangement in the atomic shells and two possibilities of the atom relaxation result in a secondary ionization:

- Fluorescence; the process through which the vacancy created by the photoelectron is filled by an outer shell electron. The form of energy released is in the x-ray range. The fluorescence photons can be absorbed by the detector gas medium or in case where these photons are not absorbed the energy of the incoming photon (x-rays in the CAST's

Micromegas) will be shifted by an energy characteristic of the gas medium; this is the origin of the escape peak in gaseous chambers.

- Auger effect; this is a radiationless transition where the vacancy of the ejected electron is filled by electron re-arrangement and an electron emission (Auger electron) of energy close to the binding energy.

In each case (fluorescence or Auger effect) a vacancy is replaced by another vacancy and the atomic relaxation results by more than one electron transitions. The deexcitation fraction through the fluorescence process is called fluorescence yield. In Argon (a common constituent of the Micromegas detector gas mixture) the K-shell fluorescence yield is 13.5%.
In the gas active volume of the detector the ionization generated, produces a signal and the fluorescence of the gas appears in the spectrum as an escape peak. Escape peaks in Micromegas detectors are most often observed due to the solid parts of the detector's housing that consists (as will be explained in next section) of metallic read-out channels, cathodes etc. That could result to the limitation of the background at low energies as can be seen in figure 6.3.

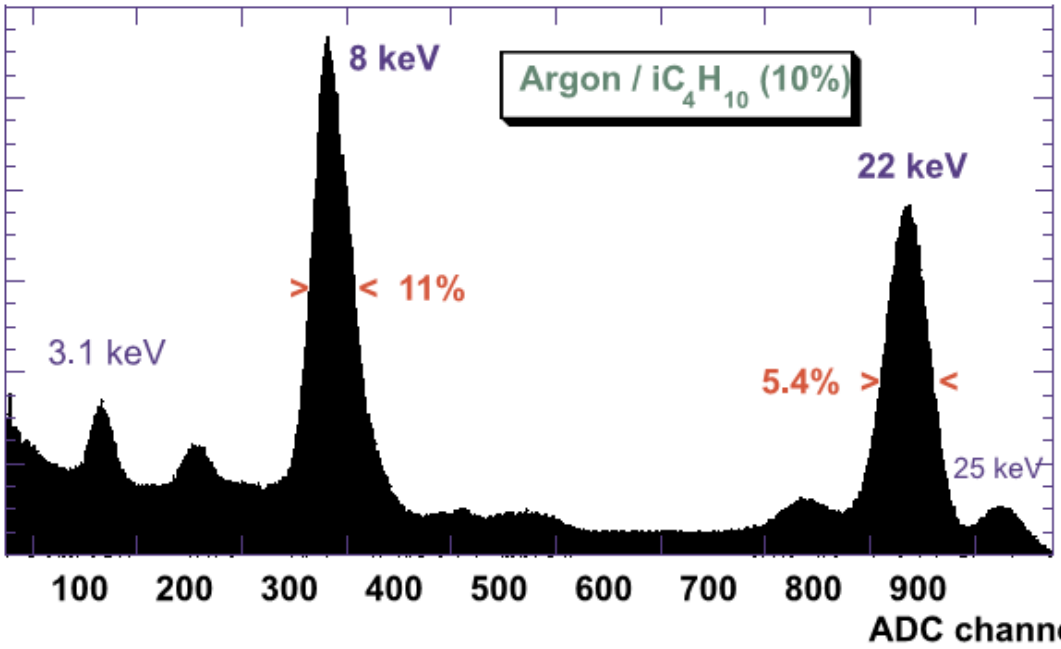

Figure 6.3 A ^{109}Cd X-ray spectra for a Ar-isobutane mixture (90%-10% respectively) at 22 and 25 keV published in [88]. The 8 keV fluorescence of Cu and Ar at 3.19 keV can be observed. The percentages shown are referred to the energy resolution as FWHM (full width at half maximum). In order to calibrate the gaseous chamber at energies close to the axion-photon energy range of interest for CAST's purposes, Ar is used as the main gas mixture constituent because the source of calibration (that is a ^{55}Fe radioactive source with a line at 5.9 keV) has only ~10% possibility to interact with an electron other than the K-shell electrons. This results to a spectrum of Ar at 5.9 keV and a smaller escape peak of Ar at 3.19 keV that they are easily distinguishable.

The effect of Compton scattering, pair production and Rayleigh scattering have a negligible

impact in the Micromegas signal used in CAST for axion detection while they contribute to the detector background.

6.1.2 Interaction of charged particles in a gas chamber

When a charged particle is passing through a gas medium, it suffers from a continuous energy loss and a deflection of its initial direction. These are results of the following mechanisms involved:

- inelastic collision with atomic electrons of the gas
- elastic scattering of nuclei
- Cherenkov radiation
- Bremsstrahlung radiation
- Nuclear reactions

In gaseous chambers the "signature" of the particles, is mainly due to Coulomb interactions. Cherenkov radiation and nuclear reactions are very rare events and beyond the energy of interest. The most important process is the inelastic collision that is mainly responsible for the energy loss and angular spread. A small fraction of the particle's energy is transferred to the gas atoms in each collision. The transferred energy is responsible for the excitation or the ionization of the atom. The primary ionized electrons can cause substantial secondary ionizations in the gas chamber.

The energy loss due to Coulomb interaction is given by the well-known Bethe-Bloch formula

$$-\frac{dE}{dx} = 2\pi N_A r_e^2 m_e c^2 \rho \frac{Z}{A}\frac{z^2}{\beta^2}\left[ln\left(\frac{2m_e c^2\beta^2\gamma^2 W_{max}}{I^2}\right) - 2\,\beta^2 - \delta - 2\frac{C}{Z}\right] \qquad (6.\ 6)$$

r_e the electron radius

m_e the electron mass

N_A the Avogadro's number

I the mean excitation potential

Z the atomic number of gas

A atomic weight of gas

ρ is the gas density

z the charge of the incident particle

β the velocity v/c of the incoming particle

γ the relativistic parameter $1/\sqrt{1-\beta^2}$

W_{max} the max. energy in single emission

δ a density correction

C a shell correction

The formula 6.6 describes the integral over all energies lost to the atoms of the medium. As $\beta\gamma$ is increased, dE/dx decreases, then it goes to a minimum and rises again for higher values of

$\beta\gamma$. The relativistic rise is expressed by the logarithmic term and its strength is given by the mean excitation energy I. It should be noted that the formula provides the mean value of the energy loss (see Figure 6.7). There are statistical fluctuations of the number of collisions taking place as also secondary charged particles, which make the distribution of the formula deviate from the typical distribution. Landau [91] calculated a distribution for the mean energy loss, but it cannot be used as a basis for calculation of energy dependence of ionization in drift chambers [92].

A statistical formulation of the problem can be treated with Monte-Carlo methods and many numerical codes have been generated for the energy loss of ions in mediums (SRIM-TRIM) or for energy loss of electrons like the Penelope code [93] that is implemented also in Geant4 [94].

Electrons

Electrons can also lose energy when passing through gaseous media. The emission of electromagnetic radiation (bremsstrahlung) arises from scattering off the nucleus field. This can be understood as radiation arising from electron acceleration while they are deflected from their direction of incidence.

Another interesting mechanism relates electrons that can form a second track in the medium. This can be achieved above a threshold where an electron is knocked out of a gas atom and will form a δ electron that is no more contributing to the initial track length.

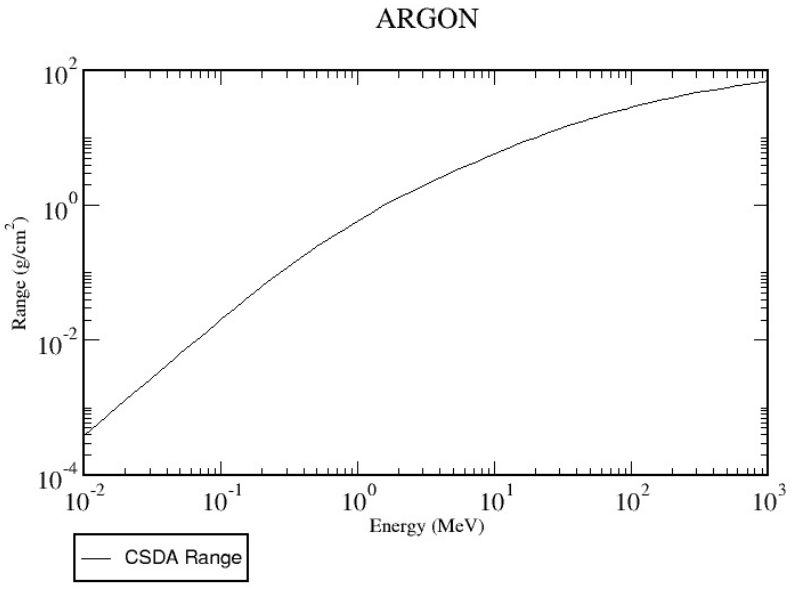

Figure 6.4 From ESTAR [95] it is extracted the CSDA (Continuous Slowing Down Approximation) range of electrons in Argon.

The secondary δ ray length, until it stops, defines a *range* that is energy dependent and it is important to be separated by electronics in a detector system or by a pattern recognition program. This should be the case if the range is comparable to the detector length and the signal is gathered in the readout. The range of secondary δ electrons is given by:

$$R\left[\frac{g}{cm^2}\right] = 0.71E[MeV]^{1.72} \quad (6.\ 7)$$

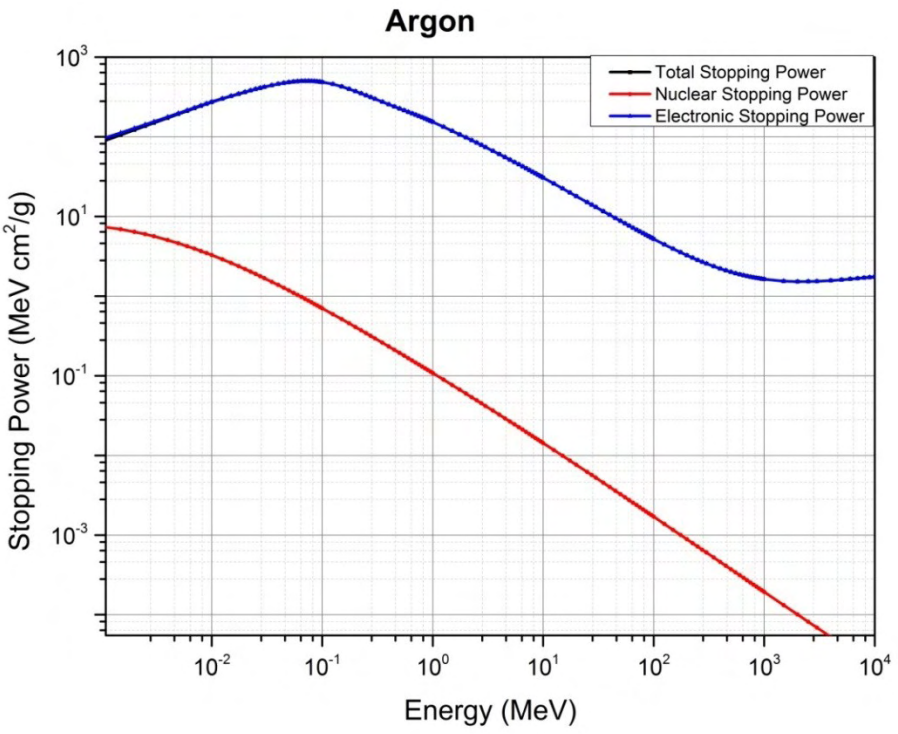

Figure 6.5 Energy loss of a proton passing through Argon as a function of proton kinetic energy in MeV. As can be seen the total stopping power comes from the electronic stopping power contribution. The data are obtained from the NIST database and use of PSTAR code [95]. Collision stopping powers are calculated from Bethe theory with a density effect correction. The mean excitation energy is calculated by taking into account experimental data. The uncertainty of calculations is about ~3% due to the shell correction term above 100 keV.

The stopping power of electrons in Argon is plotted against energy in figure 6.6.

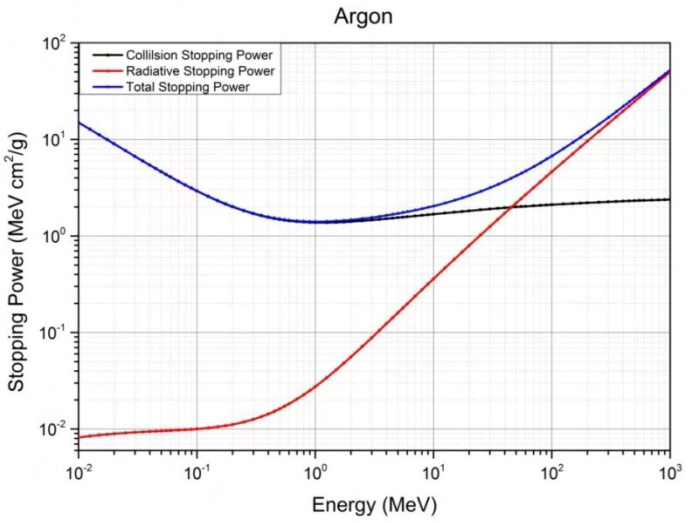

Figure 6.6 Electrons stopping power versus energy. The pressure is ~1 bar. The plot has been obtained from the NIST database using the ESTAR software.

The stopping power in solids can be deduced using the Bethe formula and an example of positive muon collision in Cu as a function of $\beta\gamma$ is shown in Figure 6.7 that is extracted from [96]

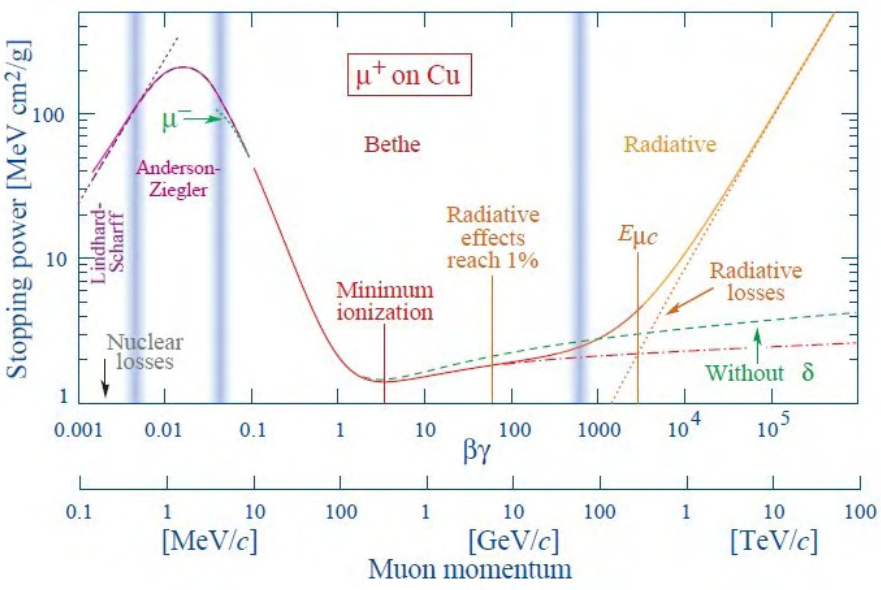

Figure 6.7 Stopping power versus $\beta\gamma$ in a 9 orders of magnitude plot. (The short dotted lines indicate the “Barkas effect” that defines the difference in stopping power between particles and anti-particles and is of no interest for this work.)

6.2 Excitation and Ionization in Gases

The interactions of photons or charged particles can transfer their energy to the gas medium, freed electrons from gas atoms or create electron-ion pairs. Every atom in the gas medium eventually returns to its stable state, usually with the emission of a photon. The energy loss can be transferred by two mechanisms, excitation or ionization.

Excitation Process

In the case where a discrete amount of energy is added to the atom, the atom changes its energy state from the ground state to an excited one. In this case no ion-electron pairs are created. The atom returns to its stable state by a photon emission. The mechanism for molecular excitation is similar with the atomic one, but in molecules transitions of rotational or vibrational nature can also occur. Excitation can also result in ionization in drift chambers of gas mixtures that are composed by a noble gas and molecular additives (quencher), required for the stability of the chamber operation. Quenchers are usually hydrocarbons that can be ionized by the excited state of the noble gas. This mechanism works like in Penning mixtures where the Penning effect[30] takes place. Polyatomic quenchers have more degrees of freedom and thus their photoabsorption coefficient is larger. The photons released from de-excitation processes can be absorbed by these quenchers and dissipate the photons energy through dissociation or elastic collisions that can increase the system stability.

The excitation mechanism can be described by the following reaction

$$X + q \rightarrow X^* + q$$

where X is referred to the noble gas atom and q is a charged particle that excites the atom state.

[30] Penning ionization refers to interaction of a neutral gas molecule that is excited and deexcitation occurs through a target molecule that has ionization potential lower than the neutral gas has.

Ionization Process

Any charged particle that traverses the gas medium of a drift chamber creates an ionization track along its trajectory. The mean free path is defined between the random ionizing encounters and is given by relation 6.8. The mean free path λ, is inversely proportional to the ionization cross section σ_I and the electrons density N.

$$\lambda = 1/N\sigma_I \qquad (6.\ 8)$$

The encounters number along a path of length L has a mean of L/λ and the frequency is a Poisson distribution.

By using the Bethe-Bloch formula and specific relativistic velocities, experiments on different gas mixtures can provide the minimal primary ionization cross-sections as shown in table 6.1

Gas	σ_p (10^{-20} cm^2)	γ_{min}	Gas	σ_p (10^{-20} cm^2)	γ_{min}
H_2	18.7	3.81	*i*-C_4H_{10}	333	3.56
He	18.6	3.68	*n*-C_5H_{12}	434	3.56
Ne	43.3	3.39	neo-C_5H_{12}	433	3.45
Ar	90.3	3.39	*n*-C_6H_{14}	526	3.51
Xe	172	3.39	C_2H_2	126	3.60
O_2	92.1	3.43	C_2H_4	161	3.58
CO_2	132	3.51	CH_3OH	155	3.65
C_2H_6	161	3.58	C_2H_5OH	230	3.51
C_3H_8	269	3.47	$(CH_3)_2CO$	277	3.54

Table 6.1 Primary ionization cross-sections σ_p for charged particles in some gases. The relativistic velocity factor γ_m (Lorentz factor) is according to measurements done in [92]

In ionization processes, an electron-ion pair is created and this can happen if the charged particle that crosses the gas medium has energy above the ionization potential of the medium. When the incident particle itself creates the ionization the mechanism is called primary ionization; in case where the ionized electron of the electron-ion pair creates further ionizations

(having energy above the ionization potential) the mechanism is called secondary ionization. The secondary ionization process can be continuous until the ionization potential of the medium is reached. The ionization potential of neutral elements can be seen in figure 6.8.

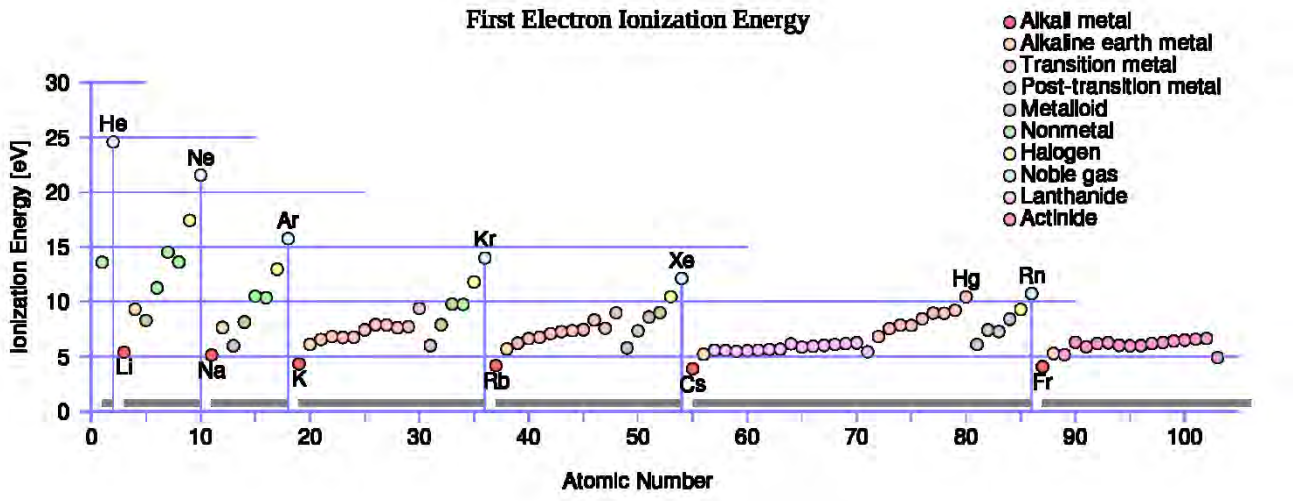

Figure 6.8 Trend of ionization energy of atoms that demonstrate a periodic behaviour. The abrupt decrease in ionization potential after noble gas atoms reveals the emergence of a new atomic shell.

The primary ionization process of the noble gas X is

$$X + q = X^{+} + q + e^{-} \tag{6. 9}$$

where q is the charged particle. The secondary ionization process can be stabilized as mentioned, in the presence of a quencher that can absorb the energetic electrons created.

In order to calculate the number of primary ionized pairs produced, the Poissonian distribution is used and the probability to have k ionizations in one event is given by the relation

$$P_k^n = \frac{n^k}{k!} e^{-n} \tag{6. 10}$$

where n is the average number of primary ionizations. A mean value for the total number of pairs (electron-positron) produced is given by the relation

$$N_e = \frac{E_0}{W} \tag{6. 11}$$

where E_0 is the initial energy and W is the mean energy needed for an electron-ion pair creation. The energy W depends on the gas properties; i.e. its composition and density and on the nature of the particle. Experimentally it is found that W is independent of the initial energy E_0 above some keV for electrons.

Gas	W_α (eV)	W_β (eV)	I_{min} (eV)	Gas mixture	W_α (eV)
H_2	36.4	36.3	15.43	Ar(96.5%)+C_2H_6 (3.5%)	24.4
He	46.0	42.3	24.58	Ar(99.6%)+C_2H_2(0.4%)	20.4
Ne	36.6	36.4	21.56	Ar(97%)+CH_4(3%)	26.0
Ar	26.4	26.3	15.76	Ar(98%)+C_3H_8(2%)	23.5
Kr	24.0	24.05	14.00	Ar(99.9%)+C_6H_6(0.1%)	22.4
Xe	21.7	21.9	12.13	Ar(98.8%)+C_3H_6(1.2%)	23.8
CO_2	34.3	32.8	13.81	Kr(99.5%)+C_4H_8(0.5%)	22.5
CH_4	29.1	27.1	12.99	Kr(93.2%)+C_2H_2(6.8%)	23.2
C_2H_6	26.6	24.4	11.65	Kr(99%)+C_3H_6(1%)	22.8
C_2H_2	27.5	25.8	11.40		
Air	35.0	33.8	12.15		
H_2O	30.5	29.9	12.60		

Table 6.2 The average energy spent of one ionization electron in various gases and gas mixtures. W_α and W_β are from measurements using α and β radioactive sources. The minimum ionization potential (I_{min}) is also shown. The total ionization in a noble gas can be increased by adding a small concentration of a quencher with low ionization potential.

In a gas mixture the total number of primary electrons created can be calculated by a weighted average of N_e in each pure gas mixture component. The relative weights correspond to the relative composition C of each substance and the ionization cross-sections σ. For a given mixture composed by A and B gases the value of W_{AB} is

$$\frac{1}{W_{AB}} = \frac{C_A \sigma_A}{W_A} + \frac{C_B \sigma_B}{W_B} \tag{6. 12}$$

where $\sigma_A + \sigma_B = 1$.

6.3 The Fano factor

The collisions of electrons with a gas molecule are statistical in nature and as a consequence the number of primary electrons created is subject to statistical variations. The number of ionizing collisions is constrained by the initial energy of the charged particle, the process is not Poissonian and the number of primary electrons exhibits a reduced variance. The process that each individual charge carrier created is not independent as the discrete number of electron shells limits the number of ways available for the atom's ionization.

The standard deviation for the process is given by the Fano factor [132]

$$\sigma_{n_e}^2 = F \cdot n_e \tag{6. 13}$$

The factor indicates the magnitude of the fluctuations on the number of primary electrons created from a charged particle of initial energy E_0, with values ranging between 0 and 1. Higher values of the factor indicate a broader distribution of the number of electrons n_e. Values of the factor lie between 0.15-0.20 for noble gases and between 0.2-04 for molecular gases.

Gas	*F*	Energy (keV)	Particle
He	0.17		*β*
Ne	0.17		
Ar	0.17		
Ar	0.22		*α*
	0.23±0.05	5.9	*γ*
	0.23±0.05	5305	*α*
Xe	≤. 15	1.49	*γ*
	0.170±0.007	1.49	*γ*
	0.13±0.01	5.9	*γ*
C_4H_{10}	0.26	1.49	*γ*
CO_2	0.33	1.49	*γ*

Table 6.3 Measured Fano Factors for various gas mixtures and particles [133].

6.4 Ions and electrons transport in Gases

The number of ion-electron pairs created when a charged particle of unit charge passes through a gas, for standard conditions (STP), will be on the order of 100 $cm^{-1}atm^{-1}$. These are not the number of electrons that can be detected since recombination or electron attachment might take place in the electrons tracks. In the absence of an external electric field (or in a presence of a low electric field), electron-ion pairs will be recombined by their electric attraction and a photon will be emitted from each pair. In the presence of electronegative gases, electrons can be captured by the gas atoms and the energy released is defined by the electron affinity. The attachment probability *h* is high for gases like oxygen while it goes to zero for noble gases.

The classical kinetic theory of gases can be used to estimate the motion properties of electrons when a field is applied. This results because the mean free path of electrons is much greater than their Compton wavelength in the rarefied gases used in drift chambers[31].

The equation of motion describing the phenomenon in the presence of an electric field E, or a magnetic field B is

$$m\frac{du}{dt} = eE + e[u \times B] - Ku \qquad (6.\ 14)$$

where m and e are the mass and the charge of the particle, u is the particle's velocity vector and K is a frictional force between the charged particle and the gas.

Electrons or ions that drift through the gas are scattered on the gas molecules and their direction of motion is randomised for each collision. In the drift mechanism macroscopic quantities such as the drift velocity and isotropic diffusion coefficient are derived as also microscopic quantities like the electron velocity, the mean time between collisions and the fractional energy loss.

6.4.1 Drift of electrons and Ions in Gas chambers

Between two collisions the electrons scatter isotropicaly and in the absence of any external force there is no preferred direction for the scattered electrons. In a gas of temperature *T* the electrons move around with a Maxwellian energy distribution with a most probable value of *kT* (0.04 eV at room temperature). In the presence of an electric field, electrons are accelerated along the field lines towards the anode. Collisions of electrons with gas molecules can interrupt the acceleration, but in general a constant drift velocity can be assumed along the direction of E.

[31] A drift chamber is an apparatus for measuring the space coordinates of the trajectory of a charged particle. This is achieved by detecting the ionization electrons produced by the charged particle in the gas of the chamber and by measuring their drift times and arrival positions on sensitive electrodes.

The extra velocity the electrons gain is due to the acceleration along the field and it can be expressed as

$$u = \frac{eE}{m}\tau \tag{6. 15}$$

The extra energy gain is generally lost in collisions through recoil or excitation. In order to evaluate the energy balance between the energy gain from the field acceleration and the energy loss because of collision losses we can evaluate the number of encounters for a drift distance:

$$n = \left(\frac{x}{u}\right)(1/\tau) \tag{6. 16}$$

that is the time of drift $\left(\frac{x}{u}\right)$ divided by the average time τ between collisions. If λ defines the fraction energy loss per collision, the energy balance is given by the following relation:

$$\frac{x}{u\tau}\lambda\varepsilon_E = eEx \tag{6. 17}$$

The mean time between collisions can be expressed in terms of the cross-section σ and the molecular density *N* as follows

$$\frac{1}{\tau} = N\sigma v \tag{6. 18}$$

where v is the instantaneous velocity of the drifting particles.

Quantum mechanical processes occur when the electron approaches the gas molecule that cause τ and the cross-section σ to vary strongly with E[32].

The total energy of the drifting electron is

$$\frac{1}{2}mv^2 = \varepsilon = \varepsilon_E + \frac{3}{2}kT \tag{6. 19}$$

[32] The Ramsauer–Townsend effect, also sometimes called the Ramsauer effect or the Townsend effect, is a physical phenomenon involving the scattering of low-energy electrons by atoms of a noble gas.

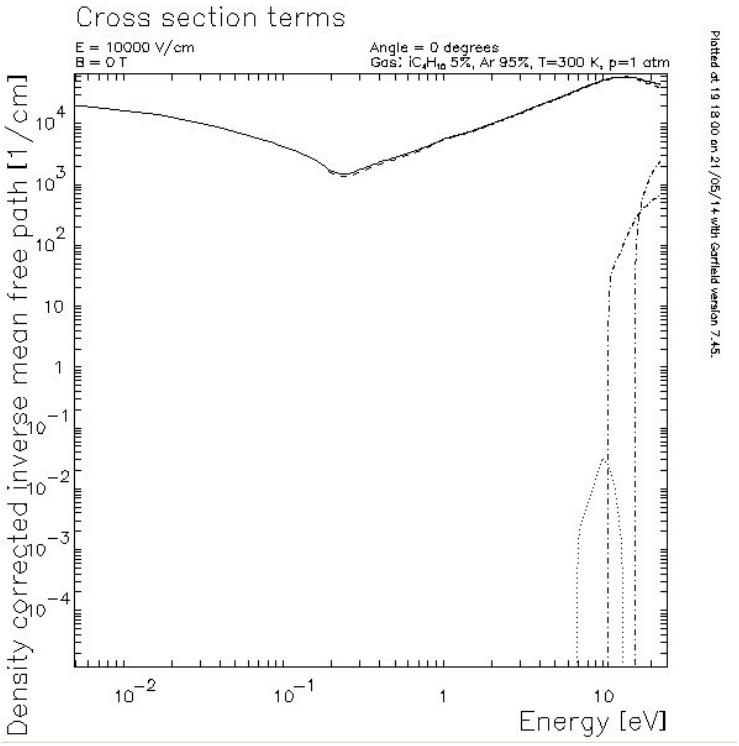

Figure 6.9 Cross-section for a mixture of Ar 95% and methane of 5% as extracted from Garfield software [97]. The Ramsauer minimum is obvious due to quantum-mechanical effects.

The total energy is composed by two parts; the energy received from the electric field and the thermal energy. For electron drift in particle detectors it usually holds that $\boldsymbol{\varepsilon_E}$ >> (3/2)·kT and the thermal motion can be neglected. Combing the equations (6. 15), (6. 15) and (6. 19) we can derive the velocities equations for drift $\boldsymbol{u}$ and the instantaneous randomly oriented velocity $\boldsymbol{v}$

$$u^2 = \frac{eE}{mN\sigma}\sqrt{\frac{\lambda}{2}} \tag{6. 20}$$

$$v^2 = \frac{eE}{mN\sigma}\sqrt{\frac{2}{\lambda}} \tag{6. 21}$$

where $e = \left(\frac{1}{2}\right)mv^2 \approx e_{exc} \gg \left(\frac{3}{2}\right)kT$

The average energy loss in collisions $\boldsymbol{\lambda}$ and the cross-section are functions of the drifting particle's kinetic energy, so in the case where the energy loss is vanished the drift velocity becomes zero. It is clear that the drift velocity of electrons in drift chambers depends on the exact gas composition. Even small additions of a quencher gas like isobutene to a noble gas can dramatically increase the fractional energy loss by energy absorption in collisions through the rotational state mechanism.

The drift velocity and the electron energy depend strongly on the E field and the gas pressure P. The term E/P is defined as the *reduced drift field*, implying that the drift velocity for different gases must be obtained for the same E/P ratio.

Garfield [97] is open source software that is used for the detailed simulation of particle detectors that contain a gas medium or mixture of gases as a medium. Garfield can perform Monte Carlo simulations for calculating the transport properties of electrons in gas mixtures by the use of Magboltz [98]. The drift values provided give accuracy better than 2%.

Drift curves (electrons drift velocity) can be generated by the use of Garfield, by applying the reduced E field for various gas mixtures like Argon and isobutene (the mixture used by CAST Micromegas detectors) in the simulated detector apparatus. The simulated detector properties like electric field, geometry and gas medium can be defined through Garfield. Another feature provided by Garfield software is to introduce the detector model properties form a FEM (Finite Element Method) software like Ansys or COMSOL [99]. In the figure 6.10, the drift velocity is presented for a gas mixture of Ar 95% -Isobutane 5%, computed by Monte Carlo methods applied in Garfield.

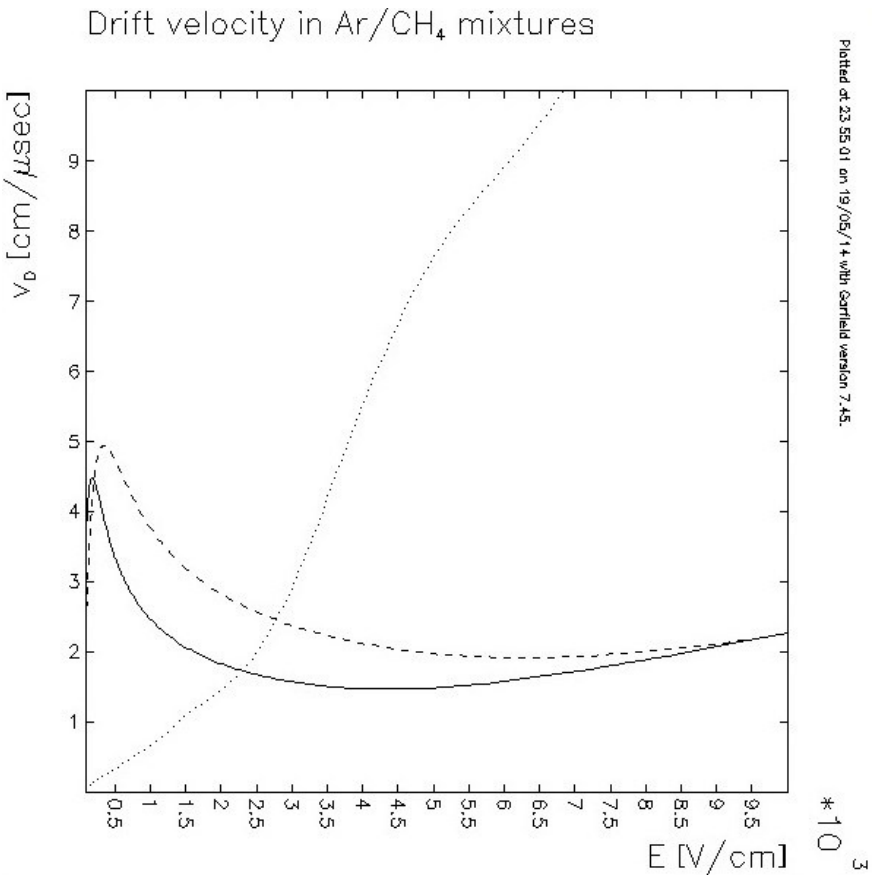

Figure 6.10 Electrons drift velocity for a gas mixture of Ar 95%-Isobutane 5% for different field values represented by the solid line. Dashed line represents the same gas for mixtures (Ar90%-iC_4H_{10}10%) and the dot line the 80% Ar and 20% isobutene.

COMSOL provides a graphical user interface (GUI) that can model physical applications like the electric field generated in a gas chamber when voltage is applied at specified boundaries. In this study, the AC/DC Multiphysics module of COMSOL has been used in addition to the Particle Tracing module, in order to generate the electron trajectories when they are released in a gas medium like argon. Results from the Comsol will be presented in the next sections. The complete study of different particle trajectories inside a specified detector, like Micromegas, for different gas mixtures and pressures is under development and beyond the purpose of this study.

Drift of Ions

When the electric field is present in drift chambers, the movement of ions is no longer random. They follow on average the field direction where they are accelerated. Electrons accelerate much faster than ions which lose energy mostly due to causes of thermal nature because of the continuous collisions with gas molecules. Collisions limit the ions velocity to an average value named as *drift velocity* that depends linearly on the ratio E/P. A useful parameter for the ions (and electrons) is the mobility that is defined as:

$$\mu = u/E \tag{6. 22}$$

where u is the drift velocity. The mobility of ions is practically constant even in high electric fields.

Gas	λ [cm]	u [cm/sec]	D [cm^2/sec]	μ [$cm^2 sec^{-1} V^{-1}$]
H_2	1.8×10^{-5}	2.0×10^{5}	0.34	13.0
He	2.8×10^{-5}	1.4×10^{5}	0.26	10.2
Ar	1.0×10^{-5}	4.4×10^{4}	0.04	1.7
O_2	1.0×10^{-5}	5×10^{4}	0.06	2.2

Table 6.4 Values of the mean free path λ, the average velocity u, the diffusion coefficient D and the mobility μ of ions in their own gas.

6.4.2 Electron Diffusion

While drift electrons continue to diffuse in the gas medium of the detector and their drift velocity deviates from the average due to the random nature of collisions, gas molecules losing their energy. Electrons will come quickly into thermal equilibrium with the gas mixture and eventually recombine.

Charge velocities can be described by the Maxwell distribution that gives a mean energy

$$u = \sqrt{\frac{8kT}{\pi m}} \tag{6.23}$$

where k is the Boltzmann's constant, T is the temperature and m is the particle's mass. As noted the average speed of electrons is much greater than that of ions. At room temperature electron speed is some cm/μs while the positive ion speed is around 10^{-2} cm/μs.

A point like cloud of electrons that begin to drift by a field $\vec{E} = -E\hat{z}$ at time t=0 in the z-direction, will have a Gaussian density distribution after some time t that is given by the relation:

$$n(x, y, z, t) = \frac{1}{\sqrt{4\pi D_L t}}\left(\frac{1}{\sqrt{4\pi D_T t}}\right)^2 \exp\left(-\frac{x^2 + y^2}{4D_T t}\right) - \frac{(z - ut)^2}{4D_L t} \tag{6. 24}$$

where r is the particle's coordinate and D_T and D_L is the diffusion constant in the direction of the field and perpendicular to it respectively. In the case where there is some change in energy distribution, imposed by the electric field, the diffusion coefficient is

$$D(E) = \int \frac{1}{3} u\lambda(\varepsilon)F(\varepsilon)d\varepsilon \tag{6. 25}$$

where $u = \sqrt{2\varepsilon/m}$ and ε is the electrons energy. Recalling the expression for the electron mobility

$$\mu = \frac{e}{m}\tau \tag{6. 26}$$

the electron energy can be determined by measurement of the ratio D/μ

$$\varepsilon = \frac{3}{2}\frac{De}{\mu} \tag{6. 27}$$

In case where the diffusing body has thermal energy, $\varepsilon = 3/2kT$ equation (6. 27) becomes

$$D/\mu = \frac{\kappa T}{e} \tag{6. 28}$$

which is known as the Nernst–Townsend formula, or the Einstein formula. An example of the diffusion coefficients produced by Monte Carlo methods in Magboltz is shown in Figure 6.11. The gas mixture used for this plot is Argon 94% and CO_2 6%.

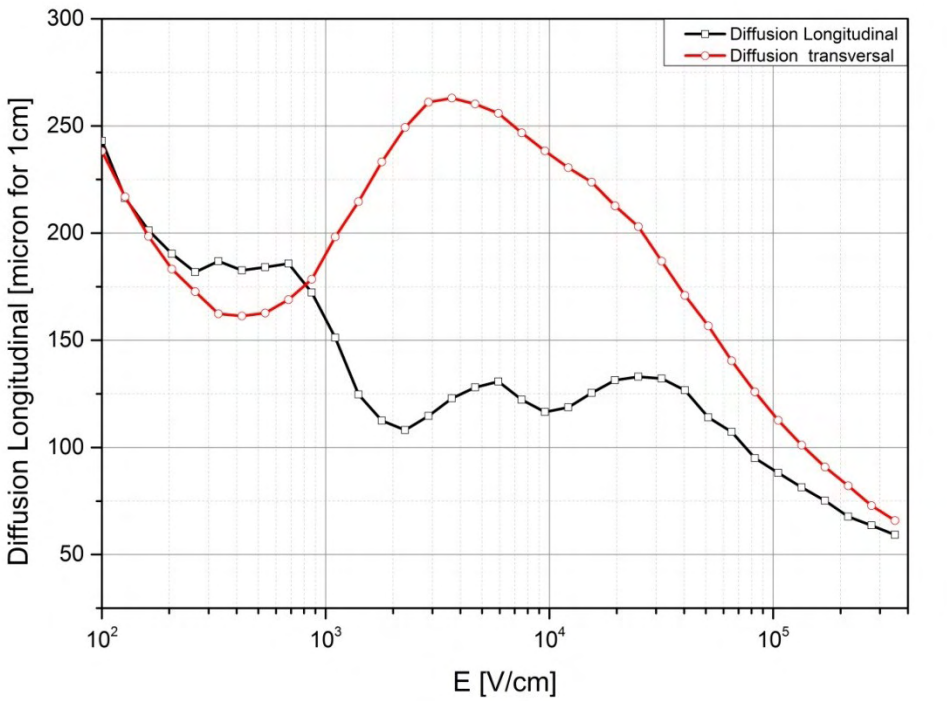

Figure 6.11 Longitudinal and transversal diffusion coefficient for different field values. Data obtained from Magboltz-Garfield. This plot represents a mixture of Ar-CO_2 (94%-6% respectively).

6.4.3 Electron attachment and recombination

Electron attachment is the absorption of the electron by a molecule of the gas during the drift. Because of attachment there is an impact on detectors signal and resolution. All gas molecules have a certain attachment cross-section with the lowest ones corresponding to the noble gases. Attachment is generally provoked by impurities of high electron affinities like water and air. Origins of this effect can be looked for in outgassing phenomena. Outgassing can be defined as the emission of gas molecules from the detector's inner walls.

Recombination is another undesirable effect that happens when electrons drifting towards the detectors anode, meet the ions that drift in the opposite direction. The Micromegas detector structure prevents the recombination because ions produced and back-flow, are absorbed by the mesh and do not enter in the drift region.

6.4.4 Avalanche Multiplication of electrons

When an electron drifts inside a drift chamber where an electric field is applied, it will carry in average a rather constant energy because of random collisions with gas molecules. In case where the field intensity increases, the electron's energy may be increased between the collisions events. If the energy of the electron is above the first ionization potential of the gas molecule, it can create another electron-ion pair while it continues to drift. The electron will probably create more pairs if during the time between collisions it can acquire the amount of energy required.

The ionization of gas molecules can thus result in secondary ionization by the first generated electron, so the mechanism can be repeated many times generating an **avalanche**. A cloud front of electrons, created by the ionization process, will manifest in a drop like distribution because ions as slower positive particles, will be moving to the back of this cloud.

An example of the electron avalanche can be seen in the Monte Carlo simulation with the Comsol Multiphysics software (Figure 6.12) where a voltage has been applied to a portion-slice of a Micromegas detector made of Cu plates and the gas used is Argon.

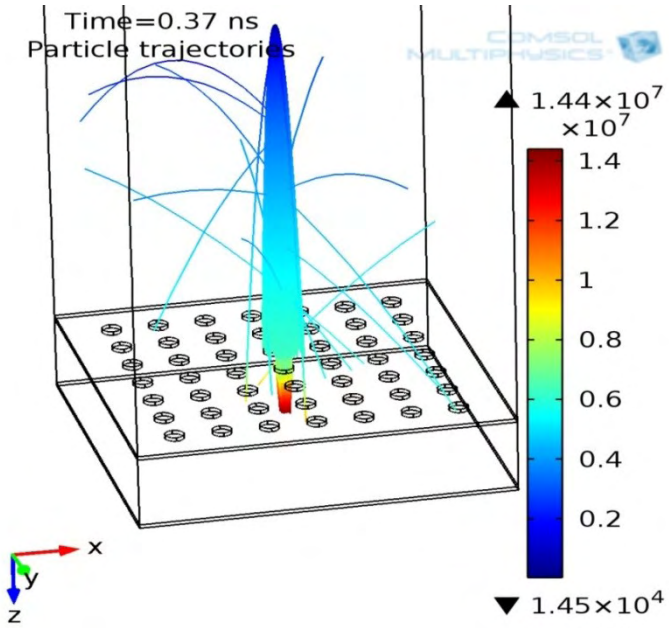

Figure 6.12 236 electrons have been released 200 μm above the mesh with zero energy and zero velocity and in the presence of the field created, they drift towards the anode. The transient simulation has been performed for 1nsec in total, with 0.01nsec step, and the view is at time=0.37 nsec. The numbers of particles created are also coloured.

In figure 6.13 a simulation in Garfield shows the avalanche process in a Micromegas detector in a gas medium of Ar 95% and Isobutane 5% .

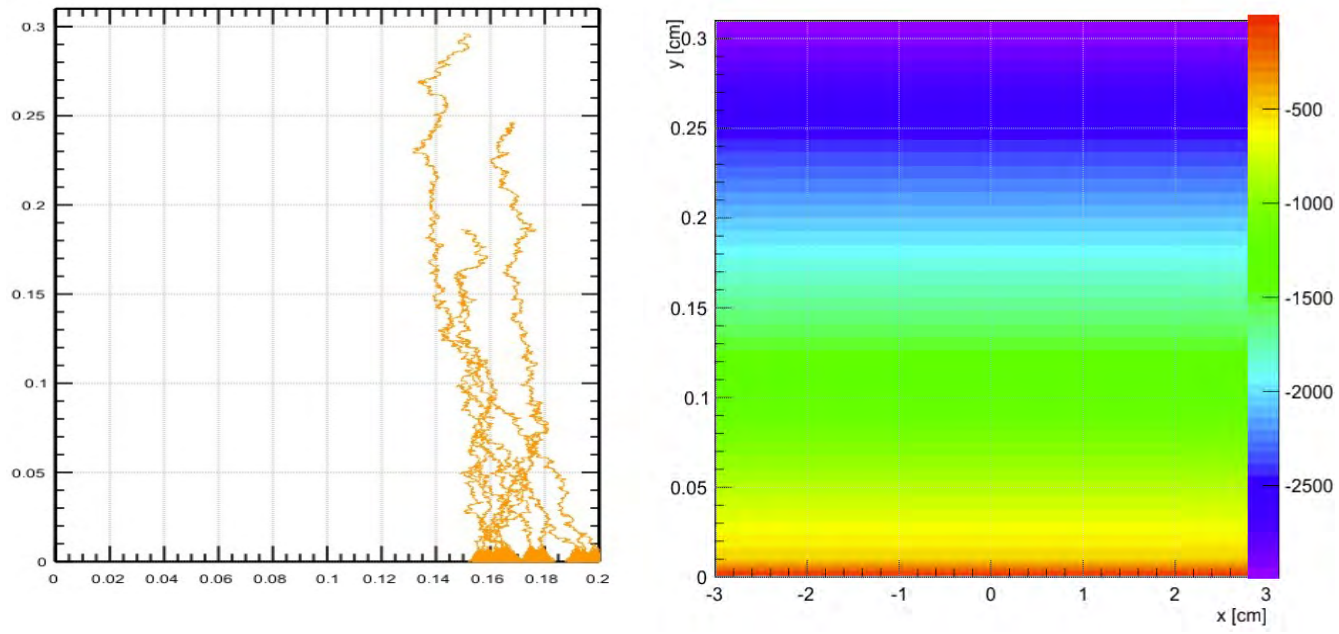

Figure 6.13 On the left the 2D x-y projection of the avalanche is shown, while on the right the contour plot of the electric potential is shown. Units of x coordinate is in [cm], units of electric potential is in [V/cm].

The mean free path of an electron for ionization is defined as the distance that the electron will travel until ionization. The inverse of this quantity is known as the *first Townsend coefficient* α, that represents the number of ion pairs created per unit length. In the case where multiplication occurs, the increase of the number of electrons N per path ds is given by

$$dN = N\alpha ds \tag{6. 29}$$

The first Townsend coefficient α can be determined by the excitation and ionization cross sections of the electrons in the field that have acquired enough energy. The total number of electrons created in a path *s* is

$$N = N_0 e^{as} \tag{6. 30}$$

The Multiplication factor or *Gas Gain* can be defined as

$$G = \frac{N}{N_0} = e^{as} \tag{6. 31}$$

The Multiplication factor cannot be increased at will because eventually a spark breakdown will occur. The limit to the factor G increase is set by the Raether[33] limit that which sets the upper

[33] The Raether limit is the physical limiting value of the multiplication factor (M) or gas gain in an ionization avalanche process

value for G < 10^8. An example of the Townsend coefficient and the attachment calculated by the Magboltz module in Garfield for an Ar 94%-CO_2 6% mixture and pressure at 2.96 atm is given in Figure 6.14.

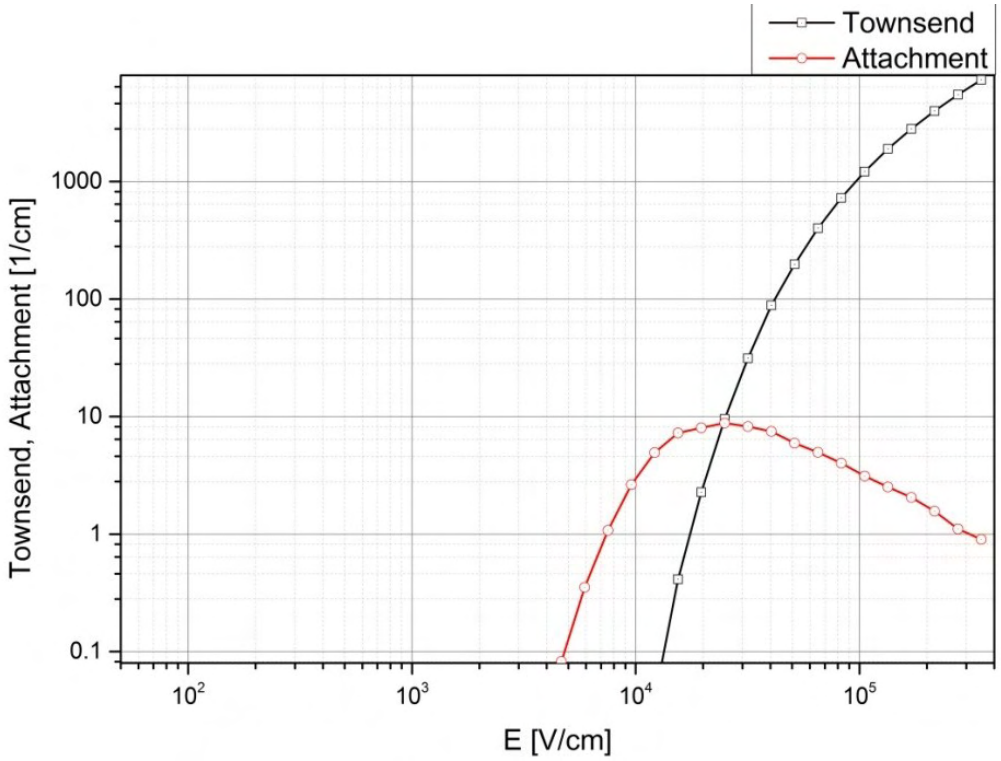

Figure 6.14 Townsend coefficient and Attachment as extracted for an Ar-CO_2 mixture versus different fields. It holds that Townsend coefficient $\alpha(\varepsilon)=\rho_e\sigma_i(\varepsilon)$, depends on the electron energy from the ionization cross section and it is proportional to the electronic energy of the gas.

6.4.5 Signal generation

The drifting electrons induce electronic signals in the detector electrodes; this mechanism is described by the Ramo's theorem which stands for the charge q induced in a particular electrode, depending only on the electric field created by the electrode itself and the trajectory followed by the charge. The current induced in a particular electrode is defined as

$$I_n^{ind}(t) = -\frac{dQ_n(t)}{dt} = \frac{q}{V_w}\nabla\psi_n[x(t)]\frac{dx(t)}{dt} = -\frac{q}{V_w}E_n[x(t)]v(t) \qquad (6.\ 32)$$

where $E_n(x) = -\nabla\psi_n(x)$ is the weighted field of electron *n* and is defined as the electric field calculated with the electrode *n* biased to V_w volt and the rest being grounded. It is important that the current induced depends not only from the sign of q but also on the relative orientation of $\vec{v}$ and E_n.

6.4.6 Gas choice for Micromegas detectors

There are several requirements for the gas choice in Micromegas detectors that have to be fulfilled. The most important of them are

- Low operating voltage
- High gain
- High rate capability
- Low cost
- Non-flammable mixtures

During years of research the choice of the above gas requirements is met in gas mixtures. The base of a mixture is usually a noble gas with some quenching organic molecular gas. These gas mixtures fulfil the important requirement that:

1. the electron lifetime should be sufficiently long and
2. the gas mixture can sustain a stable amplification process without discharges

As shown in Figure 6.10 the drift velocity of an argon-isobutene mixture (when the isobutene concentration is sufficiently low ~5%), can sustain a rather stable drift velocity for rather long values of the drift field. In pure argon, gain values higher than 10^3-10^4 cannot be achieved due to high excitation energy (11.6 eV) that can cause discharges in the detector. Argon atoms when de-excited emit photons of visible light or UV that can interact with the gas and cause the avalanche to spread along the anode with further ionizations.

The quencher added in argon gas, which is an organic constituent like isobutene in low concentration, can absorb these photons but unlike the base ingredient, it cannot be ionized. Inorganic quenchers can also be used like CO_2 or BF_3, but the usual choice for Micromegas detectors is methane or isobutene. The material which the detector is made of is of great importance because it can contaminate the gas mixture with electronegative impurities that can emanate from the material. The proportional gas (as also the detector's material) should not contain electronegative components like oxygen, CO_2 or H_2O.

6.5 Gaseous detectors

For the study of ionizing radiation, gaseous detectors have been used since the beginning of the twentieth century with the invention of the single wire proportional counter, the Geiger-Müller counter and the ionization chamber. The very important moment for gaseous detectors, worthy of the Nobel Prize, was the invention of the MultiWire Proportional Chamber (MWPC) by G. Charpak in 1968 [100].

The breakthrough of this invention was that each anode wire belonging to an array of closely spaced anodes could act as an independent proportional counter. Transistorized electronics were used to amplify every wire onto the chamber frame and thus make the detector capable for position sensing.

The MWPC detector was quickly adopted in High Energy Physics because of its excellent position accuracy, good space resolution of a few hundred μm and a modest rate capability (10^4 counts $mm^{-2}s^{-1}$). This kind of chamber is also used in fields other than particle physics like for medical imaging, neutron and crystal diffraction, single photon detection and others.

In 1986 A. Oed invented the Micro-Strip Gas Chamber (MSGC) [101] which is the first kind of detectors, known as micropattern detectors. Improvements in microelectronics and the development of the photolithography process enhanced the detector performance. The improvements rely on the imprinting of very thin strips on an isolated board in a succession of anodes and cathodes. Because of the electric field shape the ions produced by avalanche are rapidly evacuated, increasing the rating capability a 100 times above that of MWPC.

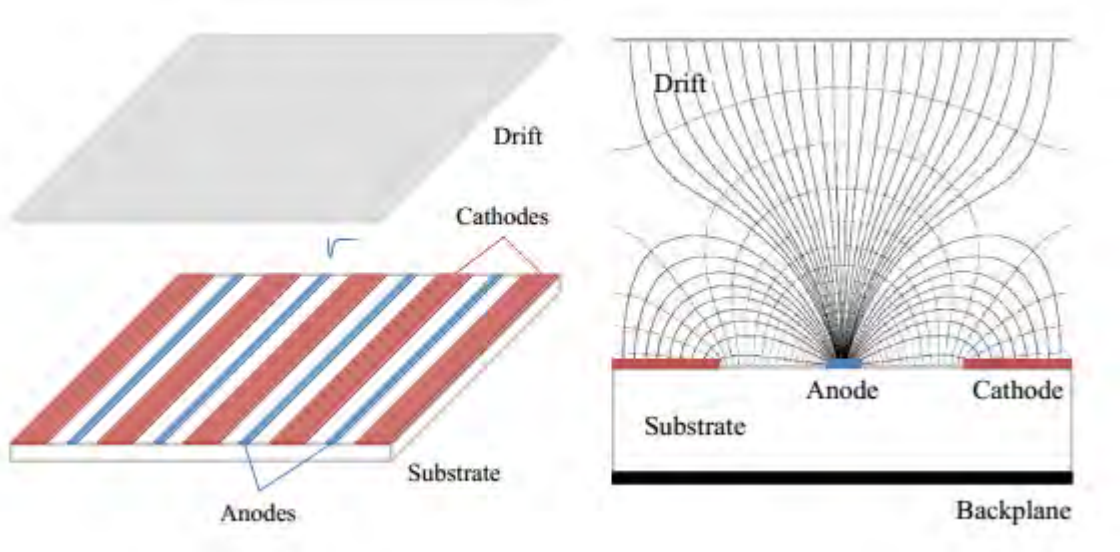

Figure 6.15 On the left anode and cathode strips imprinted on an isolated substrate is shown. The distance between anode and cathode is 50-100μm. On the right the form of the electric field produced is shown.

The dipole field, created by the application of the proper voltage between the anode and the cathode strips, amplifies the electron avalanche process. Electrons are drifting towards the anode strips and the ions are collected in the cathode.

In 1996 Sauli [102] introduced another gaseous detector known as Gas Electron Multiplier (GEM) that was built at CERN, by a standard chemical etching process. It consists of a thin (~50 μm) kapton foil that is clad in both sides with of 5 μm of Cu. The clad foil has double-conical holes with a pitch of around 140 μm and a diameter of 60-70 μm.

The field structure can be shown in figure 6.16. The field lines are focused in the holes, where the resulting electric field is ~100 kV/cm inside the holes. The setup of this detector consists of 2 or 3 successive GEMs with lower amplification per GEM but higher amplification in the whole system. With this setup the detector's performance is stable and not sparking.

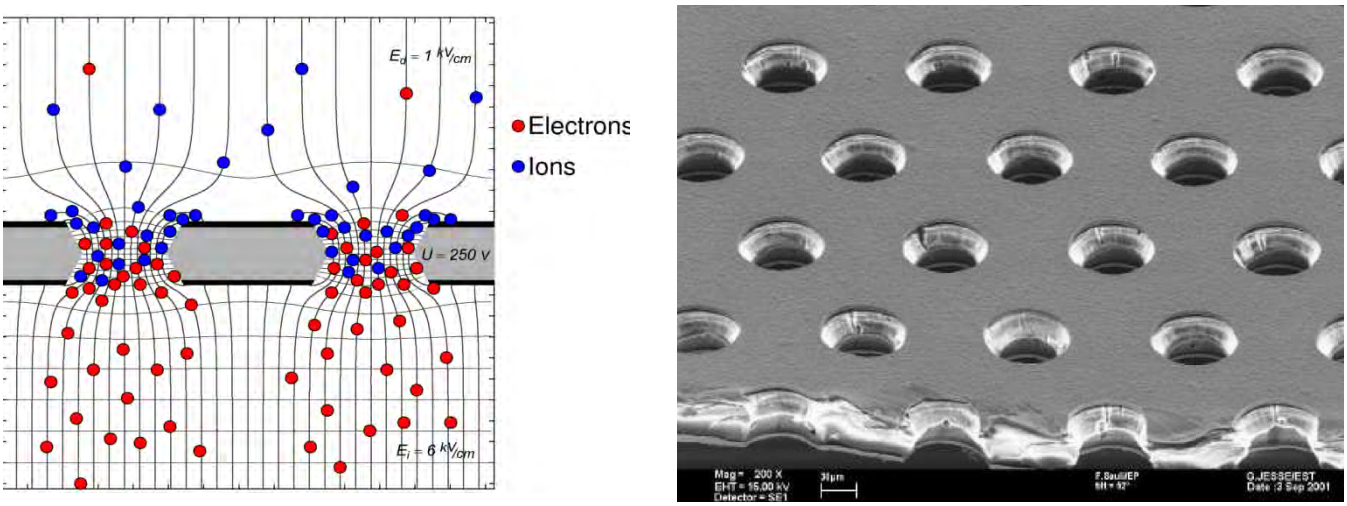

Figure 6.16 On the left, a suitable difference of potential applied across the thin layer generates the field structure of a GEM. The field lines compressed at the holes central axis and electrons released in the upper conversion volume drift into the holes. Electrons are multiplied into the holes but only 50% of the electron avalanche can exit into the transfer region. On the right, a microscope picture of the GEM structure is shown.

GEM detectors are used at the Large Hadron Collider (LHC) as a part of the LHCb muon system [103] and they are used for triggering and tracking purposes in the TOTEM experiment [104].

6.6 Micromegas detector: A Micro-Pattern Gas Chamber

The Micromegas (acronym for MICRO MEsh GAseous Structure) is a parallel-plate detector invented in 1996 by I. Giomataris and G. Charpak [106]. The wire plane of the MSGC detector was replaced by a thin electroformed Ni mesh.

The mesh was stretched and glued on an insulated frame and the distance between the mesh and the anode plane is in the rage 20-100 μm. Inside the chamber the mesh and the cathode plane define the conversion space or the drift region while the mesh and the anode plane define the amplification gap as can be seen in Figure 6.17.

The basic principle of Micromegas detector operation is illustrated in the figure 6.17.

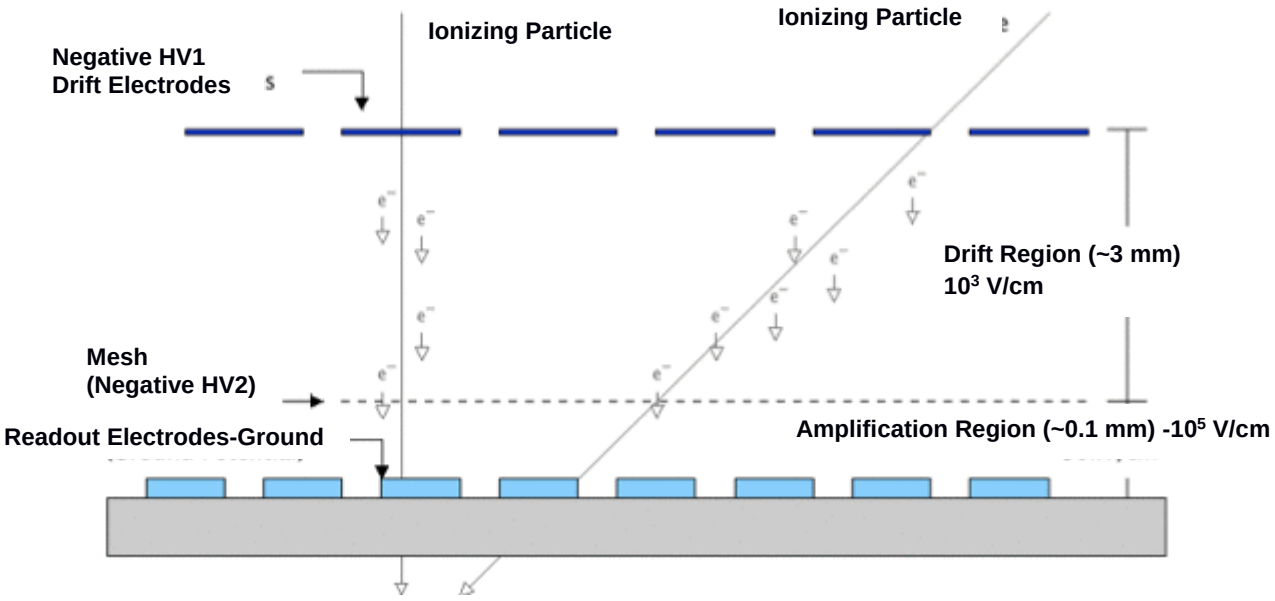

Figure 6.17 A planar drift electrode is placed a few mm above the readout electrode. The metallic mesh is placed ~0.1 mm above the readout electrode. The volume is filled with ionization gas, e.g. a mixture of argon and isobutene. The region between drift electrode and mesh is called the drift region, whilst the region between mesh and readout electrodes is called the amplification region.

By applying a positive voltage (HV2 ~ 500 V) to the micromesh and a higher positive voltage to an electrode plane HV1, the ratio of the electric field in the amplification gap over the field in the conversion gap, is large. The bigger the ratio the higher the electron transmission[34] to the amplification gap reached. The readout plane is kept grounded. By this formation, ions are

[34] The electronic transparency or transmission of the mesh is defined as the percentage of the electrons that reach the amplification region.

quickly collected to the micromesh and only a small fraction defuses to the drift region. The electrons will follow the electric field lines.

For a given amplification field when the drift field decreases, more field lines are passing through the Micromegas holes and for certain values transparency can reach unity. At very low field values, drift velocity in the gas is very low and attachment events become more evident.

But in general mesh transparency is not a purely geometrical aspect. Monte Carlo simulations of electrons trajectories reveal that transparency is affected by collisions and so it concerns gas properties as well. In Figure 6.18 the transparency trend for different gas mixtures versus the Field Rate (FR) is shown. From figure 6.18 it is evident that diffusion effects can affect the mesh transparency.

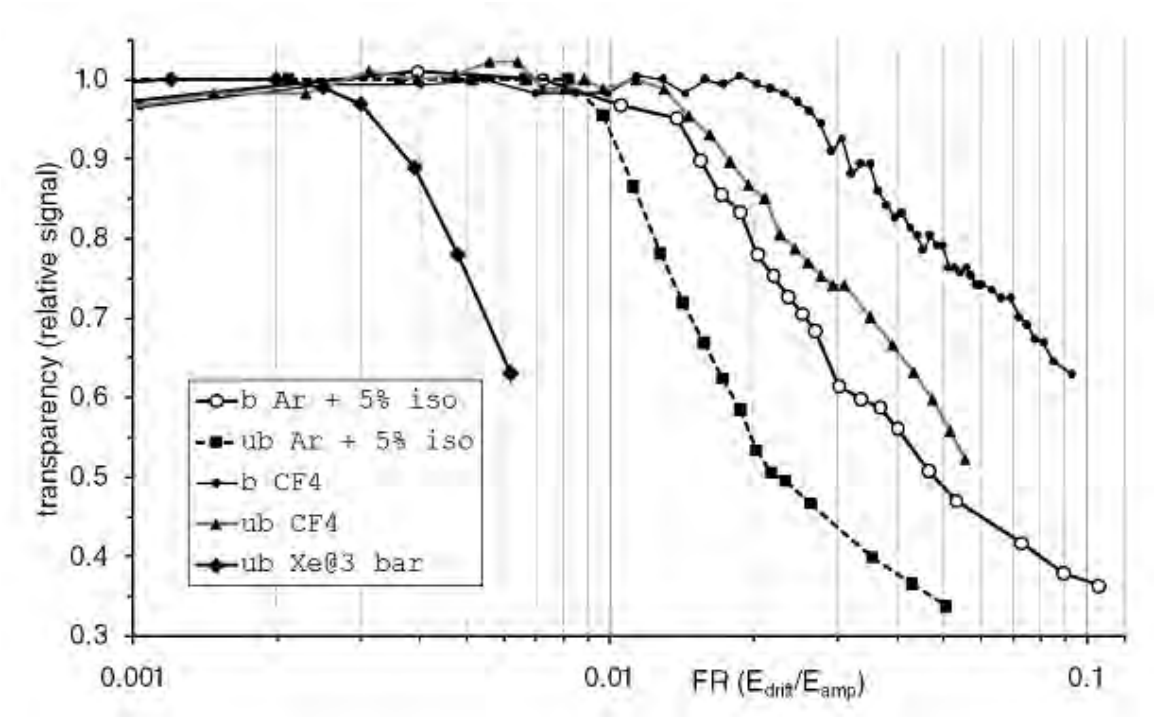

Figure 6.18 Transparency curves with a classical microbulk Micromegas for different gas mixtures and for Xe at 3 bars. [107]

After the electron transmission and the amplification of the avalanche, electrons are accumulated in the anode strips. The signal in the micromesh is derived from the positive ions collected. The signal of ions collected takes place in ~100 ns and depends on the amplification gap width and the gas mixture used. The electrons collection time is about 1 ns.

For the geometry given in figure 6.19, the transparency can be calculated from the relation

$$n_e = \frac{\Phi_{13}}{\Phi_{13} + \Phi_{12}} \qquad (6.\ 33)$$

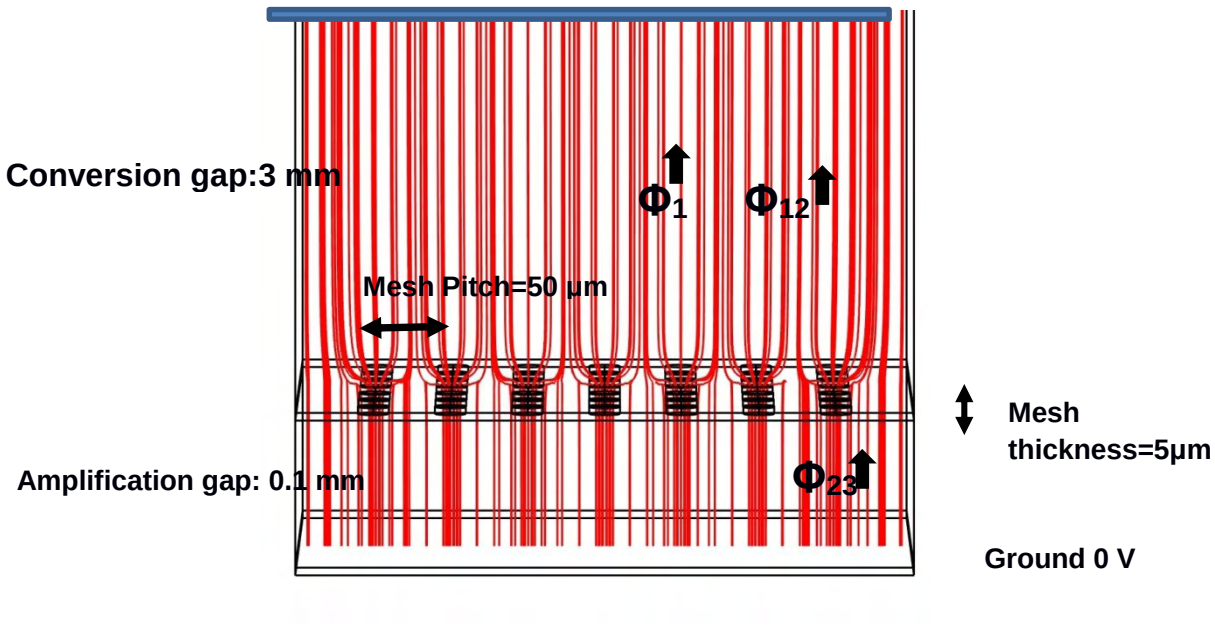

Figure 6.19 Electric field lines as extracted from COMSOL electrostatic simulation in this work. Φ_{xy} is the flux to electrode x from electrode y, with 1: the drift cathode, 2: the Micromegas mesh and 3: the anode. Drift cathode (in blue) has been sketched for visual reasons since the distance from the anode is 3 mm.

6.6.1 Micromegas properties

Gain

The multiplication factor or gain has been expressed in (6. 31) as a function of the Townsend coefficient. An early theoretical model that has been developed for Townsend calculation in different gases as a function of the amplification field is the Rose and Korff model [108]. This model neglects the secondary ionization and is defined by the formula

$$\alpha = \frac{1}{\lambda} exp\left(\frac{-I_e}{E_{amp}\lambda}\right) \quad (6.\ 34)$$

where λ is the electron mean free path, E_{amp} is the amplification field and I_e is the energy threshold for ionization. Combining relations (6. 31) and (6. 34) an important parameter of Micromegas can be deduced; the gain of the Micromegas detector that is given by the following relation:

$$G = exp\left(APde^{-\frac{BPd}{V}}\right) \quad (6.\ 35)$$

with $V=E\cdot d$ the voltage applied between the micromesh and the anode (having distance d), P is the pressure and A,B are the gas mixture parameters.

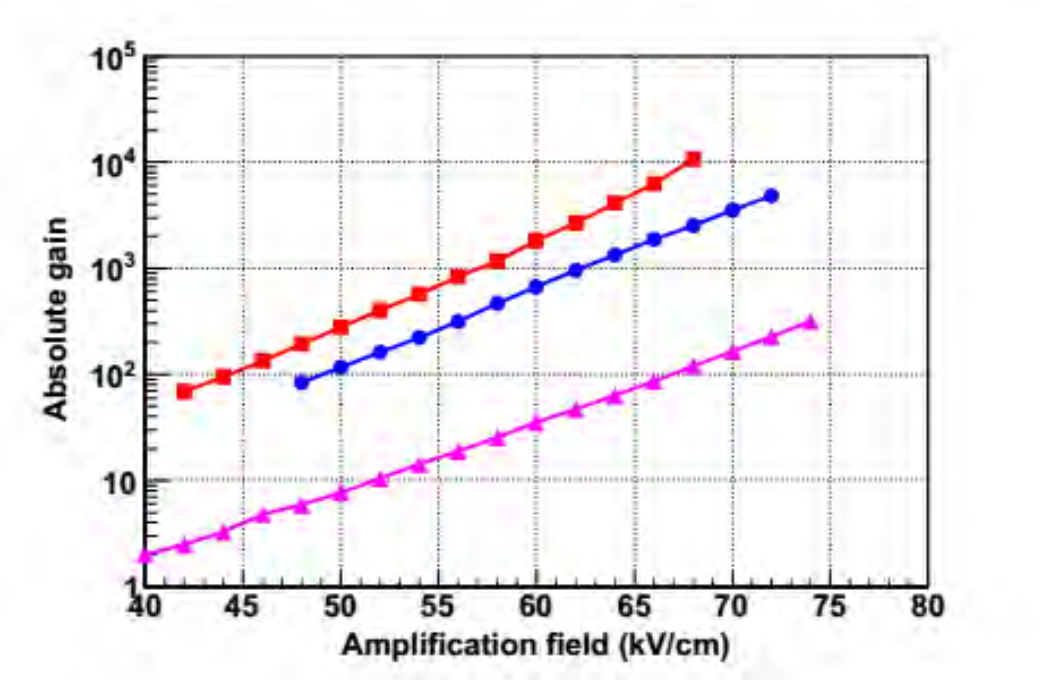

Figure 6.20 Gain curves as extracted from [109] for different gas mixtures. Red squares represent a mixture of argon-isobutene 2%, blue circles are for the same mixture of 5% isobutene and pure xenon is represented by magenta triangles points.

Differentiation of (6. 35) with respect to d can give the maximum value of the distance between the micromesh and anode, for specific gas and operation conditions:

$$\frac{\partial G}{\partial d} = G\alpha\left(1 - \frac{BPd}{V}\right) \tag{6. 36}$$

The amplification gap can be chosen by using this condition and tuning its value to acquire the maximum detector's gain. A beneficial value for micro-gaps detectors is found to be ~50 μm. A variety of gas mixtures have been used to test Micromegas detectors. The mixtures represented in figure 6.20 are the ones used in CAST (in different composition of the quencher) except the pure xenon gas that is plotted for comparison. Krypton or xenon gas can be used for applications like x-ray digital radiography, crystallography and synchrotron radiation studies.

Energy Resolution

The ability of the detector to distinguish between two energies with close lying values, defines the detector's energy resolution. This parameter is one of the most important for detector design. Processes like gas ionization, signal readout, attachment, mesh transparency etc.

contribute to the pulse signal distribution. The ideal signal pulse shape should be a delta-function peak but in reality a Gaussian-like distribution is measured.

Resolution is given in terms of *full width at half maximum* (FWHM) of the signal generated. Energies that are lying inside this width cannot be resolved. Assuming primary and avalanche fluctuations, the energy resolution can be defined as a function of the number of electrons

$$R\ (\%\ FWHM) = \frac{2.35\sigma_{n_e}}{n_e} = 2.35\sqrt{\frac{F+b}{n_b}} = 2.35\sqrt{\frac{W}{E_0}(F+b)} \qquad (6.\ 37)$$

where the factor 2.35 relates the standard deviation of a Gaussian distribution to its FWHM, E_0 is the particle's energy, W is the mean energy per electron-ion pair of the gas, F is the Fano factor and b is the readout contribution. Therefore, in the accumulation of n_b avalanches from n_e primary electrons, the final energy resolution scales with ~$E_0^{-1/2}$.

The energy resolution for the Micromegas detector is measured using a radioactive iron source ^{55}Fe. The isotope emits two x-ray photons of energy 5.9 and 6.5 keV respectively, in proportion 9:1.

The value obtained and usually mentioned in the literature is the 5.9 keV peak. For an argon-isobutene mixture, with isobutene concentration of 2%, the FWHM is about 11% at 5.9 keV. In figure 6.20 a typical spectrum of the Micromegas detector is shown. It should be noted that no appreciable deterioration was seen after a year of detector use [113].

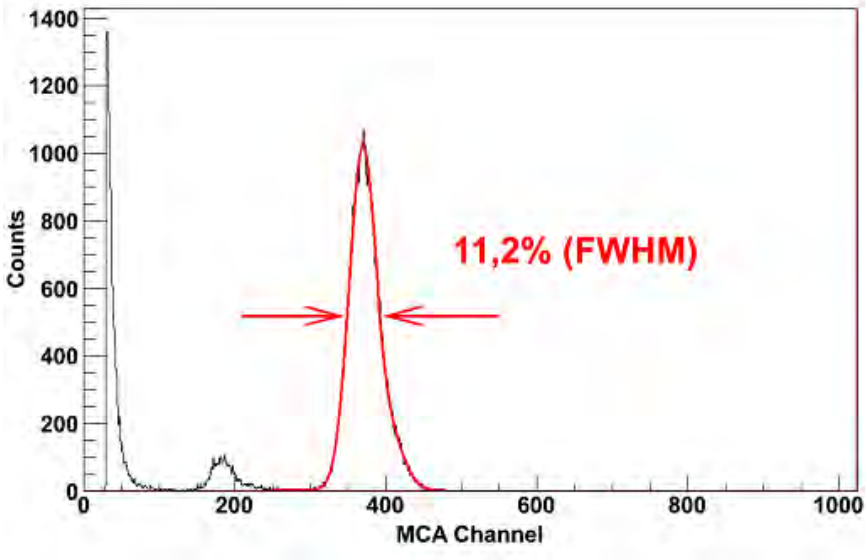

Figure 6.21 Energy resolution of the Micromegas readout. The spectrum was obtained with a ^{55}Fe source in Argon-2%iC_4H_{10}.

Spatial Resolution

This type of resolution defines the spread of electrons observed due to the transverse diffusion. The spatial resolution depends on the amplification gap, the pitch of the strips and the pitch of the mesh. In table 6.5 (extracted from [111]) a world record of a spatial resolution 14±3 μm is mentioned.

Gas Mixture	Measured Resolution $[\mu m]$	Transverse Diffusion coefficient $[\mu m/\sqrt{cm}]$	Strip Pitch $[\mu m]$	Drift field $[kV/cm]$
Ar+10%iC_4H_{10}	42.5	370	100	1.0
He+6%iC_4H_{10}+5%CF_4	35	180	100	1.8
He+10%iC_4H_{10}+5%CF_4	30	160	100	1.8
He+20%DME	25	130	50	1.0
CF_4+20%iC_4H_{10}	18	170	100	0.4
CF_4+20%iC_4H_{10}	11	100	100	2.7

Table 6.5 Micromegas spatial resolution data, performed with different configuration of the detector used and for different gas mixtures.

The detector mesh configurations can be shown in the next figure where different types of detectors are displayed.

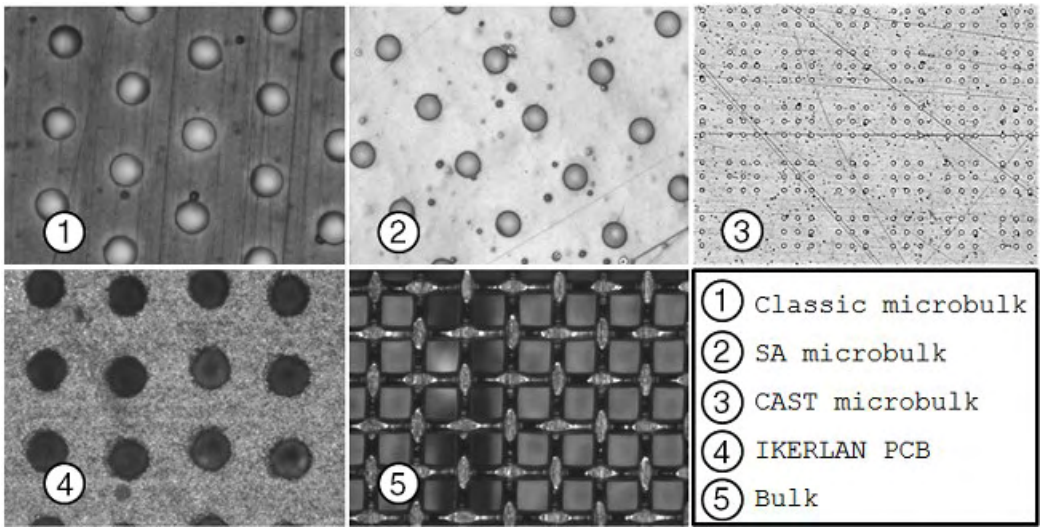

Figure 6.22 Mesh types of Micromegas detectors from a microscope view. Mesh design parameters are given in the next table.

Detector type	Pattern	Pitch (μm)	Interior square side
1 Classic	hexa	100	30
2 SA	square	100	30
3 CAST	square[2]	100	30
4 IKERLAN PCB	square	100	50
5 Bulk	woven	80	50

Table 6.6 Mesh parameters of the detector types displayed in figure 6.22. Detectors 1,2 and 3 belong to the microbulk category.

Aadvantages of Micromegas detectors

The advantages of Micromegas detectors are the following:

- The track time resolution of a Micromegas detector is found to be less than 0.60 ns [112].
- Very stable operation during long periods [114]
- The space resolution can reach about 11 μm. Space resolution is limited only by diffusion and the result has been achieved by the use of CF_4 + 20%iC_4H_{10} [115]
- High counting rate capabilities. Their fast response is due to the small path that ions have to travel (amplification gap length ~100 μm) and the strong field applied. Electrons and ions produced in the gap can be collected in 1 ns and 30-100 ns respectively and as a result rates of proton fluxes at 2×10^9 counts mm^{-2} s^{-1} can be measured [116]
- New concept designs of the detector have decreased by far the sparking probability.

6.7 CAST Micromegas detectors

The CAST scientific research program evolution runs in parallel to the Micromegas development and progress. The continuous progression on detector performance is due to detector design plans for better sensitivity, new readout patterns and manufacturing techniques. This progress has resulted in a background decrease and the enhancement of the detector's

discrimination capabilities.
Replacement of radioactive materials, shielding upgrades, acquisition upgrades and development in analysis of micromegas data improve continuously the detector's performance.

Micromegas is used also by the COMPASS and NA48 experiment at CERN and that set the standards for better performance and stability always higher. The ATLAS detector upgrade of the LHC makes use of a large-area detector based on the bulk-micromegas technology for muon detection.

Fabrication

The first Micromegas prototypes [106] were composed by two frames on which the mesh and the anode plane were glued. The meshes used were made of Ni (using electroforming processes) and the anode plane contained anode strips of gold-coated Cu, were fabricated by the metal deposition technique. The main technological challenge is the parallel suspension of the thin mesh (~3-5 μm thick) all over the anode area. Inhomogeneity of the gas could produce gain spatial dependence or sparks in bended zones. The solution for parallelism of the mesh plane was given by the use of pillars between the mesh and the anode. The same solution holds for all Micromegas versions. In early Micromegas versions, pillars were glued to the anode. Later versions, as will be explained in the next sections, use modern manufacturing techniques that can build the complete amplification system of the detector as a unit. The first detector's characteristics was a grid of 3 μm thickness with 17 μm openings every 25 μm.

6.7.1 Bulk Micromegas technology

In the bulk micromegas technology [118] the electroformed micromesh is replaced by a commercial woven wire mesh. The manufacturing process is fast, inexpensive and there is a variety of materials that could be used for the micromesh like Cu, Fe or Ni. The mesh thickness lies between 30 μm to 80 μm. The process, results to a robust and flexible micromegas detector that cannot be easily damaged by touching or by sparks and can be glued to a conventional PCB readout[35].

The base materials, consisting of an insulating material (FR4[36]) that carries the Cu strips and a photoresistive film (Vacrel) of thickness equal to the amplification gap, are laminated at high

[35] A printed circuit board (PCB) mechanically supports and electrically connects electronic components using conductive tracks, pads and other features etched from Cu sheets laminated onto a non-conductive substrate
[36] FR-4 is a composite material composed of woven fiberglass cloth with an epoxy resin binder that is flame resistant

temperature to form a single entity. By applying a photolithographic process, the photoresistive film is etched producing the pillars that are of cylindrical shape of 300 μm in diameter and have a pitch distance of 2 mm.

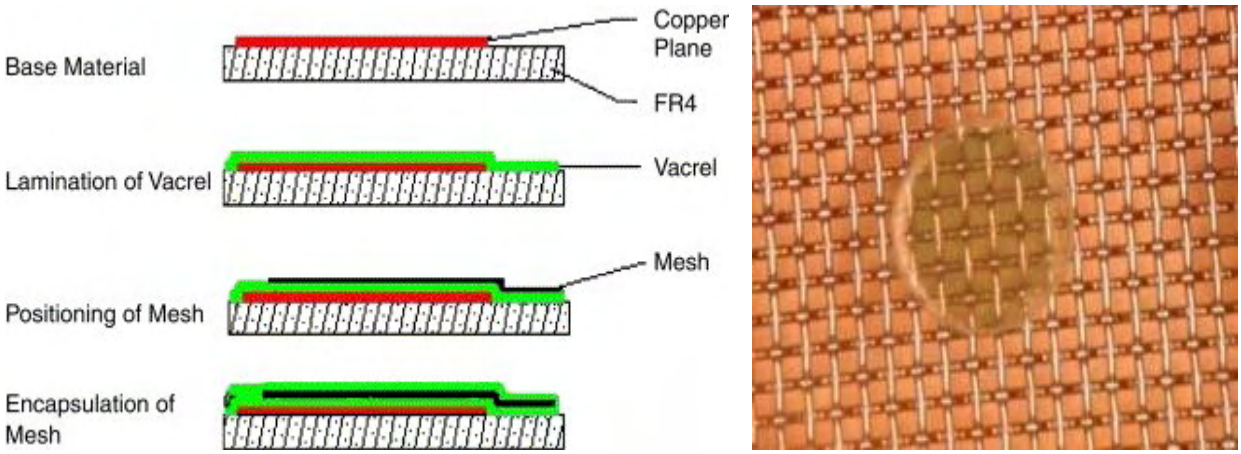

Figure 6.23 On the left a sketch of the fabrication process. On the right a detailed image of the woven mesh with a pillar.

Although, bulk micromegas have many advantages (low noise due to low capacitance, a good maximal gain before breakdown and an acceptable energy resolution ~18% FWHM at 5.9keV), their performance is limited by the mesh nature which is relatively thick. The gap is also long to ensure stability because of the thick mesh and a usual bulk detector gap is ~128 μm. The long gap limits the drift velocity and operates at a lower amplification field than other micromegas.

Large areas of the bulk detector are possible to be constructed like the MAMA (Muon ATLAS Micromegas Activity) for the ATLAS detector upgrade for sLHC[37].

6.7.2 Microbulk Micromegas

The microbulk type of micromegas is fabricated by a novel technique that achieves very thin meshes (~5 μm) and narrower amplification gaps (~25-50 μm). The manufacturing process makes use of a state-of-the-art lithography technique and the raw material is a Cu clad kapton foil (Cu-kapton-Cu). Mesh, the pillars and the anode are built as a unit. The amplification volume is produced by etching the kapton through the mesh holes.

A thin photoresistive film is used as a mask that can be put on the top of the double clad kapton

[37]sLHC is a proposed upgrade to the Large Hadron Collider. The upgrade aims at increasing the luminosity of the machine by a factor of 10, up to 10^{35} $cm^{-2}s^{-1}$.

and a lithographic method is applied to produce the mesh pattern. With this method, the amplification gap accuracy is high (about 1μm) and the homogeneity created can lead to an outstanding energy resolution. In [110], energy resolution of 11% FWHM at 5.9 keV has been obtained for a mixture of Ar+5%iC_4H_{10}.

The mesh produced for the first microbulk prototypes, had holes of 30 μm in diameter and a pitch of 80 μm. Etching process is applied to remove the kapton inside the gap and create the tiny pillars bellow the Cu mesh. The higher capacity is a source of noise but low capacity microbulk detectors are now being developed.

The microbulk unit can be glued to a complex readout plane that can also be made by standard lithographic methods, using the same materials as the amplification gap unit. By this method high radiopurity detectors have been made and their use in CAST offered upgraded results.



Figure 6.24 Left: Etching methods applied in the shadow of the mesh to create the pillars with a step of 500 μm. Right: Photo of the mesh with Cu spots used to protect the polyimide bellow during etching process [119]

6.8 The CAST Micromegas detector

The CAST experiment is using Micromegas detectors since the start of data taking in 2003 for the Phase I and in the CAST Phase II run. In the ^{3}He Phase II, CAST used bulk and microbulk micromegas detectors in three out of four exits of the coldbores. In that way, the evolution of CAST Micromegas detectors ran in parallel with the detector development. Microbulk detectors are provided as the suitable choice for the CAST experiment.

Their advantages like the energy resolution, the high radiopurity in parallel with the detector stability over the time of use, offer to CAST a reduced background and enhancement of the discrimination capabilities.

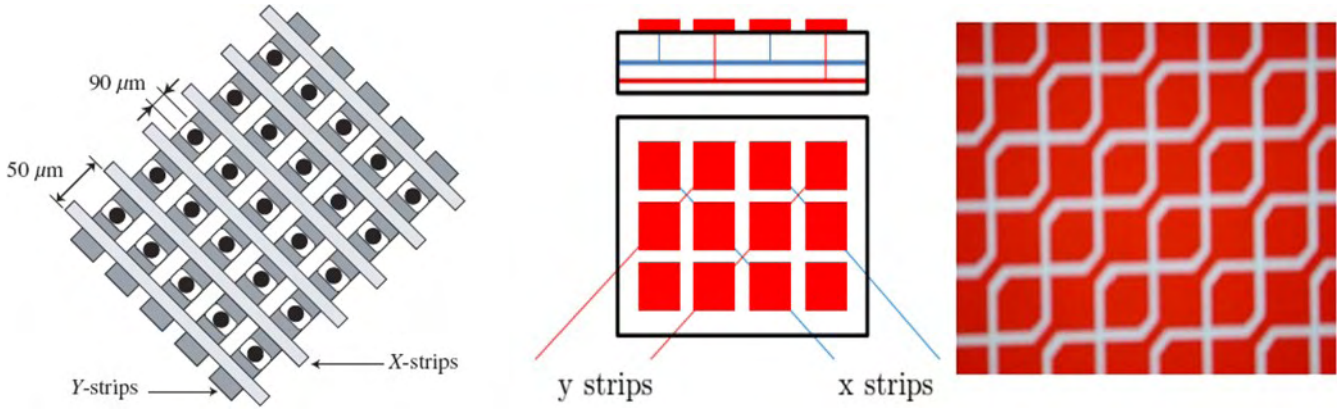

Figure 6.25 Left: The X-Y strip charge collection structure in the classical CAST readout (2002). The strips pitch is 350 μm. X-strips are in light grey and Y-strips (underneath layer) in dark grey. The holes of 90 μm diameter allow the surface charge collection for the Y-strips. Middle: Pixel like readout composed by 3 layers (2007). Right: pixel like readout composed by two layers (2009).

The CAST Micromegas shape composed of a circular base on which strips are lying. The active area is 33.9 cm^2 and comfortably covers the magnet cold-bore area of 14.55 cm^2. The readout plane is a 2D structure with X and Y Cu strips (~350 μm pitch) printed on a kapton foil. The kapton foil with the strips attached is glued on a Plexiglas base, the *raquette* (racket). Due to diffusion, the spatial resolution is better than 100 μm. The strips connections are attached to the *raquette* and extended to the readout planes through the neck of the detector and they are welded to connectors in groups of 96. The amplification gap is ~50 μm thick. Above the mesh there is the conversion gap that is 25 mm thick and ends at the drift window that is made of aluminised Mylar[38] 5 μm thick. The Mylar foil is attached to an aluminium strongback net as shown in Figure 6.26 (left) and the system is attached to the vacuum line of the magnet.

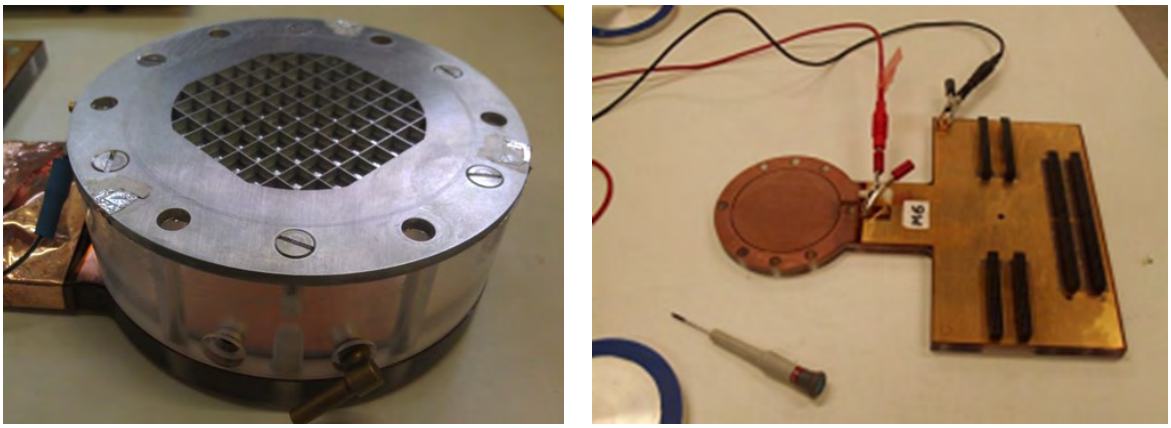

Figure 6.26 On the left picture the Plexiglas chamber and the aluminised Mylar drift window that is connected to the CAST Micromegas is shown. Right: A photo of the mesh side of the microbulk detector *raquette* without the readout cards and the Plexiglas chamber.

The construction process for the CAST microbulk detector is shown in figure 6.27.

Kapton foil (50 μm) both side Cu clad (5 μm)

[38] mylar is the brand name of ($C_{10}H_8O_4$)

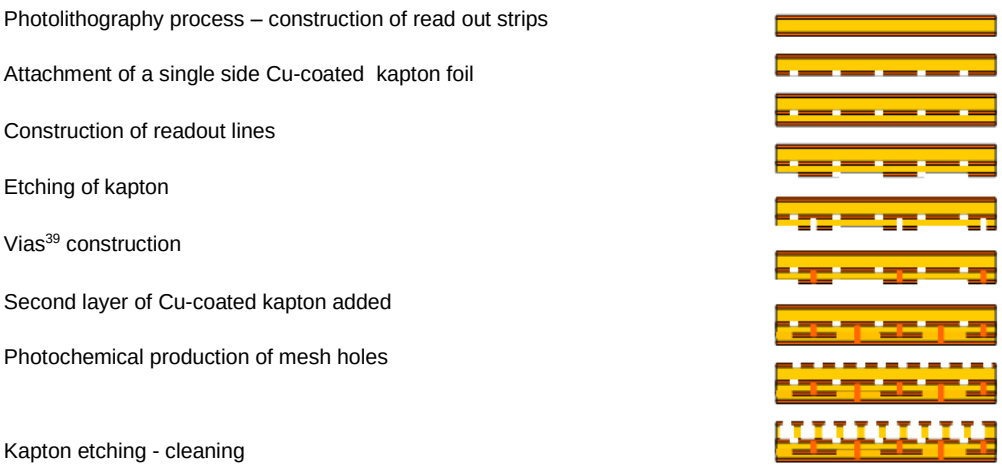

Figure 6.27 The construction process of a microbulk Micromegas detector

6.9 Sunset Micromegas System

In 2007, a general upgrade of the CAST experiment was developed and in the sunset side of the magnet (MRB), a TPC detector was replaced by 2 Micromegas detectors; i.e. one for each cold-bore line. One detector was a bulk micromegas (which was replaced with a microbulk one at a later upgrade) while the other was of a microbulk type. Each detector was positioned at the centre of the cold-bore line as can be seen in figure 6.28.

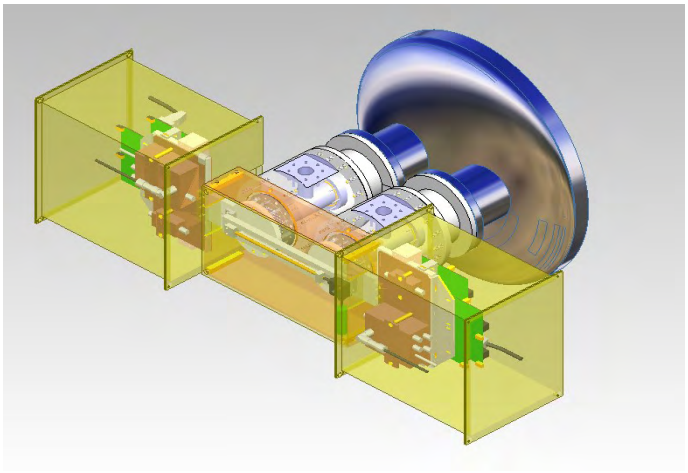

Figure 6.28 A drawing of the Sunset Micromegas detectors in the MRB side.

The new Sunset detectors setup allowed a better performance since the detector read-out was re-designed. The cross-talk problems of early micromegas detectors were diminished by a symmetric readout strip pattern in the anode. The concept of the readout design in 2007

[39] electrical connection between layers in a physical electronic circuit that goes through the plane of one or more adjacent layers

microbulk detector (figure 6.29) is based on a pixel readout scheme that uses two or three lower planes of orthogonal tracks of X and Y strips. The pitch increased to 550 μm and the number of lines reduced to 106 covering a 36 cm^2 of active area. In order to increase the readout homogeneity the mesh pattern is aligned with anode layout. Every pixel is complemented with an array of 3×3 holes with 40 μm in diameter and 100 μm pitch. The electrons crossing the mesh will always find a spatial defined anode below.

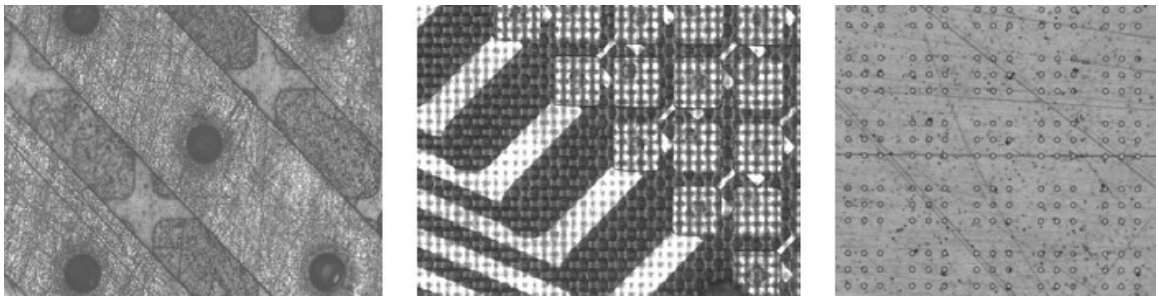

Figure 6.29 Back and front view of the anode plane of the 2007 micromegas in left and middle respectively from a microscope. Right: the mesh pattern of the microbulk, where holes distributed in 3×3 arrays that are correlated with pixel position below.

The gas mixture of the micromegas detector was changed in order to comply with CERN safety rules and the amount of the flammable gas iC_4H_{10} was reduced to 2.3% in the sunrise and 2% in the sunset side. The gas line starts from a premixed bottle of 100 bar pressure and it is regulated in 1.4 bars. The line is connected with a 5 litre volume that is installed close to detectors and this bottle sends the gas into the two detectors that are connected in series. The regular flow in the sunset micromegas is 2.5 lt/h.

6.9.1 Vacuum system

In the Sunset Micromegas detectors system there are two vacuum regions separated by a *differential window*. In the side which is close to each detector, a cylindrical Plexiglas piece is connected to the drift window of the detector with O-rings and bolts and it is pumped by a diaphragm and a turbo pump. The pressure in this region lying between 10^{-4} – 10^{-3} mbar. The vacuum side that is close to the magnet bore is pumped by two turbo pumps and a primary one and the pressure in this region is very low (10^{-8}-10^{-7} mbar).

The differential window that separates the two regions is made of 4 μm polypropylene and prevents the gas molecules that could diffuse out of the drift detector window and condense onto the cold windows. A differential *by-pass valve* is protecting the fragile *differential window* in case that the pressure difference between the two vacuum regions exceeds a safety limit (~1.5 mbar). Two *gate-valves,* positioned between the magnet-bores and the differential windows, can be used in order to separate the detector vacuum system from the magnet vacuum. During the data taking period they are normally open. The gas system and the vacuum system are shown in figure 6.30.

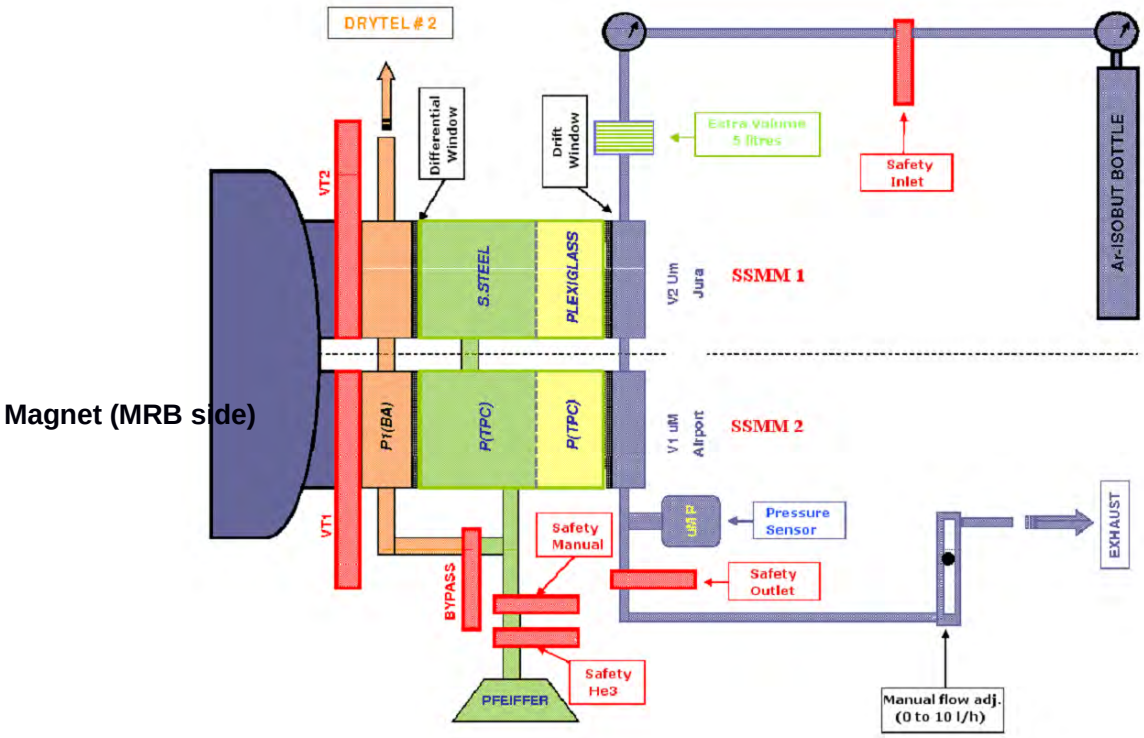

Figure 6.30 Magnet bores are connected by a differential window and a Plexiglas cylinder to the Micromegas detectors. Gate valves VT1 and VT1 (in red) can be used as interlocks (safety valves) or manually close in case of interventions. A gas bottle through a safety inlet can provide the gas mixture of the detectors.

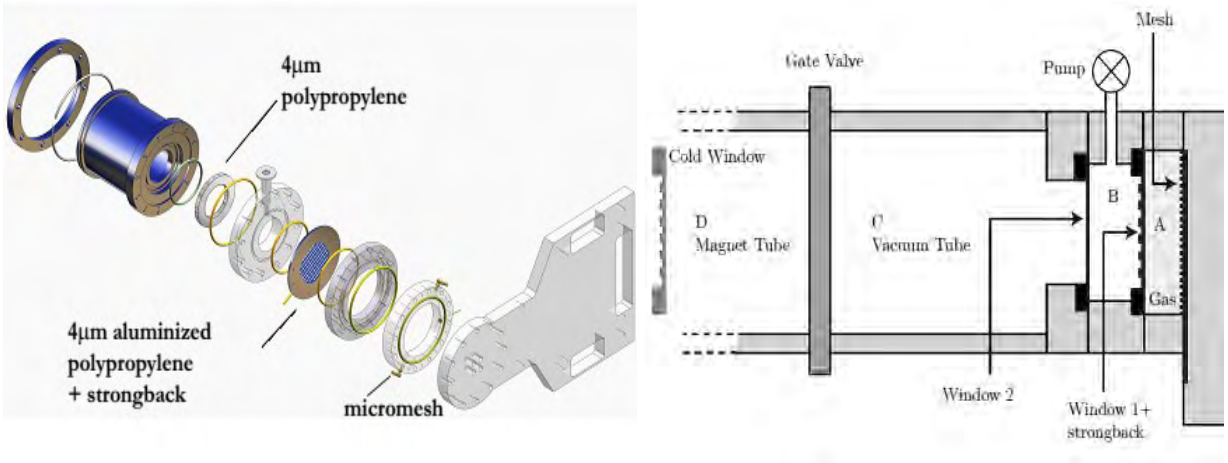

Figure 6.31 Left: An exploded 3D view of the detector, where components are being separated. Right: the Micromegas vacuum line.

6.9.2 CAST Micromegas Efficiency

The hardware efficiency of the Micromegas detector has been measured by simulations in Geant4 software package [121]. The simulations performed can also reveal the nature and origin of the detector background events. Such events are due to cosmic rays, external gamma radiation, internal radioactivity of the materials used and radon contamination. The model built in Geant4 package is presented in figure 6.32.

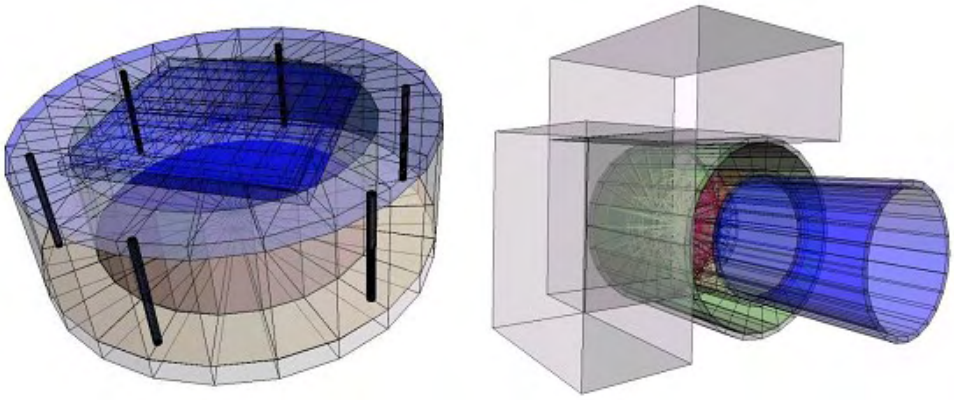

Figure 6.32 Micromegas geometry implemented in Geant4. On the right the implementation of the shielding is shown.

The Micromegas detectors have been designed and optimized for X-rays photon detection in the energy range of 2-7 keV. The total efficiency of the detector is a contribution of the materials used in the windows, the gas mixture absorption and the detector's dimensions. The x-rays that could have been converted from axions inside the magnetic field are attenuated by the following parameters

- 15 μm of polypropylene (Cold window) with 17.5% strongback
- 4 μm of polypropylene (Differential window)
- 5 μm Aluminized Mylar (Drift window) with 5% strongback.

By combination of the attenuation in x-rays of the materials used and by adding the attenuation of the gas mixture (Ar +2% Isobutene) one can obtain the efficiency curve that is plotted in Figure 6.33.

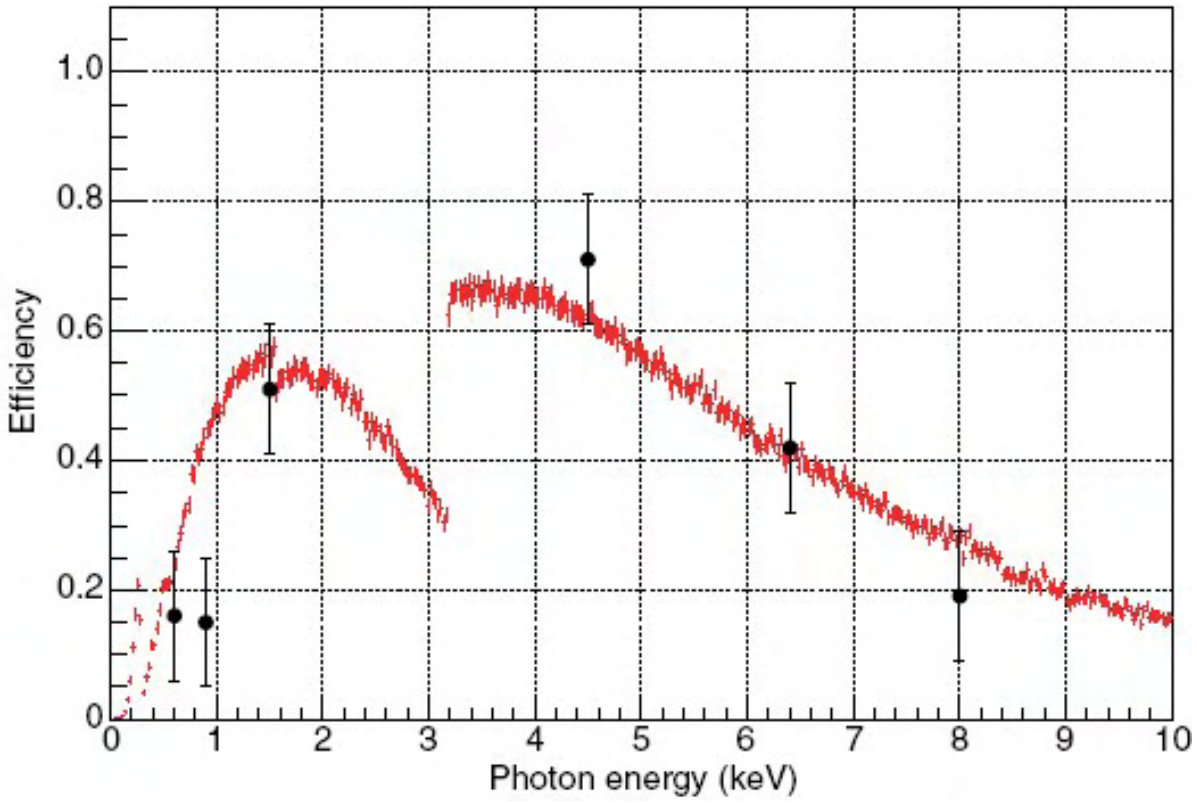

Figure 6.33 Simulated Micromegas efficiency versus energy, compared with experimental points measured at PANTER[40]. Detector efficiency is measured for gas pressure of 1 bar.

6.9.3 Calibration System

A ^{55}Fe radioactive source is used for the Sunset detectors calibration by an automated system. The system was updated in 2010 and two pneumatic calibrators were installed in the Sunset line as shown in Figure 6.34. The calibrators move the ^{55}Fe source with the help of compressed air and they are controlled by the detectors DAQ (Data Acquisition). During the data taking periods, the calibration in the Sunset system is performed twice per day. This procedure is a prerequisite for the detector data analysis since it provides valuable information about the variation of uniformity or problems in detector's stability. The uniform illumination of the detector is performed by the high X-ray source that in November 2010 had intensity of ~35 MBq.

The X-ray profile created by the ^{55}Fe illumination is used to form the sequential cuts (selection criteria) that all background events are compared with, in order to distinguish X-ray like events from background events. Every X-ray event has a characteristic shape and distribution. In the case where a background event has the same distribution as the X-ray calibration event distribution and passes the applied sequential cuts, then it can be considered as an X-ray event.

[40] PANTER is an X-ray test facility located in Germany that is mostly used for X-ray telescopes characterization

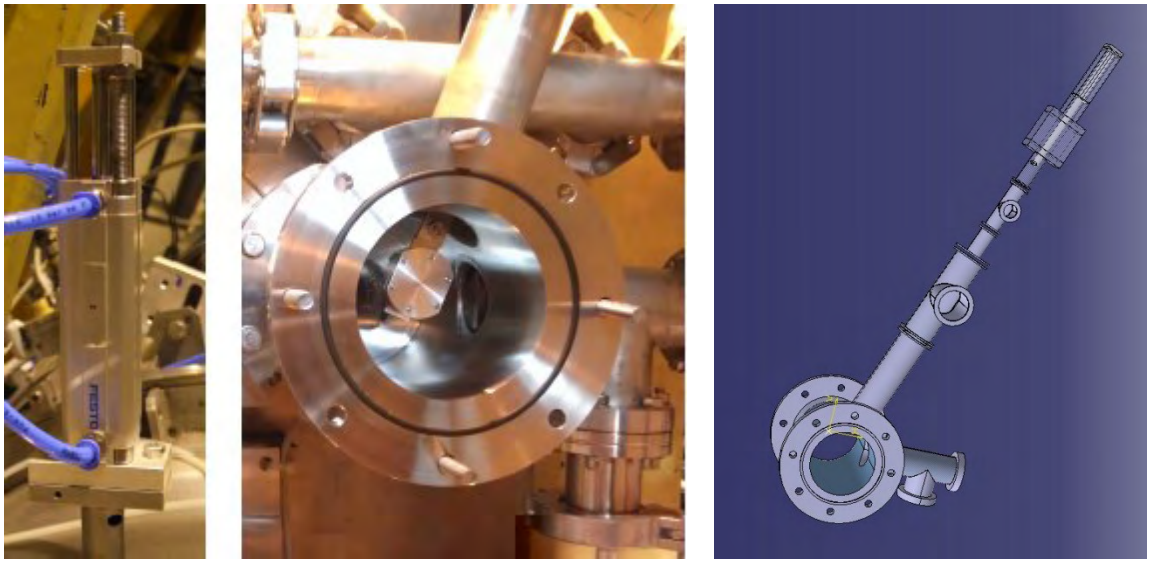

Figure 6.34 Left: the pneumatic piston that moves the ^{55}Fe source inside the vacuum tube as seen in the middle picture. Right: A drawing of the system created in this work for the upgrade of 2010 in CATIA R-19 mechanical design software.

6.9.4 The Sunset Micromegas Background and Shielding

The magnitude of the background level corresponds to the detectable radiation level and its minimization is of great importance for the Micromegas performance. The main sources of background radiation can be categorized as follows

- Radiation of the materials used for the detector construction as also the materials of the earth surface in the experimental area
- Radioactivity of the air
- Cosmic radiation
- Radioactivity of the materials used in the detector vicinity (pipes, shielding etc.)

The Earth's radioactivity as also the radioactivity of the detector's construction materials is due to the low, but important, concentrations of natural radioactive elements like potassium, thorium, uranium and the products of their decay chain. These radioactive elements can emit α, β and γ rays. In order to avoid radioactive materials, electrolytically prepared Cu, magnesium and steel can be used in the detector's manufacture, which show low levels of radioactivity.

The electrical soldering and some circuit board materials are also sources of background and it is better to use electronic circuit boards outside of the detector shielding. Short lived radioactive gas products are the ^{222}Rn (half-life 3.825 yr.) and ^{220}Rn (half-life 55.6 sec), which can be found in the ambient air surrounding the detector or outgassing from the cement used

in the experimental hall. The airborne radioactivity sources can be reduced by evacuating the detector's surrounding as also by flushing the detector with a clean gas like nitrogen.

Another source of Micromegas background is cosmic radiation. Cosmic radiation is composed primarily of high-energy protons and atomic nuclei of mysterious origin, mainly originating outside the Solar System. After the primary cosmic particle has collided with the air molecule, the main parts of the first interactions are pions. Also kaons and baryons may be created. Pions and kaons are not stable, thus they may decay into other particles[41].

The energy band of the incoming particles of extra-terrestrial sources is wide and their interaction with the material surrounding the detector can affect the background level. At sea level, muons constitute the 80% of the cosmic radiation flux and their rate is 1 muon/cm^2/sec. The archaeological Roman Pb blocks are used to reduce the environmental gammas, while they are not able to reduce the flux of cosmic muons. However most of the muons can be rejected during the offline analysis. This type of Pb is pure of radioactive material concentration, but Cu is also used to stop the fluorescence x-rays (77 and 170 keV) generated by the photoelectric absorption of gamma rays.

Alloys of high density like W, Ni, Fe or Cu can also be used to reduce the high energy gammas. The polyethylene blocks are used to stop the thermal neutrons since their concentration at sea level is rather high and can influence the low background x-ray measurements. Polyethylene is used to quickly reduce the fast neutrons energy because of its high neutron absorption cross section. Materials that contain hydrogen, like water paraffin, can also be used. Another layer of material should be used in order to absorb the thermal neutrons produced and for CAST purposes, a thin layer of 5 mm Cd has been chosen due to its high absorption cross section.

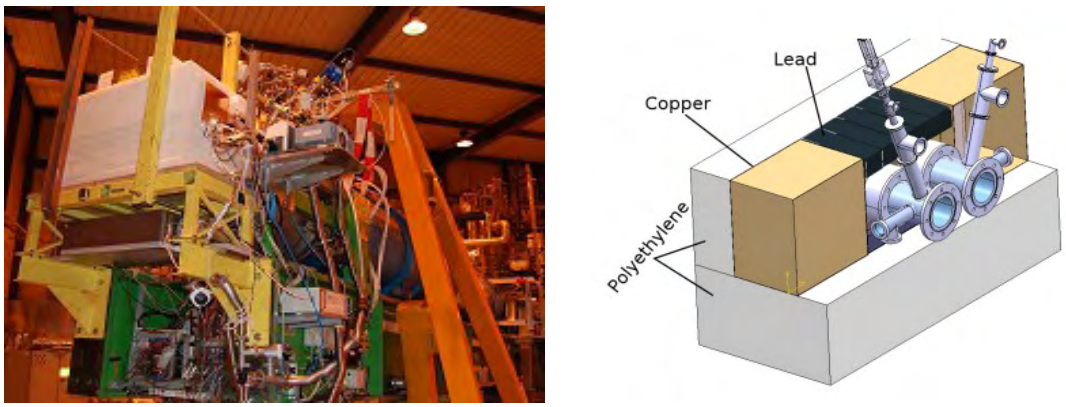

Figure 6.35 On the left the Sunset Micromegas setup on the CAST moving platform. On the right a design in CATIA R-19 is shown, of the shielded Sunset Micromegas detectors as a part of this work.

In 2007 a first attempt for the Sunset micromegas shielding update was made in order to reduce the background level. The Sunset shielding is composed of an inner layer of Cu that is used

[41] The neutral pions π^o decay into photons γ in a process $\pi^0 \rightarrow \gamma+\gamma$. The charged pions $\pi^{\pm}$ preferentially decay into muons and neutrinos in the processes $\pi^+ \rightarrow \mu^+ + \nu$ and $\pi^- \rightarrow \mu^- + \nu$. Kaons decay into muons or they can also produce pions.

also as a Faraday cage and covers both detectors, a layer of archaeological Roman Pb that covers the Cu layer in form of 5 cm thick bricks, and Polyethylene bricks that cover the whole setup. Because of the main valves and gates of the Sunset setup, the resulting shielding is not tight enough in some directions.

In order to evaluate the impact of shielding upgrade in the background reduction, a direct comparison of the background level by the same detector before and after the shielding installation was made. The Sunset installation shielding yielded a reduction factor of 3 and typical values of the background were lying in the range 5-8 $\times 10^{-6}$ $keV^{-1}cm^{-2}s^{-1}$. Bulk Micromegas can show background levels almost as good as the contemporary microbulk, but the reliability of the microbulk detectors and the stability shown in the vibrating platform of CAST made them the optimum choice. In Figure 6.36 the background evolution of the micromegas detectors is shown.

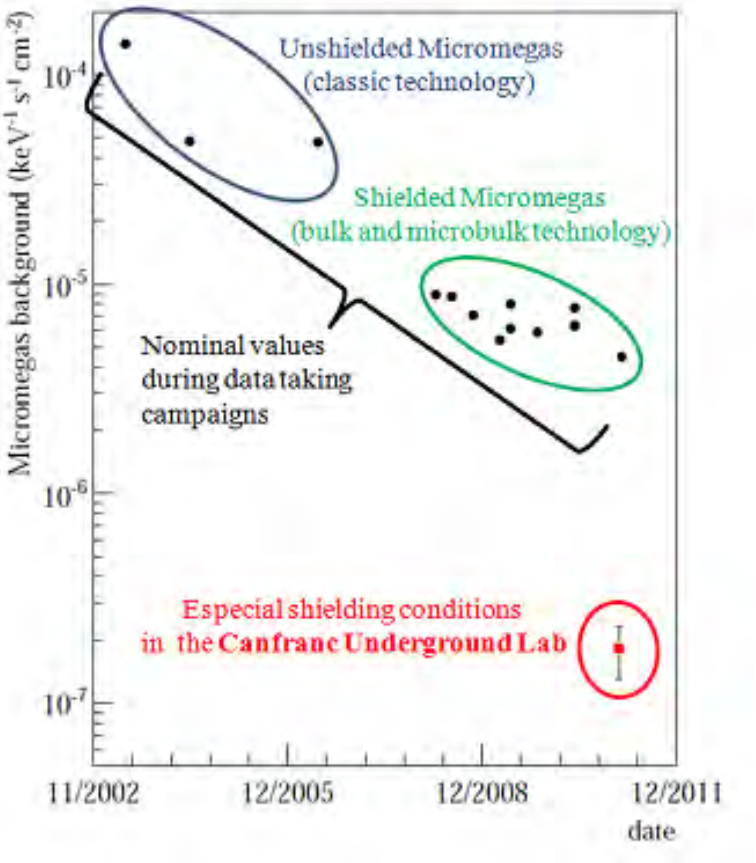

Figure 6.36 Historical background levels for the CAST micromegas detectors. In red the background level in the Canfranc laboratory in Spain, that is located in 2500 m depth, is shown for comparison [121]

6.10 The Sunset Micromegas upgrades

In this section general upgrades in the Sunset Micromegas system will be presented.

6.10.1 Cable Trays

Micromegas detectors are sensitive to the electronic noise produced in the CAST experiment because of various electronic instruments and motors attached to the moving platform. It has been observed that when the tracking motors were turned ON the electronic noise levels in the sunset micromegas were increased. Power cables that are connected to the detectors and the signal cables attached in the gassiplex cards[42] are sensitive to the inductive current produced by the high frequency motors used for the magnet movement. The solution proposed to eliminate the electronic noise level that increased the trigger rate and the dead time of the detector was the installation of cable trays. Grounded cable trays, isolate the signal and power cables of the detectors and protect them from outside word electronic noise. Voltage cables were also “dressed” with a wire-mesh that used as a Faraday cage inside the trays. Technicians also re-examined the electronic connections and ground cables of all instruments attached to the moving platform. The installation of the cable trays was a part of this work. The cable trays setup can be seen in the following figure.

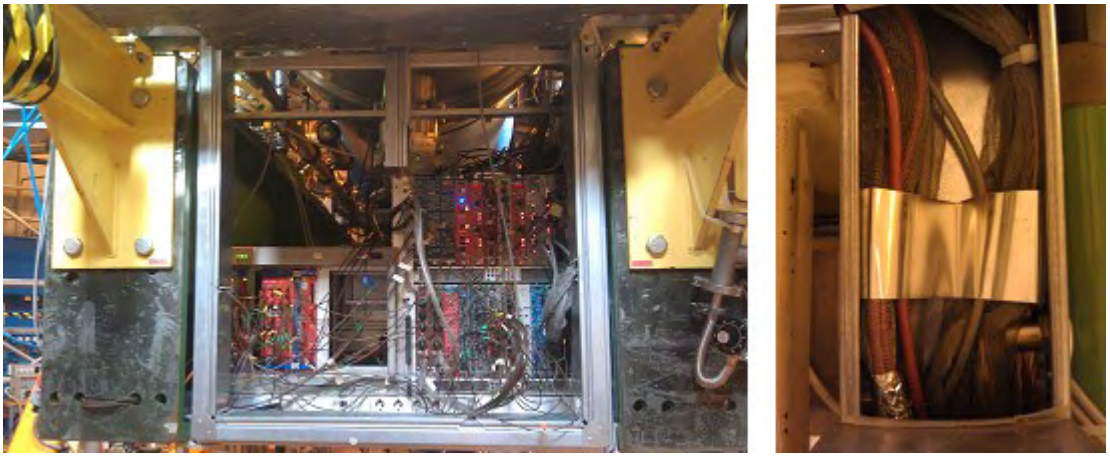

Figure 6.37 On the left, a general view of the cable trays installed in the perimeter of the detectors electronics crate. On the right, cables inside the trays “dressed” with a wire mesh.

[42] A readout system composed by four front-end electronics cards connected to the Micromegas detector

6.10.2 2012 upgrade of the Sunset setup

In 2012 a significant upgrade of the Sunset shielding was carried out before the summer data taking. Underground laboratory tests in Canfranc and Geant4 background simulations of the Micromegas detectors motivated the new shielding and detectors setup. Simulations and underground laboratory tests revealed that the main background contribution to the Micromegas detectors in CAST setup is due to the environmental γ flux that produces a 6 keV peak. The 6 keV peak is originated from the steel fluorescence in vacuum pipes and the cathode. Interactions of the environmental gammas with the vacuum pipes and the drift window can produce fluorescence photons that are able to penetrate the detector.

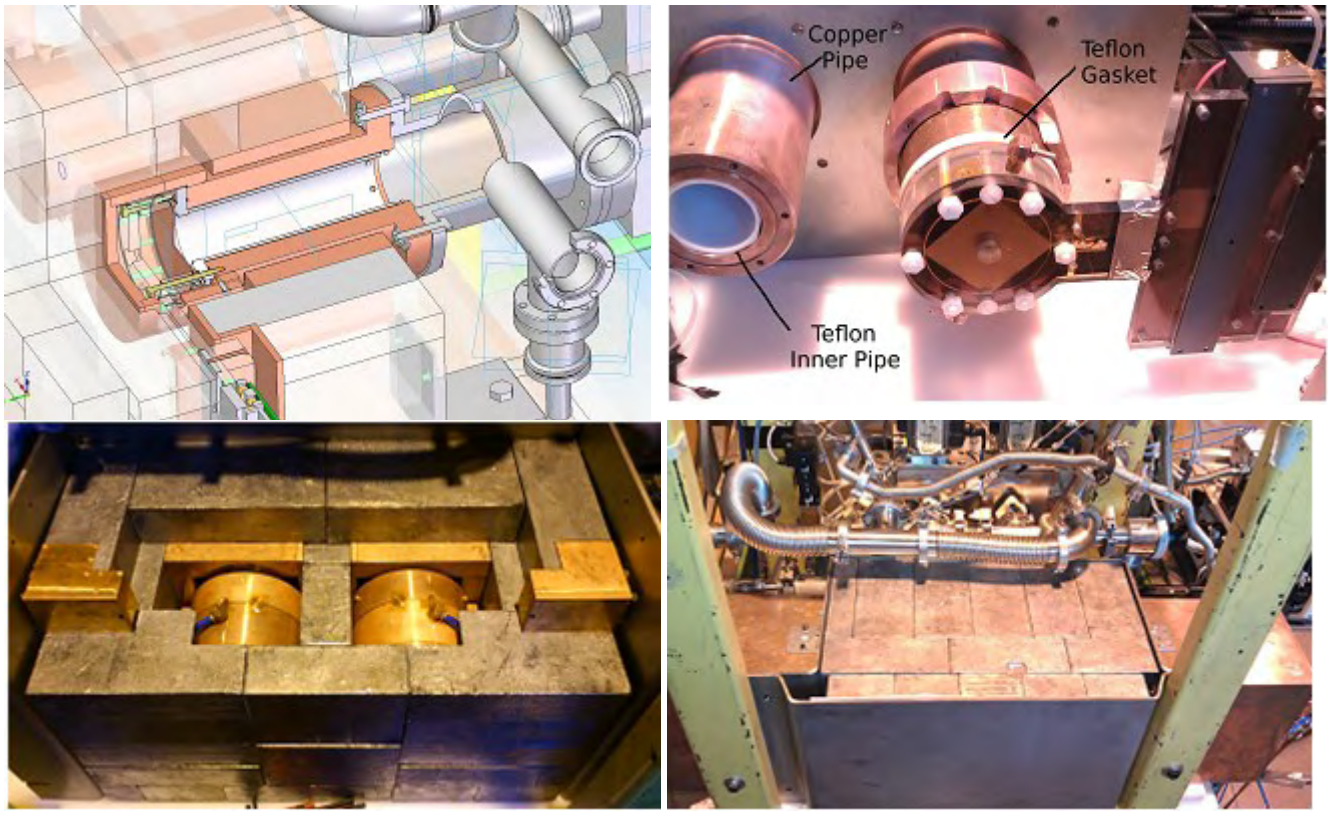

Figure 6.38 In the upper left a drawing view of the sunset micromegas shielding. Upper left figure shows the Cu pipe with an inner Teflon coating visible in the left (Jura side) magnet bore. In the upper right figure (Airport side) the installation of the detector consists of the new Teflon screws, nuts and gasket, the new gas connection and the front piece of the new Cu shielding part that fits the pipe. Lower left figure shows a later step of the shielding where Pb blocks have been adjusted carefully in the mounting process. Cu shielding is also visible as also the Faraday cage that has been adjusted to the detector's setup. In this type of setup not only detectors are shielded but the radiopure pipes as well. In the lower right figure the last step of shielding setup is shown. For the last shielding upgrade step a muon veto counter has been installed over the top of the Pb surface.

The underground tests in Canfranc have proved that shielding the detector by 10 cm thick Pb that covers the detector in a 4π solid angle can reduce the background level substantially. The

innermost Cu layer of the shielding increased from 0.5 cm to 1 cm thickness in order to attenuate the natural gamma emission from the Pb shielding layer. The polyethylene layer was decreased leaving the available space for the Pb layer extension. A significant background level reduction is also achieved when the aluminum drift window of the micromegas detector is replaced with a Cu one. A Cu pipe (20 cm long and 1.5 cm thick) has also been used; this caused a transformation of the detector away from the magnet. The Cu pipes were also shielded by Pb. In that way all the stainless steel parts near the detector have been replaced by Cu ones in order to prevent the 5-7 keV fluorescence and improve the detector intrinsic radiopurity. This was achieved by the replacement of the cathode and the gas connections to the chamber and the pipe itself. In order to prevent the fluorescence of Cu, a Teflon pipe was installed inside the Cu one.

The upgrade of the shielding resulted in the disappearance of the 6 keV peak and led the background level to 1.7-2.3 $\times 10^{-6}$ $keV^{-1}cm^{-2}s^{-1}$ in the 2-7 keV energy range. The reduction factor was about 4.5 regarding the previous sunset Micromegas detector's setup. The detectors used in this setup are the M18 and M19 that were tested and characterised in CEA Saclay while the shielding has been designed and installed by the University of Zaragoza.

6.10.3 Muon Veto setup

In May 2012 a cosmic muon veto was also installed over the sunset shielding setup because the tests performed in Zaragoza showed that a percentage of the x-rays events accepted in the offline analysis are correlated with cosmic muons. The muon veto is built from a 120cm×40cm scintillator coupled to a photomultiplier that is powered at 1kV and gives an output signal that is amplified with a NIM amplifier. The scintillator was installed on top of the sunset shielding covering both detectors. Due to a lack of space and the present setup constraints, the scintillator is installed at an angle of 45º.

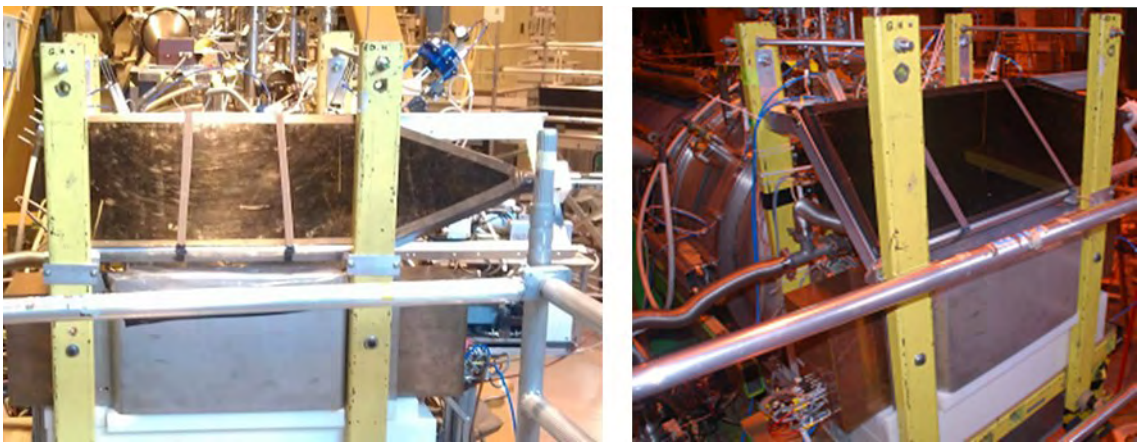

Figure 6.37 The muon veto setup (plastic scintillator) at the top of the shielded sunset micromegas

By measuring the muon spectrum energy, an output signal of the veto that is higher from a specified muon energy threshold triggers a counter that counts the time until the time between the veto event and the trigger of the micromegas. The events recorded as muons are rejected in the offline analysis. The Muon veto implementation has decreased the background to the level of 1.6-1.2×10^{-6} $keV^{-1}cm^{-2}s^{-1}$. Before the summer of 2014 data taking, a new scintillator has been installed in the back side of the shielding setup.

6.10.4 Calibration system

In 2010 a calibration system was installed to the Sunset Micromegas side. In section 6.9.3 the installation and working principles of the pneumatic calibration system are reviewed.

6.11 Data Acquisition System of Micromegas

In this chapter a review of the data acquisition system is presented. The signal from the detector's mesh and strips is read by a Data Acquisition system (DAQ) that controls the electronic hardware module. The information for each event is recorded into a file for the offline analysis. The process is decomposed in the read out analysis of the signal from the electronic modules and the software implementation of the signal that can be used in the offline analysis.

Read out electronics

6.11.1 Strips Signal

The signal generated by the avalanche of the electrons in the amplification region is collected from the X and Y strips. The strips signal is read out with the help of four Front End (FE) electronic cards that are based on the Gassiplex chip. Each of the Gassiplex card can be connected to 96 strips and operates at a maximum clock speed of 1 MHz.

The cards are controlled by a CAEN sequencer with two CRAMS modules (CAEN Readout for Analog Multiplexed Signal) in a VME crate. The cards are powered by a standard 6V power supply (positive and negative).



Figure 6.38 The Gassiplex card (inputs/outputs) used in the Micromegas detector of CAST

The Gassiplex card has three digital inputs (Track and Hold, Clock and Clear) and one output. The timing signal is provided by the sequencer as follows

- The Track and Hold pauses the card's acquisition and storage the strips charge signal in its memory
- For each Clock signal sent, one channel of the card is read
- The Clear signal resets the card's memory

The output signal is multiplexed in a multilevel voltage shape, where each level corresponds to a particular strip. The CRAMS digitize and store the signal from each Gassiplex and the 10-bit VME crate reads the signal and sends it to a PC for permanent storage and analysis.

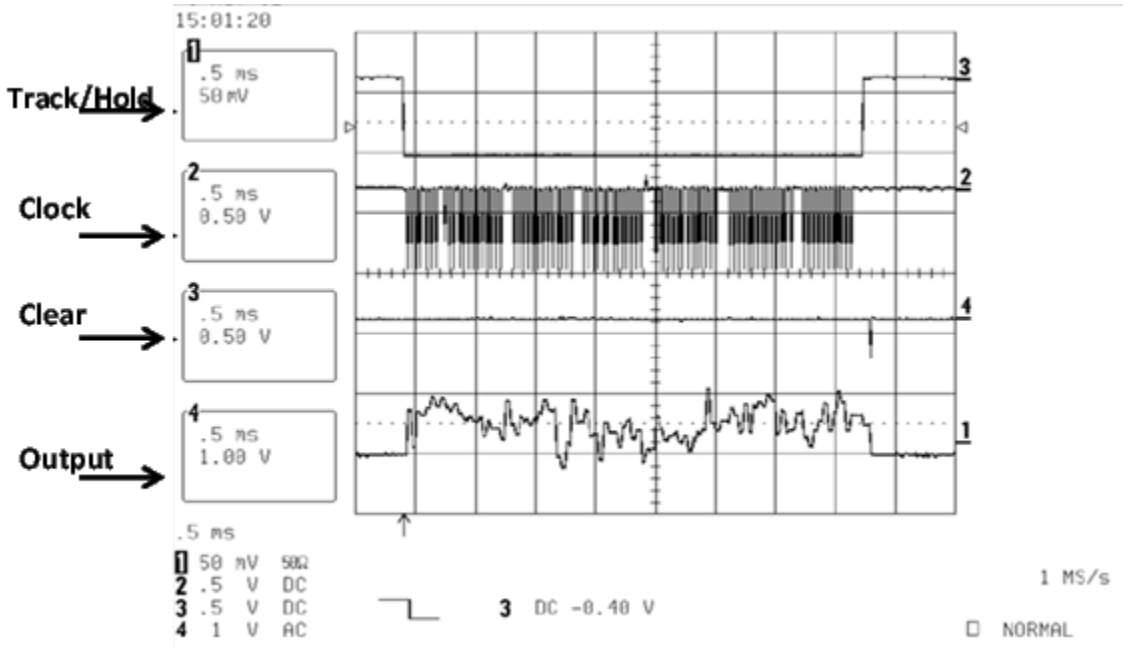

Figure 6.39 The signal sequence that triggers the Gassiplex acquisition.

In parallel with the strips signal, the Mesh signal is recorded after shaped and amplified in order

to trigger the Track/Hold signal of the sequencer.

A delay time is provided to the gassiplex card after the Mesh trigger to start reading the maximum charge accumulated. The delay time is set to 900 ns. During the signal recording a busy signal is sent by the VME to block incoming signals other than the one being read at that time. At the end of the event recording the busy signal is removed.

6.11.2 Mesh Signal

The signal that triggers the Micromegas detector is obtained by a preamplifier (ORTEC 124B) which also provides the high voltage for the micromesh cathode. The signal in the Mesh is generated by the positive ions created in the amplification region. The output of the preamplifier is shaped and amplified in order to produce the trigger signal for the strips. The Mesh signal passes to NIM timing amplifiers and is then duplicated via a Fan In-Fan Out module. One of the duplicated signals is sent to a quad discriminator and provides the digital trigger. In the case where a mesh pulse in one of two detectors exceeds a predefined threshold that is set to be above the electronic noise and corresponds to ~2 keV, 2 NIM signals are sent to the VME crate and the information of the mesh and strips signals are recorded. The second duplicated signal of the Mesh is sent to the MATACQ module (Matrix for ACQuisition) that stores timing information for the mesh pulse.

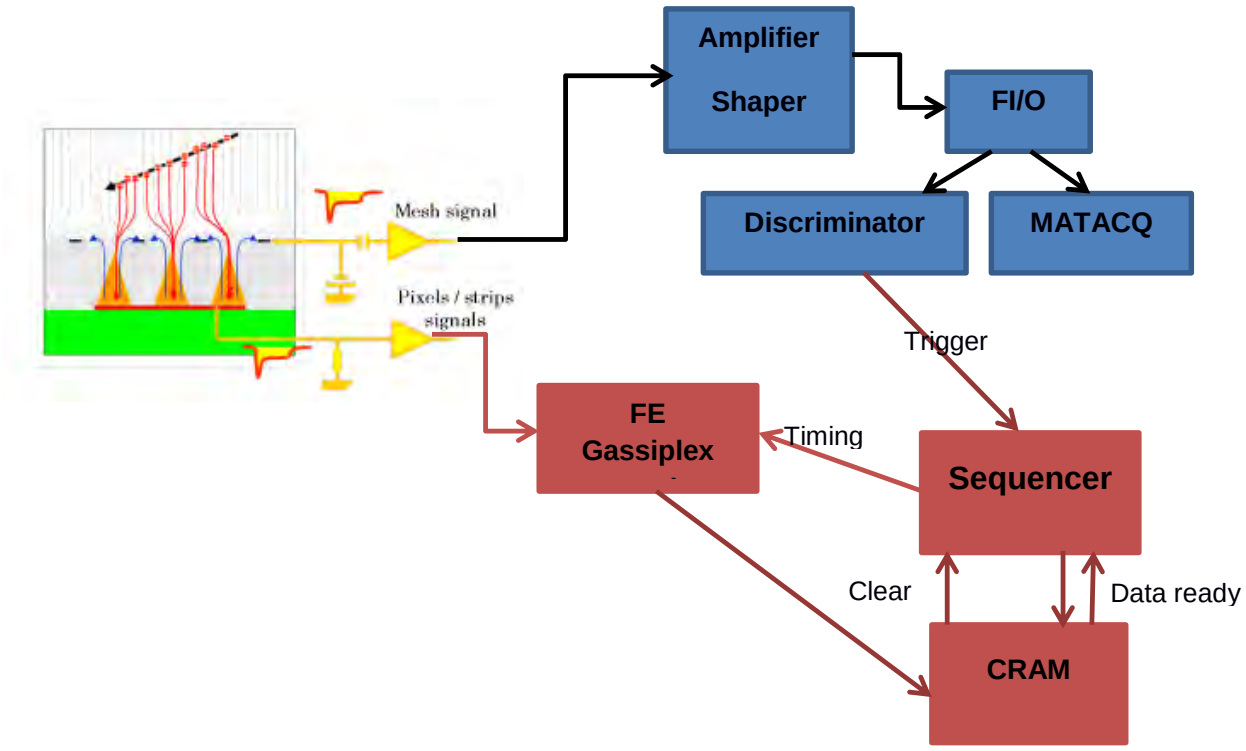

Figure 6.40 Electronic modules sequence of CAST's Micromegas detector.

Both mesh and strips signals are acquired in less than 20 ms and during the acquisition time the system cannot detect any other signal generated because the electronic modules are receiving a veto. This is the dead time of the CAST Micromegas setup and since the normal trigger rate of the background is ~1 Hz, the dead time of the signal is less than 2%.

6.12 Data Acquisition system

The data acquisition and monitoring system is based on the LabView software package of National Instruments. The DAQ software runs on a RedHat Linux (CERN distribution) and is connected to the VME controller via a fiber optic cable. The software runs in autopilot or manual mode and controls both Sunset Micromegas detectors. In autopilot mode that is used in data taking periods, the software can carry out a pre-defined schedule for each detector operation. A graphical user interface (GUI), as shown in Figure 6.41, allows the operator to control the system modules and in the manual mode to run specified types of operations as follows

- Pedestal Run. External trigger of 100 Hz frequency is sent to the strips and the strips signal is recorded. Pedestal is an estimation of the modules and strips electronic noise. The Mesh pulse is not read.
- Background Run. This is the default choice during data taking periods where background and tracking are recorded.
- Calibration. Each callibrator receives a signal to move it's X-ray source in front of each detector

Different virtual instrument (VIs) can be used from the operator to view important parameters like the trigger rate of the DAQ, or the counter rate that is the total number of events.

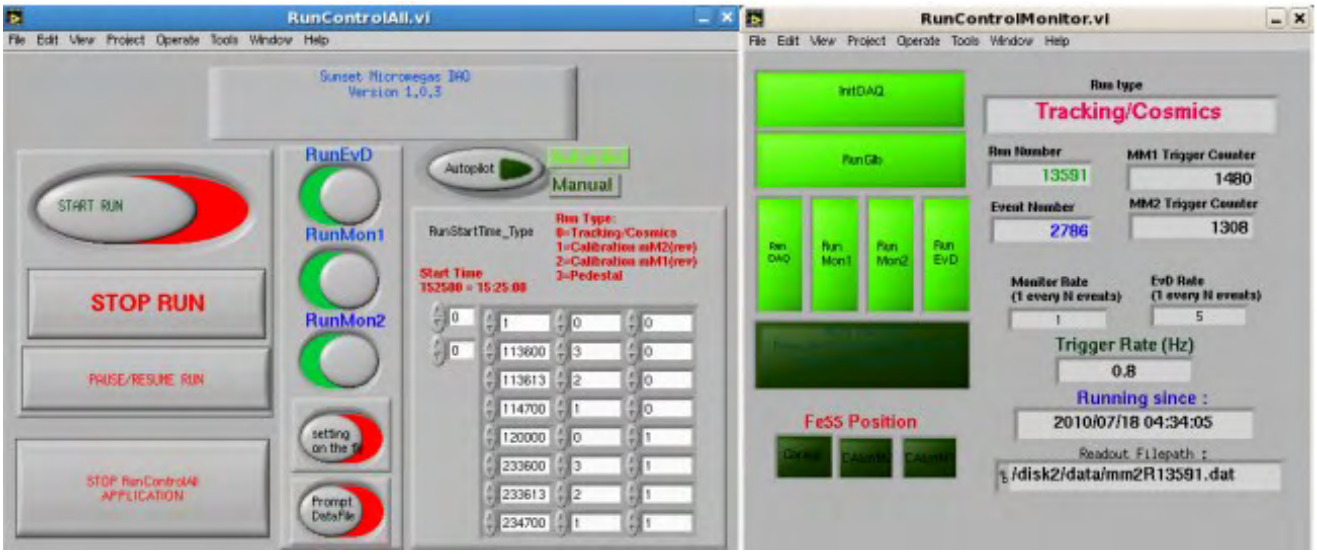

Figure 6.41 The RunControlAll.vi (left) and the RunControlMonitor.vi (right) of the DAQ system. The first one controls the initialization, open/close monitoring tools and the Autopilot process. The RunControlMonitor.vi can display the run status, the Run number, events number, recorded file etc.

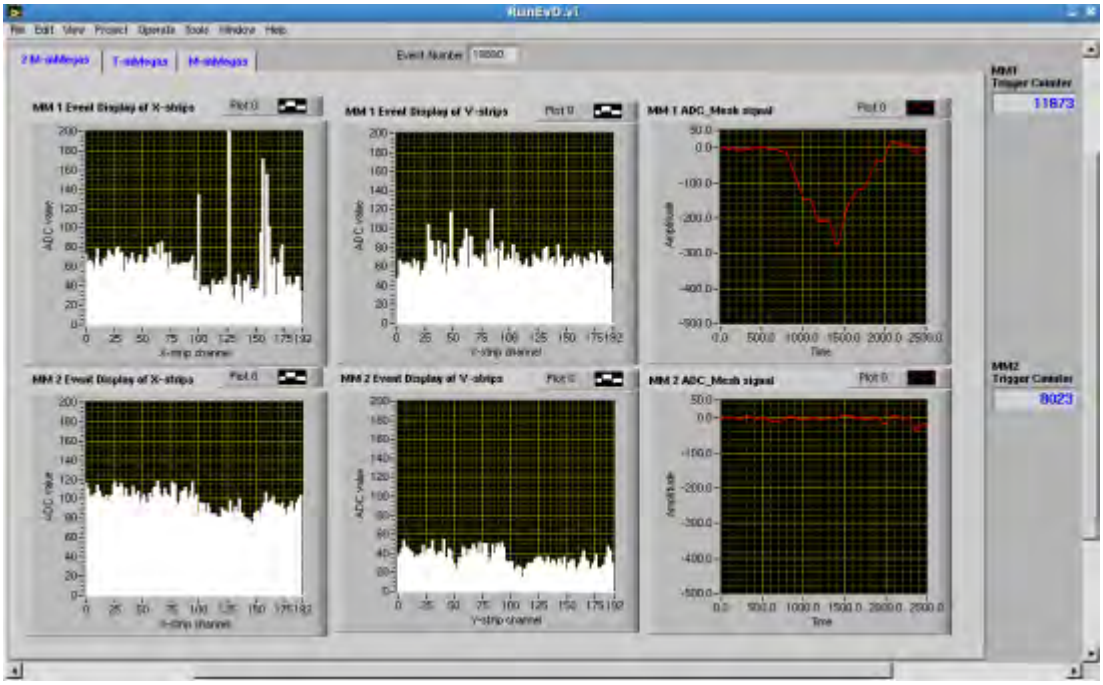

Figure 6.42 The RunEvD.vi that displays the Mesh and X-Y strips charge in real time

The trigger rate of the background run is around 1Hz and most of the events are due to cosmic muons that are passing through the detector. In the case of a Calibration run, trigger rate increases up to 100 Hz and is correlated with the ^{55}Fe source activity. The events of every trigger are recorded into a file that is stored and then transferred twice a day to CASTOR (CERN Advanced STORage manager), in form of binary files, for safety and backup by another vi (National Instruments) routing programm. The form of the raw binary files created will be described in the next section.

7. Raw Data Analysis of the Sunset Micromegas Detectors

During the data-taking period in 2009 and 2010, the Sunset DAQ system acquires three types of runs that are pedestal, calibration and background into one file. Raw data files have a specified format and each event written in a raw file, contains the information of the mesh and strips for each detector. The raw files of the sunset Micromegas are separated into three run files for each procedure (pedestal, calibration and background). Each binary file produced has to be decoded and all the necessary information has to be extracted. Each event recorded is composed by the signal read from the strips that triggered the Gassiplex and the mesh pulse.

The event is defined as the readout of the integrated number for every strip and 2500 samples from the mesh signal after each trigger. The offline data analysis is applied in order to extract the valuable information from the raw data files and distinguish the X-ray events from the background that are cosmic muons or high-energy gammas. In addition, the analysis estimates the energy and the position of the x-ray events. Energy can be extracted from the strips while position of the event can be given from the mesh or the strips. In parallel, the timing information is extracted from the signal collected in the mesh.

For the purpose of this study, a modification of the existing sunrise Micromegas recognition code was made and applied to the Sunset micromegas DAQ raw files. The Sunset raw files include information of both detectors and each event should be distinguished from the main raw file and ascribed to each detector.

The pattern recognition algorithm was designed to reproduce primary ionization events with energy less than 10 keV and localized in less than 1 mm. Muons and high-energy gammas produce pulse shapes that are wider and, as will be explained in a next section, show different pulse characteristics.

Each event triggered, which was stored in the raw file includes the data information from all 106 strips and the 2500 samples of the mesh pulse. The procedure followed from the implemented code is to transform the data into observables and reduce the file size. The observables selected are written into ROOT [135] files by applying selection criteria such as localized x-rays events with energy less than 7 keV which can be recognizable. The 6 keV events from the ^{55}Fe calibration source and the 3 keV of the Argon escape peak can be used as standard X-rays events.

Daily calibration can define the updated X-ray signal that incorporates any systematic effect that could affect the detector response. Parameters like detector's gas pressure, flow of the gas

and temperature are variable because of climate changes and these effects should be taken into account.

The off-line analysis can be divided in two main steps that are the *raw-data analysis* and the *background discrimination*. The former procedure involves the data-reduction as mentioned while the latter uses the gained information from the data-analysis to select the true X-ray events and reject the rest as background.

7.1 Raw-Data Format

Raw binary files are made of 4 byte (32 bits) words. The file starts with a run-header start flag that contains the information of the run. After the header, the triggered events are written individually to the raw file. Each event is written starting with an event header providing information about the event timestamp and the trigger counter. Firstly the pulse information of both detectors is written and next the strips information is written from both channels of each CRAM. The event format finishes with an event end label. At the end of the run file, a run-footer is written that includes information about the total number of events and the run end time.

Run Header	**Header Start Label 0x90000000**
	Run Number
	Date
	Date Offset
	Start time
	Run type
	Magnetic Field
	High Voltages
	Header end Label 0x9FFFF000
Event Header	**Event start flag 0x80000000**
	Event ID
	Event time (LabView timestamp)
	Event type
	Trigger 1
	Trigger 2
	Counter

	N_{ADC1} (Number of ADC data of detector 1)
	word×N_{ADC1} Bits 0-16: ADC data
	Bits 16-32: ADC data
	N_{ADC2} (Number of ADC data of detector 2)
	word×N_{ADC2} Bits 0-16: ADC data
	Bits 16-32: ADC data
Strips Data ×4 (Gassiplex 0-3)	**Strips Charge**
	Strip ID
	Validity
	Event end Label
Run Footer	**Foote start label 0x90000000**
	Total number of events
	Run end time

Table 7.1 Data format of Micromegas Raw files where Header, Footer and each event format and information is presented.

The files are stored in a single format named mmRXXXXX.dat, where XXXXX is an increasing number for each run.

7.2 Raw Data Reduction

As noted, the valuable information is extracted from the raw-data file for each event from the strips and the mesh pulse. In order to analyze the background, the closest calibration and pedestal run is used to take into account the systematic effects that affect the detector's conditions.

7.2.1 Strips signal analysis

7.2.1.1 Pedestal subtraction

In order to take into account the analysis of the strips fired, the characterization of each strip is needed. This can be accomplished by the analysis of each strip *pedestal.* The pedestal can be understood not only as the absence of a signal for the strip but also as its typical variance. The strips have an intrinsic electronic noise when there is no trigger from the Matacq to the Gassiplex card. The pedestal can be defined as the level of this noise and it has to be

subtracted from the amplitude of the real event in order to measure the exact charge deposition. The pedestal level is considered in any event and evaluated with the mean and the standard deviation (σ). The strip is considered as *hit* if the charge deposition on this strip is higher than its 3-sigma pedestal level.

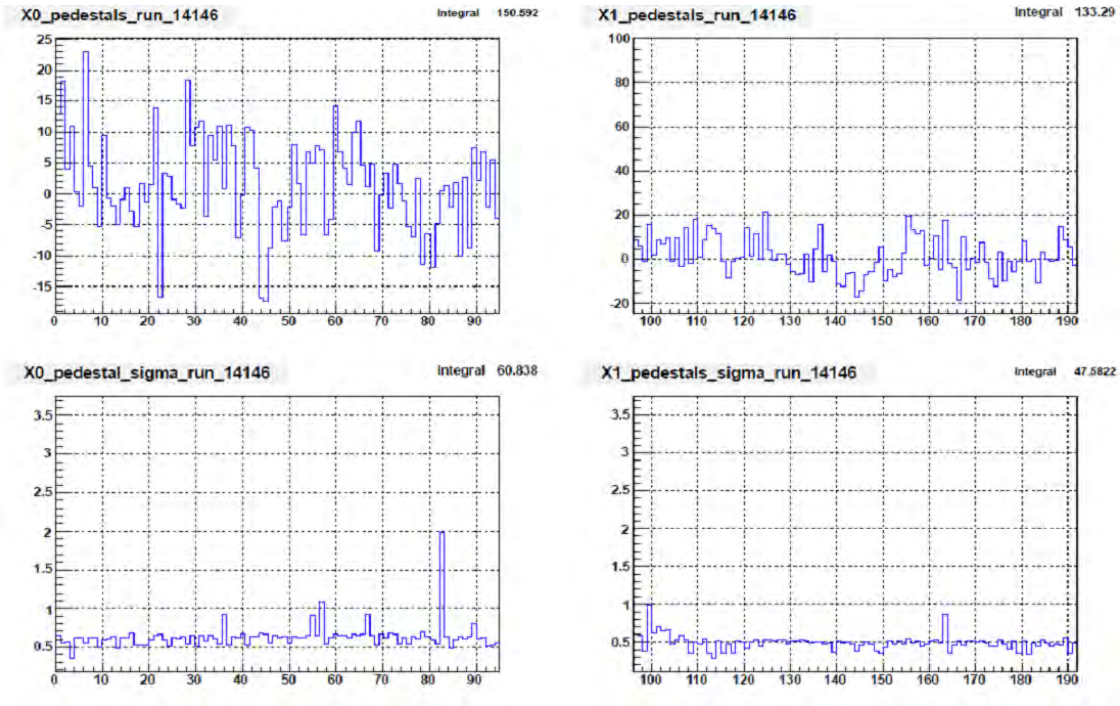

Figure 7.1 Pedestal level for two electronic cards reading the X strips (upper right and left) of the background Run-14146 during 2010 data taking. The corresponding sigmas are plotted in the lower left and right. A similar plot is evaluated for the Y strips.

7.2.1.2 Clustering

After pedestal subtraction, the strips that have been fired are identified and grouped and the events can be evaluated one by one. A cluster can be defined as two or more consecutive strips that have recorded a charge accumulation. Clusters can be identified in X and Y strips. In the case of a missing or a broken strip the algorithm condition allows up to two strips with no charge inside the cluster. When three consecutive strips are found with no charge the condition for the end of the cluster is met.

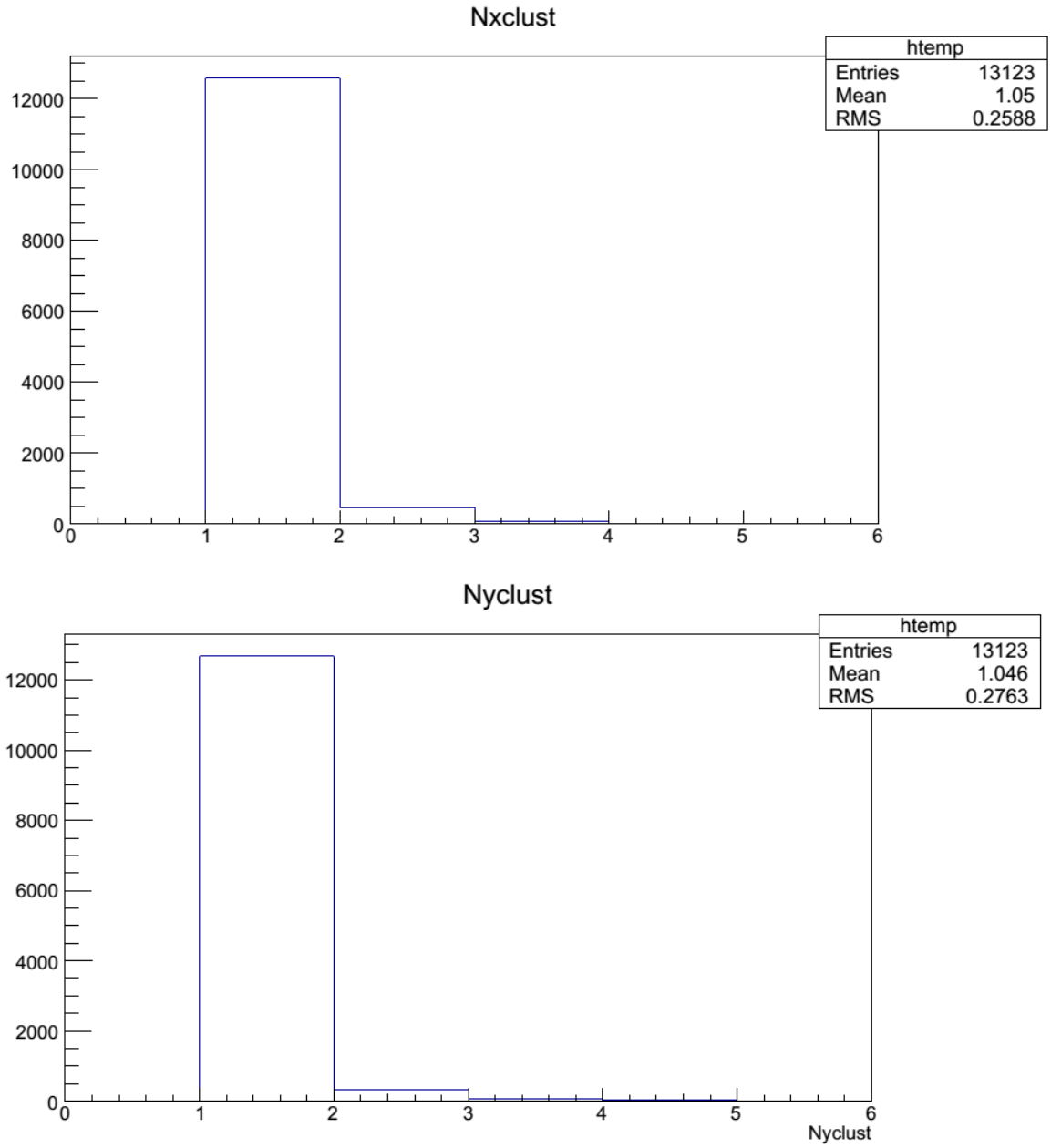

Figures 7.2 X and Y identified clusters per event in a ^{55}Fe calibration run. Note that the entries number are low (13123 events) for a calibration file.

The information that can be extracted from the clusters produced for each event is valuable and can be identified as the following

- *Cluster Multiplicity*: that is the cluster size in terms of the number of strips that have been activated inside the cluster
- *Cluster charge*: A value proportional to the number of electrons that generated the cluster. It is the total charge recorded in each strip of the cluster.
- *Cluster sigma*: It is the cluster size weighted according to the charge detected in each strip
- *Cluster position*: The position of the cluster in strips space

- *Total charge of an event*: the total charge accumulated in X and Y strips from a single event

The X-ray events produce a unique cluster signal by inducing a charge accumulation in some X and Y strips. In the off-line analysis most of the background events can be rejected by imposing the condition that an X-ray event can produce only one cluster.

7.2.2 Mesh signal and Pulse shape analysis

The Matacq card can record the mesh signal with a rate of 1GHz and produces 2500 samples that are recorded in the raw file and analyzed in the off-line analysis. The crucial parameter to be determined is the baseline of the pulse because it affects the rest of the pulse parameters. The noise in the mesh signal can disturb the baseline determination.

There are a few parameters described below that can define the mesh pulse shape and they can be used in a posterior discrimination analysis. The mesh signal provides the energy and temporal information from the triggering event and the energy of the event can be described by the amplitude and the area of the generated pulse. The parameters that are commonly used to describe the pulse shape are the *risetime* and the *width* of the pulse.

The pulse characteristics and observables that are used in this study can be summarized in the following list

***Pulse baseline*:** the baseline voltage offset that is calculated as an average value of the first 100 samples (100 ns). The actual peak starts in 400 ns.

***Baseline fluctuation*:** the standard deviation of the baseline.

Pulse Amplitude (*Peak Amplitude*): the height of the peak in mV that is the *pulse center* value after subtracting the *pulse baseline*.

***Peak Time*:** the time at which the pulse reaches its maximum height.

***Peak Start*:** the time when the pulse has reached the 15% of the peak height before reaching the *peak time*.

***Peak End*:** the time after the *peak time* point, when the pulse has reached the 15% of the peak height.

***Peak Risetime*:** the time length between the *Peak start* time and the time at which the pulse reaches the 85% of the *pulse amplitude*.

***Peak Integral*:** the integral between the *Peak Start* and the *Peak End*.

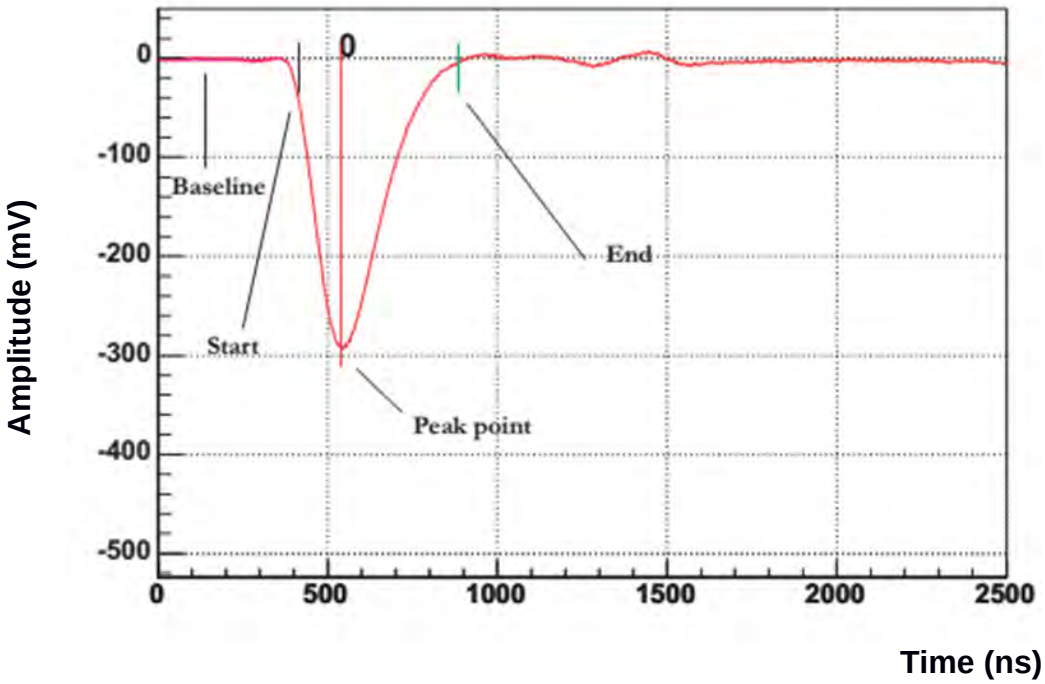

Figure 7.3 A typical pulse signal and the parameters definition is shown

7.2.3 Sunset detector's Calibration and files implementation

In the Sunset Micromegas, calibration is performed daily with a ^{55}Fe source in front of each detector. The main energy peak of this source is at 5.96 keV while the escape peak observed for the Argon gas is at 2.9 keV. The calibration runs determine the energy calibration of the detector because of small daily climate variations observed in the experimental area. A file of this type (calibration run) is written in parallel with the pedestal and the background run in the main file of both detectors.

After the main low level analysis that consists of reading the raw data of the binary file, subtracting the pedestal and creating the clusters, ROOT files are created with the mesh pulse shape analysis variables included. For each run, two ROOT files are created that include the information of the Calibration and the background and where strips variables are estimated after pedestal subtraction.

The calibration file is used in order to set the optimum set of observables for timing, spatial and energy estimation. The closest calibration file can be used in the case when a calibrator is malfunctioning or any intervention is performed in the Sunset micromegas.

A typical XY distribution of events in the Sunset Micromegas 2 (Jura side) can be seen in Figure 7.4. The energy calibration can provide the actual energy calibration of the instrument and the events produced can be used to create the X-ray profile in the detector.

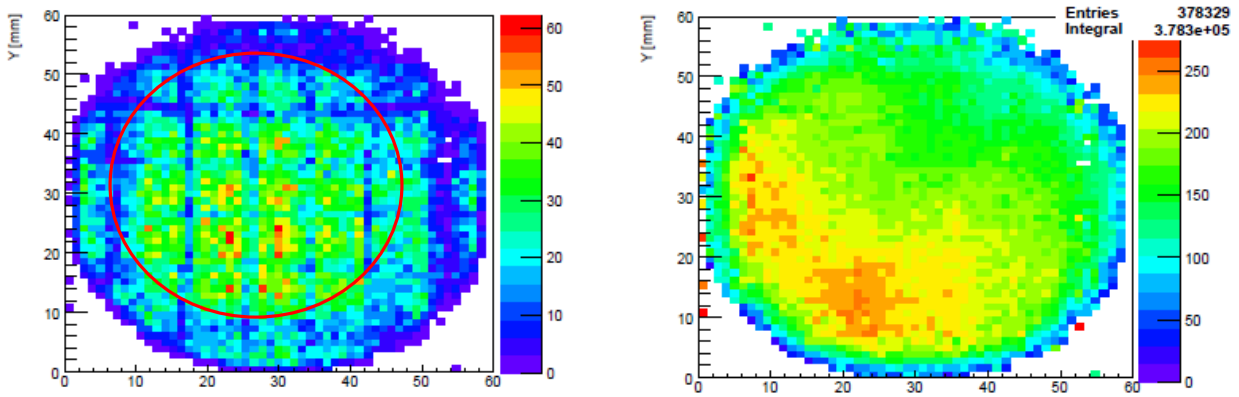

Figure 7.4 On the left the X-Y distribution of events produced in the strips of the Sunset detector 2. The cold bore area is denoted with the red circle. On the right the charge distribution of the Sunset Micromegas 2 in the same calibration run is shown. As can be seen the accumulation of the charge is not so uniform and that has an impact on the detector's gain and efficiency.

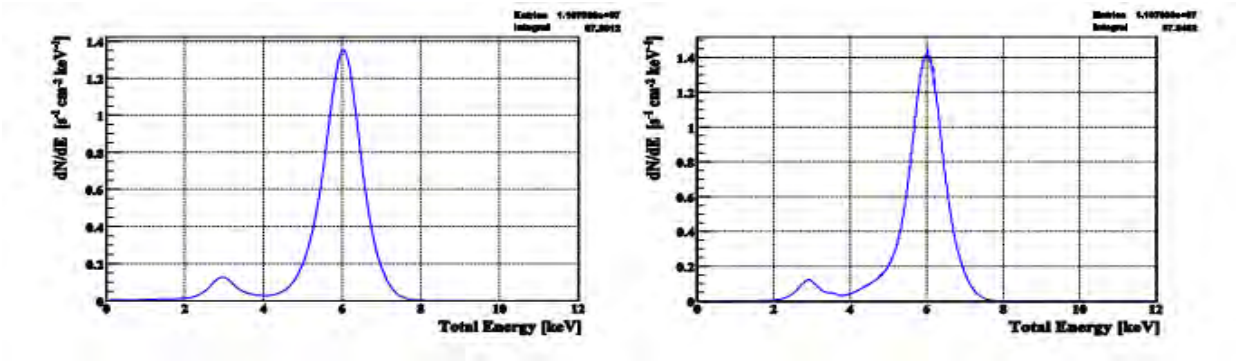

Figure 7.5 Calibration energy spectra for strips (right) and mesh (left) in SS1

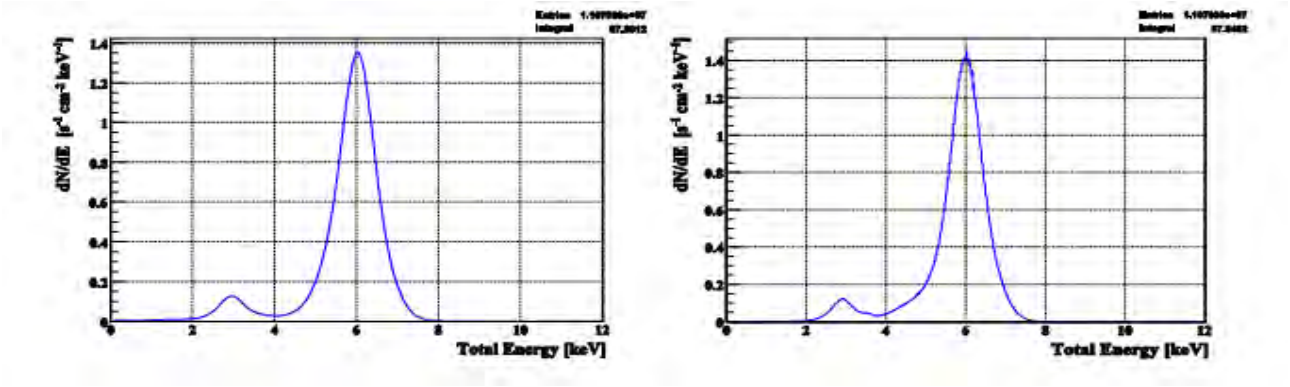

Figure 7.6 Calibration energy spectra for strips (right) and mesh (left) in SS2

The parameters, like the cluster energy, the charge accumulated in the strips and the mesh pulse amplitude, can be also extracted because these parameters provide valuable information about the energy of the background events. These parameters are plotted in the figure 7.7.

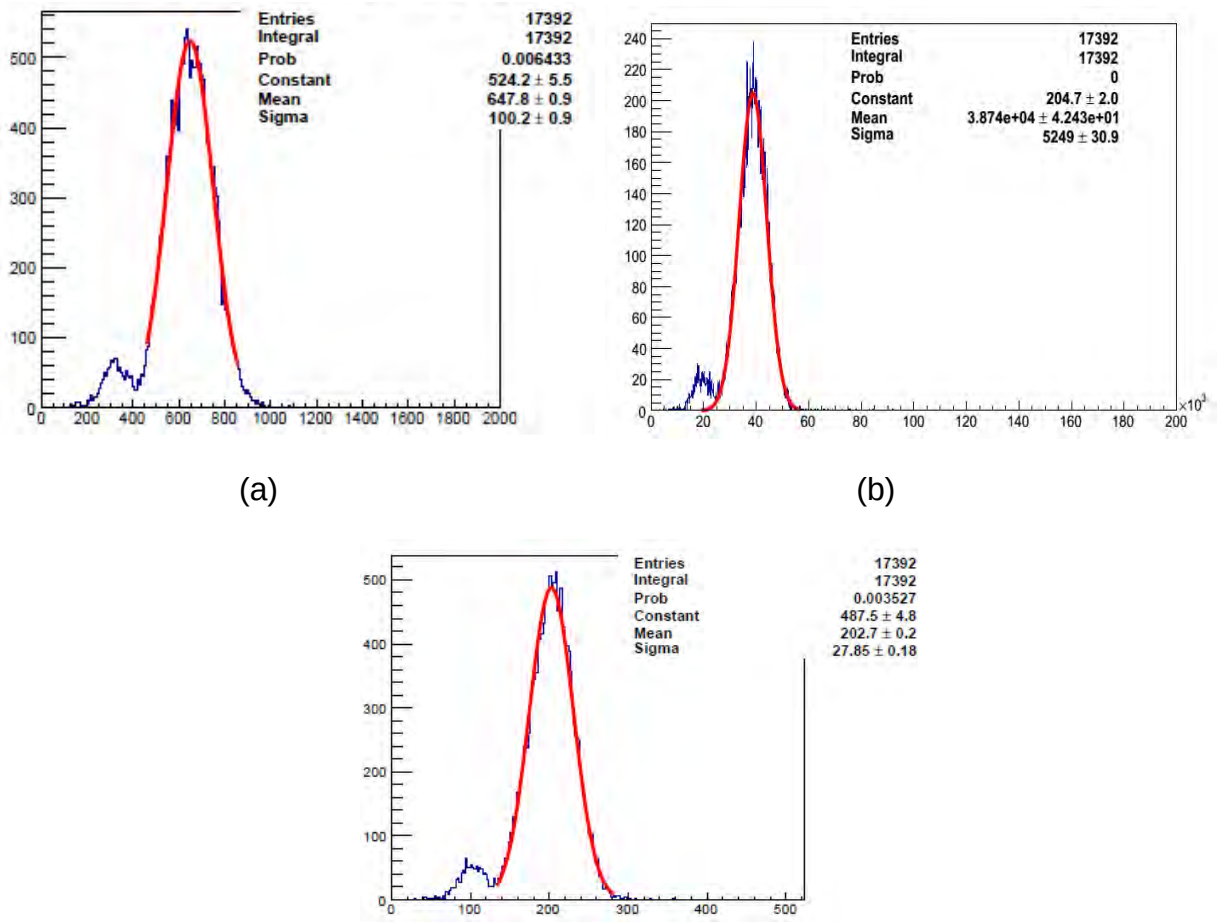

Figure 7.7 In (a) the strips charge is plotted, while in (b) the pulse integral. In (c) the pulse amplitude is shown. In all plots the fit is represented in red and the fit parameters are used to determine valuable information such as the total number of counts, the energy and the strips total charge.

7.3 Background discrimination

In order to apply the selection analysis many versions of algorithms have been designed. The common idea relies on the definition of *n observables* that can show similar characteristics to the calibration runs. Discrimination criteria can be applied to all events observed in the background runs and events that their *observables* are alike to the ones extracted from the calibration runs are identified as X-rays.

A straightforward analysis implementation is the ***Selection Criteria Analysis*** **(SCA)** first used by Dr. Theopisti Dafni [122] in CAST's Micromegas data, with the main development supporter of this algorithm being Dr. Thomas Papaevangelou.

For any observable, a tolerance range is defined from the calibration distribution and that defines an upper and a lower limit. The distribution can be considered as Gaussian and by

fitting methods limits, it can be deduced that this affects also the software efficiency. Correlations between different observables can be used as defined criteria that are applied sequentially in all events produced in the mesh and the strips. One or two dimensional criteria are used in order to define the acceptance range or area of interest. These criteria named as *cuts* are applied to the calibration data in order to estimate the software efficiency; that is the percentage of events that are accepted by applying the cuts and to background runs in order to estimate the background level.

The performance of the evaluated discrimination criteria (and CAST's experiment sensitivity) depends on the factor

$$\varepsilon/\sqrt{b} \tag{7. 1}$$

Where ε is the total detector efficiency and b the background level. This factor is called Figure Of Merit (FOM) and defines the discovery potential and the capability of better exclusion when no axion signal has been observed.

7.3.1 Manual selection cuts

The selection criteria used in case of SCA and in Multivariate analysis (MVA), first introduced in CAST by Dr. Kostas Kousouris, make use of two preliminary cuts that are applied to data after manual selection:

Fiducial selection

X and Y strips should be inside a circle that corresponds to the cold bore aperture

$$\sqrt{X^2 + Y^2} \leq 21.5 \text{ mm} \tag{7. 2}$$

All photons that are converted in the magnet conversion region should fall into this area.

One-cluster selection cut

$$N_{Xcluster} = 1 \quad \& \quad N_{Ycluster} = 1 \tag{7. 3}$$

This cut assures the charge deposition on X and Y strips in only one cluster.

7.3.2 Automatic selection cuts

The selected observables define a parameter space and the statistical methods used in SCA provide a *selection volume* where mainly X-rays events are likely to be found. The *selection volume* is chosen by inspecting raw-data and by using basic geometrical shapes that include the main X-ray population events on the parameter space. These 1D or 2D dimensional selection cuts are applied one after the other at different projections on the parameter space.

The selections are based on the contour plotting abilities of ROOT that is an analysis tool developed at CERN.

7.3.2.1 2D Multiplicity Cut

In this cut a selection of the strips multiplicity is applied to a 2D space. The selection is based on the requirement that the multiplicity in both axes could not be more than 13.

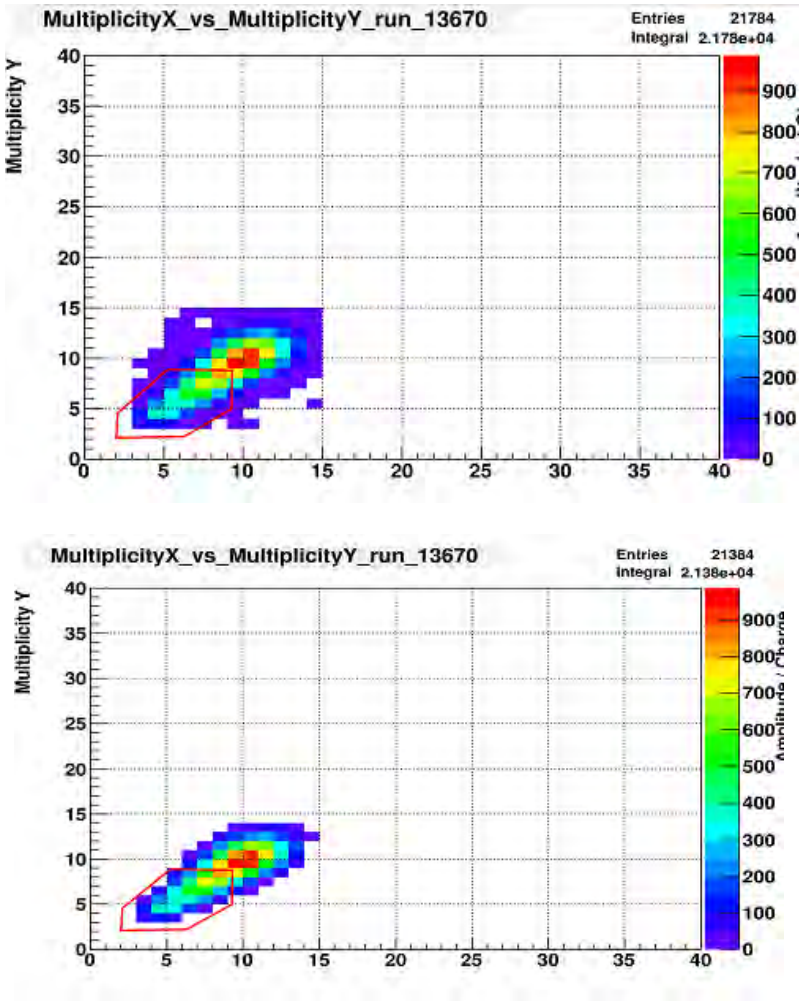

Figure 7.8 A 2D multiplicity cut where the original contour is shown in the top picture and the selected at the bottom.

7.3.2.2 2D sigma cut

Cluster sigma defines the cluster size weighted with the charge detected in each strip. By applying this cut, the width of the cluster shape and charge distribution is finite and topologically defined.

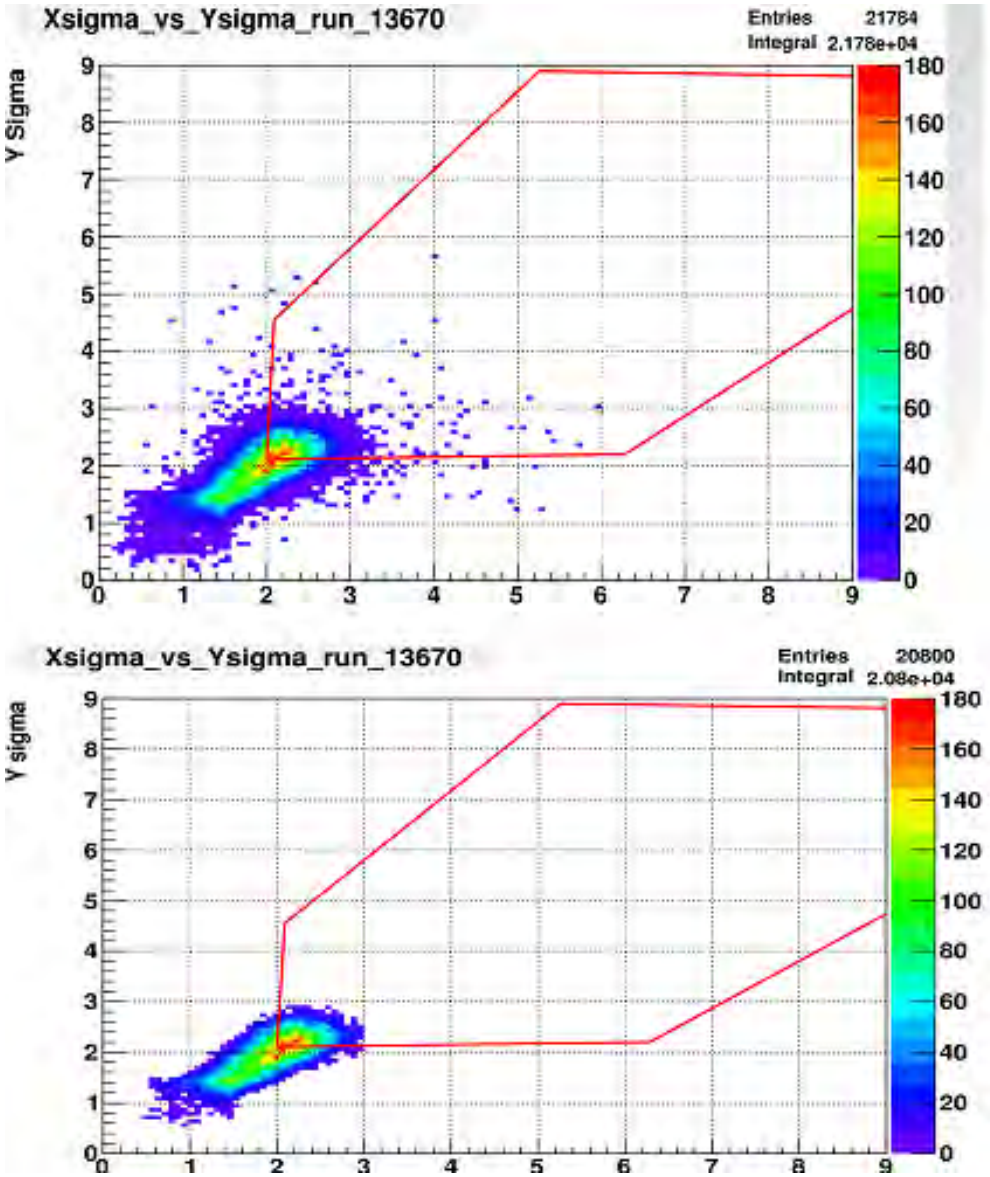

Figure 7.9 The original (top) and the cut selected (bottom) 2D sigma distribution of a calibration run.

7.3.2.3 2D mesh defined selection cuts

More complicated selection criteria can be defined by using the mesh information and observables. The ratios of the *peak amplitude/peak integral*, *peak risetime/pulse duration* and the ratio of *peak mean time/peak pulse width* can be used by specifying geometrical values that define x-ray events.

The ratios mentioned can be used in addition with other observables by fixing the parameter space of acceptance. The method applied for these selection criteria is the following:

A contour plot is created and its geometrical shape is divided in 100 equal species that are bin dependent. The cut is weighted according to the entries (number of events) and the 3 or more outer species that are less populated are rejected.

This procedure is also known as a **contour cut analysis**. The contour levels of acceptance are in general the most populated. In the figures 7.9 and 7.10 the 2D plots of this method using the observables ratios are presented.

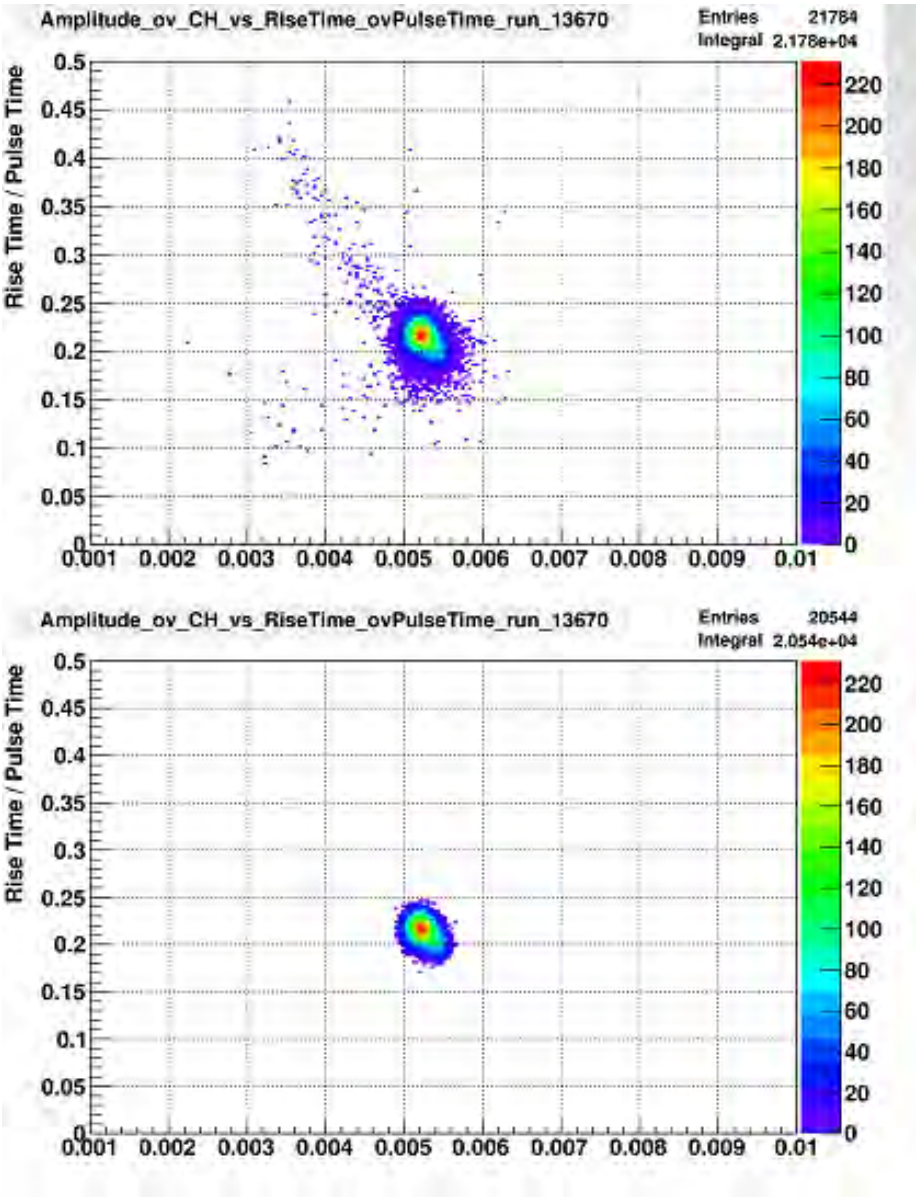

Figure 7.10 The X-axis is defined by the ratio *peak amplitude/peak integral* while the Y axis is defined by the ratio *peak risetime/pulse duration*. A weighted contour gets created in ROOT that is composed of 100 equal weighed species. The outer three are rejected and the selection is shown at the bottom plot.

The next selection cut (Figure 7.10) is defined by the ratio of *peak risetime/pulse duration* versus the ratio of the *peak amplitude/peak charge*.

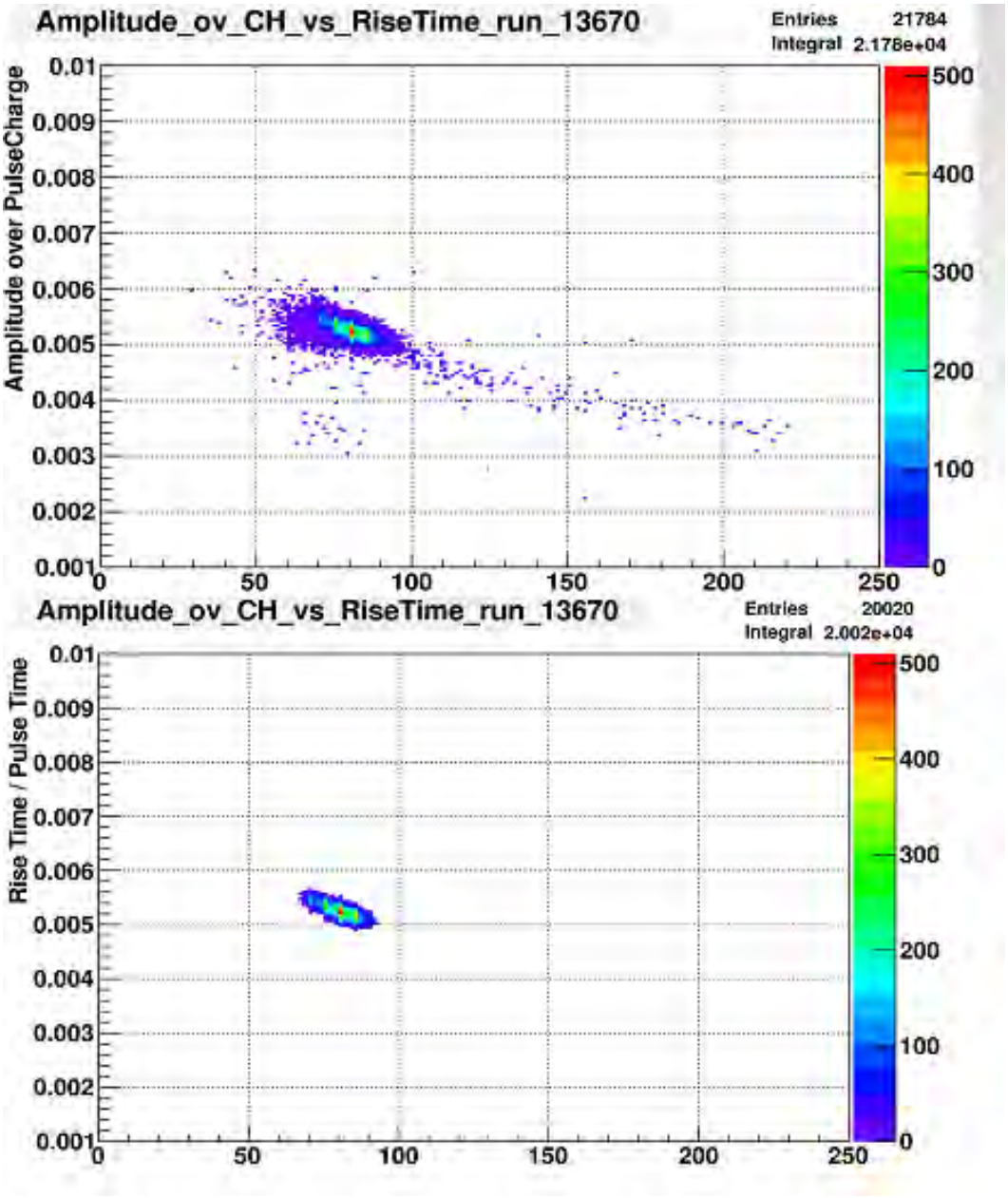

Figure 7.11 Y-axis is defined as the ratio of *peak amplitude/peak charge* and the X-axis is the *peak risetime/pulse duration* in a calibration run.

7.3.2.4 Baseline Fluctuation

The baseline fluctuation is the calculated standard deviation of the baseline. The 98% of the x-ray events distribution is selected from the calibration runs. Background events that have baseline fluctuations outside of the selected region are rejected.

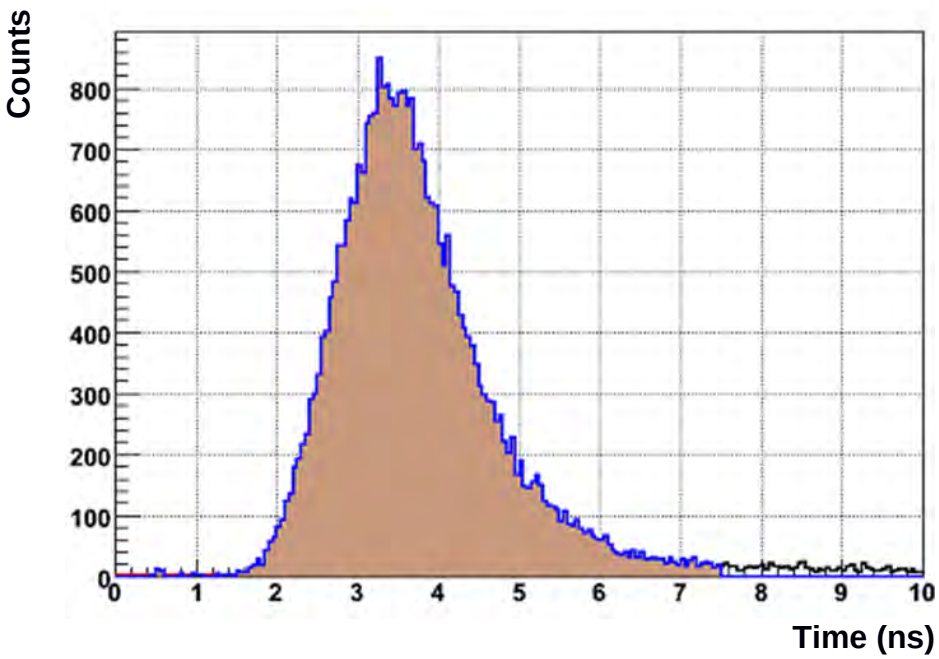

Figure 7.12 The 98% of the distribution of the baseline fluctuation is reserved from the calibration runs as shown in the figure. Events with baseline fluctuation outside of this region are rejected as background.

7.3.3 Conclusions

Contour cuts are advantageous when distributions are not Gaussian and the observables correlations are not linear. Multivariate statistical methods for the Sunset Micromegas detectors background discrimination have been studied in [123] by Cenk Yildiz, for 2008 data. The FOM for 6 keV events is method independent and for 2.9 keV the method comparisons show that it is detector dependent. In a stable and reliable Micromegas detector of good energy resolution the SCA can be beneficial and advantageous to background discrimination.

8. Sunset Micromegas data taking and background levels of 2009 and 2010

8.1 Introduction

In 2007, the CAST experiment moved to the second part of the Phase II, for which the system was thoroughly upgraded to use ^{3}He inside the magnet cold bore instead of ^{4}He. The advantage of ^{3}He is that it has higher vapour pressure than ^{4}He (135 mbar c.f 16.4 mbar) at 1.8 K, permitting CAST to use higher densities inside the cold-bores and thus continue exploring higher axion masses. That led CAST to explore the most interesting area in the axion phase-space and close the upper Hot Dark Matter axion mass limit of 1 eV. Data taking with ^{3}He started in 2008 and continued in 2009 and 2010. The status and analysis of the data taken in 2009 and 2010 with the Sunset Micromegas will be presented in this study. The final background and tracking analysis of the data measured will also be presented, as also the upper-limit of the axion-photon coupling in the axion mass range explored.

8.2 Data taking overview in the 2009 run

In 2009, the CAST system operated with the X-rays windows unheated and so the temperature profile of the pipes connected to the magnet cold-bores changed significantly. Since the gas density inside the cold-bore increased, the heat load on the cryogenic circuit also increased to an unacceptable level. In order for the experiment to run with unheated X-ray windows the vacuum system of the magnet and detectors has been upgraded.

CAST started the 2009 data taking on 15/07/2009 at the density setting #420 that corresponds to 37.5 mbar at 1.8 K. The 2009 run finished on 08/12/2009 and during that period 247 density settings were covered with a density step size of 1.4 dP (dP is the nominal pressure setting of 0.1 mbar).

The data taking efficiency for the 2009 run was 83%. The density that corresponds to the 2009 run end setting was 65.2 mbar at 1.8 K. During the 2009 run there were stoppages for interventions or due to quenches that are presented as gaps in Figure 8.1. The last pressure setting measured on the 8th of December was the #647 and the axion mass range covered is 0.66-0.88 eV/c^2.

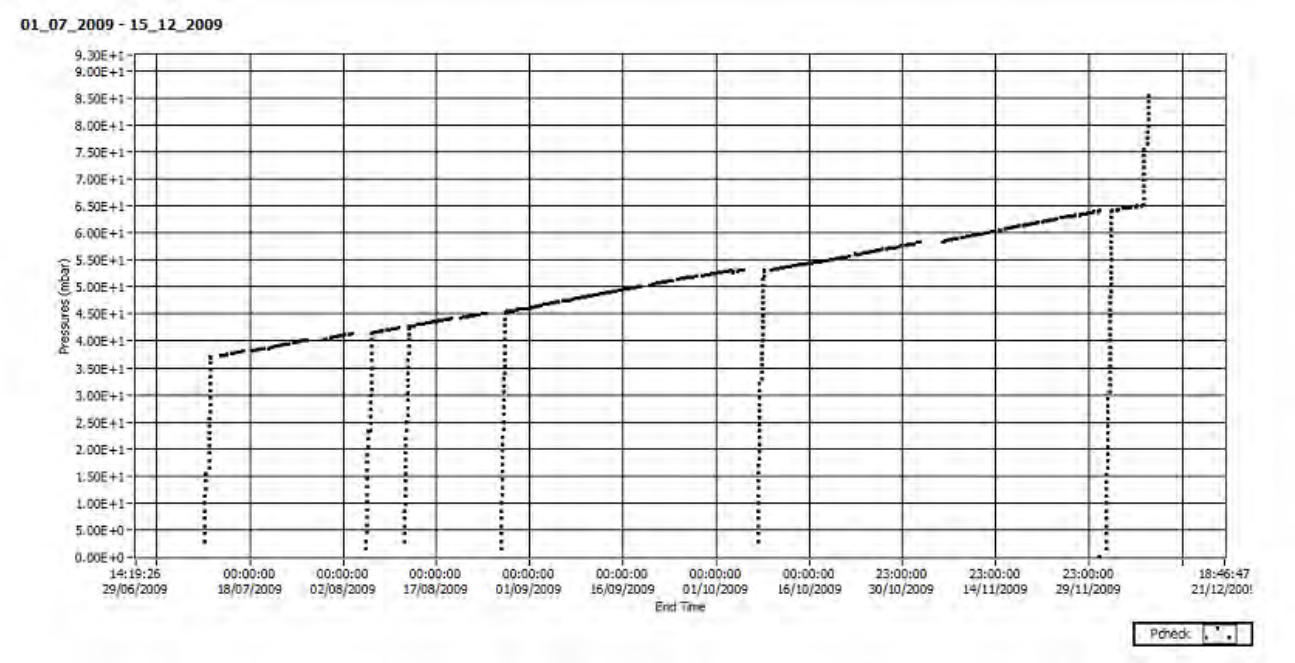

Figure 8.1 The pressure evolution in the cold bore for the data taking period of 2009. The time gaps shown represent the stoppages due to interventions, emptying of the cold-bore because of bake-outs, quenches and power cuts. P_{check} refers to the cold-bore pressure being corrected to 1.8 K.

As noted in Figure 8.1 there are some time gaps because of events that delayed the data taking. The most important events that occurred can be summarized in the following

- *PLC ^{3}He control program bug on 27th of July 2009*

There was a programming bug in the PLC software that controls the ^{3}He circuit of the CAST gas system. The bug resulted in a false quench signal and the Helium gas evacuated to the expansion volume.

- *Quench on the 3rd of August 2009*

A power cut in the CAST experimental area discharged the quench heater of the magnet. Due to this event, it was decided to perform a bake-out procedure for the cold windows. After refilling the ^{3}He into the cold-bore, data taking started again on the 7th of August.

- *Normal quench on the 25th of August 2009*

The magnet quenched before the morning tracking. Data taking was resumed on the 29th of August *2009*.

- *Planned stoppage for windows bake-out*

In early October 2009 there was a planned stoppage (5th -8th) of 3 days during which the ^{3}He gas was removed from the cold-bores and a bake-out of the cold windows was performed at ~200K. During these days there was a regeneration of the filters and cold traps of the ^{3}He system.

- *The "bird and baguette" incident of the 3rd of November 2009*

There was an incident in the short circuit of the LHC machine 18kV power supply at PA8 that occurred in the switchyard directly opposite to the CAST zone. The incident resulted in a power cut, but surprisingly no quench occurred. The ^{3}He gas evacuated from the cold bores to the storage vessel. After three days the system recovered and data taking restarted.

- *Quench on the 2nd of December 2009*

The quench was caused by a power cut in SR8 (CAST site area) that triggered the quench heaters to discharge into the magnet. The ^{3}He was rapidly recovered by the system and refilled into the cold-bore in order to complete the 2009 running period.

8.3 Sunset Detectors Data Taking in 2009

The Sunset detectors used in the data taking period of 2009 were the M10 for Sunset 1 (Jura side in CAST experimental area) that later on was replaced by M14 because of sparking problems. In the Sunset 2 (Airport side) the M9 detector was used for all the data taking period of 2009. All detectors used are microbulk detectors.

In 2009 many incidents and changes were performed in Sunset Micromegas detectors. This was due to CAST user interventions and various noise problems that occurred and the malfunction of the Sunset 1 (M10) that led to the change of the microbulk detector to a M14 version. This rather peculiar year for Sunset detectors included incidents that affected the detectors performance and stability, but fortunately for a short period during data taking. The incidents can be summarized as follows

- 24.08.2009: Because of noise problems Sunset 1 detector's threshold changed from 30 mV to 60 mV. The Sunset 2 threshold changed from 90 mV to 110 mV.
- 22.08.2009: the trigger rate increased from 1 Hz to 8 Hz.
- 30.08.2009: In Sunset 2 the threshold changed to 65 mV and in Sunset 1 to 40 mV.
- 05.09.2009: The concentration of isobutane in the gas mixture used for the Sunset Micromegas changed. The bottle used had isobutane concentration 2%, while the next one used had 2.3% isobutane concentration.
- 07.09.2009: There were high currents observed in Sunset 1. The gas flow rate was changed to 5 L/h, from the previous rate of 2 L/h.
- 10.09.2009: The gas flow rate was reduced to 2 L/h.

- 15.09.2009: Due to Sunset 1 detector problems (bad strips, sparks etc.) the detector was replaced by M14.
- 16.09.2009: A new Gassiplex card was connected to the Sunset 1 Micromegas.

In the raw data analysis performed there were problems in the strips decoding. That affected the clustering and the results of the detectors analysis. The problem was solved after contacting the Gassiplex Company, which provided a new decoding numbering system for the strips.

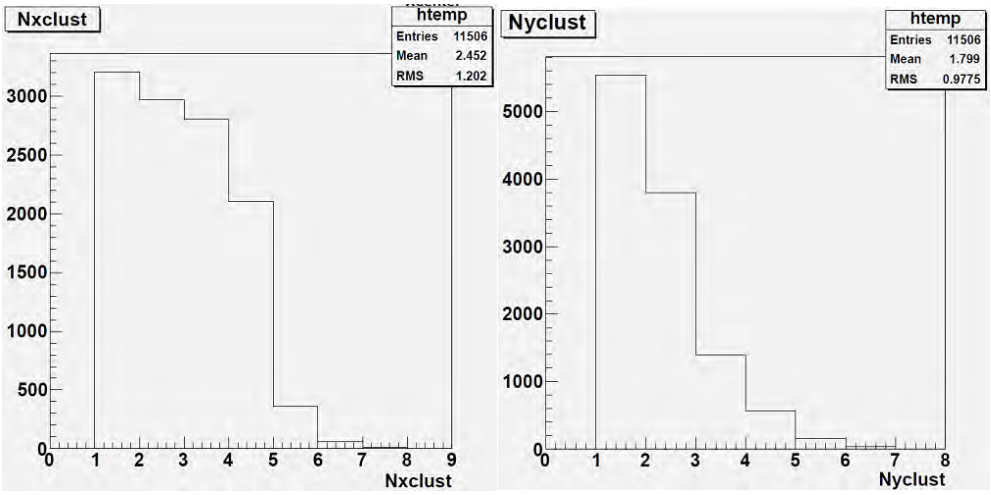

Figure 8.2 The result of the wrong decoding in Sunset 1 Micromegas detector. Cluster is defined as two or more consecutive strips that recorded a charge. The number of clusters per strip axis X or Y should be 1 for most of the events. The plot shows that more of the events recorded has number of cluster ≥ 1.

In the figure 8.3 the Calibration overview shows the bad Sunset 1 detector performance due to broken strips.

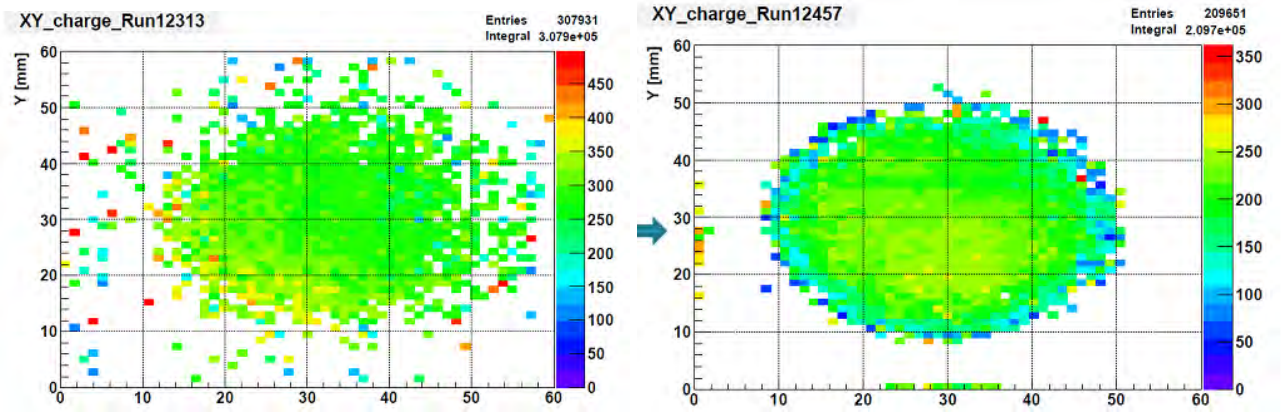

Figure 8.3 On the left the charge accumulation before the Sunset 1 detector change. The right plot shows the much better performance of the detector after its replacement by M14.

On 15th of July 2009 after the test shift of the 13th of July, the data taking starts for Sunset Micromegas.

8.3.1 Sunset detectors stability and gain performance

Figure 8.4 shows the gain evolution as a function of time for both sunset detectors. As noted, the Sunset 1 detector was replaced on the 15th of August, and a M14 microbulk detector was used for data taking after the intervention procedure. The problems of the detector stability before change, as also the voltages modifications applied by CAST users in both detectors, are exposed in the figures 8.4 and 8.5. Those changed were made due to noise problems or by high currents induced during the data taking period. Mechanical stresses and vibrations produced by the magnet movement can also affect the gain history.

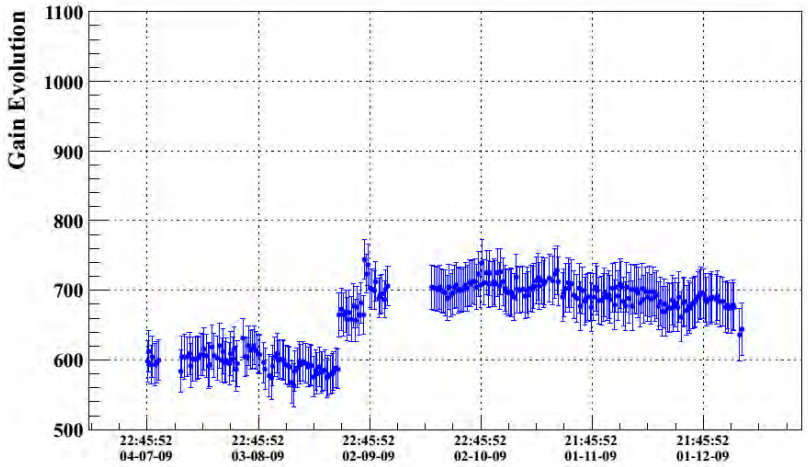

Figure 8.4 Gain evolution for strips in the Sunset 1 detector. After sparking and low detector performance the detector was replaced on 15/09 from M10 to M14. The Sunset 1 detector shows better gain stability after its replacement.

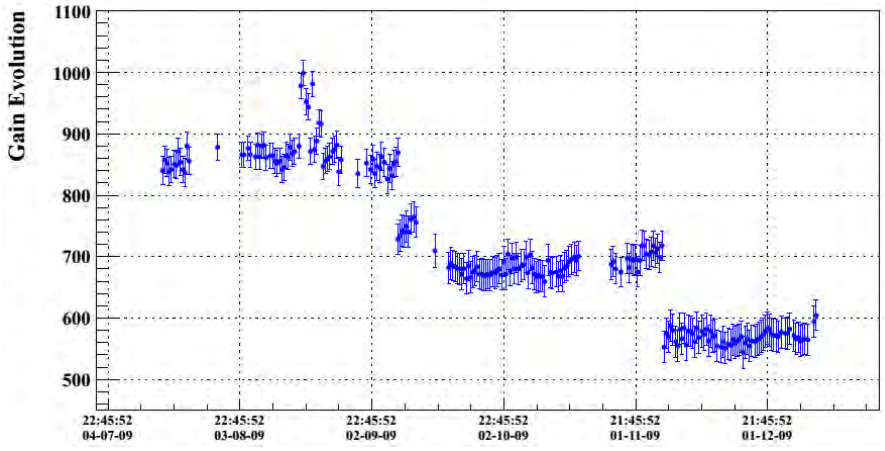

Figure 8.5 Strips Gain evolution for Sunset 2. Many voltage changes are seen that affect and modify the detector's Gain during the 2009 data taking. Due to interventions there are also some gaps because of a lack of calibrations in Sunset 2 in October 2009.

In figure 8.6, the energy resolution for both Sunset detectors is shown. The energy resolution of Sunset 1 shows the sparking problems and its instability. Sunset 2 (M9) shows robustness and low energy resolution.

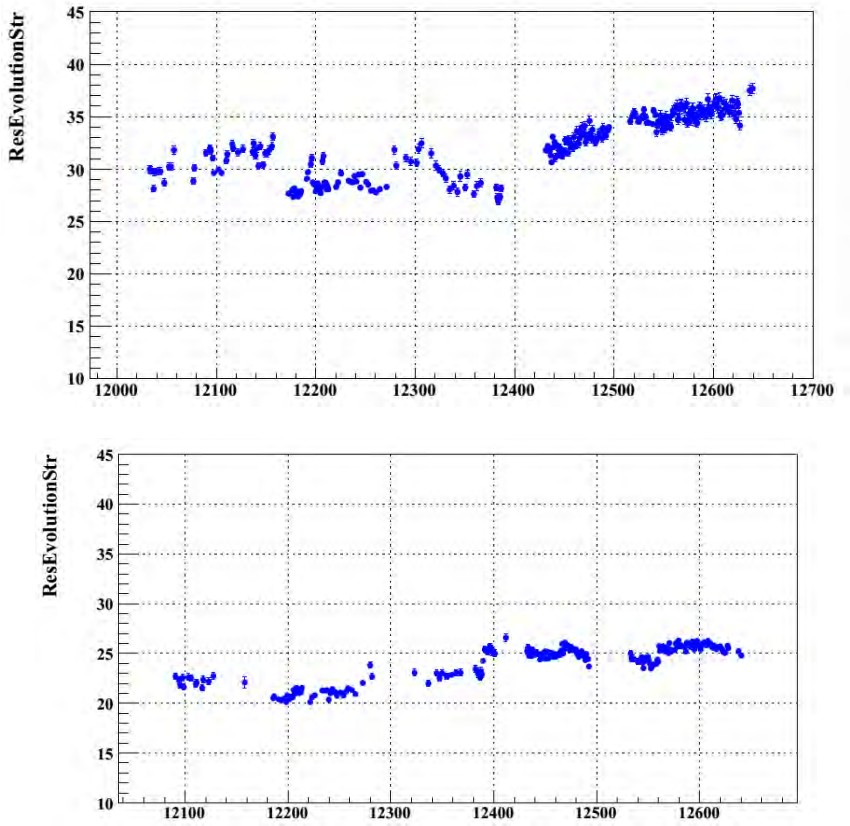

Figure 8.6 Energy resolution on the Sunset detector's strips versus Run number files. In the upper figure the Sunset 1 detector shows instability and high energy resolution even after its change to detector M14. In the lower figure Sunset 2 (M9) shows better performance and lower energy resolution.

The Sunset 1 detector's problems before its replacement on the 15th of September can also be shown in the energy resolution plot of the Mesh. The energy resolution of the Sunset 2 (M9) is remarkably stable and around 18%, while the Sunset 1 energy resolution after its change is ~30%. Figure 8.7 shows the Mesh energy resolution for both detectors in 2009.

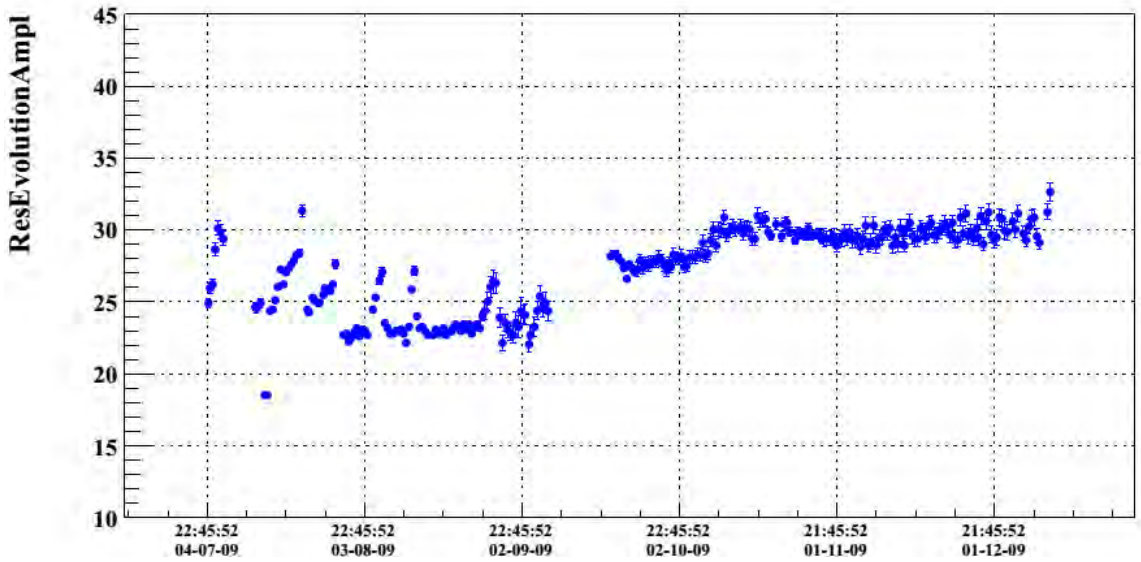

Figure 8.7 The energy resolution of the mesh signal in Sunset 1 is shown. Before the detector replacement (15/09/2009), the resolution is unstable because of sparking problems.

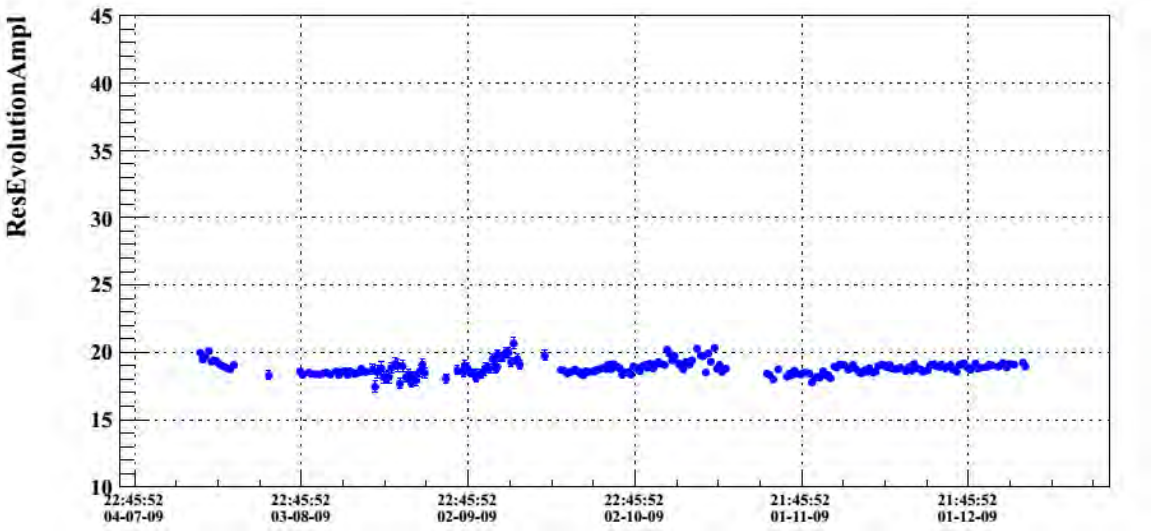

Figure 8.8 The Sunset 2 energy resolution is shown, that is remarkably stable and ~18%.

8.3.2 Efficiency of the selected criteria

The desired X-ray selection becomes optimum when the *selection volume* chosen, maximizes the number of calibration accepted events and that defines the software efficiency. The relation that can be used to estimate the selection criteria efficiency is the following

$$Efficiency\ [\%] = \frac{\int_{m-0.25}^{m+0.25} dN(after\ cuts)}{\int_{m-0.25}^{m+0.25} dN(before\ cuts)} \qquad (8.\ 1)$$

where m= 5.9 keV is the peak of the ^{55}Fe calibration events.

The efficiency is calculated for the events recorded on strips and the mesh separately, according to the selection criteria applied, since in high rate triggering during calibration there are uncorrelated mesh and strips characteristics. In the next figures calibration profiles, spectra and the efficiencies in both detectors are shown. The calibration method used is by applying a moving source of ^{55}Fe behind the detectors. The calibration system changed in 2010 and the detector illumination is made from its front side.

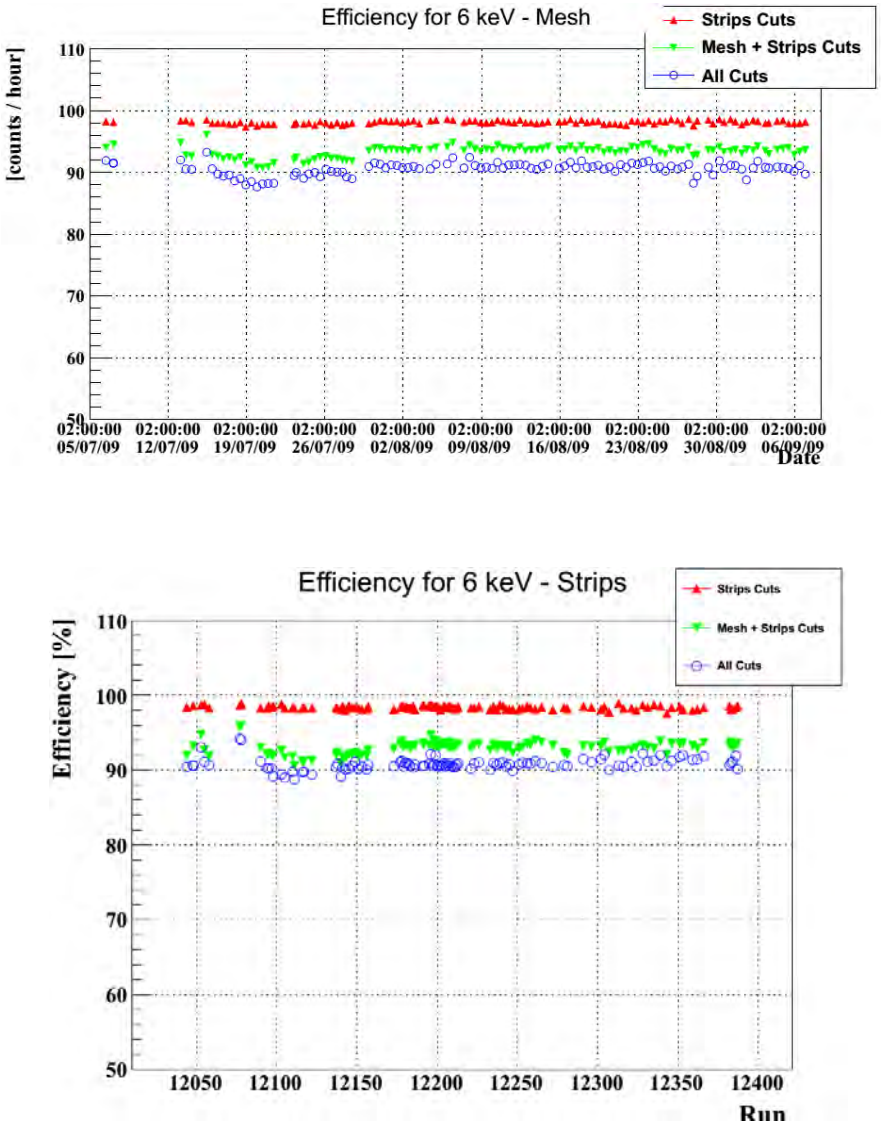

Figure 8.8 The software efficiency in the mesh (top) and strips (bottom) for the 5.9 keV events of the Sunset 1 detector before its replacement. The efficiency is quite stable and ~90%. In the top plot the efficiency is plotted against date while in the bottom against Run number.

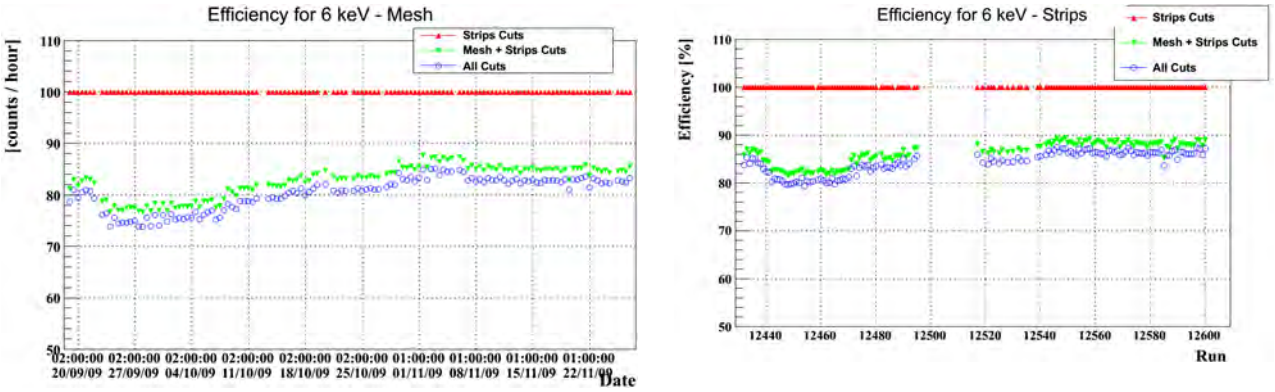

Figure 8.9 The software efficiency with the mesh (left) and the strips (right) for the 5.9 keV events of the Sunset 1 detector after its replacement. The efficiency is not so stable and it is around 85%. In the left plot the efficiency is plotted against date while in the right the efficiency is plotted against Run number.

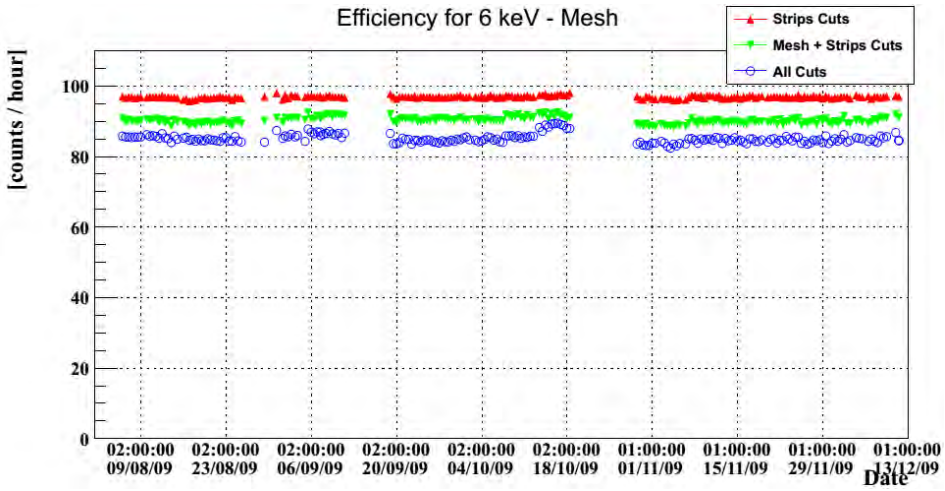

Figure 8.10 The software efficiency with the mesh signal for the 5.9 keV events of the Sunset 2 detector.

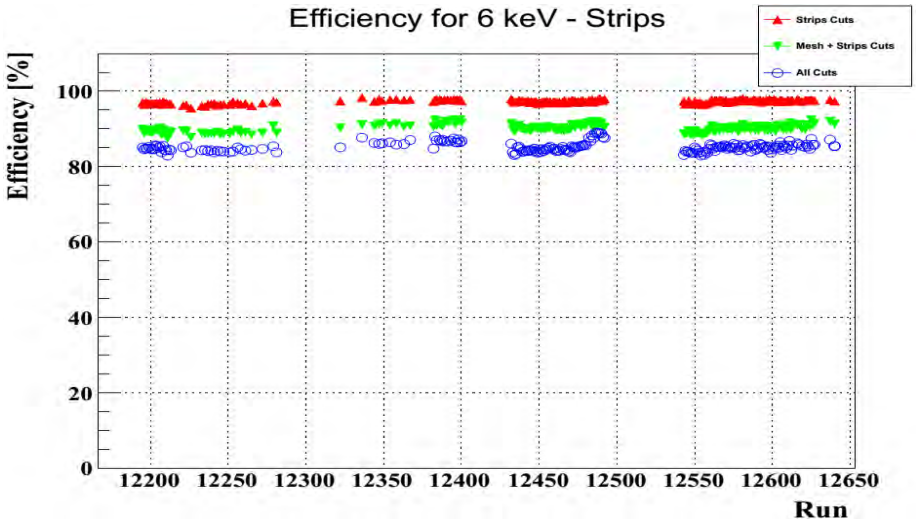

Figure 8.11 The software efficiency in the strips for the 5.9 keV events of the Sunset 2 detector.

Calibration Plots

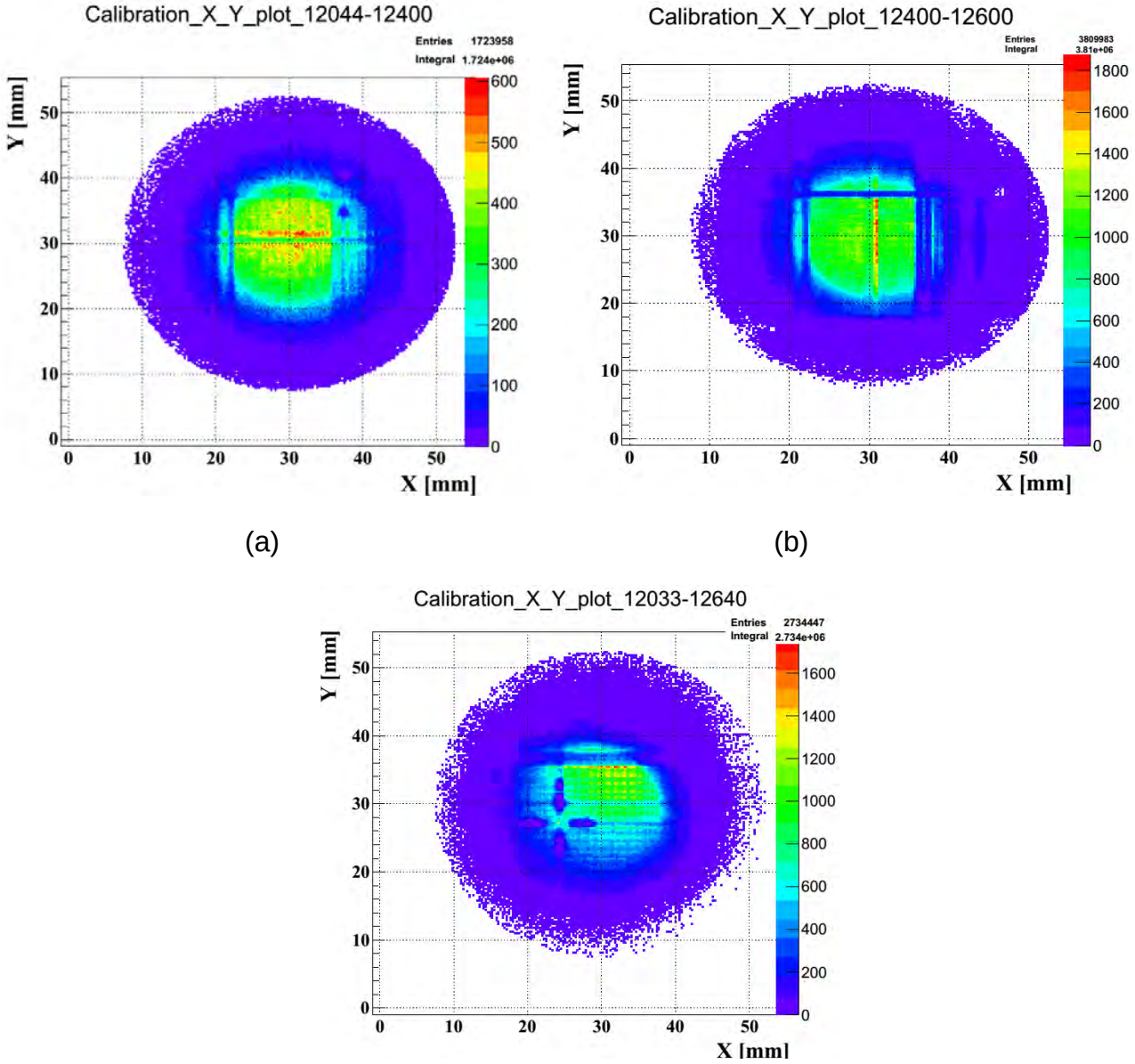

Figure 8.12 The Calibration profiles of the Sunset detectors. In (a) and (b) the profile of the Sunset 1 is shown before (left) and after (right) the detector change. In (c) the X-Y profile of all the calibration events in 2009 for the Sunset 2 detector is shown.

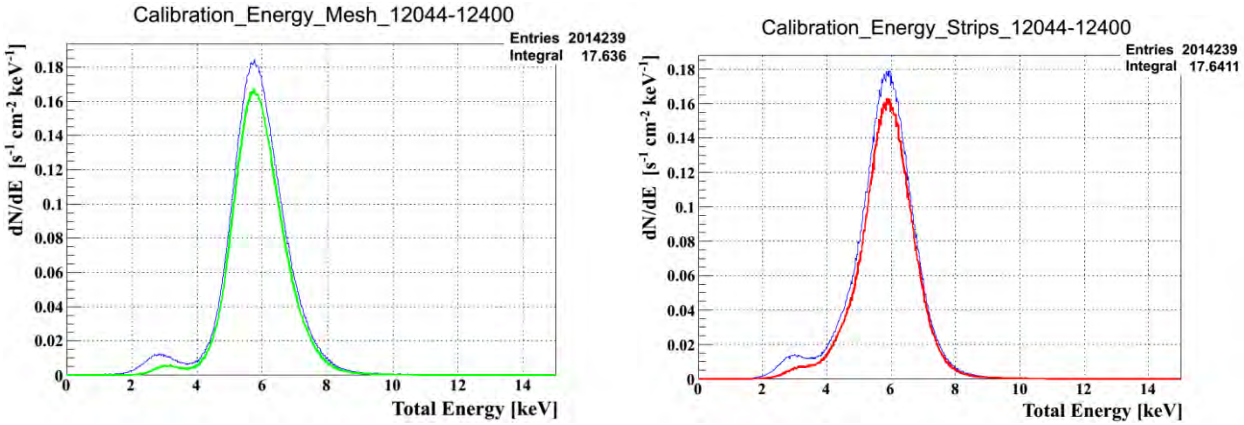

Figure 8.13 Calibration spectra for the mesh (left) and strips (right) for the Sunset 1 before its replacement. The blue line corresponds to the spectra without selection criteria applied, while the green and red lines show the energy spectra after the cuts application.

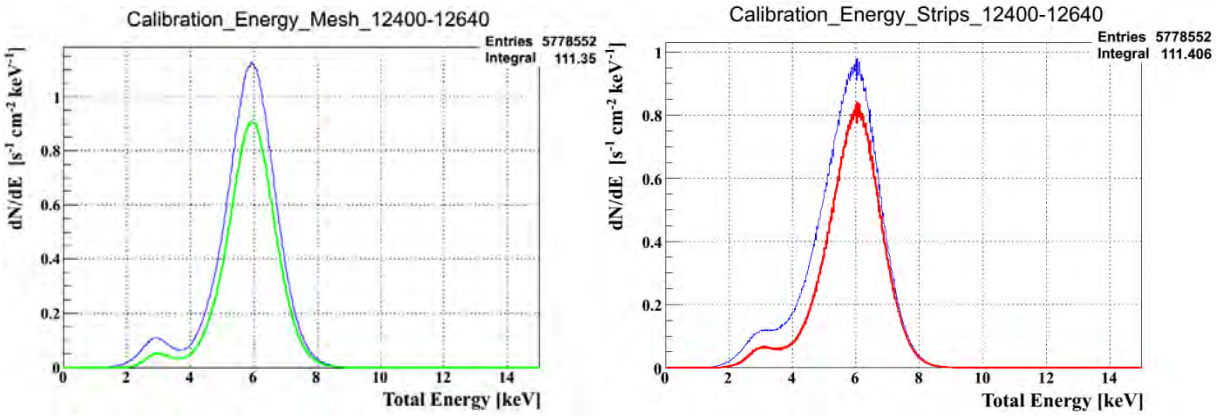

Figure 8.14 Calibration spectra for the mesh (left) and strips (right) for the Sunset 1 after its change. The blue line corresponds to the spectra without selection criteria applied, while the green and red lines show the energy spectra after the cuts application. The energy resolution in the strips is not sufficient good.

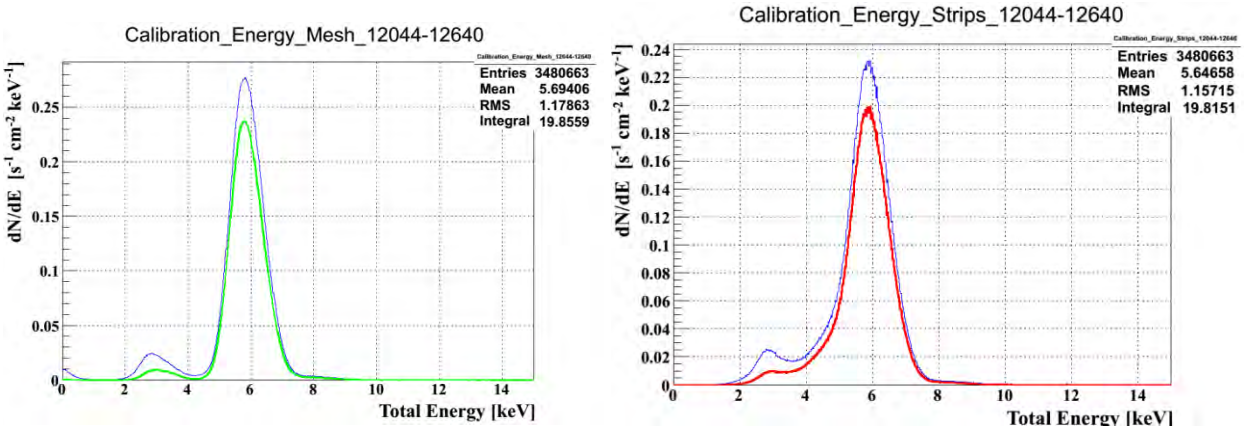

Figure 8.15 Calibration spectra for the mesh (left) and strips (right) for the Sunset 2. The blue line corresponds to the spectra without selection criteria applied, while the green and red lines show the energy spectra after the cuts application.

8.3.3 Background and Tracking Data of 2009

The final background of 2009 was obtained by applying the selection criteria (cuts) described in the previous sections. The cuts efficiency at 6 keV for both detectors is above 85% and the software efficiency for the 3 keV peak (estimated from the Argon escape peak in calibration selection), allows to take into account low energy axions. The selection criteria were used for the three detectors in the Sunset side of the magnet for 2009 data.

Background events are selected from the raw files generated twice a day (that include also the tracking information) and X-ray discrimination rules are applied in order to reject the non-X-rays events. Background files with recording time less than 5 hours are rejected unless they include tracking information. This is due to the estimation of the mean background of the surrounding days. For each tracking, 6 nearby days are taken into account for the mean background estimation.

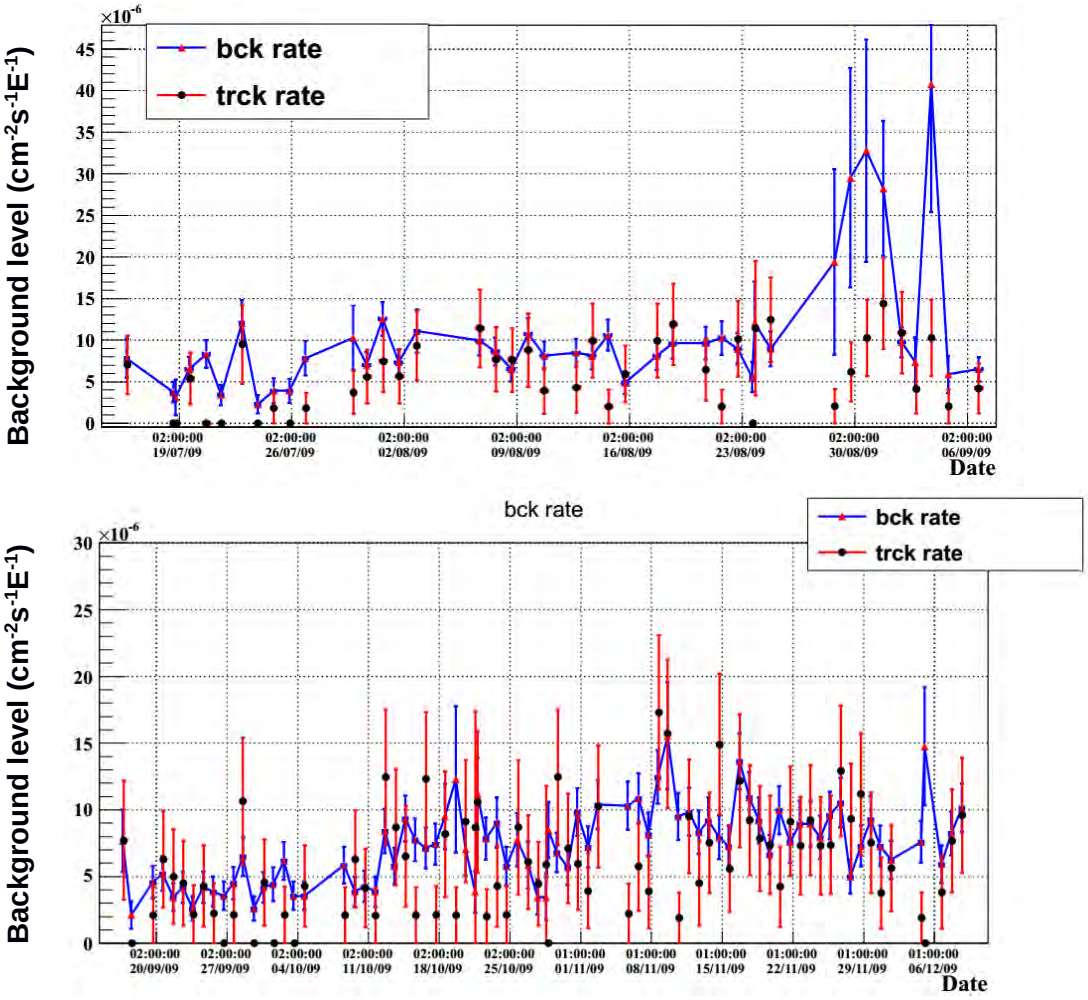

Figure 8.16 Background and tracking levels of the Sunset 1 detectors used in 2009. In the upper plot the M10 levels are shown while in the bottom that of the M14. The background rate is higher when sparking or electronic noise appears.

Tracking events can be distinguished with a series of criteria that can be formed from data recorded from the Tracking and the Slow Control program. In order to declare that a detected signal count in a background file during CAST tracking corresponds to a photon converted in the magnet, some selection rules have been applied. The conditions that define the tracking must fulfill all the selection rules following:

- ✓ Tracking PC is set to solar Tracking mode and Sun is reachable.
- ✓ Horizontal and Vertical magnet position has precision < 0.01 degrees
- ✓ Magnetic field is ON
- ✓ Gate Valve in front of Sunset detector is OPEN (VT1 or VT2)

The tracking counts detected for each tracking are resulting from the background selection by imposing the tracking conditions described. The tracking counts are estimated for the first and the second half of the tracking as also for the time during which Helium gas is inserted into the magnet bores.

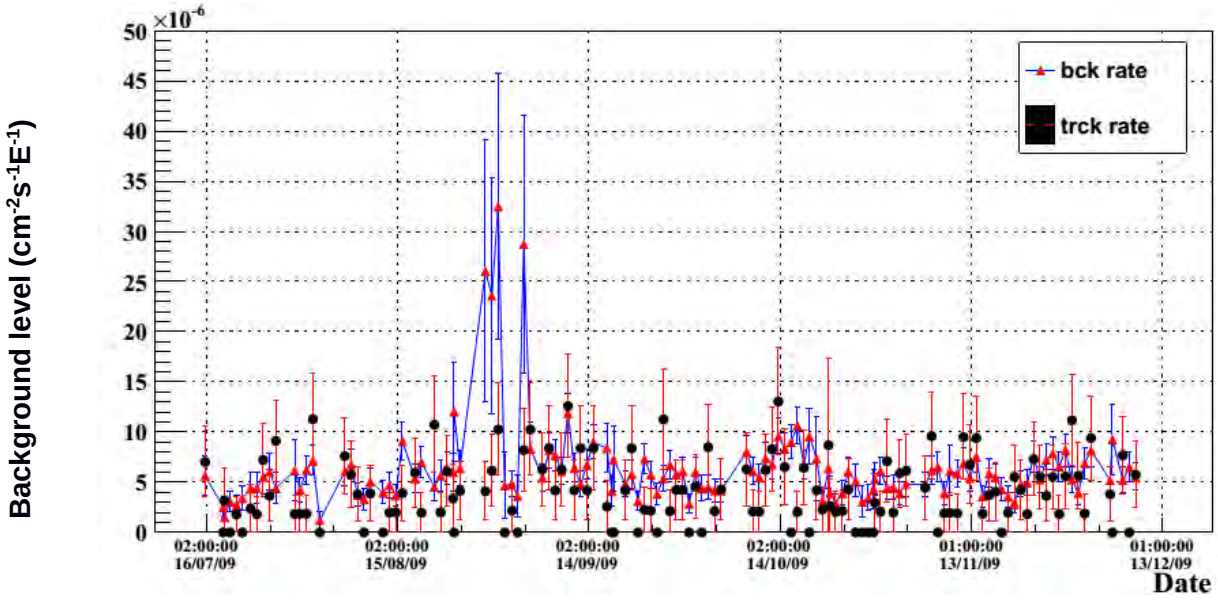

Figure 8.16 Background and tracking level of the Sunset 2 detector for the 2009 data taking period. The background rate is high for some periods where the detector electric noise was increased. In order to take into account tracking information that was included into background files of very short times, because of intervention, the rate is affected. On the 26th of October the detector Sunset 2 was disconnected and during the next days there were problems because of electronic noise. This can explain the four zero consecutive counts on those tracking days.

The energy spectra of the three detectors used in Sunset side (M10, M9 and M14) in the range of 1-10 keV are shown in the next figures. The Sunset 1 microbulk Micromegas before its replacement, was taking background measurements for 949 hours and during that time there were 42 trackings recorded that lasted for 60 hours. After the detector change to M14, there were 78 trackings of 112 hours and the background recorded time was 1599 hours.

The Sunset 2 detector (M9) was taking background data for 2776 hours, while its tracking time was 184 hours. The detector statistics for 2009 are summarized in table 8.1.

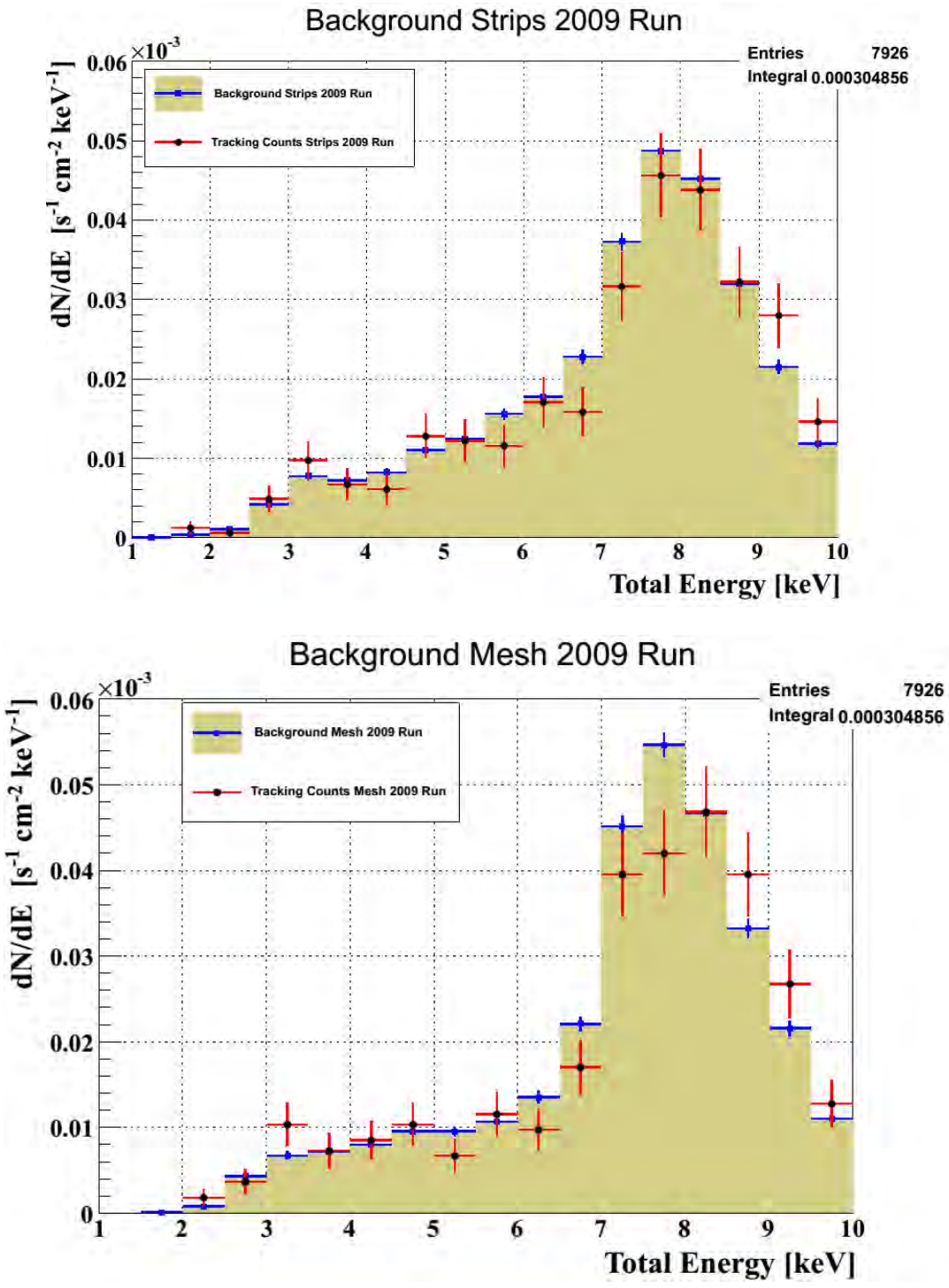

Figure 8.17 The background and tracking energy spectra for Sunset 1 detector (M10). Before the Sunset 1 detector replacement, the Cu fluorescence peak at 8 keV is noticeable. Another peak is from Fe at 6 keV, which is found in the large metallic mass of the magnet and the vacuum pipes in front of the detector. The Argon escape peak at 3 keV is also obvious. At the top the background and tracking spectra refer to the strips, while at the bottom to the mesh signal respectively.

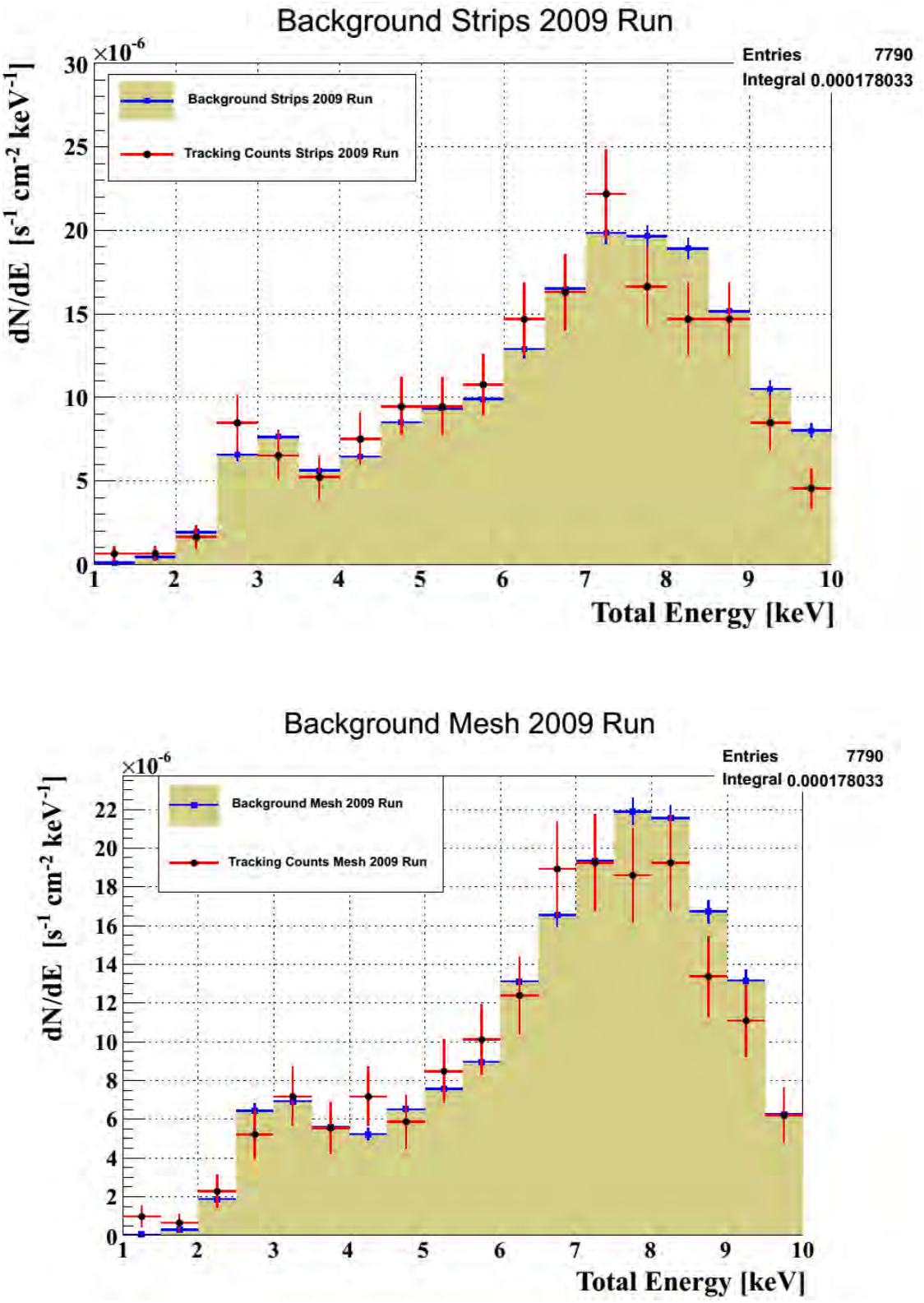

Figure 8.18 The Sunset 1 (M14) background and tracking energy spectra after the detector replacement. The background and tracking level have been reduced. At low energies the background level measured in tracking conditions is higher than the background measured in non-tracking conditions. This can be a systematic effect because of noise increase during the tracking times as also from the Sunset side movement towards the experimental wall area.

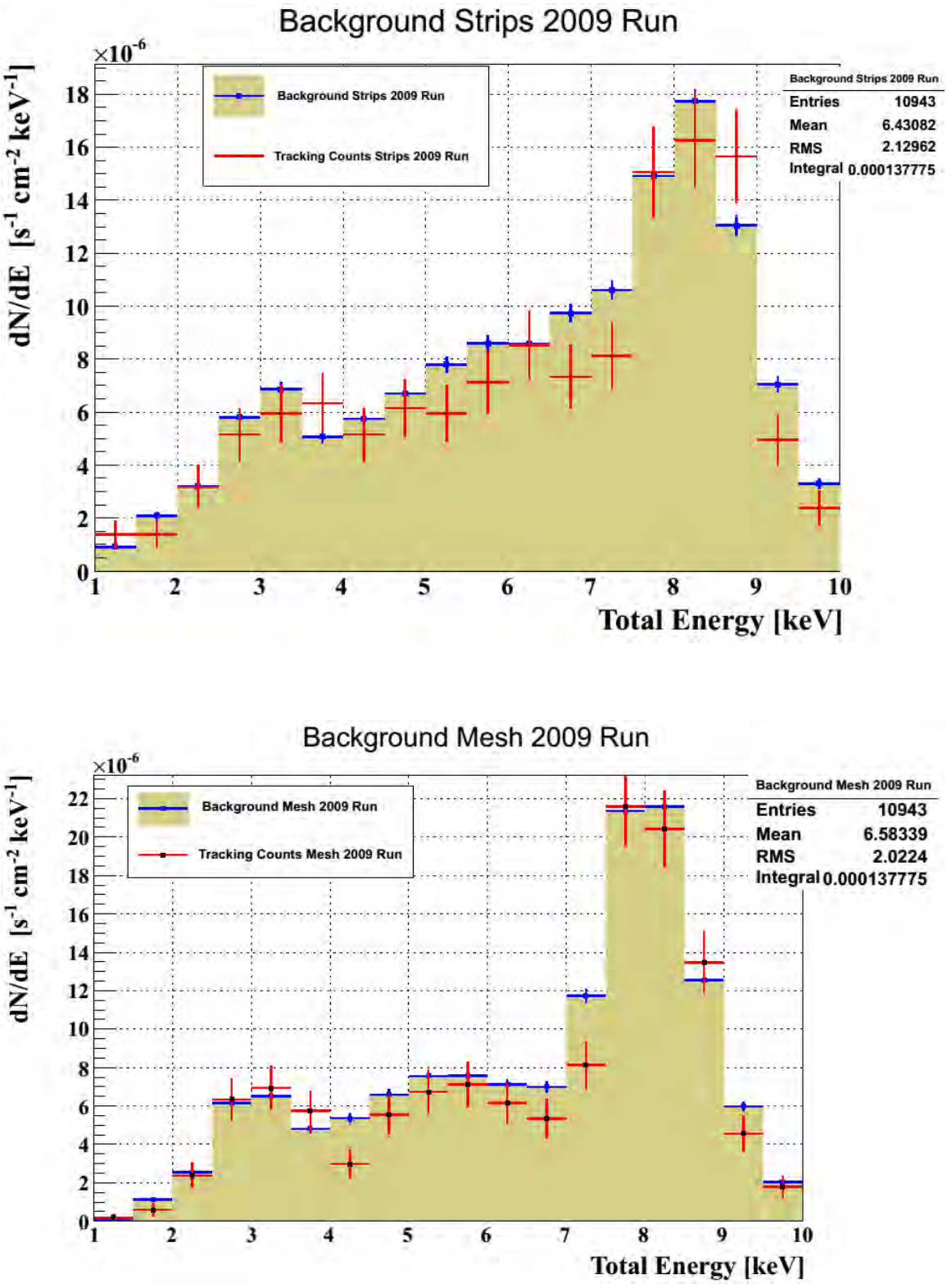

Figure 8.19 The Sunset 2 (M9) background and tracking energy spectra for the 2009 data taking period. As shown in previous sections the detector performance was remarkably good during the year and the background – tracking level is quite low for low energies (in the range of interest 2-7 keV).

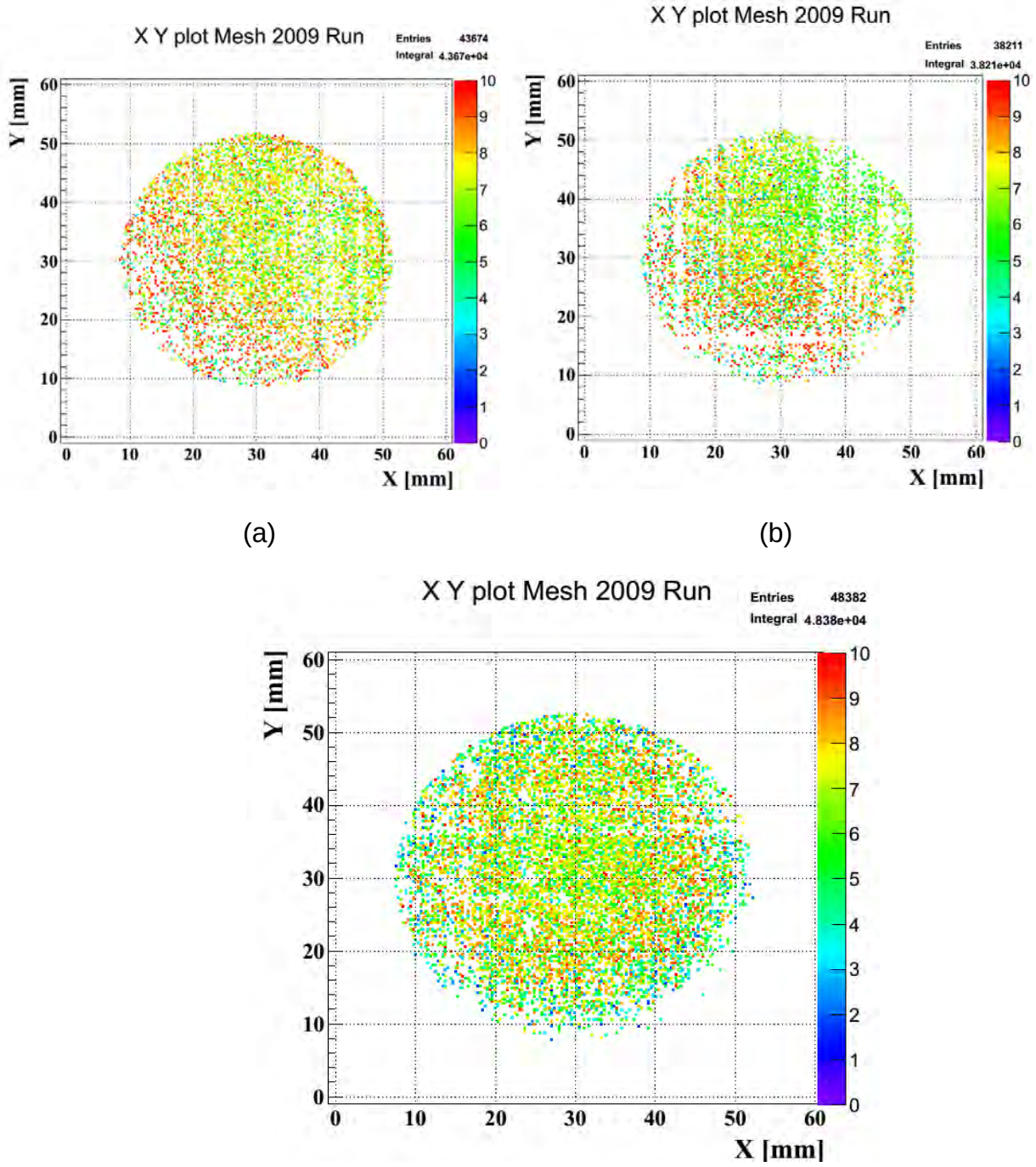

(a) (b)

(c)

Figure 8.20 The background distribution of events in the Mesh for M10 (a), M14 (b) and M9 (c) in Sunset 2.

A summary of the detectors statistics (2009 data taking period) is presented in table 8.1.

Sunset 1 (M10)	**Tracking**	**Background**
Time (h)	60	950
Counts	120	2070
Mean Rate 2-7 keV ($cm^{-2}\,s^{-1}\,keV^{-1}$)	(6.082±0.092)×e-06	(7.019± 0.1)×e-06
Sunset 1 (M14)	**Tracking**	**Background**
Time (h)	112	1599
Counts	227	3166
Mean Rate 2-7 keV ($cm^{-2}\,s^{-1}\,keV^{-1}$)	(6.17±0.093)×e-06	(6.46±0.096)×e-06
Sunset 2 (M9)	**Tracking**	**Background**
Time (h)	184	2776
Counts	256	4380
Mean Rate 2-7 keV ($cm^{-2}\,s^{-1}\,keV^{-1}$)	(4.228±0.07)×e-06	(5.084±0.08)×e-06

Table 8.1 Summary of the Sunset Micromegas performance in 2009

8.4 Data taking overview in 2010

The 2010 data taking period for CAST started on the 5th of May, 2010, and data was taken until the 30th of November, 2010. The running period was punctuated with four quenches and a ten day loss of data taking due to problems on the cryo roots pump shaft seals. Another three days were lost due to a Quench Protection rack threshold tuning.

The first part of the data taking period in 2010 was dedicated to cover all missing density settings due to ^{3}He leak problem in 2008. The second part of the run, started on 10th of August, continued the higher axion mass search at the setting that corresponds to 65.1 mbar (axion mass 0.85 eV). The new pressure settings covered with a density step of 1.4 dP (nominal pressure setting of ~0.1 mbar). The data taking efficiency was 69% (excluding stoppages due

to cryo problems) and the 2010 run finished at the density setting that corresponds to 82.7 mbar at 1.8 K (axion mass 1.01 eV). The pressure settings covered and the gaps due to quenches and cryo problems are shown in the next figure. The last pressure increase in December 2010 was due to a test performed for the CFD simulations.

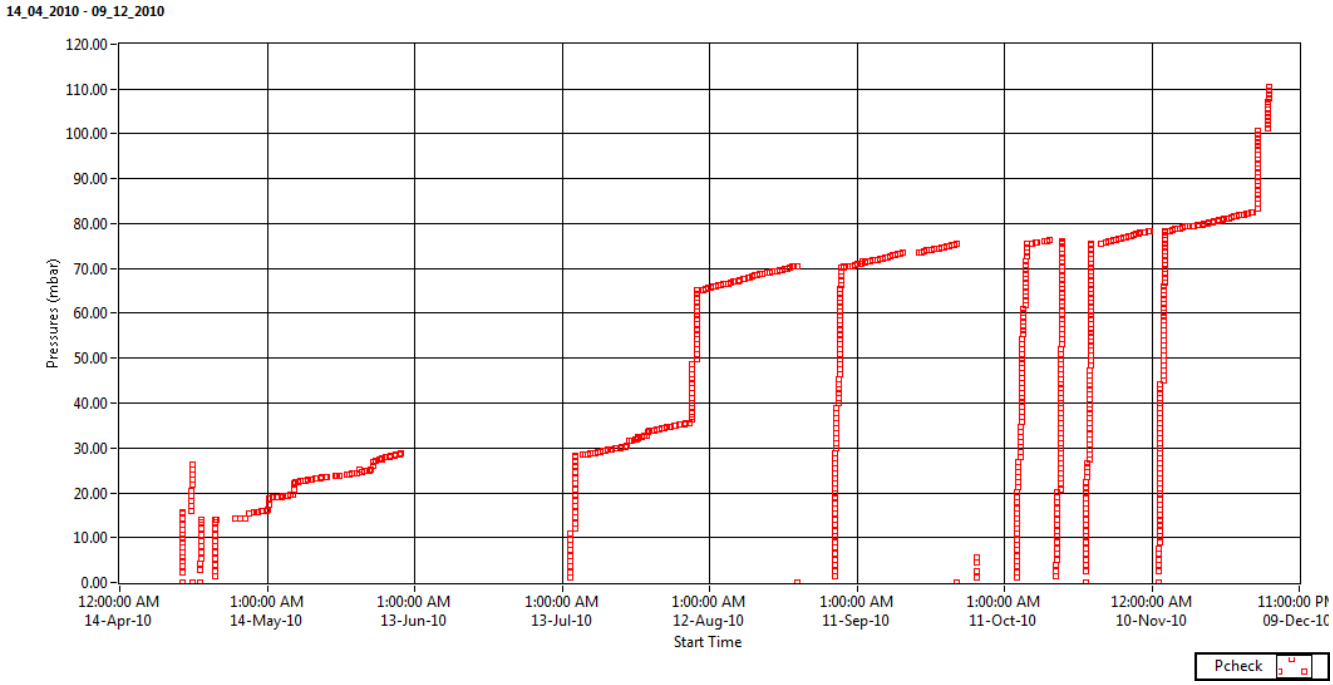

Figure 8.21 The cold bore pressure evolution in the 2010 data taking period. The gaps shown are due to cryo problems and/or quenches that occurred. The last pressure increase is due to CFD related tests.

From the pressure evolution as seen in figure 8.21 there were many gaps due to events that took place during the run; the most significant of which are

11.06.2010 Cryo problems and cold windows bake out. The root pump of the cryogenic system failed and caused six days stoppage. During this time a cold windows bake out was implemented. The system recovered on the 17th of July.

30.08.2010 Magnet movement tests and second phase preparation. During recovery the Gas analyzer was tripped off. After interventions data taking started again on the 10th of August for the second part of the 2010 run.

01.10.2010 Quench occurred. A quench signal was triggered. There were also many cryogenic problems that delayed the data taking until the 16th of October.

20.10.2010 A natural quench occurred: A quench signal was triggered due to a stoppage of the water cooling system for the 13kA cables.

26.10.1010 A natural Quench occurred. During the ramp up procedure of the evening shift a natural quench occurred. The system recovered on 29th of October for an evening shift.

09.11.2010 A natural quench occurred. No external parameter was found responsible for this natural quench.

8.4.1 Sunset detectors Data taking in 2010

In accordance with the cryo problems which occurred in the CAST run during 2010, there were also some incidents in Sunset detectors during that time. The Micromegas detectors worked well during the data taking period and their data taking efficiency was 90.5% (the 5-week break due to the cryo pump problem is excluded) covering all the pressure settings. The incidents that are important to mention are the following:

12.05.2010 - Calibrator box problems. The source was not well adjusted after the new calibrator installation and an intervention was needed to fix it. There were many tests in order to adjust the calibration system, but that did not affect the data taking.

11.08.2010 – the Mesh current was changed (decreased) in both Sunset Micromegas detectors by CAST users.

30.08.2010 – The Sunset gas flow rate was changed because of sparks observed. The flow rate was decreased to 3Lt/h.

8.4.2 Sunset detectors stability for 2010

The detectors showed good stability as can be seen in figures 8.22-8.26 for the 2010 data taking period. The Sunset 1 detector on the Jura side has been replaced with a M14 in 2009 as mentioned in section 8.3, while the Sunset 2 detector operated with the M9 detector during the data taking period.

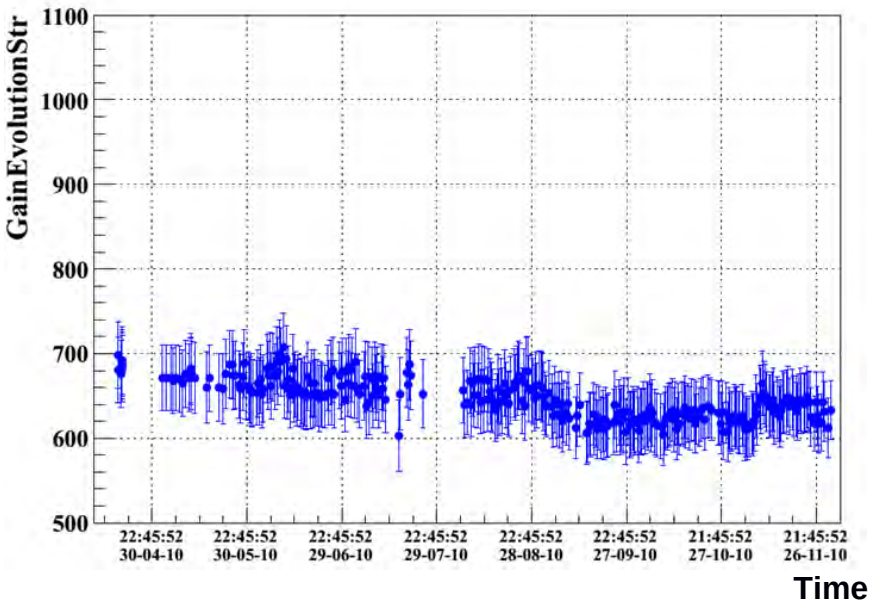

Figure 8.22 The strips Gain evolution for the Sunset 1 detector during 2010. The gap shown is due to stoppage for the detector calibrator system.

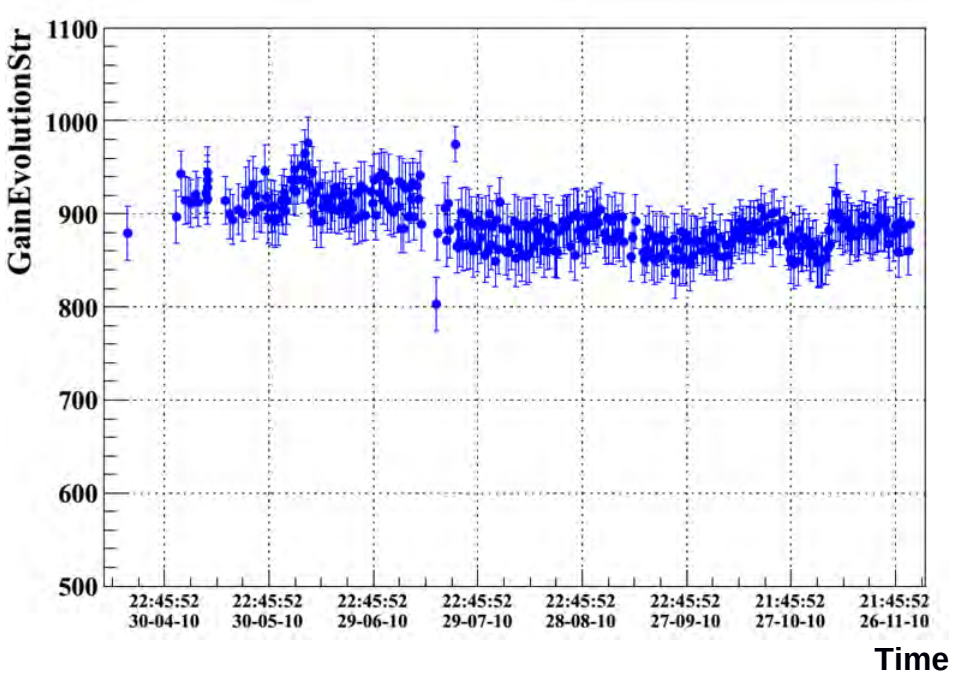

Figure 8.23 The Strips Gain evolution for the detector Sunset 2.

In figure 8.24, the Gain evolution for the mesh is shown. As for the gain in the strips, it is quite stable during the run period.

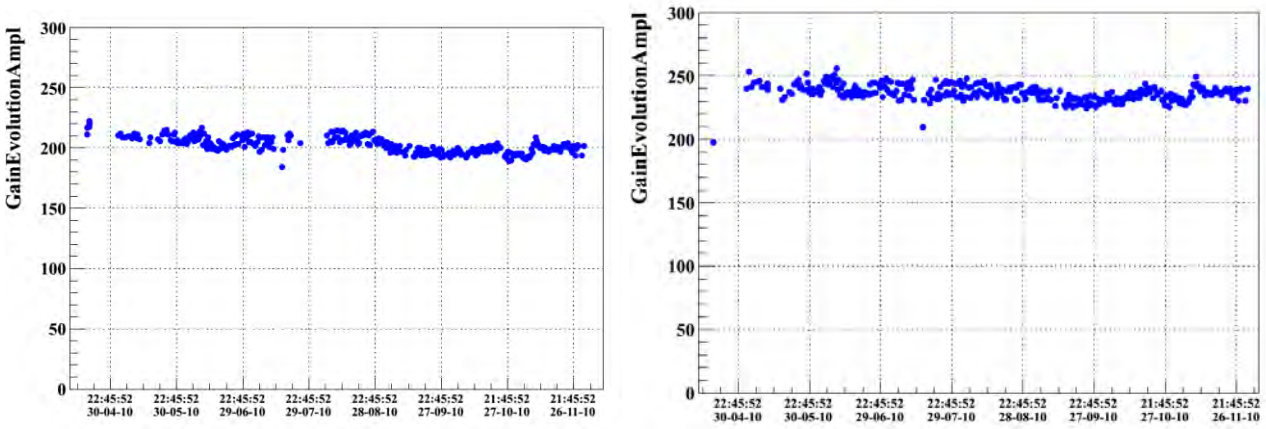

Figure 8.24 The Gain evolution for both detectors of the mesh signal as a function of time. On the left the Sunset 1 gain evolution is shown, while on the right the Sunset 2 gain evolution.

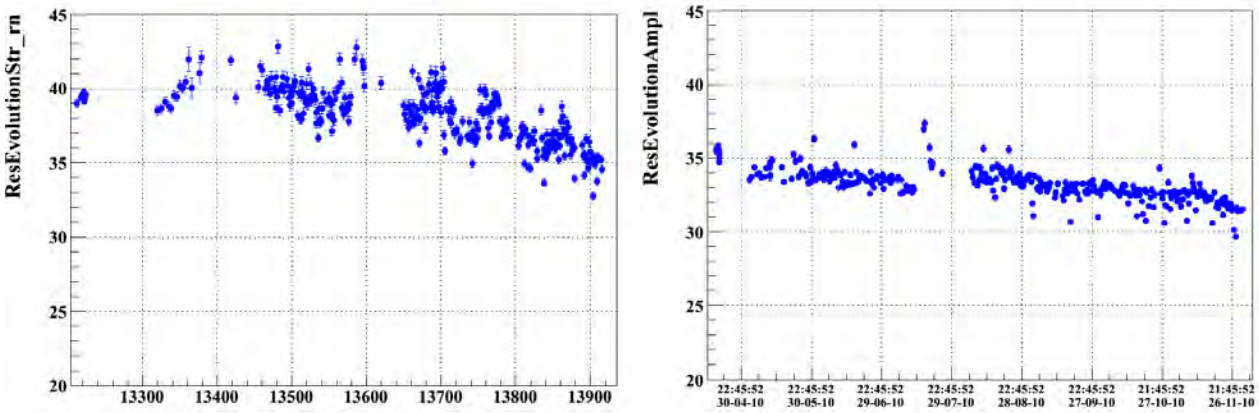

Figure 8.25. Energy resolution of the strips signal (left) and in the mesh signal (right) as a function of time for the Sunset 1 detector (M14).

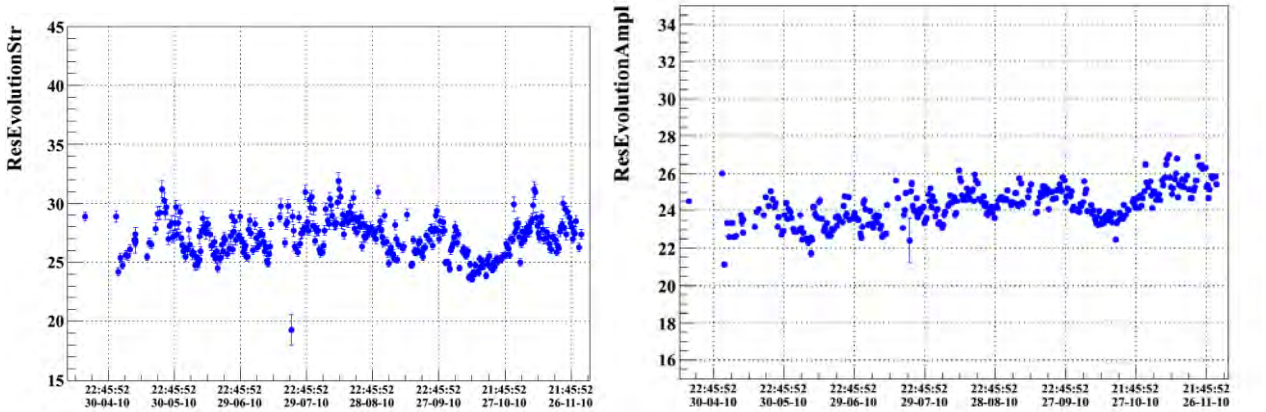

Figure 8.26. Energy resolution of the strips signal (left) and of the mesh signal (right) as a function of time for the Sunset 2 detector (M9). The energy resolution is much better than detector Sunset 1 but still above ~20%.

8.4.3 Efficiency of the Sunset detectors in 2010

The same selection criteria were used in the 2010 efficiency calculation as for 2009. The Sunset 1 detector showed poorer energy resolution and in both detectors, the efficiency was reduced compared to 2009 data. The figures displaying the calibration map for both detectors during 2010 data are the following

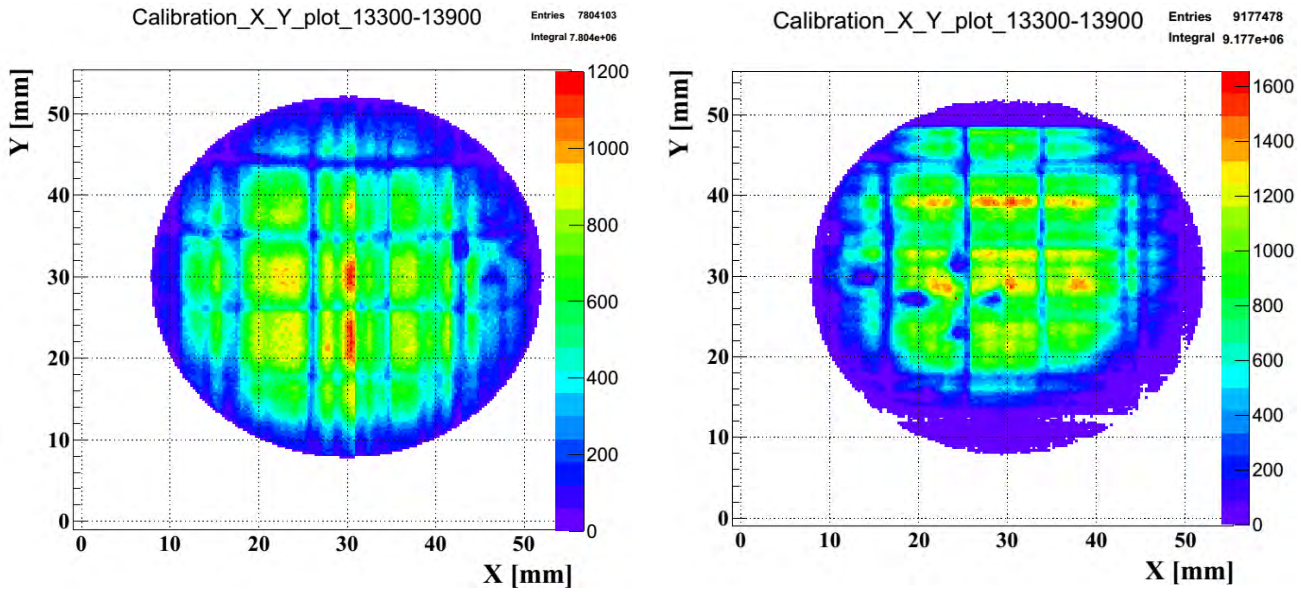

Figure 8.26 The calibration plots for the Sunset 1 (left) and Sunset 2 (right) for the data taking period of 2010.

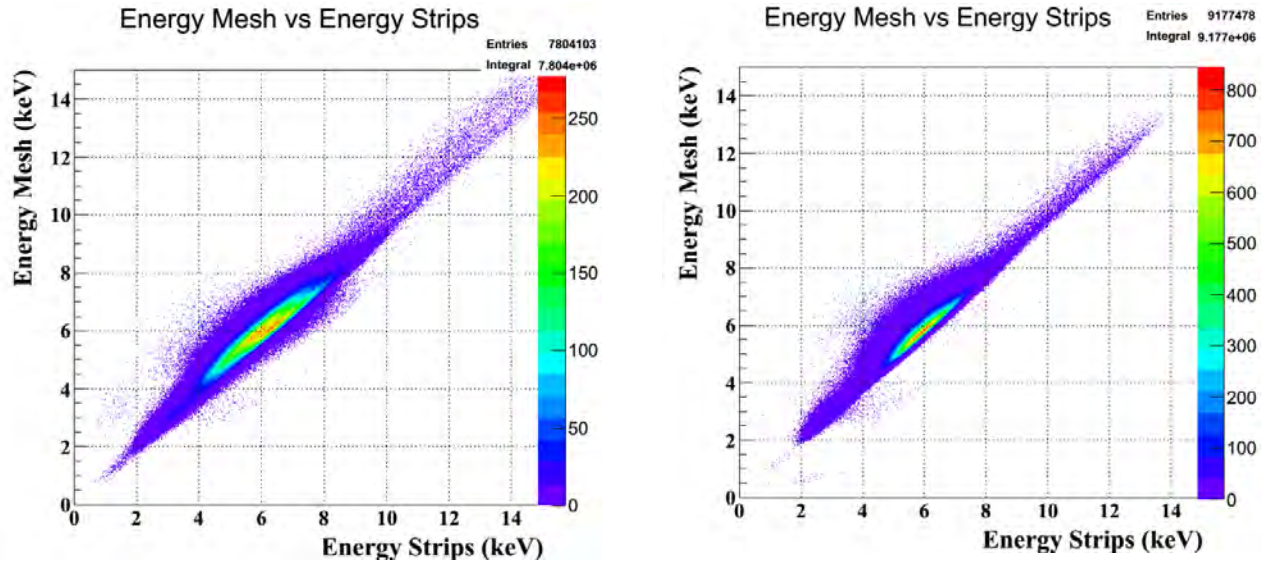

Figure 8.27 Calibration of the energy attained from the Mesh versus the energy from the Strips for the Sunset 1 detector (left) and Sunset 2 detector (right). The events after selection cuts are accumulated close to the peak of the ^{55}Fe source as expected and there are also events in the 3 keV region because of the Argon escape peak.

The software efficiency in 2010 was lower than in 2009 and being in the range 70-80 %. Nevertheless, the efficiency is in an acceptable region and the selection cuts can be used to define the background during 2010. The software efficiency for both detectors is shown in figure 8.28.

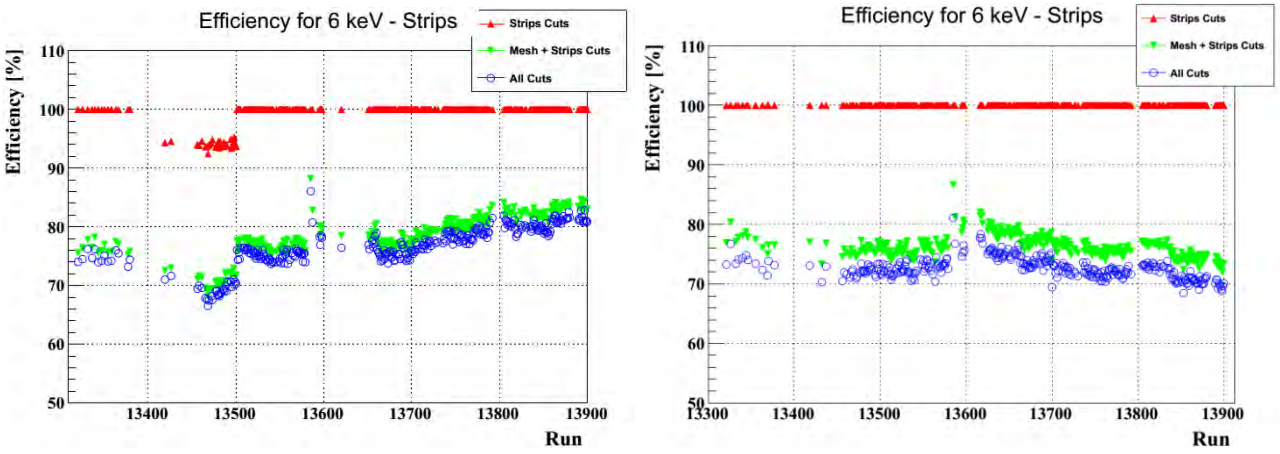

Figure 8.28 The software efficiency in Sunset 1 (left) and Sunset 2 (right) versus the Calibration Run file number.

The Calibration energy spectra for both detectors showing the mesh and strips energy resolutions are plotted below. The Sunset 1 energy resolution, as shown in a figure 8.28, is not so good for 2010.

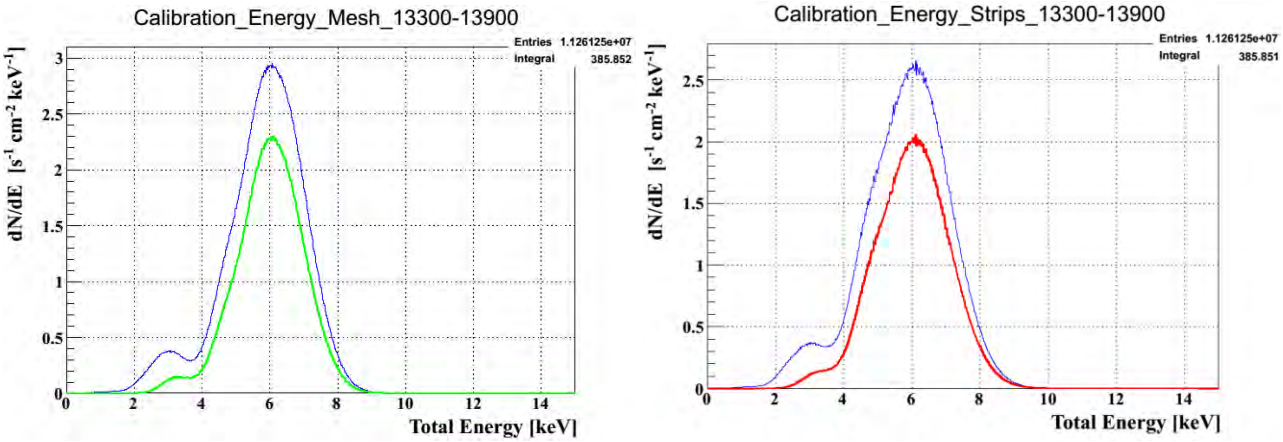

Figure 8.29 Calibration spectra for the Sunset 1 detector for the Mesh (left) and the Strips (right). The spectra in blue refer to the calibration energy spectra before the selection cuts application, while in green and red for mesh and strips after the selection cuts application respectively.

The next plots display the calibration energy spectra for the Sunset 2 detector in 2010.

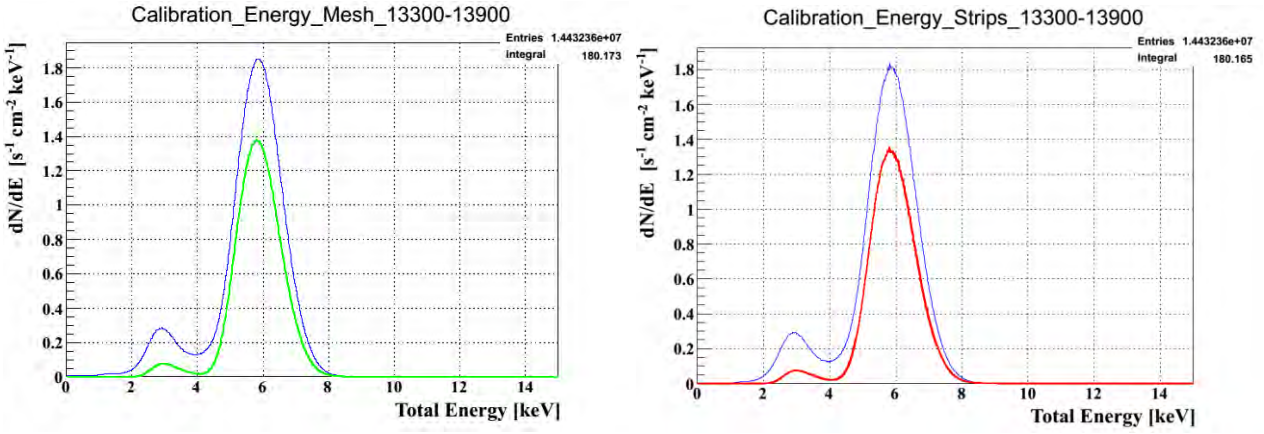

Figure 8.30 Calibration energy spectra for the Sunset 2 detector during 2010. The energy resolution is much better than detector Sunset 1, although the cuts efficiency for the 3 keV events is still low.

The Sunset 1 detector was running for 4378 hours taking background data, while the tracking time was 189 hours. The Sunset 2 detector lost one shift because of noise and the running time was 187.5 hours, while the background running time was 4445 hours. By the same method discussed in section 7.3.2, application of the selection cuts can give the background spectra, while by applying the tracking conditions to the background files the tracking events are recorded.

In the next table 8.2 the summary of the Sunset Micromegas detectors for 2010 is given.

Sunset 1 (M14)	**Tracking**	**Background**
Time (h)	189	4378
Counts	306	6687
Mean Rate 2-7 keV ($cm^{-2}\,s^{-1}\,keV^{-1}$)	(4.92±0.08)×e-06	(4.86±0.08)×e-06
Sunset 2 (M9)	**Tracking**	**Background**
Time (h)	187.5	4445
Counts	236	6151
Mean Rate 2-7 keV ($cm^{-2}\,s^{-1}\,keV^{-1}$)	(3.82±0.073)×e-06	(4.37±0.078)×e-06

Table 8.2 Summary of the 2010 Sunset Micromegas detectors performance

Background and Tracking performance in 2010

The energy spectra of the detectors used in Sunset side in the range of 1-10 keV are shown in figures 8.31, 8.32.

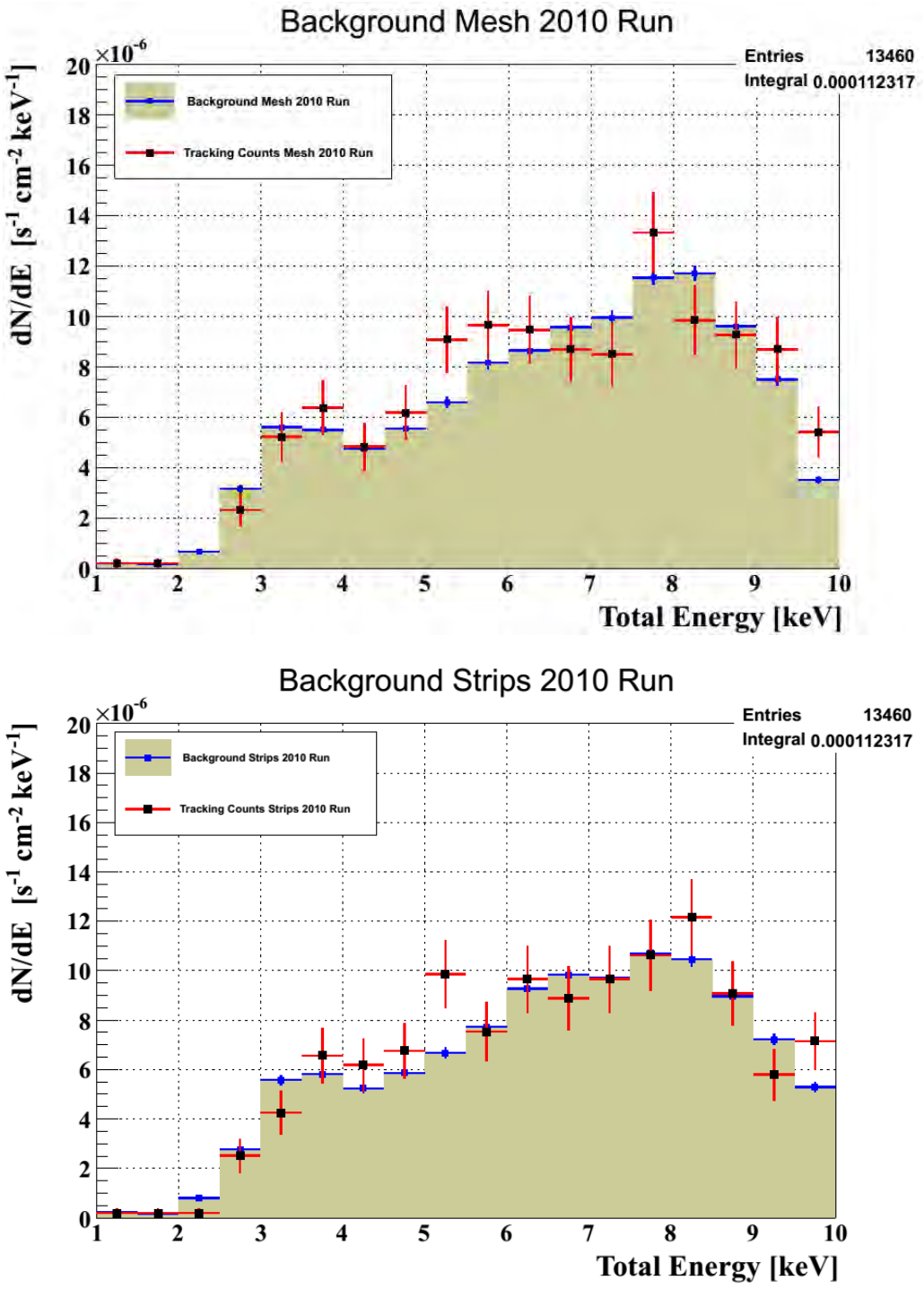

Figure 8.31 Background and tracking energy spectra for Sunset 1. Because of low energy detection efficiency at 3 keV and bad energy resolution of the detector Sunset 1 at low energies, there are very few events recorded. Noise problems during tracking also affected the tracking distribution in low energies; i.e. many low energy events were rejected as background because of noise problems.

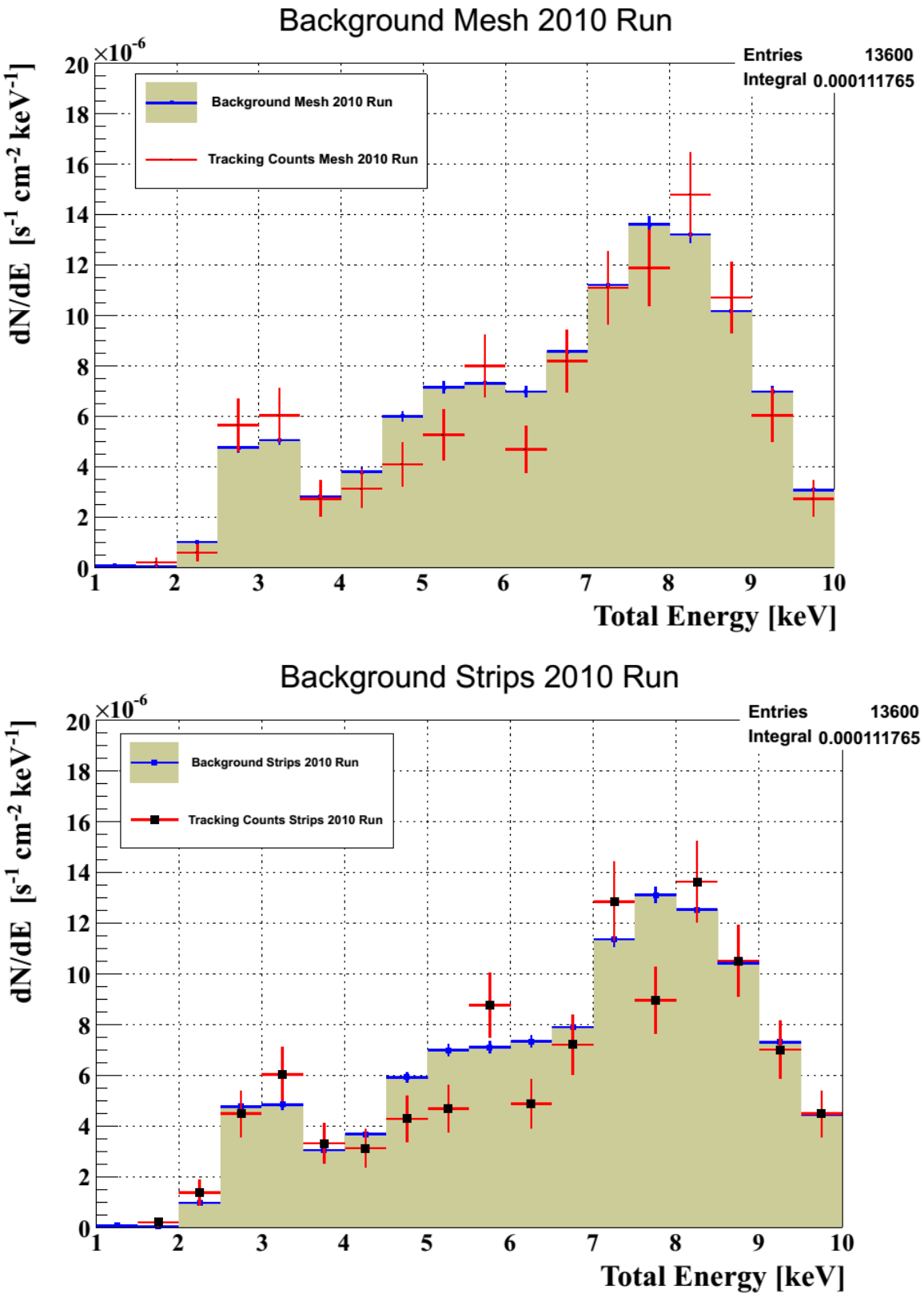

Figure 8.32 Background and tracking spectra for the Sunset 2 detector. The background energy distribution is normal, showing the peaks at 3 keV and at 8 keV as expected.

8.4.4 Statistical evaluation of the 2010 data

During the 2010 data taking period the count rate was quite stable with ~2.5 counts/hour and the background level evolution for both detectors is plotted in figure 8.33.

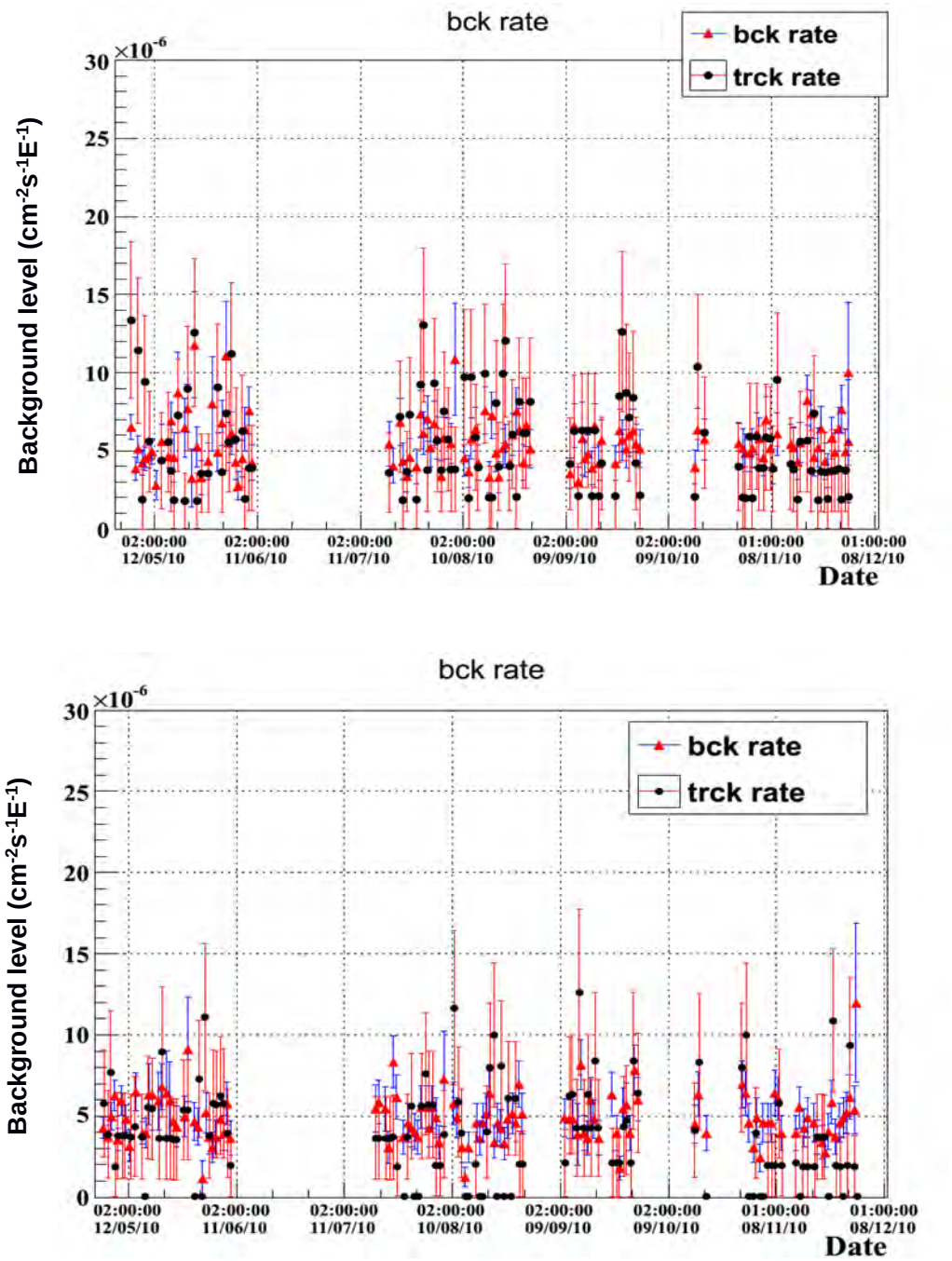

Figure 8.33 The background and tracking level evolution for Sunset 1 (top) and Sunset 2 (bottom) during the 2010 data taking period. The gaps observed are due to stoppages and there are noisy short periods in both detectors during tracking conditions.

The low number of events observed in the Sunset detectors of CAST should follow a Poisson distribution at small time bins (15-60 minutes). Figure 8.34 shows the Poisson distribution of background and tracking for both Sunset detectors in 2010.

The mean of the background counts in this timing binning is μ_B=0.760, while the tracking counts mean is μ_T=0.785, showing a good agreement with the theoretical value. For the Sunset 2 Micromegas (bottom plot in figure 8.35) the agreement is also good for background and tracking counts.

The mean value for the background is μ_B=0.681, while the tracking events mean is μ_T=0.615.

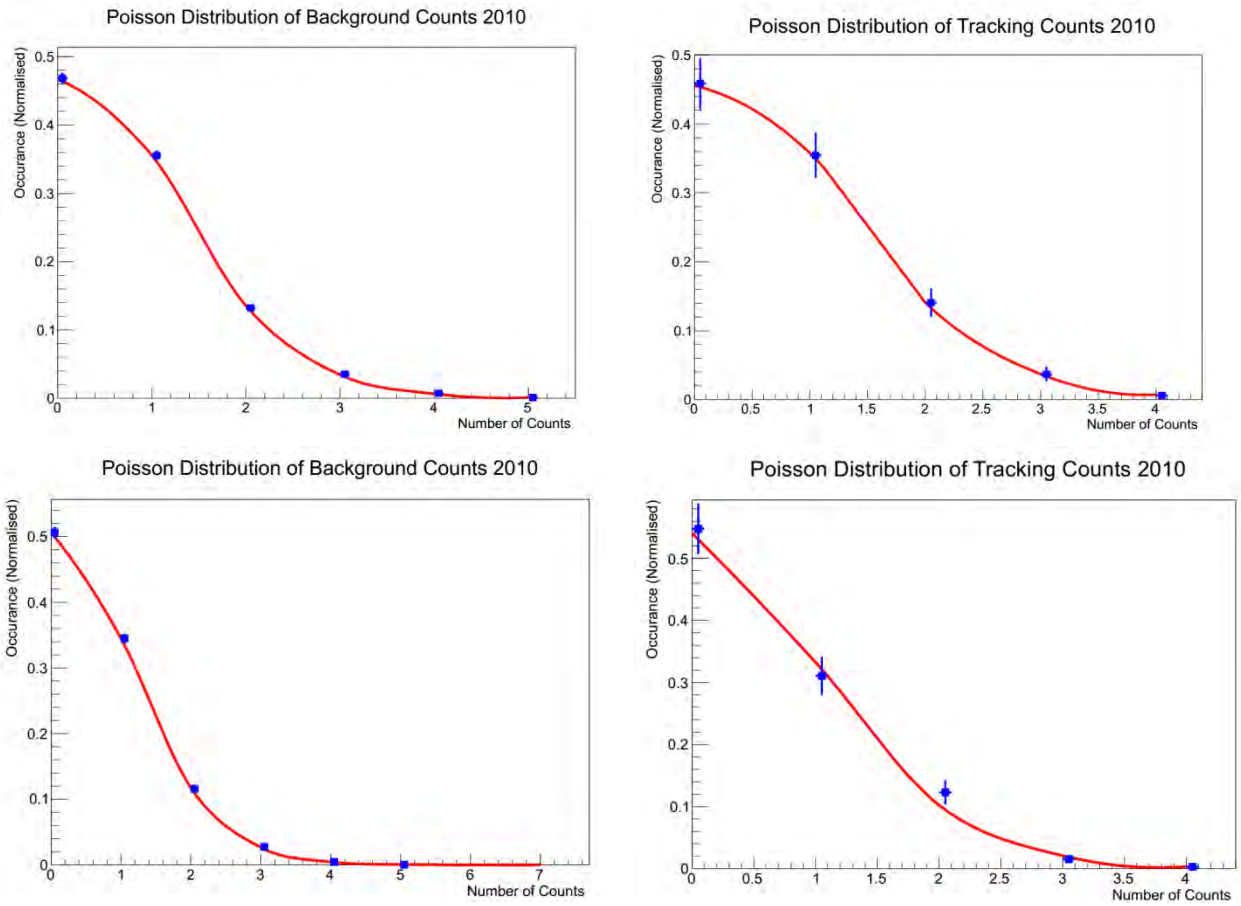

Figure 8.34 Poisson distribution of the Background (left) and tracking counts (right) for the Sunset 1 detector (top) and the Sunset 2 (bottom) in 2010 data.

9. A limit for the axion-photon coupling constant

The purpose of the methodology used in this section is to test the null hypothesis, i.e. the absence of any signal observed in the data taking analysis of 2009 and 2010, of the Sunset Micromegas detectors. However, in the absence of an axion signal from CAST data, the results obtained can be used to imply a limit on the axion parameter space that is defined by the axion mass versus the axion-photon coupling constant.

In the previous CAST Phase (Phase **I**), the method of the maximum Likelihood has been used in analysis and it is based on building likelihoods of detecting the number of counts observed, by using the coupling constant as a free parameter and maximizing the likelihood function. The statistical procedure that has been followed in order to derive the exclusion limit in the Phase **I** cannot be applied for the ^{3}He data of 2009 and 2010. The first reason is that a leak of ^{3}He was detected in 2008 and the second is the dynamical variation of the gas pressure inside the cold bores at high gas densities. The method used in Phase I has been modified and the limit in CAST Phase II is obtained using an unbinned likelihood method.

9.1 The CAST expected X-ray signal

The sensitivity of the axion-photon coupling is directly related to the CAST x-ray expected signal that is obtained by combining the following contributions:

- The solar axion flux on Earth $(d\Phi_\alpha)/dE)$
- The conversion probability ($P_{\alpha\to\gamma}$)
- The detectors efficiency (ε_d)
- Attenuation length (Γ)
- Exposure time for specified gas density (Δt)

The differential axion flux and the conversion probability in a buffer gas immersed in a transverse magnetic field have been described in a previous section. The relation which gives the flux of solar axions on Earth is the following

$$\frac{\mathrm{d}\Phi_\alpha}{\mathrm{d}E} = g_{10}^2 6.0 \times 10^{10} cm^{-2} s^{-1} keV^{-1} E^{2.481} e^{-E/1.205} \quad (9.1)$$

The solar axion flux depends on the axion energy E_α and the coupling constant $g_{\alpha\gamma}$. The conversion probability at the axion energy E_α is controlled by the buffer gas density ρ_{cb} , the attenuation length Γ, the effective photon mass m_γ and the coherence length (equation 3.15) . The attenuation length inside a medium of constant density is obtained by using the formula

$$\Gamma = \rho_{gas}\left(\frac{\mu}{\rho}\right) \quad (9.2)$$

where the total photon mass attenuation coefficient μ/ρ, is provided by the National Institute of Standards and Technology (NIST) database [124]. Photons interact when traveling in a medium and the inverse absorption length Γ depends on the gas type, the gas pressure and the photon energy.The NIST data have been fitted in the energy range of 1-15 keV and the following expression describes the fit provided in terms of $\mu/\rho(cm^2/gr)$.

$$\log \mu/\rho\,(E) = -1.5832 + 5.9195 \cdot e^{-0.3538 \cdot E} + 4.035 \cdot e^{-0.97055 \cdot E} \quad (9.3)$$

where E is the X-ray photon energy in keV.

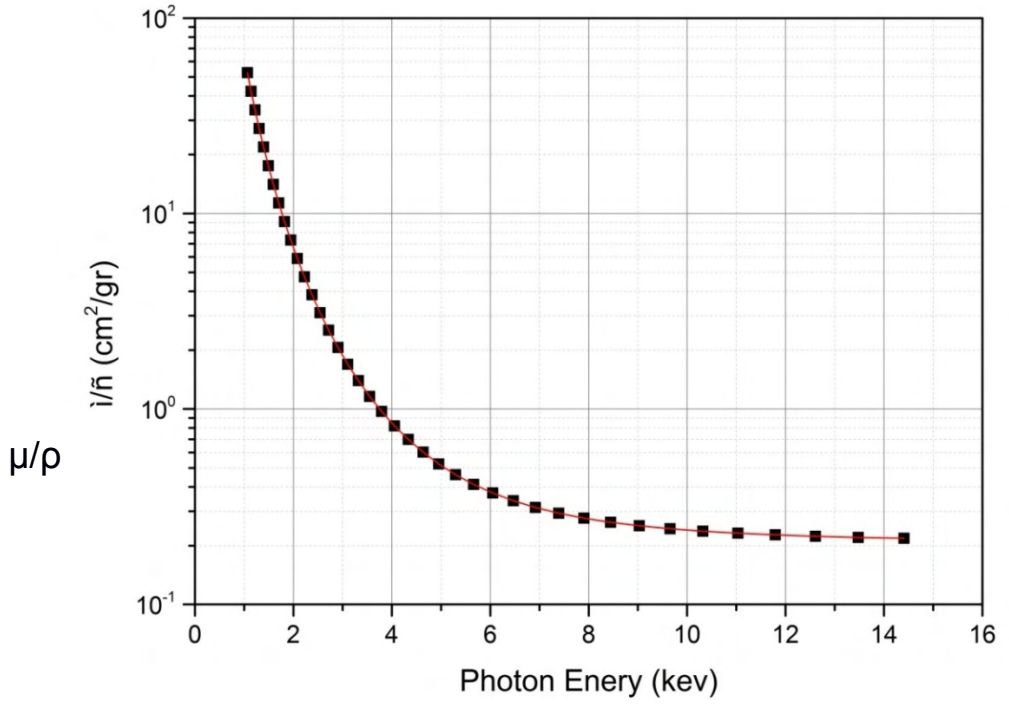

Figure 9.1 The Helium mass absorption coefficient data obtained from NIST database and the interpolated curve fitting as expressed from the equation (9.3)

The detector efficiency was introduced and calculated in section 6.3.2 for the specific materials used and the detector gas mixture (Figure 6.31).
Finally the number of photons, from converted axions, that are expected to reach the detector is given by the equation 3.14. By combining the axion flux formula and the conversion probability relation it implies that

$$N_\gamma \propto g_{\alpha\gamma}^4 \tag{9.4}$$

The contributions that account for the final expected signal during a tracking are integrated for the exposure time of the run setting and the signal expected can be expressed as

$$S\left(g_{\alpha\gamma}, m_\alpha, m_\gamma, E\right) = g_{\alpha\gamma}^4 \int_0^{t_{track}} \varepsilon_s(E)\varepsilon_d(E)\frac{d\Phi_a}{dE} P_{\alpha\to\gamma} A_{cb} \Delta t_{track}[keV^{-1}] \tag{9.5}$$

where ε_s is the software efficiency for the Sunset Micromegas detectors described in chapter 8. The effective length of the magnet and the cold bore density have also been described and calculated in chapter 6. In this study, a density stability threshold (DST) of 0.003 kg/cm^3 can be used in order to estimate the coherence length as given from the relation 5.45. By using such a not so strict bound for the energy range 2-7 keV the effective length calculation is improved for the tilted magnet at the extreme angles.

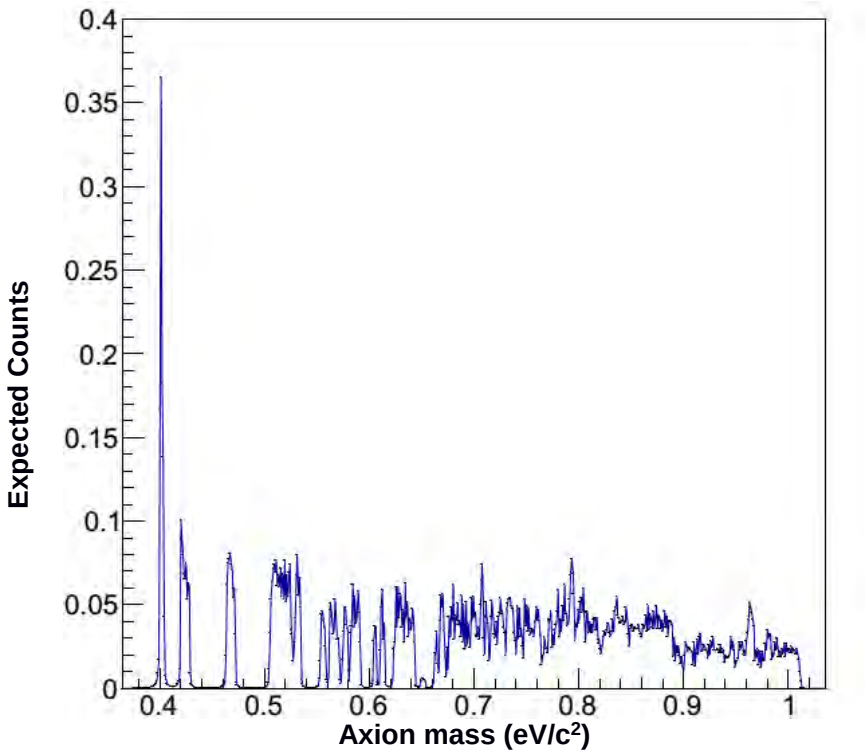

Figure 9.2 The expected x-ray signal in the Sunset 2 detector for the 2009 and 2010 runs in the energy range 2-7 keV with a value for $g_{\alpha\gamma} = 10^{-10} GeV^{-1}$

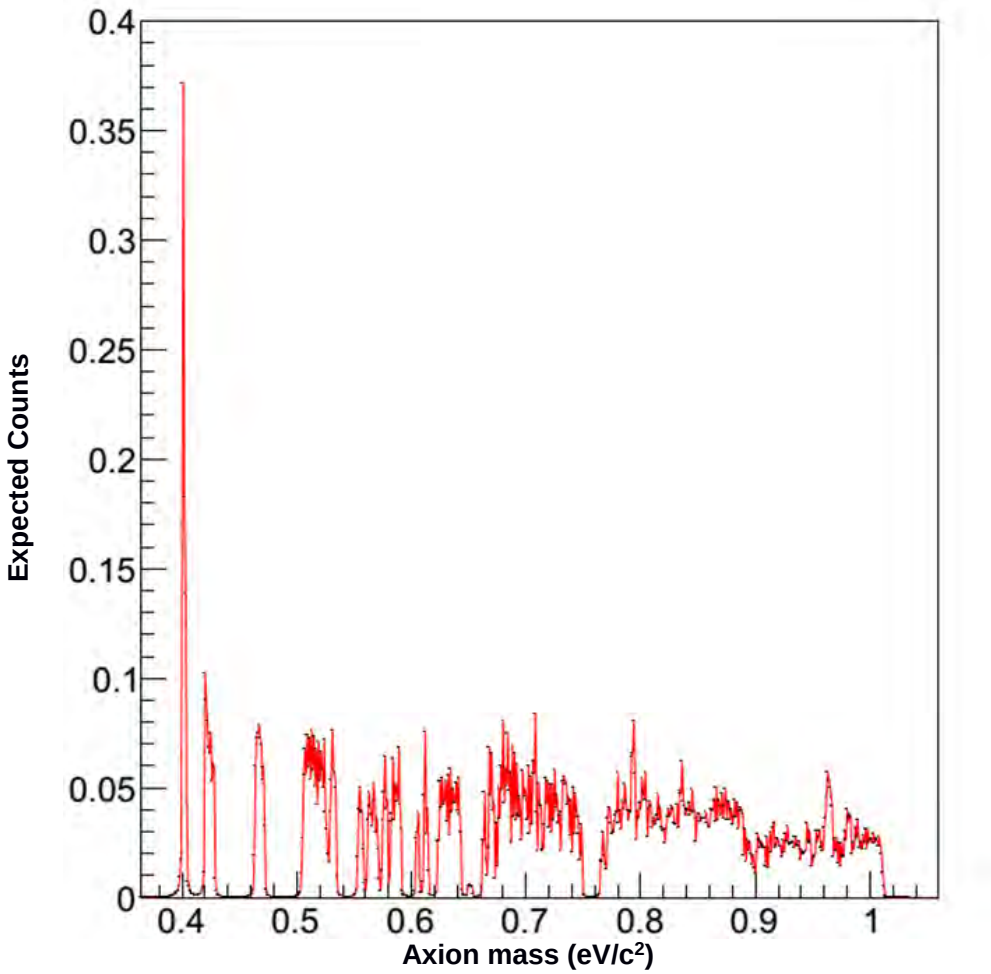

Figure 9.3 The expected x-ray signal in the Sunset 1 detector for the 2009 and 2010 runs in the energy range 2-7 keV with a value for $g_{\alpha\gamma} = 10^{-10} GeV^{-1}$

Since the tracking count rates of the Sunset micromegas are compatible with background rates, there is no statistical significant excess of counts during trackings for 2009 and 2010. However, background and tracking data are used to define the contribution of the detected counts into the upper limit of the coupling constant calculation. The expected axion rate for each detector and for each axion mass m_α can be calculated by taking into account the pressure P_{check} (that is associated with the cold bore density) and the effective photon mass m_γ. Each detected tracking count is associated with the energy bin of the mean background level which is also defined in the energy range 2-7 keV.

The exclusion plot calculated for the coherence length is provided from the chapter 5 analysis by using the CFD simulations. The moving magnet is taken into account and the density homogeneity length is provided according to the CFD results. The exclusion limit calculated according to the CFD scenario in order to define the sensitivity reached by the Sunset Micromegas of CAST for the data taking periods of 2009 and 2010. The limit provided by CAST corresponds to the combined data with the Sunrise detector. The total time exposure is given in tables 8.1 and 8.2.

9.2 Unbinned Likelihood method

As any experiment, in CAST there are a set of observables n, that contain the information about phenomena under investigation being related to the axion-photon coupling constant. That set of observables, can construct a vector $\vec{x}$ in a n-dimensional space. In case of N experimental data from the CAST experiment a set of vectors $\{\vec{x}_i\}; i = 1,..,N$ is constructed. The function that describes the frequency of occurrence of data at $\vec{x}$ is the probability distribution function (*pdf*). In case of m fixed unknown parameters $\vec{a}_0$ and $\vec{x}$ observables, the probability distribution function for any observation is

$$p = P(\vec{x}|\vec{a}) \tag{9.6}$$

where $\vec{a}$ is a more general vector that allows to vary the shape of the *pdf* in vicinity of the true shape of the parent distribution of observables. The *pdf* function has been normalized as follows

$$\int_V d^n x\, p(\vec{x},\vec{a}) = 1 \;\; \forall a \tag{9.7}$$

Averaging over the N events in each bin $\Delta^n x$ of the n-dimensional space of independent variables, the mean number of events $\mu(\vec{x})$ in the bin $\Delta^n x$ located at $\vec{x}$ is

$$\mu(\vec{x}) = P(\vec{x},\vec{a})\, \Delta^n x \tag{9.8}$$

The unbinned limit corresponds to the limit $\Delta^n x \to d^n x$ so that all bins contain either zero or one event. From Poisson statistics one gets

- Probability of Zero events in a bin $= e^{-\mu(\vec{x})} = \; e^{-d^n x P(\vec{x},\vec{a})}$
- Probability of One Event in a bin $= \mu(\vec{x}) e^{-\mu(\vec{x})} = \; d^n x P(\vec{x},\vec{a})\; e^{-d^n x P(\vec{x},\vec{a})}$

For a given set of N events the likelihood $\mathcal{L}_N$ to find the limit in unknown parameters of the experimental data is the product of the probabilities of all bins with zero events in them, and of the probabilities for all the bins with one event in them.

$$\mathcal{L}_N \propto \left[\prod_{all\ bins} e^{-d^n x P(\vec{x},\vec{a})}\right]\left[\prod_{i=1}^{N} d^n x P(\vec{x},\vec{a})\right] \tag{9.9}$$

The first term in brackets (equation 9.9) contributes a factor e^{-N} that is retained for the maximum likelihood fit. The second term depends on the events and variations in $\mathcal{L}_N$ is coming

from this term. The *pdf* has now been converted into likelihood, by exchanging fixed and variable terms in the limit of a very small bin.

All observations are combined by individual likelihoods and they are multiplied in order to produce the global likelihood of all variables in the data set provided.

$$\mathcal{L} = (a|\vec{x}_i, \ldots., \vec{x}_N) = \prod_{i=0}^{N} \mathcal{L}_i(\vec{a}, \vec{x}_i) \tag{9.10}$$

The maximization of $\mathcal{L}$ will give the maximum likelihood estimator (MLE) of a that can estimate the closest approximation of the true value a_0, by using the observables $\vec{x}_i$ as the "fixed parameters" and $\vec{a}$ values will be used as the function's variables that can vary freely. The maximization of likelihood can be written as

$$ln\mathcal{L} = ln\left(\prod_{i=0}^{N} \mathcal{L}_i\right) = \sum_{i=0}^{N} ln\mathcal{L}_i \tag{9.11}$$

In order to obtain the coupling limit in the period 2009-2010 from CAST Micromegas experimental data, the following Likelihood expression is used

$$L_k = \frac{1}{L_{0k}} \prod_i e^{-\mu_i} \frac{{\mu_{ik}}^{n_{ik}}}{n_{ik}!} \tag{9.12}$$

where i is the energy bin and n_{ik} is the number of photons observed during the tracking.

The μ_{ik} term is the expected number of counts in each energy bin for a given event k and it is given as the sum of the expected background b_{ik}, plus the theoretical axion signal s_{ik} that depends on the theory parameters $m_\alpha$and $g_{\alpha\gamma}$.

$$\mu_{ik} = b_{ik} + s_{ik}(m_\alpha, g_{\alpha\gamma}) \tag{9.13}$$

The signal s_{ik} is given by the equation (9.5). Recalling the expression 3.14 for the expected number of photons and substituting it into (9.5), the expected signal becomes

$$s_{ik}\left(m_\alpha, g_{\alpha\gamma}\right) = g_{\alpha\gamma}^4 \int_E^{E+\Delta E} \frac{dn_{\alpha\gamma}}{dE} \cdot \Delta t_k \cdot dE \tag{9.14}$$

CAST global likelihood is generated by adding the contributions of all detectors. In this thesis the combined detectors Likelihood is constructed by the Sunset Micromegas.

$$L_{m_\alpha}(g_{\alpha\gamma}) = \prod_{detector} \prod_{k} L_k \tag{9.15}$$

For a fixed value of m_α, L_k is maximized and the best fit value for the coupling constant is obtained that is the $(g^4_{\alpha\gamma})_{min}$. As noticed already, the time interval Δt_k is chosen small enough that the Likelihood terms can be split into two groups, one group with no tracking count and one with a single tracking count.

The Likelihood referred to a short period of time Δt_k instead of the full tracking time selection in Phase I period. For the ^{3}He analysis the index i runs over the energy bins of the event k. The $L_{0k} = \prod_i e^{-n_{ik}} \frac{{n_{ik}}^{n_{ik}}}{n_{ik}!}$ term is the normalization factor.

$$L_{m_\alpha}(g_{\alpha\gamma}) = \prod_{k} L_k(n_i = 1) \prod_{k} L_k(n_i = 0) \tag{9.16}$$

Where k is an index that runs over the whole time bins (Δt_k) during trackings.

The unbinned Likelihood distribution can be tested with the χ^2 method, assuming a Poissonian distribution of background and signal. The advantage of using χ^2, besides the computational accuracy, is the goodness of fit test. The expression $-2lnL_k$ behaves asymptotically as a χ^2-function and from equation (9.12) it follows

$$-\frac{1}{2}\chi^2_{m_\alpha} = \log\left(L_{m_\alpha}(g_{\alpha\gamma})\right) = -N_c - \sum_{k_{n_i=1}} -\mu_{ik} + log(\mu_{ik})] - \sum_{k_{n_i=0}} \mu_{ik} \tag{9.17}$$

where i refers to the corresponding energy bin and N_c is the total number of counts detected in 2009 and 2010. By introducing equation (9.13) in (9.17) and simplifying terms that do not contribute to the upper limit of $g_{\alpha\gamma}$calculation we obtain:

$$-\frac{1}{2}\chi^2_{m_\alpha} = \underbrace{-g^4_{\alpha\gamma} \int_E \int_{t_k} \frac{d^2 n_\gamma}{dE \cdot dt_k} dE \cdot dt_k}$$

$$+ \underbrace{\sum_{k_{n_i=1}} log \int_E^{E+\Delta E} \left(\frac{db_{ik}}{dt_k} + g^4_{\alpha\gamma} \frac{d^2 n_\gamma}{dE \cdot dt_k} dE \right)} \tag{9.18}$$

The general expression 9.18 was obtained by taking the limit $\Delta t_k \to 0$. In equation 9.18 there are two main contribution terms.

The first term accounts for the number of counts that should have been detected for a given axion mass m_α, integrating to all gas densities that might have a considerable contribution.

The second term is related with the one count contribution from equation (9.16), and is taking into account every tracking count detected for a specific background level at the energy bin.

In a simpler form equation (9.18) can be written as

$$-\frac{1}{2}\chi^2 = -R_{SSMM} + \sum_i^N logR(E_i, t_i, d_i) \tag{9.19}$$

where the sum runs over the N detected counts for the event rate R expected at the time t_i , energy E_i and detector d_i for each event i , while R_{SSMM} is the integrated expected number of events over all exposure time, energy and detectors in Sunset Micromegas (SSMM).

9.3 The Sunset Micromegas limit obtained for 2009-2010 mass range scanning

In the case, an axion signal has not been being detected, a limit in the coupling constant can be obtained with a 95% confidence level. The upper limit can be estimated by integrating the Bayesian probability on $g_{\alpha\gamma}^4$ over the physical region from zero up to 95% of its area and is given by the following expression

$$\frac{\int_0^{g_{\alpha\gamma}^4} e^{-\frac{1}{2}\chi^2} dg_{\alpha\gamma}^4}{\int_0^{\infty} e^{-\frac{1}{2}\chi^2} dg_{\alpha\gamma}^4} = 95\% \tag{9.20}$$

where χ^2 is calculated for each axion mass m_α using the global Likelihood defined in (9.16). By looping on each value of m_α one gets the full contour of $g_{\alpha\gamma}(m_\alpha)$.

$$-\frac{1}{2}\chi^2_{m_\alpha} = \log\left(L_{m_\alpha}(g_{\alpha\gamma})\right) \tag{9.21}$$

The limit was derived for the 2009-2010 data taking period with Sunset Micromegas and the exclusion plot presented in figure 9.3 is showing the coupling constant limit $g_{\alpha\gamma}$ as a function of the axion mass m_α.

The axion masses scanned in this period is 0.4-1.01 eV/c^2. A part of this scan purpose was to fill the gaps created by the ^{3}He leak in 2008 and the limit obtained for the mass range 0.39-0.64 eV/c^2 had an average value of 2.81×10^{-10} GeV^{-1} at a 95% confidence level [140].

In this thesis a combined limit in the $g_{\alpha\gamma}$ coupling, is provided from both Micromegas detectors in CAST for the years 2009-2010.

The average value of the coupling constant obtained for this work lying in the range of interest 0.65-1.01 eV/c^2 is:

$$g_{\alpha\gamma} \leq 4.29 \times 10^{-10}\ GeV^{-1}\ at\ 95\%\ CL.$$

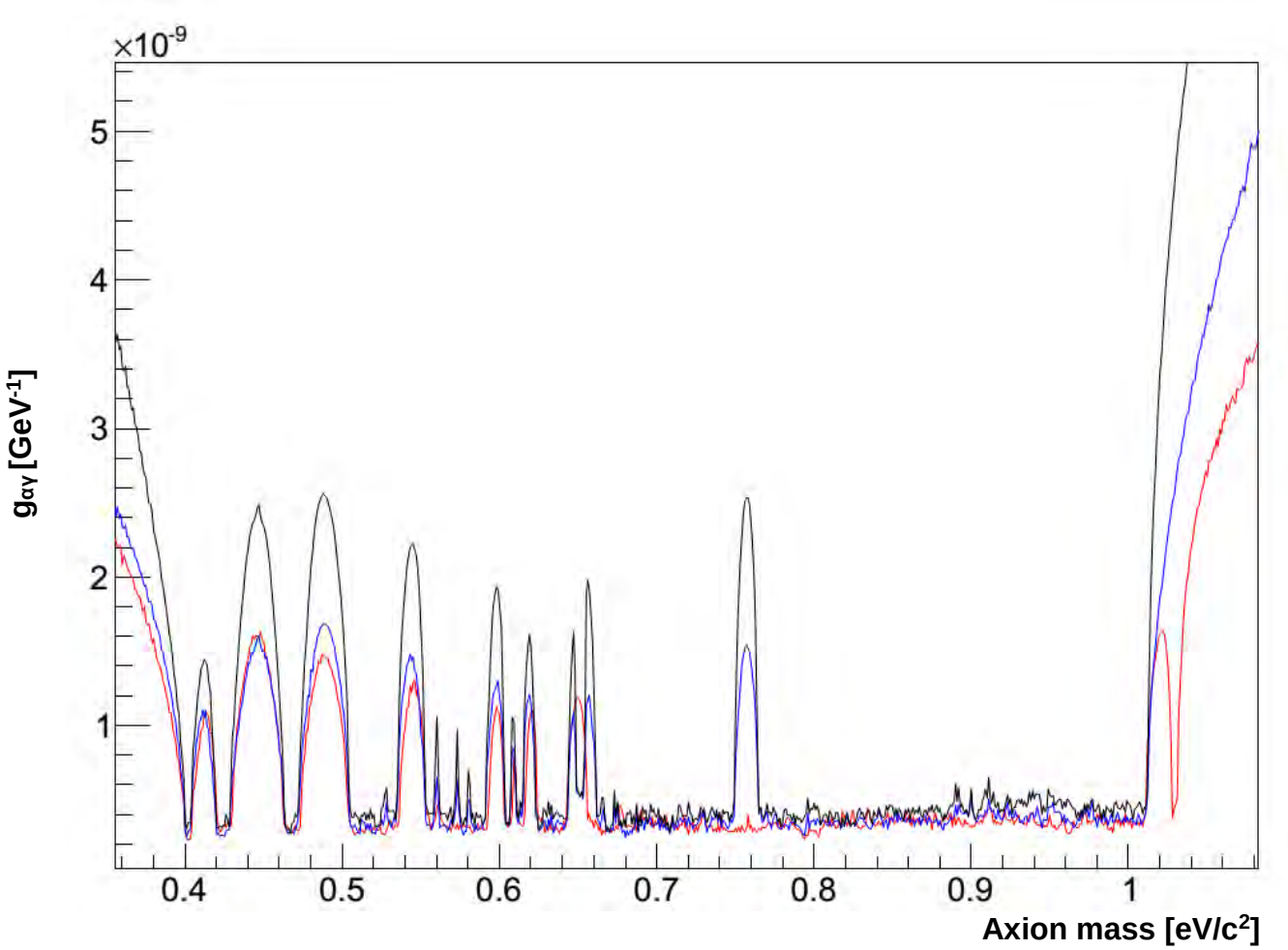

Figure 9.4 Exclusion plot obtained from Sunset Micromegas data. The coupling constant limit is plotted as a function of the axion mass for the period of 2009 and 2010. The axion mass region 0.4-0.64 eV/c^2 corresponds to the period of 2008 gaps, where a leak problem occurred in CAST. In red the coupling constant is calculated for Sunset1 detector while in blue Sunset 2 is presented and in black the combined plot is drawn.

The other CAST detectors (Sunrise Micromegas and CCD) contribute to the final exclusion plot provided by CAST experiment and improve the coupling constant limit.

The data is combined by using the total expected counts for the total tracking time exposure for the years 2009-2010 as a function of m_α and the total counts that CAST detected in both Sunset detectors.

The most conservative limit is given in Figure 9.5 combining the three Micromegas lines from 2009 to 2011. The data acquired by the CCD/Telescope are under analysis and are not included in this plot. The plot represents 418 axion mass steps in addition with the first 252 ^{3}He steps that already released in a previous publication [125]. As a result an axion mass coverage has been obtained in the range between 0.39 and 1.17 eV.

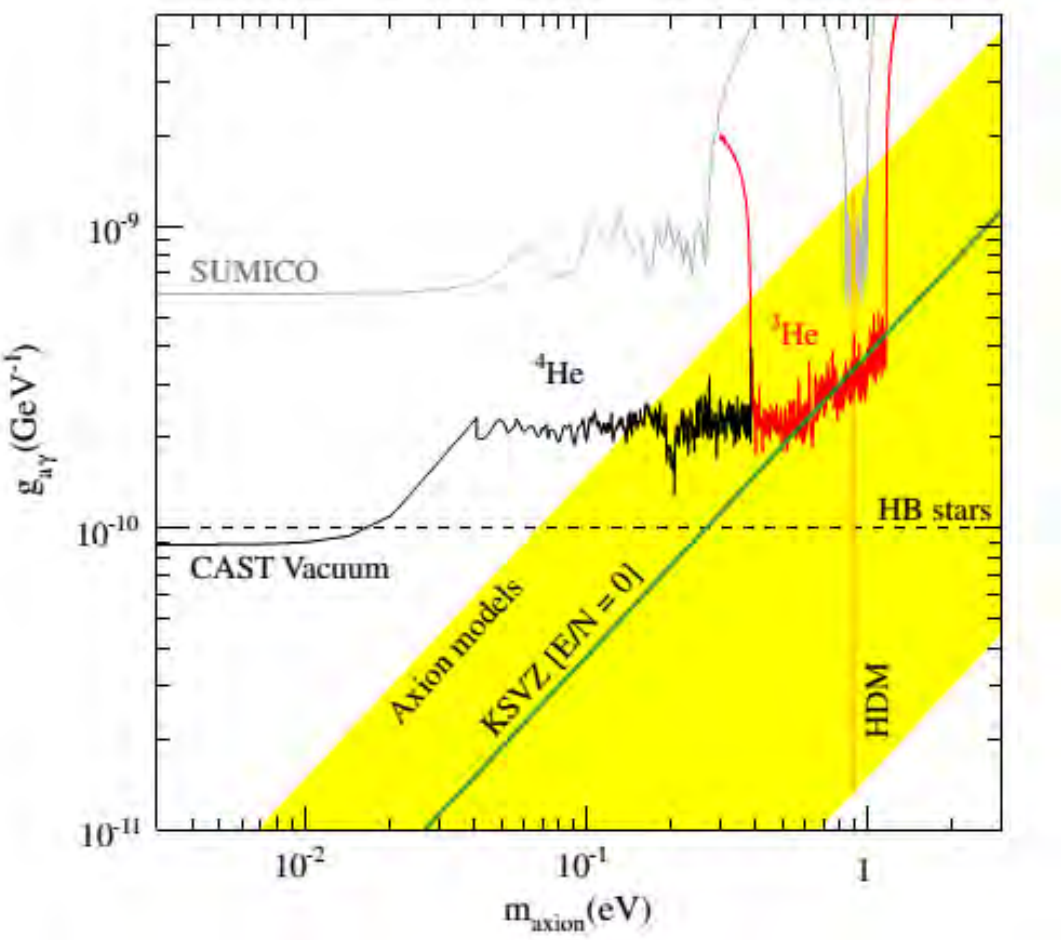

Figure 9.5 Exclusion regions in the $m_\alpha - g_{\alpha\gamma}$ plane achieved by CAST in vacuum [137],[138], ^{4}He [139], the first part of the ^{3}He phase [140], and the latest results that closing the hot dark matter gap in 2011 [125] (all in red). Constraints from the Japanese Sumico detectors are also shown [141],[142], horizontal branch (HB) stars [143] (a somewhat more restrictive limit stems from blue-loop suppression in massive stars [144]), and the hot dark matter (HDM) bound [145]. The yellow band represents typical theoretical models with |E/N−1.95|=0.07–7. The green solid line corresponds to E/N=0 (KSVZ model).

10 Dark energy

CAST presence and future prospects include the extension of its physics program to the dark energy sector. The focused interest of CAST, that is the detectors performance in the sub-keV range, covers also the spectral range expected for solar chameleons which are particle candidates from the dark energy sector. In parallel with the axion dark matter searches performed, effort has also been given (as a part of this thesis) to the chameleon dark energy search.

10.1 Introduction

Physics adopts the idea that space contains a form of energy whose gravitational effect resembles that of Einstein's cosmological constant, Lambda (Greek capital letter: Λ) and this concept is nowadays referred as Dark energy. This form of energy permeates all of space and tends to accelerate the Universe expansion as astrophysical observations of type Ia supernovae [151],[152] indicate[43].

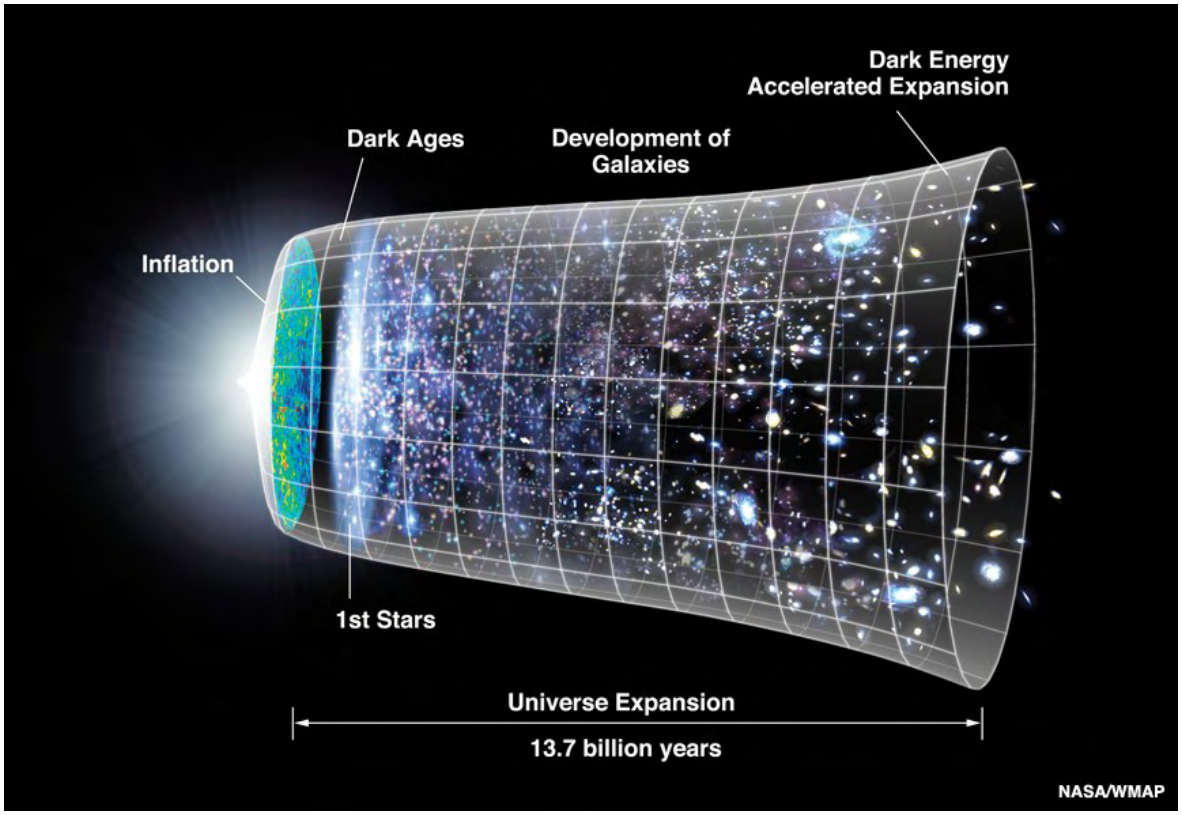

Figure 10.1 The expansion history of the Universe since the Big Bang

[43] The Nobel Prize in Physics was awarded to Saul Perlmutter, Brian P. Schmidt and Adam G. Riess for their leadership in the discovery of the expanding Universe in 2011.

The standard model of the Dark Energy is that of Cosmological Constant but the cosmic expansion acceleration effects has led to the proposal of a Fifth Force or Quintessence. The Quintessence theory introduces a slim scalar field which couples to matter fields. However, a new theoretical proposal has been made in which the scalar field has a mass that is a function of the ambient background density. The novel scalar field is named Chameleon.

Dark energy should be homogeneous and not very dense since it is quite rarefied (10^{-30} g/cm^3). Although Dark energy is not known to interact through any of the fundamental forces, is making up to 68% of the universal density. Both leading models that are a cosmological constant and quintessence have a common characteristic: they both show the strong negative pressure that explains the observed expanding of the universe.

Astrophysical observations and measurements have been corroborated the High-Z Supernova Search Team [152] and gave additional support to the Dark energy existence. Measurements of the cosmic microwave background, gravitational lensing and improved analysis of supernovae data have been consistent with the dark energy models proposed as the Lambda-CDM model or the Quintessence model [153]. Supernovae are excellent standard candles across cosmological distances and they can provide the expansion history of the universe by measurements, which reflect the relation between the distance to an object and its redshift. Therefore, supernovae are useful for cosmology and dark energy observations through their apparent magnitudes.

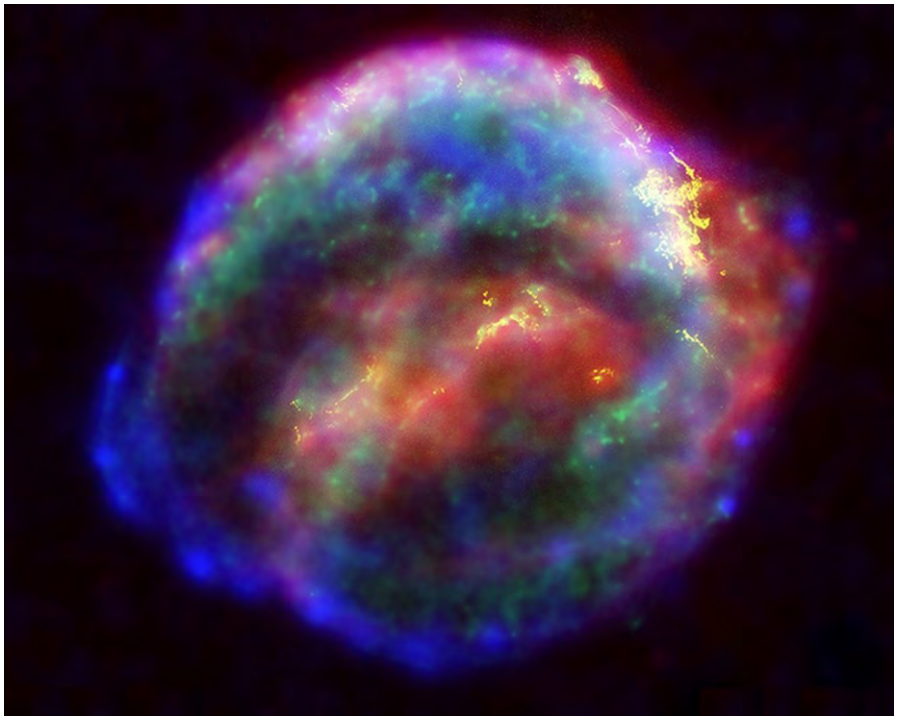

Figure 10.2 Multi-wavelength X-ray, infrared and optical compilation image of Kepler's supernova remnant, SN 1604.

Cosmic microwave background anisotropies indicate the geometry of space with the total amount of matter in the universe. Since the universe shape is close to flat the critical density ρ_c of the Friedmann universe[44] should be equal to the observed density ρ. The total amount of matter in the Universe (baryonic and dark matter) accounts for only 30% of the critical density.

The remaining amount of ~70% implies the existence of an additional form of energy and according to the Wilkinson Microwave Anisotropy Probe (WMAP) seven year analysis 72.8% of the Universe is made up of dark energy.

Cosmological observations like Weak Gravitational Lensing, Baryon Acoustic Oscillations (BAO), Large scale Structure (the theory of which, governs the formation of structures in the Universe) and finally Hubble constant data analysis, suggest the dark energy existence.

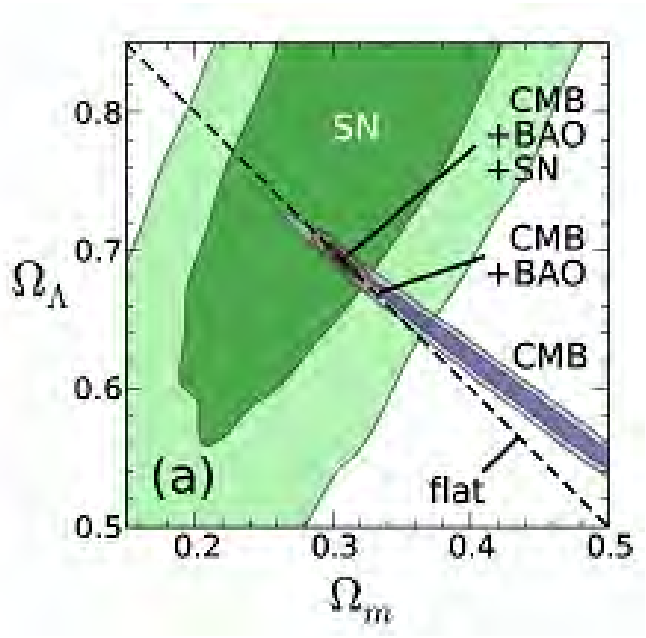

Figure 10.3 Constrains of the Dark energy model parameters and Dark matter content of the Universe (Ω_m). The intersection of Supernovae (SNe), CMB and BAO ellipsis, indicate a topologically flat universe composed of 68.3% dark energy and 26% dark and baryon matter.

10.2 Quintessence

The property of dark energy is characterized by the equation of state $w = P/\rho$ where P is the pressure and ρ is the energy density. The dark energy has a negative pressure and according to measurements, w is less than $-1/3$. The acceleration of the flat Friedmann-Robertson-Walker (FRW) universe is given by the equation

[44] The Friedmann equations are a set of equations in physical cosmology that govern the expansion of space in homogeneous and isotropic models of the universe within the context of general relativity.

$$\frac{\ddot{\alpha}}{\alpha} = -\frac{4\pi G}{3}(\rho + 3p) \quad (10.\ 1)$$

where $\alpha(t)$ is the scale factor of the universe and the second derivative represents the acceleration. In order to achieve acceleration the second derivative should be positive and thus, negative pressure is acquired from the $(\rho + 3p)$ term.

A well-known entity that fills the present day universe and has negative pressure is the cosmological constant Λ, which have the sense of the vacuum energy density. However it is evident that the cosmological constant cannot have the same value in different epochs like in the case of phase transitions and at inflation era. The cosmological constant can arise from the vacuum energy in particle physics that quantum field theory predicts, but there is a huge discrepancy between the value of the quantum vacuum and the observed energy scale.

The search for an alternative explanation to accelerated cosmic expansion has led to the proposal of a Fifth Force [153] that is usually dubbed Quintessence. This force should permeate all of space and time in order to explain the accelerated expansion. The difference between the Cosmological constant and Quintessence is that, Quintessence is a dynamical field that it can change over time and can be either attractive or repulsive depending on the ratio of its kinetic and potential energy.

A scalar tensor gravity model that introduces a gravitational coupled scalar field has the following action form:

$$S = \int d^4x\sqrt{-g}\left(\frac{\mathcal{R}}{16\pi G} - \frac{1}{2}(\partial\varphi)^2 - V(\varphi)\right) + S_m[g^J] \quad (10.\ 2)$$

where φ is the gravitational coupled scalar field with potential $V(\varphi)$, g is the determinant of the metric $g_{\mu\nu}$, $\mathcal{R}$ is the Ricci scalar, G the gravitational constant and S_m the matter action.

The Quintessence theory predicts the existence of a slim scalar field which couples to all matter fields. Experimental searches have ruled out deviations to the Equivalence principle and thus a novel proposal made by Khoury and Weltman [155] introduces the idea of a slim scalar field that has a mass which is a function of the background density.

Since the density close to large scale structure as the earth is enormous, the scalar field should have a large mass term and thus not contradict with local tests of gravity. Contrary, on cosmological scales, the field would be slim with a mass term $m_\varphi \approx H_0$ where H_0, is the Hubble constant today.

Therefore the field is changing in accordance with the density background and so is called a Chameleon field. The chameleon model theory avoids the bounds set on the quintessence theory by the gravitational experiments.

10.3 Solar Chameleons

Chameleons are scalar particles that couples to matter and they have been postulated as Dark Energy particle candidates. Their coupling to matter is non-trivial and leads to a density depended potential.

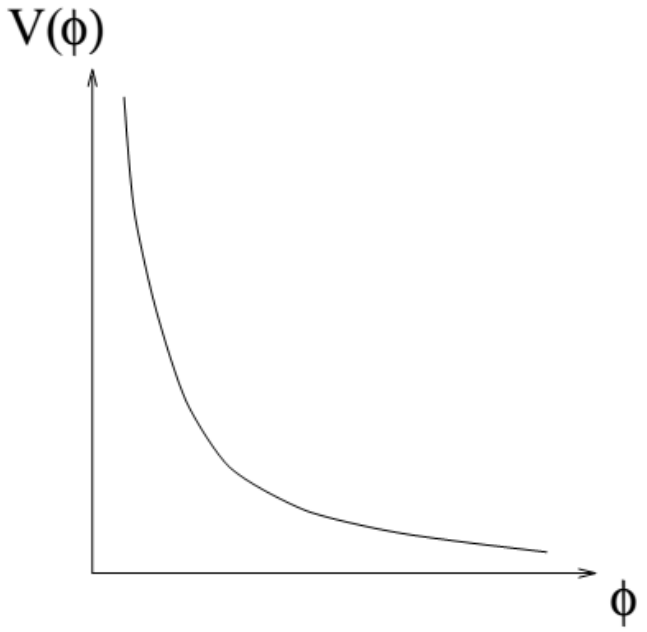

Figure 10.4 The scalar potential $V(\varphi)$for the chameleon field as a function of gravitational coupled scalar field φ

Therefore, their mass is crucially affected by the environment. Quintessence models postulate the existence of a scalar field φ that is rolling along a potential $V(\varphi)$. When the field value is large, as shown in Figure 10.4, the potential decreases and this can lead to the universe acceleration.

At the present day cosmic acceleration, the dynamical scalar field is of the order $m_{\varphi}{\sim}H_0{\sim}10^{-33}\ eV$. Such a small value of the field that couples to matter would lead to violations to Newton's law and the presence of the fifth force. This can be avoided if the scalar field that is coupled to matter modifies the Newton's constant as follows:

$$G_N(\varphi) = e^{2\beta\varphi/M_{Pl}} G_N \tag{10. 3}$$

where $M_{Pl} \cong 2 \cdot 10^{18} GeV$ is the reduced Planck mass and the coupling β is a model free parameter. The dynamics of the chameleon field is governed by an effective potential that in the presence of matter takes the following form:

$$V_{eff}(\varphi) = V_{\varphi} + e^{2\beta_m\varphi/M_{Pl}}\rho_m + e^{2\beta_\gamma\varphi/M_{Pl}}\rho_\gamma \tag{10.4}$$

where ρ_m is the matter density around the scalar field, $\beta_{m,i} \equiv \beta_m$ is a universal chameleon-matter coupling for every matter species i, $\rho_\gamma = \frac{1}{4}F^{\mu\nu}F_{\mu\nu}$ is the Lagrangian density of the electromagnetic field. The chameleon-photon coupling exists at tree level or through fermion loops.

The potential V_φ that is used has the inverse power law form:

$$V_\varphi = \lambda \frac{\Lambda^{4+n}}{\varphi^n} \tag{10. 5}$$

where Λ is a mass scale and n the discrete index. In case, $n \neq -4$ the λ parameter can be absorbed into Λ.

By solving the Klein-Gordon equation for the effective potential, one can obtain the minimum of the field that is also density depended. The mass obtained for a dense environment is such that the force mediated range is smaller than 0.1 mm and thus undetectable.

Chameleons can be produced in high photon density regions where strong magnetic fields are present like inside the Sun. Photons mix with chameleons in regions of strong magnetic fields. In the Sun, strong magnetic fields are found in the tachocline[45], which is a thin transition region between the core region and the convective region of the sun.

Chameleons' couple to the polarization orthogonal to the magnetic field and this is the difference that distinguishes the potential signal of axions that couples with the polarization parallel to the magnetic field.

The conversion probability for photons of energy ω to chameleons in a magnetic field B that travels by a length L is given by the relation [156]

$$P_{chameleon}(\omega) = sin^2(2\theta) \cdot sin^2\left(\frac{\Delta}{\cos 2\theta}\right) \tag{10. 6}$$

where

$$\Delta = \left(m_{eff}^2 - \omega_{pl}^2\right)L/4\omega \tag{10. 7}$$

ω_{pl} is the plasma frequency and the mixing angle θ is given by the relation

$$\tan(2\theta) = \frac{2B\omega\beta_\gamma}{\left(m_{eff}^2 - \omega_{pl}^2\right)M_{Pl}} \tag{10.8}$$

Chameleons should have an effective momentum $k^2 = \omega^2 - \left(m_{eff}^2 - \omega_{pl}^2\right) \geq 0$ in order to

[45] A region inside the Sun at a distance of around 0.7 $R_\odot$.

travel inside the Sun while is forbidden to propagate when $k^2 < 0$. Inside the Sun, chameleons have this specific property ($k^2 \geq 0$) and once produced in the tachocline, they leave the Sun unscathed. There is however a probability that a small chameleons fraction can reconverted into photons at the magnetized solar photosphere by the inverse Primakoff effect.

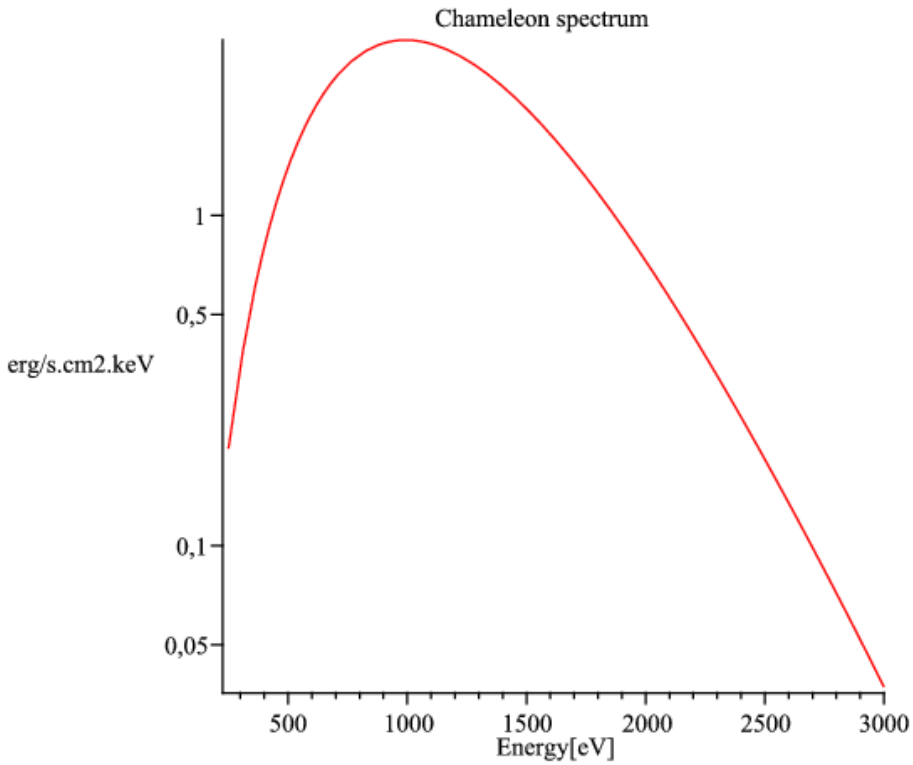

Figure 10.5 The energy spectrum of the chameleons escape from the Sun. The coupling was chosen to be $\mathbf{M_\gamma = 10^{5.8}\ GeV}$ and the magnetic field used in the calculations is B=30T. The integrated flux at the solar surface is 4 erg·s^{-1}·cm^{-2} [157]

10.4 Detection of Solar Chameleons with the Inverse Primakoff effect

Chameleons couple to photon in a similar way to the axion coupling. The electromagnetic action for chameleons can be defined as:

$$S_{EM} = -\int d^4x \sqrt{-g}\frac{e^{\varphi/M_\gamma}}{4}F^2 \qquad (10.\ 9)$$

where g is the determinant of the metric $g_{\mu\nu}$ and $F^2 = F_{\mu\nu}F^{\mu\nu}$ is the square of the photon field strength. Detection prospects for Solar and terrestrial Chameleons [157] imply that the chameleon parameter space depends on the discrete index n (Equation 10.5) and the coupling

to matter and photons. The photon coupling parameter can be defined as β_γ and stellar evolution, constrains $\beta_\gamma \leq 10^{10}$ for a big part of the parameter space.

Chameleons leaving the Sun can arrive unhindered in the earth's atmosphere that they penetrate because of their high energy. Therefore they can be back-converted into photons in magnetic Helioscopes. In CAST Helioscope, chameleons emerging from the Sun can be back-converted to photons that their energy is higher than their mass in the atmosphere and in matter in front of the magnetic pipes.

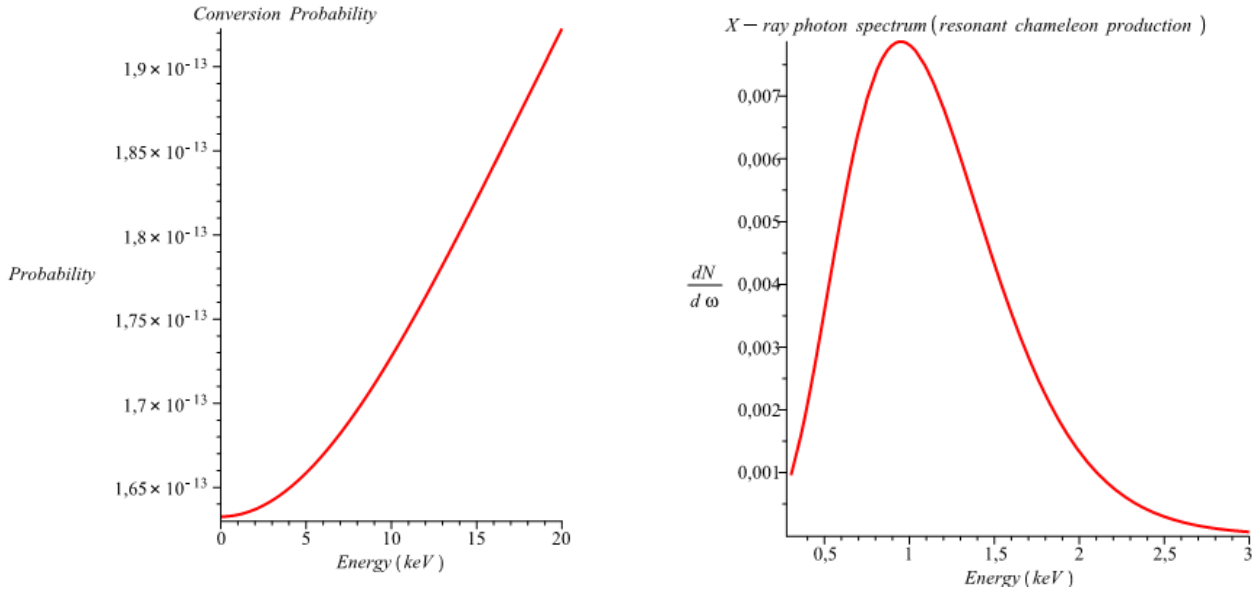

Figure 10.6 Left: The conversion probability in CAST magnetic pipes (in vacuum), as a function of the photon-chameleon energy in keV. The probability calculated by using $\boldsymbol{\beta_\gamma = 10^{10.29}}$. Right: The resonant spectrum of back-converted photons from solar chameleons in counts per hour and per keV. The matter coupling has been chosen to be $\boldsymbol{\beta_m = 1.8 \cdot 10^7}$ and the shell magnetic field in the Sun of 30 T.

In 2013 CAST began to search for dark energy particles (chameleons) and upgraded its program to include a windowless silicon drift detector (SDD) with high quantum efficiency, good energy resolution and relatively large area.

The detector collected ~15 hours of background data in the range of interest that is 400-1500 eV. The results of the data analysis are shown in Figure 10.7. The absence of X-ray excess allows the derivation of a preliminary limit to the chameleon to photon coupling

$$\beta_\gamma \leq 9.26 \cdot 10^{10} \; at \; 95\% \; C.L.$$

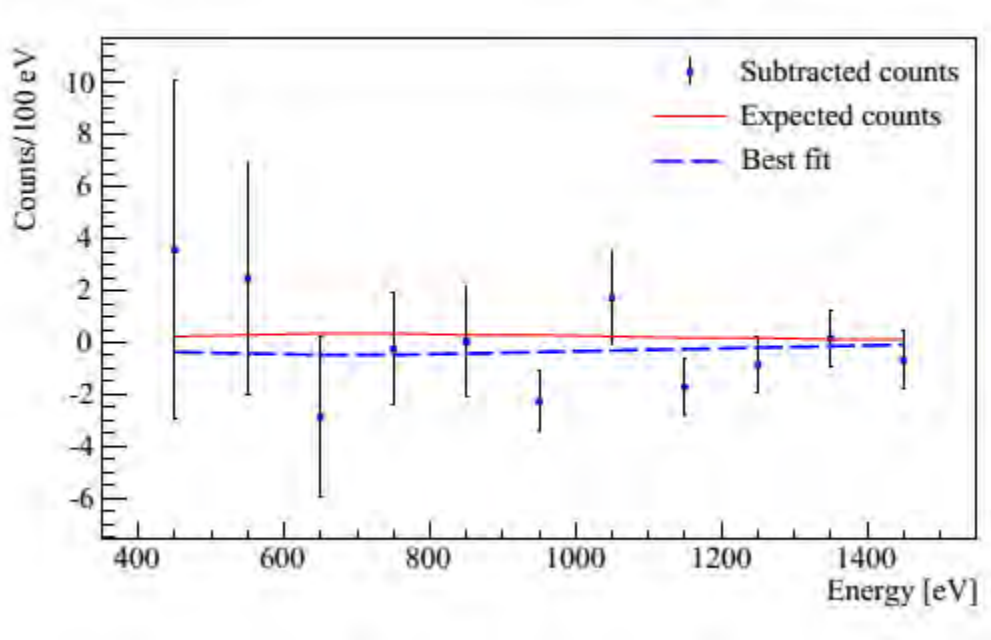

Figure 10.7 The plot shows the expected number of counts in the SSD detector from chameleon conversion in CAST magnetic pipes, the subtracted counts (tracking-background) and the best fit to data.

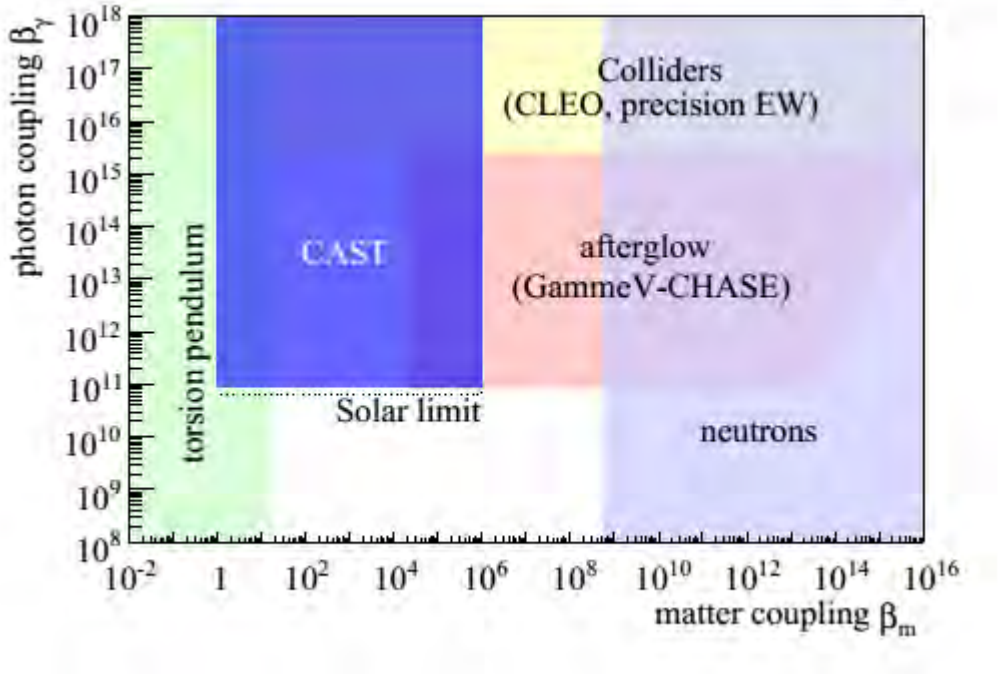

Figure 10.8 Constrains on the coupling of the chameleons to photon and matter achieved by CAST (purple) in 2013. Bound set by torsion pendulum tests (in green), resonance spectroscopy measurements of quantum states of ultracold neutrons (lilac), CHASE (pale orange) and collider experiments (yellow) are also shown [146]

10.5 Detection of Solar Chameleons through Radiation Pressure

Solar chameleons reaching Earth could also be detected by exploiting their coupling to matter β_m with an opto-mechanical force sensor [158]. CAST is ready to use a force sensor that is called KWISP for “Kinetic WISP detection” (Weakly Interactive slim Particles). The sensor is under development at INFN[46] in Italy and it is based on a thin micro-membrane that can be displaced from its rest position by a force (or equivalent pressure) applied to it. A thin but quite dense foil is utilized for chameleons reflection that is a density depended effect. Chameleons that incident into a dense slab of material, result in a momentum transfer that has the same effect as the radiation pressure. It has been estimated that solar chameleons originated from Sun’s tachocline has a broad spectrum distribution peaking at ~600 eV.

The KWISP sensitivity to solar chameleons depends on the chameleon model used. The detection principle of this experiment is more sensitive to strongly coupled chameleons that present large matter coupling β_m and large mass scales Λ. There are quantum corrections like fragmentation and loop corrections that could affect and modify the shape of the effective potential. However the proposed experiment is not a precision probe but has a purpose to distinguish between particles which do and do not reflect.

The detection principle is based on the KWISP’s membrane displacement that is sensed by optical means like interferometry which giving a direct measurement of the force (pressure) acting on the membrane. The maximum sensitivity to radiation displacement is enhanced if the membrane is placed inside a high sensitivity Fabry-Perot (FP) optical resonator, which multiplies the gain factor.

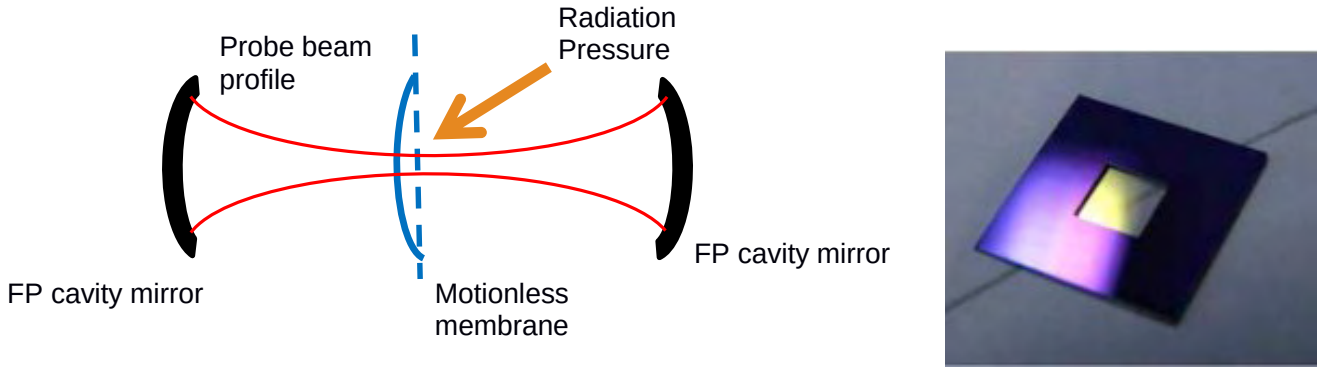

Figure 10.9 Left: Sketch of the membrane in a cavity. The membrane displacements (solid blue line) with respect to the motionless membrane (dashed blue) will modify the spatial mode of the probe beam responding to external pressure. Right: A picture of 1×1 mm and 50 nm thick Si_3N_4 micro-membrane mounted on a 200 μm thick Si substrate.

[46] Istituto Nazionale di Fisica Nucleare

Chameleons flux can distort and displace the micro-membrane from its equilibrium position and thus excite its vibrational states. Sub nanometer movement of such membrane can be detected by placing it inside a Fabry-Perot optical resonator [159].

Fabry-Perot cavities have found applications in several advanced fields as quantum electrodynamics (QEDs) test, and gravitational wave detection. The high sensitivity of the membrane displacements can be reached by the cavity finesse (Q resonator).

During the operation the FP is kept at resonance with a probe laser beam by using a feedback loop. The control signal of this loop contains the information of the membrane motion and hence on the solar chameleon flux that can distort the membrane movement.

An opto-mechanical sensor for radiation pressure measurements (called KWSIP) prototype has already built at INFN Trieste. The micro-membrane is placed inside a FP cavity as shown in Figure 10.10

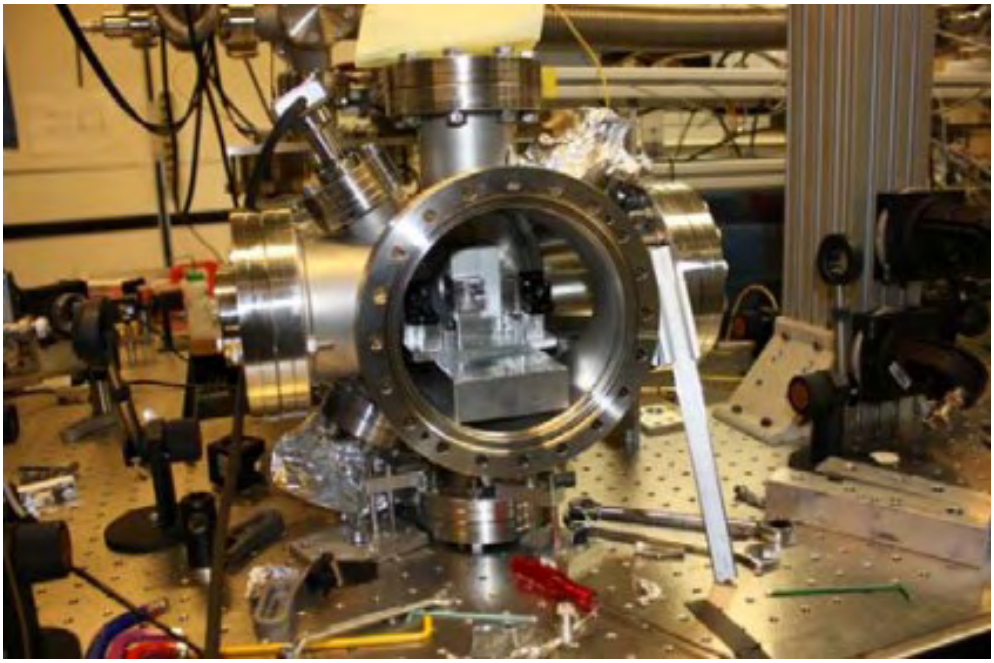

Figure 10.10 A photograph of the KWISP opto-mechanical force sensor prototype during alignment of the optics at INFN in Trieste. [168]

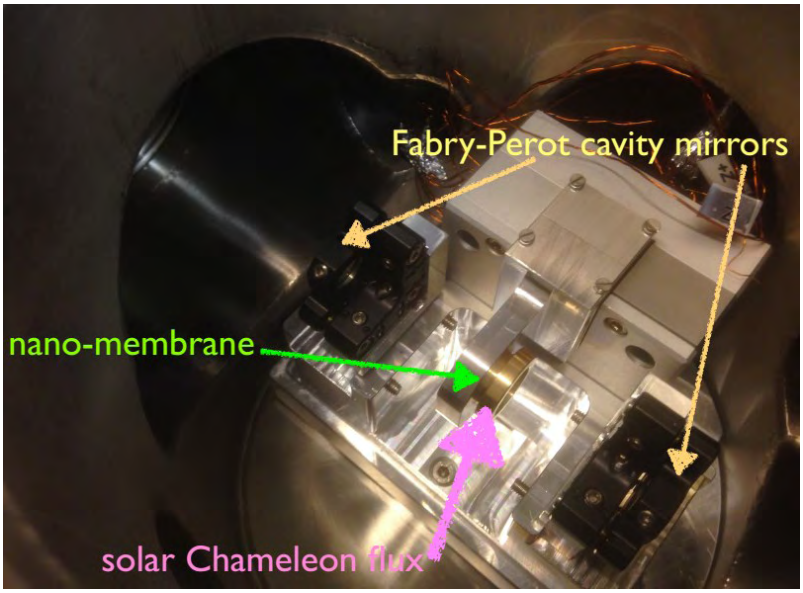

Figure 10.11 A photograph of the FP cavity optics support set inside the vacuum chamber. The FP cavity mirrors are mounted on two black tilting mounts. The membrane holder is mounted at the center of the cavity on a 5-axis PZT movement stage (Pentor model by Piezosystem Jena inc.). [168]

The KWISP's prototype sensitivity to external radiation pressure can be tested by subjecting the micro-membrane to the pressure exerted by a laser beam. To test and monitoring the membrane movements a second probe beam is applied. The optical setup is schematically shown in the next figure.

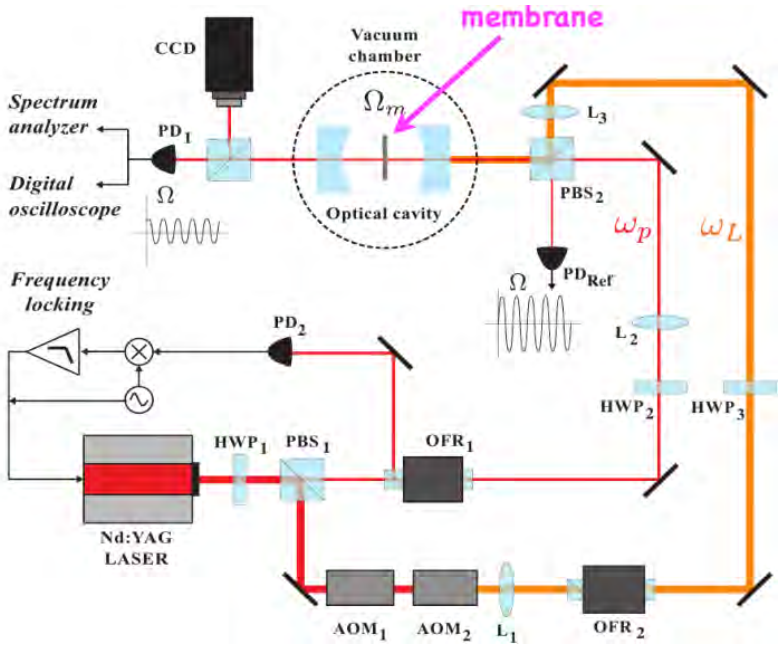

Figure 10.12 The optical setup for measuring the KWISP detector sensitivity to an external force impact. The probe beam (ω_p) at 1064 nm is frequency-locked to the FP cavity and senses the membrane movements. An intense frequency-shifted pumping beam (ω_L) exerts a control radiation pressure on the membrane for calibration purposes. [168]

The working principle of the KWISP detector relies to the FP optical resonator cavity that is frequency-locked to a laser beam using an electro-optic feedback. The feedback acts on the laser active medium, that is a crystal in case of a Nd:YAG laser. The instantaneous distance between the cavity mirrors that is left “free” to float, is always a half-integer multiple of the laser wavelength. In case where cavity is on resonance, its normal modes are not perturbed if a thin micro-membrane, transparent to the laser wavelength, is aligned and positioned in a node of the standing intra-cavity electric field.

In case of the membrane’s displacement, the membrane mechanical modes are coupled to the TEM modes of the cavity and a detuning mode appears with a typical oscillatory signature that is membrane position dependent. The detuning curve can be used to estimate membrane displacements and therefore by using the membrane’s mechanical characteristics, the force acting on it can be detected [160].

The KWISP sensor employs a 5 mm×5 mm, 100 nm thick, Si_3N_4 micro-membrane (Norcada Inc., Canada) with density $\rho=3.2$ g/cm^3 that is set inside a 85 mm long FP cavity in concave-concave configuration. The FP-membrane assembly is contained inside a vacuum chamber that is evacuated at $\approx 10^{-4}$ mbar. By proper alignment, the FP cavity finesse was measured to be $F\approx 60000$.

10.6 Finite elements simulations of the KWISP membrane

Radiation pressure can provide a direct coupling between the electromagnetic field and the translational degrees of freedom of macroscopic objects. An Optomechanical device as the KWISP sensor, in which a mechanical oscillator detunes an electromagnetic cavity is a field of ongoing research in astrophysics, cosmology, quantum optics, and nanoscience.

As explained in section 10.5, the KWISP detector consists of an optical cavity into which a membrane is suspended on a PZT-actuated vacuum compatible 5-axis movement stage (“Pentor” model). When the membrane is deflected by an amount x, the cavity experiences a detuning Δ which is proportional to x. Henceforth, the light stored in the cavity exerts a force (radiation pressure) on the membrane that is proportional to the intracavity power.

In order to reach the quantum regime of the KWISP device, the force per photon exerted by the cavity field to the membrane assembly, should be maximized. It is also crucial to maximize the membrane response to the radiation pressure. An advantageous action to increase the detector performance is also to decrease the cavity thermal bath temperature.

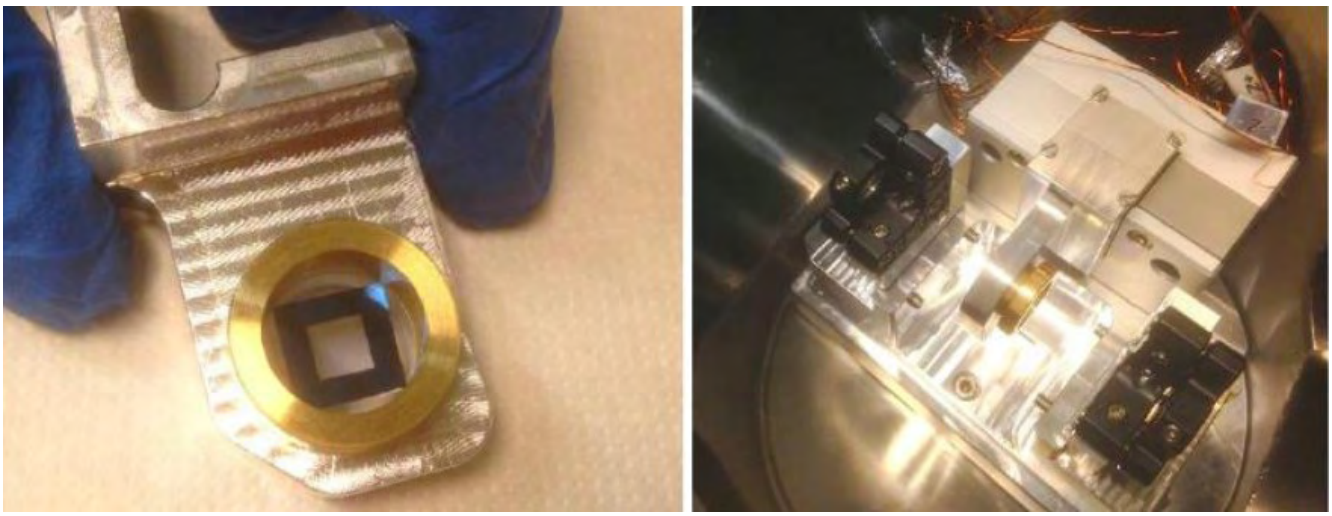

Figure 10.13 The micromembrane is mounted inside a holder (left). A photograph of the FP-membrane assembly set inside its vacuum chamber (right). [168]

The varying transmission function of the cavity is caused by interference between the multiple reflections of light between the two reflecting surfaces. The constructive interference occurs if the transmitted beams are in phase and that corresponds to a cavity with high-transmission peak.

The transmission spectrum of a FP-interferometer cavity will have a series of peaks, where constructive interference occurs, spaced by the "free spectral range" or FSR. Free spectral range is the separation (measured either in terms of frequency, wavenumber or wavelength) between adjacent transmission maxima (Figure 10.14).

The FSR is related to the full-width half-maximum, $\Delta\nu$, of any one transmission band by a quantity known as the *finesse*:

$$Finesse \equiv \frac{FSR}{\Delta\lambda} \tag{10. 10}$$

Cavities with high finesse show sharper transmission peaks. Finesse is a function of reflectivity and very high transmission peaks require highly reflective mirrors. High quality factor (Q factor) is also a prerequisite for lower rate of energy loss because the Q factor characterizes a resonator's bandwidth relative to its center frequency.

The Quality factor is defined as the ratio of the transmission peak to the FSR.

$$Q \equiv \frac{w}{FSR} \tag{10. 11}$$

where w is the transmission peak value in Megahertz.

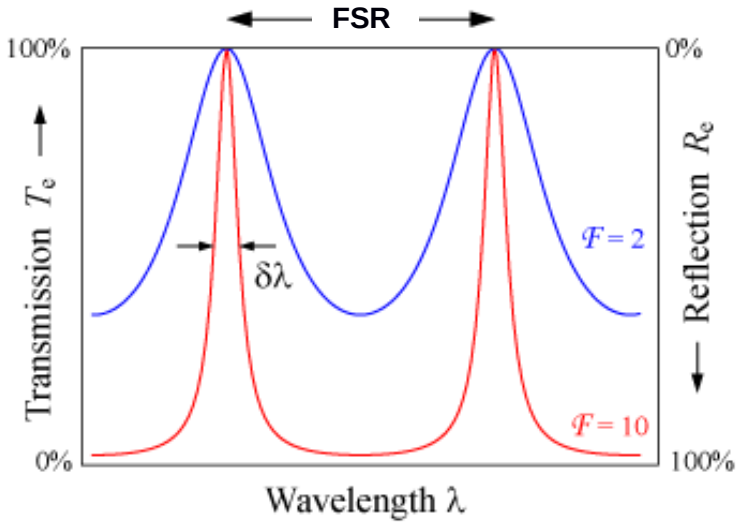

Figure 10.14 The transmission of a cavity as a function of the wavelength. A high-finesse cavity (red line) shows sharper peaks and lower transition minima than a low-finesse cavity (blue line). The FSR is $\Delta\lambda$ as shown in the plot.

Finesse measurements performed in INFN in Trieste, reveal the finesse of the KWISP detector and the resonant mode transmission peak.

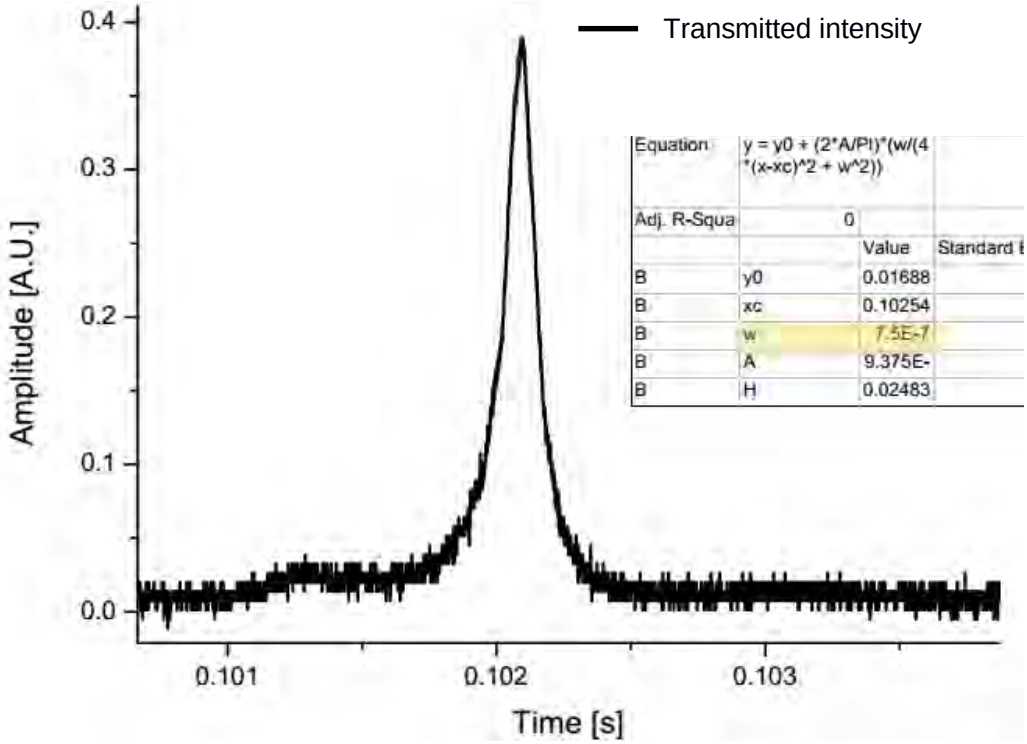

Figure 10.15 Resonant mode transmission peak fitted with a Lorentzian in order to estimate the FWHM from the fit. As noticed the finesse was estimated ~60000. In the fit window *w* represents the free spectral range, FSR.

In order to derive the force sensitivity figure for the KWISP sensor the membrane was inserted in a Michelson-type interferometer that corresponds to a single-pass FB. The displacement sensitivity that was measured and that is the minimum membrane displacement detectable in 1 sec of measuring time, was 0.18 $\mathrm{nm}/\sqrt{\mathrm{Hz}}$.

A finite element simulation program has been performed (as a part of this thesis work) to model the Si_3N_4 membrane. The simulations implemented initially to simulate a 5 mm × 5 mm and 100 nm-thick membrane model, as a simple "spring" that its spring constant can be used for the force sensitivity estimation. Later on, Finite Element Analysis (FEA) simulations have been performed in order to estimate the Frequency response and henceforth, the transmission peak of the membrane to a nano-Newton force load. Simulations have been implemented in FEA software Ansys 15.

The geometry of the micro-membrane has been designed into Ansys Design Modeler [161] and the material properties of the Si_3N_4 have been assigned to the specimen created. The first model simulated, has dimensions of 1 mm ×1 mm ×50 nm.

The density of the material assigned is ρ=3184 kg/m^3. The Young modulus that Norcada Inc. Company provides is 314 GPa and the Poisson ratio is equal to 0.27. The KWISP sensor that is under tests in INFN in Trieste has dimensions 5 mm × 5 mm ×100 nm and the simulation performed for this membrane is still under development.

The theoretical analysis carried out is based at a plane silicon nitride membrane that is homogeneously stretched across a rectangular aperture in silicon substrate with a pre-tension per unit length T. The density of the membrane per unit area is μ and its boundaries are clamped. In the absence of external forces, the wave equation that describes the motion of different points in the xy plane of the membrane is:

$$\nabla^2 U(x,y,t) = \frac{\mu}{T}\frac{\delta^2 U(x,y,t)}{\delta t^2} = \frac{1}{v^2}\frac{\delta^2 U(x,y,t)}{\delta t^2} \qquad (10.\ 12)$$

where the Laplace operator is

$$\nabla^2 = \frac{\partial^2}{\partial x^2} + \frac{\partial^2}{\partial y^2}$$

and the wave velocity in the membrane

$$v = \sqrt{\frac{T}{\mu}}$$

The transverse displacement of any point (perpendicular to the membrane plane) is given by the function $U(x,y,t)$. By setting up the boundary conditions and applying separation of variables the transvers displacement becomes:

$$U(x,y,t) = X(x)Y(y)\exp(i2\pi\nu t) \tag{10. 13}$$

The standing wave mode solution can be expressed as

$$U(x,y,t) = \begin{cases} sin(k_m x)sin(k_n y)sin(2\pi\nu_{m,n}t) \begin{cases} 0 < x < x_0 \\ 0 < y < y_0 \end{cases} \\ 0 \begin{cases} x \leq 0 \\ x \geq x_0 \\ y \leq 0 \\ y \geq y_0 \end{cases} \end{cases} \tag{10. 14}$$

where x_0, y_0 are the length and width along the x and y axis respectively and the resonant frequency $\nu_{m,n}$ is depended on the modes of vibrations k_n and k_m that can be expressed as:

$$\left(\frac{2\pi\nu_{m,n}}{\nu}\right)^2 = k_m^2 + k_n^2$$

Because of the clamped boundaries k_m and k_n can have the following values:

$$k_m = \frac{m\pi}{x_0}$$

and

$$k_n = \frac{n\pi}{y_0}$$

In case of the KWISP membrane $x_0 = y_0$ and the above equations can be combined and rearranged to yield [162]

$$\nu_{m,n} = \frac{1}{2}\sqrt{\frac{T}{\mu}}(m^2 + n^2)$$

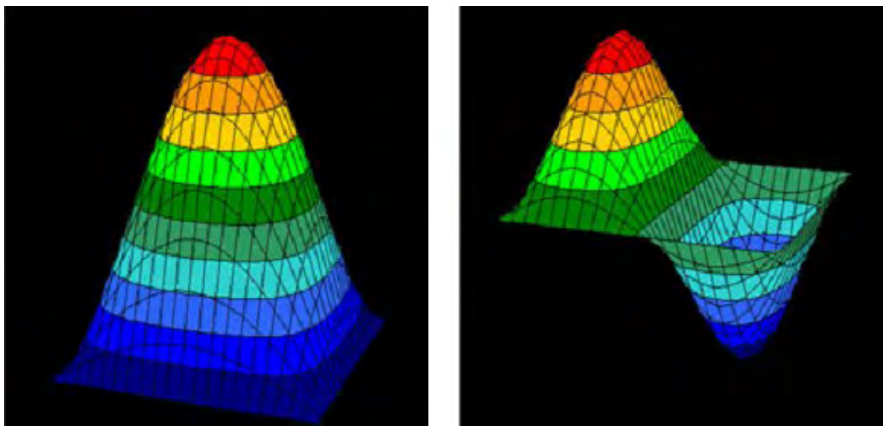

Figure 10.16 The theoretical transverse displacement of the first two modes of vibration Left: The [1, 1] mode of vibration and right: the [1, 2] mode of vibration.

The Finite element analysis performed in Ansys 15, is a 3D model of the silicon nitride membrane. The Finite Elements Analysis is composed by three parts:

- **A Static Structural Analysis**. A static structural analysis determines the displacements, stresses, strains, and forces in structures or components caused by loads that do not induce significant inertia and damping effects.

- **A Modal Analysis**. A modal analysis determines the vibration characteristics (natural frequencies and mode shapes) of a structure or a machine component.

- **Harmonic Response Analysis**. A modal analysis determines the vibration characteristics (natural frequencies - mode shapes) of a structure or a machine component.

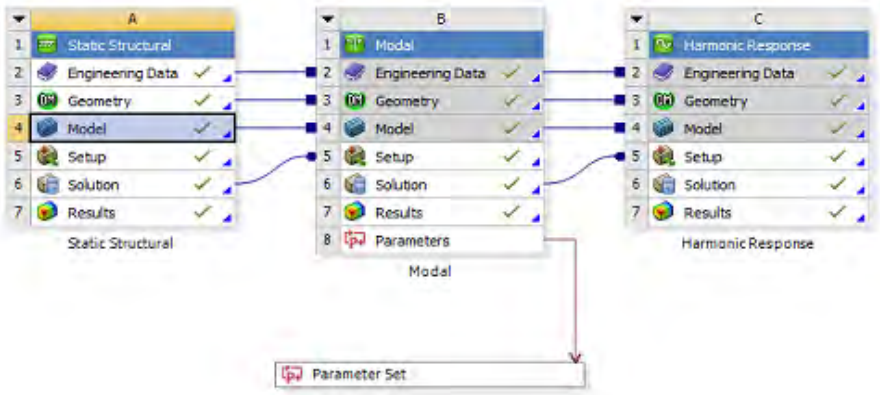

Figure 10.17 The Ansys Workbench environment that combines the Static structural, the Modal and the Harmonic response Analyses. Every module is solved (having in common the Engineering data-material properties, the Geometry and the model Mesh) separately and the solution is provided to the right module.

The simulated membrane model was meshed (as described in chapter 5.5) and 4e+04 elements were created that contain ~3e+05 nodes. Because of the membrane's thickness (50 or 100 nm) there is only one layer in the Z axis. The square elements width in XY plane is between 2-8 μm and depends on the membrane size. The mesh production in Ansys Workbench was accomplished by using the automatic method and the face sizing function.

In the static structural analysis a pressure of 800 MPa was defined in X and Y boundaries because the membrane is pre-stressed.

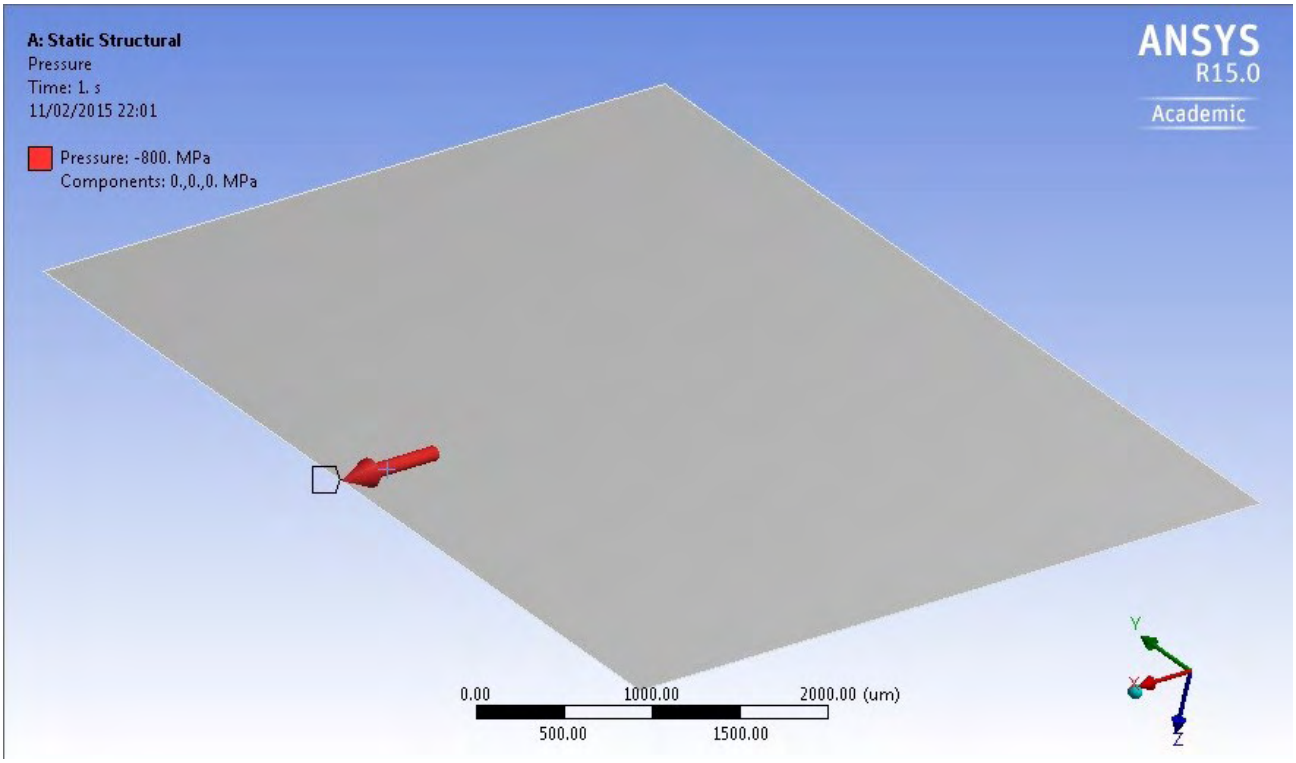

Figure 10.18 The pre-stressed Static structural analysis of the 5 mm × 5 mm ×100 nm model.

The solution of the static structural analysis is inserted in the modal analysis as a pre-stressed model. The results of the stress applied to the membrane can be seen in the figure 10.19.

In the modal analysis the pre-stressed membrane is checked for vibration characteristics, i.e. the natural frequencies of the element and the mode shapes.

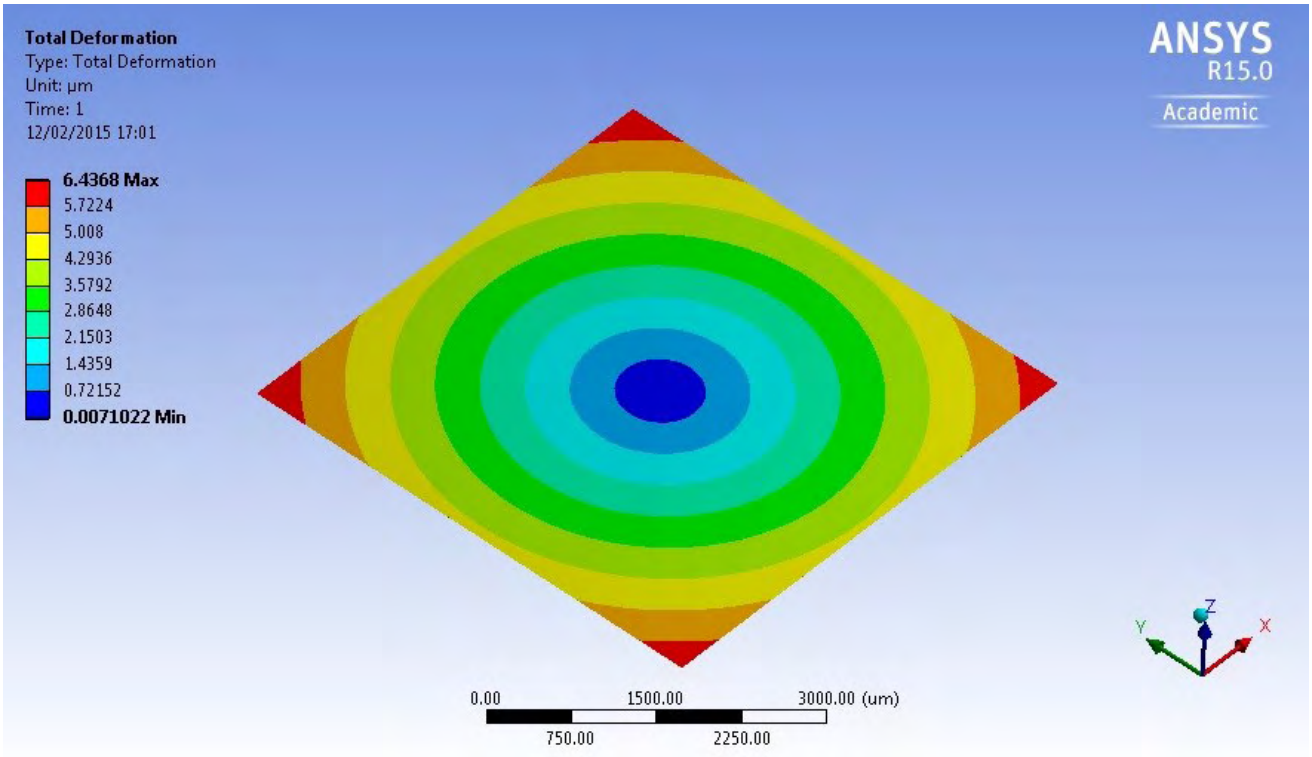

Figure 10.19 The total deformation of the membrane to the 800 MPa stress applied to it from the Static Structural Analysis. (5 mm × 5 mm ×100 nm model)

The normal modes that the Modal solution provides can be seen in table 10.1.

Mode	Frequency [MHz]
1.	9.104671e-004
2.	9.131335e-004
3.	1.525024e-003
4.	0.354442
5.	0.5604231
6.	0.5604231
7.	0.7088864
8.	0.79256
9.	0.7925602
10.	0.9036585
11.	0.9036586
12.	1.033376

Table 10.1 The first 12 normal modes of the Modal analysis. The shaded shell provides the mode of the highest amplitude. (1 mm × 1 mm × 50 nm model)

The modal Analysis solution is coupled to the Harmonic Response analysis in the Ansys Workbench environment (Figure 10.17). A force is applied to the center of the membrane with magnitude 1 Nn and direction vertical to the membrane's surface in order to compare the simulated results with the experimental procedure of the Quality factor estimation. Figure 10.20 shows the transmission peak amplitude and the Lorentz fit provided.

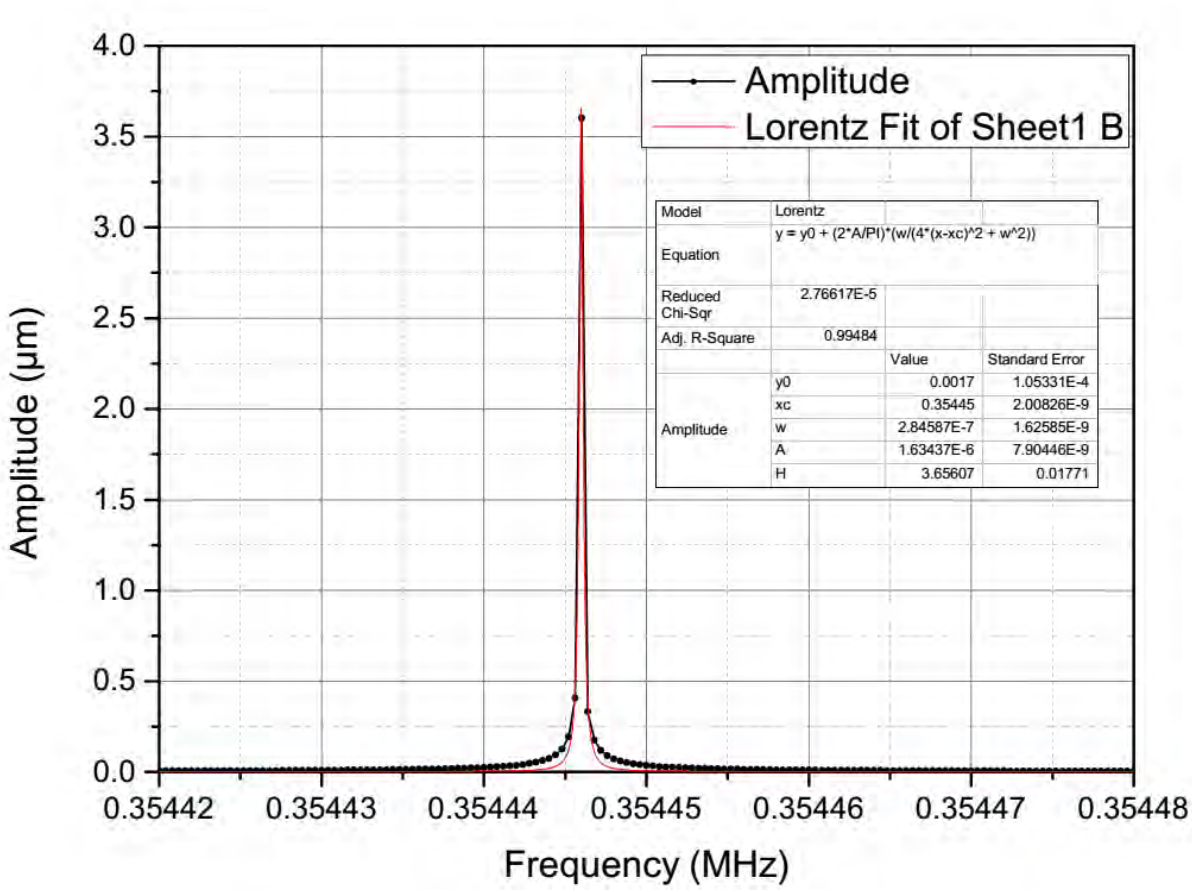

Figure 10.20 The Harmonic Response analysis provides the transmission peak amplitude to the micromembrane when 1 nN force is applied to its center. The Lorentz fit delivers the FSR and the peak value in order to estimate the Q factor. (1 mm × 1 mm × 50 nm model)

The Q factor (Equation (10. 11)) is computed from the fit parameters and was found ~$1.2 \cdot 10^6$. This value is very close to the experimentally value provided from INFN and plotted in figure 10.21. The simulated transmission peak value has ~1% error compared to the experimental value.

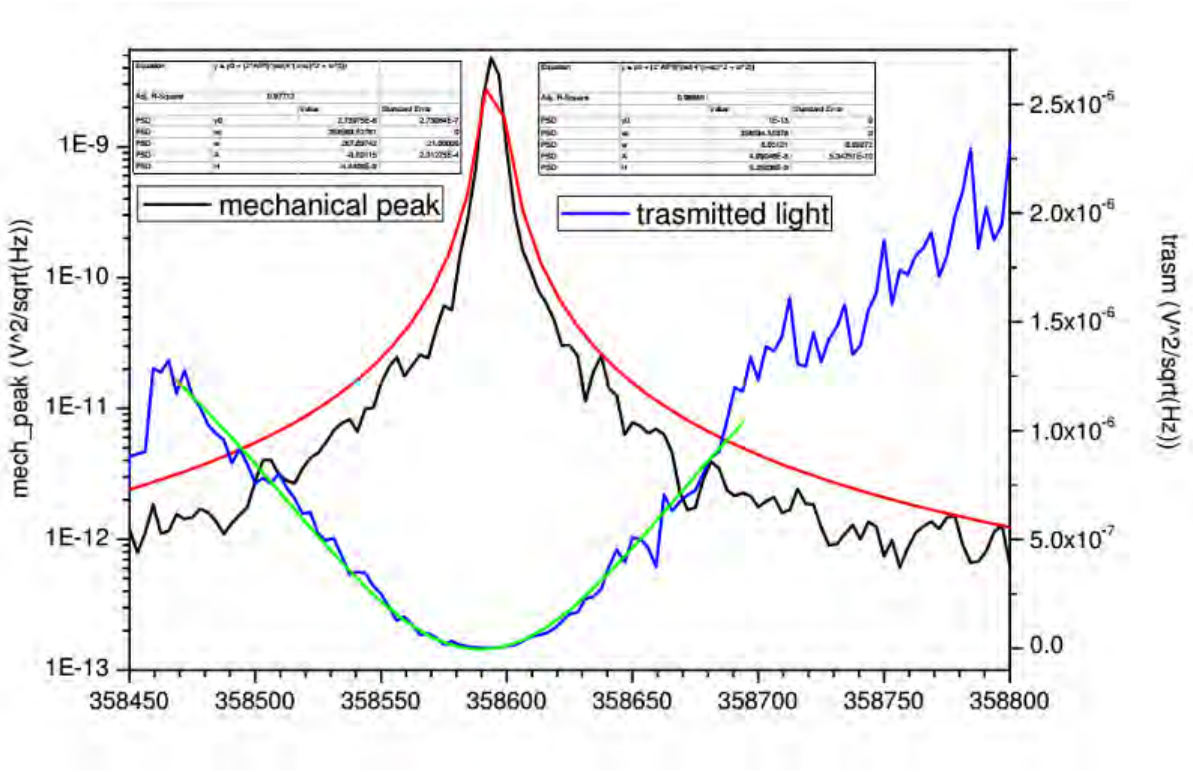

Figure 10.21 The plot shows the transmission mechanical peak as measured at INFN in Italy (black line). The red line shows the Lorentz fit that provides the parameters for the Q factor estimation. (1 mm × 1 mm × 50 nm model) [168]

As shown the agreement between the experimental and the simulated values from the FEA method is quite good. The FEA simulations are still under development for different membrane sizes. The results provided in this section were presented in CAST collaboration meeting in 2014 and 2015.

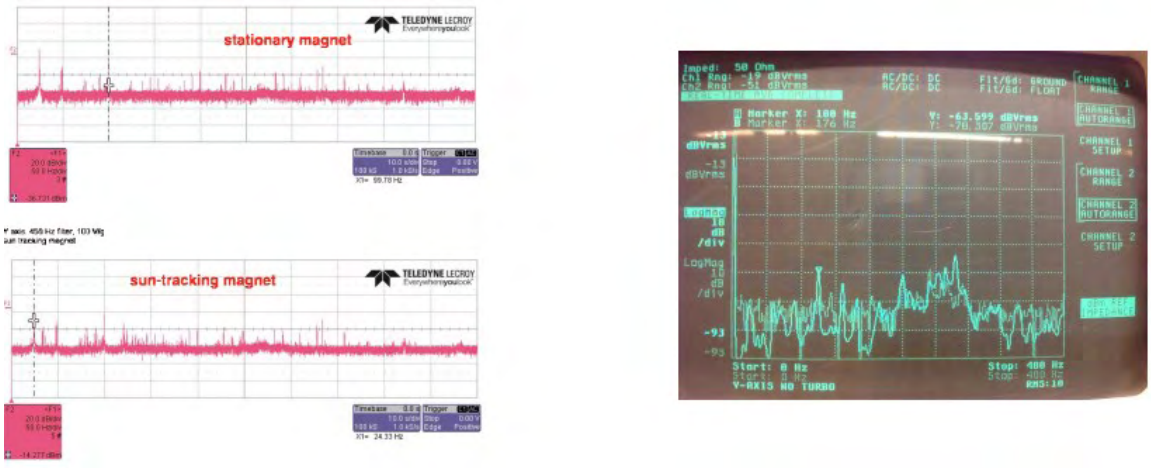

Figure 10.22 (left) Sample accelerometer spectra taken on the sunrise end of the CAST magnet. (right) Sample accelerometer spectrum taken on the Trieste laboratory optical bench. [168]

In order to setup the KWISP sensor in CAST magnet, accelerometer measurements have been performed in CAST sunrise end and in Trieste laboratory (INFN). The measurements show that mechanical vibrations (when the CAST magnet is moving) have no impact to the FP transmission peak. In Trieste peak accelerations of ~ 7×10^{-6} g occur around 100 Hz, while on the CAST magnet, peak accelerations at around 25 Hz (and higher harmonics) of about 1.7×10^{-2} g, with the magnet stationary, and 5×10^{-2} g with the magnet moving. Options to isolate the sensor against mechanical vibrations are still ongoing.

The mechanical characteristics of the KWISP vibrating silicon nitride micromembrane were determined by FEA simulations performed in Ansys 15 software package. In parallel, experiments with the KWISP sensor are still ongoing at INFN in Trieste, in order to complete the sensor's performance before the final setup in CAST. The solar chameleon spectrum for a range of model parameters has been calculated in [158]. The KWISP setup in CAST is sufficient to explore chameleon models with matter coupling $\beta_m \sim 10^3 - 10^{12}$ and photon coupling down to $\beta_\gamma \geq 10^7$. The KWISP sensor is a unique pioneer effort in the field of experimental searches for dark energy.

10.7 Conclusions

In the present thesis an overview of the CAST experiment has been given along with the analysis of the experimental data taking during the 2009-2010 period. CAST continue searching for solar axions but also for other exotica like Axion Like Particles (ALP's), paraphotons and as proposed in the SPSC (CERN), dark energy particles like chameleons. The commissioning, operation and analysis of the data taken with the Sunset Micromegas detector are presented in detail for the Phase II of the CAST experiment.

The CAST scientific research program in Phase II for axion detection relies on the accurate coherence length computation inside the magnet bores that are filled with ^{3}He gas. The axion to photon conversion probability depends sensitively on its coherence length; that is the resulting constructive interference length inside the magnetic field between axions and photons waves.

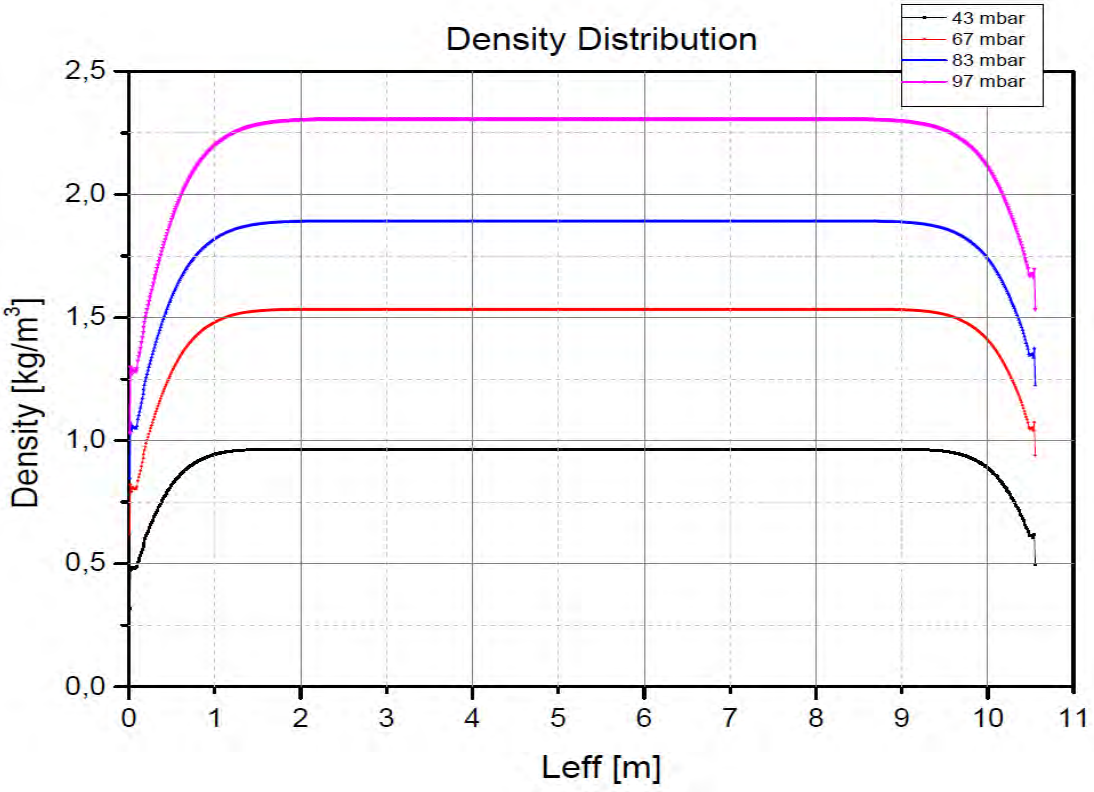

Figure 1. Density distribution along the axis of the central line of the cold bores inside the magnet. The condition imposed in order to consider homogeneity inside the cold bores, is $\Delta\rho \leq 0.003$ kg/m^3. The plot represents the density distribution when the magnet is in a horizontal position for several Helium 3 pressures, but an extensive study has been performed for the tilted magnet as well.

In order to simulate the gas behavior inside the cold bores and calculate the exact coherence length in the magnet bores at any tracking position, Computational Fluid Dynamics (CFD) methods have been applied.

Therefore, an extensive study of the ^{3}He gas dynamics was performed, in order to qualitatively and quantitatively understand the behavior of the gas system.

Monitoring the evolution of the gas density inside the magnet and comparing it to the simulations results have helped to understand the thermodynamic behavior of the system and how effects like buoyancy and convection can affect the coherence length. The length that can be considered as the effective length of the cold bores whose density is uniform does not have any impact on the physics of CAST.

The effective length of the magnet is calculated using CFD methods and the density distribution at the center of the cold bore is shown in Figure 1.

In 2009 the data collected in the period 13 July to 08 of December covered 247 density steps. The data taking efficiency of this period was 83%. The full data taking period in terms of pressure is presented in the next figure.

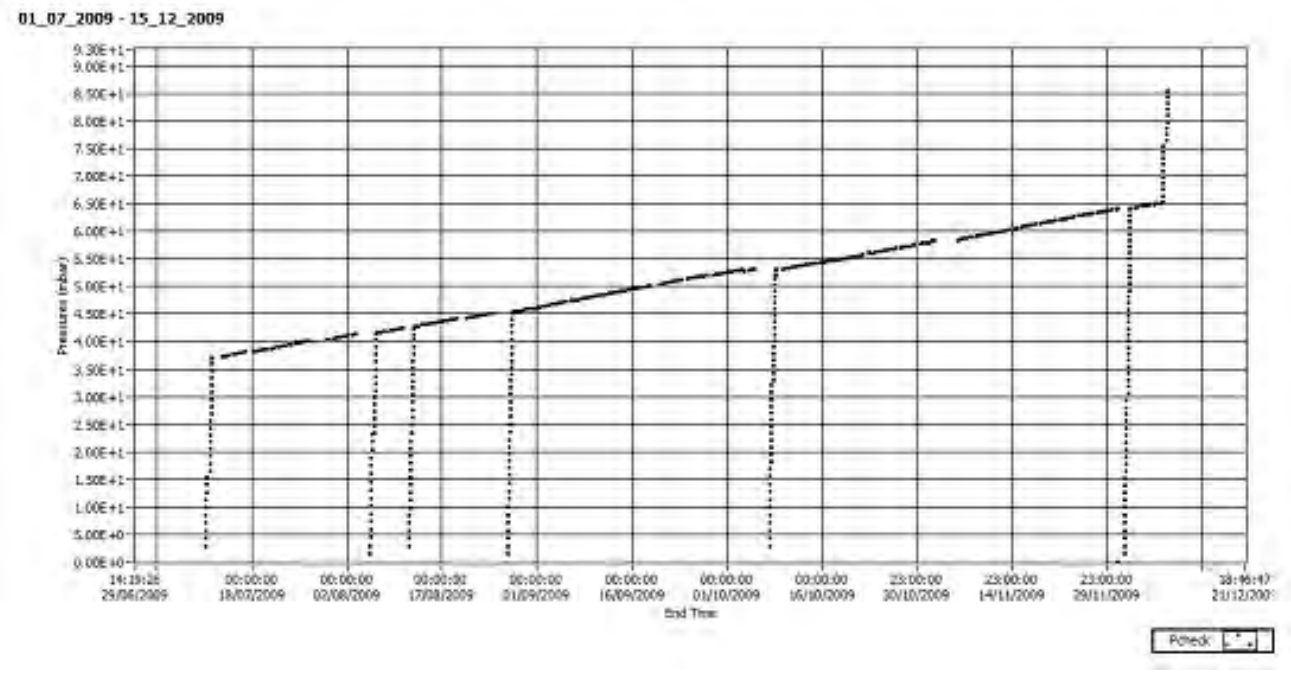

Figure 2. The cold bore pressure versus time for the 2009 run period. The gaps shown were due to stoppages and emptying the cold bore for the bake out of the cold windows procedure.

CAST started the data taking of 2010 on 05 May after many interventions with the electromagnetic noise suppression and also using improved Micromegas detectors.

The first part of the run in 2010 was dedicated to cover the missing steps of 2008 due to the ^{3}He leak problem. The data of the Sunset Micromegas detectors for this period were also

analyzed and the limit obtained in addition with the other CAST detectors in the axion rest mass range 0.39-0.64 eV/c^2 is

$$g_{\alpha\gamma} \leq 2.27 \times 10^{-10}\ GeV^{-1}\ at\ 95\%\ CL.$$

In the second part of the 2010 data taking period started on 10 August at a setting that corresponds to 65.1 mbar (axion mass 0.85 eV/c^2), 40 new pressure settings were covered with a data taking efficiency of 69% (excluding stoppages due to cryogenics problem). The 2010 run finished at the density setting that corresponds to 82.7 mbar at 1.8 K (axion mass 1.01 eV).

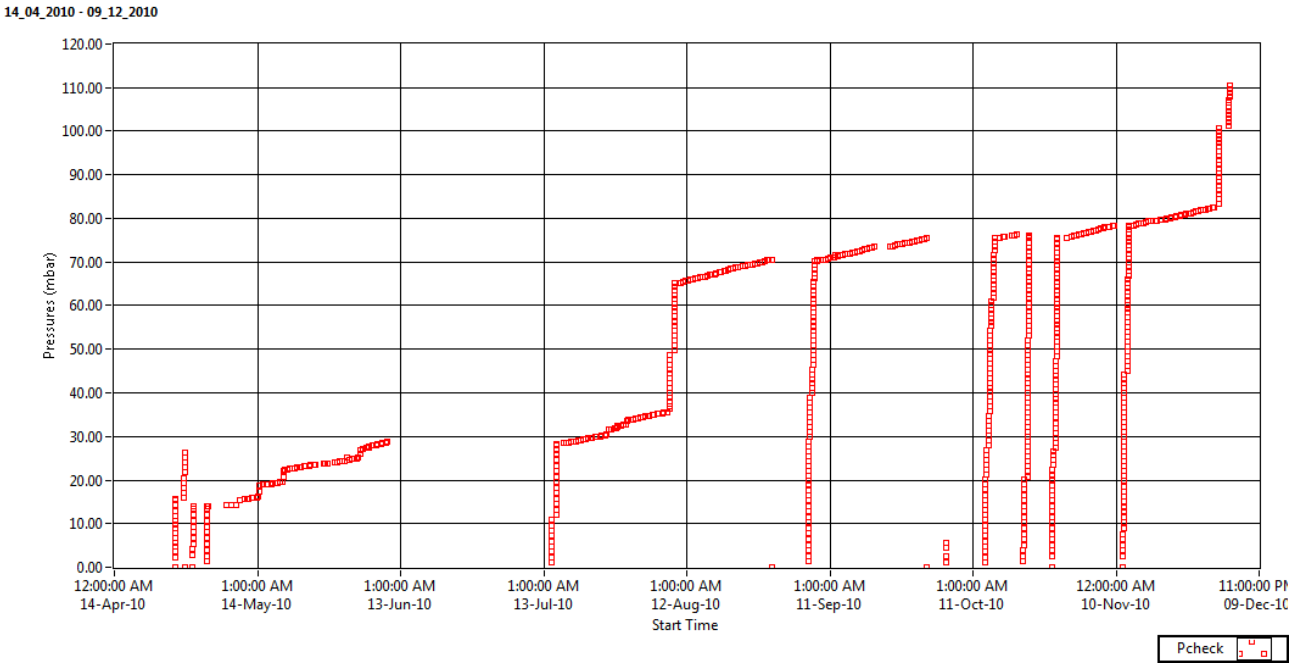

Figure 3. Cold bore pressure evolution during the 2010 data taking period.

An extensive analysis of the data taken during the period 2009-2010 showed no signal of axion above the background level with the Sunset Micromegas data. The CAST search, performed in the axion mass range 0.655-1.01 eV/c^2 and a limit for the axion to photon coupling constant can be set:

$$g_{\alpha\gamma} \leq 4.29 \times 10^{-10}\ GeV^{-1}\ at\ 95\%\ CL.$$

that is slightly improved by the CCD and Sunrise Micromegas detectors contribution.

The absence of signal was verified with the null hypothesis test and the value obtained of the coupling constant fit best the data. The limit is improved by adding the other CAST's detection lines. Therefore, CAST experiment entered in the $g_{\alpha\gamma} - m_{\alpha}$ parameter space favored by the theoretical axion models.

At the time of writing this thesis, CAST has finished its phase of using ^{3}He as a buffer gas and reached the limit of a pressure setting that corresponds to a search mass of 1.17 eV/c^2. The search range of CAST now overlaps with the current cosmic hot dark matter bound of ≤0.9 eV/c^2.

The experiment has found no hint of axions but it has set the strictest experimental limit to date for the axion mass coverage and has also excluded part of the QCD axion model region. The absence of excess X-rays when magnet is pointing to the Sun set a typical upper limit on the axion to photon coupling

$$g_{\alpha\gamma} \leq 3.3 \times 10^{-10}\ GeV^{-1}\ at\ 95\%\ CL$$

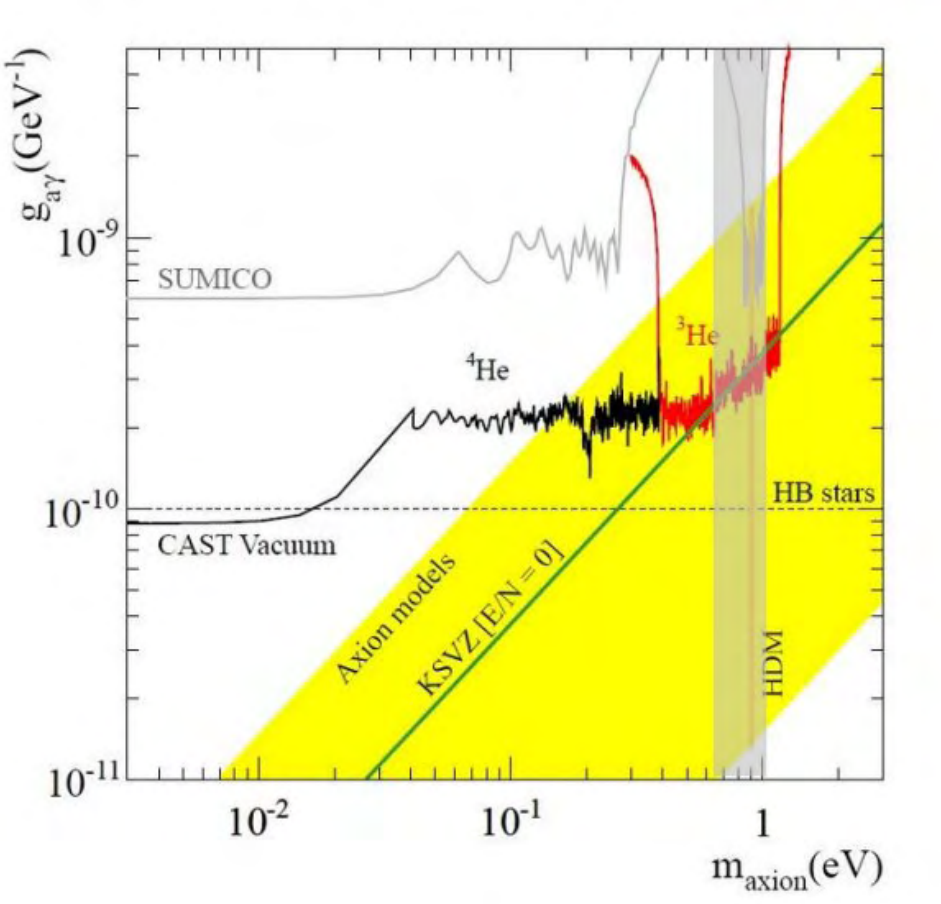

Figure 4 Exclusion regions in the $m_\alpha - g_{\alpha\gamma}$ plane achieved by CAST in vacuum, ^{4}He (black line), the first part of the ^{3}He phase and the latest results that closing the hot dark matter gap in 2011 (all in red). The grey region represents the mass range coverage of axion scanning that has been computed as part of this thesis (2 of 3 Micromegas detectors were analyzed)

The data delivered to the data analysis responsible of CAST, referred to the years 2009-2010, both Sunset micromegas detectors and include information such as: Background level, counts, times and rates for background and tracking in each pressure setting.

In 2013 CAST has started again to take data with vacuum inside the cold bores. By using better performing detectors CAST can improve its own best record for the axion-to photon coupling constant for in the axion mass range bellow ~0.02 eV/c^2.

CAST has extended its scientific program in the field of dark energy (which is responsible for the accelerated expansion of the universe) research for solar chameleons. The so called "chameleon" mechanism renders candidate particles that their effective mass depends on the local matter density. If chameleon particles exist they can be produced in the Sun's tachocline[47] and detected on Earth by the following ways:

- By exploiting the equivalent of the radiation pressure produced in a micro-membrane
- By the Primakoff effect inside the transverse magnetic field of CAST magnet bores

A part of this thesis was dedicated (section 10.6) to the solar chameleons detection through radiation pressure. Solar chameleons can be reflected from a dense medium if their effective mass becomes greater than their total energy. A suitable opto-mechanical force/pressure sensor (silicon nitride micromembrane) placed inside a Fabry-Perot cavity, has been built at INFN Trieste in order to detect the total instantaneous momentum transfer from solar chameleons flux.

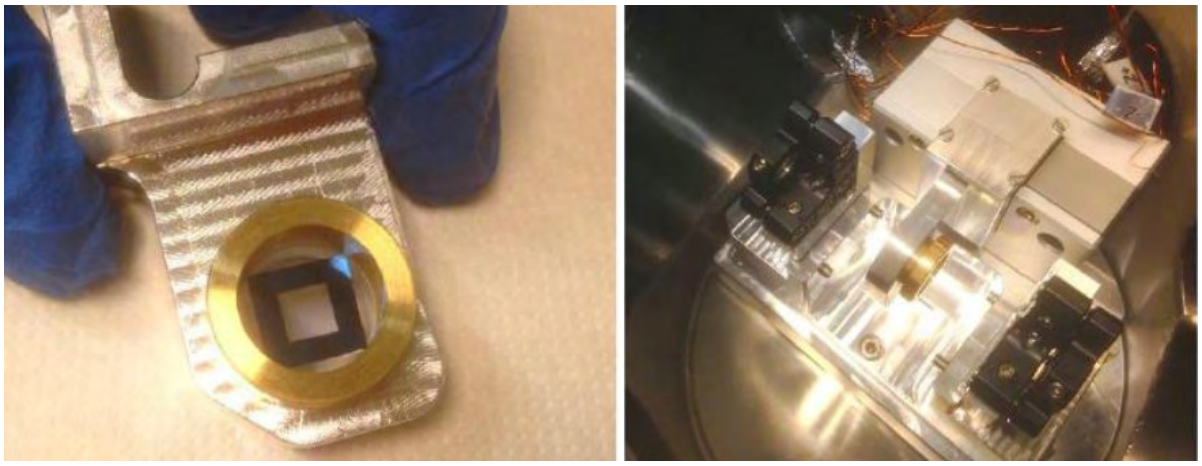

Figure 5. The micromembrane is mounted inside a holder (left). A photograph of the FP-membrane assembly set inside its vacuum chamber (right).

Finite Element Analysis (FEA) simulations have been performed with Ansys 15 for the mechanical characterization of the Si_3N_4 micromembrane. The micromembrane was modeled and analyzed in Ansys 15 in order to estimate (and compare with experimental values):

- The force sensitivity of the micromembrane
- The natural modes of micromembrane's vibration (eigenfrequenies)
- The quality factor of the membrane Q

[47] Tachocline is a region inside the Sun at a distance of around 0.7 $R_\odot$ from the center, where intense magnetic fields are widely believed to be present.

The simulated results were in good agreement with the experimental values delivered from INFN (figure 6) for a 1 mm×1 mm and 50nm thick micromembrane. The simulations are still under development for different micromembrane sizes and the first simulated results are encouraging.

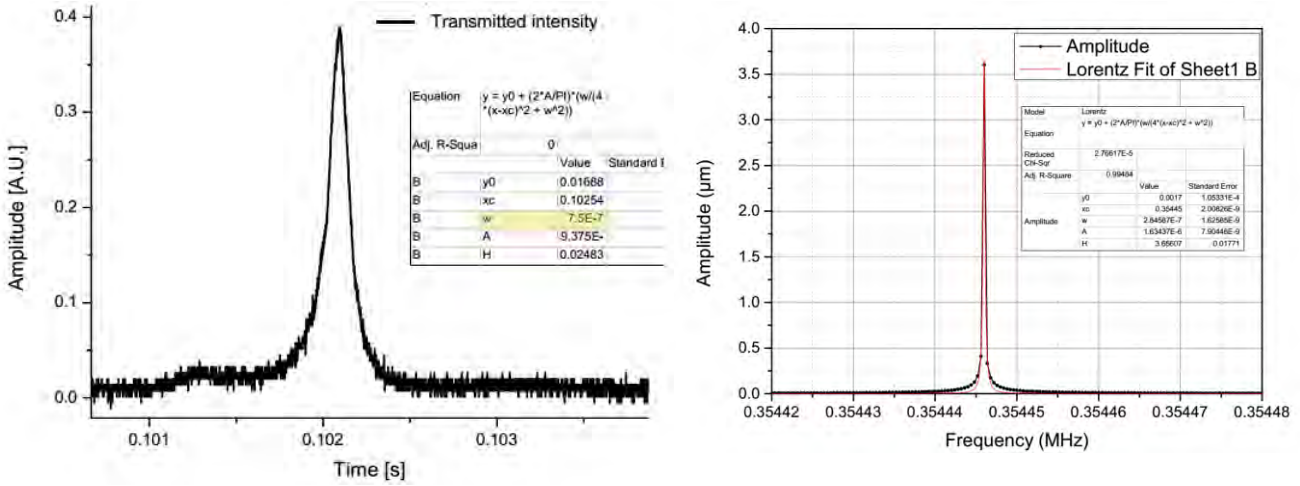

Figure 6. The left plot shows the resonant mode transmission peak fitted with a Lorentzian. The resonant peak is at 0,358 MHz. . The right plot shows the simulated transmission peak amplitude to the micromembrane when 1 nN force is applied to its center. The Lorentz fit delivers the FSR and the peak value in order to estimate the Q factor. The resonant peak is at 0,354 MHz.

References

[1] **Leutwyler Gasser**, *Quark masses*. . Phys.Rept., 87:771. 1982.

[2] **F. Zwicky**, *Die Rotverschiebung von extragalaktischen Nebeln*. Helvetica Physica Acta 6. 1933, p. 110–127.

[3] **K. Freeman and McNamara**. *In Search of Dark Matter*. s.l. : Birkhäuser, 2006.

[4] **F. Zwicky**, *Nebulae as Gravitational Lenses*. Physical Review 51(4). 1937, pp. 290.

[5] **R. D. Peccei and Helen R. Quinn** *CP Conservation in the Presence of Pseudoparticles*. . Phys. Rev. Lett. 38(25). June 1977, p. 1440–1443.

[6] **Steven Weinberg**, *The U(1) problem*. Phys. Rev. D 11(12). June 1075, pp. 3583–3593.

[7] **G. 't Hooft**. *Computation of the quantum effects due to a four-dimensional pseudoparticle*. . Phys. Rev. D, 14(12). Dec 1976.

[8] **Maxim Pospelov and Adam Ritz**, *Electric dipole moments as probes of new physics*. Annals Phys., 318. 2005, p. 119-169.

[9] **C. A. Baker, D. D. Doyle, P. Geltenbort, K. Green, M. G. D. van der Grinten, P. G. Harris, P. Iaydjiev, S. N. Ivanov, D. J. R. May, J. M. Pendlebury, J. D. Richardson, D. Shiers, and K. F. Smith,** *Improved Experimental Limit on the Electric Dipole Moment of the Neutron***,** Phys. Rev. Lett. 97, 131801 –2006

[10] **Masahiro Kawasaki, Kazunori Nakayama**. *Axions : Theory and Cosmological Role*. hep-ph. Jan 2013, arXiv:1301.1123.

[11] **Steven Weinberg** *A new light boson?* Phys. Rev. Lett., 40(4). Jan 1978, pp. 223-226.

[12] **Leutwyler Gasser,** Phys.Rept., 87. 1982, p. 771.

[13] **R. D. Peccei and Helen R. Quinn**, CP Conservation in the Presence of Pseudoparticles. . Phys. Rev. Lett., 38. Jun 1977, pp. 1440–1443.

[14] **Georg G. Raffelt**., *Astrophysical axion bounds*. Lect. Notes Phys. 741. 2008, pp. 51-71.

[15] **G. G. Raffelt,** *Astrophysical methods to constrain axions and other novel particle phenomena*. Phys. Rep. 198. 1990.

[16] **H. Leutwyler,** *The ratios of the light quark masses*. Physics Letters B, 378. Feb 1996, pp. 313-318.

[17] **M. Srednicki**, *Axion couplings to matter*. Nucl. Phys. B260. 1985, pp. 689.

[18] **M. S. Turner**, *Windows on the Axion*. Phys. Rep. 197. 1990, pp. 67.

[19] **W. Keil et al.,** *Fresh look at axions and SN 1987A.* Phys. Rev. D56. 1997, pp. 2419.

[20] **G. G. Raffelt**, *Stars as Laboratories for Fundamental Physics*. s.l. : Chicago University Press, 1996.

[21] **J. E. Kim**, *Light Pseudoscalars, Particle Physics and Cosmology*. Phys. Rep.150. 1987, pp. 1.

[22] **F. C. Porter and K. C. Königsmann**, *Unambiguous test for the axion*. Phys. Rev. D25. 1993, pp. 1982.

[23] **M. Dine, W. Fischler and M. Srednicki**. *A simple solution to the strong CP problem*. Phys. Lett. B104. 1981, pp. 199.

[24] **M. A. Shifman, A. I. Vainshtein and V. I. Zakharov**. *Can confinement ensure natural CP invariance of the strong interactions?* Nucl. Phys.B166. 1980, pp. 493.

[25] **S. L. Cheng, C. Q. Geng, and W. T. Ni**. *Axion - photon couplings in invisible axion models*. Phys. Rev., D52. 1995, pp. 3132–3135.

[26] **H. Primakoff**. *Photoproduction of neutral mesons in nuclear electric fields and the mean life of the neutral meson.* Phys.Rev., 81. 1951, pp. 899.

[27] **Dine, Michael et al.** *A simple solution to the strong CP problem with a harmless axion*. Phys.Lett.B104. 1981, pp. 199.

[28] **Leanne D Duffy and Karl van Bibber**, *Axions as dark matter particles*. New J. Phys. 11. 2009, pp. 105008.

[29] **D. Harari and P. Sikivie**, *On The Evolution Of Global Strings In The Early Universe*. Phys. Lett. B 195. 1987, pp. 361.

[30] **Biljana Lakic, Raul Horvat and Milica Krcmar**. *Axions and Large Extra Dimensions. Axions: Theory, Cosmology and Experimental Searces* . s.l. : Springer-Verlag, 2008, pp. 250.

[31] **Georg G. Raffelt**, *Astrophysical axion bounds*. Lect. Notes Phys. 2008, pp. 51-71.

[32] **P. Sikivie**, *Experimental Tests Of The *Invisible* Axion*. Phys. Rev. Lett. 51. 1983, pp. 1415.

[33] **S. De Panfilis et al**., *Limits On The Abundance And Coupling Of Cosmic Axions At 4.5 μeV < ma < 5.0 μeV*. Phys. Rev. Lett. 59. 1987, pp. 839.

[34] **C. Hagmann, P. Sikivie, N. S. Sullivan and D. B. Tanner**. *Results From A Search For Cosmic Axions*. Phys. Rev. D 42. 1990, pp. 1297.

[35] **Dieter Horns, Joerg Jaeckel, Axel Lindner, Andrei Lobanov, Javier Redondo, Andreas Ringwald**. *Searching for WISPy Cold Dark Matter with a Dish Antenna*. arXiv:1212.2970. 2012, pp. 16.

[36] **R. A. Battye and E. P. S. Shellard**, *Axion string constraints*. Phys. Rev. Lett. 73. 1996, pp. 2954.

[37] **M. T. Ressell,** *Limits to the radiative decay of the axion,* Phys. Rev. D 44, 3001 (1991)

[38] **R. Cameron, G. Cantatore, A. C. Melissinos, G. Ruoso, Y. Semertzidis, H. J.Halama, D. M. Lazarus, A. G. Prodell, F. Nezrick, C. Rizzo, and E. Zavattini**. *Search for nearly massless, weakly coupled particles by optical techniques.* Phys.Rev. D, 47(9). 1993, pp. 3707–3725.

[39] **E. Zavattini et al. (PVLAS Collaboration).** *Experimental observation of optical rotation generated in vacuum by a magnetic field.* Phys. Rev. Lett. 96. 2006, pp. 110406.

[40] **R. Cameron, G. Cantatore, A. C. Melissinos, G. Ruoso, Y. Semertzidis, H. J. Halama, D. M. Lazarus, A. G. Prodell, F. Nezrick, C. Rizzo, and E. Zavattini**. *Search for nearly massless, weakly coupled particles by optical techniques.* Phys. Rev. D,47(9). 1993, pp. 3707–3725.

[41] **Robin Bähre, Babette Döbrich , Jan Dreyling-Eschweiler, Samvel Ghazaryan, Reza Hodajerdi , Dieter Horns , Friederike Januschek, Ernst-Axel Knabbe, Axel Lindner , Dieter Notz, Andreas Ringwald , Jan Eike von Seggern , Richard Stromhagen , Dieter Trines , Benno Willke**. *Any Light Particle Search II Technical Design Report - ALPS II Technical Design Report* JNIST. 2013

[42] **Paschos, E.A.** ***et a.l*** *A proposal for solar axion detection via Bragg scattering*. Physics Letters B. 323. 1994, pp. 367–372.

[43] **Z. Ahmed et al. (CDMS Collaboration).** *Search for Axions with the CDMS Experiment*. Phys. Rev. Lett. 103, 141802 – Published 1 October 2009

[44] **P. Sikivie,** *Experimental tests of the "invisible" axion*. Phys. Rev. Lett 51(16). 1983, pp. 1415–1417.

[45] **D. M. Lazarus, G. C. Smith, R. Cameron, A. C. Melissinos, G. Ruoso, Y. K. Semertzidis and F. A. Nezrick.** *A Search for solar axions*. Phys. Rev. Lett. 69. 1992, 2333.

[46] S**. Moriyama, M. Minowa, T. Namba, Y. Inoue, Y. Takasu and A. Yamamoto**. Direct search for solar axions by using strong magnetic field and X-ray detectors. Phys. Lett. B 434. 1998, 147.

[47] **Biljana Lakic, Raul Horvat and Milica Krcmar**. *Axions and Large Extra Dimensions*. G. Raffelt,B. Beltran M. Kuster. *Axions: Theory, Cosmology, and Experimental Searches*. Springer, Berlin Heidelberg : Springer-Verlag Berlin Heidelberg, 2008.

[48] **A. Ringwald,** *Axions and axion-like particles,* [hep-ph] 2 Jul 2014

[49] **George G. Raffelt** *Astrophysical axion bounds diminished by screening effects.* Physical Review D 1986. Volume 33

[50] **G. G. Raffelt**, Plasmon Decay Into Low Mass Bosons In Stars. Phys. Rev. D. 1988, Vol. 37.

[51] **H.Primakoff**. Photo-production of neutral mesons in nuclear electric fields and the mean life of the neutral meson. Phys. Rev. 1951, 81, pp. 899–899.

[52] **K. Van Bibber, P. M. McIntyre, D. E. Morris, G. G Raffelt**. Design for a practical laboratory detector for solar axions. Phys. Rev. D. 1989.

[53] **George Raffelt and Leo Stodolsky**,. *Mixing of the photon with low-mass particles*. Phys. Rev. D. 1988, Vol. 37, 5.

[54] **Naval observatory vector astrometry subroutines** (NOVAS). http://aa.usno.navy.mil/software/novas/novas_info.php

[55] **Zioutas et al**.,. *First results from the CERN Axion Solar Telescope (CAST).* Phys.Rev.Lett. 2005, Vol. 94.

[56] **K Zioutas et al**. *Axion searches with helioscopes and astrophysical signatures for axion(-like) particles*. New Journal of Physics. 2009, 11.

[57] **K. Zioutas et al**. *A decommissioned LHC model magnet as an axion telescope*. NIM. 1999, A425.

[58] **K. Barth et al**. *Commissioning and First Operation of the Cryogenics for the CERN Axion Solar Telescope (CAST)*. Departmental Report CERN/A. 2004-1.

[59] **Remy Battesti et al**. *Axion searches in the past, at present, and in the near future*. Lect. Notes Phys., 741. 2008, pp. 199–237.

[60] **T. W. Donnelly et al**. *Do axions exist?* Phys. Rev. D18. 1978, pp. 1607.

[61] **J. Ruz et al**., *CAST constraints on the axion-electron coupling*. Jounal of Cosmology and Astroparticle Physics. 2013.

[62] **K.A. Olive et al**., *Particle Data Group*. Chin. Phys. C, 38, 090001. 2014.

[63] **K Zioutas et al**,. *An improved limit on the axion-photon coupling from the cast experiment*. Journal of Cosmology and Astroparticle Physics. 2007, Vol. 04, 010.

[64] **M. Arik et al**., *Search for Sub-eV Mass Solar Axions by the CERN Axion Solar Telescope with He3 Buffer Gas.* Physic. Review Letters. 2011, Vol. 107.

[65] **R. Kotthaus, H. Braeuninger, P. Friedrich, R. Hartmann, D. Kang, M. Kuster, G. Lutz, and L. Strueder**. *The X-ray Telescope of the CAST Experiment*. ArXiv Astrophysics e-prints. 2005.

[66] **M. Kuster, et al**. *The x-ray telescope of CAST*. New Journal of Physics. 2007, Vol. 9.

[67] **J. Altmann et al., and W. J. Egle et al**. *Mirror system for the German X-ray satellite ABRIXAS, parts I and II*. Proceedings of SPIE. 1998, Vol. 3444.

[68] **M. Freyberg, H. Brauninger, W. Burkert, G. Hartner, O. Citterio, F. Mazzoleni,G. Pareschi, D. Spiga, S. Romaine, P. Gorenstein, and B. Ramsey.** *The MPE X-ray test facility PANTER: Calibration of hard X-ray (15-50 kev) optics.* Experimental Astronomy. 2005.

[69] **L. Strüder et al**,. *The x-ray telescope of CAST.* New Journal of Physics. 2007, 49.

[70] **E. Arik et al**. *Probing eV-scale axions with CAST*. JCAP. 0902, 2009, Vol. 008.

[71] **M. Arik et al**., *Search for Solar Axions by the CERN Axion Solar Telescope with He3 Buffer Gas: Closing the Hot Dark Matter Gap*. Physical Review Letters. 2014, Vol. 112.

[72] **Konstantin Zioutas, M Davenport, Martyn Davenport, N Elias, and T O Niinikoski**. *Technical Design Report of the CAST 3-He Gas System.* Geneva : Technical Report SPSC-TDR-001. CERN-SPSC-2006-029, CERN, 2006.

[73] **K. Barth, D. Delikaris, G. Passardi, M. Pezzetti, O. Pirotte, L. Stewart, B. Vullierme, L. Walckiers, and K. Zioutas.** *Commissioning and First Operation of the Cryogenics for the CERN Axion Solar Telescope (CAST).* American Institute of Physics Conference Series. 2004, 710.

[74] **National Institute of Standards and Technology**, ***NIST***. http://www.nist.gov/srd/nist23.cfm.

[75] **Eric W. Lemmon**, *FEQ short Helmholtz equation of state for Helium-3*. 2002.

[76] *Technical Design Report of the CAST 3-He Gas System*. Technical Report SPSC-TDR-001. **Konstantin Zioutas, M Davenport, Martyn Davenport, N Elias, and T O Niinikoski. Geneva** : s.n., CERN-SPSC-2006-029.

[77] *Thin cryogenic x-ray windows*. **T O Niinikoski, B Bellanger, M Davenport, N Elias, S Aune, and J Franz**. Technical Report CERN-AT-2008-034, CERN, Geneva : s.n., 2008.

[78] **ANSYS®** *Academic Research, Release 15.0, Help System, Meshing User Guide, ANSYS, Inc*

[79] **ANSYS®** *Academic Research, Release 15.0, Help System, CFX-Pre User's Guide, ANSYS, Inc*

[80] **E D Marquardt, J P Le, and Ray Radebaugh**. *Cryogenic material properties database. 11th International Cryocooler Conference, 12(6):1–7,2000.* *URL* http://www.springerlink.com/index/P4953622131314K3.pdf

[81] **ANSYS®** *Academic Research, Release 15.0, Help System, CFX-Solver Modeling Guide, ANSYS, Inc*

[82] **F. R. Menter**, *Zonal two-equation 'k-omega' turbulence models for aerodynamic flows. AIAA Journal. 1993.*

[83] A Correlation based Transition Model using Local Variables Part 1- Model Formulation. **Menter, F.R., Langtry, R.B., Likki, S.R., Suzen, Y.B., Huang, P.G., and Völker, S**.,. Vienna : s.n., 2004.

[84] **Langtry, R.B., Menter, F.R.,** "*Transition Modeling for General CFD Applications in Aeronautics*", AIAA paper 2005-522, 2005.

[85] **ANSYS®** *Academic Research, Release 15.0, Help System, CFX-Solver Manager User's Guide, ANSYS, Inc*

[86] **K Zioutas et al**, *Axion Searches with Helioscopes and astrophysical signatures for axion(-like) particles* . New Journal of Physics. 2009, Vol. 11.

[87] **N.Elias, B.Lakic, T.Vafeiadis**, Notes on density stability threshold, 47th CAST collaboration meeting.

[88] **A. Delbart, R. de Oliveira, J. Derre, Y. Giomataris, F. Jeanneau, Y. Papadopoulos, P. Rebourgeard.** *New developments of Micromegas detector.* Nucl.Instrum.Meth. A461 (2001) 84-87

[89] **M. J. Berger et al.,** XCOM: Photon Cross Sections Database, National Institute of Standards and Technology (NIST)

[90] **W.R. Leo**, *Tachniques for Nuclear and Particle Physics Experiments*. s.l. : Springer-Verlag, 1994.

[91] **L.D. Landau and E.M. Lifshitz**, *Electrodynamics of Continuous Media*. s.l. : Pergamon Oxford, 1960.

[92] **Walter Blum, Werner Riegler, Luigi Rolandi**, Particle *Detection with Drift Chambers*. s.l. : Sprienger, 2008.

[93] **NEA-1525** PENELOPE2011. http://www.oecd-nea.org/tools/abstract/detail/nea-1525. 2014.

[94] **S. Agostinelli et al.** *Geant4- a simulation toolkit***.** Nuclear Instruments and Methods in Physics Research Section A: Accelerators, Spectrometers, Detectors and Associated Equipment, Volume 506, Issue 3, 1 July 2003, Pages 250-303

[95] **M.J. Berger, J.S. Coursey, M.A. Zucker and J. Chang ,** PSTAR, ESTAR and ASTAR**,** Stopping power and range tables for protons in various materials http://physics.nist.gov/PhysRefData/Star/Text/PSTAR.html

[96] **K.A. Olive et al**. *The Review of Particle Physics*. http://pdg.lbl.gov/. 2014.

[97] **Garfield** - *simulation of gaseous detectors*. http://garfield.web.cern.ch/garfield/. 2010.

[98] **Stephen Biagi,** Magboltz - transport of electrons in gas mixtures.

http://consult.cern.ch/writeup/magboltz/ 2014

[99] **Comsol Multiphysics**. http://www.comsol.com/. 2014.

[100] **I. Giomataris**, "Georges Charpak (1924–2010). Nature . 2010, 467 .

[101] **A. Oed,** *Position-sensitive detector with microstrip anode for electron multiplication with gases*. Nucl. Instrum. Meth A. 1988, 263.

[102] **F. Sauli**, *GEM: A new concept for electron amplification in gas detectors*. Nucl. Instrum Meth. A. 1997, 386.

[103] **D. Raspino et al**. *Status of triple GEM muon chambers for the LHCb experiment*. Nucl. Instrum. Meth. A. 2007, 581.

[104] **Bozzo, M., Oriunno, M. , Ropelewski, L. , Sauli, F. ,Orava, R. , Ojala, J. ,Kurvinen, K., Lauhakangas, R., Heino, J. , Snoeys, W. ,Ferro, F., Van Stenis, M. , David E.,**
Design and construction of the triple GEM detector for TOTEM , Nuclear Science Symposium Conference Record, 2004 IEEE Vol.1

[105] Proc. of the XI International Conference of Elastic and Diffractive Scattering Towards the High Energy Frontiers. **Ruggiero, G. Blois**, France : s.n., 2005.

[106] **Y. Giomataris, P. Rebourgeard, J. P. Robert and G. Charpak**. *MICROMEGAS: A high granularity position - sensitive gaseous detector for high particle - flux environment*. Nucl. Instrum. Meth. A. 1996, 376.

[107] **Alfredo Tomas Alquezar**. *Development of Time Projection Chambers with Micromegas for rare events Searces*. PhD Thesis. 2013.

[108] **M. E. Rose and S. A. Korff**, *An Investigation of the Properties of Proportional Counters*. Phys. Rev. 1941, 59.

[109] **Francisco Jose Iguaz Guterrez**, *Development of a Time Projection Chamber Development of a Time Projection Chamber search of the Double Beta Decay of 136Xe*. Zaragoza : s.n., 2010.

[110] **T. Dafni et al.,** *Energy resolution of alpha particles in a microbulk Micromegas detector at high pressure Argon and Xenon mixtures.* arXiv:0906.0534v2. 2009.

[111] **J. Derre, Y. Giomataris, H. Zaccone, A. Bay, J.P. Perroud, F. Ronga**. *Spatial resolution in Micromegas detectors*. Nuclear Instruments and Methods in Physics Research A. 2001, 459.

[112] **B. Peyaud et al**, *KABES: a novel beam spectrometer for NA48*, Nucl. Instrum. Meth. A 535 (2004) 247.

[113] **Dafni et al**. *Energy resolution of alpha particles in a microbulk Micromegas detector at high pressure Argon and Xenon mixtures.* arXiv:0906.0534v2. 2009.

[114] **T. Dafni et al,. New Micromegas detectors for rare event searches: axions and ββ decay.** Proceedings of the 7th International Workshop on The Identification of Dark Matte : s.n., 2008**.**

[115] **J. Derre et al**. *Spatial resolution in Micromegas detector*. Nucl. Instrum. Meth. A. 2001, 459.

[116] **J. Derre et al**. *First beam test results with Micromegas, a high-rate, high-resolution detector*. Nucl. Instrum. Meth. A. 1998, 412.

[117] **Y. Giomataris, P. Rebourgeard, J. P. Robert and G. Charpak**. *MICROMEGAS: A high granularity position - sensitive gaseous detector for high particle - flux environments*,. Nucl. Instrum. Meth. A . 1996, 376.

[118] **I. Giomataris et al.** *Micromegas in a bulk*, Nucl. Instrum. Meth. A., 560. 2006

[119] **T. Papaevangelou et al.** *Development and performance of Microbulk Micromegas detectors***.** Proceedings of the 1st International Conference on Micro-Pattern Gaseous Detectors MPDG : s.n., 2009.

[120] **S. Agostinelli et al,**. *Geant4 - A Simulation Toolkit.* Nuclear Instruments and Methods A. 2003, 506.

[121] **A. Tomas et al**., *CAST microbulk micromegas in the Canfranc Underground Laboratory*. Proceedings of the 2nd International Conference on Technology and Instrumentation in Particle Physics TIPP. 2012, Vol. 37.

[122] **Theopisti Dafni**, *A Search for Solar Axions A Search for Solar Axions in CAST*. Darmstadt : s.n., 2005.

[123] **Yıldız, Suleyman Cenk**. *SEARCH FOR AXIONS WITH MICROMEGAS DETECTORS IN THE CERN CAST EXPERIMENT*. Instambul : s.n., 2013.

[124] **NIST** Atomic Spectra Database. http://www.nist.gov/pml/data/asd.cfm. 2013.

[125] **M. Arik et al**. *Search for Solar Axions by the CERN Axion Solar Telescope with He3 Buffer Gas*: *Closing the Hot Dark Matter Gap* . Phys. Rev. Lett. 2014, 112.

[126] **W. A. Bardeen and S. H. H. Tye**, *Current Algebra Applied to Properties of the Light Higgs Boson*. Phys. Lett. 1978, B74.

[127] **C. Edwards et al**. *Upper Limit for J/ψ->γ+Axion*. Phys. Rev. Lett. 1982, 48.

[128] **Daniel Grin, Giovanni Covone, Jean-Paul Kneib, Marc Kamionkowski, Andrew Blain, Eric Jullo**. A Telescope Search for Decaying Relic Axions. Physical Review D. 2007, 75.

[129] **R. Ohta, Y. Akimoto, Y. Inoue, M. Minowa, T. Mizumoto, S. Moriyama, T. Namba, Y. Takasu, A. Yamamoto.** *The Tokyo Axion Helioscope*. Nuclear Instruments and Methods in Physics Research Section A. 2012, 670.

[130] **M.J. Berger, J.H. Hubbell, S.M. Seltzer, J. Chang, J.S. Coursey, R. Sukumar, D.S. Zucker, and K. Olsen**. *XCOM: Photon Cross Sections Database*. http://www.nist.gov/pml/data/xcom/. 2010.

[131] **A. Delbart, R. De Oliveira, J. Derre, Y. Giomataris, F. Jeanneau, Y. Papadopoulos, Ph. Redbourgeard**. *New developments of micromegas detector*. Nucl.Instrum.Meth. A. 2001, 461.

[132] **U. Fano**, *Ionization Yield of Radiations. II. The Fluctuations of the Number of Ions*. Phys. Rev. . 1947, 72.

[133] **M. Chefdeville**, *Development of Micromegas-like gaseous detectors using a pixel readout chip as collecting anode*. s.l. : University of Amsterdam, 2009. PhD Thesis.

[134] **Rob. Veenhof**, *Garfield - simulation of gaseous detectors*. http://garfield.web.cern.ch/garfield/. 2010.

[135] **Pere Mato, Philippe Canal, Bertrand Bellenot, Olivier Couet, Axel Naumann, Gerardo Ganis, Danilo Piparo, Lorenzo Moneta, Vasil Vasilev.** *ROOT A data analysis Framework*. http://root.cern.ch/drupal/. 2014.

[136] **M. Arik et al**., *Search for Sub-eV Mass Solar Axions by the CERN Axion Solar Telescope with Buffer Gas*. Physical Review Letters. 2011, 107.

[137] **K. Zioutas et al**., *First Results from the CERN Axion Solar Telescope*. Physical Review Letters. 2005, p. 95.

[138] **S. Andriamonje et al**., *An improved limit on the axion–photon coupling from the CAST experiment*. Journal of Cosmology and Astroparticle Physics. 2007.

[139] **E. Arik et al**., *Probing eV-scale axions with CAST*. Journal of Cosmology and Astroparticle Physics. 2009.

[140] **M. Arik et. al.,** *Search for Sub-eV Mass Solar Axions by the CERN Axion Solar Telescope with He-3 Buffer Gas*. Physical Review Letters 107, 261302. 2011.

[141] **S. Moriyama, M. Minowa, T. Namba, Y. Inoue, Y. Takasu and A. Yamamoto**. *Direct search for solar axions by using strong magnetic field and X-ray detectors*. Physics Letters B. 1998.

[142] **Y. Inoue, Y. Akimoto, R. Ohta, T. Mizumoto, A. Yamamoto and M. Minowa**. *Search for solar axions with mass around 1 eV using coherent conversion of axions into photons*. Physics Letters B. 2008.

[143] **G. G. Raffelt.** *Axions Theory, Cosmology, and Experimental Searches*. Lect. Notes Phys. 2008.

[144] **A. Friedland, M. Giannotti, and M. Wise**. *Constraining the Axion-Photon Coupling with Massive Star*s. Phys. Rev. Lett. 2013.

[145] **S. Hannestad, A. Mirizzi, G. G. Raffelt, and Y. Y. Y. Wong**,. *Neutrino and axion hot dark matter bounds after WMAP-7* . Journal of Cosmology and Astroparticle Physics. 2010.

[146] **CAST Collaboration (V. Anastassopoulos et al.)** *Search for chameleons with CAST* e-Print: arXiv:1503.04561

[147] **G. W. Fraser, A. M. Read, S. Sembay, J. A. Carter , E. Schyns**. *Potential solar axion signatures in X-ray observations with the XMM-Newton observatory. High Energy Astrophysical Phenomena*-arXiv. 2014- Accepted for publication in MNRAS.

[148] **Leanne D. Duffy and Karl van Bibber**., *Axions as Dark Matter Particles*. New Journal of Physics. 2009, Vol. 11.

[149] **Pierre Sikivie**,. *Axion cosmology*. Lect. Notes Phys. 2008, 741.

[150] **Michael S. Turner***, Cosmic and local mass density of "invisible" axions*. Phys. Rev. D. 1986, Vol. 33.

[151] **C.L. Bennett et.al.** *Nine-Year Wilkinson Microwave Anisotropy Probe (WMAP) Observations: Final Maps and Results (WMAP collaboration).* ApJS. 2013, Vol. 208**.**

[152] **Adam G. Riess et al (Supernova Search Team),** *Observational evidence from supernovae for an accelerating universe and a cosmological constant*. Astronomical J. 1998, Vol. 116.

[153] **Shinji Tsujikawa**, *Quintessence: A Review*. . Class.Quant.Grav. 2013, Vol. 30.

[154] **RD Peccei, J Solà, C Wetterich***. Adjusting the cosmological constant dynamically: cosmons and a new force weaker than gravity.* Physics Letters B . 1987, Vol. 195, 2.

[155] **Justin Khoury and Amanda Weltman**. *Chameleon Fields: Awaiting Surprises for Tests of Gravity in Space.* Phys. Rev. Lett. 2004, Vol. 93.

[156] **Philippe Brax, Konstantin Zioutas**. *Solar Chameleons*. Phys.Rev. D. 2010, Vol. 82.

[157] **Philippe Brax, Axel Lindner, and Konstantin Zioutas**. *Detection Prospects for Solar and Terrestrial Chameleons*. Phys. Rev. D. 2012, Vol. 85.

[158] **S.Baum, G.Cantatore, D.H.H. Hoffmann, M. Karuza, Y.K. Semertzidis, A. Upadhye, and K. Zioutas .** *Detecting solar chameleons through radiation pressure* Physics Letters B Vol. 739: 167-173. 2014

[159] **A. M. De Riva, G. Zavattini, S. Marigo, C. Rizzo.** *Very high Q frequency locked Fabry–Perot cavity*. Review of Scientific Instruments. 1996, Vol. 67.

[160] **M Karuza, C Molinelli, M Galassi, C Biancofiore, R Natali, P Tombesi, G Di Giuseppe and D Vitali.** *Optomechanical sideband cooling of a thin membrane within a cavity*. New Journal of Physics. 2012, Vol. 14.

[161] **ANSYS®** Academic Research, Release 15.0, Help System, Design Modeler User's Guide, ANSYS, Inc

[162] **G. McRobbie, Z. Wu, S. Cochran and F. Clark,** *Solutions to the Vibrating Silicon Nitride Membrane Problem,* MicroScale Sensors, School of Information and Communication Technologies, University of Paisley, Paisley, PA1 2BE, UK. 2004

[163] **G. McRobbie, Z. Wu, S. Cochran and F. Clark.** *Solutions to the Vibrating Silicon Nitride Membrane Problem*, Paisley UK : School of Information and Communication Technologies : s.n., 2004.

[164] **Fraser, G. W. et al.** *Potential solar axion signatures in X-ray observations with the XMM-Newton observatory* arXiv:1403.2436 (2014).

[165] **John N. Bahcall, Aldo M. Serenelli, and Sarbani Basu.** *New solar opacities, abundances, helioseismology, and neutrino fluxes*. Astrophys. J., 621:L85–L88, 2005. 13

[166] **Adam Burrows, M. Ted Ressell, and Michael S. Turner**, *Axions and SN 1987A: Axion trapping*. Phys. Rev. D 42. 1990

[167] **W. U. Wuensch, S. De Panfilis-Wuensch, Y. K. Semertzidis, J. T. Rogers, A. C. Melissinos, H. J. Halama, B. E. Moskowitz, A. G. Prodell, W. B. Fowler, and F. A. Nezrick**. *Results of a laboratory search for cosmic axions and other weakly coupled light particles.* Phys. Rev. D, 40(10):3153–3167, Nov 1989. 17

[168] Personal communication with Professor Giovvani Cantatore.

[169] **J. Galan** *Probing eV-mass scale axions with a Micromegas detector in the CAST experiment*, PhD. Thesis, arXiv:1102.1406 [astro-ph.IM], 2011